



Piotr Kowalczyk

Validation and application of advanced soil constitutive models in numerical modelling of soil and soil-structure interaction under seismic loading



UNIVERSITY OF TRENTO - Italy
Department of Civil, Environmental
and Mechanical Engineering



Doctoral School in Civil, Environmental and Mechanical Engineering
Topic 1. Civil and Environmental Engineering - XXXII cycle 2016/2019

Doctoral Thesis - September 2020

Piotr Kowalczyk

Validation and application of advanced soil
constitutive models in numerical modelling of soil
and soil-structure interaction under seismic loading

Supervisor

Alessandro Gajo: University of Trento

Credits of the cover image: Piotr Kowalczyk



Except where otherwise noted, contents on this book are licensed under a Creative
Common Attribution - Non Commercial - No Derivatives
4.0 International License

University of Trento
Doctoral School in Civil, Environmental and Mechanical Engineering
<http://web.unitn.it/en/dricam>
Via Mesiano 77, I-38123 Trento
Tel. +39 0461 282670 / 2611 - dicamphd@unitn.it

Validation and application of advanced soil constitutive models in numerical modelling of soil and soil-structure interaction under seismic loading

Abstract

This thesis presents validation and application of advanced soil constitutive models in cases of seismic loading conditions.

Firstly, results of three advanced soil constitutive models are compared with examples of shear stack experimental data for free field response in dry sand for shear and compression wave propagation. Higher harmonic generation in acceleration records, observed in experimental works, is shown to be possibly the result of soil nonlinearity and fast elastic unloading waves. This finding is shown to have high importance on structural response, real earthquake records and reliability of conventionally employed numerical tools. Finally, short study of free field response in saturated soil reveals similar findings on higher harmonic generation.

Secondly, two advanced soil constitutive models are used, and their performance is assessed based on examples of experimental data on piles in dry sand in order to validate the ability of the constitutive models to simulate seismic soil-structure interaction. The validation includes various experimental configurations and input motions. The discussion on the results focuses on constitutive and numerical modelling aspects. Some improvements in the formulations of the models are suggested based on the detailed investigation.

Finally, the application of one of the advanced soil constitutive models is shown in regard to temporary natural frequency wandering observed in structures subjected to earthquakes. Results show that pore pressure generated during seismic events causes changes in soil stiffness, thus affecting the natural frequency of the structure during and just after the seismic event. Parametric studies present how soil permeability, soil density, input motion or a type of structure may affect the structural natural frequency and time for its return to the initial value. In addition, a time history with an aftershock is analysed to investigate the difference in structural response during the earthquake and the aftershock.

To my mother and my sister

Acknowledgments

First of all, I would like to thank my supervisor prof. Alessandro Gajo for sharing his time, knowledge, advice and finally for his patience when waiting for the results of my research. I hope the final results were worth it.

I would also like to say great thank you to:

Prof. Francesco Cecinato for all his valuable help during the first year of my PhD research.

Prof. Oreste Bursi for giving me a chance to be a part of the XP-Resilience project and for all the project organisation later.

Prof. Rosario Ceravolo and the Polito team (Erica, Giorgia, Lili, Gaetano, Mahesh and others) for being my company during the secondment times at Politecnico di Torino. Thanks for all the technical and non-technical activities we have undertaken!

Prof. Mohammed Hjiij and his little team from INSA (Noussaiba, Hamza, Laura and others) for hosting me in Rennes. Thank you for your company and sharing experience in the extremely hectic last months of the third year of my PhD.

All the XP-Resilience ESRs (Moritz, George, Bled, Francesca, Alex, Massimiliano, Jerome, Stefano, Elizabeth, Muhammad and other mentioned before) for sharing PhD life experience and all the formal and non-formal discussions we have had during our meetings.

My colleagues from office (Gian, Marco, Matteo, Costanza, Diana, Stefano and others) and fellow PhD students from Mesiano (Alessandro, Giovanni, Gabri, Marco, Silvia, Stefano and many others) for sharing the PhD research experience. Your excellent results were motivation for me to progress my own work. Thank you also for the time we spent together to “escape” from our research life. If you have a chance to read these acknowledgments, you should also see the epilogue where the message can be found.

Maria Giovanna Durante and Prof. Di Sarno for the raw examples of the experimental data of the shear stack tests. Without a doubt, these were very valuable when progressing my work. And even more thanks to Margo for the email exchange we have had, the meeting in Rome and her help in understanding at least partly the experimental nuances.

My family and friends, to whom I owe where I am and who I am today in life.

There are even more people who contributed to the developed ideas and the final presentation of the results in this thesis. Thus, I would also like to show my gratitude to:

Prof. Colin Taylor for his insightful remarks (via email correspondence with Prof. Gajo) on soil physical modelling in shear stacks thanks to which more confidence could be obtained when presenting results in this thesis.

Prof. David Mašin for his tips on the hypoplasticity model which I needed especially at the beginning of my PhD research.

Dr Stephan Roth for help and advice when using his numerical tool ABAQUSER.

Dr Dirk Wegener for a very short email correspondence but in the very hectic period of my PhD research, thus very useful in obtaining more confidence when presenting the numerical results in this thesis.

The anonymous reviewers of the Soil Dynamics and Earthquake Engineering journal whose comments led to the improvements in Chapter 4.

My sister Agata for helping with preparation of some of the CAD sketches.

The Mesiano administration staff, in particular Ivano, Irena, Luciana, and Claudia, who all dedicated their working time to limit my involvement in administrative issues, thus, allowing fuller immersion in my research.

The night watchmen from the “*portineria*” of the Mesiano building, especially to Nicola, for allowing my constant late evening or sometimes even night working shifts. I must have been literally your nightmare! Hopefully for you, there will be no other PhD student like me in the next couple of years...

Finally, thanks to ... the mountains. The dream of doing a PhD in mountains came true in Trento. There is so many memories which will always stay with me when recalling my PhD time. Just to mention few: climbing in “zona Arco”, skiing on Paganella, the mighty Dolomites, lonely hikes to the underestimated Marzola with its amazing top ridge, hiking all the summits around Trento within the “Balcony Project” (Angelika, 2017), driving the old red van in and out of the magnificent Valle del Sarca, winter silence at the feet of Cima D’Asta, tens of falls on still unfinished “Zelda”, lunch and ... after lunch “escapes” from Mesiano to “Trento Falesie” (Conz, 2016), lonely nights on Marzola watching perseids or the moon eclipse, or finally, almost killing myself on Cima D’Asta just early this year (uffa...) or even just a rocky ledge on Sant’Agata which became my small mountain during the pandemia time.

One of the last thoughts developed in this thesis was born during lonely nights on the Vigolana mountain. I also absolutely loved the Mesiano terrazza (Figure 1). I have no doubts that the Trentino mountains gave me rest, a group of friends, revealed beauty, showed a different perspective and taught me a lesson in humility. All that influenced my way of thinking in some chaotic mathematically indescribable manner (to the best of the author’s knowledge, a mathematical model accounting for the effects of leisure activity in mountains on scientific performance has not yet been developed).

Thanks to all my friends who accompanied me in these wonderful moments in My Mountains.



Fig. 1. My office.

Funding acknowledgment:

The research presented in this thesis is a part of the XP-Resilience project. This project has received funding from the European Union's Horizon 2020 research and innovation programme under the Marie Skłodowska-Curie grant agreement No 721816.

Publications:

The most important findings from this thesis are summarized in the future journal publications*:

Kowalczyk, P., Gajo, A. (2020) Influence of pore pressure on natural frequency wandering of structures subjected to seismic loading (*submitted, currently under revision for the final resubmission*).

Kowalczyk, P., Gajo, A. (2020) The effects of elastic unloading waves in seismic behaviour of soils (*under completion*).

Kowalczyk, P., Gajo, A. (2020) Validation of advanced soil constitutive models on shear stack simulations on piles (*under development*).

*supplementary journal papers may also be written, subject to confirmation after the PhD defence

Table of contents

Introduction

Chapter 1. Soil constitutive models

1. Introduction to soil constitutive models
 2. Severn-Trent sand model
 - 2.1. Model mathematical formulation
 - 2.2. Model parameters
 3. Hypoplastic sand model
 - 3.1. Model mathematical formulation
 - 3.2. Model parameters
 4. Dafalias Manzari sand model
 - 4.1. Model mathematical formulation
 - 4.2. Model parameters
 5. Calibration of constitutive models
 - 5.1. General approach
 - 5.2. Model parameters for Severn-Trent model
 - 5.3. Model parameters for Hypoplastic model
 - 5.4. Model parameters for Dafalias-Manzari model
 6. Initial validation of constitutive models on laboratory tests
- References

Chapter 2. Higher harmonic generation due to elastic unloading waves

1. Introduction
 2. Methodology
 - 2.1. Experimental work
 - 2.2. Finite element analysis
 3. Results
 - 3.1. Shear wave propagation in semi-infinite column with simplified hyperbolic law
 - 3.2. Shear wave propagation in semi-infinite column with example elastoplastic model
 - 3.3. Shear wave propagation in shear stack in dry sand
 - 3.4. Compression wave propagation in shear stack in dry sand
 - 3.5. Impact of generated higher harmonics on kinematic pile
 - 3.6. Shear wave propagation in centrifuge in saturated soil
 4. Discussion
 5. Conclusions
- References

Chapter 3. Numerical simulations of shear stack experiments on piles

1. Background
2. Methodology
 - 2.1. Experimental tests in shear stack on piles
 - 2.2. Finite element analysis
3. Results
 - 3.1. Free head piles
 - 3.2. Pile group with oscillator
 - 3.3. Summary on comparison of numerical and experimental results
4. Discussion
 - 4.1. Stress-strain behaviour and stress paths
 - 4.2. Importance of elasticity and soil fabric in simulations of shear stack tests
 - 4.3. Effect of smooth stress-strain response
 - 4.4. Settlement predictions
 - 4.5. Ratchetting in low strain cycles
 - 4.6. Pressure dependence of models in large range of mean stresses
 - 4.7. Occasional problems with ST model
 - 4.8. Occasional problems with HP model
 - 4.9. Effect of addition of viscous damping on higher frequencies
 - 4.10. Minimum corrections to constitutive features and their optimal complexity to simulate dynamic soil behaviour and seismic soil-structure interaction
 - 4.11. Computational time
 - 4.12. Additional comments
5. Conclusions
- References

Chapter 4. Seismic frequency wandering of structures due to changes in soil pore pressure

1. Background
2. Methodology
 - 2.1. Numerical model for “basic case”
 - 2.2. Calibration of constitutive model
 - 2.3. Parametric studies
3. Validation of constitutive model on laboratory tests
4. Results
 - 4.1. “Basic case”
 - 4.2. Parametric studies
5. Discussion
6. Conclusions
- References

Summary

Epilogue

Appendices

Introduction

Earthquakes are one of the most disastrous natural hazards that cause death, damage buildings and result in enormous economic losses. Earth seismic activity is still a mystery for humankind in many aspects. As a result, one of the most important challenges for scientific community, including engineers, seismologists, geologists, geophysicists and others, is improved understanding of earth seismicity in order to protect society from its disastrous effects. It is recalled that nearly 60% of the earth population lives in cities and this number increases. The great majority of cities is founded on soil deposits which overlie rocky crust. Earthquakes are initialized in the earth crust, deep under the earth surface, from where, seismic waves propagate into soil layers before reaching the surface. Therefore, understanding of soil seismic behaviour, wave propagation within soil mass, soil-structure interaction under earthquake loading conditions and improved numerical modelling of all these aspects are of paramount importance for a resilient society of the future. This thesis discusses new findings on such aspects of the earthquake geotechnical engineering.

Soil behaviour is known to be complex and highly nonlinear. Dependence on density and confining pressure is well appreciated. In contrary to many other materials, changes in shearing cause also changes in volume. Soil behaviour is even more difficult to model at cyclic loading when changes in density and stress state take place and affect subsequent load cycles.

Numerical studies are a powerful tool for simulating complex boundary value problems of soil behaviour and soil-structure interaction under various loading conditions, including seismic actions. Therefore, robust soil constitutive models are of paramount importance in predicting and analysing real field cases. Many advanced soil constitutive models have been developed in recent years. They origin from different constitutive frameworks and contain different constitutive ingredients in order to account for the complexity of soil behaviour. Representatives of such constitutive models relevant to advanced sand modelling are used in this thesis.

The development of new constitutive models and improvements in the existing constitutive models requires their validation on high-quality benchmark experimental works. This typically involves laboratory testing in centrifuge or on a shaking table for seismic applications. The appropriate scaling laws allow to model real size problems. Numerous experimental works have been carried out by geotechnical research centres all over the world in order to simulate various types of structures and soil conditions. Examples of such experiments on dry sand behaviour are used in this thesis for the comparison with the chosen sand constitutive models.

The primary objectives of this thesis are validation of the chosen advanced soil constitutive models in analysing seismic soil-structure interaction against benchmark experimental data from shear stack tests and a proposal of potential

improvements in numerical and constitutive modelling of soil seismic behaviour. A finite element method is chosen as the most popular and robust. Most important findings on the constitutive and numerical aspects of modelling of soil seismic behaviour are discussed in this thesis. Some improvements in the formulation of the chosen advanced soil constitutive models are suggested in order to enhance their future performance in seismic analysis of soil and soil-structure interaction.

During the course of the research, the original objective has been extended to cover other related research areas. Firstly, the observation of the effects of fast elastic unloading waves in seismic wave propagation in soil has been made and some revision in the interpretation of soil dynamic behaviour based on numerical studies and examples of experimental evidence is discussed in detail in this thesis. Secondly, an application of one of the constitutive models to a novel engineering problem of seismic frequency wandering of structures is also shown in this thesis. The latter work has been carried out as a result of the secondments and collaboration with Politecnico di Torino, which was one of the partners within the XP-Resilience project, under which the research in this thesis has been conducted.

The thesis is organized with four chapters. Firstly, Chapter 1 presents in detail the advanced soil constitutive models along with their calibration for the simulations of shear stack experiments and the initial validation on laboratory tests. Subsequent chapters present results which, mutually, show validation and application of the used soil constitutive models in seismic loading conditions.

Chapter 2 presents 2D finite element numerical simulations of a soil column to replicate the free field response obtained in the shear stack experiments in dry sand. A simple 1D hyperbolic plasticity constitutive law and three advanced soil constitutive models are used. It is shown that the presence of higher harmonics at soil surface, measured in the experiments for the intended single harmonic motion, can be physical and attributed to soil nonlinearity and fast elastic unloading waves. The effects of the latter have never been observed before in soil dynamic behaviour. The results are shown mainly for S-waves but also to a smaller extent for P-waves. The higher harmonic generation is shown to develop with decreasing depth and to be independent of the frequency of the input motion. Shock wave formation within soil mass due to fast unloading waves is identified explicitly and is linked with the observed experimentally higher harmonics and with the computed numerically very high frequencies in the acceleration records. Finally, an example of saturated soil behaviour is analysed and reveals similar findings on the generation of higher harmonics in soils. The work in this chapter is an example of how numerical methods can be applied in order to improve the understanding of experimental measurements, and vice versa, how experiments help validating numerical methods.

Chapter 3 shows a comparison of 3D finite element numerical studies and examples of experimental results of soil behaviour and soil-structure interaction in shear stack tests in order to validate two advanced soil constitutive models. The results for various experimental setups, including different input motions and arrangements

of structural parts, are shown in terms of free field and structural responses. It is shown how the latter is affected by higher harmonics generated within soil mass presented in Chapter 2. The discussion section presents chosen constitutive and numerical aspects, highlights some of the limitations of the constitutive models and suggests potential improvements in the formulation of these models in order to improve their predictions in the future uses.

Chapter 4 presents an application of one of the advanced soil constitutive models in studying the phenomena of natural frequency wandering of structures induced by earthquakes. Changes in soil pore pressures generated during earthquakes are shown to cause temporary changes in the natural frequency of an idealized structure. Following parametric studies investigate the impact of soil permeability, soil density, input motion and a type of structure on the computed frequency wanderings. In addition, a time history inclusive of an aftershock is analysed in order to highlight the importance of aftershocks in seismic risk assessments.

Finally, the most important findings shown in Chapters 2, 3 and 4 are presented in Summary. Appendices placed at the end of this thesis supplement the content of the chapters.

Note that Chapters 2, 3 and 4 were intentionally written in the form of extended versions of scientific papers, thus, facilitating future journal publications extracted from this thesis. Therefore, the literature review relevant to the three topics discussed in the thesis is provided at the beginning of each of the chapters and limited only to the chosen soil constitutive models in Chapter 1. Similarly, the references are provided at the end of each of the chapters.

CHAPTER 1

Soil constitutive models

1. Introduction to soil constitutive models

Three advanced soil constitutive models have been used in this thesis, namely the Severn-Trent sand model (ST model) by Gajo (2010), the Hypoplastic Sand model (HP model) by Von Wolffersdorff (1996) and the Dafalias Manzari model (DM model) by Dafalias & Manzari (2004).

Two of the models used in this thesis, namely the ST model and the DM model, are based on classical elastoplasticity and both are intended to simulate soil behaviour mainly in deviatoric plane. The differences in the formulation between the two models lie in: the implemented elastic laws, namely hyperelasticity (ST model) and hypoelasticity (DM model); normalized stress space introduced in the ST model; evolving fabric tensor introduced in the DM model; and classical kinematic hardening plasticity (ST model) versus bounding surface formulation (DM model).

The third model comes from different constitutive framework of hypoplasticity. Constitutive laws within this framework are based on a single tensorial equation. This facilitates easier implementation of such laws and reduces their complexity in comparison with classical elastoplasticity. The constitutive ingredients such as yield surface, flow rule and hardening rule are not needed. On the other hand, the mathematical formulation of the hypoplastic laws allows to account for all important aspects of soil behaviour, such as pressure and density dependence, critical state concept or elastic range.

The implementation of all the three models comes in a format of umat. The implementation of the ST model with implicit integration scheme comes from (Gajo, 2017) whereas the other two models with explicit integration scheme are available on *soilmodels.info* (Gudehus et al., 2008). Abaqus (Dassault Systèmes, 2019) was chosen as a finite element platform to carry out numerical calculations.

All three models have been shown to be promising when simulating soil cyclic behaviour. An example of a drained cyclic triaxial test simulated by all three models with their initial calibration is shown in Figure 1. The detailed mathematical formulation of the models is provided below.

The following notation is adopted in this chapter. Vectors and second-order tensors are in bold letters and symbols (e.g. $\boldsymbol{\sigma}$, $\boldsymbol{\varepsilon}$, \mathbf{T} , \mathbf{D} , $\boldsymbol{\alpha}$) and fourth-order tensors are in calligraphic letters and symbols (e.g. \mathcal{T}_α , \mathcal{M}). Tensorial equations with “:” mean

an inner product with double contraction, either between two second order tensors, or a second-order and fourth-order tensors. The dyadic product of two tensors is noted with a “ \otimes ” sign whereas abbreviation tr stands for the trace of a tensor or of the product of adjacent tensors.

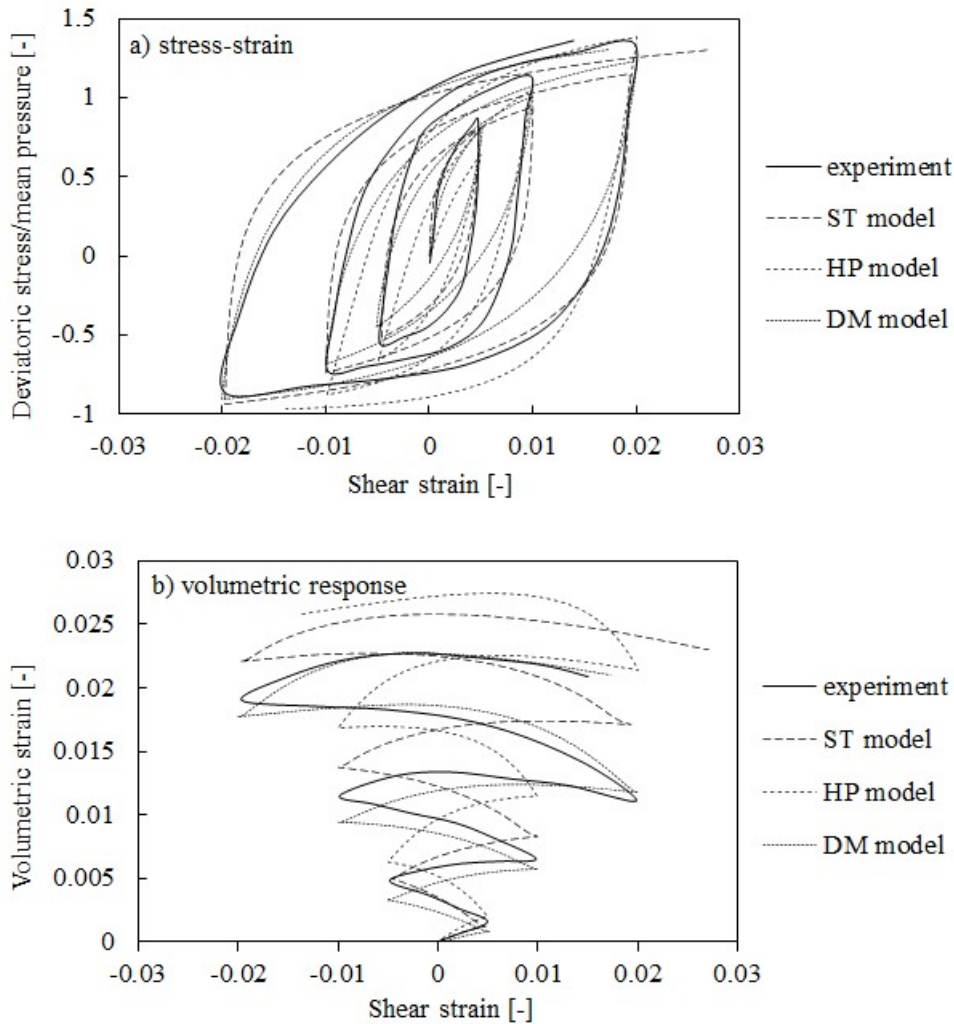


Fig. 1. Comparison of numerical simulations of drained cyclic triaxial test on Toyoura sand ($e_0=0.845$) at constant mean effective pressure of 100kPa (Pradhan et al., 1989).

2. Severn-Trent sand model

2.1. Model mathematical formulation

The Severn-Trent sand model (ST model) as presented by Gajo (2010) but without evolving elastic anisotropy has been chosen as a representative of classical elastoplastic models used to model soil behaviour. The original ST model was proposed and presented in the triaxial space by Gajo & Wood (1999a) and extended to the multiaxial space by Gajo & Wood (1999b) based on a simple model proposed by Muir Wood et al. (1994). It was shown that a single set of input parameters is enough for the model to describe a wide range of soil densities and pressures (Gajo & Wood, 1999a, 1999b). The model focuses on the deviatoric soil response, thus neglecting grain crushing under high pressures and uses the principles of kinematic hardening, equivalent to bounding surface plasticity, to maintain some history of loading. Importantly, the ST model uses well-known geotechnical concepts such as: the critical state, the Mohr-Coulomb failure, the state parameter Ψ (Been & Jefferies, 1985) to determine the dependence of the soil state on density and pressure, and the plastic hyperbolic stiffness depending on the distance from the failure surface. The two key features of the ST model are the use of a hyper-elastic law for representing soil small-strain stiffness response and the implementation with an implicit, back-Euler integration method. The more detailed model description and its ingredients are shown below.

Hyperelasticity

The model used in this thesis is based on the version by Gajo (2010) and introduces some additional constitutive features when comparing with the original formulation (Gajo & Wood, 1999a; Gajo & Wood, 1999b). The first of them is a hyper-elastic law inside the yield surface. The stress σ is obtained from the elastic potential φ . The elastic potential is a function of elastic and plastic strain and is calculated as follows:

$$\varphi(\boldsymbol{\varepsilon}^e, \boldsymbol{\varepsilon}^p) = \gamma d(-tr(\mathbf{B}\boldsymbol{\varepsilon}^e))^\eta + \zeta d(tr(\mathbf{B}\boldsymbol{\varepsilon}^e)^2)^\lambda \quad (1)$$

where: \mathbf{B} is a fabric tensor (symmetric, second-order, positive-definite) and γ , η , λ and ζ are constitutive parameters.

The original formulation of the hyper-elastic law allows the fabric tensor \mathbf{B} to evolve with plastic strain. On the other hand, the version of the model used in this thesis assumes the tensor \mathbf{B} to be constant with only initial anisotropy due to deposition to be considered. When the tensor $\mathbf{B}=\mathbf{I}$, isotropic elasticity is assumed. For this assumption, the initial stiffness can be calculated according to the empirical formula depending on the mean effective pressure p and the specific volume v as proposed by Hardin & Black (1968), i.e.:

$$G_0 = \frac{3230p_r(3.97 - v)^2}{v} \left(\frac{p}{p_r}\right)^{0.5} \quad (2)$$

Where p_r is the reference pressure of 1kPa.

The stress σ can be derived later as:

$$\sigma = \frac{\partial \varphi}{\partial \boldsymbol{\varepsilon}^e} = -\gamma d\eta (-tr(\mathbf{B}\boldsymbol{\varepsilon}^e))^{\eta-1} \mathbf{B} + 2\zeta d\lambda (tr(\mathbf{B}\boldsymbol{\varepsilon}^e)^2)^{\lambda-1} \mathbf{B}\boldsymbol{\varepsilon}^e \mathbf{B} \quad (3)$$

The use of the hyper-elasticity is a step forward from a typically assumed hypoelasticity in other advanced soil constitutive models such as for example, the DM model presented in section 4.1. Most importantly, it is thermodynamically consistent and prevents spurious energy generation or dissipation.

“Normalized” stress space

An important feature introduced in the original ST model (Gajo & Wood, 1999a) is the use of the “normalized” stress space in addition to the true stress space. This allows to avoid modelling of softening in an explicit way, although softening is still captured in the true stress space. The strength surface is related to the critical surface by the ratio $r = 1 - k\Psi$ which means that for $\Psi=0$ both surfaces coincide at large strains. This is different from what follows in the other model used here for the comparison, i.e. the DM model, where the strength surface can only be reached at infinite strains. The deviatoric “normalized” stress $\bar{\sigma}$ is given by:

$$\bar{\sigma} = \frac{1}{(1 - k\psi)} dev\sigma - p\mathbf{I} \quad (4)$$

where k is a constitutive parameter, p is the mean effective stress, \mathbf{I} is the second-order unity tensor, and Ψ is a state parameter as proposed by Wroth & Bassett (1965) and Been & Jefferies (1985) to be:

$$\psi = v - v_{\Delta} + \lambda \ln(p) \quad (5)$$

where v is the specific volume, v_{Δ} and λ are the constitutive parameters. The state parameter Ψ accounts for pressure and density effects and serves as an indicator of the distance between the current state from the critical state line.

The “normalized” stress space allows for the yield and strength surfaces to remain of constant sizes, thus only kinematic hardening occurs. Otherwise, when dense sand dilates, the state parameter Ψ tends to 0 so the bounding surface decreases or when loose sand contracts the bounding surface expands. Another simplification in the model formulation coming from the use of the “normalized” stress space is the lack of “curved” boundaries and a “curved” axis for the yield surface. The back-stress ratio tensor α is enough to describe the position of the yield surface in the “normalized” stress space, thus only kinematic hardening occurs.

The “true” stress σ is obtained subsequently through appropriate transformation laws between the two stress tensors. Here, the shape of the yield surface is more complicated, as the axis is “curved” and the angular opening changes. The yield surface shape and the position in the “true” stress space depends also on the plastic volumetric strain thus the hardening is not only kinematic but also isotropic.

Yield and strength surface

The shape of the yield surface is as per the strength surface (Argyris et al., 1974) due to easier mapping rules in the used implementation which is different from Gajo (2010) where the yield surface is a circular cone. The initial size of the yield surface can be modified depending on the parameter R which is a proportion of the strength surface. The effect of the yield surface shape has been discussed in Gajo & Wood (1999b) as generally negligible, with the Argyris yield surface giving best fit with experimental work for non-triaxial stress paths.

The yield surface in the “normalized” stress space is described with the following relationship:

$$\bar{f}(\bar{\sigma}, \alpha) = \sqrt{\frac{3}{2} \text{tr} \left(\text{dev} \bar{\sigma} - \frac{\text{tr} \bar{\sigma}}{\text{tr} \alpha} \text{dev} \alpha \right)^2} - RMg(\theta_{(\sigma)})p \quad (6)$$

where α is a second-order symmetric tensor to define the position of the axis of the yield surface to satisfy the kinematic hardening rule, R is the size of the yield surface, M represents the slope of the critical state line in the q - p plane and the function $g(\theta_{(\sigma)})$ depends on the Lode angle and is defined as:

$$g(\theta_{(\sigma)}) = \frac{2m}{1 + m + (1 - m)\cos 3\theta_{(\sigma)}} \quad (7)$$

where $\theta_{(\sigma)}$ is the Lode angle and m is a constitutive parameter chosen in a way to ensure the convex shape of the yield and strength surface.

The strength surface in the “normalized” stress space is described in the following way:

$$\bar{F}(\bar{\sigma}) = \sqrt{\frac{3}{2} \text{tr}(\text{dev}\bar{\sigma})^2 - Mg(\theta_{(\sigma)})p} \quad (8)$$

Finally, the strength surface in the “true” stress space is defined as:

$$F(\sigma, \text{tr}\epsilon^p) = \sqrt{\frac{3}{2} \text{tr}(\text{dev}\sigma)^2 - (1 - k\psi)Mg(\theta_{(\sigma)})p} \quad (9)$$

Hardening rule

A translation rule and a hardening rule are needed to define the movement of the yield surface and the change in plastic stiffness. The translation rule is given by:

$$\dot{\alpha} = \tau \mathcal{T}_\alpha [\bar{\sigma}_c - \bar{\sigma}] \quad (10)$$

where τ is a scalar quantity dependent on a plastic strain rate, \mathcal{T}_α is a fourth-order projection tensor, $\bar{\sigma}_c$ is the conjugate stress state, i.e. an image stress placed on the strength surface.

In contrast to the original formulation based on bounding surface plasticity, Gajo (2010) introduced the formulation based on classical kinematic hardening plasticity, i.e.:

$$\tau = -\frac{\beta}{B*\beta_{max}} \left(\frac{\mathbf{Q} \cdot (\bar{\sigma}_c - \bar{\sigma}_i)}{\mathbf{Q} \cdot (\bar{\sigma} - \bar{\sigma}_i)} \right)^\alpha \left((\bar{\sigma}_c - \sigma) \cdot \epsilon^p \right) \left(\frac{\partial f}{\partial \alpha} \mathcal{T}_\alpha \cdot (\bar{\sigma}_c - \sigma) \right)^{-1} \quad (11)$$

where $\mathbf{Q} = \frac{\partial f}{\partial \sigma}$ is the gradient of the yield surface in the “true” stress space, $\bar{\sigma}_i$ is the initial stress state when yielding starts which remains fixed until unloading happens.

Finally, the parameter α is a constitutive parameter that allows for smooth stiffness variation between elastic and plastic parts of stiffness. The description of β_{max} and B is given in equation (12) below.

Flow rule

The equation (11) was chosen in a way to retrieve the same stress-strain behaviour as the original ST model (Gajo & Wood, 1999a & 1999b). To recall, the change in plastic stiffness was described there according to the following relation:

$$\dot{\boldsymbol{\varepsilon}}^p = \frac{B\beta_{max}}{\beta^2} (\bar{\mathbf{Q}} \cdot \dot{\boldsymbol{\sigma}}) \mathbf{P} \quad (12)$$

where B is a constitutive parameter, β is the distance between the current stress state and its image on the strength surface, β_{max} is the maximum possible distance, \mathbf{P} is the plastic flow direction, $\bar{\mathbf{Q}} = \frac{\partial \bar{f}}{\partial \boldsymbol{\sigma}}$ is the gradient of the yield function in the “normalized” stress space.

Volumetric response is governed by a flow rule which links volumetric and distortional strain increments. The flow rule in the ST model is associated in deviatoric section and can be presented as follows:

$$\frac{\text{tr} \mathbf{P}}{||\text{dev} \mathbf{P}||} = -\frac{\sqrt{3}}{\sqrt{2}} A \frac{1}{g(\theta_{(Q)})^p} [(1 + k_d \psi) \text{dev} \bar{\boldsymbol{\sigma}}_c - \text{dev} \boldsymbol{\sigma}] \cdot \frac{\text{dev} \mathbf{Q}}{||\text{dev} \mathbf{Q}||} \quad (13)$$

where A and k_d are constitutive parameters.

The adopted associativity in the deviatoric section is one of the differences in comparison with the DM model, where the flow rule is generally non-associated in the deviatoric section due to modified plastic strain direction for non-radial stress paths. On the other hand, it has to be recalled that the parameter B in the current version of the ST model (Gajo, 2017) varies between two values B_{min} and B_{max} in order to improve the simulations of non-radial stress paths, thus being sort of equivalent to the modified plastic strain direction introduced in the DM model. A need for such a distinction of the B parameter was found in the initial studies of this research which indicated that the stiffness in simple shear tests was underestimated when being calibrated only on triaxial tests.

Summary on ST model

The above brief description of the model ingredients shows the core of the ST model formulation used in this thesis. More detailed model formulation can be found in Gajo (2010). The further model developments have been limited so far to the enhancement proposed by Corti et al. (2016), where an additional memory surface was implemented in order to improve the model capabilities to predict plastic strain accumulation under very large number of load cycles.

Model implementation

The implementation of the ST model has been provided by Gajo (2017). The model has three tensorial state variables (which include: plastic strain, back-stress ratio tensor at shear reversal for memory purpose and current total strain from a previous time step). The integration scheme is implicit, back-Euler.

2.2. Model parameters

The model input requires twelve parameters. These can be divided into different usages and are explained below.

The critical state is defined by the usual set of parameters, namely: the intercept v_A of the critical-state line in the compression plane at mean effective stress $p' = 1Pa$, and the slope A of the critical state line in the compression plane and the friction angle ϕ_{cv} .

The yield surface size and shape are controlled by the parameters R and m , respectively. The initial elastic stiffness is controlled by the parameter E_R which is namely a fraction of the very initial stiffness at very small strains. The latter parameter defines the ratio between the actual initial stiffness used and the initial stiffness calculated from Hardin & Black (1968). The parameter k is used to link changes in density and pressure with the current size of the yield surface.

The plastic stiffness parameters are B and α . The parameter B defines how fast plastic stiffness reduces with the applied strain. In the current used version of the model (Gajo, 2017), the parameter B is split into two, namely B_{min} and B_{max} , which differ with the changing Lode's angle thus allowing the plastic stiffness modification on various stress paths within the deviatoric plane. Whereas the parameter α is calibrated in order to allow smooth transition between elastic and plastic stiffnesses.

Dilatancy depends on the multiplier A and the parameter k_d , which is a contribution of the state parameter, i.e. a distance from the current state to the critical state line position.

The range of typical values of the model parameters is presented in Table 1 and is based on previously derived values in other studies (Gajo & Wood, 1999a & 1999b; Gajo, 2010; Abate et al., 2010, Rotisciani & Miliziano, 2013, Corti et al., 2016).

Table 1 Typical range of values of input parameters for ST model.

Parameter	Description	Typical value
v_A	Intercept for critical-state line in v - $\ln(p)$ plane at $p'=1\text{Pa}$	2.065-2.176
A	Slope of critical-state line in v - $\ln(p)$ plane	0.013-0.031
φ_{cv}	Critical-state angle of friction	29.5°-40°
m	Parameter controlling deviatoric section of yield surface	0.8
k	Link between changes in state parameter and current size of yield surface	2.0-3.8
A	Multiplier in flow rule	0.5-1.1
k_d	State parameter contribution in flow rule	1.0-1.7
B_{min} - B_{max}	Parameter controlling hyperbolic stiffness relationship	0.0013-0.016
α	Exponent controlling hyperbolic stiffness relationship	1.8
R	Size of yield surface with respect to strength surface	0.01-0.1
E_R	Fraction of G_0 used in computations	0.4-1.0

3. Hypoplastic sand model

3.1. Model mathematical formulation

The second model used in this thesis is the Hypoplastic sand model (HP model). The model formulation is as proposed by Von Wolffersdorff (1996) with an addition of the intergranular stain concept (Niemunis & Herle, 1997) to account for small strain stiffness and improved predictions of cyclic loading. The updated version of the intergranular strain concept is used in this thesis as per Wegener (2013) and Wegener & Herle (2014) to improve predictions of the accumulated volumetric strains in cyclic behaviour. The constitutive law is characterized by a tensorial rate equation of a general form:

$$\dot{\mathbf{T}} = \mathbf{F}(\mathbf{T}, q, \mathbf{D}) \quad (14)$$

where $\dot{\mathbf{T}}$ is the stress rate, \mathbf{T} is the stress, q is a set of state variables, and \mathbf{D} is the strain rate tensor.

Hypoplasticity is an alternative constitutive approach to elastoplasticity. It is a mathematical formulation that develops from hypoelasticity as explained by Kolymbas & Medicus (2016). The initial hypoelastic formulation is changed into incrementally nonlinear thus allowing irreversible strains. The motivation for the development of hypoplasticity was a need to avoid complexity of using classical plasticity with all its ingredients, mainly features such as surfaces in stress space and consistency condition. The justification for this approach was that the real elastic region in soils is very small thus all the complexity coming from the fact of material passing from elastic to plastic region could be avoided.

A particular feature of hypoplasticity for soils is that it is a rate-type constitutive law presented as a nonlinear tensorial function firstly shown by Kolymbas (1985, 1991) and later developed by Wu (1992):

$$\dot{\mathbf{T}} = \mathcal{L} : \mathbf{D} + \mathbf{N} ||\mathbf{D}|| \quad (15)$$

where \mathcal{L} is a fourth-order constitutive tensor, \mathbf{N} is a second-order constitutive tensor and \mathbf{D} is a stretching tensor.

However, this initial hypoplastic model formulation for sands had only stress state as a state variable, thus, was not fully suitable to model soil behaviour. It required to be recalibrated for different density and pressure states.

Therefore, the subsequent hypoplastic laws were developed in order to include barotropy and pycnotropy of soil. To achieve these, a new state variable was introduced in the rate tensorial equation, namely a void ratio. The rate of the introduced void ratio is calculated as follows:

$$\dot{e} = (1 + e) \operatorname{tr} \mathbf{D} \quad (16)$$

Gudehus (1996) developed a solution to link the previous hypoplasticity models with the critical state concept by including limiting void ratios: e_i (maximum void ratio), e_c (void ratio at the critical state), e_d (minimum void ratio) through the equation by Bauer (1996):

$$\frac{e_i}{e_{i0}} = \frac{e_c}{e_{c0}} = \frac{e_d}{e_{d0}} = \exp \left[- \left(- \frac{\operatorname{tr} \mathbf{T}}{h_s} \right)^n \right] \quad (17)$$

where e_{i0} , e_{c0} , e_{d0} , h_s and n are constitutive parameters.

The general form of the tensorial equation was amended to include barotropy and pycnotropy, namely two scalar functions f_s and f_d , according to:

$$\dot{\mathbf{T}} = f_s(\mathcal{L} : \mathbf{D} + f_d \mathbf{N} |\mathbf{D}|) \quad (18)$$

where:

$$f_s = f_b \cdot f_e \quad (19)$$

$$f_e = \left(\frac{e_c}{e} \right)^\beta \quad (20)$$

$$f_d = \left(\frac{e - e_d}{e_c - e_d} \right)^\alpha \quad (21)$$

$$f_b = \frac{h_s}{n} \left(\frac{1 + e_i}{e_i} \right) \left(\frac{e_{i0}}{e_{c0}} \right)^\beta \left(- \frac{\operatorname{tr} \mathbf{T}}{h_s} \right)^{1-n} \left[3 + a^2 - \sqrt{3} a \left(\frac{e_{i0} - e_{d0}}{e_{c0} - e_{d0}} \right)^\alpha \right]^{-1} \quad (22)$$

where α and β are model parameters, f_e and f_d are pycnotropy factors, f_b is a barotropy factor, f_s controls soil stiffness and a is expressed as:

$$a = \frac{\sqrt{3} (3 - \sin\varphi_c)}{2\sqrt{2} \sin\varphi_c} \quad (23)$$

Subsequently, the model from Gudehus (1996) was updated by Von Wolffersdorff (1996) to account for stress paths different than axisymmetric.

To enhance further the representation of soil behaviour, the intergranular strain concept (Niemunis & Herle, 1997) needed to be introduced in order to account for very high stiffness at small strains, reduce ratcheting and, therefore, improve the simulation of soil cyclic behaviour. As a result, a new state variable is introduced in the tensorial equation, which is an intergranular strain δ which evolves as follows:

$$\dot{\delta} = \begin{cases} (I - \hat{\delta} \otimes \hat{\delta} \rho^{\beta_r}) : D, & \text{for } \hat{\delta} : D > 0 \\ D, & \text{for } \hat{\delta} : D \leq 0 \end{cases} \quad (24)$$

where $\hat{\delta}$ is the direction of the intergranular strain, β_r is a constitutive parameter, I is a fourth-order identity tensor, and ρ is the normalized magnitude of δ :

$$\rho = \frac{|\delta|}{R} \quad (25)$$

where R is a constitutive parameter defining the maximum value of the intergranular strain.

The idea behind the intergranular strain concept is to model the elastic part of soil deformation, i.e. deformation which is not attributed to grain rearrangement. The hypoplastic constitutive law with the intergranular strain concept can be written in the following simplified form:

$$\dot{T} = \mathcal{M} : D \quad (26)$$

where \mathcal{M} is a fourth-order tensor that represents the tangential stiffness and it is calculated from the hypoplasticity tensors \mathcal{L} and \mathcal{N} , which are multiplied by the small strain stiffness factors m_R and m_T .

The stiffness tensor \mathcal{M} reduces to the basic hypoplastic model for non-elastic loading, i.e. when $\rho=1$, the equation (18) rules. For cases $\rho < 1$, the stiffness tensor \mathcal{M} can be calculated as follows:

$$\mathcal{M} = [\rho^\chi m_T + (1 - \rho^\chi) m_R] \mathcal{L} + \begin{cases} \rho^\chi (1 - m_T) \mathcal{L} : \widehat{\boldsymbol{\delta}} \otimes \widehat{\boldsymbol{\delta}} + \rho^\chi \mathbf{N} \otimes \widehat{\boldsymbol{\delta}} & \text{for } \widehat{\boldsymbol{\delta}} : \mathbf{D} > 0 \\ \rho^\chi (m_R - m_T) \mathcal{L} : \widehat{\boldsymbol{\delta}} \otimes \widehat{\boldsymbol{\delta}} & \text{for } \widehat{\boldsymbol{\delta}} : \mathbf{D} \leq 0 \end{cases} \quad (27)$$

where m_R , m_T and χ are constitutive parameters.

The intergranular strain concept was updated by Wegener (2013) and Wegener & Herle (2014) to reduce accumulation of strains under cyclic loading conditions. They proposed to modify equation (27) as follows:

$$\mathcal{M} = [\rho^\chi m_T + (1 - \rho^\chi) m_R] \mathcal{L} + \begin{cases} \rho^\chi (1 - m_T) \mathcal{L} : \widehat{\boldsymbol{\delta}} \otimes \widehat{\boldsymbol{\delta}} + \rho^\vartheta \mathbf{N} \otimes \widehat{\boldsymbol{\delta}} & \text{for } \widehat{\boldsymbol{\delta}} : \mathbf{D} > 0 \\ \rho^\chi (m_R - m_T) \mathcal{L} : \widehat{\boldsymbol{\delta}} \otimes \widehat{\boldsymbol{\delta}} & \text{for } \widehat{\boldsymbol{\delta}} : \mathbf{D} \leq 0 \end{cases} \quad (28)$$

The equation (28) exchanges exponent χ in the nonlinear part of the hypoplastic equation with a different exponent ϑ . This change allows to reduce the strain accumulation during cyclic loading when $\vartheta > \chi$ but does not affect stiffness in monotonic loading.

Summary and developments of hypoplastic models

The hypoplastic models have been recently developed to account for other soil types and complexities of soil behaviour. Mašín (2005) presented a hypoplastic clay model extended later to the Cam-clay hypoplastic model (Mašín, 2012) and to an anisotropic clay model (Mašín, 2014). Fuentes & Triantafyllidis (2015) formulated an enhanced hypoplastic sand model, the so-called ISA model, to account for fabric effects and inherent anisotropy. A more detailed presentation of hypoplasticity and its developments is presented in Mašín (2018).

Model implementation

The implementation of the model was provided by Gudehus et al. (2008). The model has two tensorial state variables (which include the stress state and the intergranular strain) and a scalar void ratio state variable. The integration scheme is explicit, i.e. Runge-Kutta-Fehlberg of the second and third order accuracy (RKF-32) with an adaptive substepping (Hull et al., 1996).

3.2. Model parameters

The basic hypoplastic sand model (Von Wolffersdorff, 1996) has eight input model parameters which include: the critical friction angle φ_c , the granular hardness h_s , the stiffness exponent n , the limiting void ratios at zero mean pressure e_{c0} , e_{d0} , e_{i0} and the exponents α and β . The granular hardness h_s and the stiffness exponent n determine the void limiting ratios as expressed in the Bauer's equation (17). The limiting void ratio e_{i0} is the maximum possible void ratio for a minimum density state whereas the limiting void ratio e_{d0} is the minimum possible void ratio for a maximum density state at $p'=0$. The limiting void ratio e_{c0} is the critical state void ratio at zero mean stress. The exponent α controls the peak strength and the exponent β controls stiffness in general as it scales the barotropy factor f_b in the equation (22).

The original intergranular strain concept (Niemunis & Herle, 1997) requires additional five model parameters which include: R , m_R , m_T , β_R and χ . The parameter R defines the size of the elastic range. The parameters m_R and m_T control the small strain stiffness, the former in the initial loading or unloading along the same strain path, the latter in the loading after a 90° change in the loading direction. The parameters β_r and χ define how fast stiffness reduces with increasing strain. Finally, the model enhancement proposed by Wegener (2013) and Wegener & Herle (2014) includes the additional input parameter ϑ which allows a reduction in strain accumulation in cyclic tests.

The typical range of values of the thirteen parameters are shown in Table 2. Importantly, two different “styles” of calibration can be observed for the pair of the parameters h_s and n . The first one, mostly observed in earlier works, chose h_s greater than 1000 and n smaller than 0.3. The other approach, mostly noticed in more recent studies, preferred h_s smaller than 1000 and n around 0.5.

Some calibrations from previous studies are listed in Tables 3 and 4. The last calibration in Tables 3 and 4 is the estimation of the input parameters as calculated by *Excalibre*, i.e. a calibration tool available on the *soilmodels.info* webpage (Gudehus et al., 2008). The laboratory tests used in this calibration were, as advised on the webpage: i.e. an oedometer test on loose sand and two drained triaxial tests at two

different mean effective stresses of 100kPa and 200kPa (Lanzano et al., 2016). The intergranular strain concept parameters were calibrated as per suggestions provided on the webpage, i.e. R , χ are kept with default values, m_R is calibrated for very small strain stiffness, m_T is a 0.7 fraction of m_R and finally β_r is calibrated to obtain the best possible match with experimental G/G_0 curves. The effects of this calibration are shown in Section 5.3 of this chapter.

Table 2 Typical ranges of values of HP model parameters

	Parameter	Description	Typical values
Basic hypoplasticity	φ_c	Critical friction angle	30-35
	h_s	Granular hardness [MPa]	0.05-5800
	n	Stiffness exponent ruling pressure-sensitivity	0.19-0.6
	e_{d0}	Limiting minimum void ratio at $p'=0$ kPa	0.26-0.613
	e_{c0}	Limiting void ratio at $p'=0$ kPa	0.45-1.014
	e_{i0}	Limiting maximum void ratio at $p'=0$ kPa	0.5-1.24
	α	Exponent linking peak stress with critical stress	0.1-0.25
	β	Stiffness exponent scaling barotropy factor	0.8-2.0
	Intergranular strain concept	R	Representation of elastic range size
m_R		Stiffness multiplier	5.0-10.0
m_T		Stiffness multiplier after 90° change in strain path	2.0-4.0
B_r		Control of rate of evolution of intergranular strain	0.05-0.6
χ		Control on interpolation between elastic and hypoplastic response	1.0-6.0
ϑ		Control on strain accumulation	1.0-10.0

Table 3 Example calibrations of parameters for intergranular strain concept

Reference	Soil	R	m_R	m_T	β_r	χ	ϑ
Niemunis & Herle (1997)	Hochstetten sand	0.0001	5.0	2.0	0.5	6.0	-
Reyes et al. (2009)	Lotung site	0.00015	2.0*	5.0*	0.05	1.2	-
Hleibich et al. (2014)	Leighton Buzzard, fr. E	0.0003	7.0	4.0	0.3	1.0	10.0
Mohammadi-Haji et al. (2018)	Leighton Buzzard, fr. E	0.0003	10.0	4.0	0.3	1.0	-
Ochmanski et al. (2019)	Leighton Buzzard, fr. E	0.0001	6.0	3.0	0.07	1.0	-
Hleibich & Herle (2019)	Nevada sand	0.00005	10.0	4.0	0.6	1.0	10.0
Mašín (2018)	Komorany sand	0.0002	3.4	1.7	0.12	0.7	-
<i>Excalibre</i> (Gudehus et al., 2008)	Leighton Buzzard, fr. E	0.0001	13.0	9.1	1.5	1.0	-

* possibly a mistake in Reyes et al. (2009), as $m_R > m_T$ is specified in the model formulation

Table 4 Example calibrations of model parameters for basic hypoplasticity

Reference	Sand	φ_c	h_s [MPa]	n_0	ed_0	ec_0	e_{i0}	α	β
Niemunis & Herle (1997)	Hochstetten sand	33	1000	0.25	0.55	0.95	1.05	0.25	1.0
Herle & Gudehus (1999)	Hochstetten gravel	36	32000	0.18	0.26	0.45	0.5	0.1	1.9
	Hochstetten sand	33	1500	0.28	0.55	0.95	1.05	0.25	1.0
	Hostun sand	31	1000	0.29	0.61	0.96	1.09	0.13	2.0
	Karlsruhe sand	30	5800	0.28	0.53	0.84	1.00	0.13	1.0
	Lausitz sand	33	1600	0.19	0.44	0.85	1.00	0.25	1.0
	Toyoura sand	30	2600	0.27	0.61	0.98	1.10	0.18	1.1
	Zbraslav sand	31	5700	0.25	0.52	0.82	0.95	0.13	1.0
Wegener & Herle (2014)	Karlsruhe sand	30	187	0.5	0.53	0.84	1.00	0.13	1.05
Hleibieh et al. (2014)	Leighton Buzzard sand, fr. E	33.4	65	0.6	0.613	1.014	1.166	0.1	1.0
Mohammadi-Haji et al. (2018)	Leighton Buzzard sand, fr. E	33.4	100	0.6	0.613	1.014	1.166	0.1	1.0
Ochmanski et al. (2019)	Leighton Buzzard, fr. E	31.79	600	0.47	0.504	1.01	1.21	0.2	0.8
Hleibieh & Herle (2019)	Nevada sand	31	140	0.5	0.511	0.887	1.02	0.1	1.0
Mašin (2018)	Komorany sand	35	0.05	0.2	0.35	0.87	1.04	0.26	4.0
<i>Excalibre</i> (Gudehus et al., 2008)	Leighton Buzzard sand, fr. E	34	5762	0.294	0.517	1.033	1.24	0.12	0.7

4. Dafalias Manzari sand model

4.1. Model mathematical formulation

The second representative of the elastoplastic constitutive models used in this thesis is one of the SANISAND (Simple Anisotropic Sand) family models, namely the DM model (Dafalias & Manzari, 2004) presented within a bounding plasticity theory and based on the initially proposed model by Manzari & Dafalias (1997). Both these works show that the model is capable of simulating sand under a wide range of densities and pressures with a single set of parameters. Similarly, to the original version, the model is a stress-ratio (deviatoric over mean pressure) controlled model, thus, a model that focuses on the deviatoric soil response. The yield surface has no cap to account for plastic strains under constant stress-ratio stress paths and only elastic strains for this stress path occur. The key constitutive feature of the model, which distinguishes it from the previous formulation, is a fabric tensor which accounts for dilatancy effects on subsequent compressive response. The more detailed description of the constitutive ingredients of the DM model is given below.

Hypoelasticity

The DM model uses a simple hypoelastic law inside the yield surface. The respective shear and volumetric elastic strain rates can be expressed as follows:

$$\mathbf{e}^e = \frac{\dot{\mathbf{s}}}{2G} \quad \text{and} \quad e_v^e = \frac{\dot{p}}{K} \quad (30)$$

where \mathbf{s} is a deviatoric stress tensor, p is mean effective stress, G and K are the hypoelastic shear and bulk moduli expressed as functions of the mean effective stress p and the current void ratio e as follows:

$$G = G_0 p_{at} \frac{(2.97 - e)^2}{1 + e} \sqrt{\frac{p}{p_{at}}} \quad (31)$$

$$K = \frac{2(1 + \nu)}{3(1 - 2\nu)} G \quad (32)$$

where G_0 is a model parameter, ν is Poisson's ratio, p_{at} is a reference atmospheric pressure.

Hypoelastic laws such as the one presented above, although being simple and convenient in the implementation, are known to be thermodynamically incompressible. On the other hand, this is usually considered acceptable for soils where the elastic strain range is very small, thus the error introduced due to hypoelasticity can be considered negligible.

Yield surface

The yield surface is a cone in the stress space and a circle in the deviatoric section in the multiaxial formulation:

$$f(\mathbf{s}, \boldsymbol{\alpha}) = [\text{tr}((\mathbf{s} - p\boldsymbol{\alpha})(\mathbf{s} - p\boldsymbol{\alpha}))]^{1/2} - \sqrt{\frac{2}{3}}pm = 0 \quad (33)$$

where $\boldsymbol{\alpha}$ is a back stress-ratio tensor and m is a model parameter which defines the opening of the cone in the stress space (i.e. the size of the circle in the deviatoric section) as a fraction of the strength surface.

Critical state, phase transformation and bounding surfaces

The DM model is based on the concept of critical state soil mechanics. The sand pressure and density dependence are included using the state parameter Ψ for sands (Been & Jefferies, 1985), i.e. both the dilatancy and peak-stress ratio depend on the state parameter Ψ . The critical state line position is calculated as per Li & Wang (1998):

$$e_c = e_0 - \lambda_c \left(\frac{p_c}{p_{at}} \right)^\xi \quad (34)$$

where e_0 , λ_c and ξ are model parameters.

In addition to the critical state surface, phase transformation and bounding surfaces are introduced together with the yield surface. The three surfaces are associated with back stress-ratio tensors α which represent the image back-stress ratio tensors on the critical state, phase transformation and bounding surfaces, respectively:

$$\alpha_{\theta}^c = \sqrt{2/3}[g(\theta, c)M \exp(\psi) - m]\mathbf{n} \quad (35)$$

$$\alpha_{\theta}^d = \sqrt{2/3}[g(\theta, c)M \exp(n^d\psi) - m]\mathbf{n} \quad (36)$$

$$\alpha_{\theta}^b = \sqrt{2/3}[g(\theta, c)M \exp(-n^b\psi) - m]\mathbf{n} \quad (37)$$

where:

$$g(\theta, c) = \frac{2c}{1 + c + (1 - c)\cos 3\theta} \quad (38)$$

and \mathbf{n} is the loading direction, M , n^d , n^b and c are model parameters.

All the surfaces have a shape which depends on the Lode's angle. In the original work (Dafalias & Manzari, 2004), this dependence was as per Argyris et al. (1974) but in the available model implementation (Gudehus et al., 2008), the Van Eekelen (1980) formulation was preferred due to higher accuracy for higher values of friction angle (Martinelli et al., 2016).

Hardening rule

The bisector of the yield surface, tensor α , is the back-stress ratio tensor. The translation of the yield surface in the stress space is described by:

$$\dot{\alpha} = \langle L \rangle \frac{2}{3} h(\alpha_{\theta}^b - \alpha) \quad (39)$$

where L is the loading index (plastic multiplier), h is a function of state variables (described below) and $(\alpha_{\theta}^b - \alpha)$ is a distance between the current and the bounding back-stress ratio tensors.

Flow rule

The deviatoric plastic strain is calculated as:

$$\dot{\mathbf{e}}^p = \langle L \rangle \mathbf{R}' \quad (40)$$

where \mathbf{R}' is the direction of the deviatoric plastic strain which is expressed as a function of the Lode's angle:

$$\mathbf{R}' = B\mathbf{n} - C(\mathbf{n}^2 - \frac{1}{3}\mathbf{I}) \quad (41)$$

$$B = 1 + \frac{3}{2} \frac{1-c}{c} g \cos 3\theta \quad \text{and} \quad C = 3 \sqrt{\frac{3}{2}} \frac{1-c}{c} g \quad (42)$$

Generally, $\mathbf{R}' \neq \mathbf{n}$ thus deviatoric non-associativity applies which is different from the previous model version (Manzari & Dafalias, 1997) and from the ST model. When $c=1$, $B=1$ and $C=0$ the direction $\mathbf{R}'=\mathbf{n}$ thus only triaxial stress paths can be reliably simulated as shown in the previous model version.

The volumetric part of the plastic strain is calculated as:

$$\dot{\mathbf{e}}_v^p = \langle L \rangle D \quad (43)$$

$$D = \text{tr}[(\boldsymbol{\alpha}_\theta^d - \boldsymbol{\alpha})\mathbf{n}]A_d \quad (44)$$

where D is dilatancy, $(\boldsymbol{\alpha}_\theta^d - \boldsymbol{\alpha})$ is a distance between the current and the phase transformation back-stress ratio tensors and A_d is a dilatancy parameter which evolves according to the changes in the fabric tensor as shown later.

The plastic multiplier L is a function of a stress rate and the plastic stiffness K_p :

$$L = \frac{1}{K_p} \frac{\partial f}{\partial \boldsymbol{\sigma}} : \dot{\boldsymbol{\sigma}} \quad (45)$$

$$K_p = \left(\frac{2}{3}\right) ph \cdot \text{tr}[(\boldsymbol{\alpha}_\theta^b - \boldsymbol{\alpha})\mathbf{n}] \quad (46)$$

The plastic stiffness K_p is related to the distance between the current stress state and the image stress on the bounding surface. It is also dependent on the mean

effective pressure p and the function h of the current values of state variables. The latter function h is given as:

$$h = \frac{b_0}{\text{tr}[(\boldsymbol{\alpha} - \boldsymbol{\alpha}_{in})\mathbf{n}]} \quad (47)$$

$$b_0 = G_0 h_0 (1 - c_h e) \left(\frac{p}{p_{at}} \right)^{-\frac{1}{2}} \quad (48)$$

where $\boldsymbol{\alpha}_{in}$ is the position of the initial stress state when new loading happens, G_0 , h_0 and c_h are model parameters.

Fabric tensor

The dilatancy in the model is assumed to be dependent on the changes in the fabric tensor \mathbf{z} according to:

$$A_d = A_0 (1 + \langle \text{tr}(\mathbf{z}\mathbf{n}) \rangle) \quad (49)$$

where A_0 is a model parameter, and the evolution of the fabric tensor \mathbf{z} is given by:

$$\dot{\mathbf{z}} = -c_z \langle -\dot{e}_v^p \rangle (z_{max} \mathbf{n} + \mathbf{z}) \quad (50)$$

where c_z and z_{max} are model parameters for the fabric-dilatancy tensor.

The MacCauley brackets are used in the equations (49) and (50). The activation of the content in these brackets is only when the plastic volumetric strain is dilative. As long as the volumetric response is contractive, i.e. $\dot{e}_v^p > 0$, the fabric tensor remains inactive and $A_d = A_0$. Therefore, the fabric tensor accounts for the effects of the computed dilation on the subsequent compressive response. This feature of the DM model was found especially important at low pressures for sand behaviour under undrained conditions (Dafalias & Manzari, 2004). The previous version of the model from Manzari & Dafalias (1997) predicted a response with early stabilization of the drop in effective stresses which was deemed unrealistic based on experimental works.

Summary and developments of DM model

The interested reader can find more detailed description of the DM model in (Dafalias & Manzari, 2004) and (Manzari & Dafalias, 1997).

It is noted that the SANISAND family models include also versions developed after the year 2004. The developments included a model with a fabric tensor to account for inherent anisotropy (Dafalias et al., 2004), a model with a cap on a yield surface (Taiebat & Dafalias, 2008) to include plastic behaviour with increasing hydrostatic pressure and a model with a vanishing yield surface, the so-called Z-soil model by Dafalias & Taiebat (2016). The Z-soil model limits the yield surface to a single stress point thus eliminating totally purely elastic behaviour of soil.

The other models based on the DM model are a visco-elastic-plastic model by Pisano & Jeremic (2014) and the PM4 sand model (Boulanger & Ziotopoulou, 2015). The first model introduces a zero elastic range where the deviatoric plastic strain follows the direction of the deviatoric stress. In addition, viscous damping is added to the model formulation to improve the computed damping with experimental measurements. On the other hand, the PM4 sand model modifies the original constitutive features in order to improve simulations dedicated to applications in saturated soil, effective stress analysis and liquefaction related problems.

Another development of the DM model comes from Liu et al. (2019) where an additional memory surface was implemented in between the bounding surface and the yield surface. This surface improves the ability of the DM model to account for changes in soil fabric and to deal with the problem of ratcheting due to high number of loading cycles. This helps in better recognition of the “shakedown” effect after many loading cycles.

Nevertheless, the updated versions of the DM model are not considered useful for the analysed case of the behaviour of piles in shear stack experiments. In addition, the other improved models have not yet been implemented in any numerical code mainly due to complexities because of the introduced new features (e.g. additional memory surface, or lack of a yield surface).

A note is made here that the implementation of the DM model returns an error predicting reverse softening (i.e. simultaneous reduction of stresses and strains in stress-strain behaviour) for certain stress paths. This has been particularly visible in more complex boundary value problems, thus the DM model is used only in Chapter 2 and abandoned in the studies shown in Chapter 3 of this thesis.

Model implementation

The implementation of the model has been provided by Gudehus et al. (2008). The model has three tensorial state variables (including: the back-stress ratio tensor, the back-stress ratio tensor at shear reversal for memory purpose and the fabric tensor) and a scalar state variable, namely the void ratio. The integration scheme is explicit, i.e. Runge-Kutta-Fehlberg of the second and third order accuracy (RKF-32) with adaptive substepping (Hull et al., 1996), namely the same as the one for the HP model.

4.2. Model parameters

The model parameters can be divided in few groups depending in which constitutive ingredient they are included in, i.e.: elastic behaviour (G_0 , ν), plastic modulus (h_0 , c_h), the position of the critical state line (e_0 , λ , M_c and ζ), dilatancy (A_0), dependence on the state parameter (n_b , n_d), or finally changes in the soil fabric (z_{max} , c_z).

The elastic properties are determined by providing two input parameters G_0 and ν . What is important, the G_0 parameter is related to the initial small strain stiffness but it is a unitless multiplier in equation (31).

The critical state line is defined by a set of parameters, namely: the intercept e_0 for the critical-state line in the compression plane at $p'=0Pa$, the slope λ_c of the critical state line in the compression plane, the critical stress ratio M_c in triaxial compression and the exponent ζ .

The bounding and the phase transformation surfaces depend on the distance from the critical state surface, thus depend on the state parameter ψ . The parameters n_b and n_d help controlling better the distance of the two surfaces from the critical state surface.

The calculation of the volumetric strain changes with the induced shear strain is controlled by the dilatancy parameter A_0 . The plastic stiffness is controlled by the distance from the bounding surface and the parameters h_0 , c_h related to the effects of this distance. Finally, the changes in the soil fabric are controlled by the two model parameters z_{max} and c_z .

The range of the typical values of the model parameters is presented in Table 5 and is based on the previously derived calibrations in other studies listed in Table 6 (Dafalias & Manzari, 2004; Taiebat et al., 2010; McAllister et al., 2015; Martinelli et al., 2016; Ghofrani & Arduino, 2018; Ramirez et al., 2018; Liu et al., 2019; Arduino & Ghofrani, 2019). These ranges of the values are indicative but not restrictive as recognized in a similar comparison provided by Ghofrani & Arduino (2018).

Table 5 Typical ranges of model parameters for DM model

Parameter	Description	Typical values
G_0	Shear modulus constant	37.67-740
ν	Poisson's ratio	0.01-0.35
m	Size of yield surface	0.01-0.02
e_0	Void ratio on CSL at $p=0$	0.83-0.96
λ_c	Slope of critical state line	0.019-0.055
ζ	Critical state line parameter	0.27-0.7
M_c	Slope of critical state line in $q:p$ plane, triaxial compr.	1.14-1.6
c	Control of shape of yield and bounding surfaces in deviatoric section	0.47-1.0
h_0	Plastic modulus constant	5.0-9.7
c_h	Plastic modulus constant	0.968-1.03
n_b	Plastic modulus constant	0.64-2.56
A_0	Dilatancy constant	0.704-1.06
n_d	Dilatancy constant	0.1-3.5
z_{max}	Fabric index constant	2.0-15.0
c_z	Fabric index constant	50-4000

Table 6 Calibration examples of model parameters for DM model

	Dafalias & Manzari (2004)	Taiebat et al. (2010)	Taiebat et al. (2010)	Ghofrani & Arduino (2018) *	Ramirez et al. (2018)	Liu et al. (2019)
Parameter	Toyoura sand	Nevada sand	Sacramento sand	Ottawa F-65 sand	Monterey sand	Quartz sand (Wichtmann, 2005)
$G_0 [-]$	125	150	200	82.35	130	110
ν	0.05	0.05	0.2	0.01	0.05	0.05
m	0.01	-	-	0.02	0.02	0.01
e_0	0.934	0.83	0.96	0.8	0.858	0.845
λ_c	0.019	0.027	0.028	0.055	0.02	0.049
ζ	0.7	0.45	0.7	0.5	0.69	0.27
M_c	1.25	1.14	1.35	1.46-1.6	1.27	1.27
c	0.712	0.78	0.65	0.47-1.0	0.712	0.712
h_0	7.05	9.7	5.0	15.114-17.0	8.5	5.95
c_h	0.968	1.02	1.03	0.996	0.968	1.01
n_b	1.1	2.56	1.2	0.64	1.05	2.0
A_0	0.704	0.81	0.8	0.45	0.6	1.06
n_d	3.5	1.05	2.0	0.1-0.5	2.5	1.17
z_{max}	4	5	-	14.6-15	4	-
c_z	600	800	-	2000-4000	50	-

*three calibrations were provided for class A, B and C predictions

5. Calibration of constitutive models

5.1. General approach

In the past, similar numerical studies on laminar boxes with a tunnel embedded in granular soil were calibrated explicitly for small strain behaviour (e.g. Bilotta et al., 2014; Hleibieh et al., 2014). The models in this thesis have also been calibrated for small strain stiffness G/G_0 curves as per the recommendations relevant for the analysis of shear stacks (Dietz & Wood, 2007) and for G_0 profiles varying with depth as per correlation dependent on mean effective pressure given by Hardin & Drnevich (1972). Subsequently, the calibration of the models was slightly adjusted to improve simulations of the free field response in the dynamic behaviour of shear stack. Therefore, the calibration of the model used in this thesis is for the class type C simulations (Lambe, 1973).

The initial calibration of the models was carried out on the available triaxial and oedometer tests on Leighton Buzzard sand, fraction E (Lanzano et al., 2016). This approach has not been found sufficient for obtaining reliable simulations on different stress path in the deviatoric plane (i.e. close to simple shear) and in the small strain region applicable to seismic analysis, thus, the initial calibration has been subsequently readjusted to fit better G/G_0 curves in low mean effective stresses as explained in detail later.

The critical state line position has been maintained as per the experimental results from the triaxial tests (Lanzano et al., 2016) with small readjustment to account for shear localization and not-fully developed critical state (i.e. a non-null volumetric strain rate at the end of the compressive triaxial tests). As a result of these two observations, the e_0 value in the description of the critical state line (at $p' = 1 \text{ kPa}$) has been raised to 1.01 which is also equivalent to the minimum density e_{min} measured experimentally for Leighton Buzzard sand, fraction E. The originally assessed critical state, and the derived critical state line position are shown on Figure 2 together with the examples of the triaxial tests where strain localization was observed (Figure 3). Importantly, all three constitutive models require the definition of an input parameter which corresponds to the e_0 value. However, the definition of the critical state line in each model is different, thus also the e_0 value is different for each of the models as shown later.

The G/G_0 curves chosen for the calibration are shown in Figure 4 as suggested by Dietz & Wood (2007), confirmed by the studies at low mean effective stresses by Kokusho (1980) and with the limits proposed by Seed & Idris (1970). Initial studies indicated that the maximum expected shear strain in the shear stack does not exceed the value of $0.4 \cdot 10^{-3}$, therefore, particular attention has been drawn for a good match

for strain ranges less than 10^{-3} (in case the initial studies underestimated the shear strain levels).

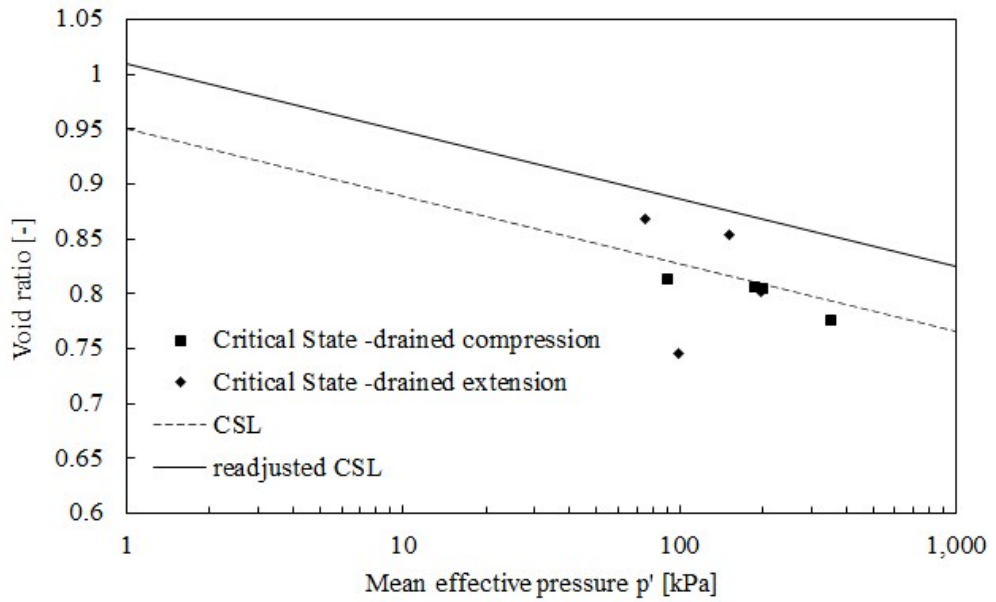


Fig. 2. Derived critical state and critical state line as proposed by Lanzano et al. (2016) and as readjusted in this thesis due to observed shear localisation and non-homogenously developed critical state in triaxial tests.

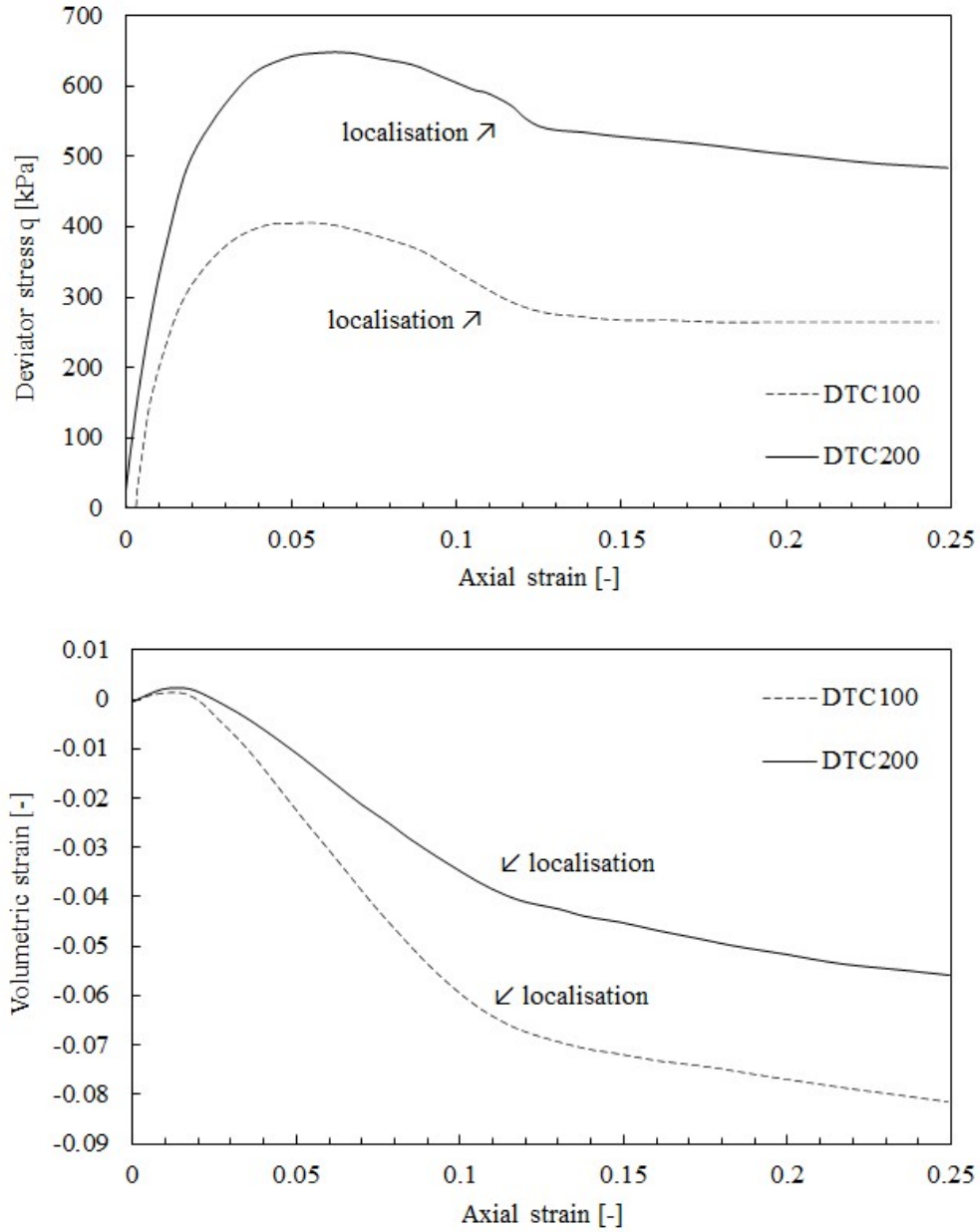


Fig. 3. Examples of experimental drained triaxial compression tests (Lanzano et al., 2016) with observed shear localisation: a) stress strain behaviour, b) volumetric response.

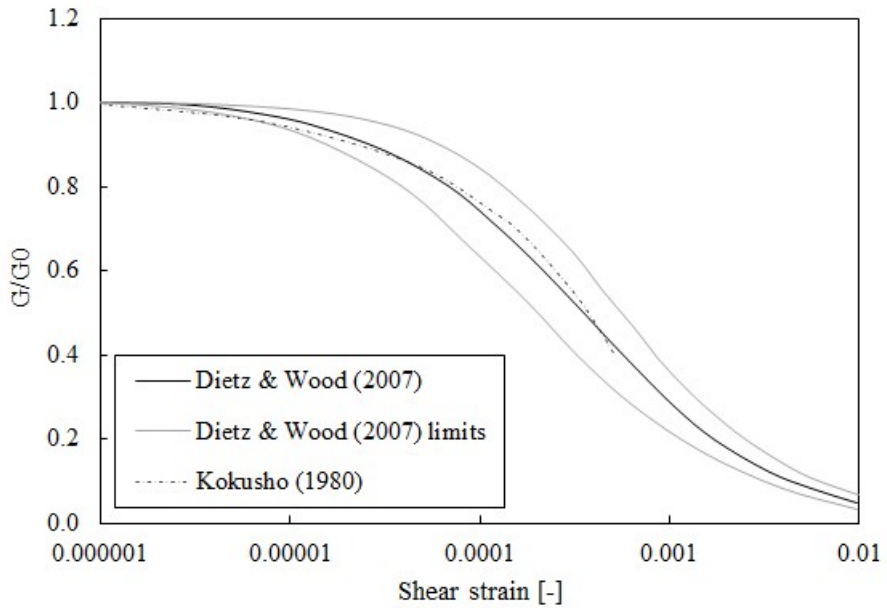


Fig. 4. Chosen G/G_0 curves and their limits for purpose of calibration of constitutive models on small strain behaviour in shear stack.

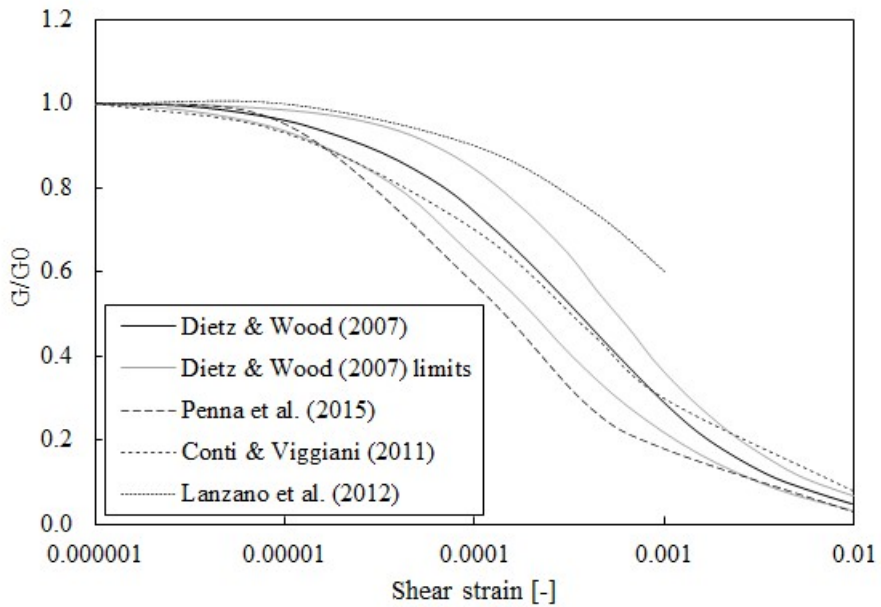


Fig. 5. Alternative G/G_0 curves considered for calibration of small strain behaviour.

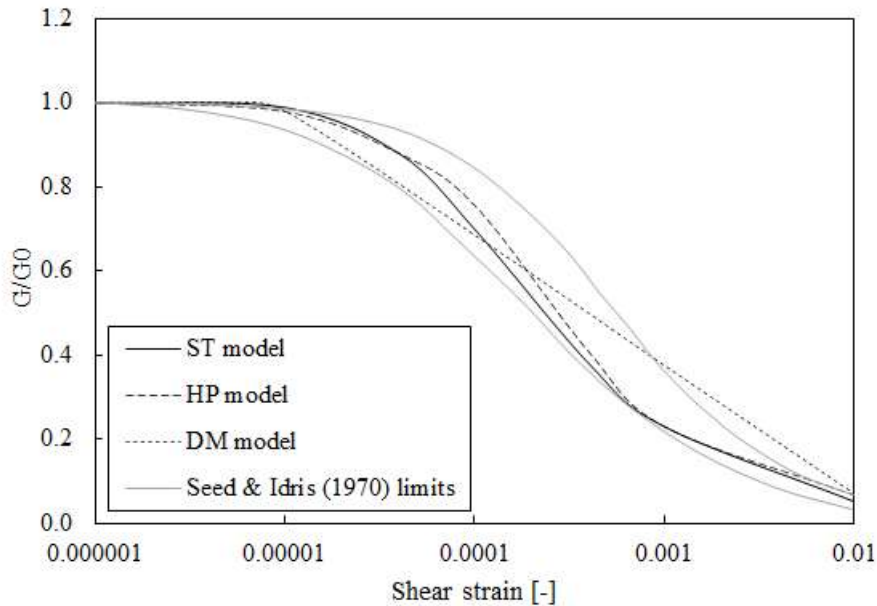


Fig. 6. Calibration of constitutive models in terms of G/G_0 curves at $p'=5\text{kPa}$ and $K_0=0.5$.

Several G/G_0 stress-strain degradation curves are available. The three models herein have been calibrated against the G/G_0 curves shown by Dietz & Wood (2007). Some other studies on small strain stiffness and its degradation in low mean effective stresses have also been considered. Figure 5 shows shear stiffness degradation from Dietz & Wood (2007), Kokusho (1980), Conti & Viggiani (2011), Penna et al. (2016), and Lanzano et al. (2016). It is highlighted that the G/G_0 curve derived by Penna et al. (2016) and Lanzano et al. (2016) are much more different from the other three. Penna et al. (2016) assumed quite high initial stiffness G_0 , thus, somehow compensating for the faster stiffness degradation with the increasing strain (all for the subsequent numerical study of a retaining wall under seismic input motion). On the other hand, Lanzano et al. (2016) predicted stiffness degradation on higher strains, this was contradicted by Conti & Viggiani (2011) and Conti et al. (2014) preferred the latter when analysing a tunnel under seismic loading. The reason for such a “delayed” stress-strain curve degradation in Lanzano et al. (2016) is the fact of obtaining it for the mean effective pressures in the range of 100-400kPa, thus outside of the range of pressures in 1-g shear stack experiments. The finally adopted G/G_0 curves from Dietz & Wood (2007) are supported by almost identical G/G_0 trends obtained by Kokusho (1980) who derived it for low mean effective stresses of approximately 20kPa.

The G/G_0 curves for the three constitutive models are derived for the mean effective pressure of 5kPa including the condition of $K_0=0.5$ as relevant for the pluviation method in shear stack experiments (Stroud, 1971). The calibration method is of type C, thus the calibration presented in Figure 6 allows for some small

readjustments in the values of the input parameters to match better the shear stack simulations, as a result some deviation of the derived G/G_0 curves can be seen when compared with the exact curve suggested by Dietz & Wood (2007). On the other hand, the derived G/G_0 curves are within the limits given by Seed & Idris (1970) for the strain range of interest, i.e. less than 10^{-3} , thus also the response of the DM model is acceptable.

Importantly, the shear stack tests (Durante, 2015) comprise an experimental setup of two layers of two different sands. The top looser layer ($D_r=25\%$) was modelled in the experiments with the Leighton Buzzard sand, fraction E, whereas the bottom layer was modelled with a denser layer ($D_r=41\%$) of the Leighton Buzzard sand, fraction B (85%) + E (15%). Table 7 and Table 8 contain the information of both sand types and sand layers. Note that no laboratory tests are known for a mixture of the two fractions (B+E) and only e_{min} and e_{max} were evaluated in the past (Moccia, 2009). Therefore, the calibration of the bottom layer has been assumed to be the same as of the top layer. The only change has been regarding the initial void ratio, which has been set to match the higher relative density of the bottom layer, which is approximately $D_r=41\%$ (i.e. $e_0=0.48$), and results in equivalent void ratio of $e_0=0.85$ in the numerical studies. All the constitutive models use void ratio as a state variable, its initial value needs to be specified, and the chosen values are 0.91 for the upper sand layer, and, to reiterate, 0.85 for the bottom sand layer.

Table 7 Properties of Leighton Buzzard sand

Sand type	γ_s [kg/m ³]	e_{min}	e_{max}	D_{10}	D_{50}	Reference
LB, fr. E	2647	0.613	1.014	0.095	0.14	Tan (1990)
LB, fr. B+E	2647	0.289	0.614			Moccia (2009)

Table 8 Sand properties within two soil layers

Layer	Height [m]	γ_s [kg/m ³]	e	D_r [%]
LB, fr. E	0.34	1332	0.91	25
LB, fr. B+E	0.46	1800	0.48	41

The appropriateness of the initial elastic stiffness, its change with depth and its implementation in the constitutive models has been confirmed when determining the first natural frequency of the soil column in the shear stack. This has been achieved numerically by using an artificial input signal of a very low amplitude and a wide flat frequency content, namely the Ormsby wavelet (explained more in Chapter 4, Section 2.1) thus a signal which is similar to a white noise. The comparison of the experimentally and numerically determined first natural frequency of the soil in the shear stack lies in the range of 31-35Hz and is shown on Figure 7. Some discrepancy between the predictions of the models and the experimental data can be observed.

However, the experimentally determined natural frequency, although obtained for a relatively low amplitude white noise input motion of 0.01g, was observed with non-negligible strain levels and the very initial stiffness was expected to be 10-20% higher (Durante, 2015). Therefore, the experimental natural frequency within a very small strain range is expected to be higher and even closer to the numerical estimation. In addition, it can be observed that the natural frequency computed for the HP model is slightly lower than those computed for the elastoplastic models. Increasing the parameter m_R from 5.0 to 6.0 results in scaling the whole hypoplastic equation and brings the natural frequency of the soil column from around 32Hz to around 35Hz. On the other hand, this resulted in obtaining less consistent (too stiff) results when comparing the initial numerical studies with the experiments, therefore, slightly lower small strain stiffness has been preferred for the case of the HP model.

To sum up, the constitutive models have been calibrated for simulating shear stack tests, thus their performance is primarily aimed at low mean effective stress environment, small shear strain ranges and stress paths similar to those of simple shear in the deviatoric section. The exact values of the input parameters for the three models are specified in subsections 5.2, 5.3 and 5.4. Although calibrated mainly for simple shear stress paths, the three models are also shown to be able to replicate at least qualitatively other laboratory tests, of different stress paths, at various mean effective stress levels. This is shown in detail in Section 6 of this chapter.

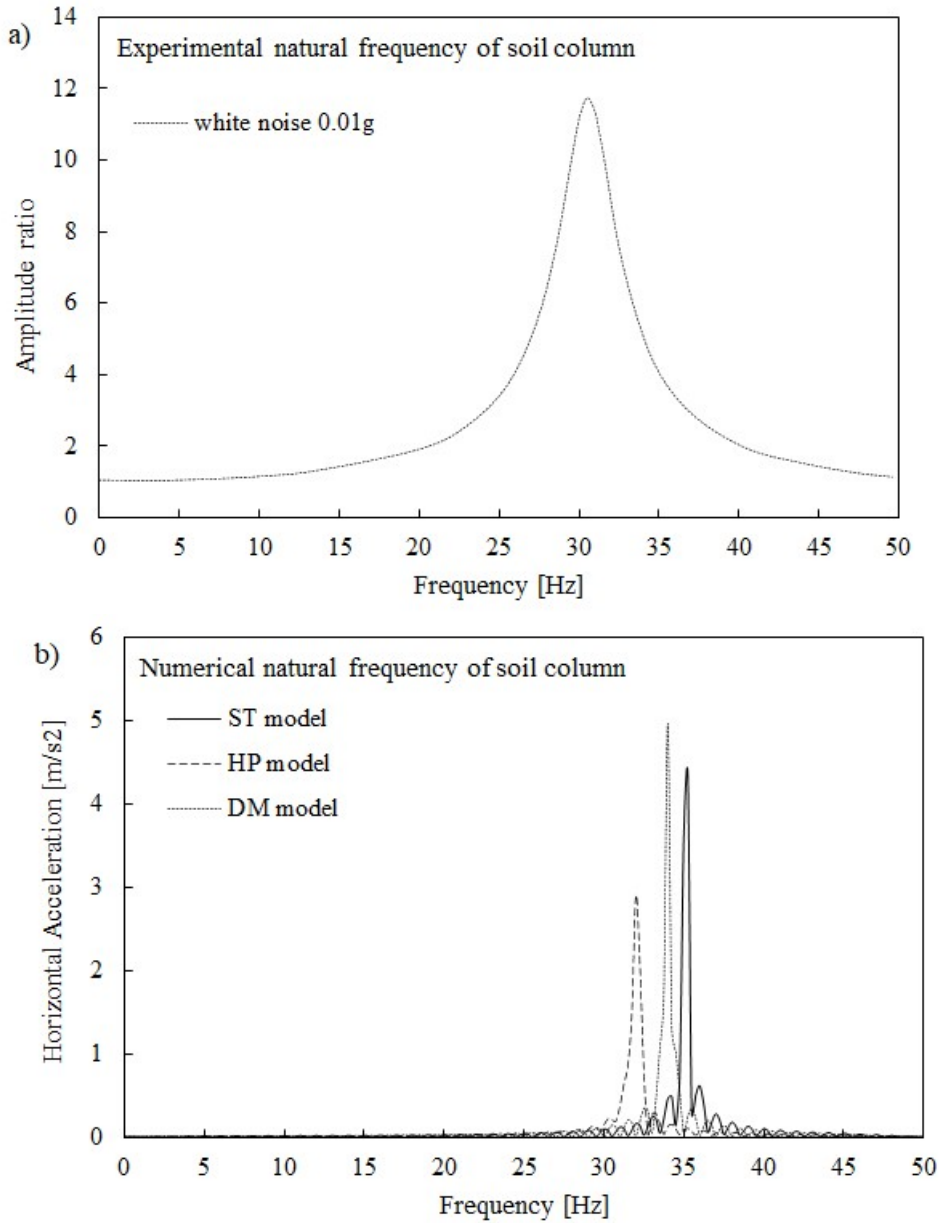


Fig. 7. Comparison of: a) experimental (Durante, 2015) and b) numerical estimation of first natural frequency of soil deposited in shear stack.

5.2. Model parameters for Severn-Trent model

The input model parameters for the ST model are listed in Table 9. The G/G_0 curve obtained at mean effective stress of 5kPa is shown in Figure 8.

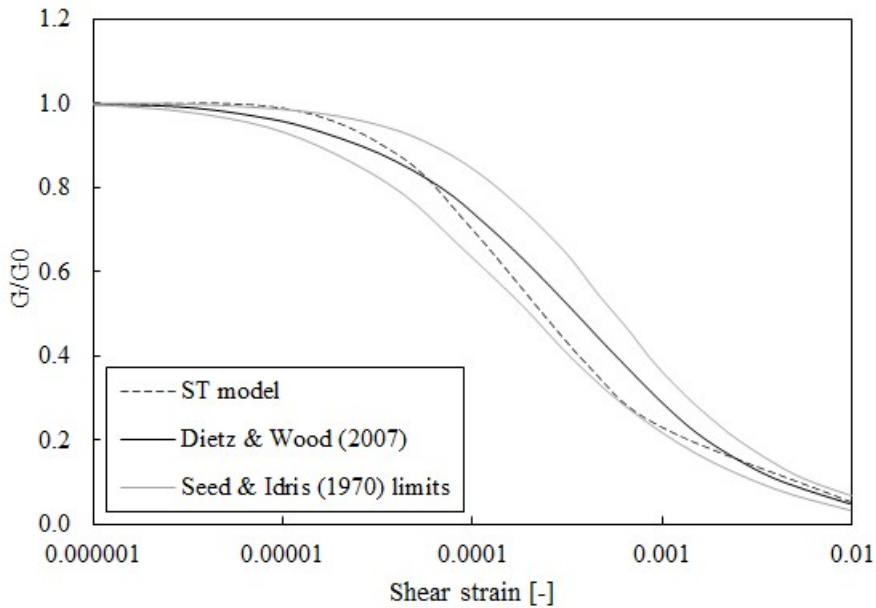


Fig. 8. Calibration of stiffness degradation curve G/G_0 for ST model obtained at $p'=5\text{kPa}$ and $K_0=0.5$.

Table 9 Input parameters for ST model.

Parameter	Description	
v_A	Intercept for critical-state line in $v\text{-ln } p'$ plane at $p'=1\text{Pa}$	2.194
Δ	Slope of critical-state line in $v\text{-ln } p'$ plane	0.0267
φ_{cv}	Critical-state angle of friction	33°
m	Parameter controlling deviatoric section of yield surface	0.8
k	Link between changes in state parameter and current size of yield surface	3.5
A	Multiplier in flow rule	0.75
k_d	State parameter contribution in flow rule	1.3
B_{min}	Parameter controlling hyperbolic stiffness relationship	0.0005
B_{max}	Parameter controlling hyperbolic stiffness relationship	0.002
α	Exponent controlling hyperbolic stiffness relationship	1.6
R	Size of yield surface with respect to strength surface	0.01/0.02
E_R	Fraction of G_0 used in the computations	1.0

The yield surface size has been defined to be 0.01 for the bottom soil layer and 0.02 for the upper soil layer. The latter is slightly greater than usually assumed for granular soils where plastic strains occur practically from the very beginning of loading. The increased yield surface size has been enforced by the numerical reasons, i.e. very low mean effective stresses at soil surface. Otherwise very large substepping numbers and computational times would be required to obtain convergence. Similar problem has been encountered with the DM model.

The implemented version of the ST model used in this thesis has a very small amount of cohesion of 1Pa in order to translate the corner of the yield surface and avoid approaching negative mean effective pressures. This was found important for shear stack simulations due to the very low mean effective pressure around the soil surface and P-wave generation due to dilation (which alternately increases and reduces the mean effective pressure).

Importantly, the calibration of the ST model in Chapter 4 will be slightly changed in order to improve the simulation of saturated soil behaviour as shown in detail in Chapter 4.

5.3. Model parameters for Hypoplastic Sand model

The input model parameters for the HP model are listed in Table 10. The G/G_0 curve obtained at 5kPa mean effective stress is shown in Figure 9.

The HP model has been initially calibrated based on the available triaxial and oedometer tests (Lanzano et al., 2016). This calibration was found to be insufficiently accurate for shear stack analysis. Therefore, it was updated later to match G/G_0 profiles as explained in Section 5.1. The required G/G_0 profiles were obtained mainly by the recalibration of the parameter n and the parameters of the intergranular strain concept. The final calibration was obtained after preliminary numerical runs of shear stack models.

This section presents the chosen set of parameters to model Leighton Buzzard sand. In addition, some consideration has been given to other calibrations for the same or similar sand, such as: Hleibieh et al. (2014), Ochmanski et al. (2019) (both for Leighton Buzzard sand, fraction E), Herle & Gudehus (1999) for Toyoura Sand (sand similar in terms of particle distribution and void ratio limits to Leighton Buzzard sand, fr. E) and the calibration obtained using Excalibre tool (Gudehus et al., 2008). The first two calibrations deal with a similar numerical study of a tunnel also embedded in Leighton Buzzard Sand (fraction E) in a laminar box in centrifuge. The third one is one of the originally proposed calibrations when introducing the intergranular strain concept. The last one is the recommended calibration method for the engineering practice purpose when triaxial and oedometer tests are available. In the case of the work in this thesis, an oedometer test on loose sand and two triaxial tests on dense sand ($p' = 100\text{kPa}$ and $p' = 200\text{kPa}$) as reported by Lanzano et al. (2016) were used to obtain

the input parameters for the basic hypoplastic model with Excalibre tool. The parameters of the intergranular strain for this calibration were obtained as per the guidelines from the webpage *soilmodels.info* (Gudehus et al., 2008), i.e. calibrating m_R as per small strain stiffness, β_R to move horizontally G/G_0 curve and using default values for the remaining parameters.

Figure 10 presents a comparison of all these calibrations with the calibration used in this thesis in terms of G/G_0 curves obtained in low mean effective stress (herein for 5kPa with $K_0=0.5$). It can be observed that the alternative calibrations cannot be used directly due to too stiff response in the small strain region.

In addition, the calibration of the Herle & Gudehus (1999) has been used to run an example of a cyclic simple shear test in a small strain range. This calibration resulted in strange behaviour, when the dilation and soil loosening lead to a stiffness increase as explained more in details in Chapter 3 (Section 4.8).

The initial void ratio has been specified as constant within the two layers, i.e. 0.91 and 0.85 for the top and bottom layers respectively, ensuring that the limiting void ratios have not been exceeded.

Table 10 Input parameters for HP model.

	Parameter	Description		
Basic hypoplasticity	φ_c	Critical friction angle	33.0	
	h_s	Granular hardness	2500	
	n	Stiffness exponent ruling pressure-sensitivity	0.42	
	e_{d0}	Limiting minimum void ratio at $p'=0$ kPa	0.613	
	e_{c0}	Limiting void ratio at $p'=0$ kPa	1.01	
	e_{i0}	Limiting maximum void ratio at $p'=0$ kPa	1.21	
	α	Exponent linking peak stress with critical stress	0.13	
	β	Stiffness exponent scaling barotropy factor	0.8	
	Intergranular strain concept	R	Representation of elastic range size	0.00004
		m_R	Stiffness multiplier	5.0
m_T		Stiffness multiplier after 90° change in strain path	2.0	
β_R		Control of rate of evolution of intergranular strain	0.3	
χ		Control on interpolation between elastic and hypoplastic response	0.5	
ϑ		Control on strain accumulation	5.0	

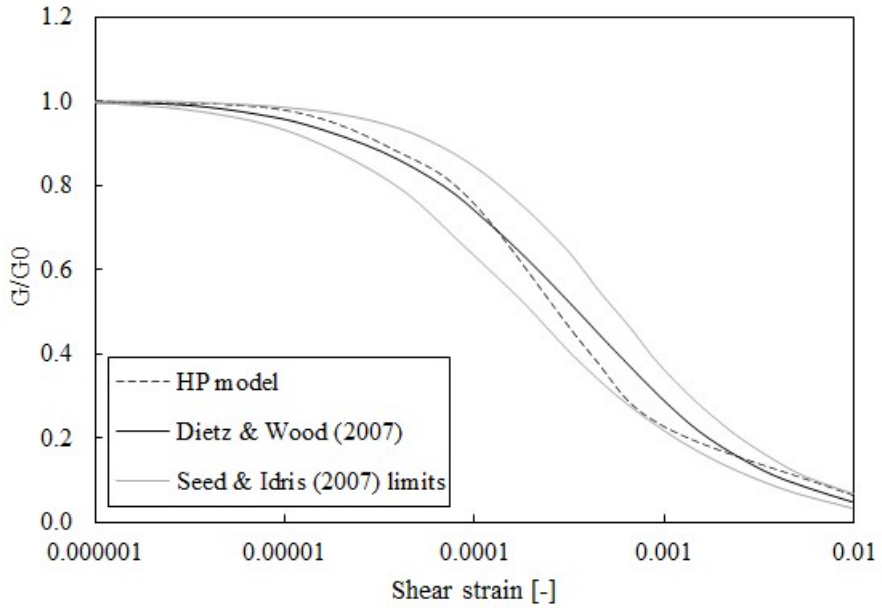


Fig. 9. Calibration of stiffness degradation curve G/G_0 for HP model obtained at $p'=5\text{kPa}$ and $K_0=0.5$.

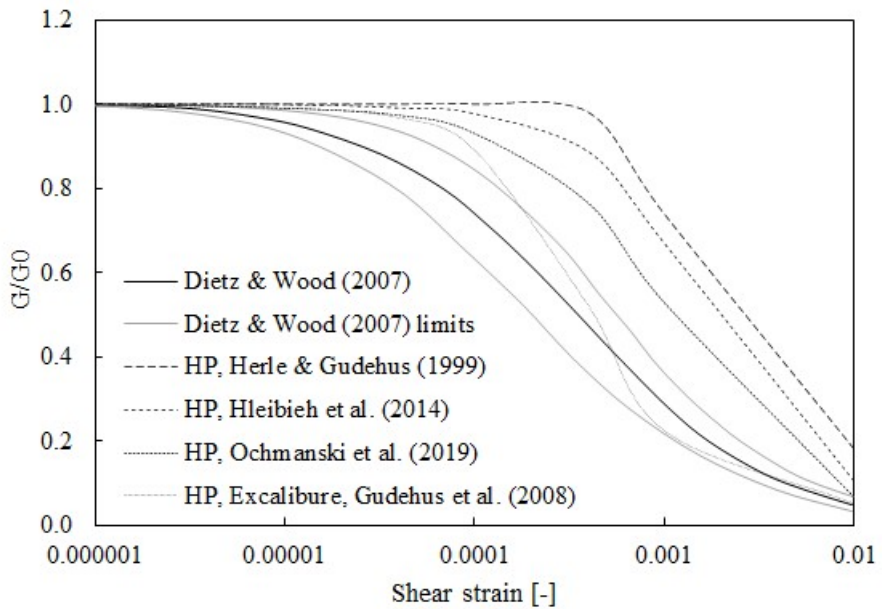


Fig. 10. Comparison of various calibrations of HP model with shear stiffness degradation curve recommended by Dietz & Wood (2007).

5.4. Model parameters for Dafalias Manzari model

The input model parameters for the DM model are listed in Table 11 and the G/G_0 curve obtained at the mean effective stress of 5kPa is shown in Figure 11.

The yield surface size for the DM model has been defined to be 0.025. This slightly increased value (when comparing with the calibration of the ST model) was needed to obtain an optimized shape of G/G_0 curves at very small strain levels. The same yield surface size was assumed for both, top and bottom soil layers. This is different from the ST model. However, it is needed due to the lack of a stiffness smoothing feature in the DM model formulation, i.e. assuming the size of the yield surface for the bottom sand layer of 0.01 would lead to smaller stiffness of the bottom layer than the upper layer in certain ranges of strains. Such lack of a stiffness smoothing constitutive feature is explained in detail in Chapter 3 in Section 4.3.

The CSL position in the DM model is defined as per equation (34) proposed by Li & Wang (1998). This is different from a more commonly used logarithmic relationship such as the one used in the ST model and shown on Figure 2 in this thesis. In this thesis, the CSL position of the DM model has been placed to match the logarithmic CSL at low pressures, i.e. up to 20kPa. In this way, the behaviour of the ST and DM models is more comparable when analysing shear stack experiments. On the other hand, this CSL placement leads to some discrepancy in the predictions of the DM model for laboratory tests at higher pressures as will be shown later in Section 6 of this chapter.

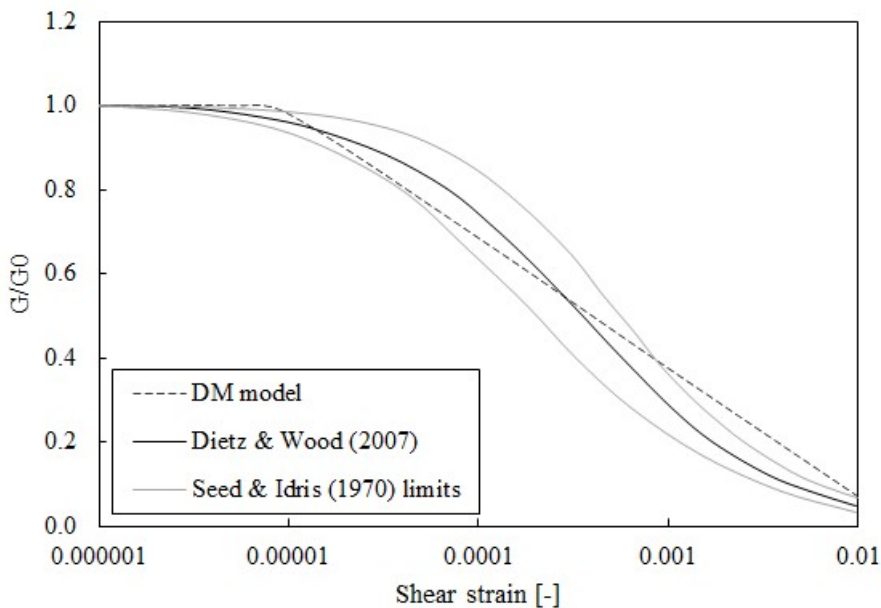


Fig. 11. Calibration of stiffness degradation curve G/G_0 for DM model obtained at $p'=5\text{kPa}$ and $K_0=0.5$.

Table 11 Input parameters for DM model

Parameter	Description	Typical values
G_0	Shear modulus constant	320
ν	Poisson's ratio	0.3
m	Size of yield surface	0.025
e_0	Void ratio on CSL at $p=0$	1.04
λ_c	Slope of critical state line	0.23
ξ	Critical state line parameter	0.45
M_c	Slope of critical state line in $q:p$ plane, triaxial compr.	1.33
c	Control of shape of yield and bounding surfaces in deviatoric section	0.821
h_0	Plastic modulus constant	25.0
c_h	Plastic modulus constant	0.95
n_b	Plastic modulus constant	1.1
A_0	Dilatancy constant	0.704
n_d	Dilatancy constant	3.5
z_{max}	Fabric index constant	2
c_z	Fabric index constant	600

Generally, the calibration adopted in this thesis introduces steps to increase small strain stiffness (i.e. quite high G_0 and h_0 values) when comparing with the original calibration (Dafalias & Manzari, 2004). However, other calibrations for small strain behaviour showed similar trends, i.e. an increase in the predicted stiffness was needed. For instance, Ghofrani & Arduino (2018), when moving from class A to class B/C predictions, increased the stiffness parameters, the critical friction angle and used a circular shape of the bounding surface (i.e. $c=1.0$ which leads to the increased distance from the bounding surface for stress paths other than triaxial). Besides, McAllister et al. (2015) indicated a need to increase the G_0 parameter when comparing to its derivation from triaxial tests (as suggested by Taiebat et al., 2010) in order to simulate seismic site response.

Different calibrations of the DM model were found to lie substantially outside the limits proposed by Seed & Idris (1970) as shown on Figure 12. In addition, the elastic initial stiffness proposed in these calibrations was too small when comparing to this observed in shear stack (i.e. $G_0=125$ for Toyoura Sand, or $G_0=82.35$ for Ottawa Sand was too low as comparing with $G_0=320$ proposed in this thesis).

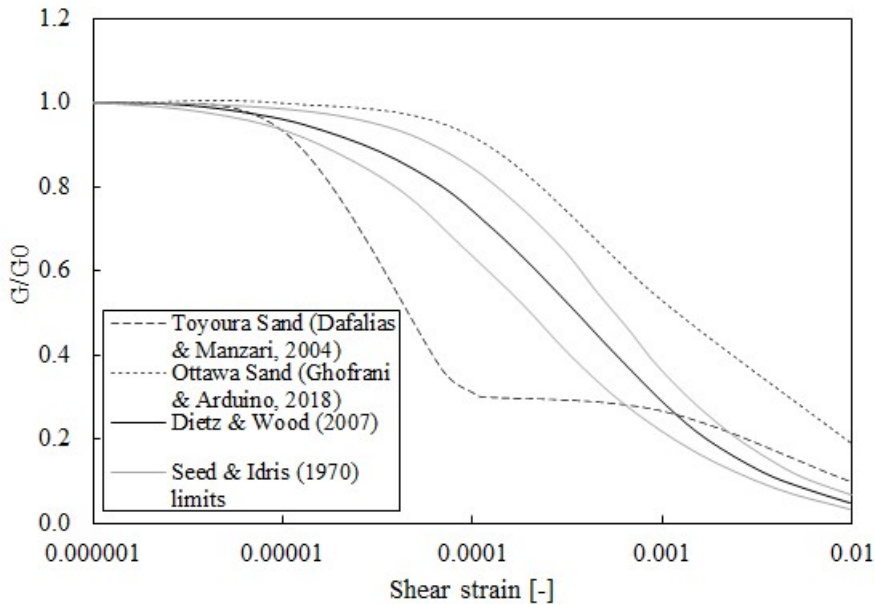


Fig. 12. Comparison of other calibrations of DM model with shear stiffness degradation curve recommended by Dietz & Wood (2007).

6. Initial validation of constitutive models on laboratory tests

This section presents the response of the constitutive models to simple laboratory tests, including one of the drained triaxial tests on Leighton Buzzard sand, fr. E (Lanzano et al., 2016), a simple shear test at low mean effective pressure on Leighton Buzzard sand, fraction B (Stroud, 1971) and a cyclic simple shear test on Toyoura sand (Shahnazari & Towhata, 2002).

The comparison of the results of the drained triaxial test is shown on Figure 13. Clearly all the three models predict stiffer response in the initial part of the loading. This reflects why, when the constitutive models were calibrated for triaxial tests, the predictions of the shear stack experiments were “too soft”. In addition, a separate comment is needed on the results computed by the DM model. This model shows quite distinctly different response when comparing with other two models, i.e. the response is as per loose sand (no peak strength and very little dilation observed). This is a consequence of readjusting the CSL position to match the CSL position of the ST model and the experiments in the mean effective stress range of up to 20kPa. Therefore, such discrepancy at $p' = 100\text{kPa}$ as shown on Figure 13 can be expected.

The comparison of the results of the drained simple shear test is shown on Figure 14. All the models predict the response as for loose sand. However, as expected,

the predicted responses differ at larger strains. Generally, all the models compute satisfactory stress-strain and volumetric behaviours.

The comparison of the results of the drained cyclic simple shear test is presented on Figure 15 to 21. Figure 15 shows the experimental results. Figures 16 to 18 show predictions of the constitutive models when the initial void ratio is specified exactly as for the experiment, i.e. $e_{ini}=0.756$ (note that the e_{min} and e_{max} values for Toyoura sand lie very close to the e_{min} and e_{max} values for Leighton Buzzard sand, fraction E). The response of the three models is quite consistent with each other, although all the models predict dense sand behaviour, i.e. dilation and not compression as per the experiment, is observed with shearing cycles. This is again associated to the position of the CSL in the $e-p'$ plane which for Toyoura sand is typically placed lower than in this thesis for Leighton Buzzard sand. To compensate for this fact, Figures 19 to 21 show the predictions of the models for higher initial void ratio, namely $e_{ini}=0.9$, for which all the models predict compression with shearing cycles as expected for loose sands.

To sum up, the calibration of the three models is considered suitable for the shear stack analysis and shows acceptable response for other stress paths and mean pressures from those predominantly experienced in shear stack tests. Some discrepancies are found but these are a confirmation of the initial conclusions of this research, i.e. the calibration of the models on triaxial and oedometer tests was not sufficient for small strain behaviour and stress paths resembling those of simple shear which dominate in shear stack experiments.

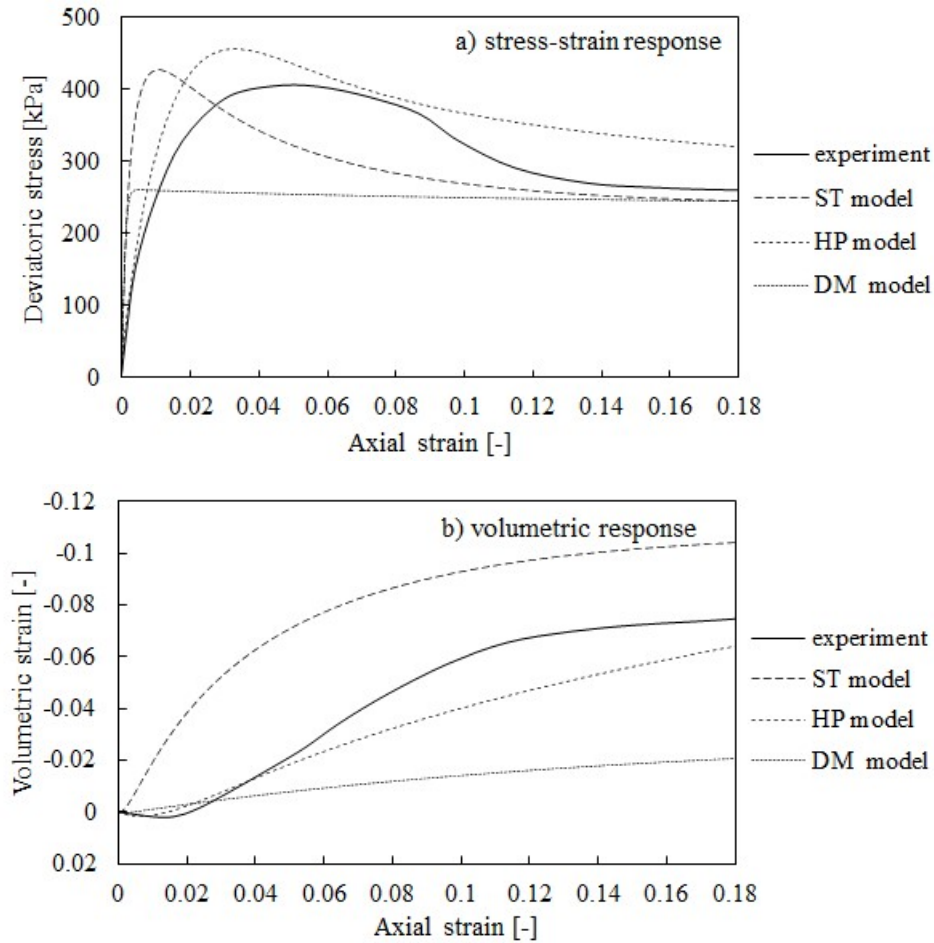


Fig. 13. Comparison of experimental and numerical results of drained triaxial test for Leighton Buzzard sand, fraction E (isotropic initial mean effective stress $p' = 100$ kPa and void ratio $e = 0.69$) from Lanzano et al., (2016) in terms of stress strain (a) and volumetric (b) response.

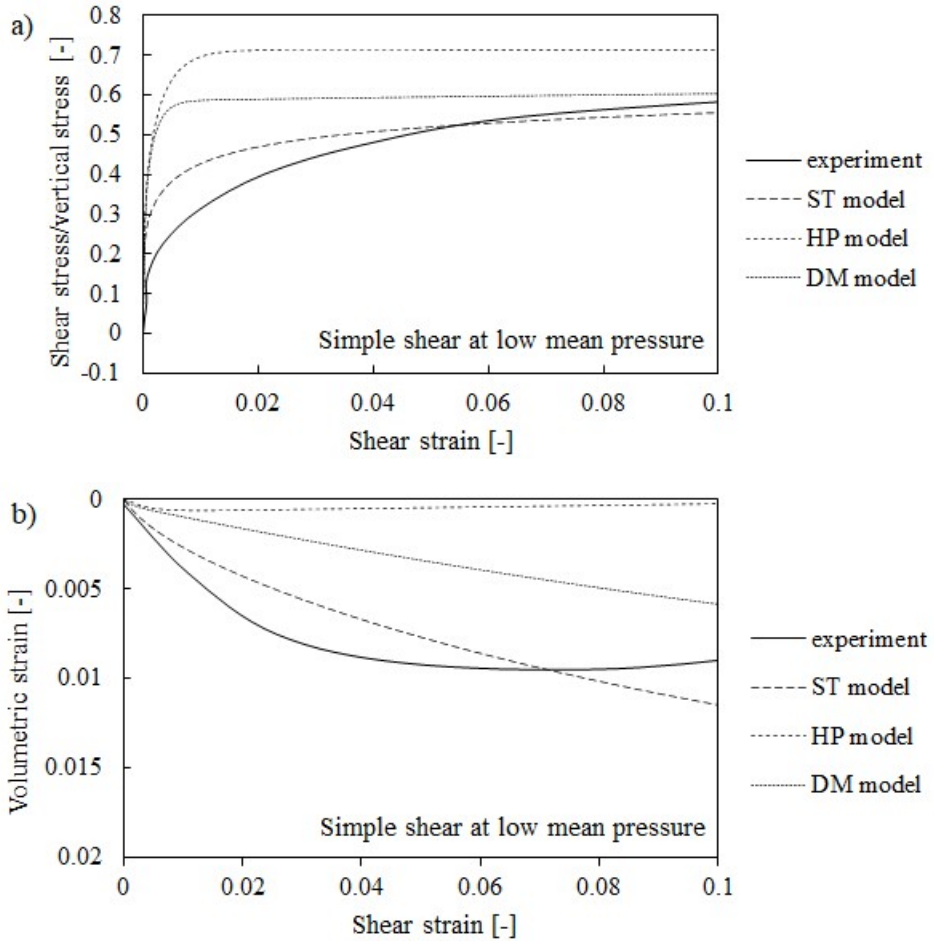


Fig. 14. Comparison of experimental and numerical results of drained simple shear test for Leighton Buzzard sand, fraction B at isotropic mean effective stress $p'=11\text{kPa}$ and void ratio $e=0.78$ (simulated with equivalent void ratio $e=0.99$) from Stroud et al. (1971) in terms of stress strain (a) and volumetric (b) response.

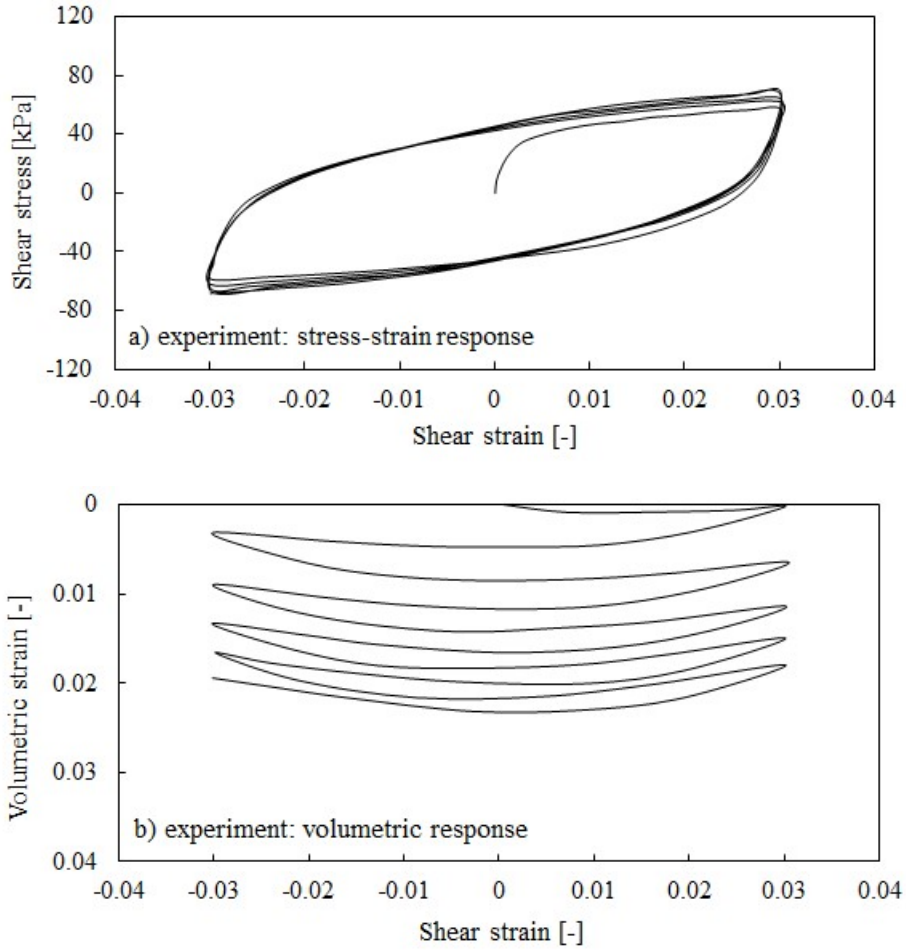


Fig. 15. Experimental results for drained cyclic simple shear test for Toyoura sand at $p'=100\text{kPa}$ and $e_{ini}=0.756$ (Shahnazari & Towhata, 2002).

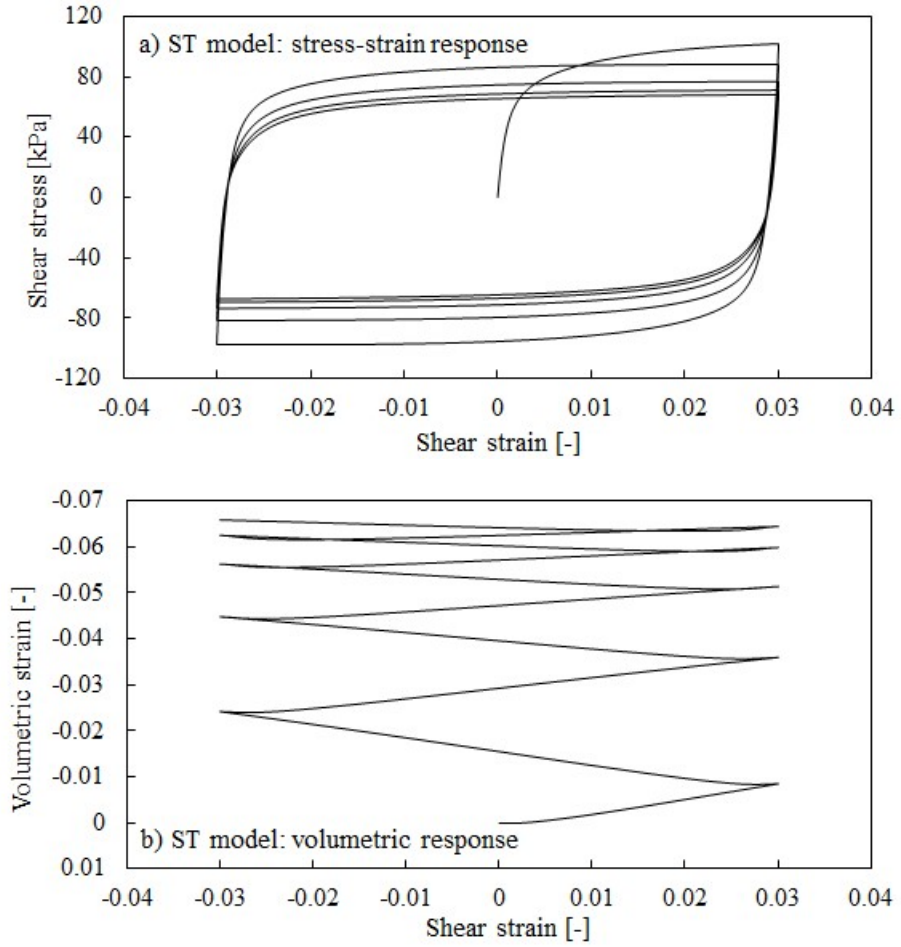


Fig. 16. Numerical results for drained cyclic simple shear test with ST model at $p' = 100 \text{ kPa}$ (initial void ratio $e_{vir} = 0.756$).

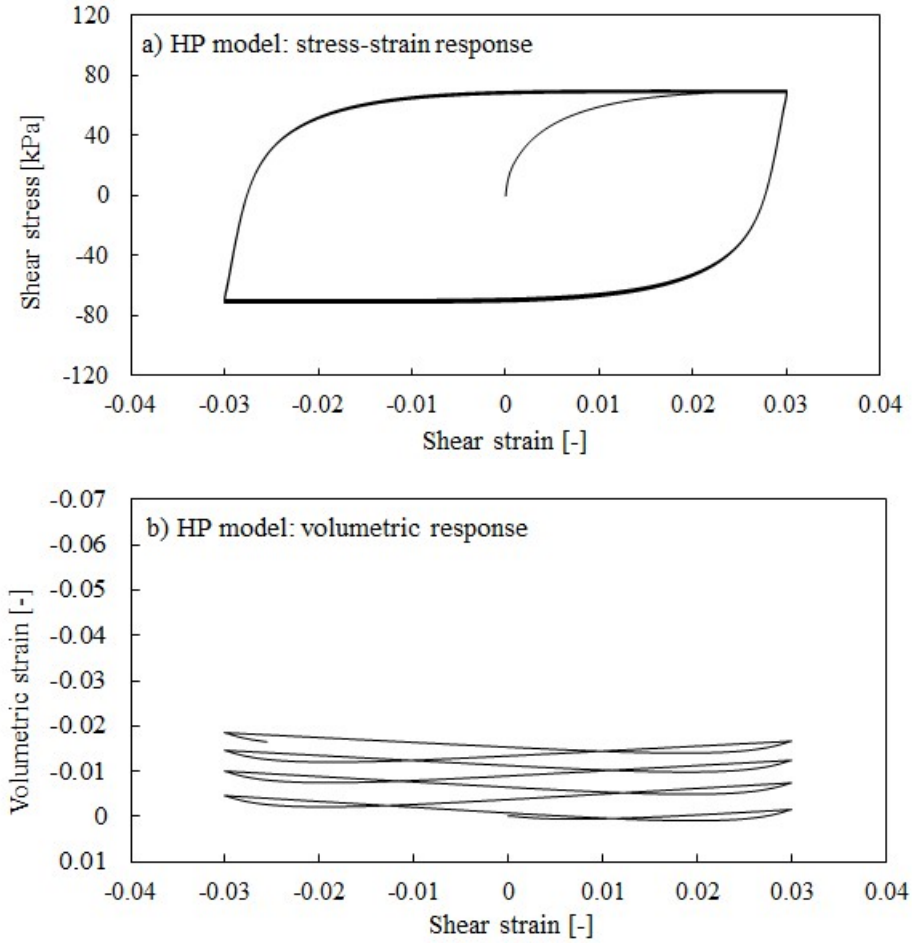


Fig. 17. Numerical results for drained cyclic simple shear cyclic test with HP model at $p' = 100 \text{ kPa}$ (initial void ratio $e_{ini} = 0.756$).

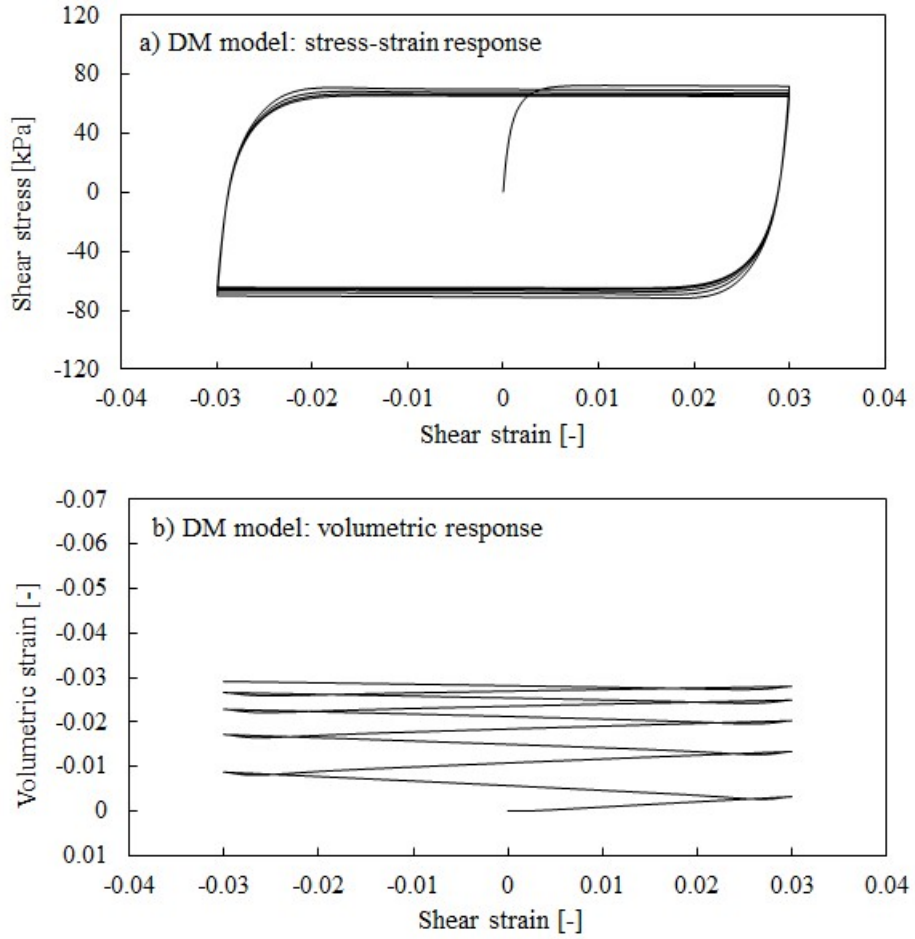


Fig. 18. Numerical results for drained cyclic simple shear cyclic test with DM model at $p' = 100 \text{ kPa}$ (initial void ratio $e_{mi} = 0.756$).

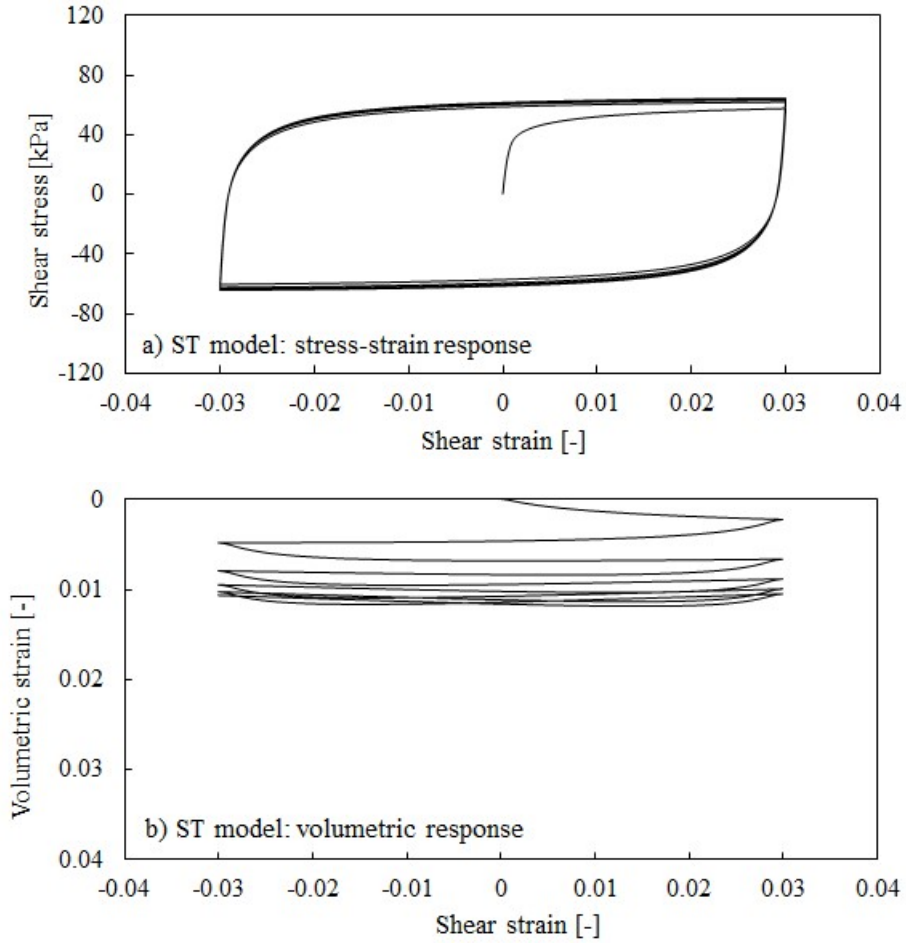


Fig. 19. Numerical results for drained cyclic simple shear cyclic test with ST model at $p' = 100 \text{ kPa}$ (initial void ratio $e_{ini} = 0.9$).

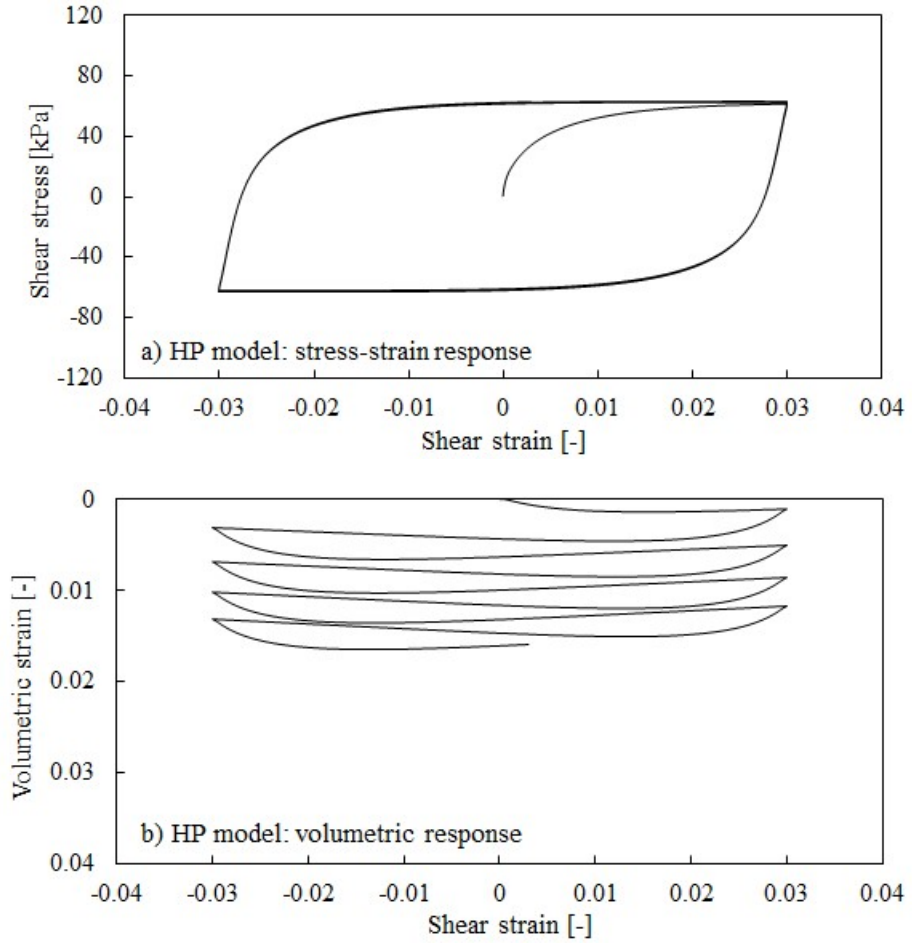


Fig. 20. Numerical results for drained cyclic simple shear cyclic test with HP model at $p' = 100 \text{ kPa}$ (initial void ratio $e_{mi} = 0.9$).

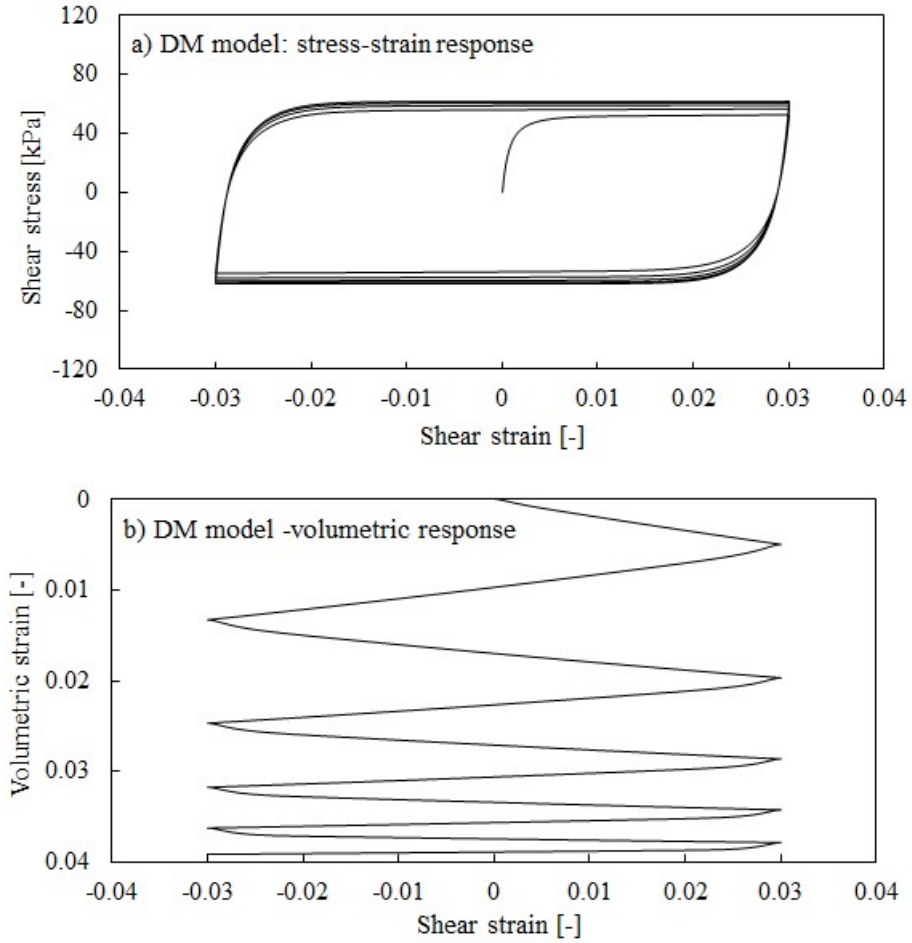


Fig. 21. Numerical results for drained cyclic simple shear cyclic test with DM model at $p' = 100 \text{ kPa}$ (initial void ratio $e_{ini} = 0.756$).

References

- Abate, G., Massimino, M., R., Maugeri, M., Muir Wood, D. (2010). Numerical modelling of a shaking table test for soil-foundation-superstructure interaction by means of a soil constitutive model implemented in a FEM Code. *Geotechnical and Geological Engineering* 28(1), 37-59.
- Arduino, P., Ghofrani, A. (2019). Modelling liquefaction effects -from lateral spreading to soil-structure interaction. *In proceedings of the 7th International Conference of Earthquake Geotechnical Engineering*, 17-20 June, Rome, Italy.
- Argyris, J., H., Faust, G., Szimmat, J., Warnke, P., William, K. (1974). Recent developments in the finite element analysis of prestressed concrete reactor vessels. *Nuclear Engineering and Design*. 28, 42-75.
- Bauer, E. (1996). Calibration of a comprehensive constitutive equation for granular materials. *Soils and Foundations* 36(1), 13-26.
- Been, K., Jefferies, M., J. (1985). A state parameter for sands. *Géotechnique* 35, 99-112.
- Bilotta, E., Lanzano, G., Madabushi, S.P.G., Silvestri, F. (2014). A numerical Round Robin on tunnels under seismic actions. *Acta Geotechnica* 9, 563-579.
- Boulanger, R., Ziotopoulou, K. (2015). PM4Sand Version 3: A sand plasticity model for earthquake engineering applications. *Technical Report*.
- Conti, R., Viggiani, G.M.B. (2011). Evaluation of soil dynamic properties in centrifuge tests. *Journal of Geotechnical and Geoenvironmental Engineering* 138(7), 850-859.
- Conti, R., Viggiani, G.M.B., Perugini, F. (2014). Numerical modelling of centrifuge dynamic tests of circular tunnels in dry sand. *Acta Geotechnica* 9(4), 597-612.
- Corti, R., Diambra, A., Muir Wood, D., Escribano, D., E., Nash, D., F., T. (2016). Memory surface hardening model for granular soils under repeated loading conditions. *Journal of Engineering Mechanics* 142(12):04016102.
- Dafalias, Y., F., Manzari, M. T. (2004). A simple plasticity sand model accounting for fabric change effects. *Journal of Engineering Mechanics* 130(6), 622-634.
- Dafalias, Y., F., Papadimitriou, A. G., Li, X. S. (2004) Sand plasticity model accounting for inherent fabric anisotropy. *Journal of Engineering Mechanics* 130(11): 1319-1333.
- Dafalias, Y., F., Taiebat, M. (2016). SANISAND-Z: zero elastic range sand plasticity. *Geotechnique*, 66(12), 999-1013.

Dassault Systèmes (2019). Abaqus Standard software package.

Dietz, M., Muir Wood, D. (2007). Shaking table evaluation of dynamic soil properties. *In proceedings of the 4th International Conference of Earthquake Geotechnical Engineering*, 25-28 June, Thessaloniki, Greece.

Durante, M. G. (2015). Experimental and numerical assessment of dynamic soil-pile-structure interaction. *PhD Thesis*. Università degli Studi di Napoli Federico II (Italy).

Fuentes, W., Triantafyllidis, T. (2015). ISA: a constitutive model for deposited sand. *In: Schanz, T., Hettler, A. (eds.) Aktuelle Forschung in der Bodenmechanik 2015*, 169-187. Springer, Berlin (2015)

Gajo, A., Muir Wood, D. (1999a). Severn-Trent sand: a kinematic hardening constitutive model for sands: the q-p formulation. *Géotechnique* 49(5), 595-614.

Gajo, A., Muir Wood, D. (1999b). A kinematic hardening constitutive model for sands: the multi-axial formulation. *International Journal for Numerical and Analytical Methods in Geomechanics* 23(9), 925-965.

Gajo, A. (2010). Hyperelastic modeling of small-strain anisotropy of cyclically loaded sand. *International Journal for Numerical and Analytical Methods in Geomechanics* 34(2), 111-134.

Gajo, A. (2017). Fortran subroutine in a format of user defined material (UMAT) of implementation of the Severn-Trent sand model.

Ghofrani, A., Arduino, P. (2018). Prediction of LEAP centrifuge test results using a pressure-dependent bounding surface constitutive model. *Soil Dynamics and Earthquake Engineering* 113, 758-770.

Gudehus, G. (1996). A comprehensive constitutive equation for granular materials. *Soils and Foundations* 36(1), 1-12.

Gudehus, G., Amorosi, A., Gens, A., Herle, I., Kolymbas, D., Mašín, D., Muir Wood, D., Nova, R., Niemunis, A., Pastor, M., Tamagnini, C., Viggiani, G. (2008) The soilmodels.info project. *International Journal of Numerical and Analytical Methods in Geomechanics* 32(12), 1571-1572.

Hardin, B. O., Black, W. L. (1968). Vibration modulus of normally consolidated clay. *Journal of the Soil Mechanics and Foundation Division (ASCE)* 94, 353-369.

Hardin, B.O. & Drnevich, V.P. (1972). Shear modulus and damping in soils. *Journal of Soil Mechanics and Foundations Division (ASCE)*, 98(7), 667-692.

Herle, I., Gudehus, G. (1999). Determination of parameters of a hypoplastic constitutive model from properties of grain assemblies. *Mechanics of Cohesive and Frictional Materials* 4(5), 461-486.

- Hleibieh, J., Wegener, D., Herle, I. (2014). Numerical simulations of a tunnel surrounded by sand under earthquake using a hypoplastic model. *Acta Geotechnica* 9, 631-640.
- Hleibieh, J., Herle, I. (2019). The performance of a hypoplastic constitutive model in predictions of centrifuge experiments under earthquake conditions. *Soil Dynamics and Earthquake Engineering*, 122, 310-317.
- Hull, T. E., Enright, W. H., Jackson, K. R. (1996). Runge-Kutta research at Toronto. *Applied Numerical Mathematics* 22(1-3), 225-236.
- Kokusho, T. (1980). Cyclic triaxial test of dynamic soil properties for wide strain range. *Soils and Foundations* 20(2), 45-60.
- Kolymbas, D. (1985). A generalized hypoelastic constitutive law. *In Proceedings of the 11th International Conference on Soil Mechanics and Foundation Engineering*, San Francisco, USA.
- Kolymbas, D. (1991). Computer-aided design of constitutive laws. *International Journal of Numerical and Analytical Methods in Geomechanics* 15, 593-604.
- Kolymbas, D., Medicus, G. (2016). Genealogy of hypoplasticity and barodesy. *International Journal of Numerical and Analytical Methods in Geomechanics* 40, 2532-2550.
- Lambe, T. (1973). Predictions in soil engineering. *Géotechnique* 23(2), 151-202.
- Lanzano, G., Visone, C., Bilotta, E., Santucci de Magistris, F. (2016). Experimental assessment of the stress-strain behaviour of Leighton Buzzard sand for the calibration of a constitutive model. *Geotechnical and Geological Engineering* 34(4), 991-1012.
- Li, X., S., Wang, Y. (1998). Linear representation of steady-state line for sand. *Journal of Geotechnical Geoenvironmental Engineering* 124(12), 1215-1217.
- Liu, H. Y., Abell, J.A., Diambra, A., Pisano, F. (2019). Modelling the cyclic ratcheting of sands through memory-enhanced bounding surface plasticity. *Géotechnique* 69(9), 783-800.
- Manzari, M. T., Dafalias, Y. F. (1997). A critical state two-surface plasticity model for sands. *Géotechnique* 47(2), 255-272.
- Martinelli, M., Burghignoli, A., Callisto, L. (2016). Dynamic response of a ply embedded into a layered soil. *Soil Dynamics and Earthquake Engineering* 87, 16-28.
- Mašín, D. (2005). A hypoplastic constitutive model for clays. *International Journal of Numerical and Analytical Methods in Geomechanics* 29(4), 311-336.

- Mašín, D. (2012). Hypoplastic Cam-Clay model. *Géotechnique* 62(6), 549-553.
- Mašín, D. (2014). Clay hypoplasticity model including stiffness anisotropy. *Géotechnique* 64(3), 232-238.
- Mašín D. (2018). Modelling of soil behaviour with hypoplasticity. Another approach to soil constitutive modelling. *Springer*.
- McAllister, G., Taiebat, M., Ghofrani, A., Chen, L., Arduino, P. (2015). Nonlinear site response analyses and high frequency dilation pulses. *In Proceeding of the 68th Canadian Geotechnical Conference. Quebec, Canada*.
- Moccia, F. (2009). Seismic soil pile interaction: experimental evidence. *PhD Thesis. Università degli Studi di Napoli Federico II (Italy)*.
- Mohammadi-Haji, B., Ardakani, A. (2018). Numerical prediction of circular tunnel seismic behaviour using hypoplastic soil constitutive model. *International Journal of Geotechnical Engineering* DOI:10.1080/19386362.2018.1438152.
- Muir Wood, D., Belkheir, K., Liu, D.F. (1994). Strain softening and state parameter for sand modelling. *Géotechnique* 44 (2), 335-339.
- Niemunis, A., Herle, I. (1997). Hypoplastic model for cohesionless soils with elastic strain range. *Mechanics of Cohesive-Frictional Materials* 2, 279-299.
- Ochmanski, M., Delli Carpini, M., Salvatore, E., Modoni, G., Bilotta, E. (2019). Numerical simulation of centrifuge seismic tests on tunnel in sandy soil. *In proceedings of the 7th International Conference of Earthquake Geotechnical Engineering*, 17-20 June, Rome, Italy.
- Penna, A., Sorrentino, G., d'Onofrio, A., Silvestri, F., Simonelli, A. L. (2016). Dynamic behaviour of the Leighton Buzzard sand-B under very low confining stresses. *In Proceedings of the 1st IMEKO TC-4 International Workshop on Metrology for Geotechnics*, March 17-18, Benevento, Italy.
- Pisano, F., Jeremic, B. (2014). Simulating stiffness degradation and damping in soils via a simple visco-elastic-plastic model. *Soil Dynamics and Earthquake Engineering* 63, 98-109.
- Pradhan, T. B. S., Tatsuoka, F., Sato, Y. (1989). Experimental stress-dilatancy relations of sand subjected to cyclic loading. *Soils and Foundations* 29(1), 45-64.
- Ramirez, J., Barrero, A. R., Chen, L., Dashti, S., Ghofrani, A., Taiebat, M., Arduino, P. (2018). Site response in a layered liquefiable deposit: evaluation of different numerical tools and methodologies with centrifuge experimental results. *Journal of Geotechnical and Geoenvironmental Engineering* 144(10) 04018073.

- Reyes, D. K., Rodriguez-Marek, A., Lizcano, A. (2009). A hypoplastic model for site response analysis. *Soil Dynamics and Earthquake Engineering* 29, 173-184.
- Rotisciani, G., M., Miliziano, S. (2013). Guidelines for calibration and use of the Severn-Trent sand model in modelling cantilevered wall-supported excavations. *International Journal of Geomechanics* 14(6) DOI:10.1061/(ASCE)GM.1943-5622.0000373.
- Seed, H. B., Idriss, I. M. (1970). Soil moduli and damping factors for dynamic response analysis. *EERC report 70-10*. University of California, Berkeley.
- Shahnazari, H., Towhata, I. (2002). Torsion shear tests on cyclic stress-dilatancy relationship of sand. *Soils and Foundations* 42(1) 105-119.
- Stroud, M. A. (1971). The behaviour of sand at low stress levels in the simple shear apparatus. *PhD Thesis*. University of Cambridge.
- Tan, F.S.C. (1990). Centrifuge and theoretical modelling of conical footings on sand. *PhD Thesis*. University of Cambridge.
- Taiebat, M., Dafalias, Y. F. (2008). SANISAND: Simple anisotropic sand plasticity model. *International Journal of Numerical and Analytical Methods in Geomechanics*. 32, 915-948.
- Taiebat, M., Jeremic, B., Dafalias, Y. F., Kaynia, A. M., Cheng, Z. (2010). Propagation of seismic waves through liquified soils. *Soil Dynamics and Earthquake Engineering* 30(4), 236-257.
- Van Eekelen, H. (1980). Isotropic yield surface in three dimensions for use in soil mechanics. *International Journal of Numerical and Analytical Methods in Geomechanics* 4(1), 89-101.
- Von Wolffersdorff, P. A. (1996). A hypoplastic relation for granular materials with a predefined limit state surface. *Mechanics of Cohesive and Frictional Materials* 1(3), 251-271.
- Wegener, D. (2013). Numerical investigation of permanent displacements due to dynamic loading. *PhD thesis*. TU Dresden (Germany).
- Wegener, D., Herle, I. (2014). Prediction of permanent soil deformations due to cyclic shearing with a hypoplastic constitutive model. *Geotechnik* 37(2), 113-122.
- Wichtmann, T. (2005). Explicit accumulation model for noncohesive soils under cyclic loading. *PhD thesis*. Bochum University (Germany).
- Wroth, C. P., Bassett, R. H. (1965). A stress-strain relationship for the shearing behaviour of a sand. *Géotechnique* 15, 32-56.

Wu, W. (1992). Hypoplastizität als mathematisches Modell zum mechanischen Verhalten granularer Stoffe. *Publication Series of the Institute of Soil Mechanics and Rock Mechanics*, No. 129, Karlsruhe University.

CHAPTER 2

Higher harmonic generation due to elastic unloading waves

1. Introduction

The most recent studies in seismic geotechnical engineering are focused on providing high quality experimental data followed by advanced numerical studies. The most important aims of the physical modelling are twofold: improved understanding of soil-structure interaction during seismic events and validation of the numerical modelling studies, thus, allowing their use in the subsequent predictive studies of full-scale problems. Although, advanced physical and numerical modelling are considered as reliable ways of investigating seismic behaviour of soil, both these methodologies often experience presence of unexpected high frequency content in recorded or computed motions.

Physical modelling of soil seismic behaviour is typically achieved in shear stacks or laminar boxes placed on shaking tables in 1g (e.g. Durante et al., 2016) or centrifuge experimental setups (e.g. Lanzano et al., 2012). Such experimental studies often record unexpected and undesired higher frequency content even though they use simplified sinusoidal input motions of a single frequency. For example, high frequency content in a form of a regular pattern of higher harmonics, e.g. 3ω , 5ω , 7ω etc. (where ω is the driving frequency), was observed by many research centres participating in the LEAP-GWU-2015 project (Kutter et al., 2018) and LEAP-UCD-2017 project (Kutter et al., 2019) on saturated soil slopes. Experimental work on dry soil also revealed the presence of undesired higher harmonics for an intended perfect sinusoidal input motion (e.g. Conti & Viggiani, 2012; Conti et al., 2012; Lanzano et al., 2012, Abate & Massimino, 2016).

The presence of higher frequency content recorded in the experimental work is not fully clear. In studies regarding saturated soil, high frequency content could be associated with “*de-liquefaction shock waves*” (Kutter & Wilson, 1999) or in other words with dilation, sudden reduction in excess pore pressure and consequent sudden increase in soil stiffness (Bonilla et al., 2005; Roten et al., 2013; McAllister et al., 2015; Wang Gang et al., 2018). On the other hand, higher frequencies in dry soil were attempted to be explained by shear band development at shallow soil depths in a shear stack under high amplitude input motions (Das, 1993; Gajo & Wood, 1997). Importantly, some past earthquakes also resulted in spectral response of regular

patterns of frequency content ω , 3ω , 5ω (where ω dominant frequency). Ruiz & Saragoni (2009) associated such spectral responses with soil natural frequencies although the presence of higher modes was not explicitly explained. In general, one is reminded that any nonlinearity in a physical system is expected to generate higher harmonics for a single sinusoidal ω driving frequency (Nekorkin, 2015). For instance, higher harmonics for a perfect sine input motion were observed in frictional base isolation systems (Kelly, 1982; Fan et al., 1988; Wiebe & Christopoulos, 2010) or in a harmonic oscillator with sliding friction (Vittorino et al., 2017), where abrupt changes in stiffness and changes in the direction of the friction force caused nonlinearity and led to such a generation of higher harmonics. Some numerical studies showed that soil inherent nonlinearity, in detail hysteretic stress strain behaviour, can also generate higher harmonics for a single sine input motions (Pavlenko, 2001; Pavlenko & Irikura, 2005; Mercado et al., 2018; Veeraraghan et al., 2019). To sum up, some physical explanations to the observed higher harmonics has been attempted by the previous studies, although none of these studies considered the effects of fast elastic unloading waves or the possibility of an elastic wave separation.

Sometimes higher harmonics of a regular pattern ω , 3ω , 5ω etc. were also recorded at base level. For example, Madabhushi (2014) showed an example input motion recorded at base in a centrifuge test to comprise higher harmonics in the regular form of ω , 3ω , 5ω , 7ω etc. As a result of this observation, the presence of harmonics is often attributed also to the actuating systems (Brennan et al., 2005). In more detail, Kutter et al. (2018) and Manandhar et al. (2019) indicated difficulties in controlling high frequency content in actuators, Lanzano et al. (2012) pointed out at the potential resonance with higher natural modes of the shakers, whereas Yao et al. (2017) showed that higher harmonics are recorded on an empty shaking table for a very high amplitude input motions and they attributed these higher harmonics to nonlinearities in the actuating system.

The occurrence of higher frequency content appears also in numerical studies. For instance, the performance of the numerical predictions in the LEAP-UCD-2017 project was presented by Manzari et al. (2019). This study highlights the fact that some constitutive models were able to represent the higher frequency content in a similar way as obtained in the centrifuge tests. Some other constitutive models were able to damp out higher frequencies. Therefore, the presence or absence of higher harmonics was attributed more to implemented numerical or Rayleigh damping and less to the constitutive models themselves. To the best of the author's knowledge, majority of the predicting teams used the input motion at base as per the one recorded in centrifuges, thus, with higher harmonics being present. Similarly, Bilotta et al. (2014) showed that different predicting teams chose different methods to remove spurious high frequencies, e.g. by means of result filtering or application of viscous damping, and were able to obtain comparable response spectra at soil surface with experimental data. However, the input motion introduced at base also contained higher harmonics. A more specific study, dealing strictly with high frequency content in numerical studies,

was presented by Tsiapas & Bouckovalas (2018) where the authors recognized such frequencies to be numerical noise. They observed that the source of these numerical oscillations can be attributed to abrupt stiffness changes or the moment of unloading, and proposed a filtering method to remove such noise from the computations of dry and saturated soil.

The problem of higher frequency content, in recorded or computed motions, appears in both, physical and numerical modelling studies. This chapter shows a potential explanation to sources of such high frequencies based on the consideration of the propagation of fast elastic unloading waves and their effects. In fact, the importance of unloading waves has been recognized in solid mechanics. The first formulation of the unloading wave problem came from Rakhmatullin (1945) who described the propagation of an elastoplastic-unloading boundary. Numerous analytical solutions predicted the propagation of an unloading shock wave and the onset of a loading-unloading boundary in elastoplastic bodies. Nowacki (1978) and more recently Wang (2007) showed an overview of unloading waves with different cases of interactions of elastoplastic longitudinal waves in bars. Wang (2007) divided wave interactions into two types: head-on and pursuing loading. The former concerns waves of opposite stress signs and opposite direction of propagation, whereas the latter happens when an unloading faster wave catches up with a slower preceding plastic wave, both propagating in the same direction. Various types of situations can then occur, including strong discontinuous waves, such as those due to sudden unloading, or weak discontinuous waves, in the case of gradual unloading. Moreover, the possibility of the separation of the elastic part of a wave from its plastic part with the increasing propagation length in the case of an elastoplastic material was also discussed.

Although the importance of unloading waves received consideration in solid mechanics, so far, it is rather missing from the consideration in seismic wave propagation in soil. Some very initial numerical studies were limited only to a soil column analysed by Fellin (2002) and a brief study by Song et al. (2018). The former analysed a compressive wave propagation under a single cycle of loading and unloading, where it was shown that a shock wave forms as a result of soil nonlinearity in oedometer-like conditions. Indeed, the fast unloading wave was not a subject to closer investigation. The latter showed a semi-infinite column with a rectangular shock pulse with loading and unloading fronts which interact with each other due to the unloading wave being faster and chasing the loading wave. However, the semi-infinite column was modelled with linearly hardening plasticity on loading and pure elasticity on unloading, thus not being representative of real soil behaviour. To sum up, these studies only briefly introduced the topic of unloading waves, none of these works showed higher frequency generation, separation of the elastic part of a wave, or comparisons with experimental data.

This chapter shows a potential explanation of the presence of higher frequencies recorded in experimental and computed in numerical studies as related to

the physical effects of fast elastic unloading waves, i.e. fast elastic unloading waves pursuing slow plastic waves and the elastic part of a wave separating from its plastic part. The study comprises advanced numerical studies compared with experimental examples (Durante, 2015). The chapter is divided into sections and subsections. Section 2 is dedicated to methodology, including brief introduction to the conducted numerical studies and a short description of the experimental data available to the author. The results of the chapter are presented in six subsections of Section 3. In detail, Section 3.1 presents a simplified numerical study with a simple hysteretic soil model to reveal the first effect of fast elastic unloading waves, i.e. shock wave formation and sine wave distortion. Section 3.2 repeats the study of the previous section with an example elastoplastic model in order to present the second effect of fast elastic unloading waves, i.e. elastic part of a wave separating from its plastic part. Both these effects are shown to be registered in the spectral response as higher harmonics of the frequency of the input motion. Section 3.3 shows comparisons of numerical and experimental results on dry sand carried out in a shear stack for S-wave propagation. Section 3.4 is dedicated to P-wave propagation in dry sand in a shear stack. In addition, the impact of the generated harmonics on the structural response is also discussed based on the example of a kinematic pile (Section 3.5). A short study on saturated soil column shows higher frequency generation and a strong discontinuous shock wave to be also a result of soil nonlinearity in Section 3.6. Finally, the discussion section (Section 4) follows with further comments on the consequences of the observed effects of soil nonlinearity and elastic unloading waves. Finally, the most important findings are listed in the conclusion section (Section 5) of this chapter.

2. Methodology

This section introduces briefly the available experimental data and the conducted numerical studies.

2.1. Experimental work

Shear stack tests in dry soil

Historically, shear stack tests were started in Bristol with work of Dar (1993) and followed by developments of Crewe et al. (1995). The examples of the experimental data used in this thesis for comparisons with numerical studies come from Durante (2015).

The free field response is a subject of the comparison in this chapter. Durante (2015) analysed a five-pile group in a bi-layered soil profile in her studies. However, the acceleration measurements away from the piles were found to be representative of the free field response and not affected by slender kinematic piles. The effects of the shear stack on the soil have also been shown to be negligible by Durante (2015). The soil profile in the shear stack experiments constitutes two soil layers, i.e. the upper “softer” layer and the bottom “stiffer” layer. However, what is important, the intended stiffness ratios were not achieved by either Durante (2015) or in the preceding work by Moccia (2009). The ratio in the average shear wave velocity between the bottom and the top layer was measured to be around 1.6. On the other hand, on the interface this value is expected to be much smaller. In fact, the relative densities for both layers indicated rather small difference, i.e. 25% for the top layer, 41% for the bottom layer (Durante, 2015). What is more, typically, sand stiffness is affected more by changes in mean stresses than in void ratio, thus the stiffness change between the two layers can be expected to be limited to weak C1 discontinuity. This was confirmed by Towhata (1996) who showed that, in fact, shear wave velocity and soil stiffness change in continuous way with increasing depth, even for substantially different soil types within the soil profile. Some further evidence comes from the results obtained by Moccia (2009) who showed that pile axial strains are nearly independent of the modelled soil profile. In detail, a single “soft” layer or a bi-layered “soft” and “stiff” soil profile resulted in the same pile axial strains being recorded. It is worth to note that Moccia (2009) achieved much higher relative density ratio (i.e. 73% at the bottom versus 4% in the top) between the two layers than Durante (2015).

To sum up, the effects of piles, shear stack interacting with soil or a bi-layered soil profile on the presence of additional waves being present in experimental free field

records can be considered negligible. In addition, some further consideration to these aspects is given in the result section of this chapter, for the completeness only.

Further detailed description of the shear stack tests is provided in Chapter 3 (Section 2.1), where the comparison of a 3D finite element analysis with experimental results is presented.

Centrifuge tests in saturated soil

In addition to the shear stack tests in dry soil, some consideration in this chapter is also given to the numerical comparison with the experimental work in saturated soil. Examples of experimental data from the LEAP-UCD-2017 project (Beber et al., 2018) are used to compare with numerical analysis.

The LEAP-UCD-2017 project is an attempt to optimize the experimental techniques in order to improve repeatability of the results obtained from the same experimental setup but from various research centres. In addition, it provides a valuable base for future validation of numerical studies.

The geometry of the analysed problem has been simplified in order to facilitate repeatability between different research groups. In detail, the studied problem attempted to model a gentle 5° slope, 4m deep and 20m long, in a rigid container. Ottawa F65 sand was used by all research groups. The numerical study which is employed in Section 3.6 considers only the free field response in the middle of the rigid box, thus assumed to be free of the boundary effects. This assumption will be discussed further when presenting results in Section 3.6.

The summary of all the centrifuge tests from all the participating centrifuge centres is provided by Kutter et al. (2019) where also other more detailed studies are referenced, such as Madabhushi et al. (2020) which is used in this chapter for the result comparisons in Section 3.6.

2.2. Finite element analysis

The finite element analysis comprises of three parts. Firstly, a semi-infinite soil column is analysed with a simplified constitutive law (Section 3.1) and an example of an elastoplastic model (Section 3.2). Secondly, the three advanced constitutive models (described in Chapter 1) are used in Sections 3.3 (S-waves) and 3.4 (P-waves) to obtain the free field response in dry soil as per geometry of a soil column in the shear stack tests (Durante, 2015). Section 3.5 is an extract from Chapter 3 where the effects of unloading waves on a kinematic pile are shown. Finally, the ST model is used to model a saturated soil column representative of the free field response in the middle of the slope analysed in the LEAP-UCD-2017 project (Section 3.6).

Simplified finite element analysis of semi-infinite column

Two constitutive models are used in this study, namely a simplified constitutive law and an example elastoplastic model (i.e. the ST model) to indicate two sources of higher harmonics generated in acceleration records.

The first constitutive relationship for a simplified study of shear wave propagation in soil has been reduced to a 1D hyperbolic law. Therefore, dilation and p-wave generation, split into elastic and plastic parts, dependence on depth are removed from consideration. The constitutive law has been implemented in the umat format by Gajo (2019) and the changing stiffness is in a form of:

$$\frac{\Delta\tau}{\Delta\gamma} = \begin{cases} \frac{(-\tau_{lim}-\tau)^2}{2 \cdot B \cdot \tau_{lim}} , & \text{for } \Delta\gamma < 0 \\ \frac{(\tau_{lim}-\tau)^2}{2 \cdot B \cdot \tau_{lim}} , & \text{for } \Delta\gamma > 0 \end{cases}$$

where τ_{lim} is the limiting shear stress (in this study $\tau_{lim}=4000\text{Pa}$ constant throughout the depth), τ is the current shear stress and B is the model constitutive parameter (in this study $B=0.001$) to modify the plastic stiffness. The chosen integration scheme is explicit. The typical model response is shown on Figure 1.

Wave propagation in the case of the use of both of the constitutive models (simplified hysteretic and ST model) has been analysed in a 1D soil column (but without depth dependence). The input motion applied at the bottom of the soil column consists of a horizontal acceleration having the shape of 25Hz sine-dwell input motion of an increasing amplitude ranging from 0 to the maximum amplitude of 0.077g. Very small element size of 0.00625m has been chosen in order to reduce amount of spurious oscillations that are described below. Eight node, quadratic finite elements have been used. To avoid the effects of reflected waves at the upper soil boundary, a very long soil column has been considered. No initial shear strains or stresses are introduced in the soil column.

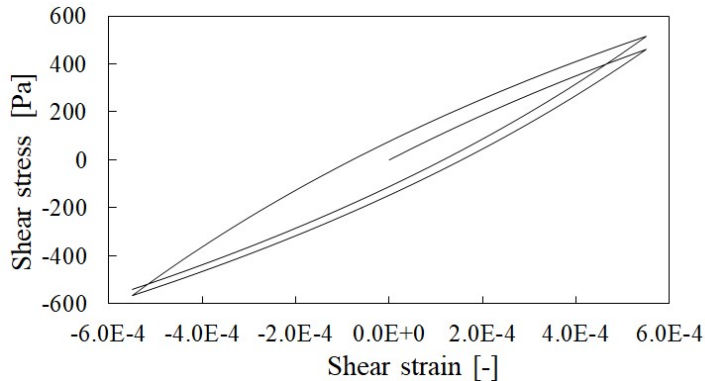


Fig. 1. Typical response of simplified 1D constitutive model.

Finite element analysis of dry soil in shear stack

The numerical analyses included a 0.8m high soil column discretized with an 8-node, quadratic finite elements of 0.05m (for 10Hz input motion for S-wave propagation and 20Hz input motion for P-wave propagation) and 0.025m size (for 25Hz input motion and earthquake input motion). This mesh refinement has been found sufficient to ensure that the conclusions on the results do not depend on the mesh size. All three advanced soil constitutive models presented and calibrated in Chapter 1 have been employed.

A short extract from the results of Chapter 3 for the 3D numerical analysis, is also shown in Chapter 2 (Section 3.5) for the completeness of the effects of soil nonlinearity and unloading waves on an example structure. Details on mesh and discretization of the 3D model are given in Chapter 3.

Finite element analysis of saturated soil in centrifuge

In addition, a case of saturated soil column has been analysed by means of the ST model. A free field response in the middle of the slope of the experimental set-up (Kutter et al., 2019) has been analysed. Several numerical studies have been carried out within LEAP-UCD-2017 project (Manzari et al., 2019) where, to the author's knowledge, the majority of the predicting teams used the input motions with higher harmonics being present as recorded at the shaking table. On the other hand, in this study, the author introduced the 1Hz input motion as a perfect sine in order to observe the capability of the numerical model to generate higher harmonics also in the case of saturated soil.

The numerical study for saturated soil has been carried out by means of a developed user element with the implemented u-p formulation for saturated media and the ST model (Gajo, 2018). The u-p formulation, which is known to have some limitations, has been used in this study within the allowable ranges as presented in (Gajo & Argani, 2020). The element size is 0.05m which is significantly smaller than in majority of the numerical studies within the LEAP-UCD-2017 project.

Soil is represented by a 4m soil column in the middle of the box. The effect of rigid boundaries is assumed to be negligible for the study in question. No effect of the slope geometry, i.e. unequal stress state on both sides of the column, has been considered. However, some consideration to this assumption will be given in Section 3.6.

The calibration of the ST model is updated as per the work presented in Chapter 4 (Section 2.2), as it was found to be more accurate to simulate saturated soil behaviour.

3. Results

The result section presents firstly numerical introduction to the topic with a simplified study on shear wave propagation followed by a comparison of advanced numerical studies and experimental evidences of higher harmonic generation due to soil nonlinearity and elastic unloading waves, primarily in dry soil but also in saturated soil. The following subsections are described: shear wave propagation in a semi-infinite column with a simple hysteretic model (Section 3.1) and subsequently with an example elastoplastic model (Section 3.2) to reveal the two sources of higher harmonics generated due to elastic unloading waves, shear wave propagation in a shear stack in dry sand (Section 3.3), compression wave propagation in a shear stack in dry sand (Section 3.4), impact of generated harmonics on a kinematic pile (Section 3.5) and shear wave propagation in centrifuge in saturated soil (Section 3.6).

3.1. Shear wave propagation in semi-infinite column with simplified hysteretic law

This section discusses S-wave propagation in a semi-infinite soil column modelled with a simple hyperbolic constitutive law without depth dependence being included (Gajo, 2019) as described in Section 2.2. The aim of this section is to show the sine wave distortion due to fast unloading waves.

Figure 2 shows the history of applied horizontal acceleration at the soil base and the computed accelerations at different distances from the soil base with accompanying shear strains. Figure 3 shows the spectral acceleration response. It can be noticed that the initially perfect sine wave loses its shape and becomes progressively distorted with the increasing height. In particular, a tendency to form a “jump” in the acceleration time history can be observed, namely the initial sine wave starts to resemble a “square wave” with the increasing propagation length. The “jump” in acceleration corresponds to the moment of unloading, i.e. a change in shearing direction. Due to the inability of a standard finite element formulation in representing shock waves, the “jump” in acceleration is followed by spurious, high frequency oscillations, with an amplitude that increases with the propagation length and generally depends on mesh and time refinement. It is worth observing that the “jump” in acceleration is associated with an “edge” in the shear strain history (i.e. weak C1 discontinuity). Note that the shear strains are also initially perfectly sinusoidal and change only with height (i.e. propagation length) into the “edgy” form.

Figure 3 shows that the change of the shape of the original sine wave in a sort of a “square wave” and is associated with the generation of higher harmonics having a regular frequency pattern 3ω , 5ω , 7ω etc. in the spectral response. The response spectra of the numerical results were computed with an FFT transform applied to a windowed part of the signal, in order to have a length of the window, which is a multiple (here typically 7-8 times) of the single input cycle, thus avoiding the generation of spurious harmonics. Importantly, high frequency oscillations following the acceleration “jumps” in Figure 2 are thought to be due to numerical effects and have a much higher frequency than those shown in Figure 3. Generally, this thesis assumes such an explanation for the very high frequency oscillations but some doubt on, whether these are only numerical or maybe partly physical (due to potential multiple interactions between fast unloading waves with slow loading waves), may be raised. Only future studies using more advanced numerical tools would allow clarification.

Since numerical simulations in Sections 3.3, 3.4 and 3.5 are compared with experimental measurements that were filtered with a low-pass filter of 80Hz, the numerical results in this section are also treated with a similar low-pass filter (a Butterworth filter 80Hz, 5th order). Figure 4 shows the numerical results after such

filtering. It can be noticed that the sudden “jump” in the computed accelerations now changes into a geometric feature resembling a sort of a “wiggle”.

To conclude Figures 2-4, the nonlinear hysteretic behaviour resulting in fast pursuing unloading waves generates higher harmonics in the semi-infinite column. In detail, the nonlinear stress-strain response induces a clearly visible distortion of the propagating waves and weak discontinuity in shear strains (Figure 2) and leads to a regular frequency pattern of 3ω , 5ω , 7ω in the spectral response (Figure 3). Note that such higher frequencies in the spectral response are representative of a “square wave” and are not physical higher frequency motion (as opposite will be shown in Section 3.2).

Moreover, the soil response is affected also by the initial conditions and by the input motion. Figure 5 shows the effects of non-symmetric acceleration input loading that was obtained by applying the maximum acceleration amplitude of $0.077g$ from the very first loading cycle (namely without an amplitude steadily growing over cycles). This input motion leads to a stronger accumulation of shear strain on one side of the soil column, inducing a sort of non-symmetrical loading (with larger shear strain in one direction with respect to the other), when comparing to the symmetric loading considered in Figures 2-4. As a result, the effect of unloading is stronger on the first unloading in the sine cycle as can be seen in the oscillations in the acceleration and in the shear strain records (Figure 5). The unsymmetrical loading leads to stronger oscillations of the accelerations in one branch of the sine curve, thus the acceleration “jumps” (and the related spurious high frequency oscillations due to the FEM discretization) are larger on both sides of the sine curve. It is worth noting that the generated harmonics in Figure 6 include now also even harmonics (2ω , 3ω , 4ω etc.) which were absent in the case of the symmetrical loading (Figure 3). The reason of the non-symmetric behaviour can be understood in Figure 7 showing the stress-strain cycles evaluated at a Gauss point placed at about 1m height above the soil base. Figure 7a shows stress-strain curves for a symmetrical loading case. Figure 7b (non-symmetrical load case) shows clearly that during the loading cycles there is a clear difference between loading and unloading stiffnesses on one side (bottom in Figure 7b), whereas on the other side the difference between loading and unloading stiffnesses is practically negligible (top in Figure 7b). For completeness, Figure 8 shows the numerical results after filtering with a low-pass filter of 80Hz, where “wiggles” appear in the computed accelerations.

Finally, Figure 9 shows a shear strain profile with height of the semi-infinite column to reiterate in a different manner the effects of the pursuing unloading wave. The “sharpening” of the shear strain profile when unloading (change in shearing direction) happens can be observed with increasing height of the column. At the bottom of the column (less than 0.5m) the shear strain profile is still smooth and resembles sinusoidal input motion applied. This changes with propagation length and weak C1 discontinuity in the shear strain profile is observed. Furthermore, for the symmetrical loading (Figure 9a), it can be observed that the initial part of the input

motion of a gradually increasing amplitude, is not sufficient to induce the strain “sharpening” effect (above 3.5m height), otherwise achieved when higher amplitude motion arrives (below 3.5m height). Such observation can be explained by low nonlinearity in the column and the little difference in the velocities between the loading and unloading waves.

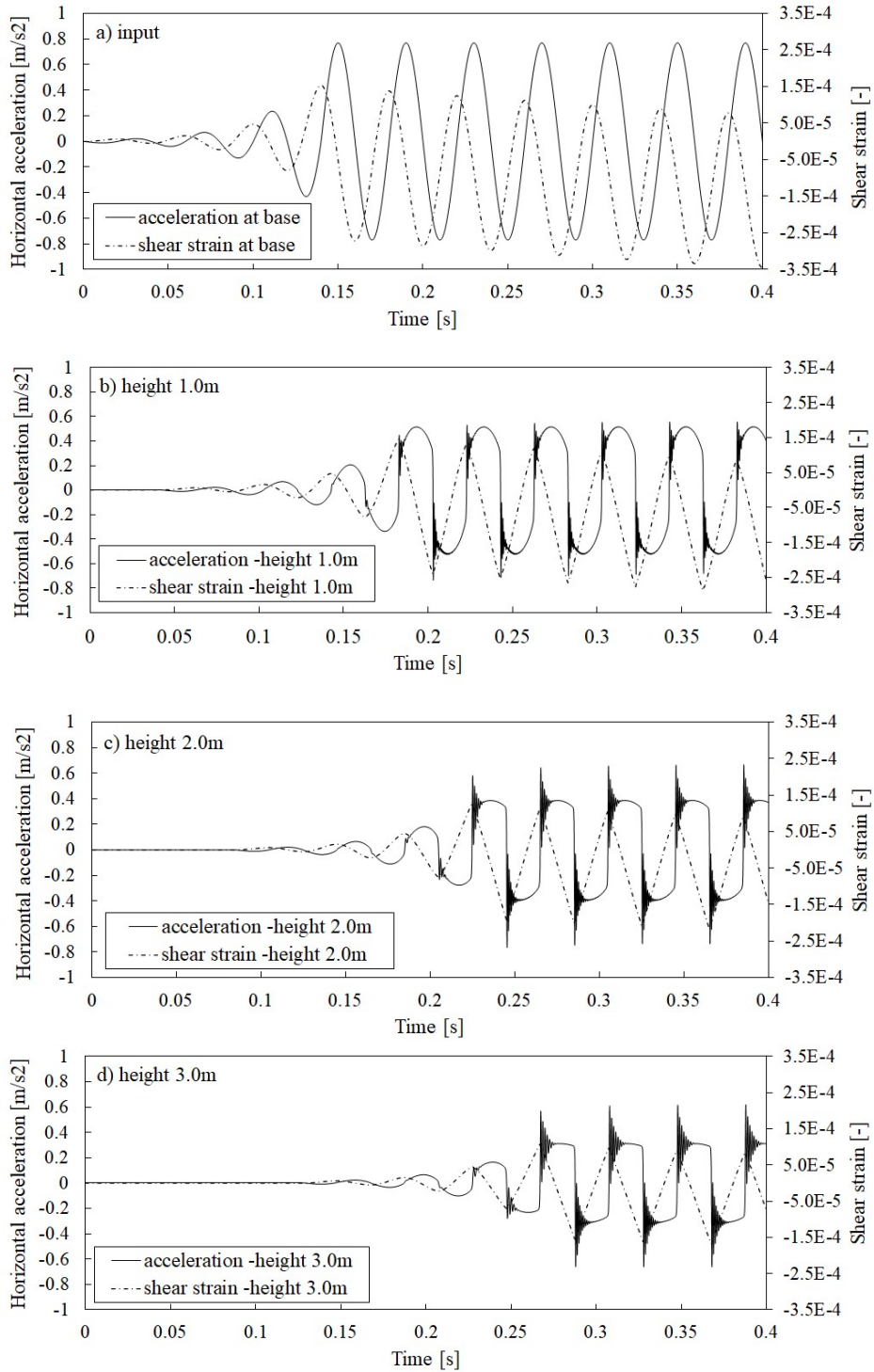


Fig. 2. Unfiltered horizontal acceleration and shear strain records: a) input motion, b) height 1.0m, c) height 2.0m, d) height 3.0m.

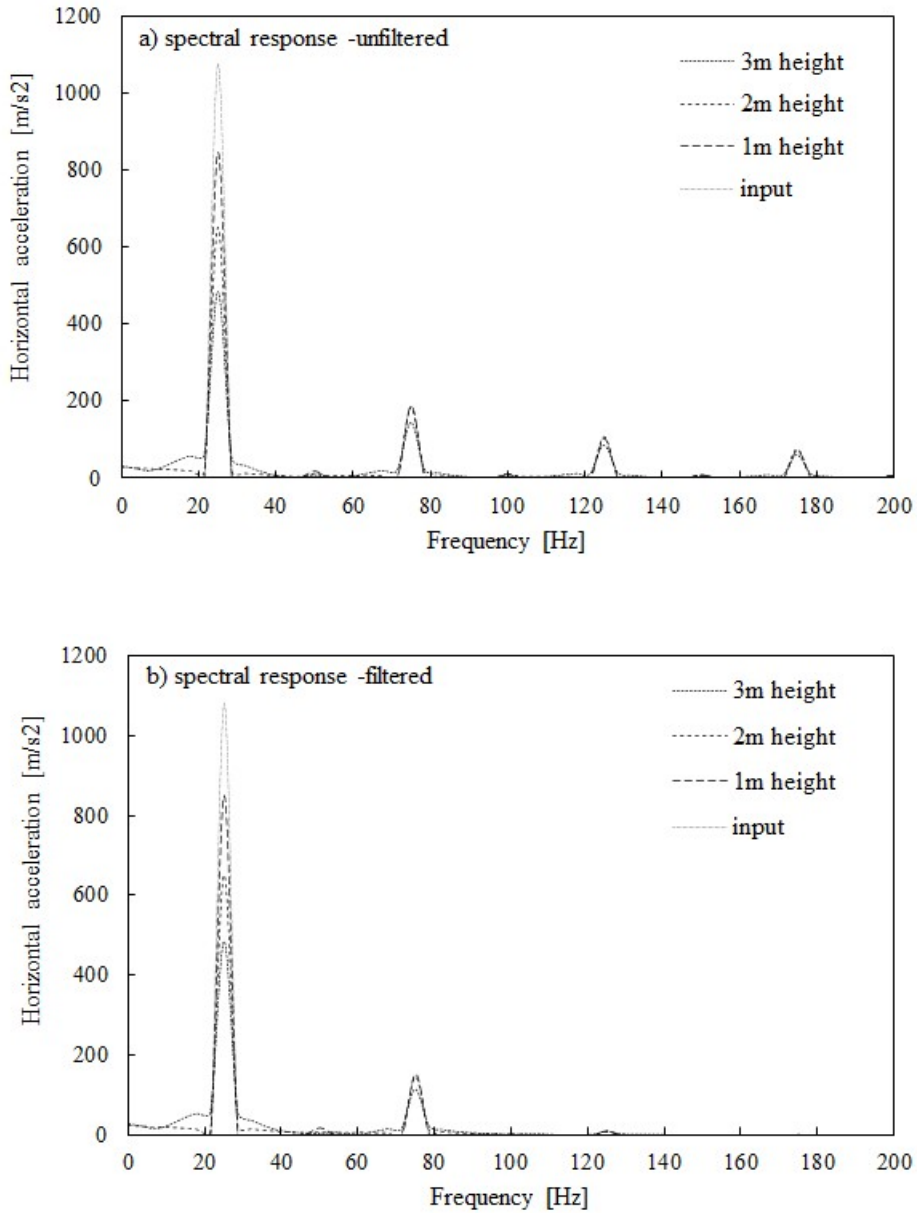


Fig. 3. Spectral horizontal acceleration changing with depth for unfiltered (a) and filtered motion (b).

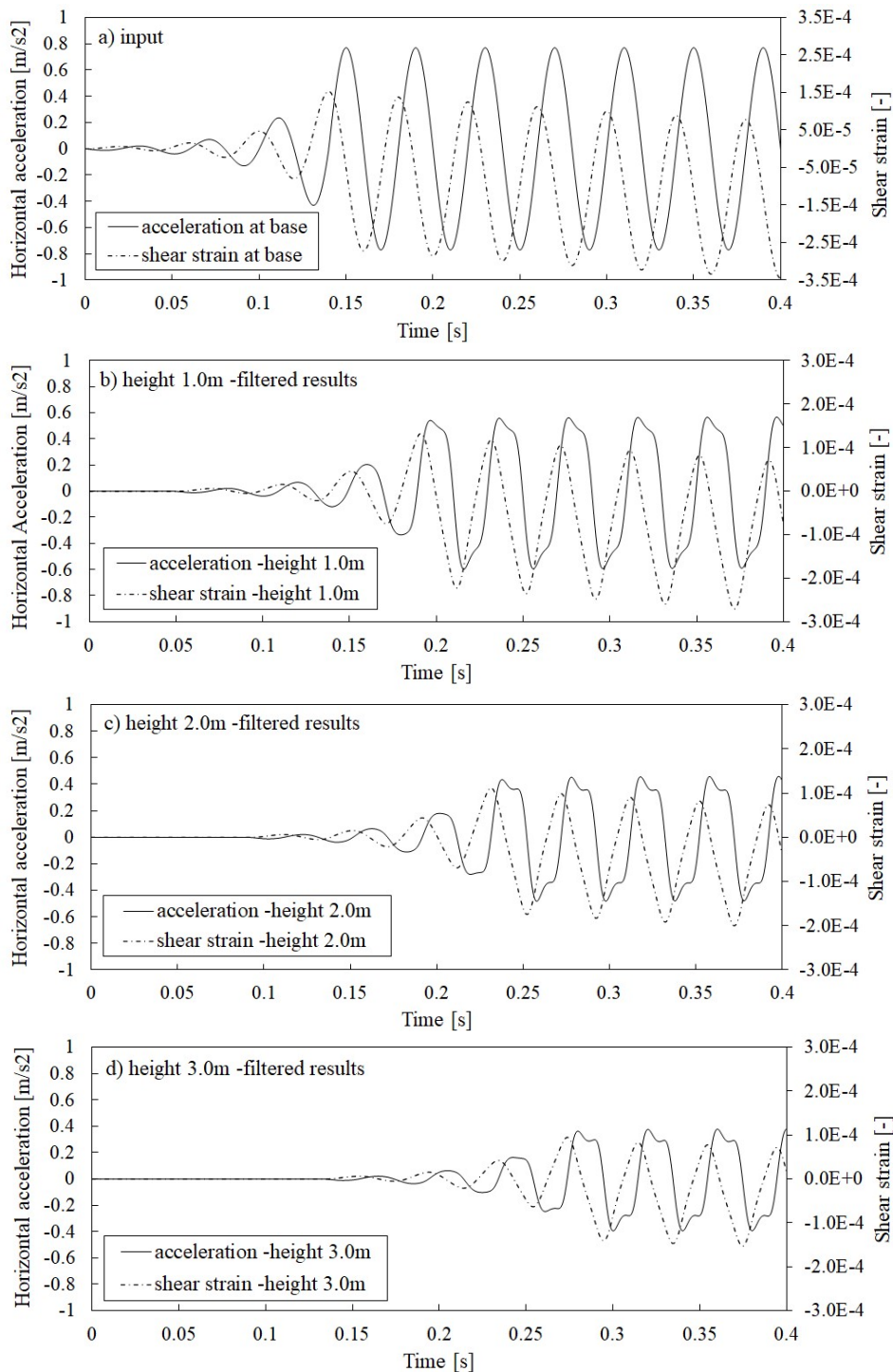


Fig. 4. Filtered horizontal acceleration and shear strain records: a) input motion, b) height 1.0m, c) height 2.0m, d) height 3.0m.

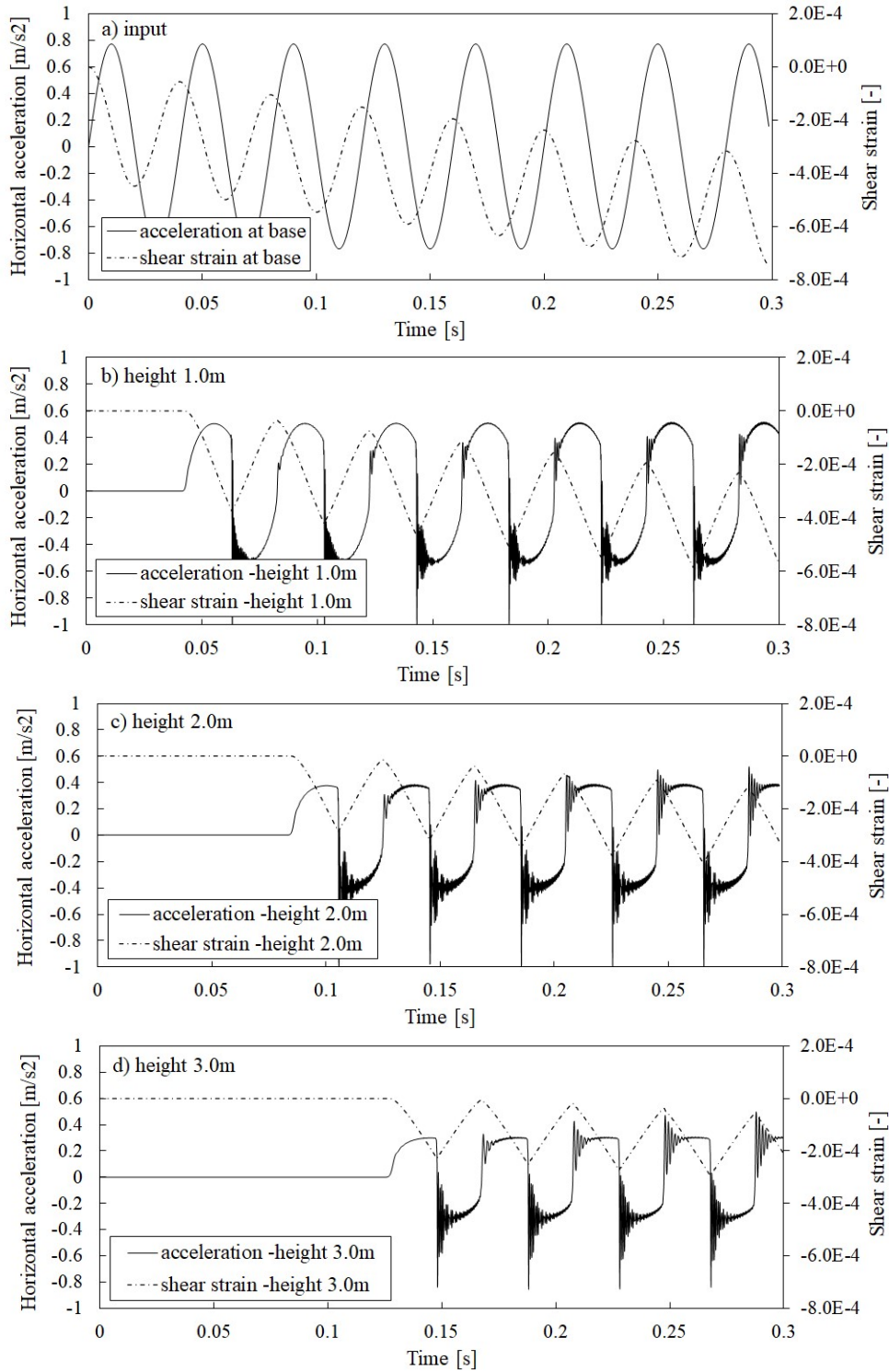


Fig. 5. Unfiltered horizontal acceleration records for nonsymmetric loading: a) input motion, b) height 1.0m, c) height 2.0m, d) height 3.0m.

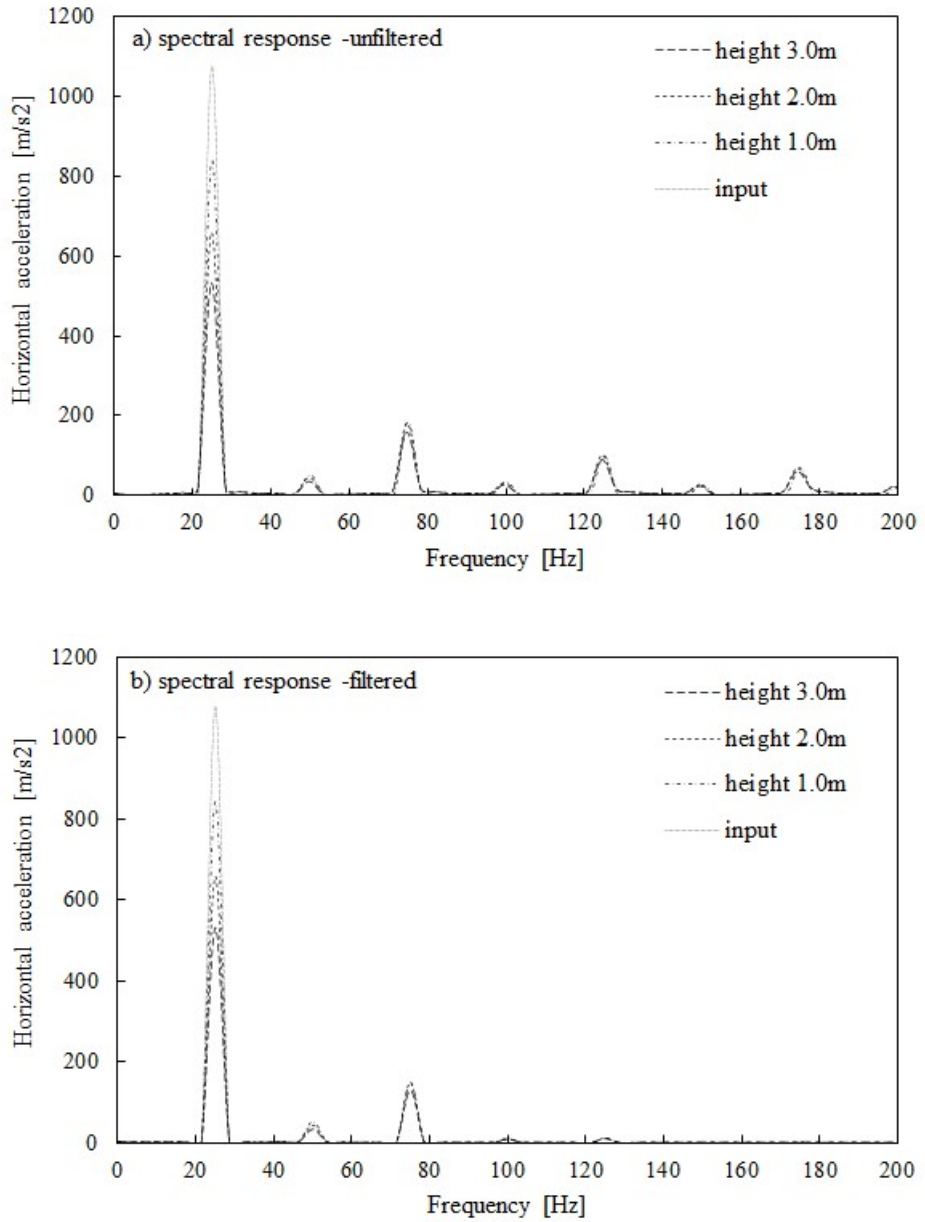


Fig. 6. Spectral horizontal acceleration changing with depth for case of nonsymmetric loading unfiltered (a) and filtered motion (b).

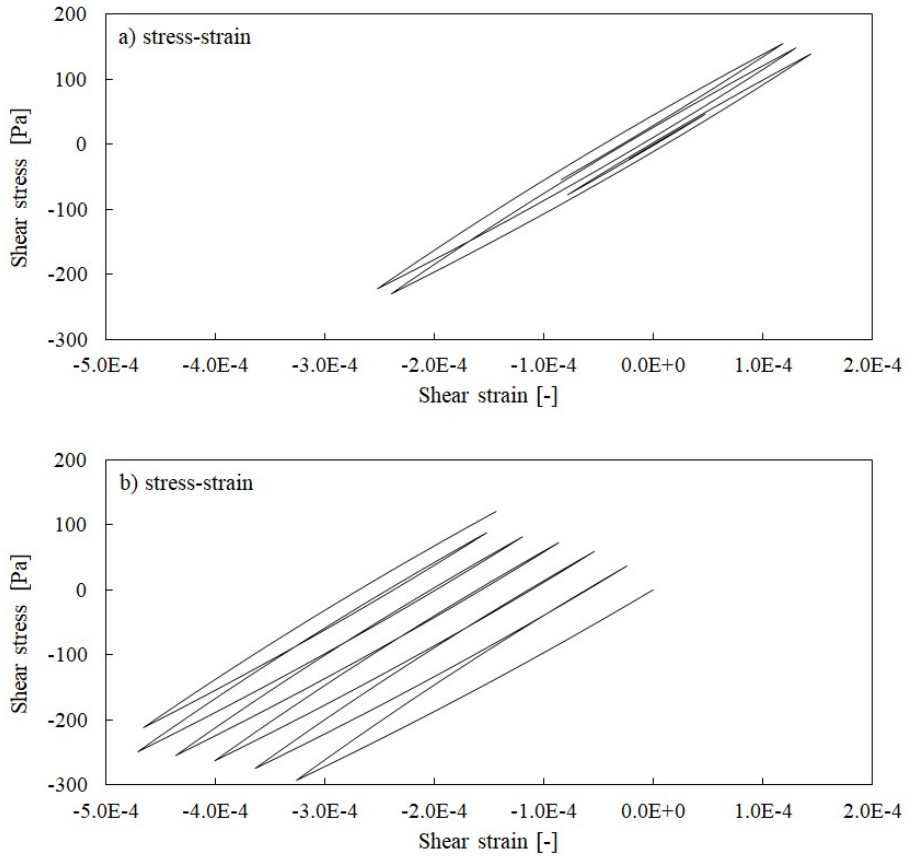


Fig. 7. Stress strain response in case of symmetrical loading (a) and unsymmetrical loading (b) as per Gauss point 1m above soil base.

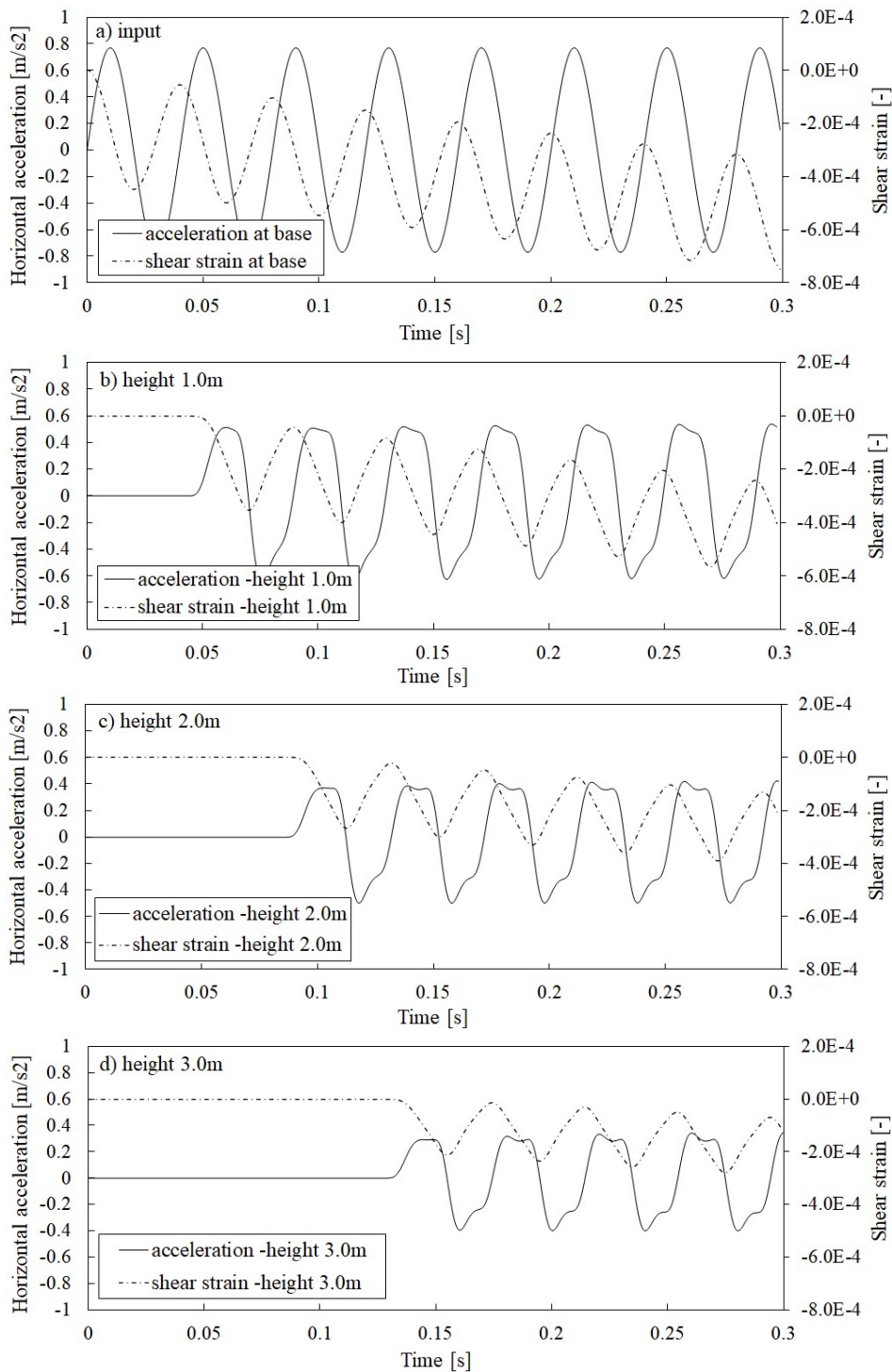


Fig. 8. Filtered horizontal acceleration records for nonsymmetric loading: a) input motion, b) height 1.0m, c) height 2.0m, d) height 3.0m.

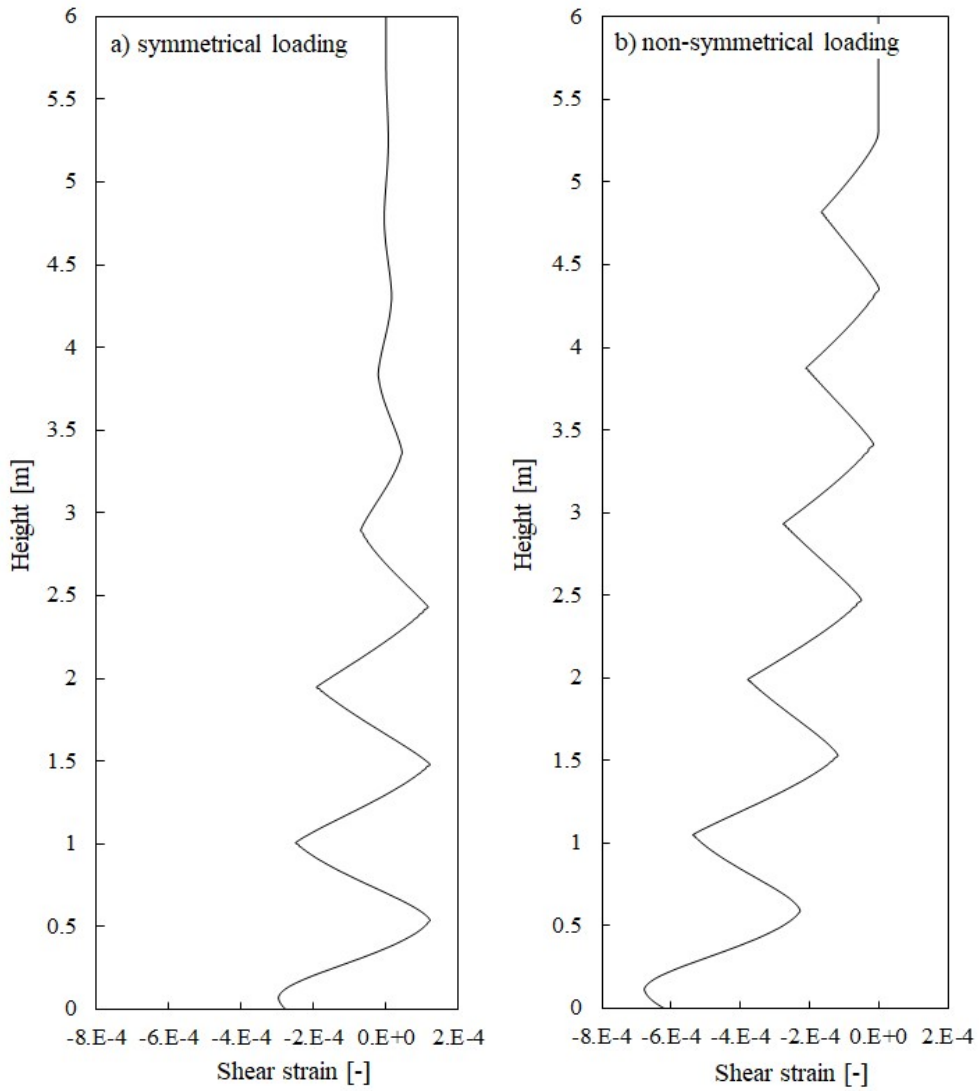


Fig. 9. Shear strain profile with increasing height of column for: a) symmetrical loading (at propagation time $t=0.2403s$), b) non-symmetrical loading (at propagation time $t=0.2250s$).

3.2. Shear wave propagation in semi-infinite column with example elastoplastic model

This section discusses S-wave propagation in a semi-infinite soil column modelled with an example elastoplastic constitutive law without depth dependence being included. The aim of this section is to show the second source of higher harmonic generation due to fast elastic waves (loading or unloading), i.e. the separation of the elastic part of a wave from the plastic part.

In this section, wave propagation has been analysed in a long 1D soil column to ensure no reflections from the free end. The chosen elastoplastic model is the Severn-Trent sand model (Gajo, 2010) described in more details in Chapter 1 although other elastoplastic models could also be used here. The input motion, the element type and the element size are as per the simplified study shown in Section 3.1. In detail, two 25Hz input motions are used here, firstly a short loading pulse (approximately half 25Hz sine of the 0.077g maximum amplitude), secondly continuous 25Hz sine input motion as per Section 3.1. The constitutive model calibration is as shown in Chapter 1. The soil column is assumed to have constant pressure along the full depth (approximately 13kPa, i.e. relevant for the mean stress at the bottom of the shear stack and resulting in elastic shear wave velocity of around 115m/s for the assumed density of 2000kg/m³). Thus, depth dependent effects are neglected in this study. In fact, the main highlight between the two simplified studies is the example elastoplastic constitutive law in Section 3.2 consisting of additive elastic and plastic strains as in opposition to the study shown in Section 3.1 where fully irreversible behaviour was modelled. The point of using an example elastoplastic model within the same geometry as shown in Section 3.1 is to show the second source of the generated higher frequencies in the shear stack, i.e. the separation of the elastic part of a wave from its plastic part. These findings will be shown to be important when discussing results in Section 3.3 and Section 3.5.

Figure 10 shows the results for pulse input motion (approximately half sine, Fig. 10a) of the maximum amplitude of 0.077g. Such a pulse has been chosen to ensure reaching plastic strains but no unloading in the semi-infinite soil column to show additional source of higher frequencies being related only to the change from elastic to plastic loading. In fact, the additional source of higher frequencies is clearly visible as a sort of a “bump” in the computed unfiltered accelerations (Figure 10bcd and 11a) and can also be observed in shear strains as a “passage of a slower strain” (in dotted circles in Figure 11b). The “bump” occurs when the plastic strain is reached and increases its amplitude with the propagation length as shown in Figure 10. Clearly, a gap between elastic and plastic part (or elastic and plastic strain) of the pulse occurs only for large propagation length (Figure 10d). Figure 11 shows that the “bump” in the acceleration time histories and the “passage of slower shear strains” travel in the soil column with the elastic shear wave velocity (1m reached in approximately 0.0085s,

i.e. with the elastic shear wave velocity of 115m/s). Thus, we can consider such effect and refer to it as the separation of the elastic part of a wave from its plastic part. The existence of such separation of the elastic part as shown in this study is expected in the theory of dynamic elastoplasticity as explained, e.g. by Wang (2007), where a faster elastic precursor wave is followed subsequently by a slower plastic wave.

Now Figure 12 shows the results for the continuous 25Hz input motion (steadily increasing to 0.077g) and the two sources of higher frequencies are shown together (i.e. wave distortion explained in Section 3.1 and elastic wave separation explained in this section). Similarly, to the results shown on Figure 2, the shock wave is formed, and the wave distortion can be clearly seen for higher amplitudes of the input motions ($t > 0.15\text{sec}$) and for larger propagation lengths (i.e. greater than 1m). In contrast to the results obtained with a simplified constitutive law (Figure 2), the second source of higher frequencies can be observed in Figure 12 for the lower amplitudes of the input motion, i.e. before the shock wave is formed (Figure 12b and 12c before 0.15sec) and for short propagation lengths even for the higher amplitudes of motion (Figure 12b). This source of higher frequency is not coincident with the moment of unloading at the referenced height (as shown before in Figure 2). Note that when the response is purely elastic, i.e. for $t < 0.1\text{sec}$, the separation of the elastic wave is not present in the computed accelerations and starts to occur only when plastic strains develop for the larger amplitudes of the input motion.

The additional reason to think that such a “bump” is related to elasticity were parametric studies (not shown in the thesis) carried out with the simplified model used in Section 3.1. These studies indicated that the position of the “wiggle” could not be moved, i.e. for the purely plastic behaviour the “wiggle” is associated only with a sharp edge in strains and represents only wave distortion towards a “square wave”. Such observation led the author to try to use an elastoplastic model in a similar study as shown in Section 3.1. Indeed, Figure 12 shows that the acceleration time history for the elastoplastic material has small irregularities (“bumps”) which were absent in Figure 2 for purely plastic material where only strain discontinuity appeared.

Note that the position of the arrival of the separated elastic part changes with the amplitude of the input motion. In more detail, for lower amplitudes (i.e. when the motion steadily grows in amplitude), such arrival takes place “late” in the sine loading cycle, just before the next unloading (see long arrows in Figures 12b and 12c). In contrast, for the increasing amplitude, the arrival of the separated elastic part is closer to the preceding unloading (see short arrows in Figures 12b and 12c). This is due to the increasing amount of plasticity in the soil column; thus, the separated elastic part appears sooner after unloading in sine loading cycles of higher amplitude.

Finally, note that once a shock wave is formed due to weak discontinuity in shear strains (as explained in Section 3.1), very high frequency numerical oscillations, attributed previously to numerical problems, dominate and overcast the presence of the separated elastic part (Figure 12c) which for relatively high amplitudes are very

close to the unloading moment (very short arrows in Figure 12b and very short arrows with question marks in Figure 12c).

For completeness, Figure 13 shows a zoom-in on the computed accelerations and strain time histories. Figure 14 shows spectral response and Figure 15 shows acceleration records being filtered as per the experimental work shown later. The applied filtering (80Hz Butterworth, 5th order) reveals how such filtering can mask the presence of the separated elastic waves which disappear in the filtered computations, as the ‘wiggles’ shown in Figure 15 correspond only to the wave distortion (i.e. harmonics lower than 80Hz) and are not representative of the separated elastic waves. This observation will be important again when evaluating results in Section 3.3.

Finally, Figure 16 presents a shear strain profile with the increasing height of the column for the continuous 25Hz sine input motion to reiterate findings shown before. In detail, at a higher height (i.e. height >20m) the response is purely elastic and the effects of fast elastic unloading waves do not occur. Slightly below, the effects of fast elastic unloading waves are limited to the separation of the elastic part as shown in the dotted circles. These are clearly present when only little plasticity develops as the amplitude of motion is not large enough to generate discontinuity in strains and shock wave formation. When the amplitude reaches its maximum, shock wave formation can be observed, i.e. C1 discontinuity in the shear strain profile can be observed. Such discontinuity forms only with longer propagation length, i.e. at the very bottom of the column, such discontinuity in shear strains is not yet reached and almost perfect sine motion can be observed.

Note that the study presented here is still not comprehensive. The interested reader is directed to Wang (2007) where some further explanation for such separation of the elastic part is provided. The effects of depth are also missing from the consideration in this section but also may play a further role and as such should be a subject to the future studies.

A separate comment is needed to justify the title of the Chapter 2, i.e. “Higher harmonic generation due to elastic unloading waves”. Actually, Figures 10 and 11 for a pulse sine input motion show that the elastic part separation happens during the loading of the soil specimen and there is no need for unloading in the time history to induce such effects. However, since the following thesis deals with earthquake loading time histories (either recorded in field or artificial in a sine dwell form) where by definition numerous loading cycles are present, the separation of the elastic part of a wave will be referred as to the effect of fast unloading elastic waves within such cycles (although for the pulse loading in this section it is the effect of fast loading elastic waves).

As a side note only, the author thinks that it would also be interesting to repeat such a numerical study with a more advanced numerical tool which allows dealing with shock wave formation. Such a repeated study would allow to give a clearer picture on the presence of the separation of the elastic part after the weak discontinuity in strains is reached. In addition, it is reminded that this simplified study neglects the

effect of depth on changes in soil stiffness (elastic and plastic). It would again be interesting to present a separated study on the depth effect on higher frequency generation. Such specific study is missing from the consideration in this work due to time constraints. However, the author may investigate this aspect in the future.

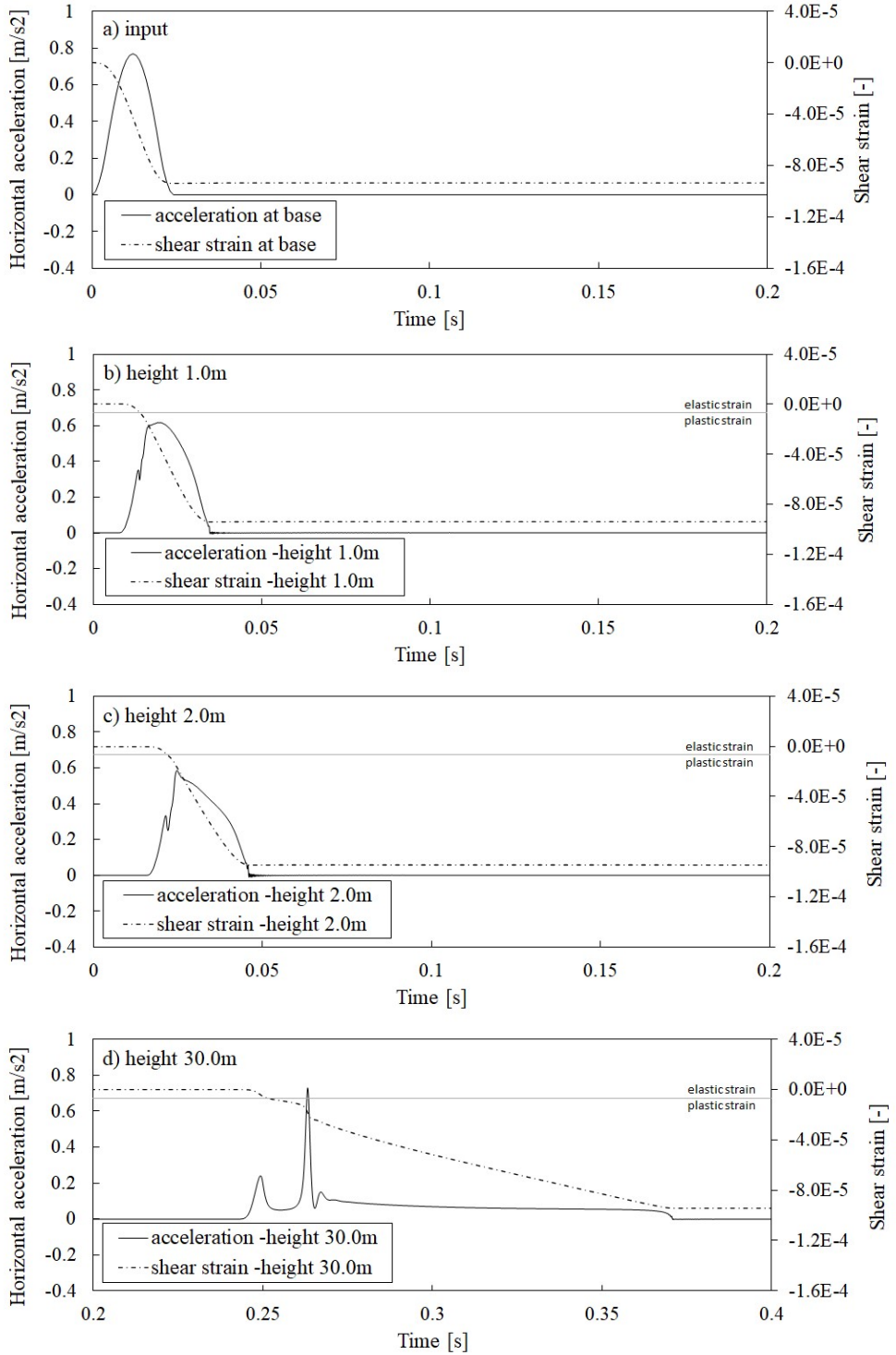


Figure 10. Unfiltered horizontal acceleration records for a semi-infinite column with example elastoplastic model: a) pulse input motion, b) height 1.0m, c) height 2.0m, d) height 30.0m.

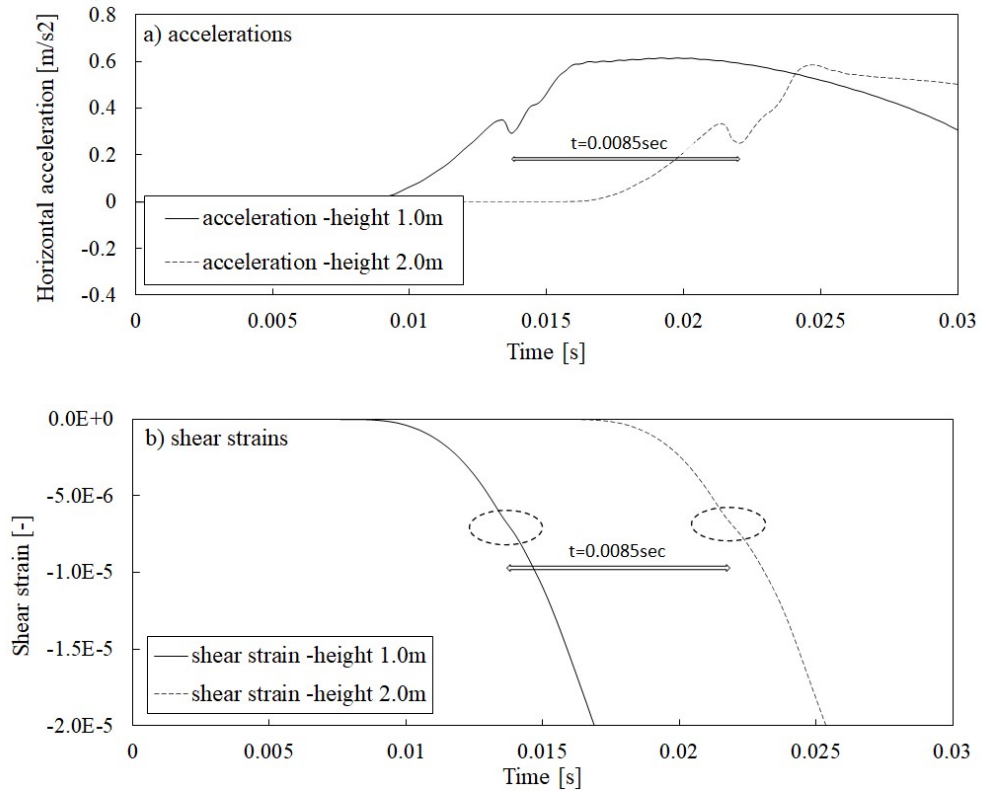


Figure 11. Zoom in of unfiltered horizontal acceleration records (a) and shear strains (b) for a semi-infinite column with example elastoplastic model under half sine pulse input motion at 1m and 2m height.

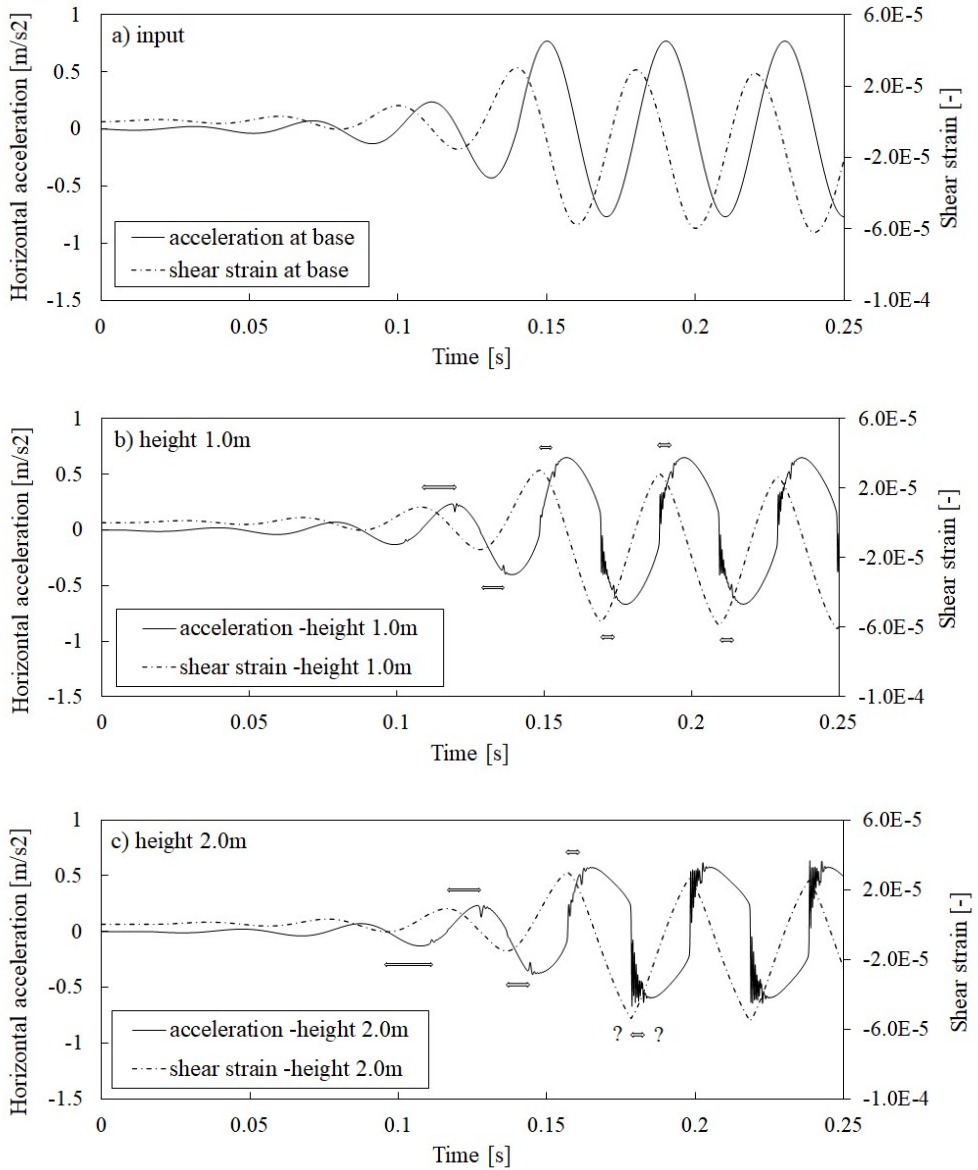


Figure 12. Unfiltered horizontal acceleration records for a semi-infinite column with example elastoplastic model: a) continuous input motion, b) height 1.0m, c) height 2.0m.

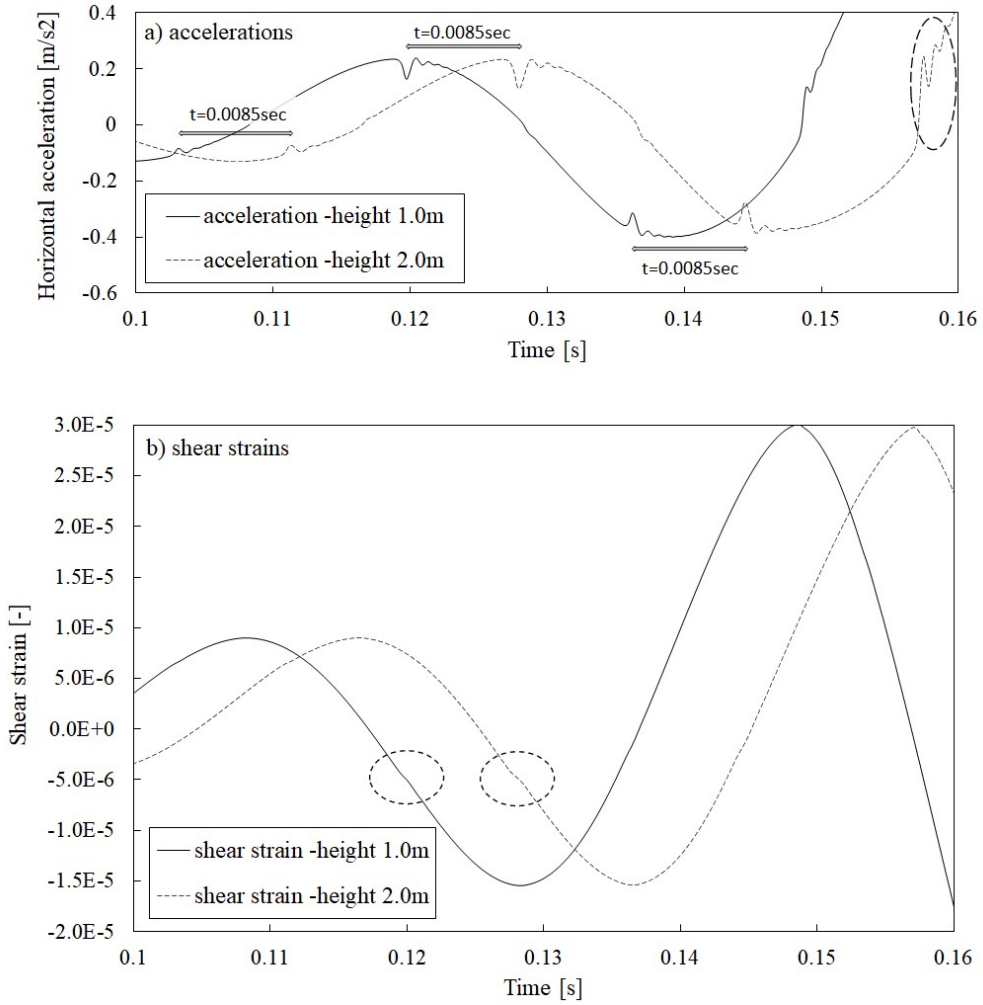


Figure 13. Zoom in of unfiltered horizontal acceleration records (a) and shear strains (b) for a semi-infinite column with example elastoplastic model at 1m and 2m height.

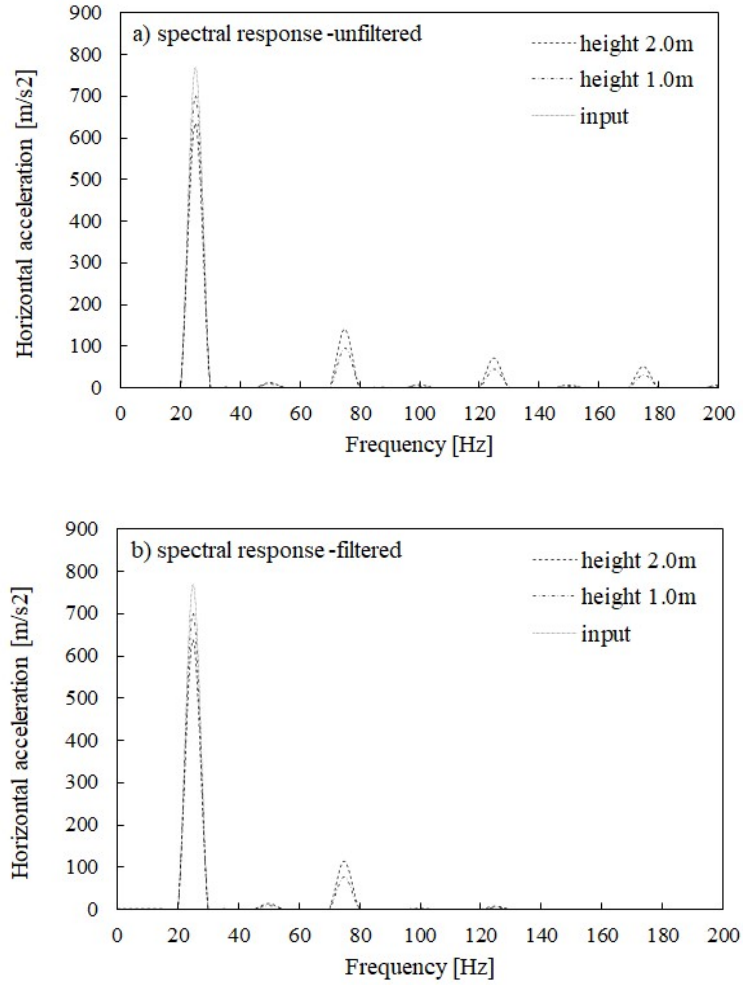


Figure 14. Spectral horizontal acceleration changing with depth for unfiltered (a) and filtered motion (b) for a semi-infinite column with example elastoplastic model.

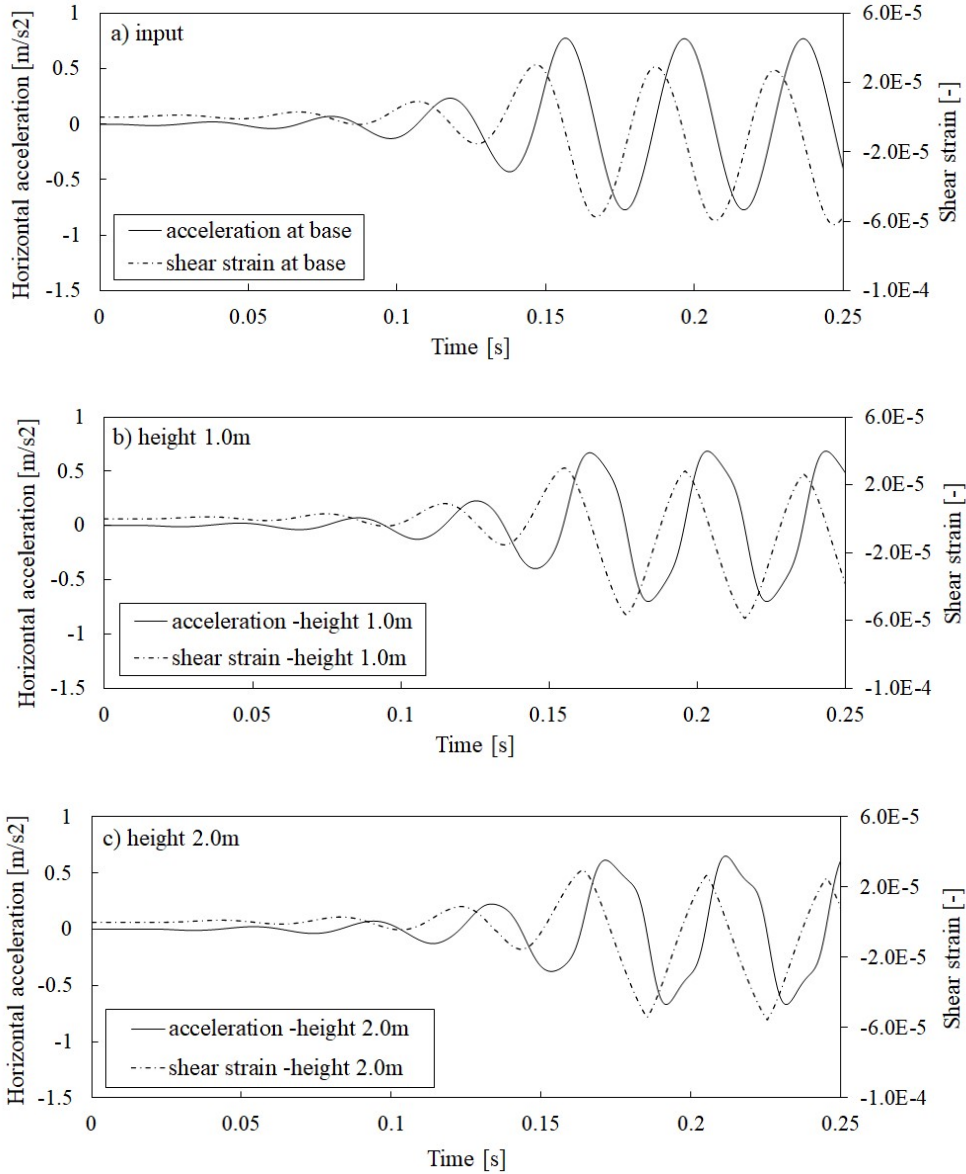


Figure 15. Filtered horizontal acceleration records for a semi-infinite column with example elastoplastic model: a) input motion, b) height 1.0m, c) height 2.0m.

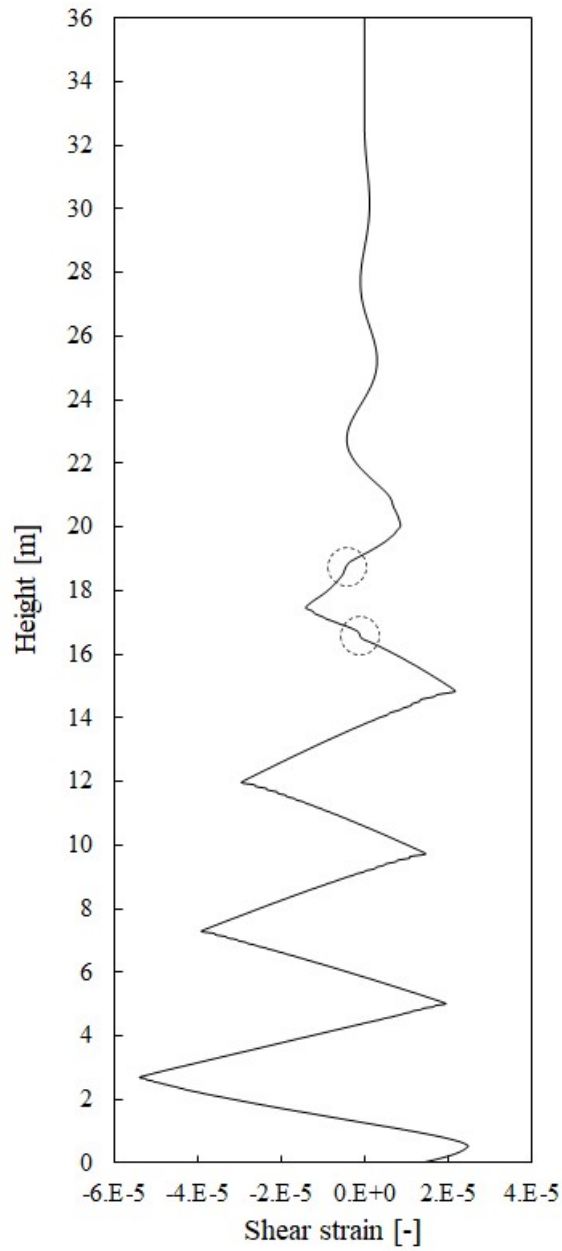


Fig. 16. Shear strain profile with clearly visible separated elastic part (in dashed circles) at propagation time $t=0.2403\text{sec}$.

3.3. Shear wave propagation in shear stack in dry sand

This section discusses numerical simulations and experimental results obtained on dry sand subjected to shear stack tests at 1g by Durante (2015) at Bristol facility (Muir Wood et al., 2002). Only shear wave propagation is analysed in this section.

Two acceleration input motions have been considered: 10Hz (in Figures 17 and 18) and 25Hz (in Figures 19-25). In the former, a sine input motion of 0.137g amplitude has been applied, whereas in the latter two different amplitudes of the input motion, i.e. 0.077g and 0.037g, have been considered, respectively.

The results of the available experimental examples are shown on Figures 17a, 19a and 21a (measurements of the horizontal accelerations at the soil surface) and Figures 18a, 20a and 22a (harmonics evaluated at the soil surface evaluated by the author). A negligible amount of higher harmonics can also be identified at the shear stack base. The input motion in the numerical studies is a perfect sine. Nevertheless, some numerical simulations were performed also with the exact input motion applied in the shear stack tests (including a negligible amount of higher harmonics) and the results practically coincide with those obtained with the perfect sine input motion (see Appendix A.1 for more). The numerical simulations neglected the physical presence of the shear stack, thus only the soil was discretized. However, the inclusion of the shear stack in the FEM model was verified to be ineffective in the higher harmonic generation (see Appendix A.2). Finally, the effect of a bi-layered soil profile of different density characteristics against a single layered soil profile has also been investigated to yield negligible changes in the computed response (see Appendix A.3).

The experimental measurements are compared with the computed acceleration time histories in Figures 17 (10Hz sine input motion), 19 and 21 (25Hz sine input motion), whereas the harmonics obtained from the experimental measurements and from the numerical simulations are compared with each other in Figures 18, 20 and 22, for one 10Hz and two 25Hz input motions, respectively.

For the sake of consistency with the experimental results, the numerical simulations were subjected to the same filtering process applied to the experimental data for eliminating undesired spurious high frequency content, thus, the numerical results were calculated with a sampling frequency of 1000Hz and were subsequently filtered with a low-pass Butterworth filter 80Hz (5th order filter). No phase correction has been applied to the filtered results since it was considered negligible for the investigated subject. As explained in Section 3.1, the response spectra were computed by windowing a part of the signal, in order to have a length of the window that is an exact multiple of the single input cycle, thus avoiding the generation of spurious harmonics.

Figure 17 compares the measured and computed filtered acceleration time histories for the 10Hz input motion. It can be observed that the experimental and

numerical results at soil top show wave distortion, i.e. “wiggles” are generated. Such wave distortion is clearly visible and symmetrical (i.e. the same for unloading on both sides of the shear stack) in the numerical analysis. These effects apparently are less visible for the experimental results, where the “wiggles” are less visible and being less symmetrical (i.e. unloading on one side of the shear stack leads to stronger “wiggles” on this side). In addition, it can be observed that the computed acceleration at soil top are fairly in phase with the input motion which is in agreement with the experimental data (i.e. propagation length is short). Finally, it can be observed that the ST and DM models capture the number of “wiggles” better than the HP model (which shows two “wiggles” after each unloading and four “wiggles” in a full sine loading-reloading cycle). Finally, Figure 18 shows the computed spectral response for the experimental and numerical results and shows that there is a good match between these, thus, beside the input frequency of 10Hz, higher harmonics with frequencies of 30, 50 and 70Hz are generated.

Similar effects can also be observed in Figures 19 and 20, where the input frequency of 25Hz (maximum amplitude of 0.077g) leads to larger “wiggles” in the experimental results (Figure 19a) with respect to 10Hz (Figure 17a). In Figure 19, the horizontal acceleration at the top and at the base of the soil column are out-of-phase with respect to each other (i.e. propagation length is longer). Numerical simulations obtained with the ST model (Figure 19b) are slightly more consistent with the experimental results when comparing to the other models as the HP model (Figure 19c) and in particular the DM model (Figure 19d) show the “wiggles” to be very close to the peak accelerations and a sort of a “flat peak” is obtained. However, the spectral analysis (Figure 20) shows that in both, the experiments and the simulations, higher harmonics with frequency of 75Hz and 125Hz are generated beside the input frequency of 25Hz. It can be noticed that the experimental data (Figure 20a but also Figure 18a) show in addition some relatively small amount of even harmonics being present. This might possibly be related to a non-symmetrical shear strain accumulation in the experiments, because each “new” seismic input motion was applied to a soil sample that was previously shaken, thus some residual shear strain could have been imposed due to previous shaking tests and the initial shear strain state might not have been zero as assumed in all the numerical simulations. Section 3.1 shows an example of when even harmonics are present due to such non-symmetrical loading.

Finally, Figures 21 and 22 investigate the effects of a smaller peak acceleration (i.e. 0.037g) applied at the soil base, for the input frequency of 25Hz. Again, “wiggles” are generated at soil top in the experimental measurements and the numerical simulations. The position of the “wiggles” differs between the experimental and numerical studies, i.e. it is halfway between the maximum and minimum acceleration in the experiment and closer to the maximum and minimum in the simulations. However, the amplitude of the “wiggles” is the same (especially for the ST and HP models) or only slightly smaller (for the DM model). This is confirmed in the spectral response shown on Figure 22, where the regular frequency pattern is shown with

higher harmonics of 75Hz and 125Hz being generated. Note that the horizontal acceleration measured and computed at the top and at the base of the soil column are fairly out-of-phase with respect to each other as shown on Figure 21 (and also Figure 19) which is in contrast to Figure 17. Such shift in phase is related to the natural frequency of the soil column, which is close to 25Hz, thus higher motion amplification is achieved for 25Hz input motions. Nevertheless, it is important to highlight that the generated harmonics for 25Hz input motions are not related to soil natural frequencies but to wave distortion as explained later.

The main conclusion that can be drawn from the application of a single sine input motion is that in both the experimental results and simulations, the frequency of the generated higher harmonics (Figures 18, 20 and 22) is mostly an odd multiplication of the input frequency (although some even harmonics with a very small amplitude are visible in the experimental data as explained above). In addition, the higher harmonics appear as “wiggles” in the distorted acceleration records at the soil surface. These effects are generally well represented by the three constitutive models taken into account. A reduction of the amplitude of the input motion causes the amplitudes of the generated higher harmonics to reduce as well (see comparison of Figures 20a and 22a). Equivalently, the amplitude of the “wiggles” in the acceleration records are also reduced (see comparison of Figures 19a and 21a) if the amplitude of the input acceleration is reduced (0.077g in Figures 19 and 20, 0.037g in Figures 21 and 22). These observations lead to the question whether for even smaller amplitude input motion, the harmonics will actually disappear due to soil behaviour limited to elastic response only (such as shown in the simplified study in Section 3.2). Some numerical consideration to the determination of purely elastic soil response in the shear stack is given in Appendix B.

Figure 23 shows the development of the “wiggle” with propagation length for the 25Hz input motion (0.077g). It can be observed that the “wiggle” becomes more prominent with decreasing depth for both, experimental and numerical results (the latter is limited to the ST model for brevity). This is also confirmed by Figure 24 where the response spectra measured and computed at various depths are compared. The computed response spectra clearly show an increase of the higher harmonics with the increase of propagation length (i.e. decrease of depth). The variation with depth of the numerical simulations is less consistent with the experimental results when comparing response at soil surface. However, the general trend is well captured, i.e. the amplitude of the higher harmonics increases with decreasing depth. Note that the numerical results shown on Figures 23 and 24, although were already satisfactory for the element size of 0.025m, have been computed with a reduced element size of 0.0067m in order to minimize the amount of numerical noise between 25Hz and 75Hz frequencies.

Figure 25 shows the horizontal velocity and displacement histories obtained by careful numerical integration of the measured horizontal accelerations for the 25Hz input motion of 0.077g amplitude. It can be observed that the “wiggles” in the acceleration history does not produce any effect in the displacement histories and only

minor distortion of the sine shape is visible in the computed velocity. The “wiggles” in the acceleration history are observed even for very low amplitude input motions (with relative horizontal displacements less than 0.1 mm), and their amplitude increases with the increase of the amplitude of the input motion and with the decrease of depth. As a result, they cannot be attributed to strain localization due to rather small relative displacement (the upper part of the soil specimen does not seem to move as a rigid block against the lower part) or to “stick-slip effects” in the shear stack (because the “wiggle” amplitude should decrease with the increase of the amplitude of the input motion, since higher driving force should easier overcome the “sticking” force if such was present somewhere in the system).

In general, the position of the “wiggle” in the acceleration time histories within a single sine loading cycle can be thought as a consequence of two effects of fast unloading waves, namely sine wave distortion (longer propagation lengths) or a separated elastic part (shorter propagation lengths). Differentiation between these two effects has been explained in Section 3.2. For example, the experimental results for the 10Hz input motion (longer wave length comparing to the available propagation length of 0.8m) possibly represent a case when the “wiggle” is related to a separated elastic part as the propagation length (0.8m only in the shear stack) versus the wave length is too short for a shock wave to form. On the other hand, the experimental results for 25Hz, 0.077g (shorter wavelength) show the ‘wiggle’ being potentially representative mainly of sine wave distortion. Note that such interpretation is a speculation as the experimental results were filtered out, thus, certain amount of information was removed from the available records. This might be a case especially for the 25Hz input motion, where only second harmonic was left in the spectral response (frequencies above 80Hz were filtered out). Thus, it is of the author’s opinion, that it would be interesting to see the future experimental work being filtered in a more careful way with much higher cut-off frequency.

To strengthen the above speculations, the computed unfiltered numerical accelerations and shear strains for the ST model are shown on Figures 26 and 27 for the 10Hz and 25Hz input motions, respectively. Indeed, these results show shear strain weak discontinuity being reached for the 25Hz input motion but not for the 10Hz input motion. As such the ‘wiggles’ in Figures 26 and 27 can be associated with two different effects of fast elastic unloading waves, i.e. the ‘wiggle’ for the 10Hz input motion is representative of a separated elastic wave, whereas the ‘wiggle’ for the 25Hz input motion can be associated with sine wave distortion, both as explained in Sections 3.1 and 3.2, i.e. the shock wave may not develop in the case of 10Hz input motion (too long wave length), but can develop in the case of 25Hz input motion (shorter wave length). Such interpretation can be supported also by the observation made in the spectral response, i.e. Figure 18b for the ST model, shows higher harmonics without the exponential decay for the 10Hz input motion (i.e. more energy in the harmonic 70Hz than in 50Hz), thus cannot be representative of wave distortion only (which is represented by higher harmonics characterized by the exponential decay).

In addition, some other experimental records (beside acceleration records) further support such speculation regarding result interpretation for the 10Hz and 25Hz input motions. For example, the experimentally measured records of settlement at soil surface are shown here on Figure 28 as well, as these probably were not filtered out. Figure 28a reveals a potential arrival of the separated elastic part of a wave on soil surface. It can be observed that upon the change in the direction of shaking compression is observed, followed by dilation. However, before the subsequent change in lateral displacements, an unexpected short phase of compression and dilation appears which could be the indication of the arrival of the separated elastic part. On the other hand, Fig. 28b presents a more predictable and expected picture, i.e. single compression is followed by dilation within a single loading cycle (some small variations are still observed but difficult to determine if not due to inaccuracy in measurements). A further proof on the presence of the separated elastic waves for the 10Hz input motion will be shown in Section 3.5 where elastic piles will be shown as potential additional measuring instruments which can pick up easier such high frequency elastic parts of waves.

In general, the position of the ‘wiggle’ depends on the amplitude and the wave length of the input motions as explained above and in Section 3.2 but it also changes with changes in elastic and plastic stiffness definition of the constitutive models (so parameters tuning the character of nonlinearity). Some parametric studies shown on Figure 29 for the ST model present how the computed unfiltered accelerations change due to changes in elastic stiffness (increased by 1.6), decrease in the amplitude of the input motion (0.1g), and a reduction in plastic stiffness definition (constitutive parameter $\alpha=1.3$). Note that the calibration of the models here is aimed at larger number of input motions and geometries and is not limited to the input motions and geometries presented in this chapter. Future studies would allow further quantification of all the mentioned effects on the position of the “wiggles”.

In addition, one may note that a bi-layered soil profile such as the one in the experiments of Durante (2015) can be a source of additional wave reflections in the soil column. However, the effects of fast elastic unloading waves are thought to be independent of such a bi-layered soil profile. To confirm that, the Appendix A.3 presents some numerical studies with a single soil layer which support the assumption of negligible effects of the bi-layered soil profile (see Section 2.1 of this chapter) on the obtained conclusions. In addition, one is reminded that typically experimental studies are carried out for a single soil layer (e.g. Lanzano et al., 2012; Kutter et al., 2019) and higher harmonics are still observed in spectral response. Importantly, also previous experimental work in the shear stack in Bristol (Abate & Massimino, 2016) showed higher harmonic generation in spectral response for a soil profile with a single soil layer. Thus, higher harmonics observed and computed for the bi—layered soil profile shown in this study can be predominantly considered to be the result of soil nonlinearity and fast elastic unloading waves, and to a negligible level as a result of wave reflections at interface of the two soil layers. Nevertheless, if future experimental

work dedicated towards the observation of wave distortion and separated elastic waves was carried out it would benefit from the assumption of a single soil layer only.

Finally, the effects of fast elastic unloading waves are important even in the analysis of real seismic input motions in shear stack tests and are expected to be important in real field measurements. Figure 30 shows the comparison between the measurements performed on dry soil in the shear stack and the simulations obtained with the three advanced constitutive models. Scaled Tolmezzo earthquake input motion with a maximum acceleration of 0.112g was applied at the soil base in the shear stack tests. The numerical results were filtered with a low-pass filter as described in Section 3.1. It can be observed that higher frequencies, not introduced with the nominal input motion, are present both in the experimental measurements and in the numerical results. Figure 30 shows that higher harmonics with frequencies around 60-80Hz are generated in the experiments and are well predicted in the numerical simulations, although not present in the nominal input motion. It is important to note that the generated frequencies have a range approximately three times larger than the dominant input frequencies (20-30Hz).

In addition, Figure 31 shows a part of the measured and computed acceleration time histories between 0.1 and 0.7 second. These possibly reveal that wave distortion (in dashed circles) and arrivals of separated elastic waves (dotted circles) can apparently be spotted in both, the experimental measurements and numerical simulations. Again, it is of the author's opinion, that the experimental results would be worth to be seen without filtering being applied, since the two effects in question could potentially be captured in a clearer way.

For completeness, Figure 32 shows a part of acceleration time history for the 1985 Mexico City earthquake where soil free vibrations were observed, i.e. the shown acceleration time history is recorded after the incident waves ceased (Ruiz & Saragoni, 2009). Importantly, also here one might be tempted to attribute the characteristics of the recorded motion to wave distortion and separated elastic waves (note that here the acceleration records were probably not filtered). Note that such interpretation as shown on Figure 32 is author's speculation only but he could not restrain himself from such pondering in this section even if it is dedicated to S-wave propagation in shear stack tests.

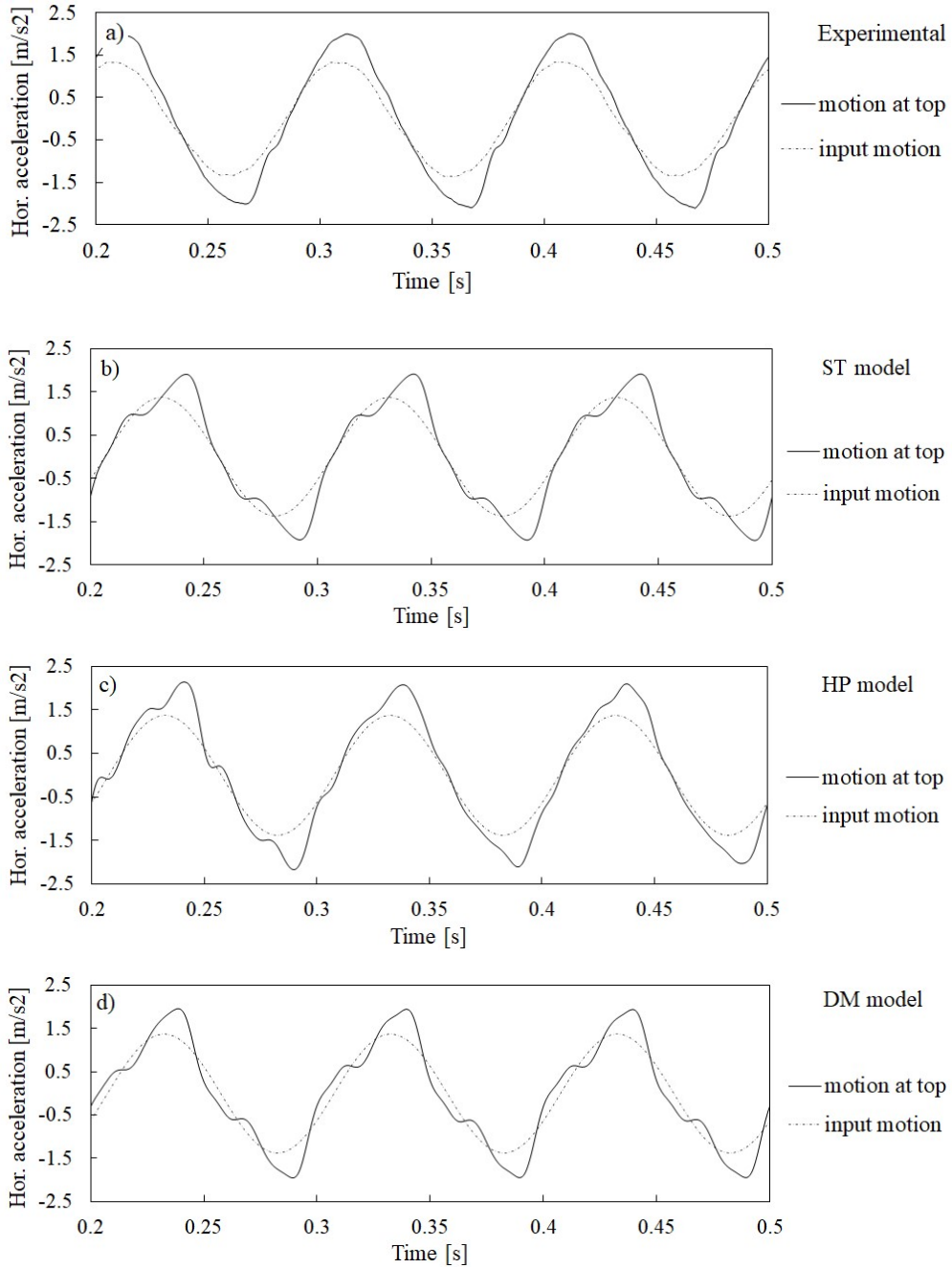


Fig. 17. Horizontal acceleration records at top and bottom of column for 10Hz sine input motion with maximum acceleration of 0.137g: a) experiment, b) ST model, c) HP model, d) DM model.

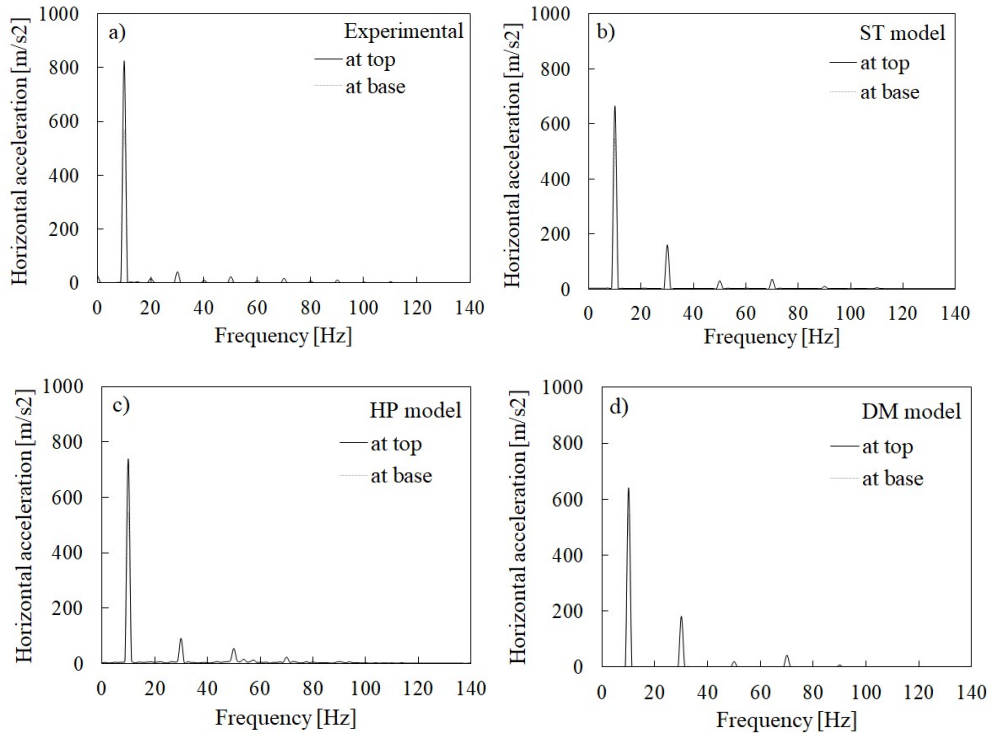


Fig. 18. Response spectra at top and bottom of column for 10Hz sine input motion with maximum horizontal acceleration of 0.137g: a) experiment, b) ST model, c) HP model, d) DM model.

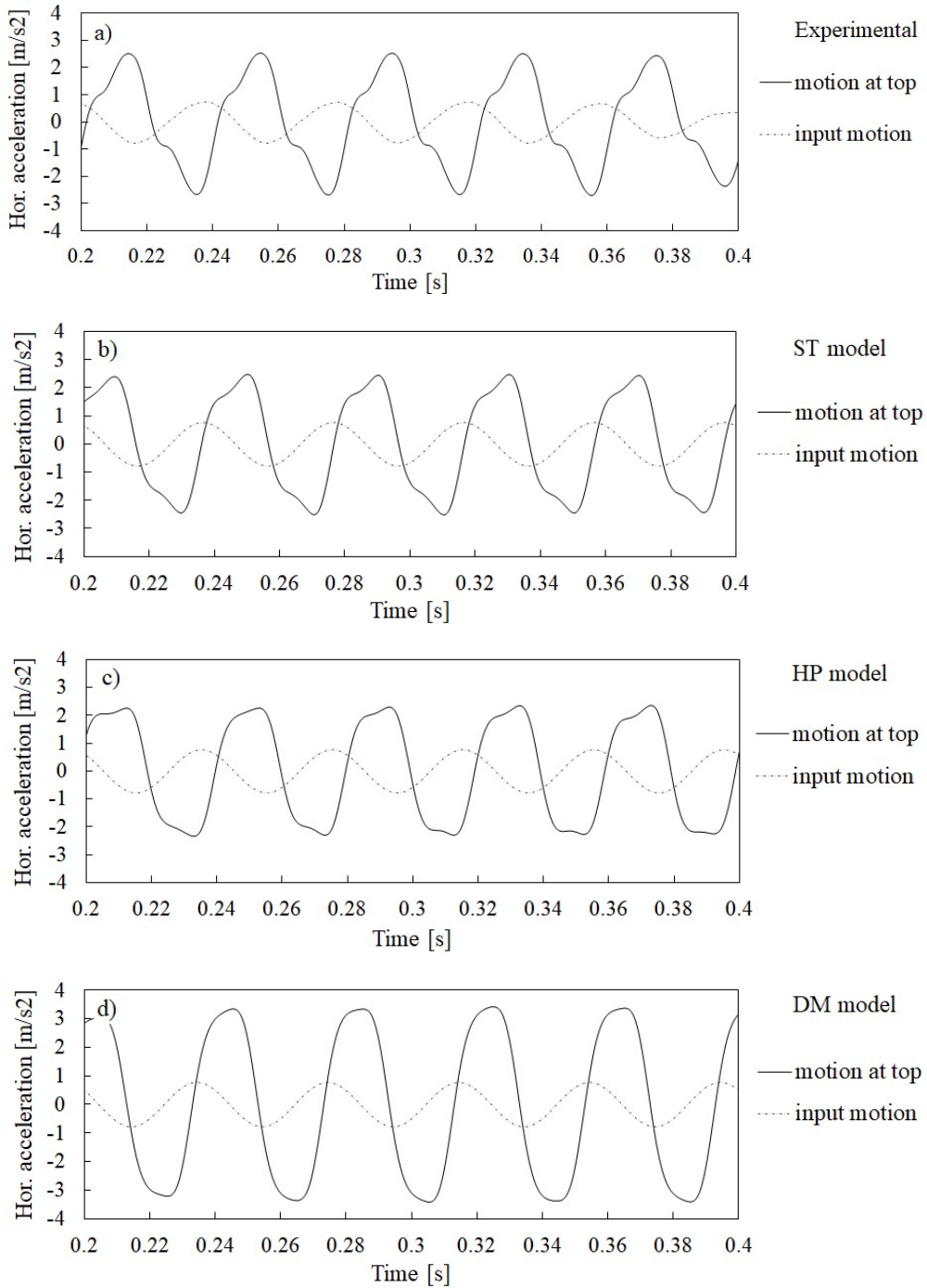


Fig. 19. Horizontal acceleration records at top and bottom of column for 25Hz sine input motion with maximum acceleration of 0.077g: a) experiment, b) ST model, c) HP model, d) DM model.

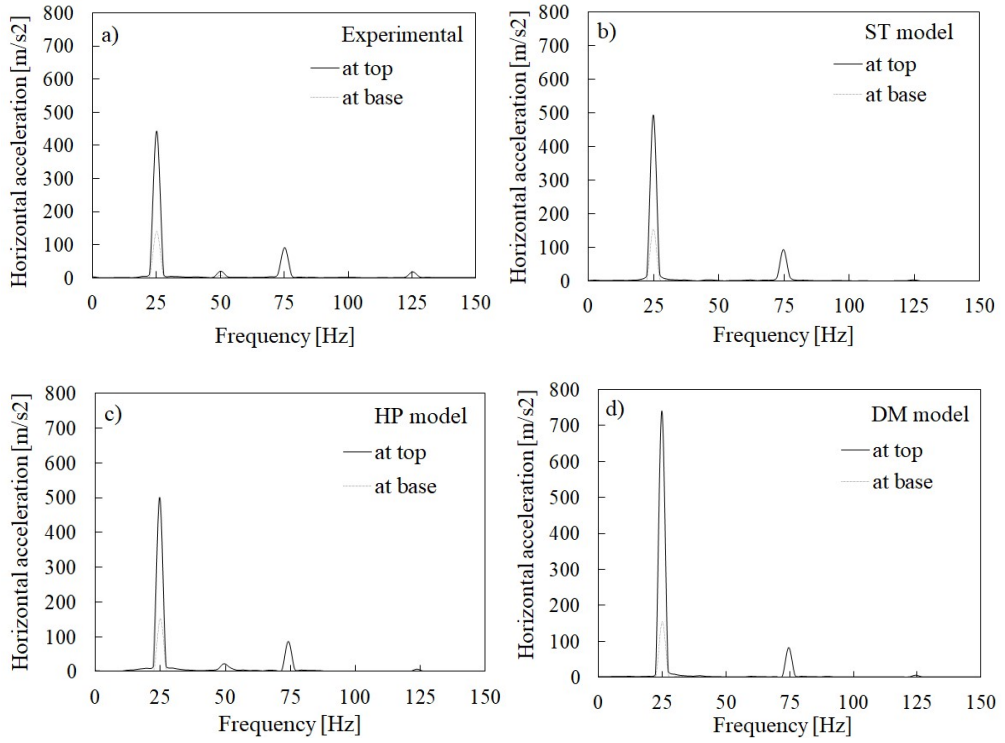


Fig. 20. Response spectra at top of column for 25Hz sine input motion with maximum horizontal acceleration of 0.077g: a) experiment, b) ST model c) HP model, d) DM model.

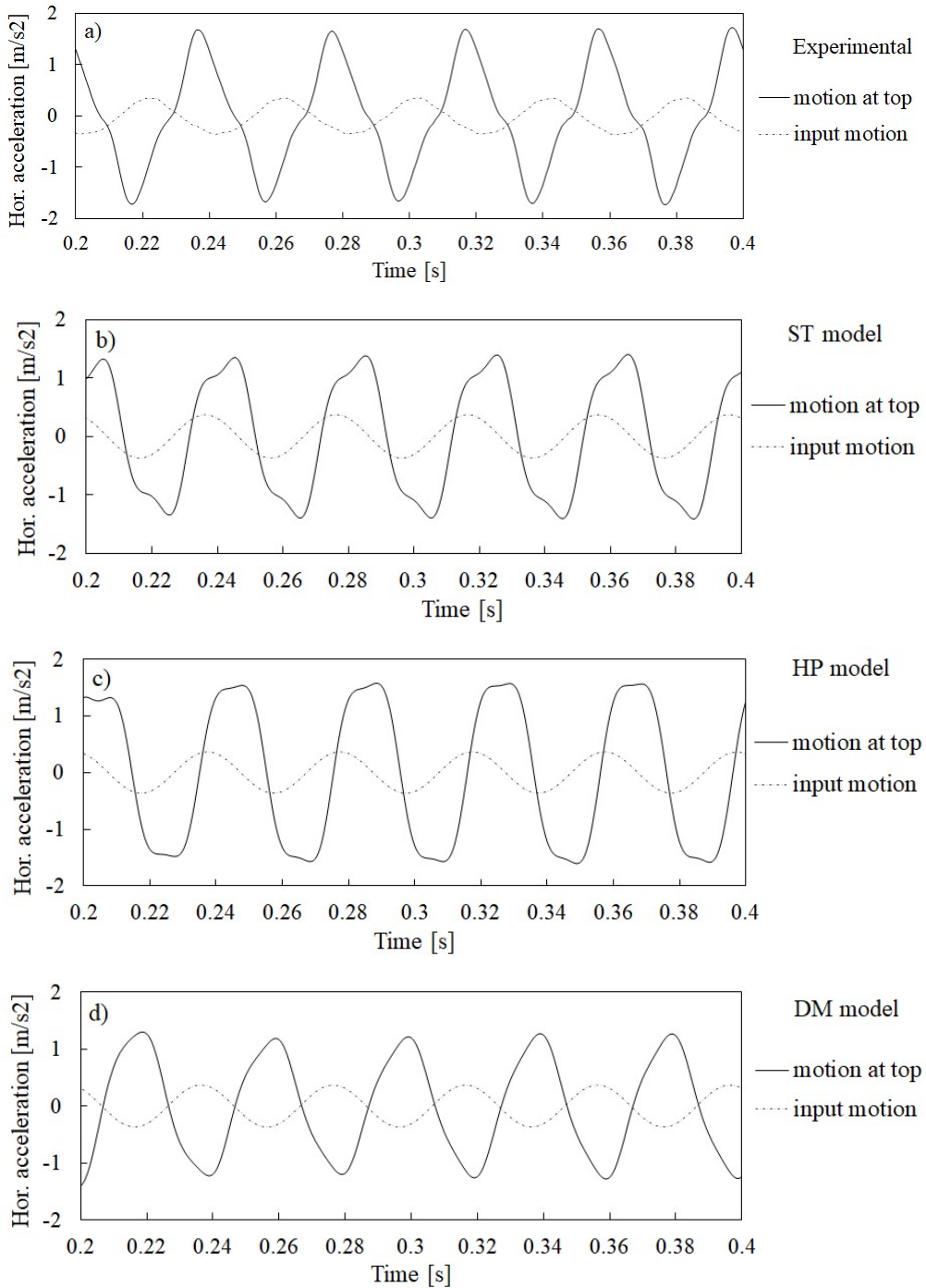


Fig. 21. Horizontal acceleration records at top and bottom of column for 25Hz sine input motion with maximum acceleration of 0.037g: a) experiment, b) ST model, c) HP model, d) DM model.

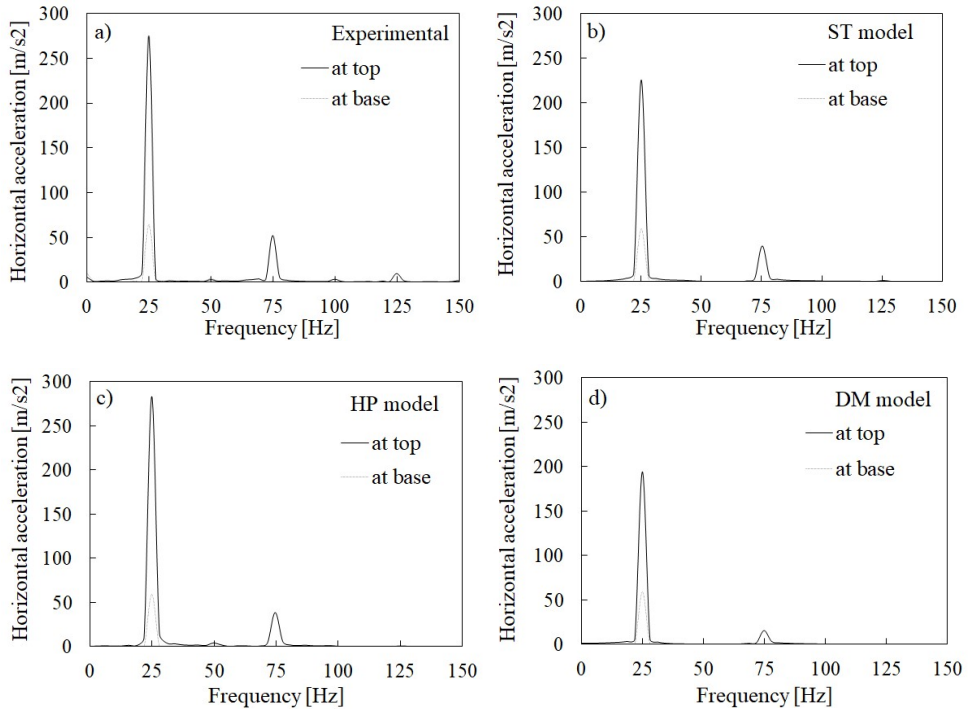


Fig. 22. Spectral response at top of column for 25Hz sine input motion with maximum horizontal acceleration 0.037g: a) experiment, b) ST model, c) HP model, d) DM model.

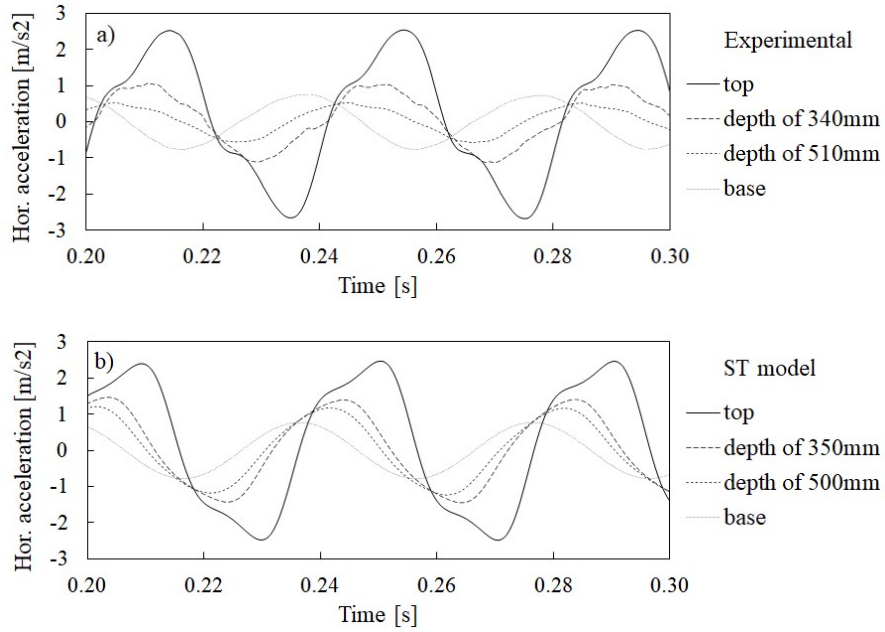


Fig. 23. Horizontal acceleration records at different depths: a) experimental, b) numerical.

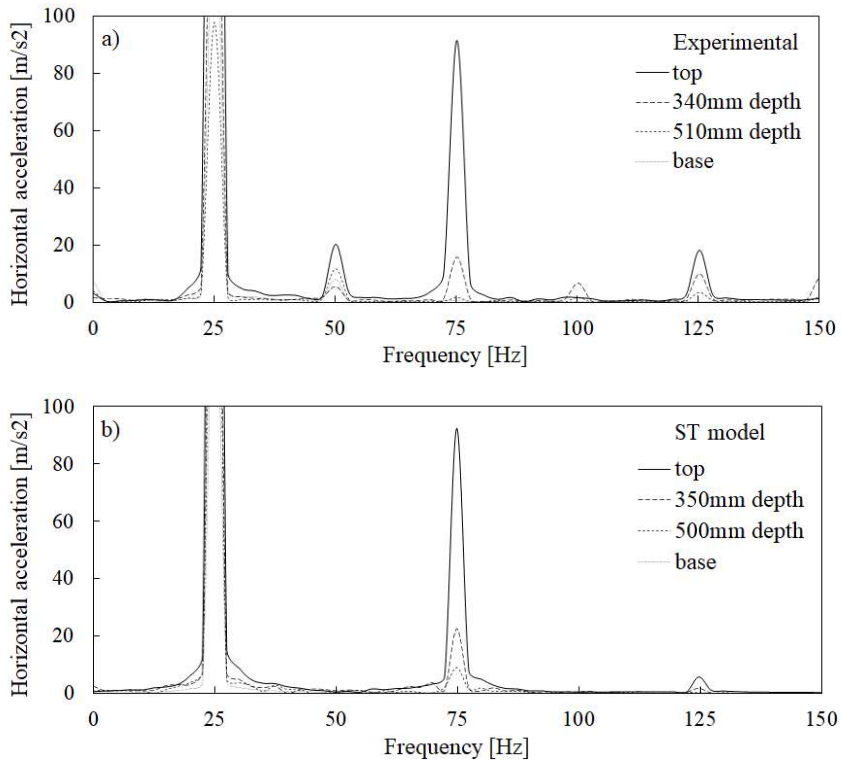


Fig. 24. Response spectra at different depths: a) experimental, b) numerical.

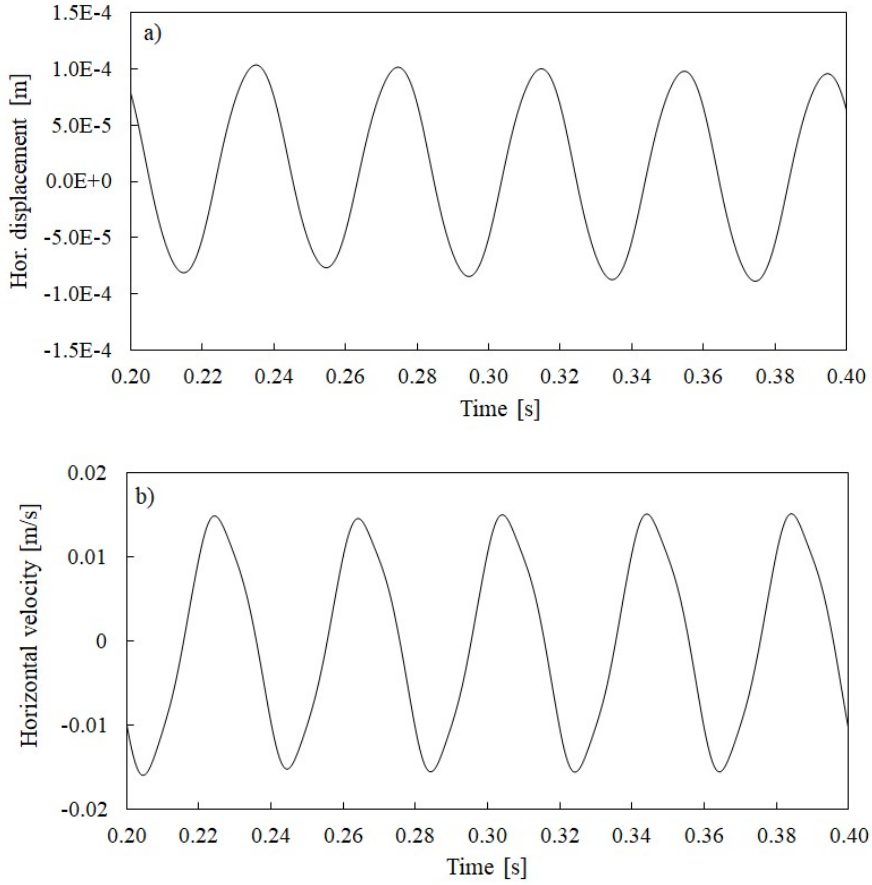


Fig. 25. Horizontal displacement (a) and velocity (b) calculated from integration of recorded experimental horizontal accelerations at top of soil column for 25Hz sine input motion with maximum horizontal acceleration of 0.077g (shown in Figure 12a).

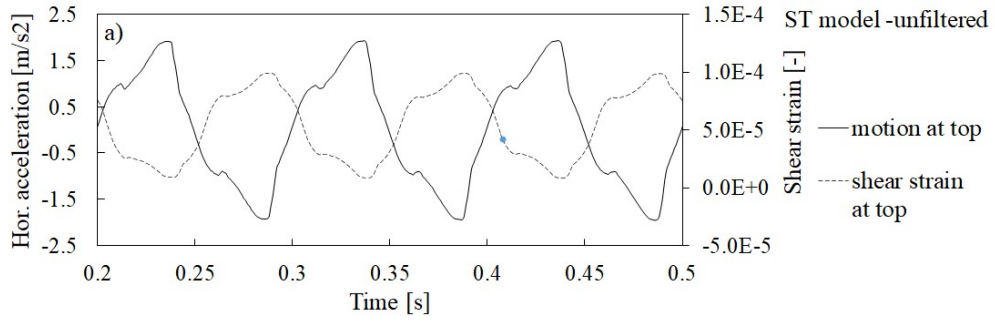


Fig. 26. Unfiltered computed accelerations with shear strains for 10Hz input motion with maximum acceleration of 0.137g for ST model.

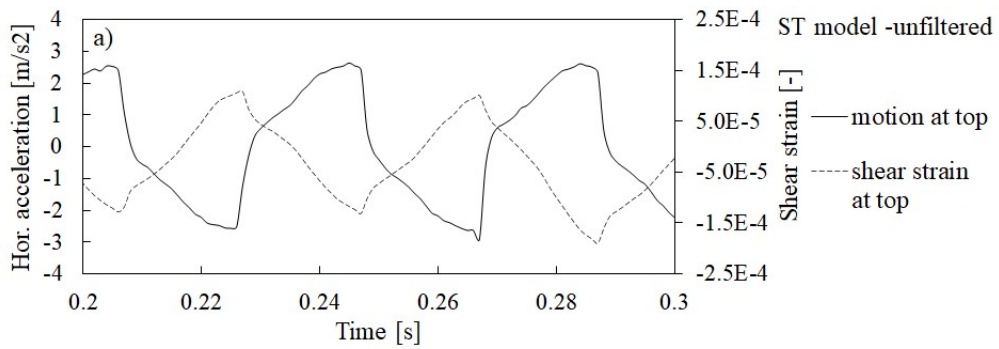


Fig. 27. Unfiltered computed accelerations with shear strains for 25Hz input motion with maximum acceleration of 0.077g for ST model.

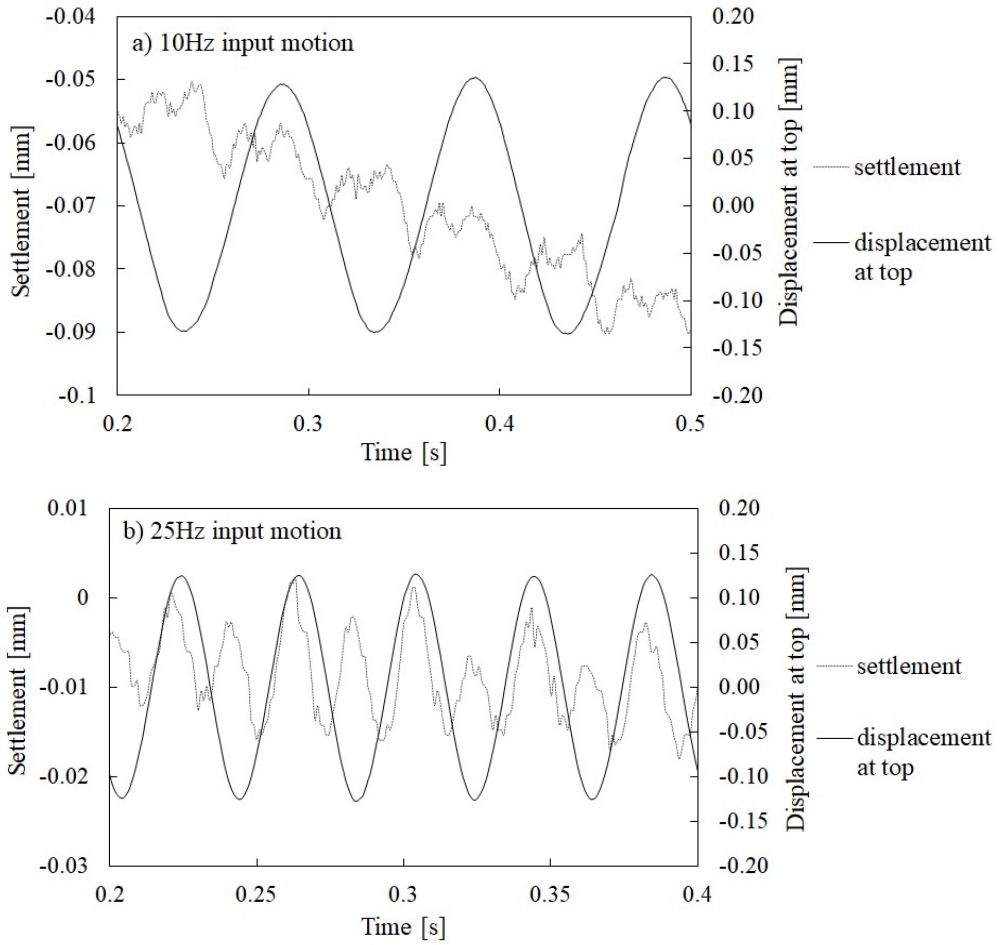


Fig. 28. Settlement experimental records within shearing cycles for a) 10Hz and b) 25Hz input motions.

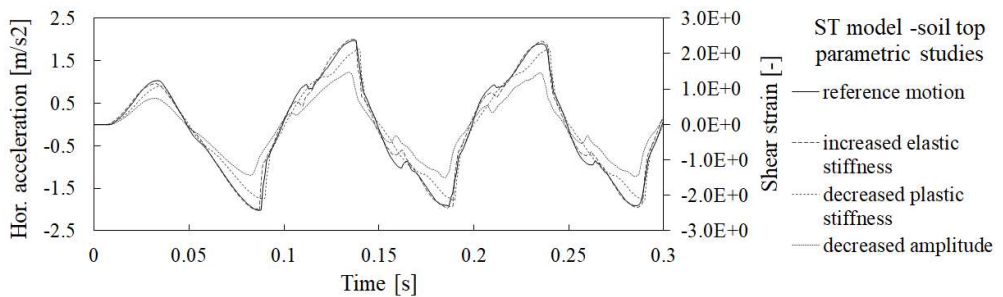


Fig. 29. Parametric studies on position of elastic part separation around soil surface in shear stack column computed by ST model for 10Hz input motion.

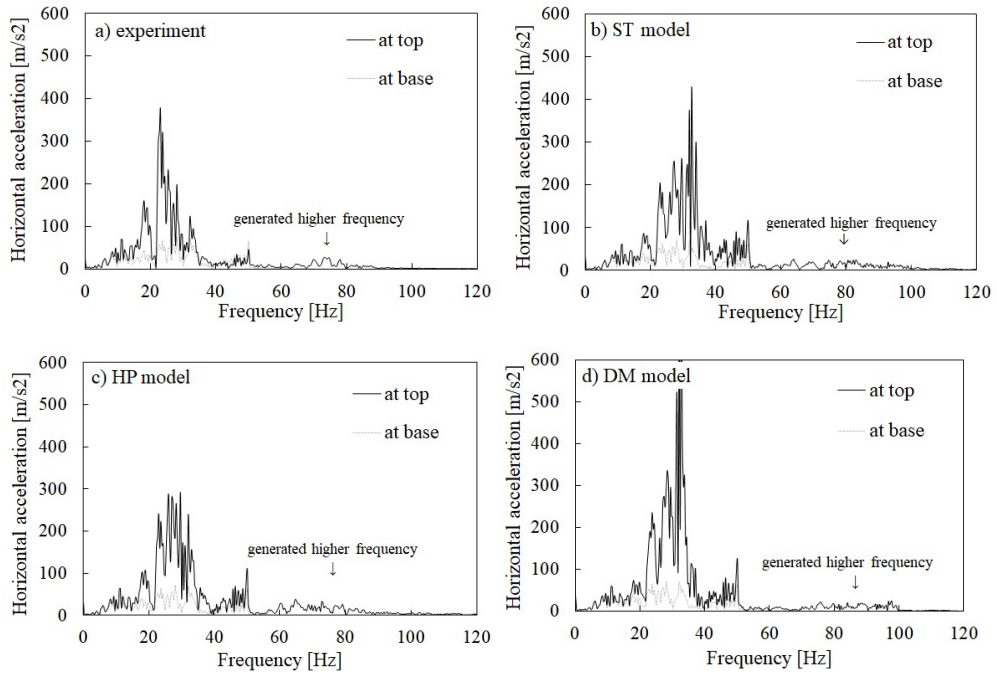


Fig. 30. Response spectra at top and bottom of soil column for scaled Tolmezzo earthquake input motion with maximum acceleration of 0.112g: a) experiment, b) ST model, c) HP model and d) DM model.

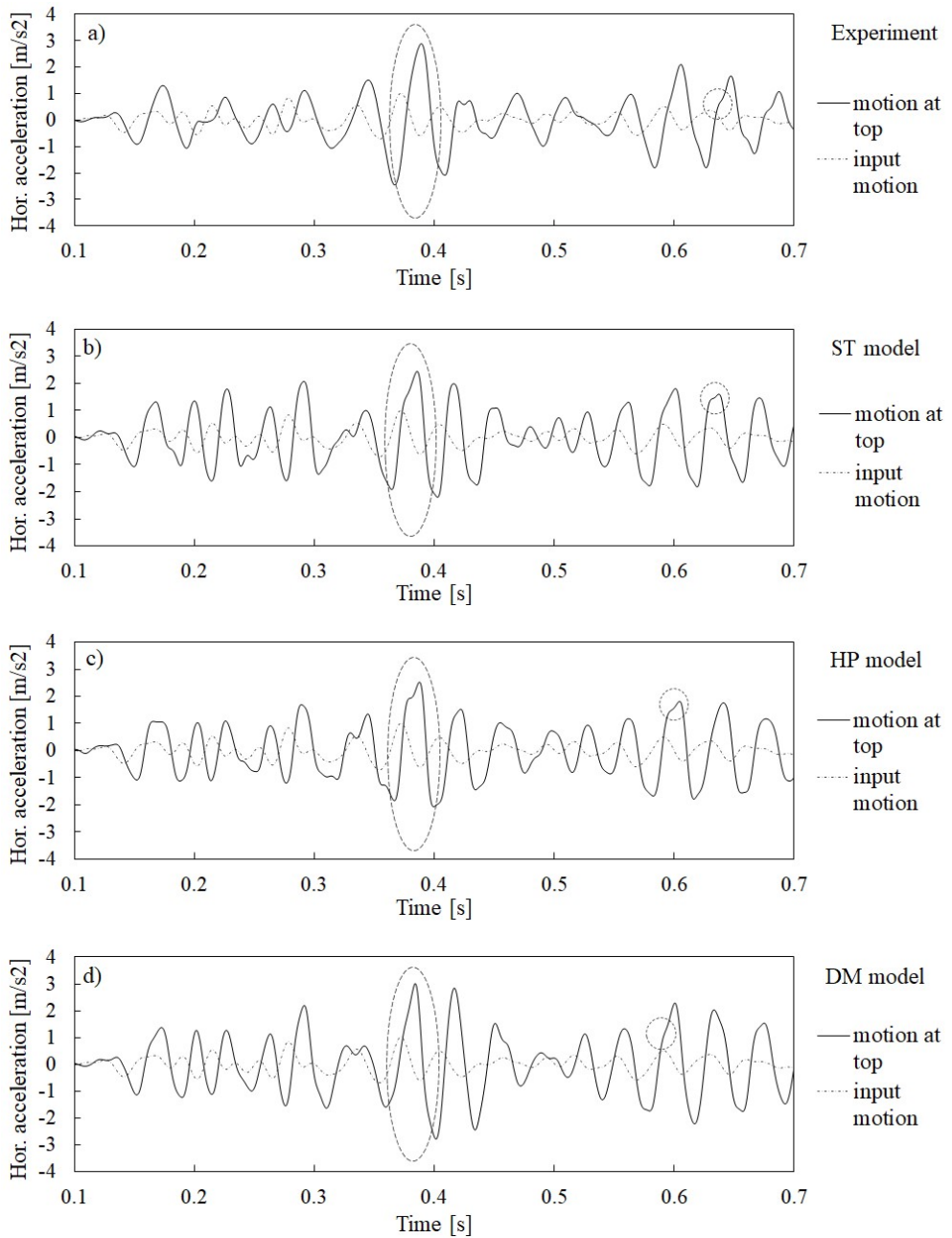


Fig. 31. Acceleration at top and bottom of soil column for scaled Tolmezzo earthquake input motion with maximum acceleration of 0.112g: a) experiment, b) ST model, c) HP model and d) DM model.

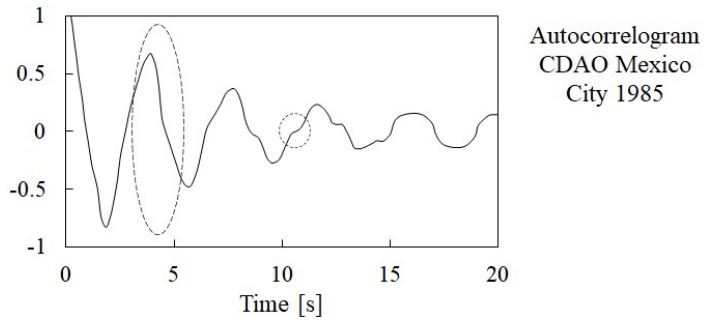


Fig. 32. Digitalized acceleration time history from Ruiz & Saragoni (2009) with recorded wave characteristics resembling these observed in shear stack tests.

3.4. Compression wave propagation in shear stack in dry sand

This section discusses experimental and numerical results of the vertical accelerations at soil surface evaluated for P-wave propagation. The numerical analyses consider a 0.8m high soil column that was discretized with 8-node, quadratic elements of 0.05m size. This has been found sufficient to ensure that the conclusions are not dependent on the element size.

Figure 33 shows P-wave propagation induced by the application of a vertical input motion having the shape of a single sine wave, at the base of the shear stack filled with dry sand (Durante, 2015). Just one single “wiggle” appears in the experimental tests (Figure 33a), whereas “wiggles” are practically absent in the numerical simulations (Figure 33b). Harmonic analysis confirms these observations: in the experimental tests, higher harmonics have a frequency that is as large as twice the input frequency, namely 2ω , if ω is the input frequency. This is in contrast with what occurs in S-waves (Section 3.3) and is more similar to the propagation of a non-symmetrical case considered in Section 3.1. P-waves can be considered non-symmetrical because the applied cyclic strains and stresses act on the initial state of strain which is not zero. Alternatively, the explanation for asymmetrical acceleration records can come from alternating changes in mean pressures due to cyclic dynamic loading with stress paths similar to the one in oedometer.

None of the selected soil constitutive models is capable of predicting the generated frequencies in a proper way, neither in terms of generated harmonics, nor in terms of their amount. Equivalently, in the simulated acceleration time histories there are no “wiggles”. This is because the constitutive models taken into account are formulated mainly for deviatoric response.

It is worth emphasising that the absence of higher harmonics in the numerical simulations, confirms the reliability of the signal processing algorithms, because the higher harmonics highlighted in S-waves (Section 3.3) cannot be attributed to any spurious processing effects (as such regular harmonic patterns are now missing for the case of P-wave consideration).

In contrast to S-waves, higher harmonics with a larger amplitude are also observed at the shaking table base in case of P-waves. This aspect is discussed later in the discussion section (Section 4) of this chapter.

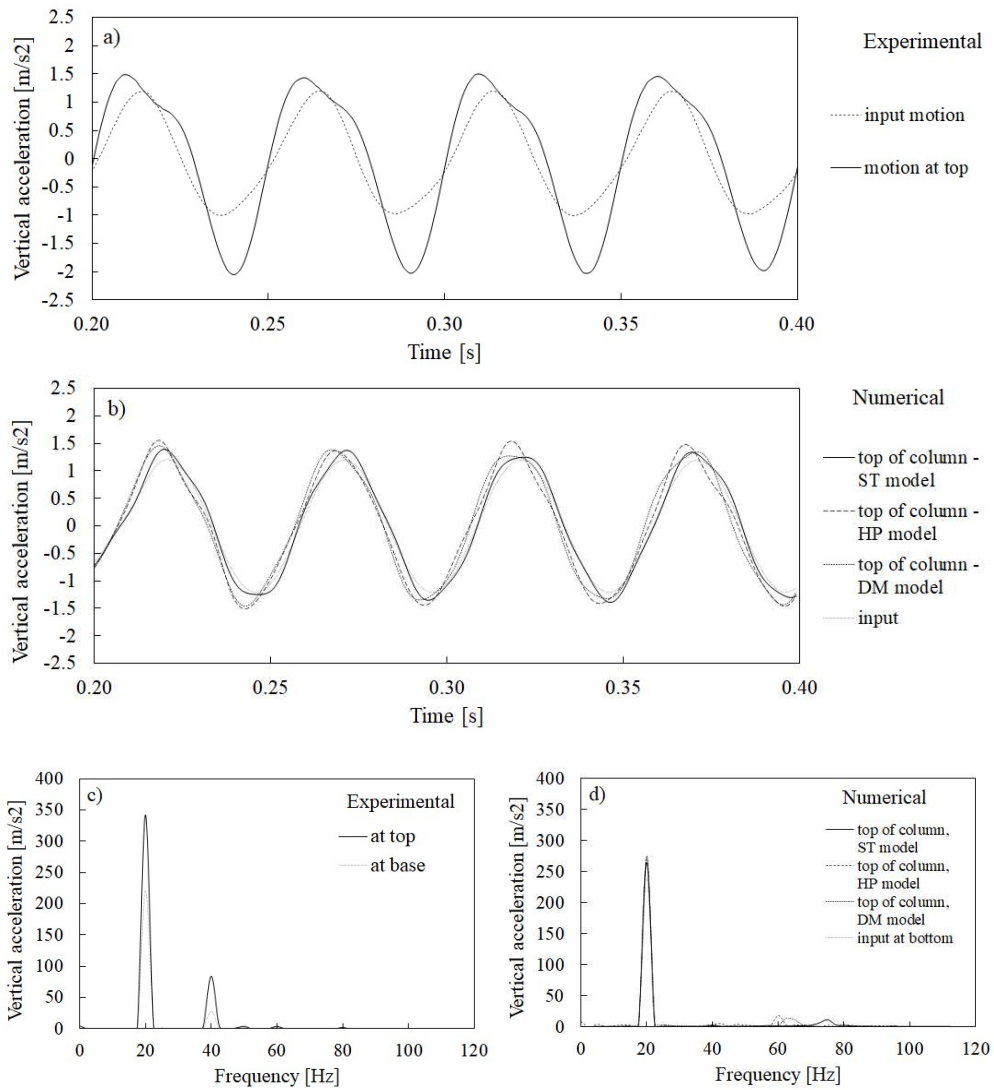


Fig. 33. Results for 20Hz sine input motion of P-wave propagation with maximum vertical acceleration of 0.120g: a) experimental acceleration records, b) numerical acceleration records, c) experimental response spectra, d) numerical response spectra.

3.5. Impact of generated higher harmonics on kinematic pile

This section of Chapter 2 presents how fast elastic unloading waves can affect a structure under dynamic conditions. As an example, a kinematic pile subjected to seismic loading in a shear stack test (Durante, 2015) is considered. The comparison between experimental data and numerical simulations is shown in Figures 34-36. A low-pass Butterworth filter 80Hz (5th order filter) has been applied to all numerical results for the sake of consistency with the measurements.

Note that this section is an extract from Chapter 3, presented also as a single example in Chapter 2, for the consistency and completeness of the topic of higher harmonic observation. More numerical and experimental analyses on soil-structure interaction are presented in Chapter 3. Note that in this section, the middle pile out of five piles from the pile group is a subject of the discussion.

In Figure 34, both experimental measurements and numerical simulations show that the slender pile is driven by the low input harmonic (10Hz) and that the higher frequencies generated within the soil mass significantly affect the pile response. The amplitude of higher harmonics is larger in piles than in soil in Figures 34a and 34b, probably because the top part of the pile is more rigid than the top soil and does not behave as a kinematic pile (in contrast with the lower part of the pile). In addition, some small mass of measuring instruments was placed at the pile top which was at about 60 mm above soil surface. As a result, the pile response would resemble more the one of an oscillator which is stiffer than the soil in the upper part of embedment. As a consequence, if the natural frequency of such oscillator is close to the frequencies of the higher harmonics, this could lead to a phenomenon of super-harmonic resonance, i.e. the coincidence of the higher harmonics generated within the soil mass with one of the natural frequencies of the pile. Importantly, we are considering here higher harmonics generated due to elastic part separation and not due to wave distortion (the latter are “artificial” as associated with representation of a “square wave” formation and not being physically present as additional waves). Thus, the increased presence of higher harmonics on the pile could be possibly associated with elastic wave separation (such as presented in Section 3.2), although further studies and more careful assessment of the experimental data would be needed for confirmation. In any case, the phenomenon of stronger presence of higher harmonics on piles than in free field has been captured by the numerical simulations and measured in the experiments. It is interesting to notice that in some way, piles (purely elastic inclusions) placed in soil can be seen as additional measuring instruments for the effects discussed in this chapter, i.e. we can think of an elastic pile being such an additional measuring instrument which picks up additional high frequency waves and brings them to the top of the pile.

Figures 35a and 35b show the results of harmonic analysis of the measured and simulated acceleration histories. It can be observed that in both cases, the higher

frequencies have a regular pattern, with dominant harmonics that are odd multiples (3ω , 5ω and 7ω of the input frequency ω).

The measured and computed axial strain histories at around the pile mid-height are finally shown in Figures 36a and 36b. The experimental results show that the loss of a perfect sine shape, and the presence of higher frequencies is not limited to the accelerometer measurements but is also confirmed by strain gauges. Although the maximum simulated axial strains are about half of the measured one, the general patterns shown by the simulations is reasonably consistent with the measurements. More consideration on discrepancies in predicting soil-structure interaction in numerical studies is given in Chapter 3 of this thesis.

Note that the results presented here (experimental and numerical) are for a five-pile group in a bi-layered soil profile. An ideal experiment should consider a single pile in a homogenous soil profile. A numerical design of such a perfect experimental setup is presented in Appendix C, for completeness and for showing directions for future works.

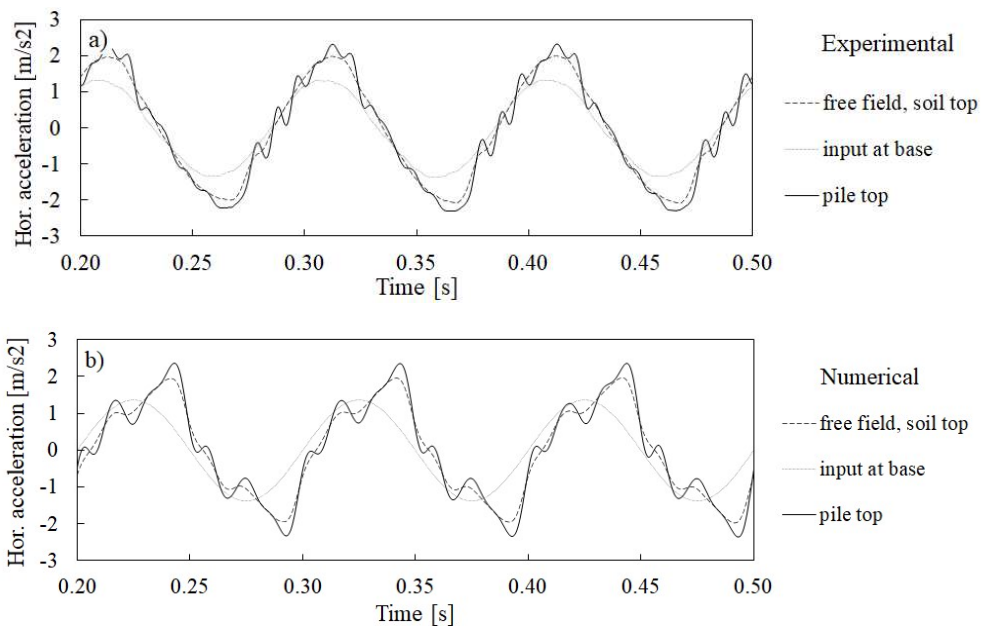


Fig. 34. The results for soil-structure interaction of a kinematic pile for 10 Hz sine input motion with the maximum horizontal acceleration of $0.137g$: a) experimental acceleration records, b) numerical acceleration records.

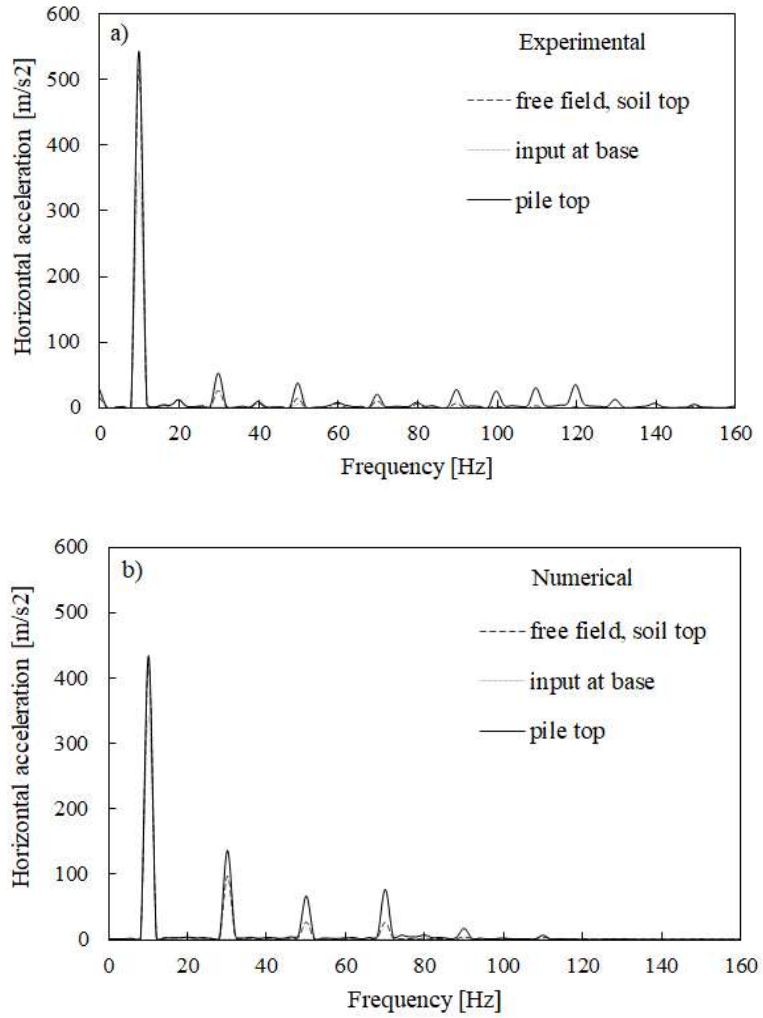


Fig. 35. The results for soil-structure interaction of a kinematic pile: a) spectral response from the experiment, b) spectral response from the numerical analysis.

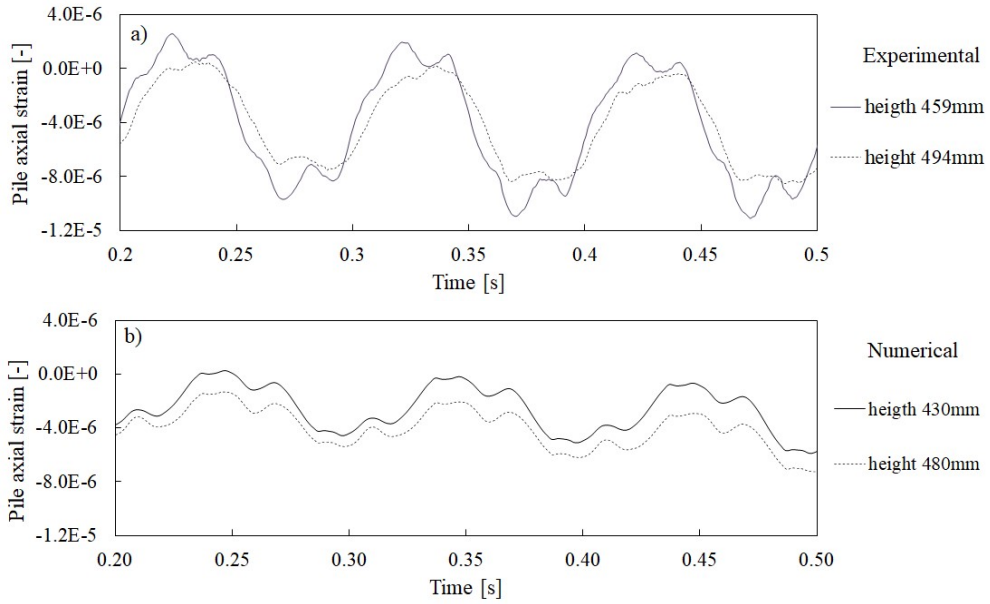


Fig. 36. Results for soil-structure interaction of kinematic pile: a) pile axial strains from experiments, b) pile axial strains from numerical analysis.

3.6. Shear wave propagation in centrifuge in saturated soil

The final subsection in the result section presents a short numerical study on higher harmonic observation in saturated soil. A saturated soil column has been analysed in order to replicate the free field response in the middle of the slope of the LEAP-UCD-2017 experimental set-up (Kutter et al., 2019). Figure 37 shows the experimental measurements in terms of recorded accelerations and their spectra for the tests carried out at Cambridge University (Beber et al., 2018; Madabhushi et al., 2020). A steadily increasing up to 0.15g, 1Hz sine input motion has been applied at the bottom of a 4m high soil column as per the centrifuge tests. Similarly, to the analysis of dry soil, the input motion applied is a perfect sine and does not contain additional harmonics. This may not be fully correct since higher harmonics have been registered at the bottom of the rigid box in centrifuge. However, this study is intended to show the ability of the constitutive model to generate higher harmonics even if a perfect sine input motion is applied at the bottom of the soil column, also in the case of saturated soil.

The results have been filtered out with a lowpass 10Hz filter in order to remove very high frequencies reaching very high amplitudes and associated with numerical problems related to shock formation as adequate also for saturated soil (see below).

The soil response in the numerical analysis can be divided into two sections: before the acceleration “spikes” occur (Figure 38a), and after the acceleration “spikes” start appearing (Figure 38b) due to dilation pulses as a result of a sudden reduction in excess pore pressure (Figure 39c). The first part of the acceleration time history (up to around 5sec) resembles the acceleration records as per dry soil with a “wiggle” on ascending and descending branches. Indeed, before 5sec the changes in pore pressure are relatively small (Figure 39c), the stress strain behaviour resembles closely the one observed in dry soil (Figure 39a in the dashed circle and Figure 39b). This changes after around 5sec, when large strains are experienced (Figure 39a) due to the induced cyclic mobility.

In terms of generated higher harmonics, the numerical study predicts generation of frequencies 3Hz, 5Hz and 7Hz (Figure 38c). On the other hand, the experimental data shows higher harmonics of 2Hz, 3Hz, 4Hz at the top of the soil, and 3Hz, 5Hz, 7Hz at the bottom of the laminar box (Figure 39b). The even harmonics are practically not present at the bottom of the column. This discrepancy is believed to be related to the non-symmetrical soil response during shaking when analysing slope with this effect being stronger at the top of the column. The numerical study assumes a symmetric soil column only (without slope geometry included), thus, the stress state is horizontally uniform, the response on both sides of the column is the same and the generated harmonics follow the odd pattern of generated frequencies 3ω , 5ω etc. as explained in Section 3.1. Most importantly, this short study shows that the soil can

generate higher frequencies also in saturated soil even if these are not present at the base level.

Noticeably, the computed shear strain changes from a smooth sinusoidal form (applied at the bottom) into firstly an “edgy” form (Figure 38a) and subsequently into a “jumpy” form (Figure 38b) with the increasing amplitude of the applied motion. At the top of the column under high amplitude motion, the shear strain resembles almost a square wave, with sudden “drops” and “jumps”. These are indicators of the formed shock wave which in case of saturated soil is of strong discontinuity. This finding was presented by Kutter & Wilson (1999) and associated with strain hardening in soil experiencing cyclic mobility such as shown also here on Figure 39a. However, to the best of the author’s knowledge, typically the shock wave formation in saturated soil is not appreciated in the numerical analysis of seismic geotechnical problems and many numerical problems might be a consequence of such a shock wave. Indeed, when comparing Figure 38b with similar spectral response shown for studies in dry soil (Section 3.3), the pattern of the generated harmonics seem to be strongly affected by other frequencies in between the dominant integer harmonics of ω , 3ω , 5ω etc, suggesting that strong discontinuity in strains is more troublesome for the ordinary finite element formulation than weak discontinuity.

Finally, one may note that the very small stress-strain reversal loops shown in Figure 39a (in dotted circles). These could be indications of separating fast elastic parts of waves arriving after the unloading happens (as explained in Section 3.2) and result in a smaller “spike” in the computed accelerations shown in Figure 38b (note also that small “wiggles” can also be potentially observed in Figure 38a before strain discontinuity occurs and also can be attributed to the presence of separated elastic parts of waves) as explained in Section 3.2. The presence of smaller acceleration “spikes” is not obvious in the experimental data at the top of the column or at its base. Nevertheless, such thinking of higher harmonic generation could be a subject in the future studies to determine the reason of higher harmonics in centrifuge experiments if inaccuracy of the actuating systems was excluded.

This section has presented higher harmonic generation and shock wave formation in saturated soil. This is due to, firstly, behaviour similar to dry sand governed by fast elastic unloading waves (0-5sec), secondly, due to strain hardening becoming more dominant (5-10sec). Therefore, the conclusion for the studies on saturated soil can be similar as per dry soil, i.e. soil nonlinearity, resulting in fast elastic unloading waves or strain hardening, results in the observation of higher frequencies in the spectral response, with the pattern of the generated harmonics depending on the geometry of the problem.

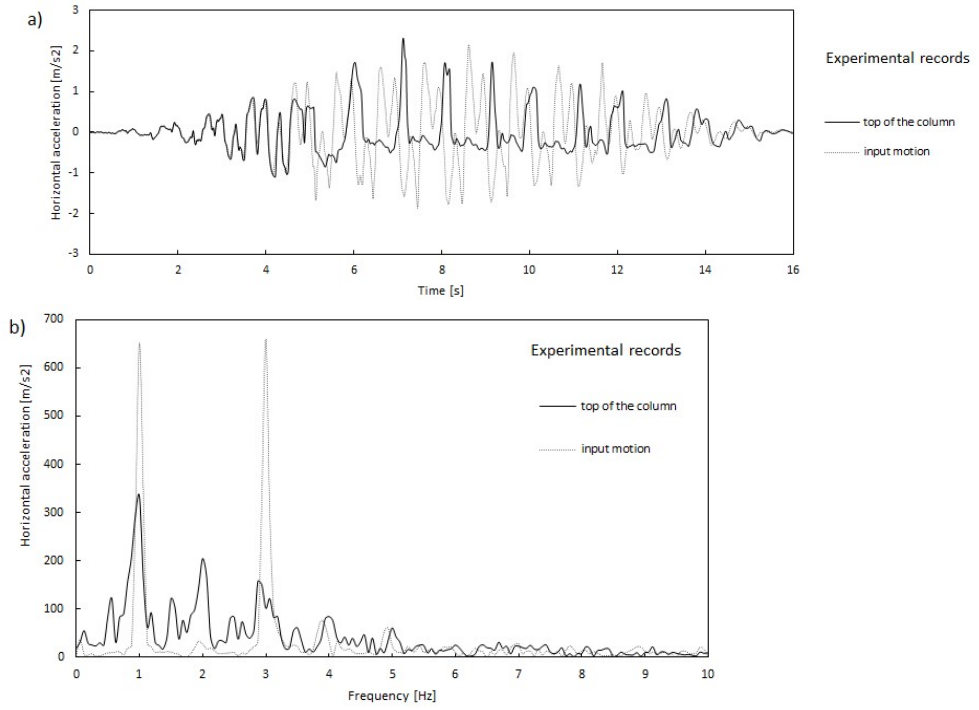


Fig. 37. Experimental results from centrifuge in Cambridge in terms of recorded: a) accelerations and b) spectral accelerations.

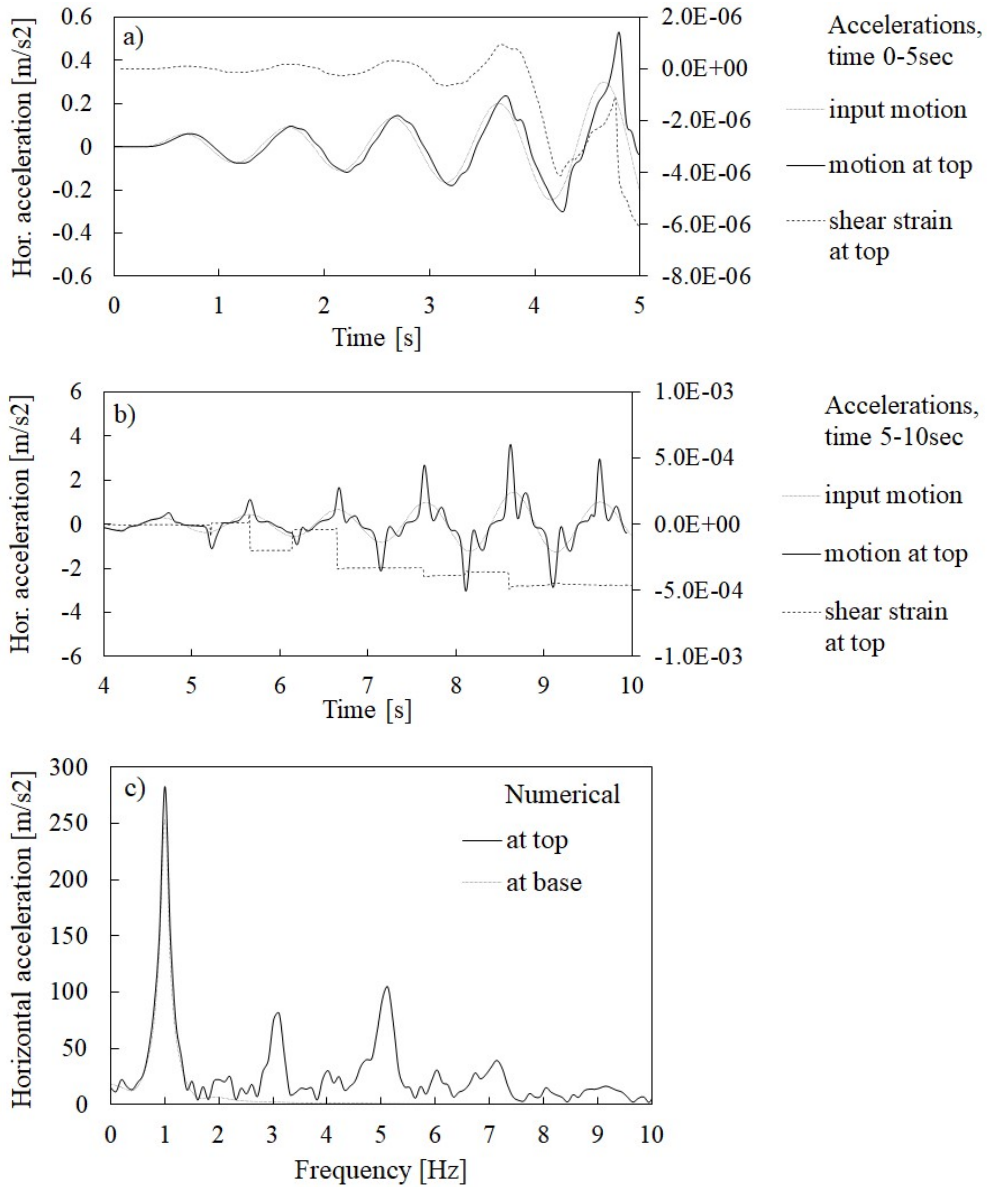


Fig. 38. Numerical results for simulations of saturated soil column as per experimental setup in the LEAP-UCD-2017 project: a) accelerations and shear strain during 0-5sec, b) accelerations and shear strain during 4-10sec, c) spectral response.

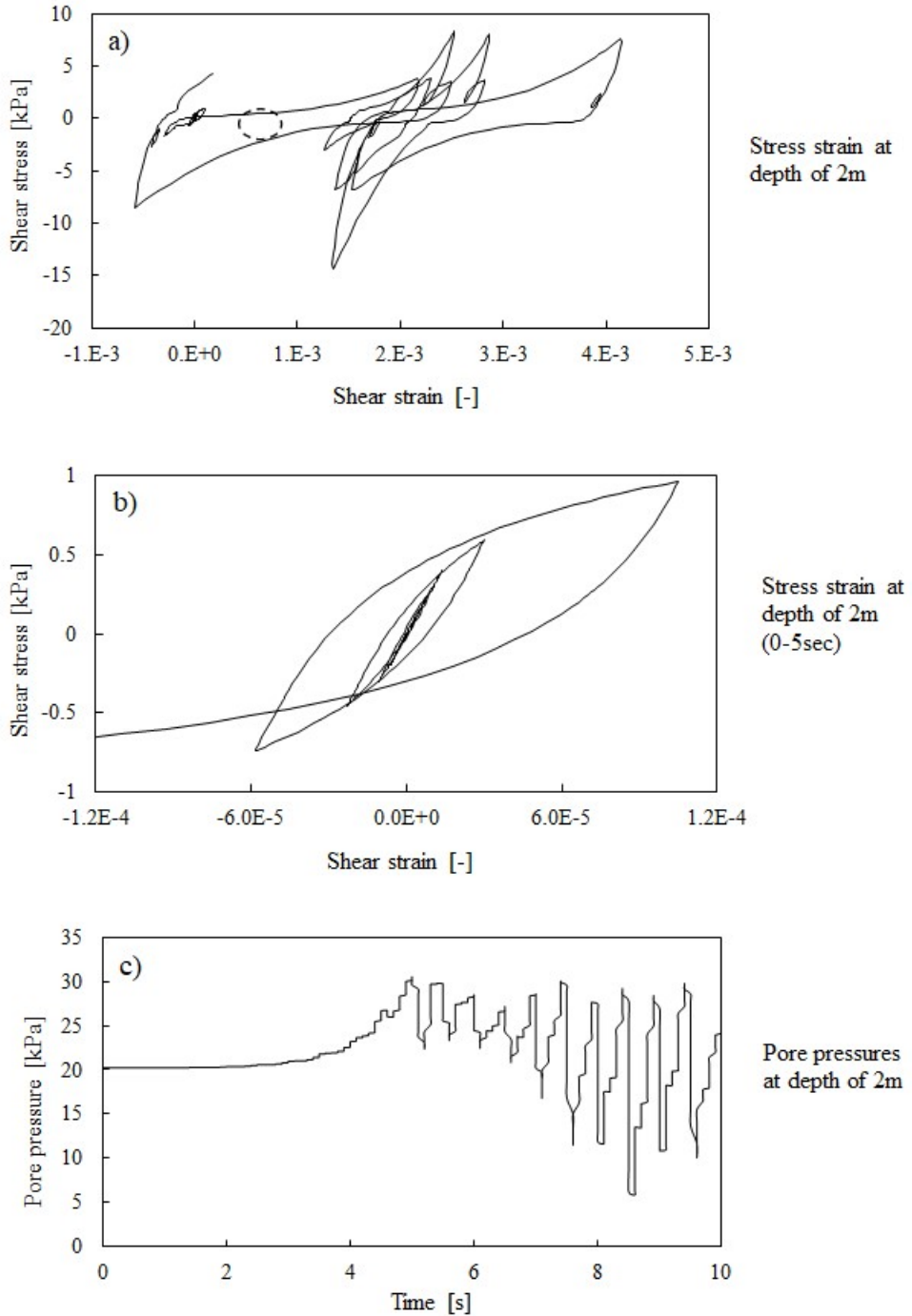


Fig. 39. Numerical results at depth of 2m in terms of: a) stress-strain behaviour, b) stress-strain behaviour in first 0-5sec, c) generated pore pressures.

4. Discussion

This chapter shows that when sinusoidal seismic input motion is applied at the base of a soil layer, either experimentally (in a shear stack) or numerically, higher harmonics are generated at the soil top surface, even in the case of a perfect sine (single harmonic) input motion applied at the soil base. This study proposes that the causes of such higher harmonics are related to soil non-linear response for both, dry and saturated soil. These findings are important for various aspects of seismic geotechnical engineering ranging from the potential observation of unknown physical effects in soils, through the reliability of advanced soil constitutive models, the proper investigation of soil-structure interaction to the choice of the most suitable numerical methods in the theoretical simulations of seismic geotechnical problems.

This work aims mainly at explaining higher harmonics in dry soil and shows that a possible source of higher harmonics with a regular pattern of frequencies are the fast elastic unloading waves, either pursuing and interacting with the slower preceding loading waves, or separating from plastic parts of waves. These effects are shown through the preliminary analysis of S-wave propagation in an idealized 1D, nonlinear, irreversible material (Section 3.1) and an example elastoplastic model (Section 3.2) in a semi-infinite column and, finally, through the comparison between the experimental evidence and the numerical simulations obtained with three different advanced soil constitutive models (Section 3.3, 3.4, 3.5). In detail, two effects of unloading waves are observed, namely wave distortion due to shock wave formation and separation of elastic waves. The first kind, visible in the shear stack for the input motions of higher input frequencies (shorter wave lengths vs shear stack height), the second one observed for lower input frequencies (longer wave lengths vs shear stack height) when the shock wave may have not fully been formed. These phenomena have long been recognized in solid mechanics (Wang, 2007) but are generally neglected in seismic analysis of soils.

The weak form of discontinuity is shown to form gradually within dry soil increasing with the increase of the length of wave propagation, i.e. the decrease of soil depth (Section 3.1 and 3.2). In fact, initially, for an ideal sine input motion, there is no discontinuity being present after short propagation lengths, in which cases the occurrence of the separated elastic parts dominate in the computed accelerations and the spectral response. However, at some distance from the source of input motion, as a result of the unloading wave pursuing and chasing up the loading wave, a sharp “spiky” edge is obtained in shear strains and shear stresses. The sharpness of this feature increases with the distance from the source. Therefore, a shock wave is formed in the accelerations due to soil inherent nonlinearity and irreversibility and the effects of wave distortion dominate over these of separated elastic parts (as shown in Section 3.2). Namely, the fast elastic unloading wave causes the strains (and stresses) to have weak discontinuity and their derivatives (accelerations) to have a strong discontinuity. This is different with respect to saturated soils, where the discontinuity is strong in

strains (and stresses) as a result of soil strain stiffening when cyclic mobility state is reached, as shown experimentally by Kutter & Wilson (1999) and numerically in Section 3.6 of this chapter.

This work validates all three advanced soil constitutive models which are considered in this chapter. In detail, the models are capable of simulating the generation of the higher harmonics having a correct frequency pattern for the S-wave propagation, although a single sinusoidal input motion has been applied at the soil base in the numerical analyses. This is different when comparing with other published numerical studies, where the applied input motion typically includes the higher frequencies that were not present in the planned input motion. In other words, the numerical analyses show that higher frequencies for S-wave propagation may be generated within the soil mass, as a result of the soil nonlinearity and irreversibility, leading to fast elastic unloading waves resulting in sine wave distortion and separation of the elastic part of a wave. Thus, fast elastic unloading waves could be considered as a further mechanism explaining the generation of higher harmonics, besides the already known mechanism of “de-liquefaction shock waves” in saturated soil (Kutter & Wilson, 1999) and the suggested shear localization in dry soil (Dar, 1993; Gajo & Wood, 1997). Interestingly, the latter was found in similar shaking table tests as these described here (Durante, 2015) but at much higher amplitudes of input motions. In fact, Durante (2015) did not apply stronger sine input motions than 0.15g. Thus, the author wonders whether also in Dar’s experiments, it could be soil nonlinear behaviour and elastic unloading waves that generated higher harmonics attributed originally to be a proof of shear localisation. Actually, the maximum lateral displacements were reported to be around 2-3 mm (in Gajo & Wood, 1997), i.e. still rather small for strain localisation occurrence. What is more, the lateral displacements of 2-3mm, i.e. ten times larger than the maximum displacements measured by Durante (2015), could be expected for approximately four times larger amplitudes of sine input motions due to increasing soil nonlinearity (see also next paragraph of the discussion). Some numerical consideration is given to this way of thinking in Appendix D. However, these are speculations only and would need confirmation in future experimental work to determine which of the mechanisms, shear localisation, unloading waves or maybe some other, generates higher harmonics in shear stack experiments under high amplitude input motions.

The characteristics of the higher harmonics are shown to depend on the amplitude of the input motion. The experimental and numerical studies show that higher harmonics have larger amplitudes for stronger input motions. This is probably related to the increasing nonlinearity (as shown also by other studies, e.g. Pavlenko, 2001) and the softer plastic response. Thus, the effects of the elastic unloading waves become stronger (because the differences between the velocities of a fast elastic unloading wave and a slow plastic loading wave become larger). Similar experimental evidence has been shown in other works (Lanzano et al., 2012) where an increase in higher frequency content could be related to an increase of the amplitude of the input

motion or with a decrease of soil relative density (in fact both effects lead to larger plastic strains and slower plastic waves). Further (numerical only) consideration in this chapter (Appendix B) has been also given to low amplitude input motions with the aim to identify purely elastic soil response. The numerical studies have shown some initial findings, with higher harmonics disappearing in low amplitude input motions. The confirmation on such findings would allow to define the limit on when the numerical approaches based on elasticity can be used in the predictions of seismic soil behaviour.

The generated higher harmonics are most often of an odd pattern (i.e. 3ω , 5ω , 7ω etc.) of the driving frequency ω . However, there are cases where even harmonics may appear. In this work, even harmonics were shown to be potentially related to P-wave propagation (Section 3.4), slope geometries (Section 3.6), or in general, to non-symmetrical loading (Section 3.1). This concept is supported by published analyses of the higher harmonic generation in optics of amorphous solids (Yong Sing You et al., 2018) where generation of the odd harmonics in crystalline quartz is associated with lack of the crystal symmetry.

The effects of fast elastic unloading waves are not limited to the problems of wave propagation only. Section 3.5 reveals how a kinematic pile can be affected by such effects of elastic unloading waves. Chapter 3 of this thesis will look on that in further details, including soil-structure interaction not limited to the case of a kinematic pile only.

Some studies say elastic region in soil is negligible and of minor importance. This work suggests that soil has a strain region where the behaviour is elastic and soil elasticity can be considered important when analysing seismic wave propagation problems. If no elastic region was present in soil, the soil response in Section 3.3 would be expected to be as shown in Section 3.1. However, there is some evidence, either numerical or experimental, shown in Section 3.3 that soils can be considered as having an elastic range in their constitutive behaviour.

Based on the findings of higher harmonic generation in soil placed in shear stacks subjected to a sine dwell input motions, it is expected that higher frequencies can also be generated on site during earthquakes. An example of this effect has been discussed in Section 3.3 supported by the experimental evidence and numerical simulations. As a result, the higher harmonic generation could contribute to the discussion on the double peak spectra (Gallegos & Saragoni, 2017) or the multiple peak spectra recorded in some earthquakes (Ruiz & Saragoni, 2009). The multi-peak spectra were found in seismic records of soil free vibration measurements, thus higher modes were associated with soil natural frequencies although the occurrence of these higher modes were not explained explicitly. It is intriguing to think that higher modes could be generated within the soil mass as a result of soil nonlinearity and elastic unloading waves. What is more, as a result of these waves some structures could experience superharmonic resonance (due to picking up the high frequency elastic parts of waves) such as the example shown in Section 3.5. In addition, some interesting findings are also obtained for field measurements of vertical accelerations due to the

propagation of compression waves. Aoi et al. (2008) found that the vertical acceleration records during the strong Iwate-Miyagi earthquake in Japan (6.9 magnitude) were remarkably asymmetric, indeed, similar in its lack of symmetry to the vertical accelerations shown in this chapter for P-wave propagation in Section 3.4. Due to time constraints, the field observations could not be further considered in this thesis; however, future studies are planned to confirm or contradict the above speculations.

Eventually, it is worth recalling that a shear stack filled with soil is an imperfect and not a completely understood 3D system aiming at simulating a 1D vertically propagating shear wave, in which imperfections, although present (such as, for instance, the different stiffnesses of the shear stack and soil, influence of shear stack inertia, the boundary effects implying a zig-zagged displacement and non-uniform stress distribution) are attempted to be minimized. The results from the examples of the experimental work in dry soil used in this thesis (Durante, 2015) come from a setup with piles, a bi-layered soil profile, a small shear stack, with slightly imperfect sine input motion and the measured results being strongly filtered (i.e. an 80Hz filter applied on 25Hz input motions). Ideally, one would want to analyse a single soil layer only, without structural elements (although a single pile could be considered as a “carrier” of separated elastic waves as explained before), possibly in a large shear stack to minimize effects of boundary conditions, under perfect sine input motion applied at base and with limited filtering on the measured results. Therefore, it is recognized that higher harmonics in the experiments such as the one used in this study could also possibly be generated due to other reasons, such as reflections of waves from piles, wave reflections and refractions between the two layers or the shear stack interacting with the soil. However, the effects of these factors on the results have been considered in more detail (Section 2.1), subsequently have been attempted to be studied numerically (Section 3.3) and shown to be rather negligible on the main conclusions drawn in this chapter.

Importantly, regarding experiments in shear stacks, some consideration is worth to be given to recorded input motions. Namely, a difference between shear stack tests performed at 1g (e.g. Durante, 2015) and in centrifuge (e.g. Madabhushi et al., 2020) is sometimes observed in terms of the recorded input motions. In particular, higher harmonics (with a regular frequency pattern) are more often observed at the soil base in centrifuge tests, notwithstanding the intended input motion should consist only of a single harmonic. In the shear stack tests at 1g performed at Bristol, the amplitude of the higher harmonics at the soil base is larger for P-waves with respect to S-waves, as observed in Section 3.4. For this reason, the higher frequencies are sometimes considered to be generated by the actuator itself (Brennan et al., 2005; Yao et al., 2017). The possibility of the higher harmonic presence at base due to actuators themselves cannot be excluded as the author lacks experimental experience. However, an alternative explanation to the presence of higher harmonics at the base level can be an interaction between soil specimen (soil in a shear stack) and actuating systems

(actuators and shaking tables). In shear stack tests at 1g performed in Bristol, the amplitude of the higher harmonics at the soil base is typically rather negligible. This is believed to be related to the difference in mass and stiffness of the actuating systems in comparisons with soil specimen in 1g and centrifuge tests. For instance, the Bristol shear stack filled with soil is of a relatively “small” mass when comparing with the mass of the shaking table, thus it is the shaking table motion that really drives the input motion and the interaction “soil specimen-actuating system” would be expected to be relatively low. On the other hand, the actuating system in centrifuge is of significantly reduced size, and the harmonics registered in soil can easier affect the response at the shaking table level, thus the interaction “soil specimen-actuating system” is expected to be stronger. Such stronger interaction could have also occurred in the case of P-waves in 1g, shear stack tests performed at Bristol facility, where undesired higher harmonics were observed at soil base, for a nominal single harmonic input motion.

Finally, some comments can be given on the finite element method which is recognized to be not perfectly suited for shock wave analysis, due to typical generation of spurious very high frequency oscillations. The shock wave formation in dry (weak discontinuity) or saturated soil (strong discontinuity), discussed in this chapter, can explain the numerical difficulties that are typically encountered in seismic geotechnical modelling. Such difficulties were also encountered by the author at the beginning of the PhD research when acceleration fields were surprisingly heavily affected by some sort of noise (due to unknown reasons at that time), whereas displacement and velocity fields showed uniform expected results. In any case, the occurrence of shock waves might demand the use of more sophisticated numerical techniques (such as the discontinuous Galerkin method or higher order finite elements, e.g. Semblat & Brioist, 2000; or Godunov’s method, e.g. Fellin, 2002) than those currently used in practice and employed in this work. It would be presumed that the use of such techniques would allow for further developments of the findings shown in this thesis. For example, the answer to which extend the very high frequencies are numerical and to which are physical could be established, as some pondering shown in this thesis suggested that the very high frequency content could also potentially be physical due to many interactions of fast elastic unloading waves and slow plastic loading waves. To distinguish between the two sources of very high frequencies, the numerical study would need to be repeated with one of the more advanced and reliable theoretical formulations.

5. Conclusions

The numerical study and its comparison with the experimental examples shown in this chapter have indicated the potential origin of higher harmonics typically observed in experimental studies of soil excited by single sine input motion. The most important findings of Chapter 2 can be summarized as follows:

- It has been shown that higher harmonics generated in experimental works, such as in a shear stack (1g) or in a laminar box (centrifuge), are physical and can be explained by soil nonlinearity and elastic unloading waves occurring in elastoplastic material such as soil and leading to sine wave distortion and separation of the elastic part of a wave. Most importantly, unloading waves in soil and their effects have not been recognized before. Thus, they should be a subject of future studies in order to develop further the findings of this chapter. This thesis can be considered as a good starting point for such further examination.

- Generally, the amplitude of the generated higher harmonics is related to the amplitude of the input motion and the amount of nonlinearity experienced by soil. The sharper the change from loading into unloading, the more severe the impact of nonlinearity and fast elastic unloading waves in dry soil.

- The occurrence of the odd pattern of harmonics, i.e. 3ω , 5ω , etc is related to symmetrical response of soil such as in S-wave propagation shown in Section 3.3. Whereas, the odd and even pattern of generated harmonics, i.e. 2ω , 3ω , 4ω , etc such as shown in the case of P-wave propagation, non-symmetrical loading or slope geometry such as studied in the LEAP-UCD-2017 project, can generally be associated with non-symmetrical soil response.

- Structural behaviour can be affected by generated higher harmonics as shown in this chapter. Additional waves of higher frequencies are shown to travel along kinematic piles. This can be potentially considered as an example of a superharmonic resonance.

- Based on the findings of this chapter, the higher frequency content would also be expected to be generated by soil in field during real earthquakes. Therefore, traditional thinking of filtering out higher frequencies in soils as a result of wave propagation from rock underneath through soil deposits may not be fully correct.

- The higher harmonic generation can be simulated correctly by soil constitutive model which possesses fully nonlinear loading and unloading behaviour such as the elastoplastic models ST and DM model or the hypoplastic HP model. Advanced soil constitutive models such as presented in this study are capable of capturing the real soil behaviour for S-wave but not for P-wave propagation. For the latter, a soil constitutive model with a “cap” yield surface would be expected to possibly perform better.

- Soil nonlinearity leads to shock wave formation of weak (dry soil) or strong discontinuity type (saturated soil). As a result, the standard finite element formulation may not be fully appropriate when shock wave is formed in soil and results in high frequency oscillations computed in numerical acceleration records. Future work should focus on developing more advanced finite element formulations, such as discontinuous non-Galerkin method or higher order finite element formulations in order to confirm to which extent the very high frequency oscillations are numerical (and related to weak discontinuity shock formation) or physical (related to numerous internal interactions between elastic unloading waves and plastic loading waves).

- The results presented in this chapter support the concept that soils have actually an elastic region and highlight the importance of such a region in engineering problems regarding seismic wave propagation in soils.

- Determination of the regions of elastic and plastic soil behaviour in seismic wave propagation problem could be potentially determined based on the generation of higher harmonics. In detail, high amplitude motions are expected to generate harmonics, whereas low amplitude input motions are not. This has been shown numerically only and would need to be confirmed further in the future experiments as could potentially lead to the determination of the range of the applicability of the simplified numerical methods assuming soil linear elastic behaviour.

- Caution is advised when filtering experimental results as excessive filtering may lead to the removal of physical high frequency motions such as discussed in this chapter.

The findings of this chapter reveal how experimental work helps validating constitutive models, but also vice versa, how application of advanced soil constitutive models can help in understanding sometimes “mysterious” measurements in experiments. The mutual interpretation of the results obtained from the advanced numerical studies and the available examples of the shear stack and centrifuge experimental works revealed unknown effects of soil nonlinearity and importance of elastic unloading waves. On the other hand, although the results presented in this chapter explain clearly the higher harmonic observation in soil seismic response, it is believed to be interesting to carry out a dedicated experimental campaign, towards a more explicit observation of elastic unloading waves and their effects on the measurements in small scale experimental works. Possibly again with the aid of numerical studies, this time using more advanced numerical techniques, capable of dealing with shock formation. As such, the results shown in this chapter, if confirmed in the future, would cast new light of seismic wave propagation in soils.

References

- Aoi, S., Kunugi, T., Fujiwara, H. (2008). Trampoline effect in extreme ground motion. *Science* 322(5902): 727-730.
- Abate, G., Massimino, M., R. (2016) Dynamic soil-structure interaction analysis by experimental and numerical analysis. *Rivista Italiana di Geotecnica* 2/2016.
- Beber, R., Madabhushi, S., Dobrisan, A., Haigh, S., Madabhushi, G., (2018-10-08), "CU1, CU2 - University of Cambridge Experiments, in PRJ-1843: LEAP-UCD-2017", *DesignSafe-CI [publisher]*, Dataset, doi:10.17603/DS2H68M.
- Bonilla, L. F., Archuleta, R. J., Lavallée, D. (2005). Hysteretic and dilatant behaviour of cohesionless soils and their effects on nonlinear soil response: field data observations and modelling. *Bulletin of the Seismological Society of America* 95(6), 2373-2395.
- Brennan, A.J., Thusyanthan, N. I., Madabhushi, S.P.G. (2005). Evaluation of shear modulus and damping in dynamic centrifuge tests. *Journal of Geotechnical and Geoenvironmental Engineering* 131(12), 1488-1497.
- Conti, R., Madabhushi, G. S. P., Viggiani, G. M. B. (2012). On the behaviour of flexible retaining walls under seismic actions. *Géotechnique* 62(12), 1081-1094.
- Conti, R., Viggiani, G. M. B. (2012). Evaluation of Soil Dynamic Properties in Centrifuge Tests. *Journal of Geotechnical and Geoenvironmental Engineering* 138(7), 850-859.
- Crewe, A., J., Lings, M., L., Taylor, C., A., Yeung, A., K., Andrighetto, R. (1995). Development of a large flexible shear stack for testing dry sand and simple direct foundations on a shaking table. *European seismic design practice, Elnashai (ed), Balkema, Rotterdam.*
- Dar, A. R. (1993). Development of a flexible shear-stack for shaking table testing of geotechnical problems. *Phd thesis*. University of Bristol.
- Durante, M. G. (2015). Experimental and numerical assessment of dynamic soil-pile-structure interaction. *Phd Thesis*. Università degli Studi di Napoli Federico II (Italy).
- Fan, F. G., Ahmadi, G., Tadjbakhsh, I. G. (1988). Base isolation of a multi-story building under a harmonic ground motion – a comparison of performances of various systems. *Technical Report NCEER-88-0010*.
- Fellin, W. (2002). Numerical computation of nonlinear inelastic waves in soils. *Pure and Applied Geophysics* 159, 1737-1748.
- Gajo, A., Muir Wood, D. (1997). Numerical analyses of behaviour of shear stacks under dynamic loading. *Report on work performed under the EC project European*

Consortium of Earthquake Shaking Tables (ECOEST): Seismic bearing capacity of shallow foundations.

Gajo, A. (2010). Hyperelastic modeling of small-strain anisotropy of cyclically loaded sand. *International Journal for Numerical and Analytical Methods in Geomechanics* 34(2), 111-134.

Gajo, A. (2018). Subroutine for a user-defined finite element with implemented constitutive law of the Severn-Trent sand model and u-p formulation for saturated media.

Gajo, A. (2019). Fortran subroutine in a format of user defined material (UMAT) of a 1D hyperbolic law.

Gajo, A., Argani, L. (2020). New insights in seismic vertical ground motion modelling with u-p and u-U formulations. (*In preparation, title to be confirmed*).

Gallegos, M. F., Saragoni, G. R. (2017). Analysis of strong-motion accelerograph records of the 16 April 2016, Mw 7.8 Muisne, Ecuador Earthquake. *In the Proceedings of: 16th World Conference on Earthquake Engineering, Santiago, Chile.*

Kelly, J. M. (1982). The influence of base isolation on the seismic response of light secondary equipment. *Research Report UCB/EERC-81/17. University of California, Berkeley.*

Kutter, B. L., Wilson, D. W. (1999). De-liquefaction shock waves. *In Proceedings of: 7th U.S. -Japan Workshop on Earthquake Resistant Design for Lifeline Facilities and Countermeasures Against Soil Liquefaction, Technical Report MCEER-99-0019, 295-310.*

Kutter, B. L., Carey, T. J., Hashimoto, T., Zeghal, M., Abdoun, T., Kokkali, P., Madabhushi, G., Haigh, S. K., Burali d'Arezzo, F., Madabhushi, S., Hung, W.-Y., Lee, C.-J., Cheng, H.-C., Iai, S., Tobita, T., Ashino, T., Ren, J., Zhou, Y.-G., Chen, Y.-M., Sun, Z.-B., Manzari, M. T. (2018). LEAP-GWU-2015 experiment specifications, results and comparisons. *Soil Dynamics and Earthquake Engineering* 113, 616-628.

Kutter, B. L., Carey, T. J., Stone, N., Li Zheng, B., Gavras, A., Manzari, M. T., Zeghal, M., Abdoun, T., Korre, E., Escoffier, S., Haigh, S. K., Madabhushi, G. S. P., Madabhushi, S. S. C., Hung, W.-Y., Liao, T.-W., Kim, D.-S., Kim, S.-N., Ha, J.-G., Kim, N. R., Okamura, M., Sjafruddin, A., N., Tobita, T., Ueda, K., Vargas, R., Zhou, Y.-G., Liu, K. (2019). LEAP-UCD-2017 Comparison of Centrifuge Test Results. *In: B. Kutter et al. (Eds.), Model tests and numerical simulations of liquefaction and lateral spreading: LEAP-UCD-2017. New York: Springer.*

- Lanzano, G., Bilotta, E., Russo, G., Silvestri, F., Madabhushi, S. P. G. (2012). Centrifuge modelling of seismic loading on tunnels in sand. *Geotechnical Testing Journal* 35(6), 854-869.
- Madabhushi, G. S. P. (2014). Centrifuge modelling for civil engineers. *Taylor & Francis Ltd.*
- Madabhushi, S. S. C., Dobrisan, A., Beber, R., Haigh, S. K., Madabhushi, G. S. P. (2020). LEAP-UCD-2017 Centrifuge tests at Cambridge. In: Kutter, B., Manzari, M., Zeghal, M. (eds) *Model Tests and Numerical Simulations of Liquefaction and Lateral Spreading*. Springer, Cham.
- Manandhar, S., Kim, S., & Kim, D. (2019). LEAP-ASIA-2018 Centrifuge Test at KAIST.
- Manzari, M. T., El Ghoraiiby, M., Zeghal, M., Kutter, B. L., Arduino, P., Barrero, A. R., Bilotta, E., Chen, L., Chen, R., Chiaradonna, A., Elgamal, A., Fasano, G., Fukutake, K., Fuentes, W., Ghofrani, A., Haigh, S. K., Hung, W.-Y., Ichii, K., Kim, D. S., Kiriya, T., Lascarro, C., Madabhushi, G. S. P., Mercado, V., Montgomery, J., Okamura, M., Ozutsumi, O., Qiu, Z., Taiebat, M., Tobita, T., Travasarou, T., Tsiaousi, D., Ueda, K., Ugalde, J., Wada, T., Wang, R., Yang, M., Zhang, J.-M., Zhou, Y.-G., Ziotopoulou, K. (2019). LEAP-2017: Comparison of the Type-B Numerical Simulations with Centrifuge Test Results. In: B. Kutter et al. (Eds.), *Model tests and numerical simulations of liquefaction and lateral spreading: LEAP-UCD-2017*. New York: Springer.
- McAllister, G., Taiebat, M., Ghofrani, A., Chen, L., Arduino, P. (2015). Nonlinear site response analyses and high frequency dilation pulses. In *Proceedings of: 68th Canadian Geotechnical Conference*. Quebec, Canada.
- Mercado, V., W. El-Sekelly, Abdoun, T., Pajaro, C. (2018). A study on the effect of material nonlinearity on the generation of frequency harmonics in the response of excited soil deposits. *Soil Dynamics and Earthquake Engineering* 115, 787-798.
- Moccia, F. (2009). Seismic soil pile interaction: experimental evidence. *PhD Thesis*. Universita degli Studi di Napoli Federico II (Italy).
- Muir Wood, D., Crewe, A. J., Taylor, C. A. (2002). Shaking table testing of geotechnical models. *International Journal of Physical Modelling in Geotechnics* 2(1), 1-13.
- Nekorkin (2015). Introduction to nonlinear oscillations. *Wiley*.
- Nowacki, W. K., (1978). Stress waves in non-elastic solids. *Pergamon Press*.
- Pavlenko, O., (2001). Nonlinear seismic effects in soils: numerical simulation and study. *Bulletin of Seismological Society of America* 91(2), 381-96.

- Pavlenko, O., Irikura, K. (2005). Identification of the non-linear behaviour of liquefied and non-liquefied soils during the 1995 Kobe earthquake. *Geophysical Journal International* 160(2), 539-553.
- Rakhmatullin, KhA (1945). On propagation of the unloading wave. *PMM* 9(1), 15-24.
- Roten, D., Fah, D., Bonilla, L. F. (2013). High-frequency ground motion amplification during the 2011 Tohoku earthquake explained by soil dilatancy. *Geophysical Journal International* 193(2), 898-904.
- Ruiz, S., Saragoni, G. R. (2009). Free vibrations of soil during large earthquakes. *Soil Dynamics and Earthquake Engineering* 29(1), 1-16.
- Semblat, J.F., Brioist, J.J. (2000). Efficiency of higher order finite elements for the analysis of seismic wave propagation. *Journal of Sound and Vibration* 231(2), 460-467.
- Song, E. X., Haider, A., Peng, L. (2018). Numerical simulation of plane wave propagation in a semi-infinite media with a linear hardening plastic constitutive model. *In Proceedings of: China-Europe Conference on Geotechnical Engineering, SSGG*, 410-414.
- Towhata, I. (1996). Seismic wave propagation in elastic soil with continuous variation of shear modulus in the vertical direction. *Soils and Foundations* 36(1), 61-72.
- Tsiapas, Y. Z., Bouckovalas, G. D. (2018). Selective Filtering of Numerical Noise in Liquefiable Site Response Analyses. *In Proceedings of: Geotechnical Earthquake Engineering and Soil Dynamics Conference, June 10-13, Austin, Texas*.
- Veeraraghavan, S., Spears, R. E., Coleman, J. L. (2019). High frequency content in soil nonlinear response: A numerical artefact or a reality? *Soil Dynamics and Earthquake Engineering* 116, 185-191.
- Vitorino, M. V., Vieira, A., Rodrigues, M. S. (2017). Effect of sliding friction in harmonic oscillators. *Scientific Reports* 7(1) 3726.
- Von Wolffersdorff, P. A. (1996). A hypoplastic relation for granular materials with a predefined limit state surface. *Mechanics of Cohesive and Frictional Materials* 1(3), 251-271.
- Wang, L. (2007). Foundations of stress waves. *Elsevier Science*.
- Wiebe, L., Christopoulos, C. (2010). Characterizing acceleration spikes due to stiffness changes in nonlinear systems. *Earthquake Engineering and Structural Dynamics* 39, 1653-1670.
- Yao, J., Han, Y., Dietz, M., Xiao, R., Chen, S., Wang, T., Niu, Q. (2017). Acceleration harmonic estimation for a hydraulic shaking table by using particle swarm

optimization. *Transactions of the Institute of Measurement and Control* 39(5), 738-747.

You, Y. S., Yin, Y., Wu, Y., Chew, A., Ren, X., Zhuang, F., Gholam-Mirzaei, S., Chini, M., Chang, Z., Ghimire, S. (2018). High harmonic generation in amorphous solids. *Nature Communications* 8(1), 724.

CHAPTER 3

Numerical simulation of shear stack experiments on piles

1. Background

Soil behaviour and soil-structure interaction (SSI) in seismic conditions has been widely studied in recent years. The latter is of paramount importance for resilient cities and societies of the future. The origins of SSI come from the fact that the soil causes a structure to vibrate, and the structure in response affects the surrounding soil. The SSI can be split into inertial interaction (when the mass of a structure affects the motion) and kinematic interaction (when an embedded structure is driven by seismic waves without its mass affecting the motion). Typically, when compared to the fixed base conditions, SSI leads to lengthening of natural periods and increased damping due to wave radiation effect and hysteretic damping due to plasticity developing in soil (Pitilakis et al., 2008). A similar point of view on soil-structure interaction was presented by Loli et al. (2010) where they indicated soil as potential placement of a plastic hinge developing during large magnitude earthquakes in a soil-structure system and protecting the structure. Although typically soil influence on a structure is considered beneficial, detrimental effects were also observed. For example, during the 1985 Mexico City earthquake double resonance was experienced, i.e. soil vibrated with its own natural frequency, and then caused structures of similar natural frequency to resonate with soil natural frequency and suffer damage (Hall & Back, 1986). Indeed, Mylonakis & Gazetas (2000) looked in detail at cases of detrimental effects of SSI and concluded that structural ductility demand can also increase due to the period elongation caused by SSI. Although the appreciation of SSI effects has been acknowledged, further advanced experimental and numerical studies follow in order to detail the knowledge on SSI and to allow reliable predictions on complex boundary value problems.

Small scale physical modelling is one of the approaches to study in more detail seismic soil behaviour and soil-structure interaction under earthquake conditions. Numerous experimental studies have been carried out in the recent past. Many of them have been carried out in shear stacks on a shaking table apparatus in 1-g stress state (Muir Wood et al., 2002). Moccia (2009) analysed a single pile of varying pile head fixity and embedded in soil profiles of various characteristics. Chidichimo et al. (2014) studied a pile group behaviour in a bi-layered soil profile. Further comments and

outcomes of similar works are shown by Simonelli et al. (2014) and Durante et al. (2016).

Another group of physical studies comprises those carried out in centrifuge, thus at increased stress levels comparing to 1-g shear stack studies. Lanzano et al. (2012) studied a tunnel embedded in granular dry soil subjected to earthquake loading in order to allow future validation of numerical tools. Conti et al. (2012) looked at the behaviour of a retaining wall, its rotation and distribution of earth pressures. Many centrifuge studies have been carried out on saturated soil. The work on a saturated slope in a rigid box studied within the LEAP-GWU-2015 and LEAP-UCD-2017 projects was summarized in Kutter et al. (2018) and Kutter et al. (2019) respectively, where the results from all the participating centrifuge centres were compared. Importantly, some differences in the obtained results for the same experimental setup were highlighted.

In addition to small scale tests, there is a lower number of large-scale tests on seismic soil-structure interaction. For instance, Tokimatsu et al. (2005) studied the kinematic and inertial interaction of a small pile group with and without a structure in dry and saturated soil. Shirato et al. (2008) showed subsequently a larger pile group subjected to a series of large-scale earthquakes.

Numerical modelling, such as the finite element method, is an alternative to physical modelling and is a powerful tool to study seismic soil behaviour and soil-structure interaction. Robust advanced soil constitutive models capable of simulating cyclic soil behaviour are needed to carry out accurate predictions in such numerical studies. There is a vast number of constitutive models which come from different frameworks and which have been shown to be able to replicate soil cyclic behaviour, thus, they are good candidates to be used in seismic analysis. For instance, Gajo & Wood (1999a, 1999b) presented a kinematic hardening elastoplastic model, namely Severn-Trent sand model, which was shown to be capable of analysing soil under various densities and pressures with a single set of model parameters. A group of sand constitutive models also based on the elastoplasticity approach comes under the name of SANISAND (simple anisotropic sand) family models. These include consecutive works from Dafalias & Manzari (2004), Dafalias et al. (2004), Taiebat & Dafalias, (2008), Dafalias & Taiebat (2016) which all are based on Manzari & Dafalias (1997) and introduced, respectively the following updates: a fabric tensor to modify volumetric response, a yield cup to model grain crushing, a fabric tensor to account for inherent anisotropy and a model without the yield surface. The SANISAND family models were also a base and inspiration for further developments. Pisano & Jeremic (2014) proposed a visco-elastic-plastic constitutive model which poses two dissipative mechanisms, i.e. the first one due to hysteric soil behaviour, the second one due to viscous damping. A popular choice among practitioners dealing with liquefaction phenomena in saturated soil is the PM4 sand model (Boulanger & Ziotopoulou, 2015) which is another of the developments of the SANISAND models.

A different family of constitutive models is based on the hypoplasticity theory (Kolymbas, 1991). Mašín (2018) provided a wide overview of the capabilities of the hypoplastic models, which include hypoplastic models for sands (Gudehus, 1996; Von Wolffersdorff, 1996) and their developments to account for small strain stiffness (Niemunis & Herle, 1997) and reduction in the accumulation of strains in loading cycles (Wegener, 2013; Wegener & Herle, 2014).

The above-mentioned models are not the only candidates to simulate soil cyclic behaviour. The number of the available advanced soil constitutive models is larger and is still growing. On the other hand, detailed validation of constitutive models, although attempted for some constitutive models in certain aspects, is still rather missing. Some constitutive models, such as those mentioned above, have been shown to replicate laboratory cyclic tests successfully and subsequently used to make predictions for large boundary value problems. However, another step in the validation of advanced soil constitutive models is their ability to simulate complex boundary value problems, including large soil domains of varying characteristics and various types of soil-structure interaction. Some studies, based on the comparisons of numerical predictions with benchmark experimental works, have been dedicated to this aspect.

One of the first such studies by Gajo & Wood (1997) used a simple Mohr Coulomb model and an advanced soil constitutive Pastor-Zienkiewicz model (Pastor et al., 1990) to simulate shear stack tests from Dar (1993) and indicated a need to develop more reliable constitutive models, in particular a model able to account for dependency of strength and dilatancy on mean pressure. A large number of codes was verified in PRENOLIN (PREdiction of NOn-LINear soil behaviour) project which dealt with nonlinear site response (Régner et al., 2018). Bilotta et al. (2014) summarized the results of five different predicting teams in the numerical round robin competition for seismic simulations of a tunnel embedded in dry granular soil. All teams fairly well were able to reproduce acceleration records in free field, both in terms of amplitude and frequency content. On the other hand, a consistent trend of underestimated settlement was shown by all five teams. In addition, the representation of bending moments and hoop forces in the tunnel was captured only to a qualitative point. Numerous advanced soil constitutive models were attempted to be validated during the series of the LEAP projects. The summary of the numerical predictions for the LEAP-2017 project was provided by Manzari et al. (2019). In addition, more detailed studies were shown by all the predicting teams. For instance, Ghofrani & Arduino (2018) used the DM model (Dafalias & Manzari, 2004) to model the response of a sloping ground analyzed in centrifuge and indicated that the DM model was capable to represent many aspects of saturated soil under seismic loading conditions.

There are some studies which aimed at validation of the hypoplastic soil models in seismic conditions. For instance, Reyes et al. (2009) validated the viscohypoplastic model (Niemunis, 2003) on the site response recorded in Lotung (Taiwan). The results showed that the hypoplastic model was capable to simulate the

site response in terms of calculated accelerations. Soil seismic behaviour analyzed by the hypoplastic sand model was also presented by Hleibieh & Herle (2018). They indicated that the hypoplastic model was able to simulate a behaviour of an embankment on saturated soil in terms of generated pore pressures and displacements. Hleibieh et al. (2014) tried to validate the hypoplastic sand model on soil-tunnel interaction experiments in centrifuge. They showed good match between computed and measured accelerations in the free field, but much less consistent results for settlements and structural bending moments. The soil-tunnel interaction was also later analysed by Mohammadi-Haji et al. (2018) and Ochmanski et al. (2019). The former presented comparison of the hypoplastic sand model with HSS model (Benz, 2007) and simple Mohr Coulomb model where all the models underpredicted the settlement. The latter study showed improved predictions of settlement although still reaching only 50% of the measured one.

The study presented in this chapter aims at detailed validation of two advanced soil constitutive models, namely the Severn-Trent (ST) sand model (Gajo, 2010) and the hypoplastic (HP) sand model (Von Wolffersdorff, 1996), on the examples of the shear stack experiments on piles in dry soil. A comparison of the numerical and experimental results is shown for various input motions and pile head conditions, including setups with a single degree of freedom structure on the top of one of the piles. The results are followed by a discussion section which looks in detail on the performance of the constitutive models and on the characteristics of soil behaviour in the shear stack. The characteristics of the soil behaviour in the shear stack are analysed in order to determine the prerequisites for the formulation of constitutive models aimed at performance in seismic conditions. Subsequently, some constitutive and numerical features are under investigation and potential improvements in the formulation of the models are suggested in order to improve simulations under seismic loading conditions in the future.

2. Methodology

2.1. Experimental tests in shear stack on piles

Introduction to shear stack experiments

The experimental work with shear stack tests on piles was carried out in Bristol and was summarized by Chidichimo et al. (2014) and Durante (2015). Two phases of the experimental campaign, namely phase I and phase II, were conducted considering identical experimental setup of five piles in a bi-layered dry granular soil profile. The preceding experiment (Moccia, 2009) considered only a single pile of various pile head conditions and soil profile characteristics. The numerical simulations in this thesis focus solely on the pile group of five piles as no raw data could be obtained for the experimental work for the single pile experiments. In addition, the experiments from Moccia (2009) suffered from a relative movement between the shear stack and the shaking table, thus were found to be of limited reliability.

The history of the shear stack development in Bristol starts with the works of Dar (1993) and Crewe (1995 et al.). The currently used shear stack consists of eight aluminium stacks put on top of each other with rubber links in between (Figure 1). The shear stack dimensions are: 1.2m length, 0.8m height and 0.65m width. The scaling laws between an experimental model and a real size prototype were given by Muir Wood et al. (2002) and are not recalled here.

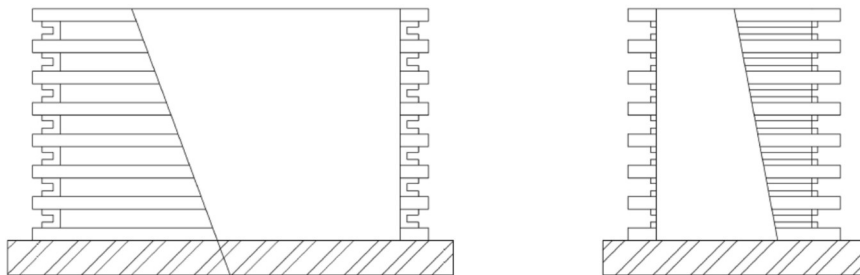


Fig. 1. Sketch of shear stack used in experimental work with pile group.

Soil Profile

The experimental work, which was simulated in this thesis, was carried out with Leighton Buzzard sand. Two different fractions of this sand were used, namely fraction E in the top “soft” layer and a mixture of fractions B (85%) and E (15%) in the bottom “stiff” layer. The properties of Leighton Buzzard sand and soil profile in the shear stack have been presented in Chapter 1 in Section 5.1 and are not repeated here.

The initial void ratio of the top loose layer is around 0.91 which is below the CSL for low pressure environment such as experienced in a shear stack at 1g, thus the soil is still expected to behave as dense sand. It is reminded here that no laboratory data was available for LB sand, fraction B+E. Thus, the bottom layer has been modelled in the numerical studies with the same input parameters as LB sand, fraction E, but with a void ratio of 0.85 which results in achieving the equivalent relative density of around 40% measured for the bottom layer. This assumption does not result in a very strong contrast in stiffnesses between the two soil layers. However, is deemed reasonable as already explained in Chapter 2 (Section 2.1).

Pile model and pile group arrangement

The tests comprised a five-pile group (Figure 2) with different pile head conditions. These included free head piles, a short cap spanning three closer piles (piles no. 1, 2 and 3), and a long cap spanning all five piles. In addition, a SDOF oscillator was placed on the pile no.3 in order to simulate a structure. The pile model is an aluminium tube of 750mm length, 22.23mm diameter and 0.71mm wall thickness.

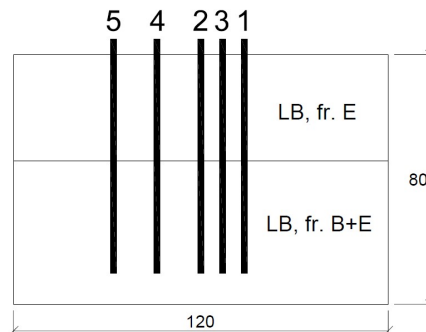


Fig. 2. Geometry of experimental setup and pile numbering of pile group in shear stack (dimensions in cm).

Importantly, following the review of the raw experimental data, it has been recognized that the piles with free pile head conditions also behave as oscillators. Chapter 2 (Section 3.5) has shown such example. This behaviour is presented here on Figure 3, where the accelerations measured on pile tops are shown, and on Figure 4, where the transfer functions for white noise input motion are shown. Durante (2015) took photos of the experimental setup (reproduced in the sketch on Figure 5) where transparent plastic caps and accelerometers mounted on the top of the piles can be seen. The weight of these two components was evaluated in this thesis as 80g (30g accelerometers, 50g plastic cap assuming low plastic density of 1000kg/m³) and was attributed to cause the top part of the pile to behave as an oscillator. The first dominant frequency of motion of the piles is as per the soil column (Figure 4) and comes from the fact that the piles generally behave as kinematic piles for majority of their length. The second peak in the frequency domain, although being close to the second peak of the soil column but much stronger in magnitude, is believed to actually be at higher frequencies, as one needs to remind that the acceleration results were filtered out with the cut-off frequency of 80Hz (5th order, i.e. gradual decline in frequencies above 80Hz). The experimental data with the white noise input motion shows different responses for the different piles, i.e. the top of the pile no.2 seems to have “more weight” and thus lower natural frequency. A speculative explanation to that could be wires and cables coming out of the pile interiors and leaning on the top of the pile, thus additionally loading the pile heads. What is more, when a real pile cap spanning three or five piles together is fixed on the pile heads, the pile tops do not show oscillator behaviour of an oscillator. This only confirms that in other cases the pile tops behave as oscillators (see the pile no. 2 on Figures 3a and 3b).

The above way of thinking, although being a speculation, seems logical to the author. The aspect of pile tops behaving as oscillators has been briefly shown in Chapter 2 (Section 3.5) and will be further discussed in the result section in Chapter 3.

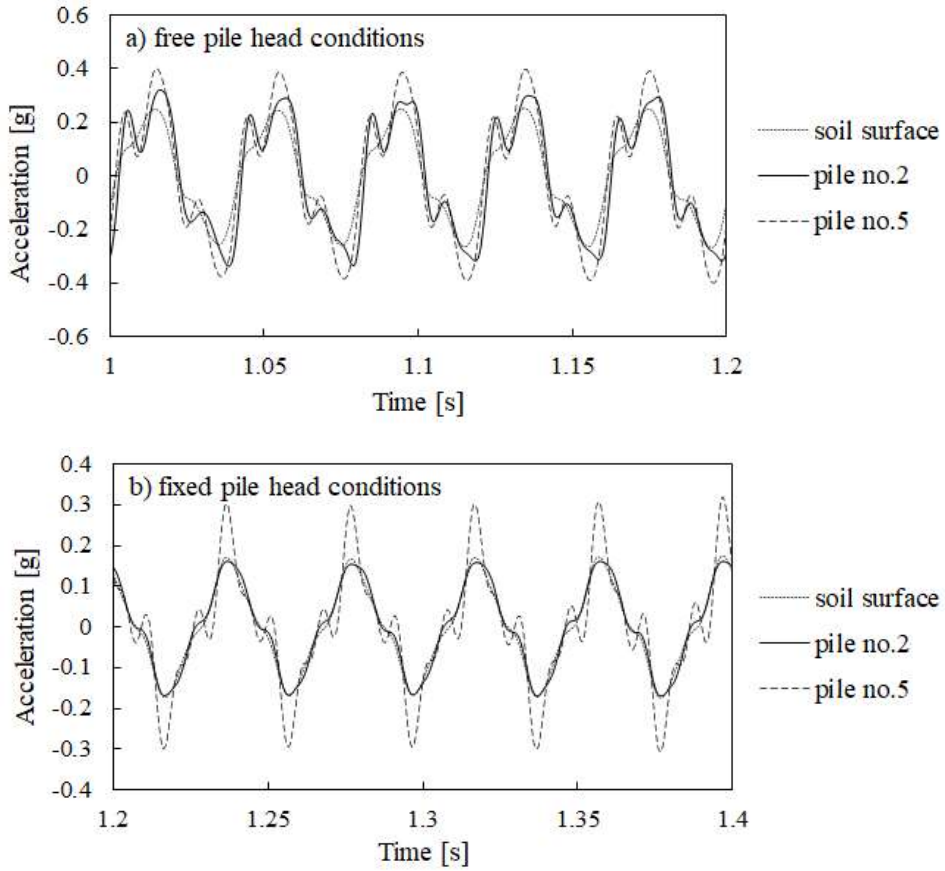


Fig. 3. Acceleration records in free field and on chosen piles for 25Hz input motion with: a) free head pile conditions (maximum amplitude 0.077g) and b) small pile cap spanning piles no. 1, 2 and 3 (maximum amplitude 0.037g).

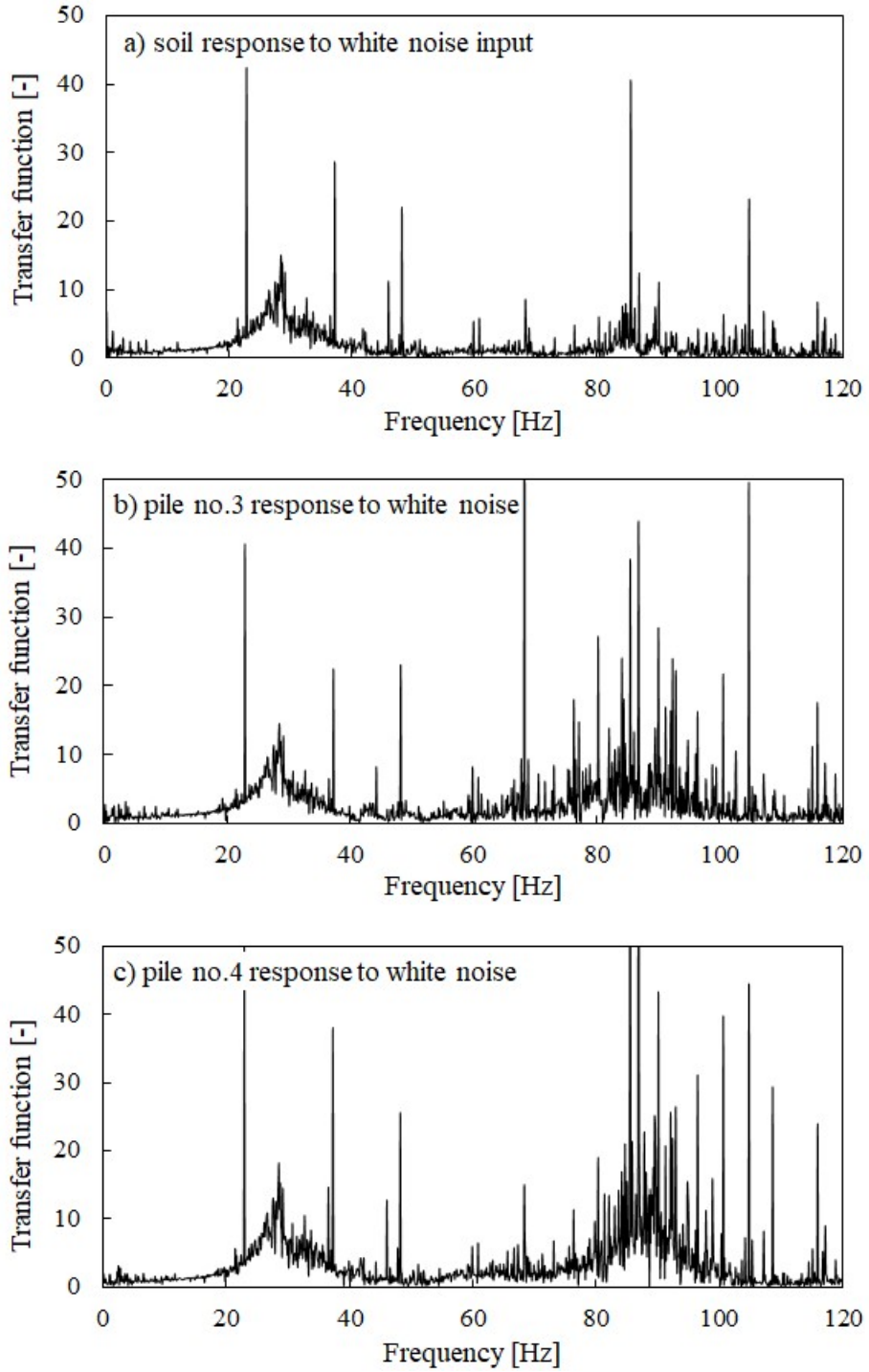


Fig. 4. Transfer functions for natural frequency assessment of: a) soil column, b) pile no. 3 and c) pile no. 4.

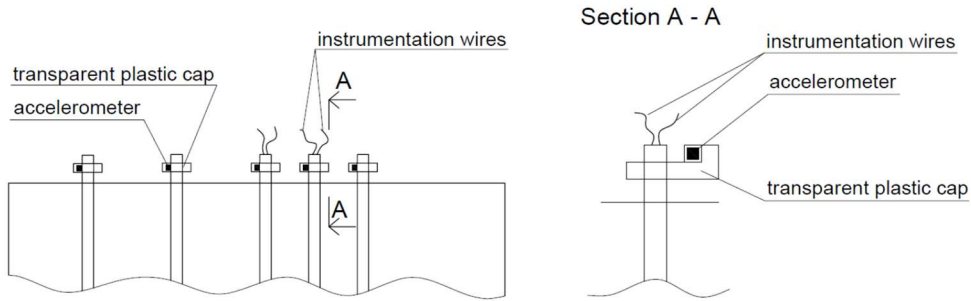


Fig. 5. Sketch of experimental setup of five-pile group in shear stack (for more see photographs in Durante, 2015).

Monitoring instruments

The monitoring instrumentation included accelerometers, displacement transducers, strain gauges and the Indikon instrument to measure settlements. The placement of the part of the instrumentation from the experimental setup used in this thesis is shown on Figure 6. The details on all data channels is available in Durante (2015).

Importantly, all the measuring channels were subject to filtering procedure (lowpass Butterworth 80Hz, 5th order) in order to remove high frequency noise (Durante, 2015). However, note that some channels, according to the author's observation, seem not to be filtered (e.g. settlements).

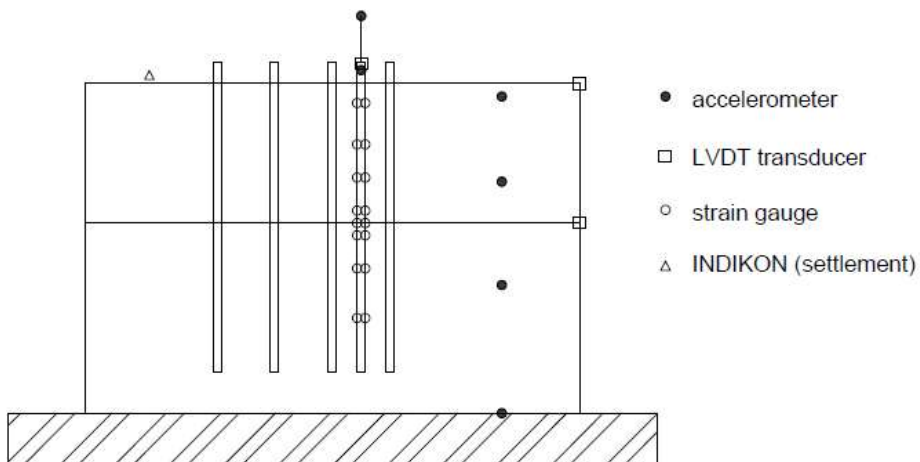


Fig. 6. Part of monitoring instrumentation installed inside shear stack and on piles.

Input motions

The chosen input acceleration time histories and the pile head conditions are shown in Table 1. Note that some part of the numerical results has been moved to Appendix E at the end of this thesis. Table 1 specifies which time histories are shown in the main body of this chapter, and which in Appendix E.

The numerical analyses in this chapter have focused solely on S-wave propagation. As a result, accelerations throughout this chapter should be explicitly understood as horizontal accelerations (unless otherwise stated).

Table 1 Input motions and pile head conditions analysed numerically

Item	Type of input motion	Maximum acceleration	Pile head conditions	Testing phase	Results
1	Sine 10Hz	0.137g	FHP	I	Chapter 3
2	Sine 25Hz	0.077g	FHP	I	Chapter 3
3	Sine 30Hz	0.041g	FHP	I	Appendix E
4	Tolmezzo scaled earthquake	0.101g	FHP	II	Appendix E
5	Sine 25Hz	0.037g	SCAP	I	Appendix E
6	Sine 10Hz	0.155g	FHP+SDOF	I	Chapter 3
7	Sine 25Hz	0.092g	SCAP+SDOF	I	Chapter 3

Test repeatability

The experimental campaign for a group of five piles was carried out in two phases, namely phase I and phase II. The experimental setups within both phases were practically the same, both in terms of soil characteristics and pile arrangements. Noticeably, the repeatability of the results in terms of measured soil accelerations in free field was typically very good as shown for the examples of similar tests from the two phases (Figures 7a and 7b). Sporadically, some discrepancies were also found, such as for the case of 30Hz input motion shown in Figure 7d. However, Cairo et al. (2011) reported stronger result filtering, i.e. 32Hz cut-off frequency for the 30Hz input motion, used at least for some of the data obtained in phase II. Such increased filtering can explain the discrepancies depicted on Figure 7d. The other measurements in free field, i.e. the horizontal displacement and settlement (the latter is of a negative value for downward movement) are shown on Figures 8 and 9, respectively. The pile head accelerations are compared in Figure 10 and show similar patterns in the repeatability of the measurements to those in free field response (Figure 7).

In terms of the pile head lateral displacements and the pile axial strains (indicator of pile bending moments) the same 25Hz and 30Hz input motions gave quite different and contradicting results between the two phases (Figures 11 and 12), i.e. the pile lateral displacements in phase I are larger but the pile axial strains are much smaller and not necessarily at the same depth as in phase II. Note that results are compared only for the pile no.3. However, the same pattern is observed for the other instrumented pile no. 2. According to Durante (2019), the measurements from the phase II “suffered” from some “mishmash” of the obtained data, therefore, the phase I is preferred in this thesis as more reliable in terms of measurements from transducers and strain gauges. The numerical results shown later confirm that the pile axial strains lie within lower order of magnitude as per the measurements in phase I.

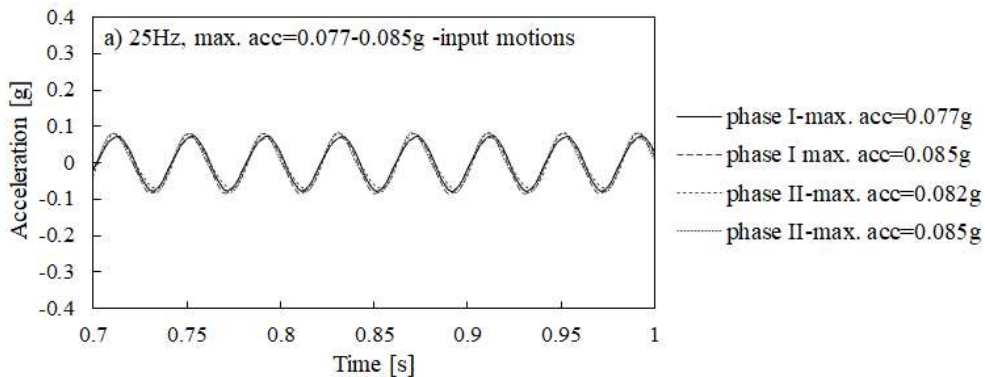


Fig. 7. (continuation on the next page)

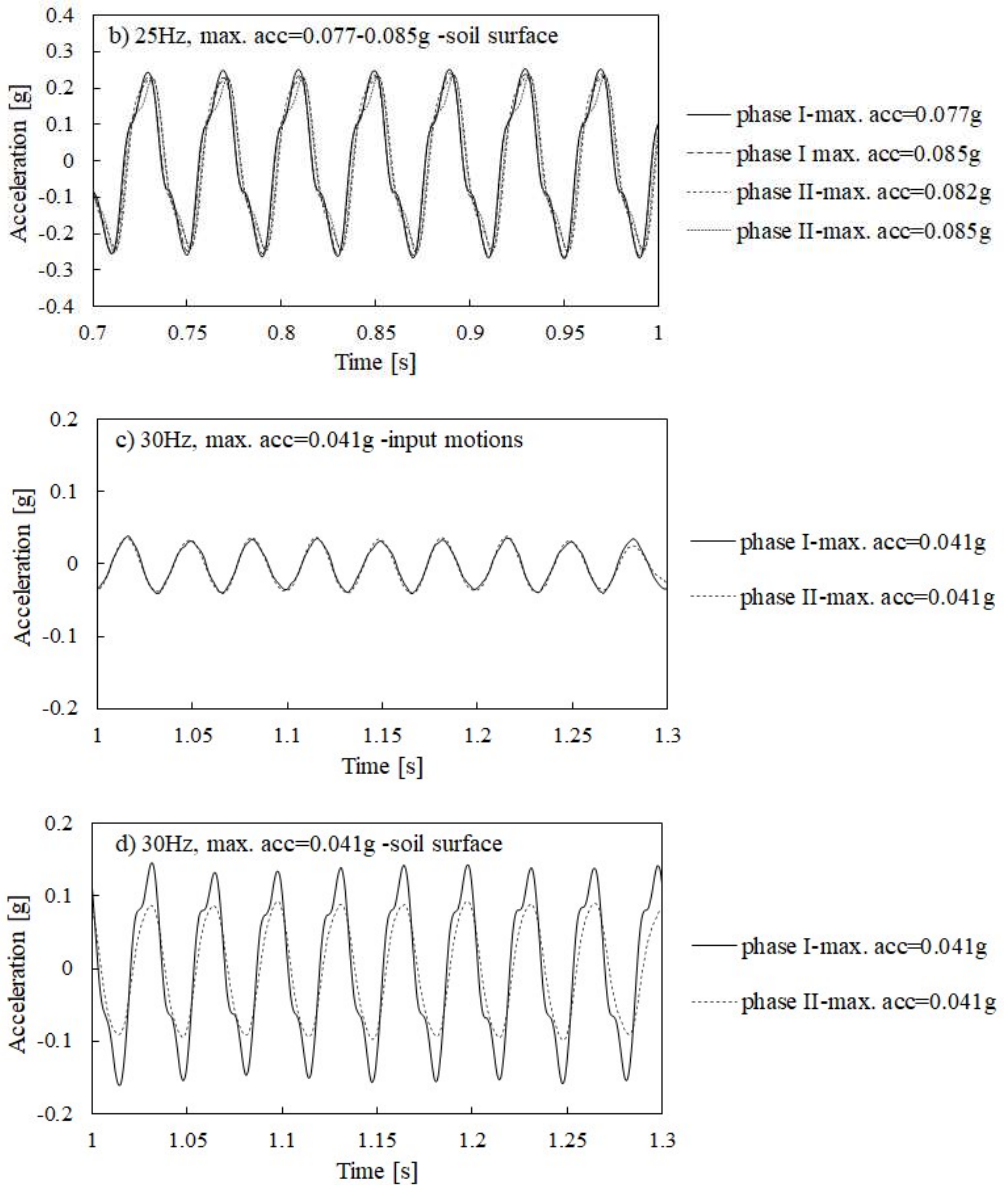


Fig. 7. Accelerations in free field at shear stack level and soil surface level for comparable input motions within testing phases I and II: a) 25Hz sinedwell -input motions, b) 25Hz sinedwell -soil surface, c) 30Hz sinedwell -input motions, d) 30Hz sinedwell -soil surface.

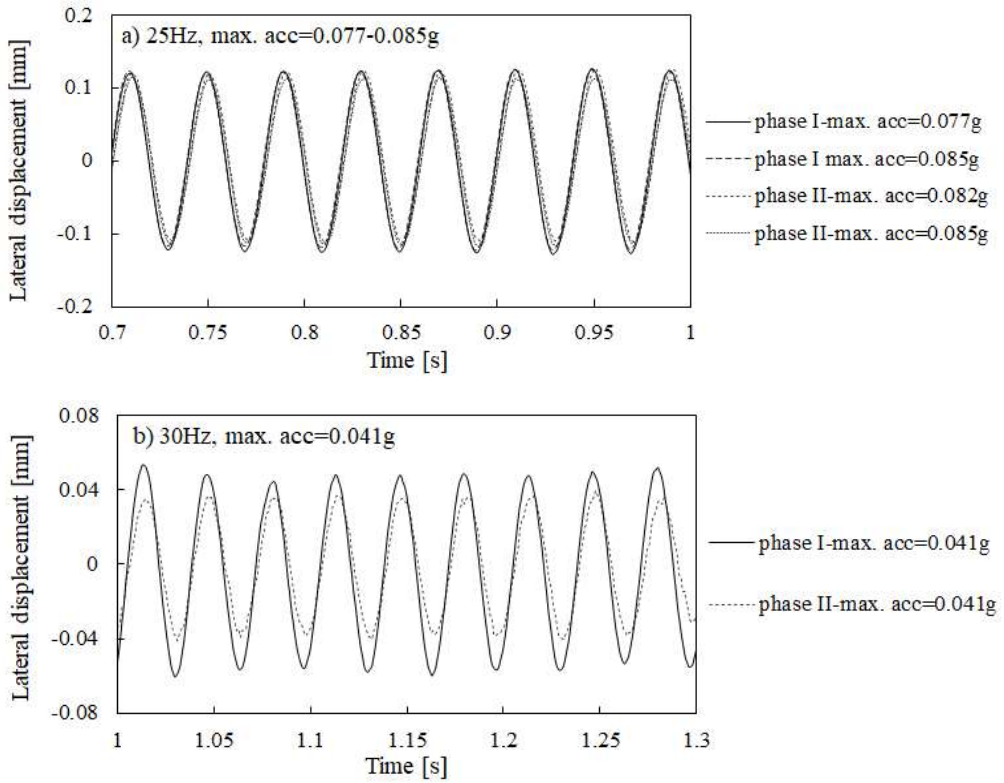


Fig. 8. Lateral displacement in free field at soil surface level for comparable input motions within testing phases I and II: a) 25Hz sinedwell, b) 30Hz sinedwell.

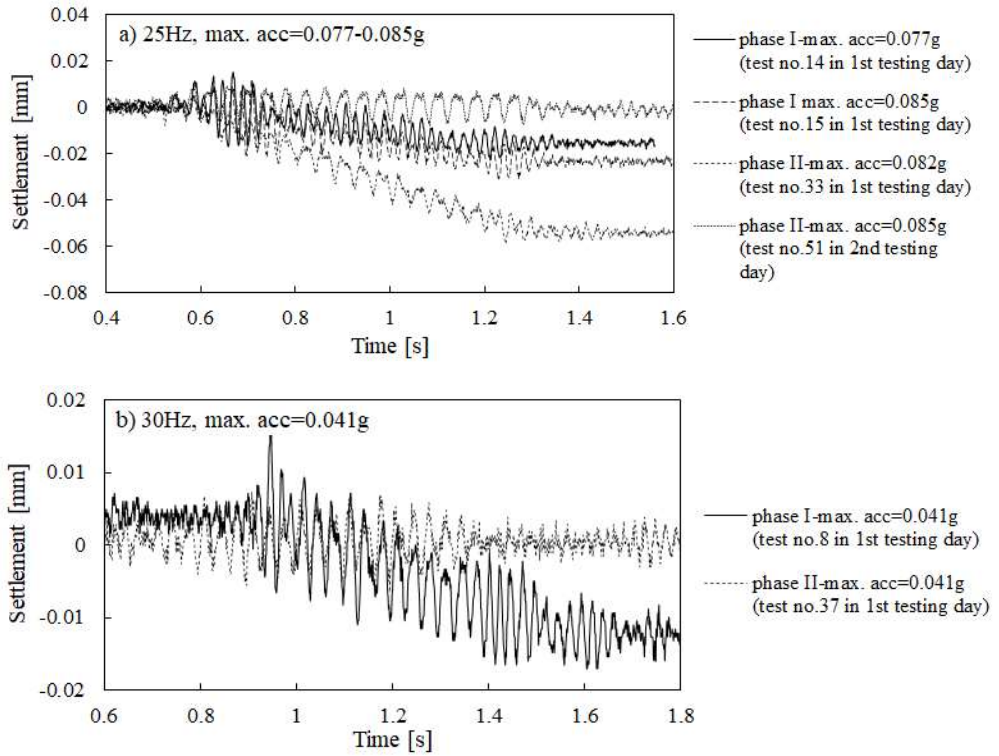


Fig. 9. Settlement at soil surface level for comparable input motions within testing phases I and II: a) 25Hz sinedwell, b) 30Hz sinedwell.

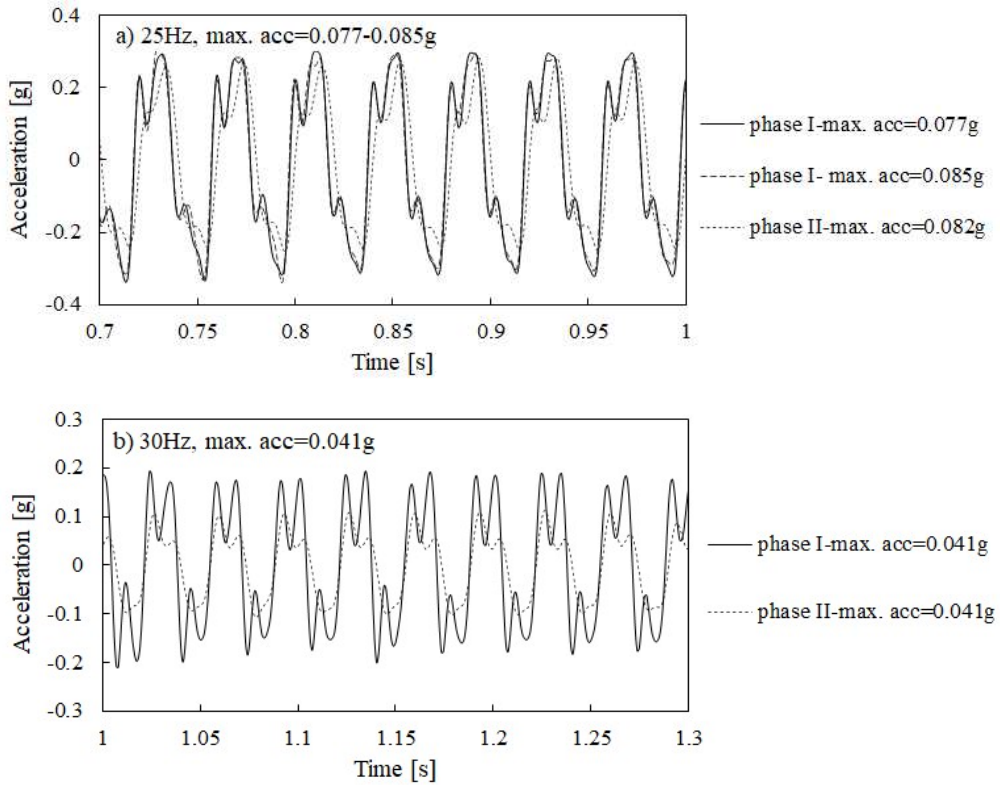


Fig. 10. Accelerations at top of pile no.3 for comparable input motions within testing phases I and II: a) 25Hz sinedwell, b) 30Hz sinedwell.

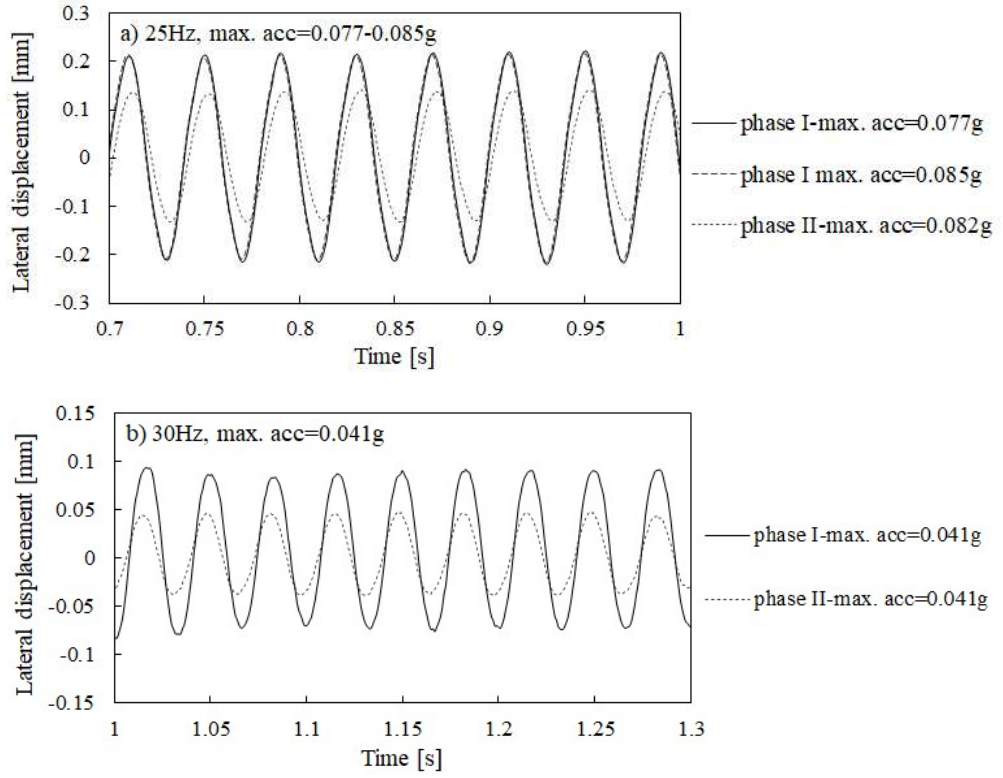


Fig. 11. Lateral displacements at top of pile no.3 for comparable input motions testing phases I and II: a) 25Hz sinedwell, b) 30Hz sinedwell.

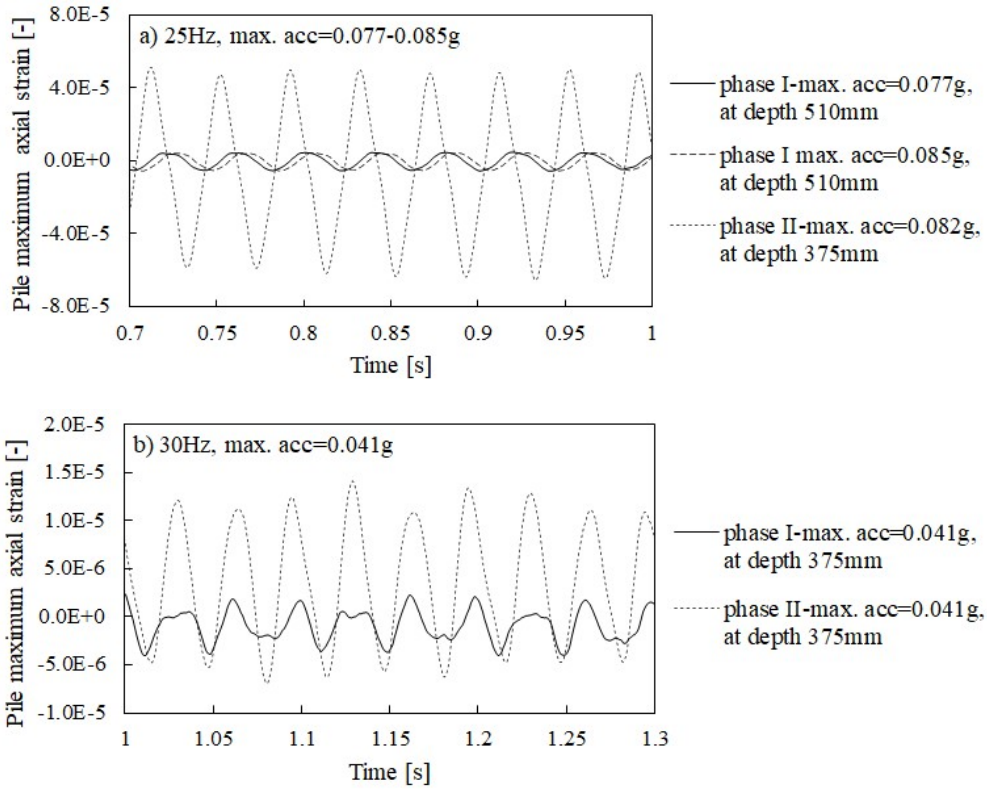


Fig. 12. Maximum axial strains at pile no. 3 for comparable input motions testing phases I and II: a) 25Hz sinedwell, b) 30Hz sinedwell.

2.2. Finite element analysis

Advanced soil constitutive models

Two advanced soil constitutive models, namely the ST model and the HP model, have been used in the 3D finite element analysis in Abaqus (Dassault Systèmes, 2019). The DM model has been abandoned in the 3D analysis due to consistent errors in the model implementation when dealing with more complex geometry including many elements. The detailed description of the constitutive models is given in Chapter 1 of this thesis.

Soil geometry and discretization

Periodic boundaries have been defined on lateral sides of the mesh through tie connectors between the side nodes. Seismic input motion has been applied as an acceleration time history at the bottom of the mesh. No non-reflective boundaries have been defined at the bottom of the mesh as some wave reflection is expected to be experienced in a shear stack placed on a rigid shaking table. The effect of aluminium stacks has been omitted as typically considered of negligible influence (Gajo & Wood, 1997; Dietz & Wood, 2007).

The element type is a quadratic C3D20R. The element size has been calculated from elastic wave propagation for the slowest wave (G_0 of around 3MPa in superficial soil) and highest frequency (80Hz to account for most important higher harmonics). This resulted in maximum distance between two nodes to be 0.06m. This has been subsequently reduced to 0.025m (quadratic element size 0.05m) in order to account for plasticity developing in soil, i.e. lower stiffness and therefore slower velocities of propagating waves (Watanabe et al., 2017). In addition, mesh sensitivity studies have been undertaken and confirmed the accuracy of the chosen element size. The mesh sensitivity studies with the ST model are shown on Figure 13 where the element size 0.05m (16 elements) is compared with 0.025m (32 elements). Some slight discrepancy can only be noticed at soil surface level. This can be associated with developing plasticity and slower waves being present in the solution at the very top of the mesh. On the other hand, the results at depth of 20cm (Figure 13b) show superposed results, therefore the slight discrepancy observed at the soil surface is considered negligible and the element size of 0.05m has been chosen for all the following studies. Note that the comparison of the computed displacements has been preferred in the mesh sensitivity studies due to that fact that the computed accelerations are inevitably affected by mesh size due to shock wave formation as explained in Chapter 2.

Sensitivity studies on time increment are shown in Figure 14. The analyses with different time increment generally superpose each other (apart from the longest time increment 10^{-3} sec). The 3D analysis in this Chapter has been carried out with time increment of $2 \cdot 10^{-5}$ sec as it was found to facilitate the convergence.

Similar task on mesh and time sensitivity studies has also been carried out for the HP model and shown on Figures 15 and 16. The chosen element size is confirmed to be suitable also for wave propagation simulated by the HP model (Figure 15). The analyzed time increment sizes (Figure 16) show efficiency of the adopted adaptive substepping scheme in the implementation of the HP model (Gudehus et al., 2008).

The final mesh used in the 3D numerical studies is shown on Figure 17. Similarly, to the results in Chapter 2, the numerical results are sampled at 1000Hz frequency and in addition the computed accelerations are presented after applying the lowpass Butterworth filter 80Hz (5th order).

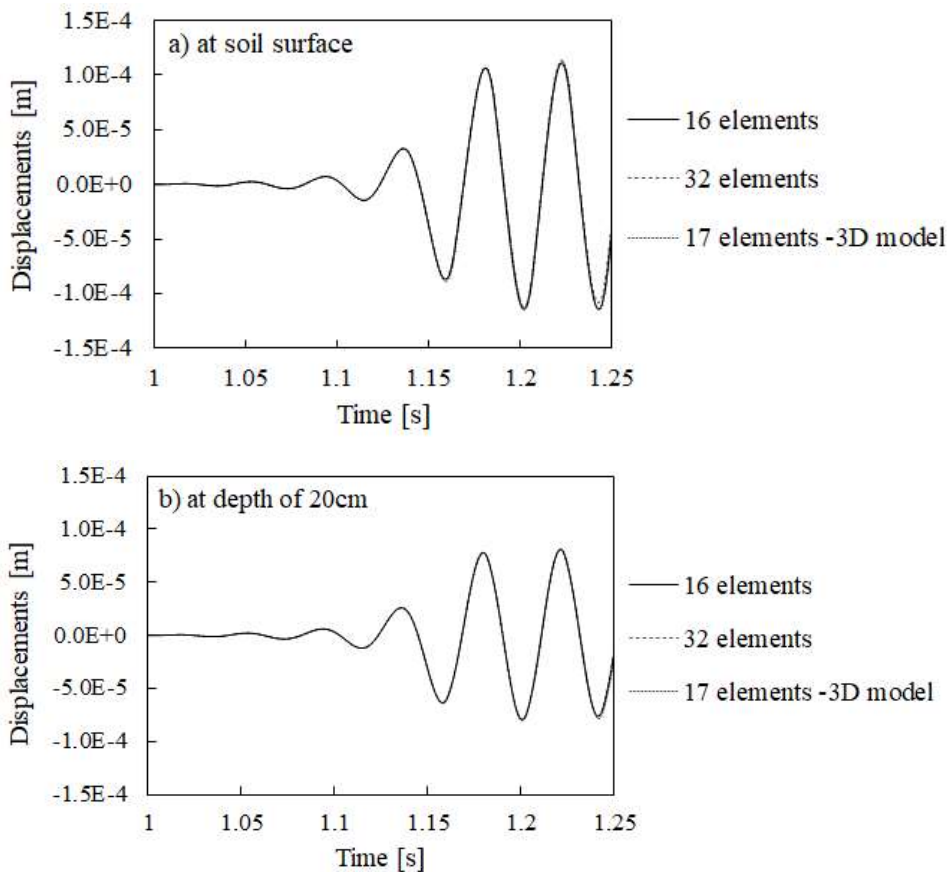


Figure 13. Lateral displacements in mesh sensitivity studies for ST model: a) at soil surface, b) at depth of 20cm.

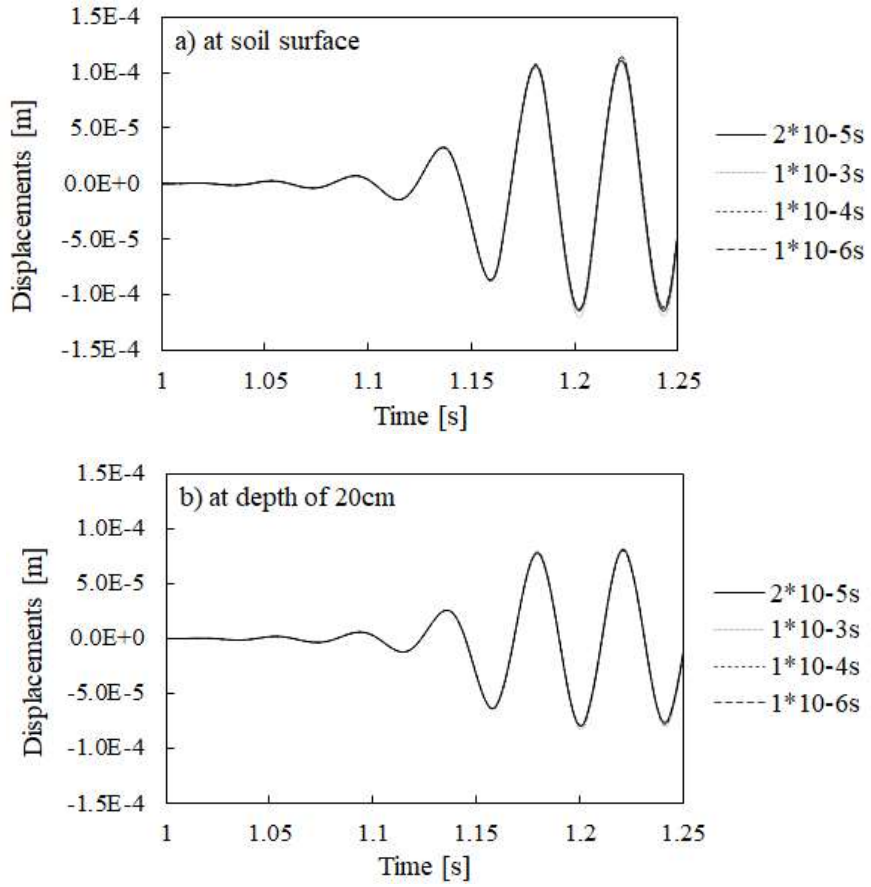


Figure 14. Lateral displacements in time increment sensitivity studies for ST model: a) at soil surface, b) at depth of 20cm.

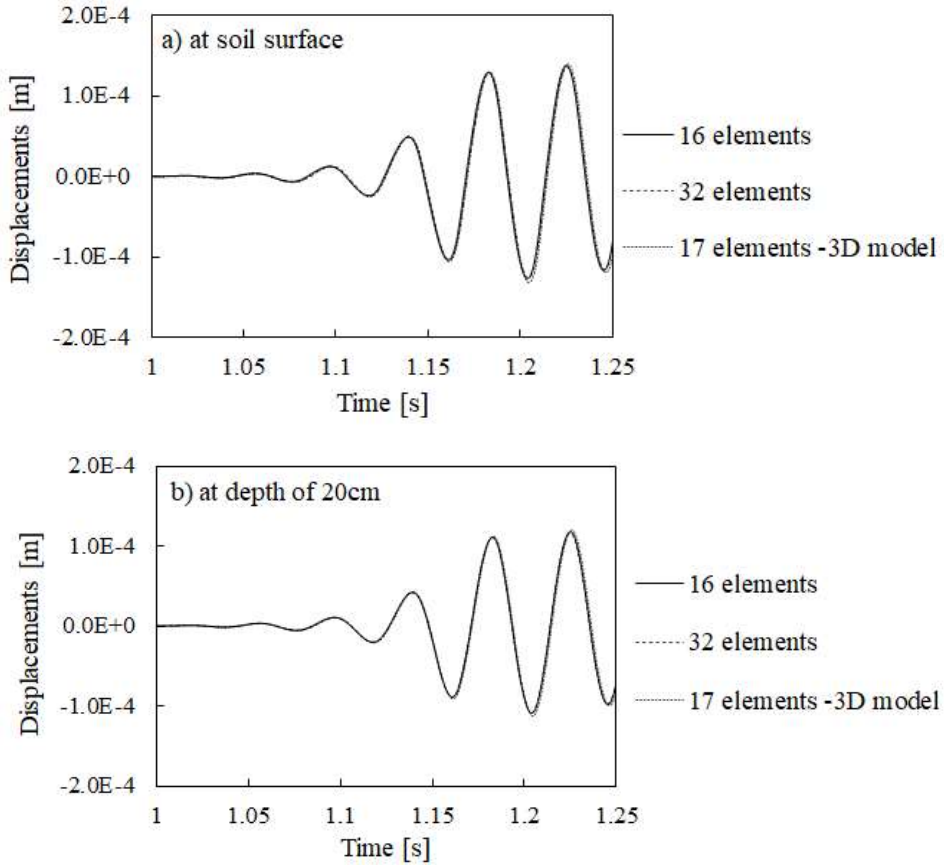


Figure 15. Lateral displacements in mesh sensitivity studies for HP model: a) at soil surface, b) at depth of 20cm.

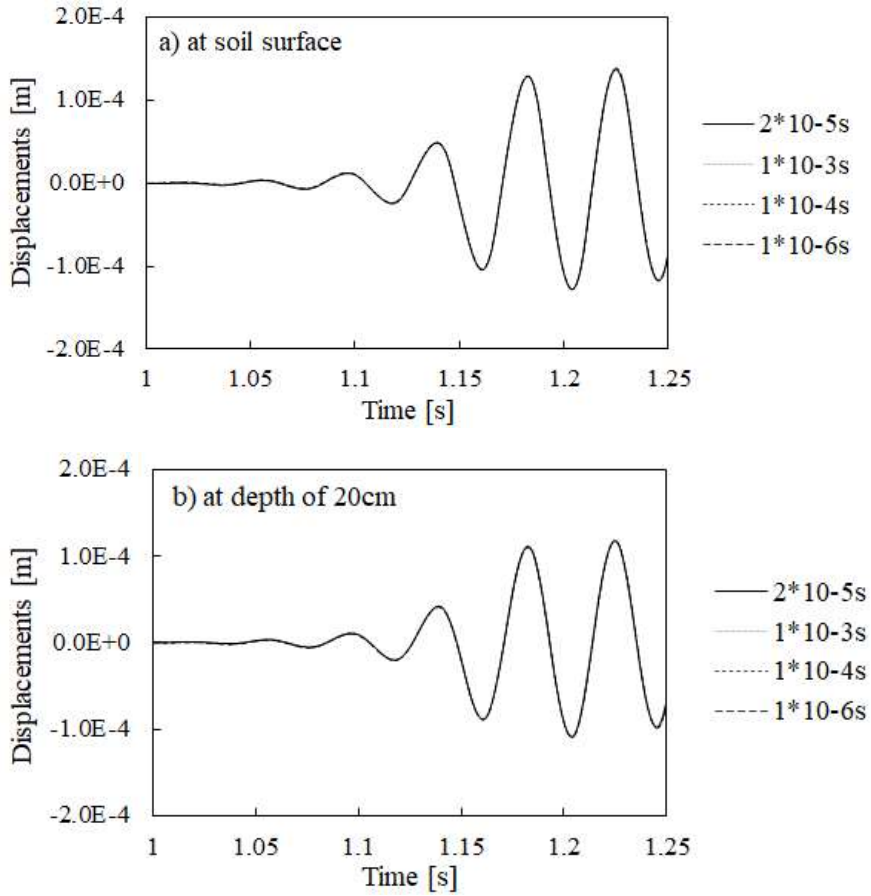


Figure 16. Lateral displacements in time increment sensitivity studies for HP model: a) at the soil surface, b) at depth of 20cm.

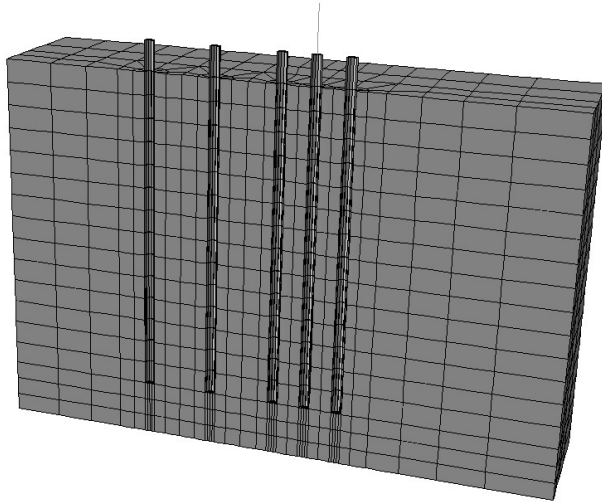


Fig. 17. Final optimal mesh discretization chosen for 3D numerical analysis.

Pile geometry and discretization

The element type S4R has been chosen to model the tubular piles of 22mm diameter. The piles have been modelled with elastic material representative of aluminium, i.e. stiffness $E=70\text{GPa}$ and Poisson's ratio $\nu=0.3$.

The contact between soil and piles has been modelled as surface to surface contact pair with pile surface being the master surface. The coefficient of friction between the piles and soil was chosen as 0.5 which is typical for steel piles in granular soil (Uesugi & Kishida, 1986).

Oscillator geometry and discretization

The single degree of freedom oscillator has been modelled as a 100mm long column of the aluminium material and with a mass of 190gr at the top (to simulate the oscillator mass) and a mass of 176gr at the bottom (to simulate the foundation mass). It has been numerically checked that the fixed natural frequency of such oscillator was 26.5Hz as per the experimentally assessed fixed-base natural frequency. The damping of 0.9% was applied in the elastic material definition to account for experimentally assessed damping for a fixed-based oscillator. The oscillator has been discretized with the B32 element type with a rectangular section 30x12mm as per the experimental setup.

3. Results

The numerical results are presented in groups depending on the pile head fixity and the presence of a simplified structure in the form of a SDOF oscillator. Note the results for settlements are shown with a sign “-“ to indicate a downward compressive movement, and with a sign “+” to indicate an upward dilative movement. The results for the pile are referred to the pile no.3 within the five-pile group (Figure 2).

Note that a part of the results is also available in Appendix E. These include the free pile head condition with 30Hz input motion and a scaled Tolmezzo earthquake, and a pile group with a small cap on the piles no.1, 2 and 3 with 25Hz input motion.

3.1. Free head piles

A comparison of the numerical and experimental results for two different input motions is presented in this section. The excitation motions include two sine dwell input motions 10Hz and 25Hz. Note that more studies with the free pile head conditions, including 30Hz input motion and a scaled earthquake input motion are shown in Appendix E.

The response in free field in terms of accelerations (Figures 18 and 24) and lateral displacements (Figures 19 and 25) is fairly well represented, especially for the 25Hz input motion with the exception of clearly overestimated lateral displacements for the 10Hz input motion by the HP model (Figure 19). In general, the computed settlements (Figures 20 and 26) are overestimated by the ST model for each of the input motions, whereas the HP model overestimates the settlements only for the 10Hz input motion (Figure 20) for which it also overestimates lateral displacements (thus the two observations can be logically linked together). More detailed consideration on the computed settlements is given in Section 4.4 of this chapter.

Regarding the pile response, the computed accelerations (Figures 21 and 27) match very well in terms of the amplitude the experimental measurements. Both models also capture the presence of the generated (within soil) higher harmonics on the piles. The amount of the generated harmonics on the piles is much greater than in the free field records, and thus, the sine wave is more distorted in the time domain. These effects have been quite well captured in the simulations by the two constitutive models. The amplification of the higher harmonics on the pile can be thought as an example of superharmonic resonance, i.e. the resonance of higher harmonics with the natural frequency of the top of a pile which behaves as an oscillator (as explained also in Section 2.1 of this chapter). Such pile behaviour is also a proof of additional waves being present in the shear stack (as explained in Section 3.5 of Chapter 2).

Looking at the pile head lateral displacements (Figures 22 and 28) some inconsistency can be observed between numerical and experimental studies. The pile

lateral displacements seem to be underestimated by both models. Note that some doubts on the experimentally measured pile lateral displacements have been highlighted in Section 2.1. Actually, the experimentally measured lateral displacement for the pile no. 2 was even larger than for the pile no. 3 and resulted in even more pronounced difference between numerical and experimental results (although both piles would be expected to experience very similar motion).

Finally, the pile maximum axial strains (representative of the pile maximum bending moments) are compared on Figures 23 and 29. The computed values are within the order of magnitude of the experimental measurements and at similar depths. The discrepancies are larger for the 10Hz input motion and smaller for the 25Hz input motion. The maximum pile axial strains are not consistent also between the two predictions of the two models. This is thought to be related to differences in shear stiffness degradation with depth predicted by the two models (as explained in detail in Section 4.6 of this chapter).

10Hz sine dwell, 0.137g (Fig. 18 to 23)

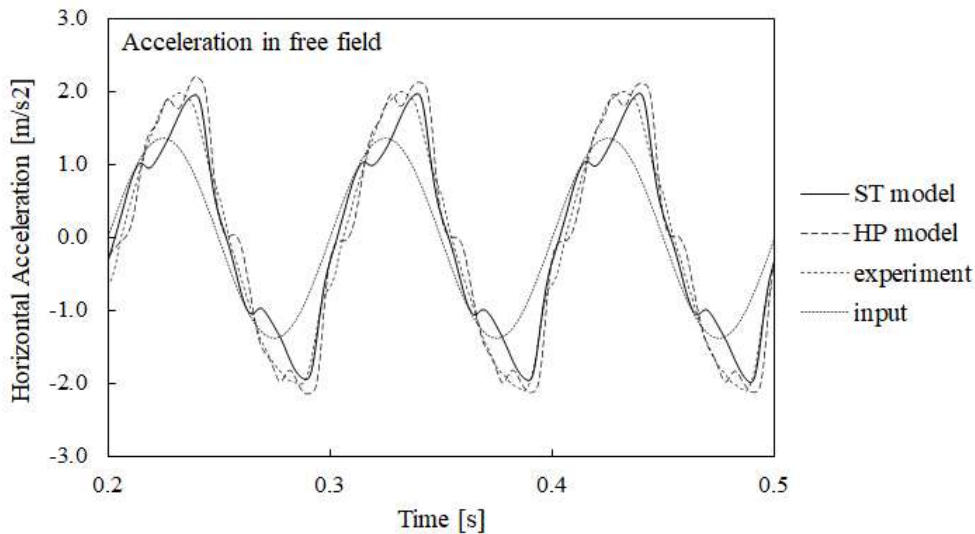


Fig. 18. Comparison of measured and computed horizontal accelerations in free field at soil surface level.

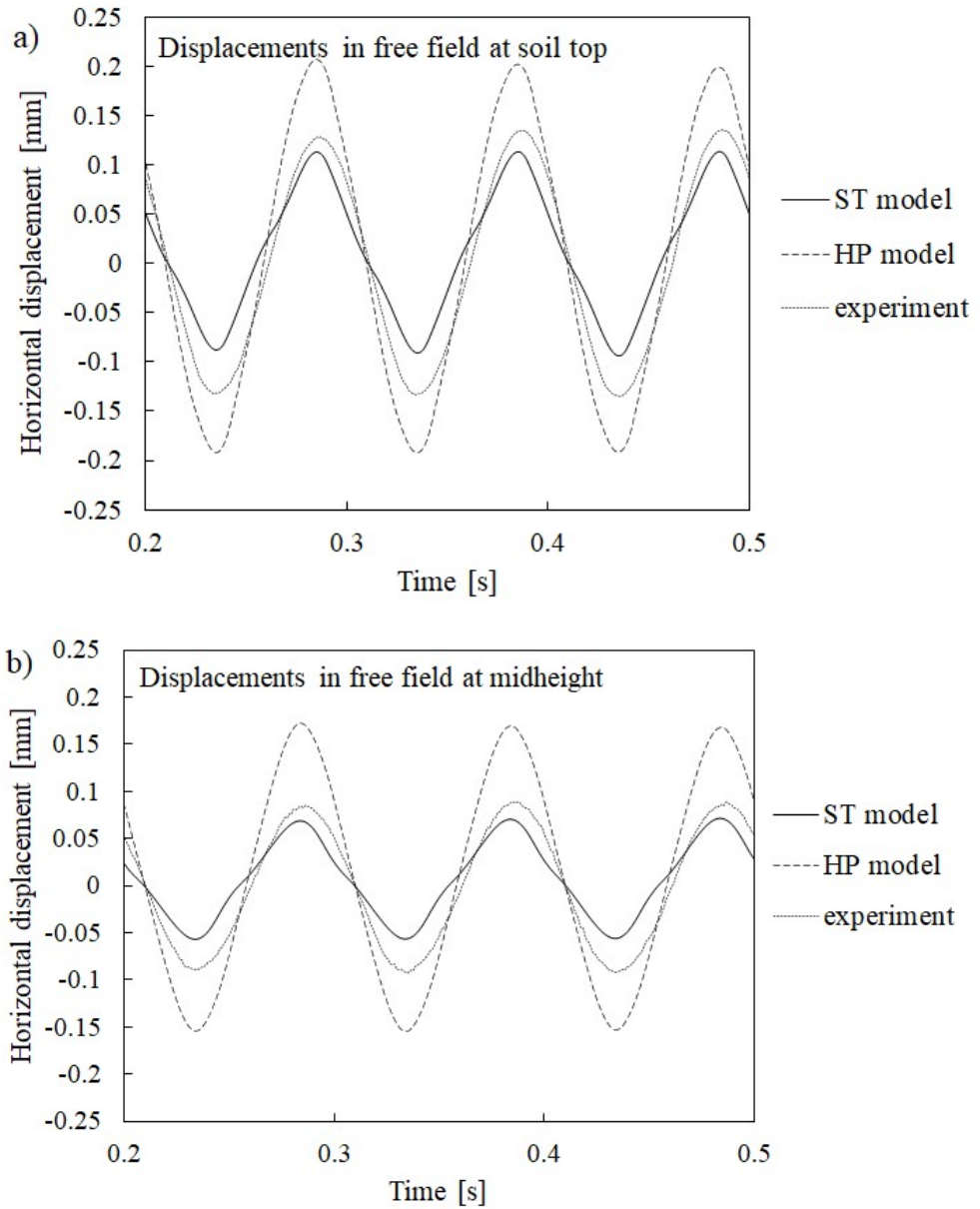


Fig. 19. Comparison of measured and computed lateral displacements in free field at soil surface level (a) and at mid-height (b).

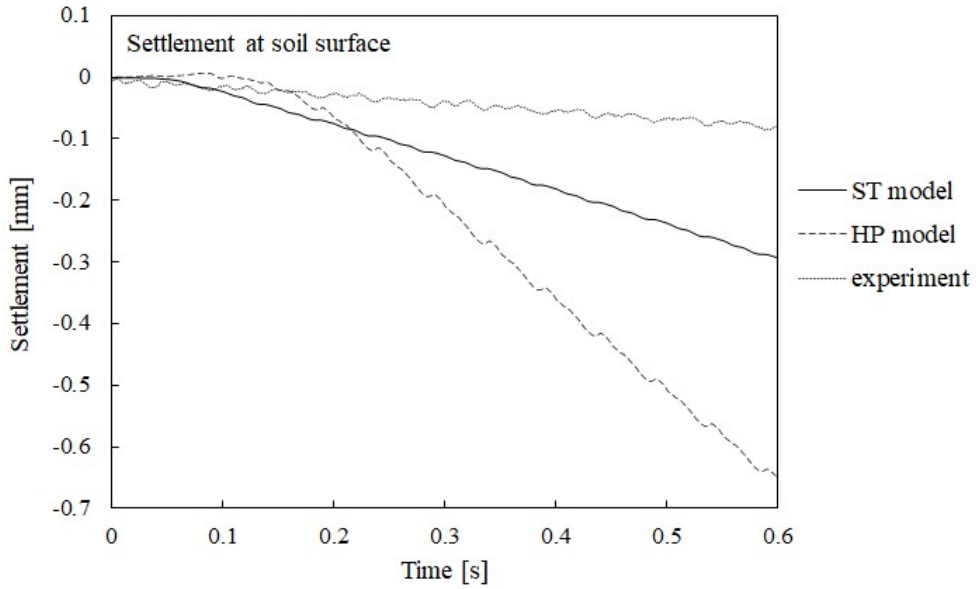


Fig. 20. Comparison of measured and computed settlements in at soil surface level.

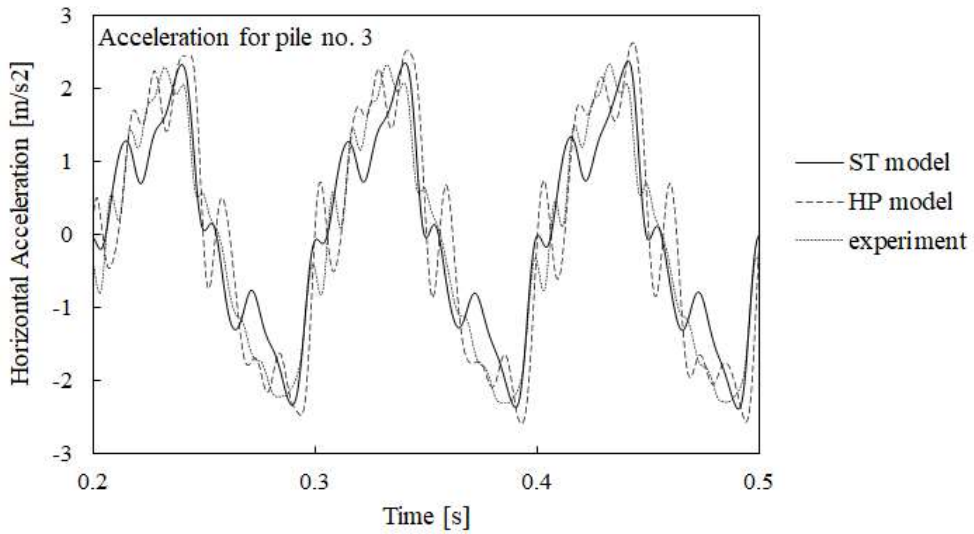


Fig. 21. Comparison of measured and computed horizontal accelerations at top of pile no. 3.

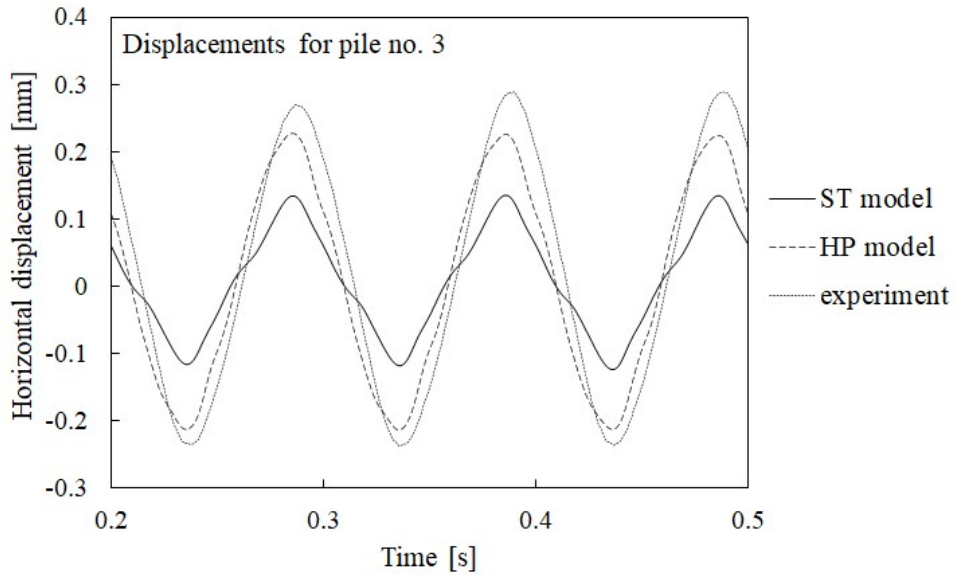


Fig. 22. Comparison of measured and computed lateral displacements at top of pile no.3.

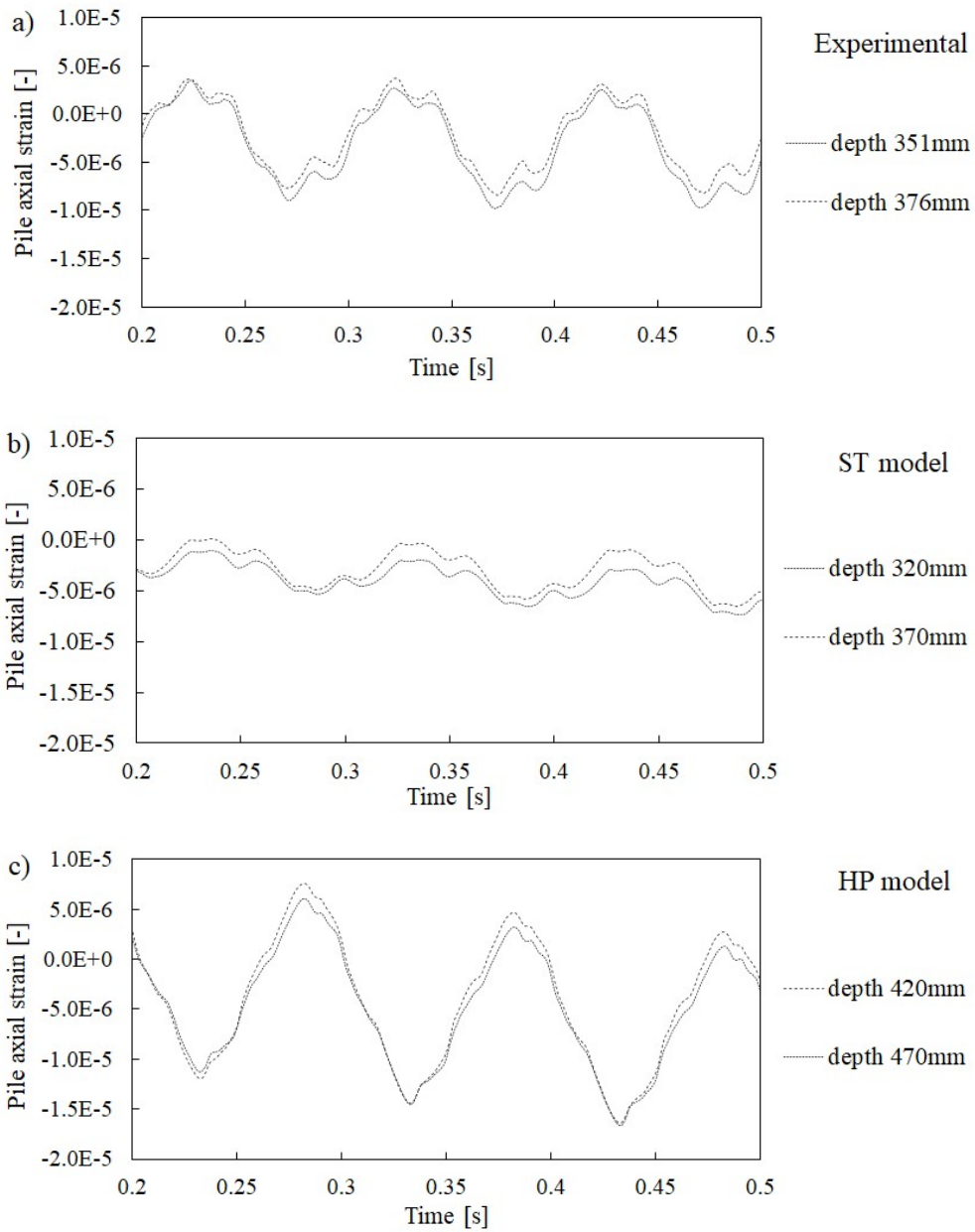


Fig. 23. Comparison of maximum measured and computed pile axial strains of pile no. 3.

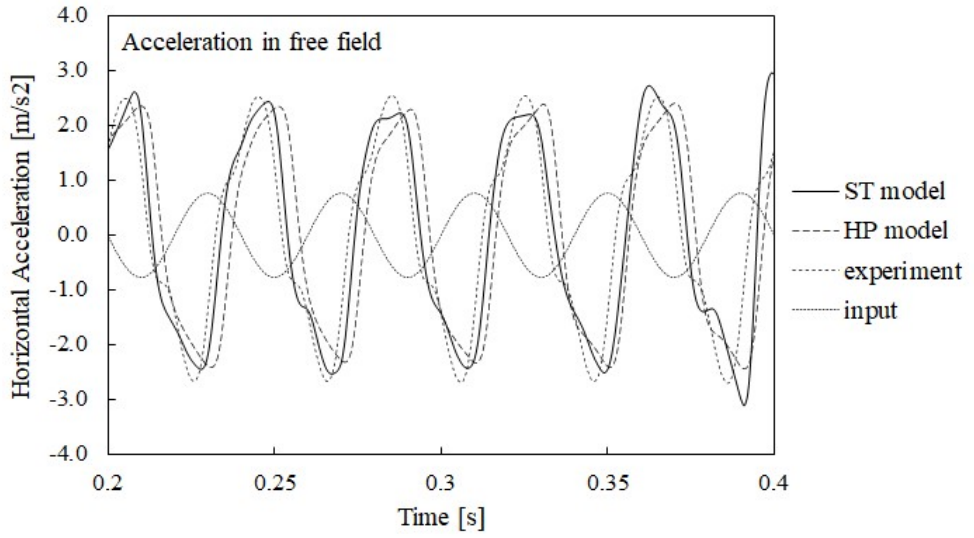
25Hz sine dwell, 0.077g (Fig. 24 to 29)

Fig. 24. Comparison of measured and computed horizontal accelerations in free field at soil surface level.

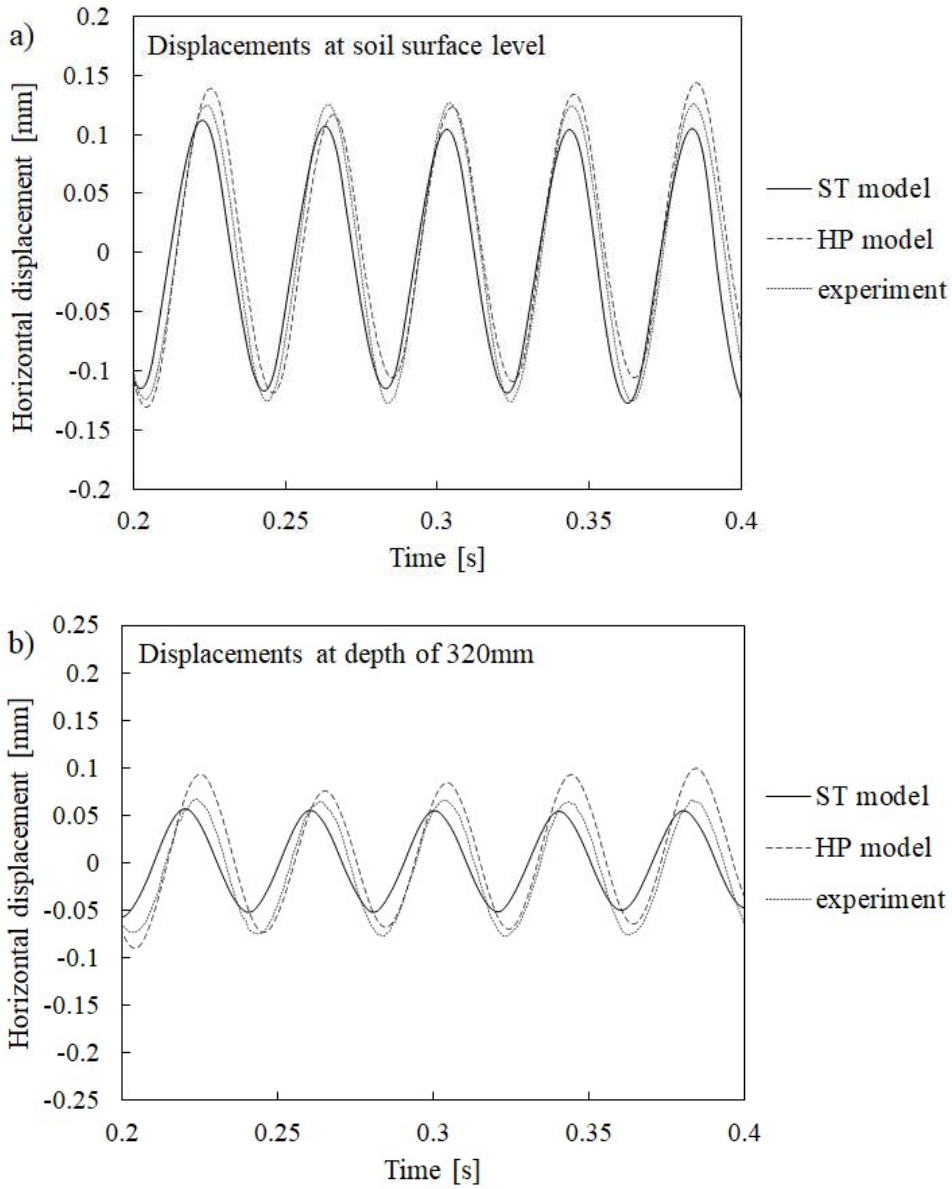


Fig. 25. Comparison of measured and computed lateral displacements in free field at soil surface level (a) and at mid-height (b).

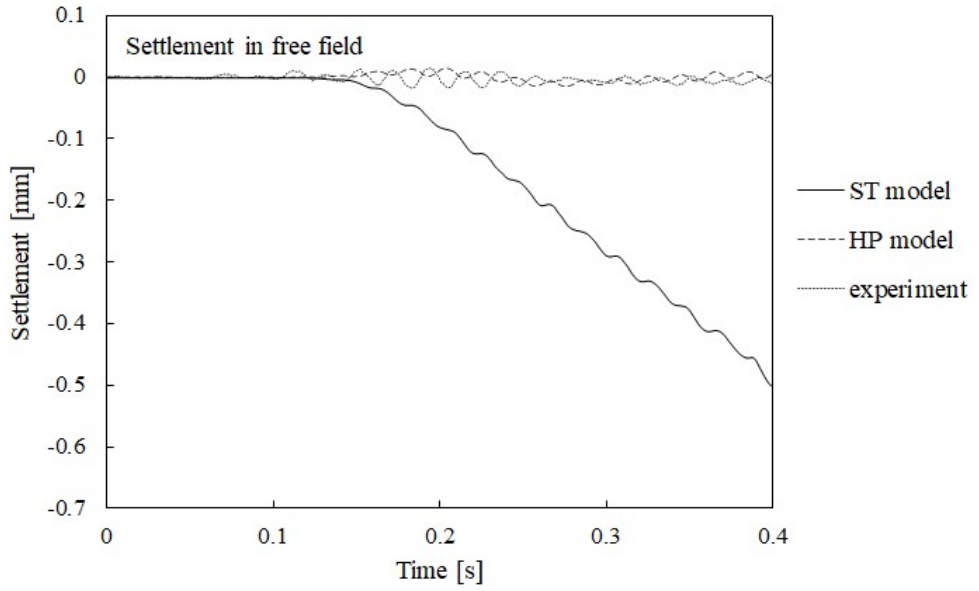


Fig. 26. Comparison of measured and computed settlements at soil surface level.

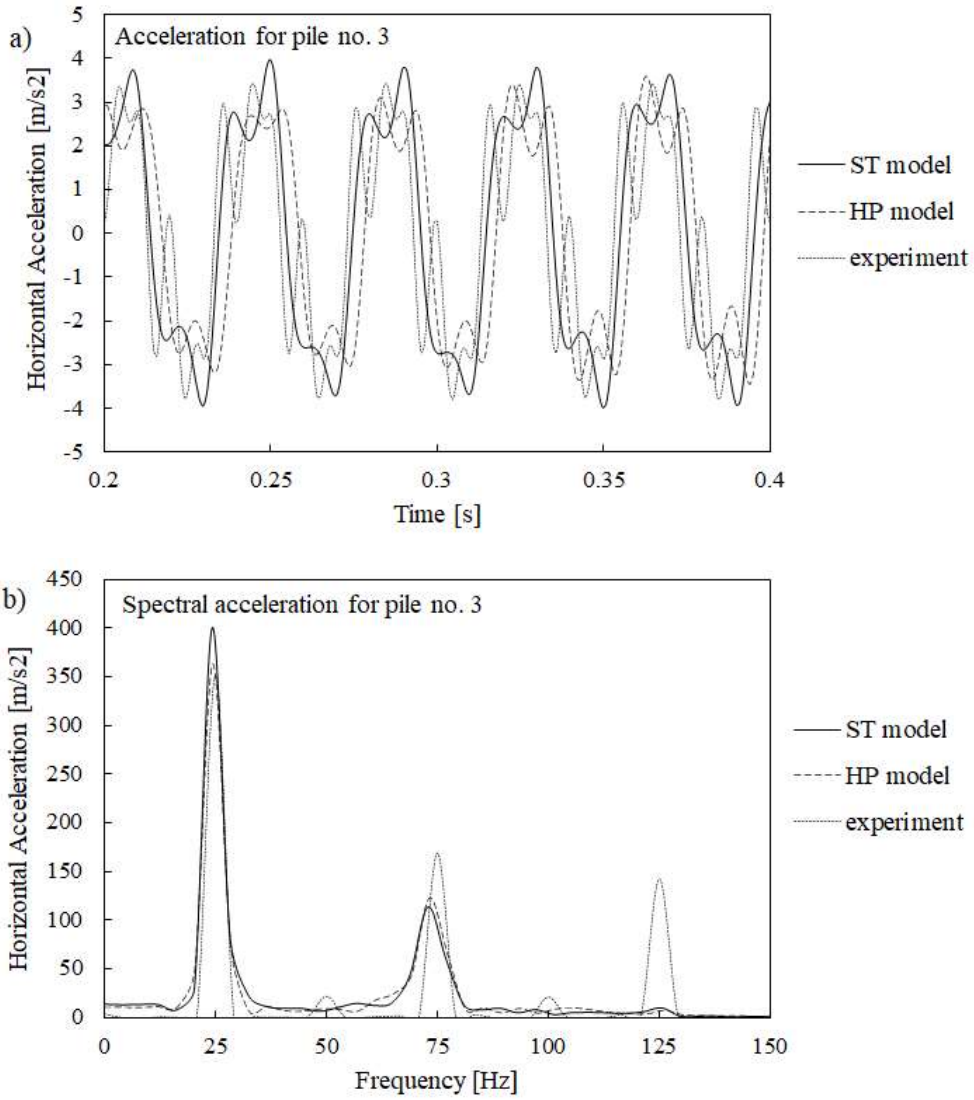


Fig. 27. Comparison of measured and computed horizontal accelerations at top of pile no.3 and corresponding spectral accelerations.

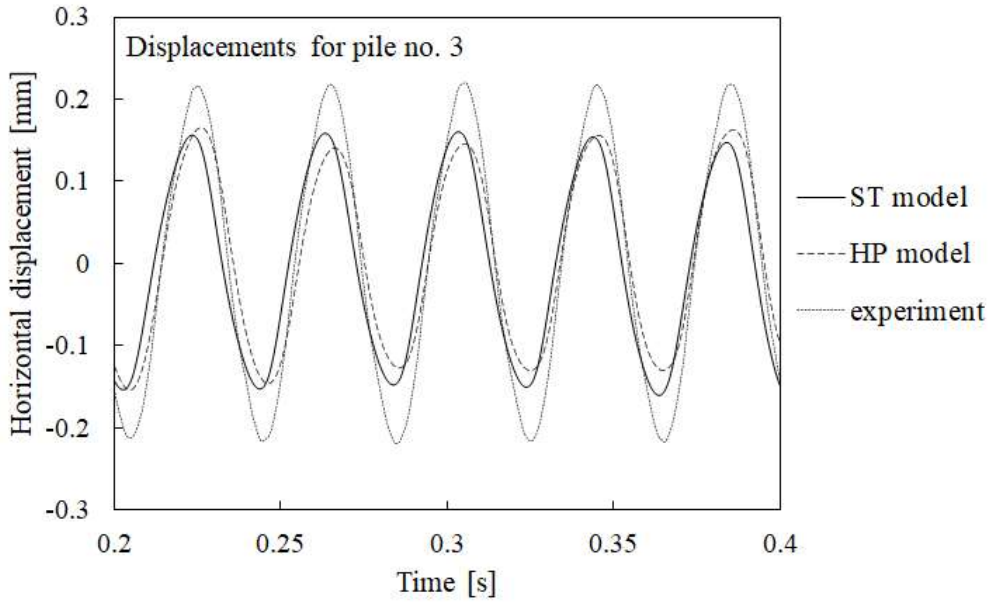


Fig. 28. Comparison of measured and computed lateral displacements at top of pile no. 3.

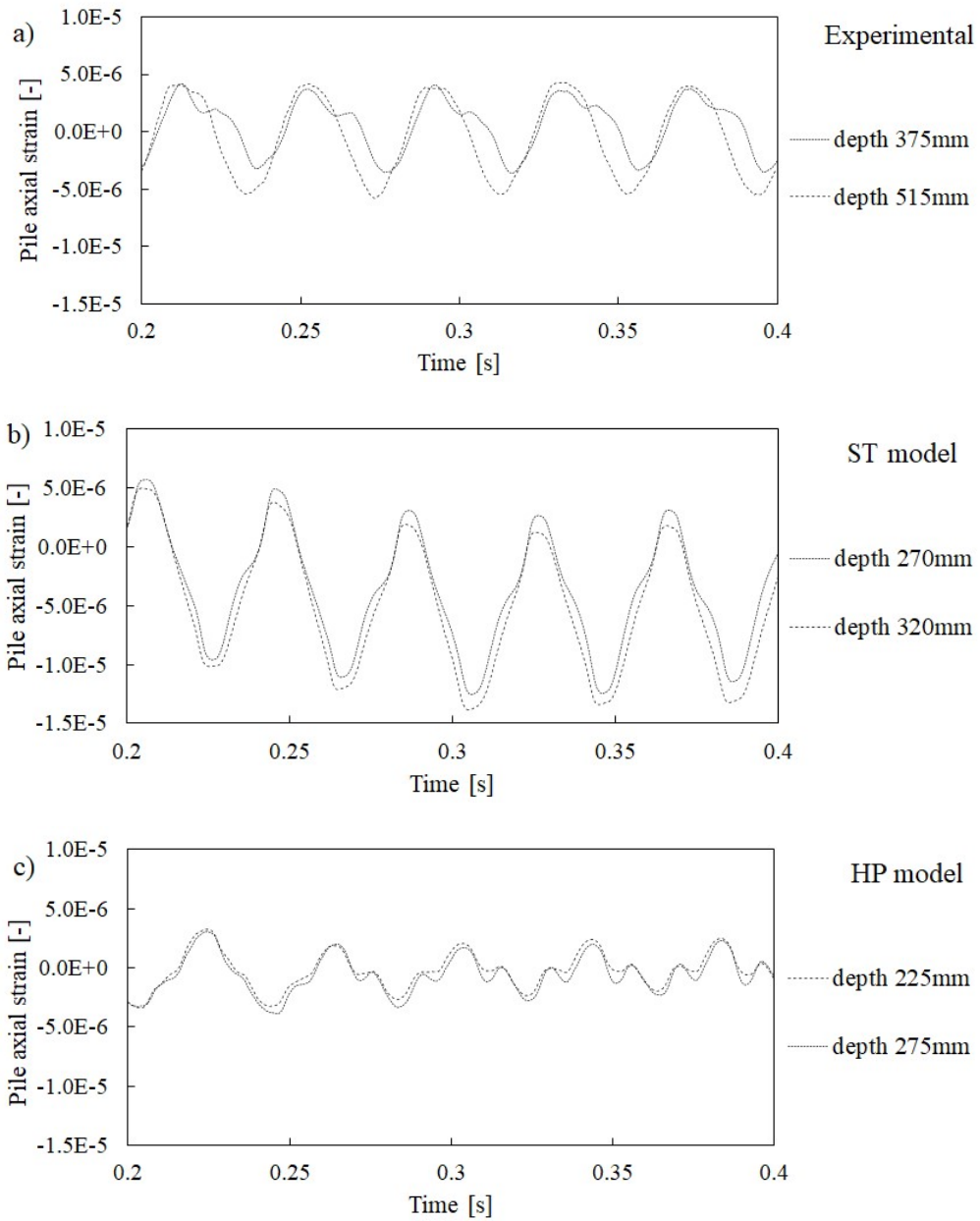


Fig. 29. Comparison of maximum measured and computed pile axial strains of pile no. 3.

3.2. Pile group with oscillator

Two input motions are subject to a comparison in this section, firstly 10Hz sine dwell (0.155g) with free pile head conditions, secondly, 25Hz sine dwell (0.092g) with a short cap spanning the piles no. 1, 2 and 3. In addition, a SDOF oscillator is placed at the top of the pile no. 3 in both analysed cases.

10Hz sine dwell, 0.155g without a cap

Firstly, the response in free field is compared (Figures 30-32). This is very similar to the input motion 10Hz (0.137g) with free pile head conditions which confirms repeatability of the experiments and the numerical studies (see Figures 18-20). The increased accelerations and the lateral displacements (when compared with 10Hz, 0.137g) are due to slightly higher magnitude of the input motion (0.155g). Generally, the response of the ST model is closer to the experimentally measured free field response, although the accelerations in the free field are matched very well by both models.

The accelerations of the pile no. 3 are shown on Figure 33 and are again in fairly good agreement for both models and the experiments, with stronger presence of higher harmonics in the numerical studies, especially the 50Hz harmonic. The lateral pile displacement and the pile maximum axial strains are shown on Figures 34 and 35 respectively. The predictions of the former by the HP model are closer to the measured data, i.e. the pile top displacement is matched very well (although some doubt arises that this match is a result of the overestimated displacements in free field by the HP model). The maximum pile axial strains are measured and computed around the top of the pile, with both models slightly overestimating the measured axial strains.

Finally, the computed accelerations at the top of the SDOF oscillator (Figure 36) show some underestimation of the maximum accelerations due to higher harmonics (or the position of the “wobble” as per Chapter 2) affecting the computed accelerations around the maximum magnitude, thus reducing the maximum amplitude. The higher harmonics are present in the motion of the oscillator; however, their amount has not been captured precisely by the two models. The dominant harmonic in the experimental measurements is at 20Hz which is close to the natural frequency of such oscillator with compliant foundation (to recall, fixed base natural frequency is 26.5Hz). On the other hand, the harmonic 20Hz has not been generated within the soil mass by the two models. As explained in Section 3.1 of Chapter 2, possibly non-symmetrical effects in the experiments (e.g. residual strains on one side on the shear stack) would allow generation of the 20Hz harmonic. Alternatively, non-symmetrical input motion

in the numerical analysis could potentially improve the numerical predictions for the behaviour of the oscillator in terms of the generated harmonics.

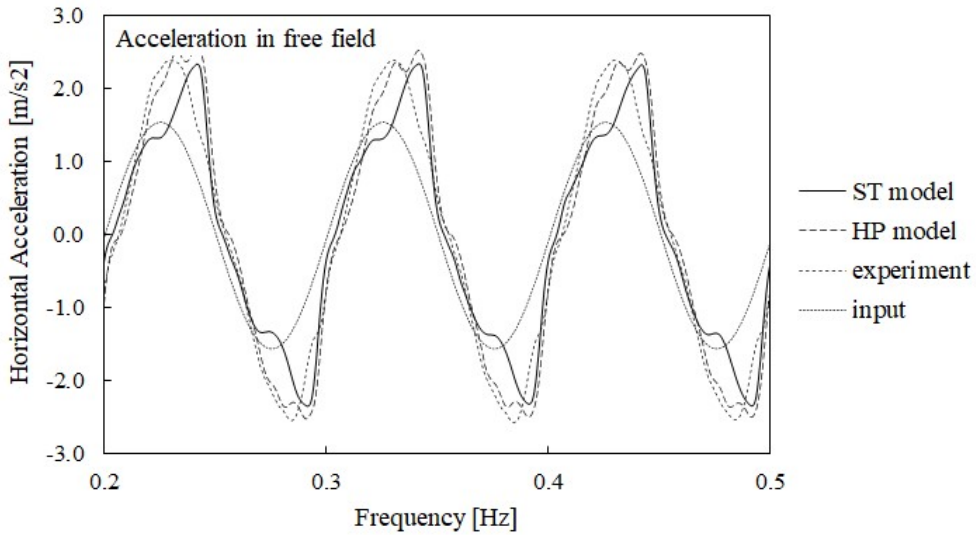


Fig. 30. Comparison of measured and computed horizontal accelerations in free field at soil surface level.

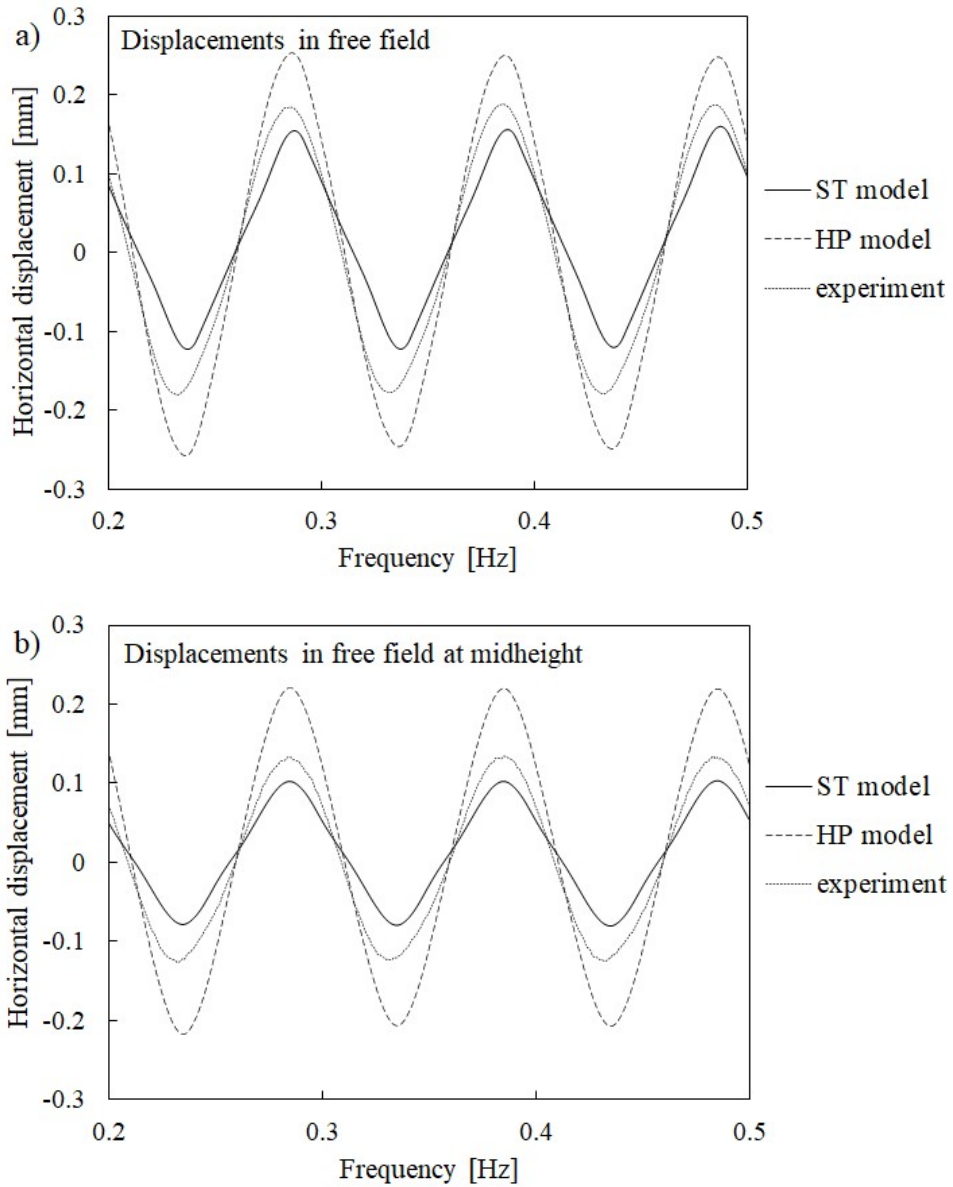


Fig. 31. Comparison of measured and computed lateral displacements in free field at soil surface level (a) and at mid-height (b).

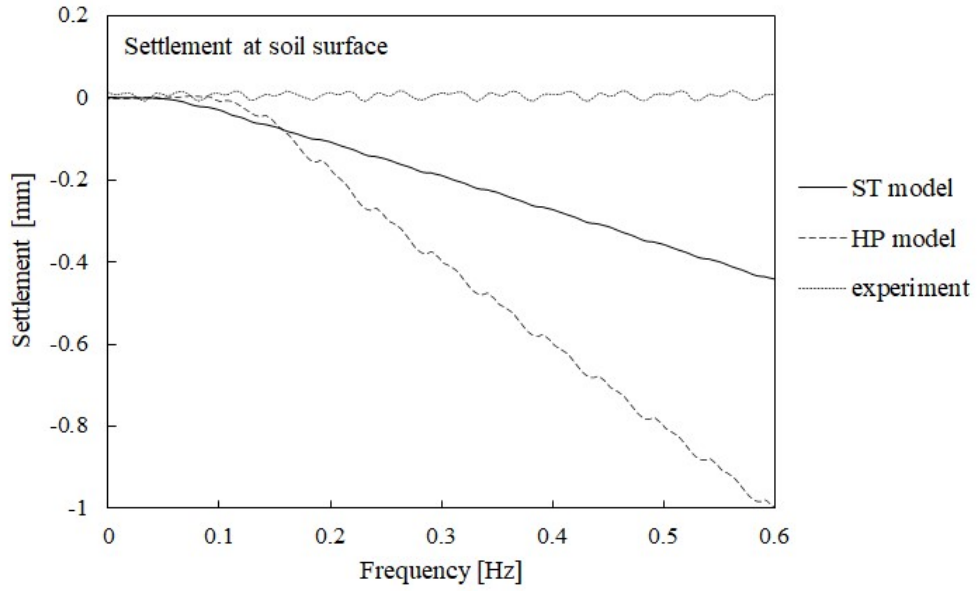


Fig. 32. Comparison of measured and computed settlements at soil surface level.

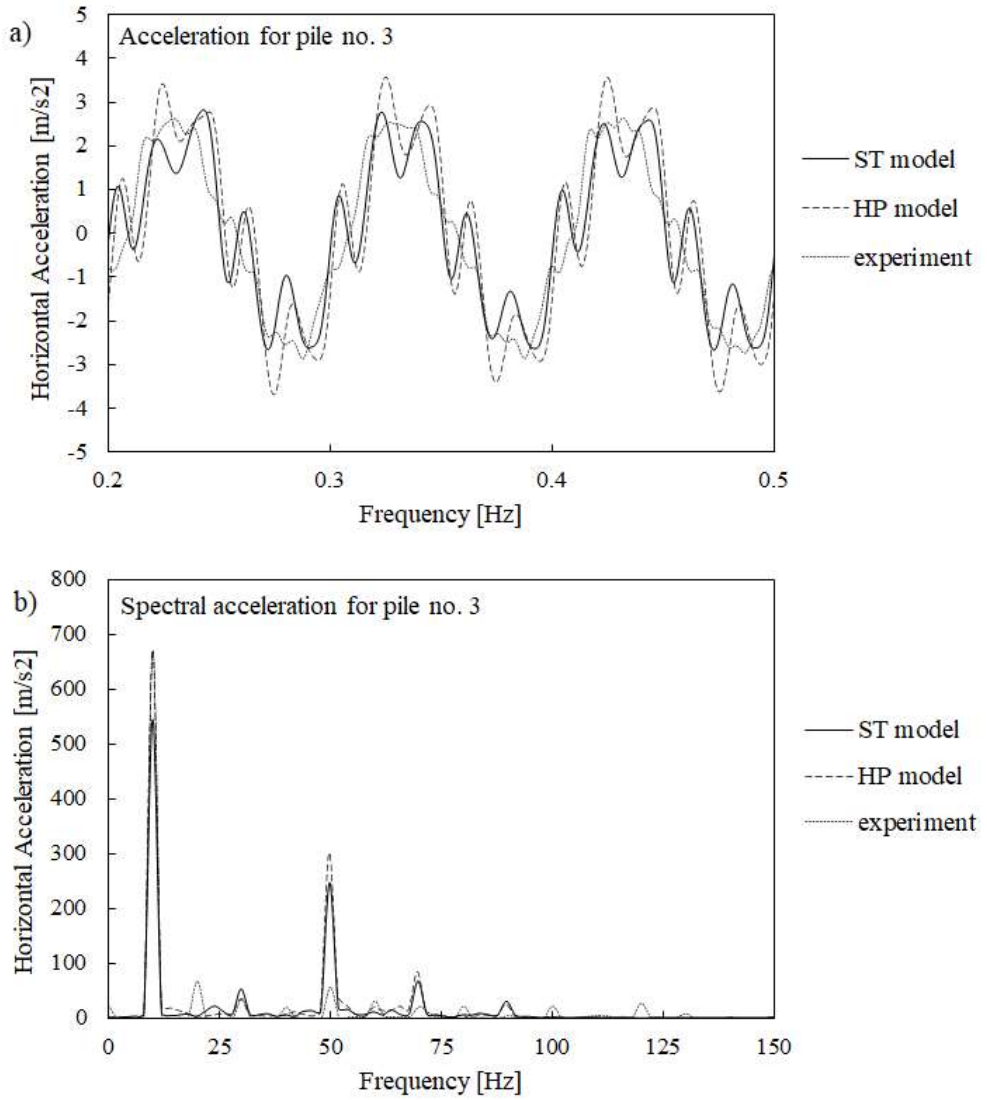


Fig. 33. Comparison of measured and computed horizontal accelerations at top of pile no.3 and corresponding spectral accelerations.

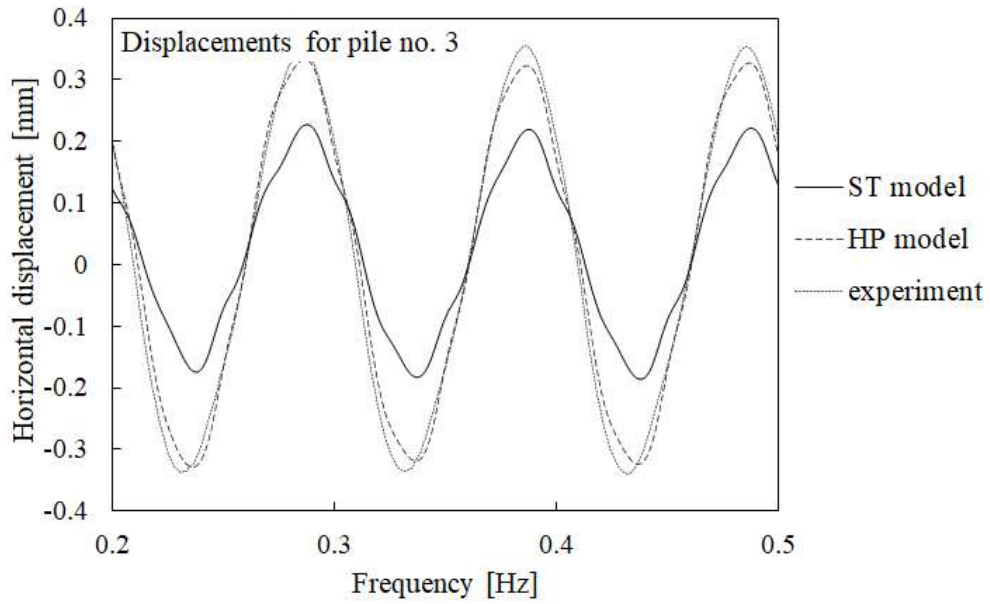


Fig. 34. Comparison of measured and computed lateral displacements at top of pile no. 3.

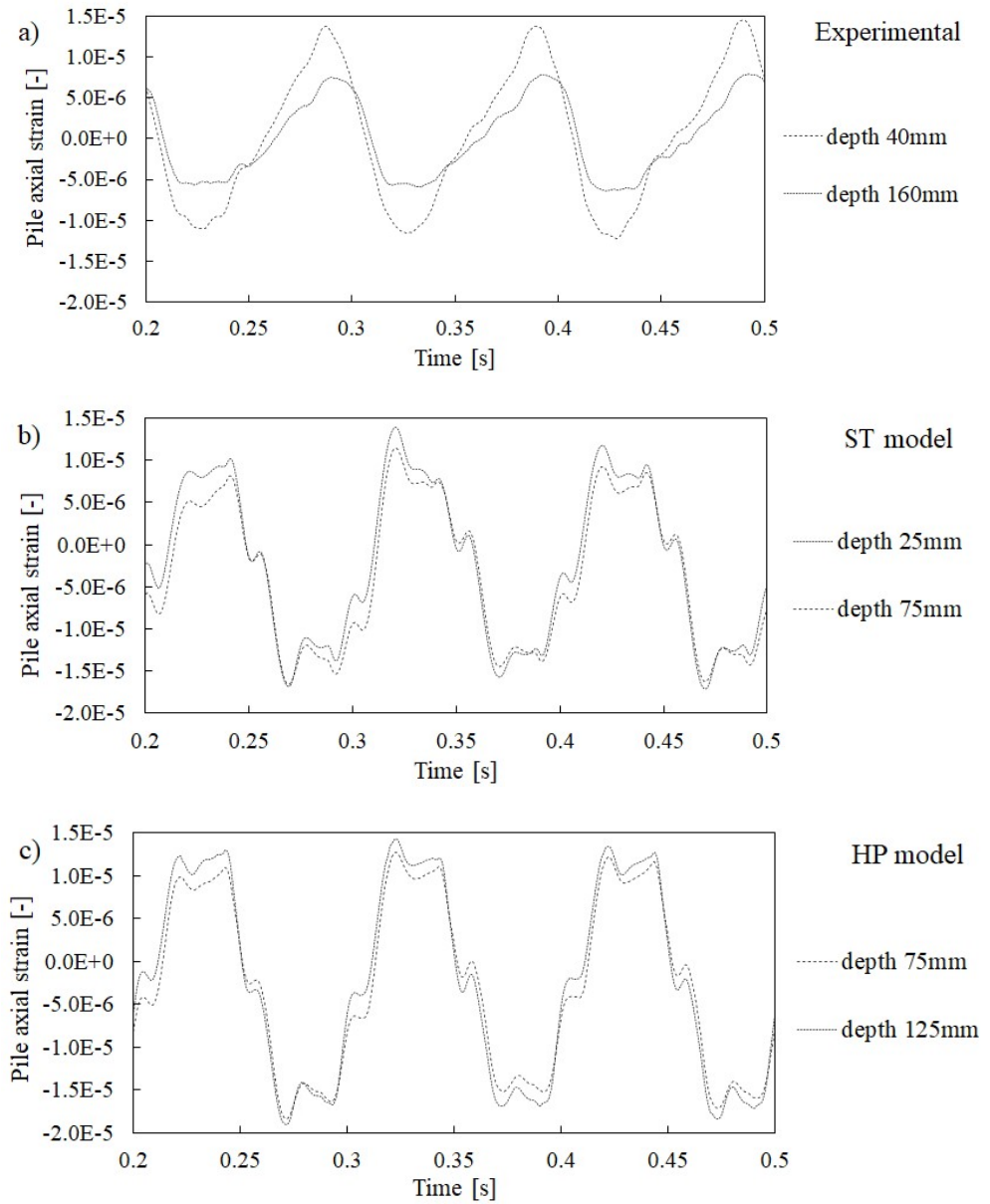


Fig. 35. Comparison of maximum measured and computed pile axial strains of pile no. 3.

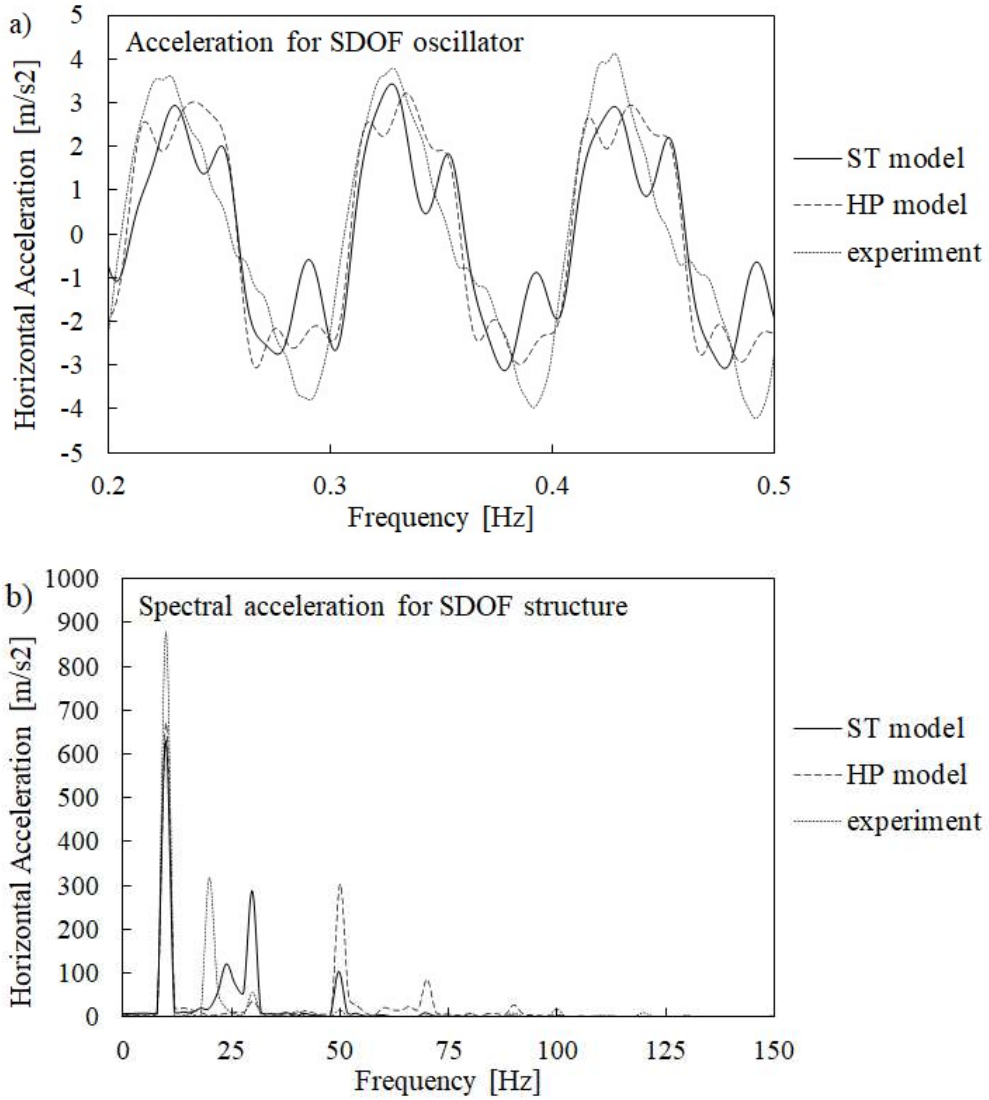


Fig. 36. Comparison of measured and computed horizontal accelerations at top of oscillator and corresponding spectral accelerations.

25Hz sine dwell, 0.092g with a short pile cap

The results in free field are presented in Figures 37 to 39. These are comparable with a similar input motion of slightly lower amplitude (25Hz, 0.077g) presented in Section 3.1 (Figures 24-26). The accelerations are very well captured by both models, in terms of the computed amplitude as well as in terms of the generated harmonics, clearly visible in a form of a “wiggle”. Figure 38 shows that the computed displacements are very close to the measured values for both models. The settlements are plotted on Figure 39 and are consistent with Figure 26 for the ST model. The HP model predicts similar settlement to that given by the ST model, however, rather not consistent with Figure 26. This change in settlement predictions can be associated with larger lateral displacements (Figure 38 in comparison with Figure 25) due to higher amplitude of motion (i.e. 0.092g at Figure 38 versus 0.077g at Figure 25).

The pile top accelerations are shown on Figure 40. Both models overpredict the measured accelerations although the lateral displacements of the pile top are very similar (Figure 41). The experimentally measured pile accelerations are very close to the accelerations in the free field, this reveals that possibly the pile cap weight (plastic cap and foundation of the oscillator) in the numerical study has not been estimated to the exact weight from the experimental setup. The computed pile maximum axial strains are measured and computed just below the fixity point for the experimental and the numerical results (Figure 42). The numerical magnitudes are around twice larger than those measured. However, one is informed that the fixity point in the numerical study is slightly below the one in the experiments, thus such difference in magnitude can be justified. Indeed, at greater depths, the numerical and experimental axial strains are close to each other. Finally, the predicted accelerations for the SDOF oscillator (which fixed base natural frequency 26.5Hz is very close to the driving frequency of 25Hz) are very well matched by the ST model and fairly well by the HP model, both numerical models and the experimental measurements showing resonance, i.e. a gradual increase in the acceleration magnitude with the loading cycles.

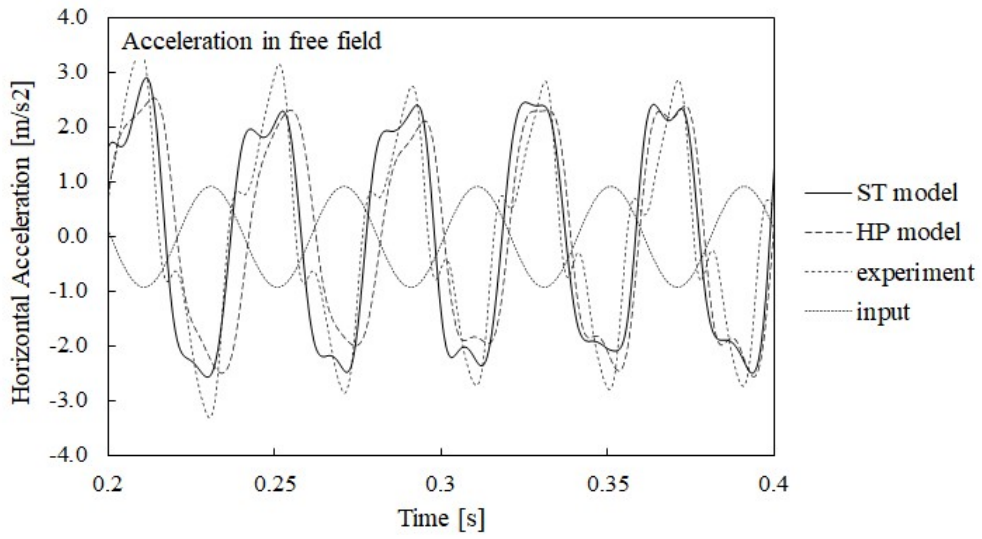


Fig. 37. Comparison of measured and computed horizontal accelerations in free field at soil surface level.

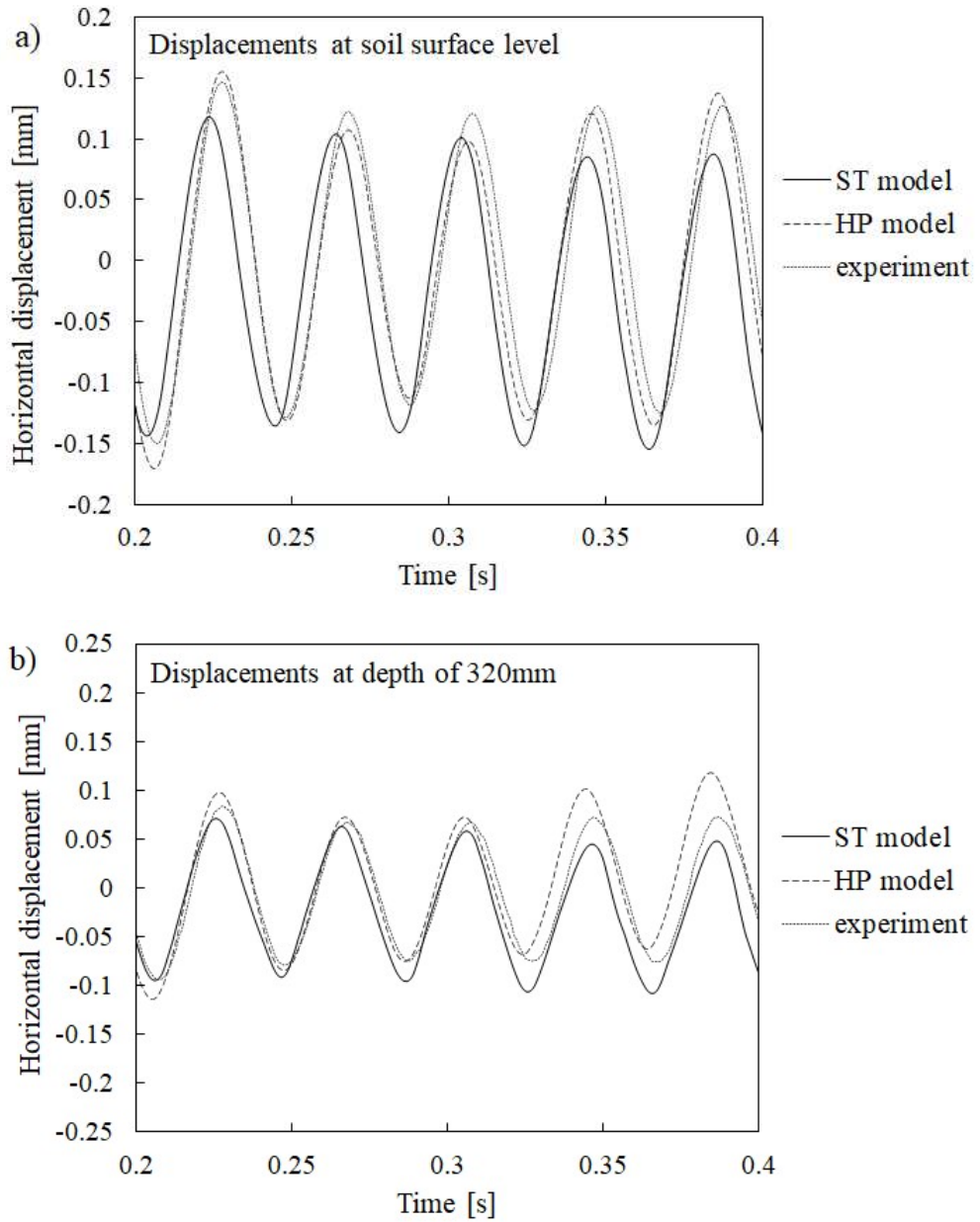


Fig. 38. Comparison of measured and computed lateral displacements in free field at soil surface level (a) and at mid-height (b).

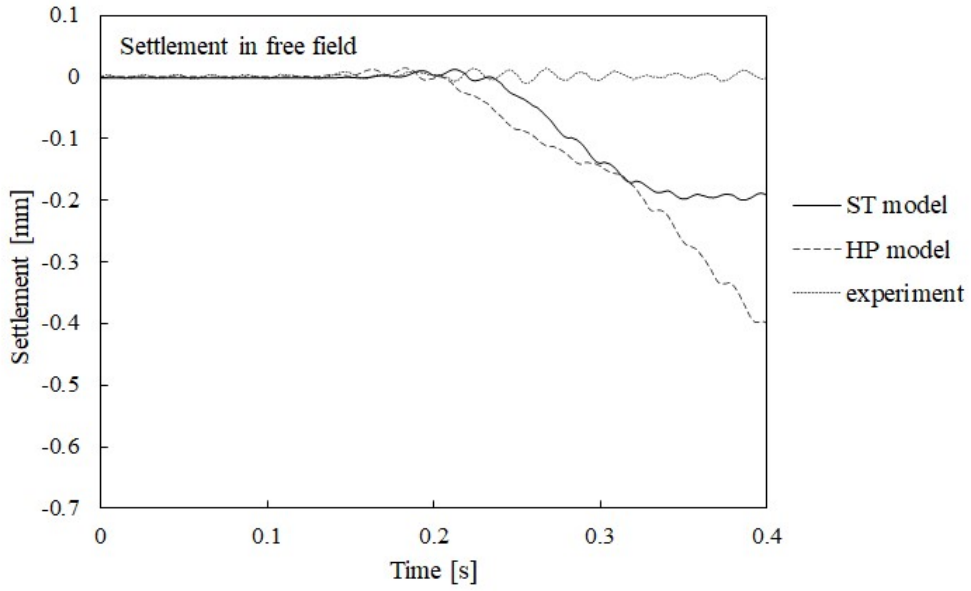


Fig. 39. Comparison of measured and computed settlements at soil surface level.

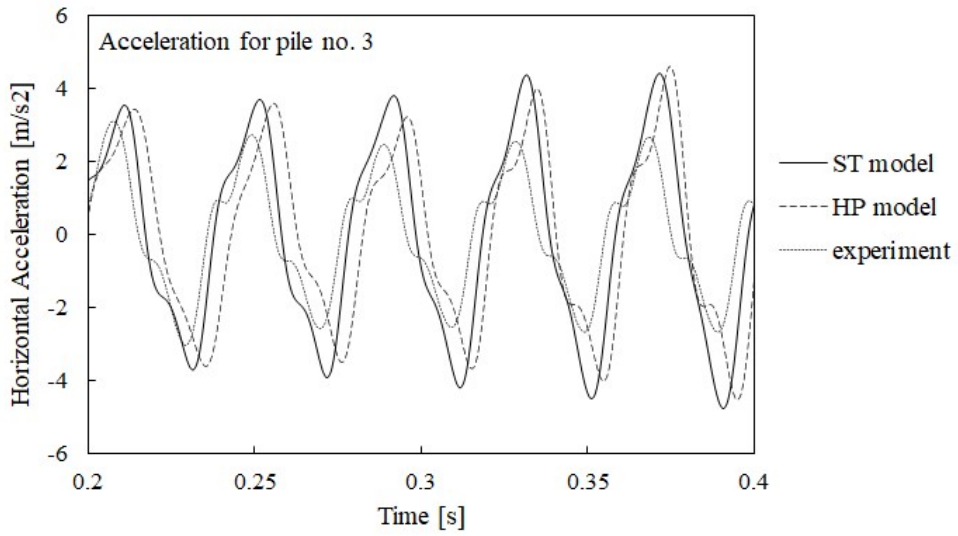


Fig. 40. Comparison of measured and computed horizontal accelerations at top of pile no.3.

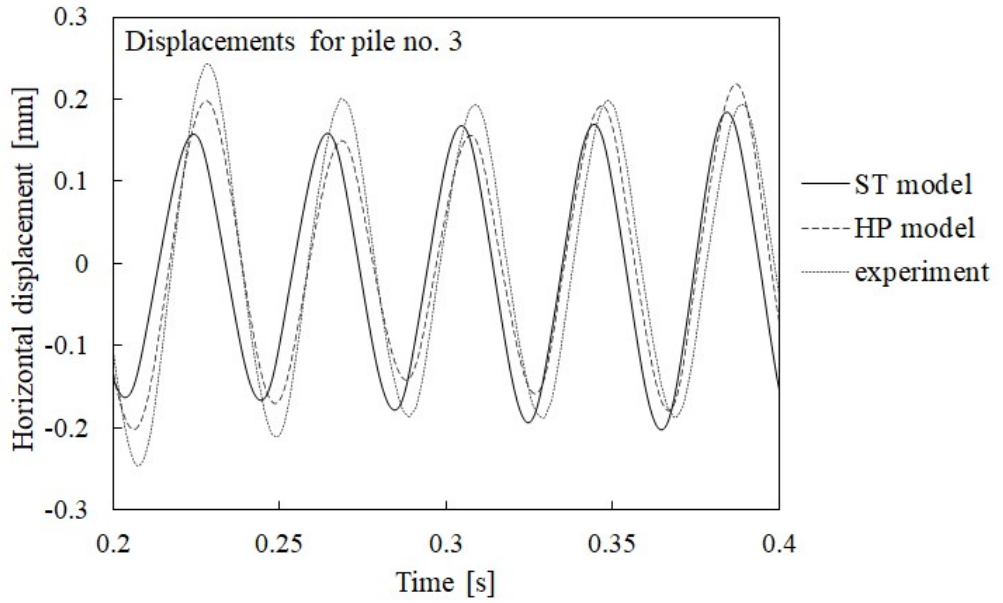


Fig. 41. Comparison of measured and computed lateral displacements at top of pile no.3.

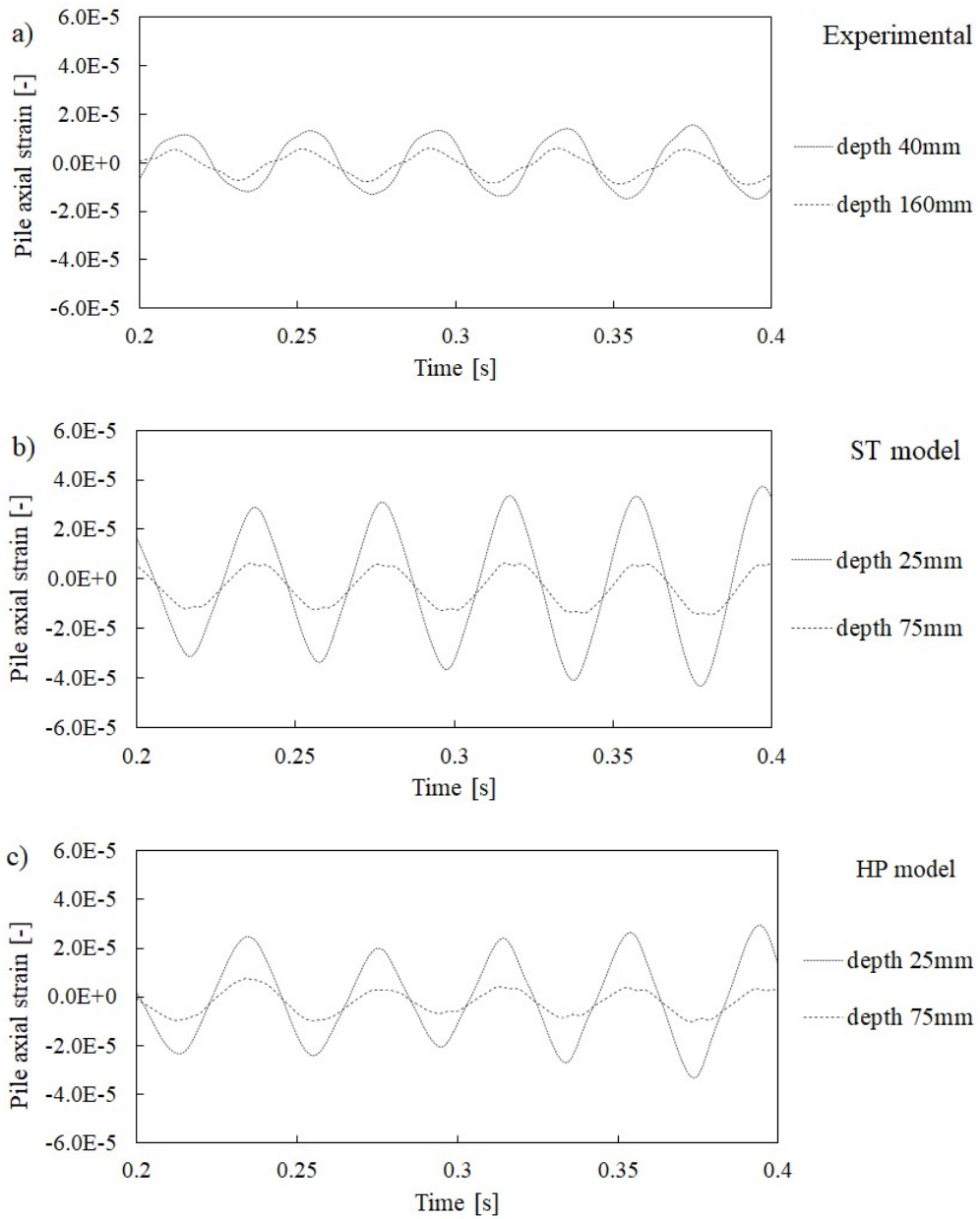


Fig. 42. Comparison of maximum measured and computed pile axial strains of pile no. 3.

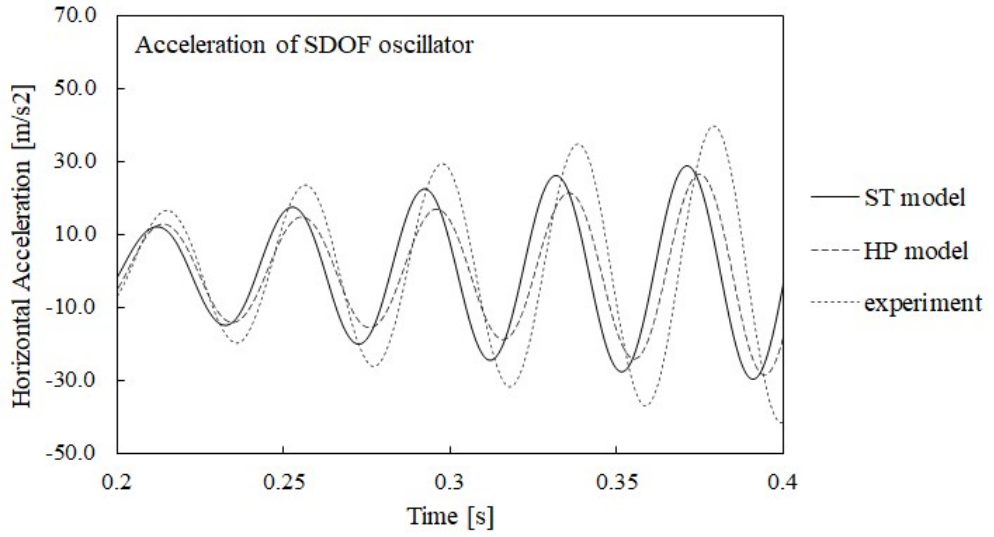


Fig. 43. Comparison of measured and computed horizontal accelerations at top of oscillator and corresponding spectral accelerations.

3.3. Summary on comparison of numerical and experimental results

The comparison of the numerical predictions and experimental measurements for numerous input motions and pile head conditions have been shown in this section of the thesis. Three additional input motions are also shown in Appendix E where the interested reader is invited. These additional acceleration time histories include also scaled earthquake input motion and a pile group with a small cap. Overall, the constitutive models have performed well when predicting the free field response and the kinematic and inertial soil-structure interaction, especially when recalling that such a vast number of input motions and pile head conditions has been analysed. Nevertheless, some discrepancies could also be found. This reveals potentially not optimized calibrations, need for improvements in the model formulations but also possibly lower experimental repeatability and reliability regarding structural response.

The comparison between the numerical and experimental study in Chapter 3 has also been linked with the findings shown in Chapter 2 of this thesis. Namely, the higher harmonic generation due to soil nonlinearity and fast elastic unloading waves, has been shown to affect the structural response. The presence of the generated harmonics has been indicated on the structure and at the pile tops. For the latter, the presence of the harmonics in the amounts different from those observed in free field, confirms the fact that in reality the kinematic piles in the shear stack behave as purely kinematic piles only to a certain depth, whereas above this depth, the piles behave as oscillators due to the piles being stiffer than soil at low depths and a small mass placed on the pile tops. In fact, an elastic pile placed in a shear stack can be treated as an additional instrumentation in order to capture higher harmonic motion generated within the soil mass.

The presented numerical studies have shown some occasional inconsistencies when comparing with the experimental results, thus, one may wonder on the reasons and consider potential improvements in the numerical predictions. First of all, it is recalled that the experimental results accumulate plastic strains during the testing sequence, thus the initial strain are not zero as in the numerical studies and this can have effect when comparing the numerical and the experimental results. Therefore, tweaking the model parameters for a specific input motion and not trying to capture a large group of experimental data would be expected to improve simulations for this particular input motion.

The next step to potentially try to improve the numerical predictions could be some parametric studies on the assumed input parameters in the numerical models, such as for example the K_0 value, the friction coefficient on the pile-soil interface or the lack of anisotropy in soil. However, any parametric studies would inevitably be still in shade of the lower repeatability of the experimental measurements for piles as highlighted before in this chapter.

Finally, one needs to remember about how the bottom layer has been modelled (i.e. the same calibration as the top layer with the only modification in the initial void ratio to account for higher relative density). Due to this assumption, although there are some indications listed in Section 2.1 in Chapter 2 showing it to likely be reasonable, it is possible that the behaviour of the bottom layer has still not been captured very accurately. Therefore, an obvious improvement, or at least higher confidence in the obtained numerical results (if the above assumption was actually verified to be representative of the behaviour of the bottom layer), would be to calibrate the bottom layer in the shear stack tests on laboratory tests of Leighton Buzzard sand, mixture between fractions B and E (currently not available to the best of the author's knowledge).

In conclusion, it is reiterated that both models predicted soil and soil-structure interaction in a satisfactory way, especially when recalling a large number of different test configurations. Therefore, the conducted analyses and the presented results can still be a valuable source for an interesting discussion on some aspects of numerical and constitutive modelling. These are shown in detail in the following Section 4 of this chapter.

4. Discussion

The following section discusses various numerical and constitutive aspects of soil modelling which contribute to reliable simulation of soil seismic behaviour. The performance of the models is also subject to more detailed investigation. Some reference is made also to Chapter 2 of this thesis in order to incorporate the response of the DM model regarding some of the studied aspects. Some additional computational runs of a 2D soil column are done in this section in order to develop the discussion.

The discussion includes the following aspects: stress strain behaviour and stress paths (4.1), importance of elasticity and soil fabric (4.2), effects of smooth stress-strain curves (4.3), settlement predictions (4.4), ratchetting (4.5), pressure dependence of the two models (4.6), occasional problems encountered during the course of the research with the ST model and HP model (4.7 and 4.8 respectively), effect of addition of viscous damping on higher frequency motion (4.9), a set of minimum corrections to the formulation of elastoplastic models in order to improve soil seismic behaviour (4.10), computational times (4.11) and final additional remarks (4.12).

4.1. Stress-strain behaviour and stress paths

This section presents stress-strain behaviour and stress paths in the chosen five elements from the 3D mesh (Figure 44) in their bottom Gauss points for the 10Hz input motion (0.155g) with a SDOF structure on the top of the pile no. 3. The elements can be divided in three groups, representing free field, vicinity of a kinematic pile and vicinity of a pile with a SDOF structure.

Figures 45 to 49 depict shear stress against shear strain curves for the five chosen elements. The elements no. 1, 2 and 4 (Figures 45, 46 and 48 respectively) show clearly hysteretic fairly smooth behaviour as in simple shear, i.e. as expected in free field or close to the pile but at depth, where the response of kinematic piles is driven by soil. On the other hand, the elements no. 3 and 5 show very erratic stress strain curves. In these regions, the response is no longer dominated by the simple shear behaviour since the impact from the very stiff pile becomes dominant. Note that the response of the models in corresponding elements sometimes differs to some extent, e.g. for the element no.1, where the ST model at the top predicts softer response than the HP model. This difference in predictions of both of the models is explained in Section 4.6 later in this chapter.

Figures 50 to 52 show a sort of “biaxial” loading on the soil elements 1, 3 and 5, respectively. It can be observed that this type of loading is negligible in free field, has some significance close to the kinematic pile no. 3, and is of major importance for the pile with an oscillator on its top. In addition, the stress paths of ratio σ_v/σ_h versus the normalized mean effective stress p'/p_o are shown on Figure 53 for the element no. 5 to highlight the dramatic changes in stress state in soil around the pile with the structure.

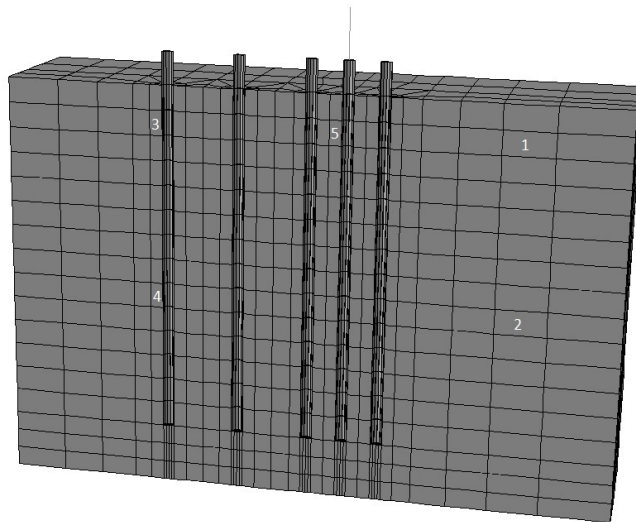


Fig. 44. Chosen elements for stress strain and stress path presentation.

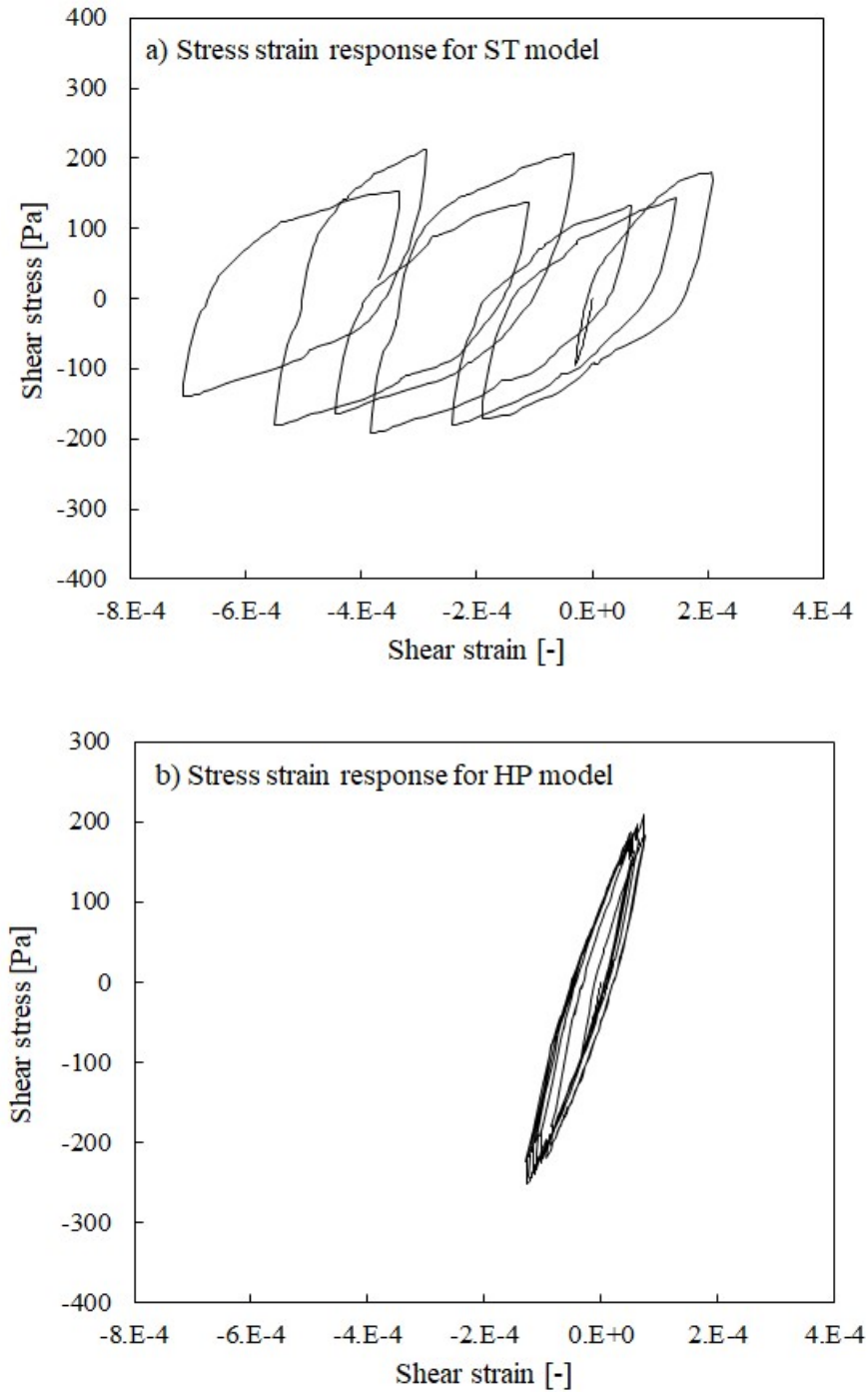


Fig. 45. Stress-strain curves for element no.1 in free field at around 90mm depth for: a) ST model, b) HP model.

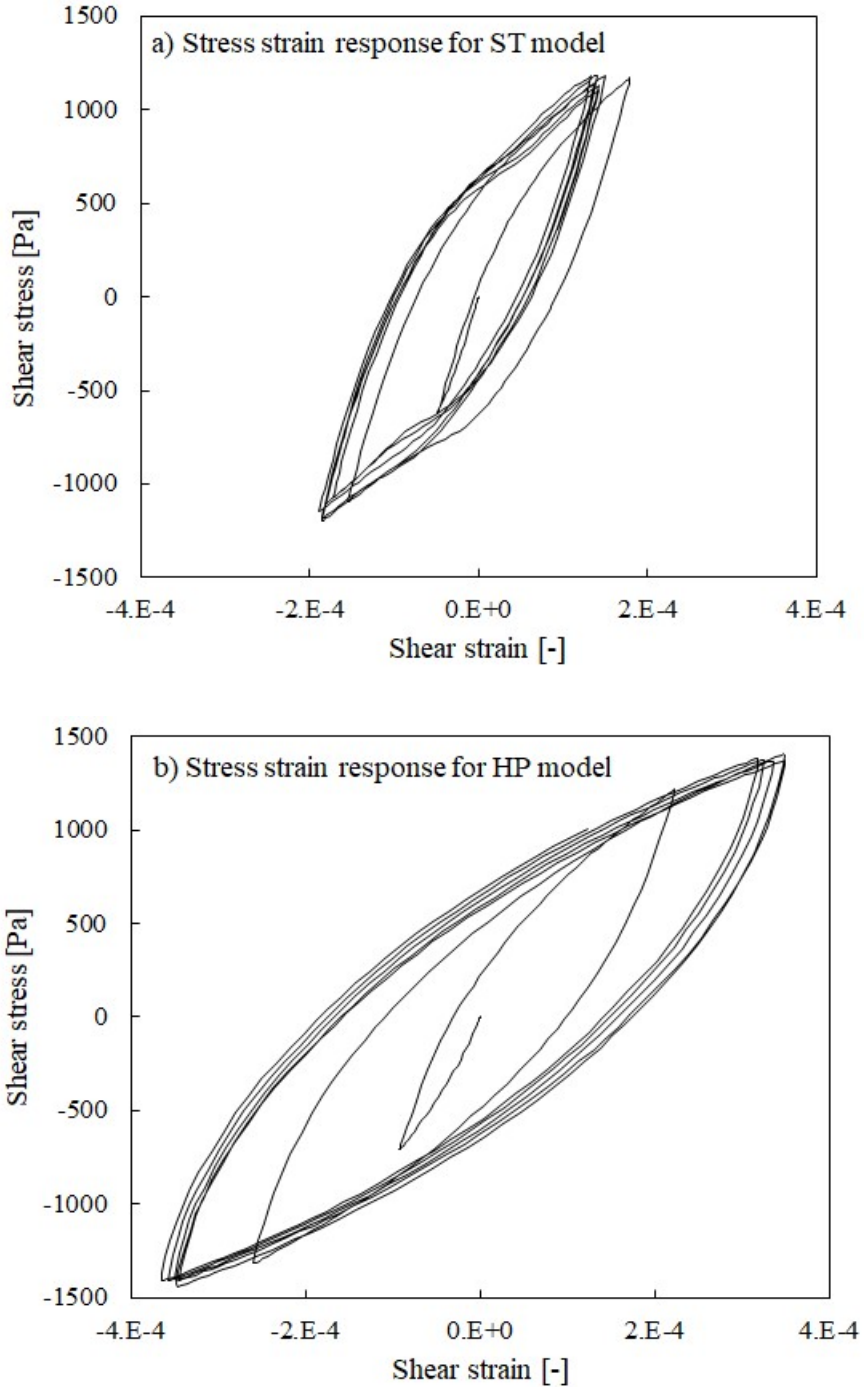


Fig. 46. Stress-strain curves for element no.2 in free field at around 430mm depth for: a) ST model, b) HP model.

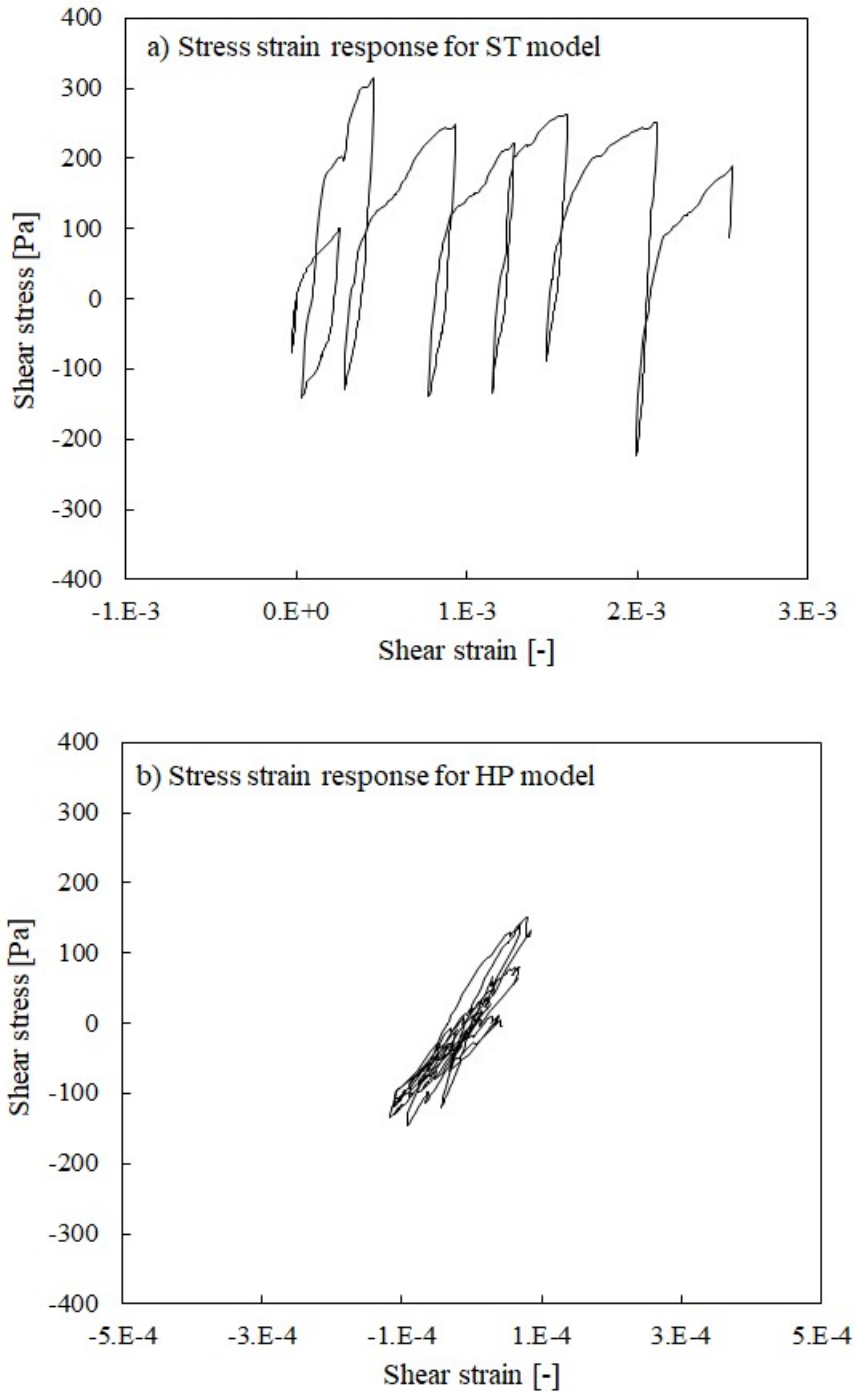


Fig. 47. Stress-strain curves for element no.3 in vicinity of kinematic pile at around 90mm depth for: a) ST model, b) HP model (note different scale on shear strain axis).

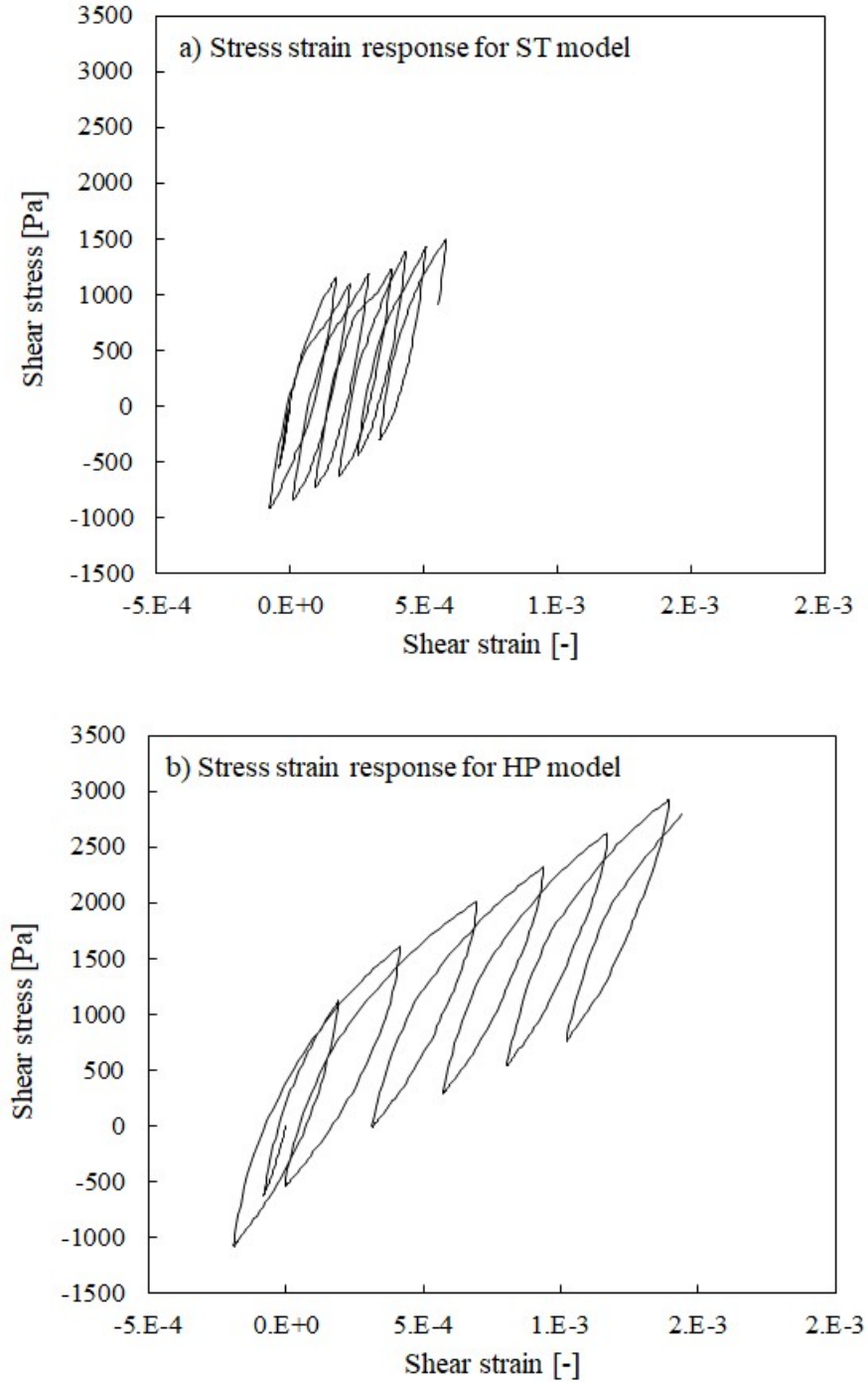


Fig. 48. Stress-strain curves for element no.4 in vicinity of kinematic pile at around 430mm depth for: a) ST model, b) HP model.

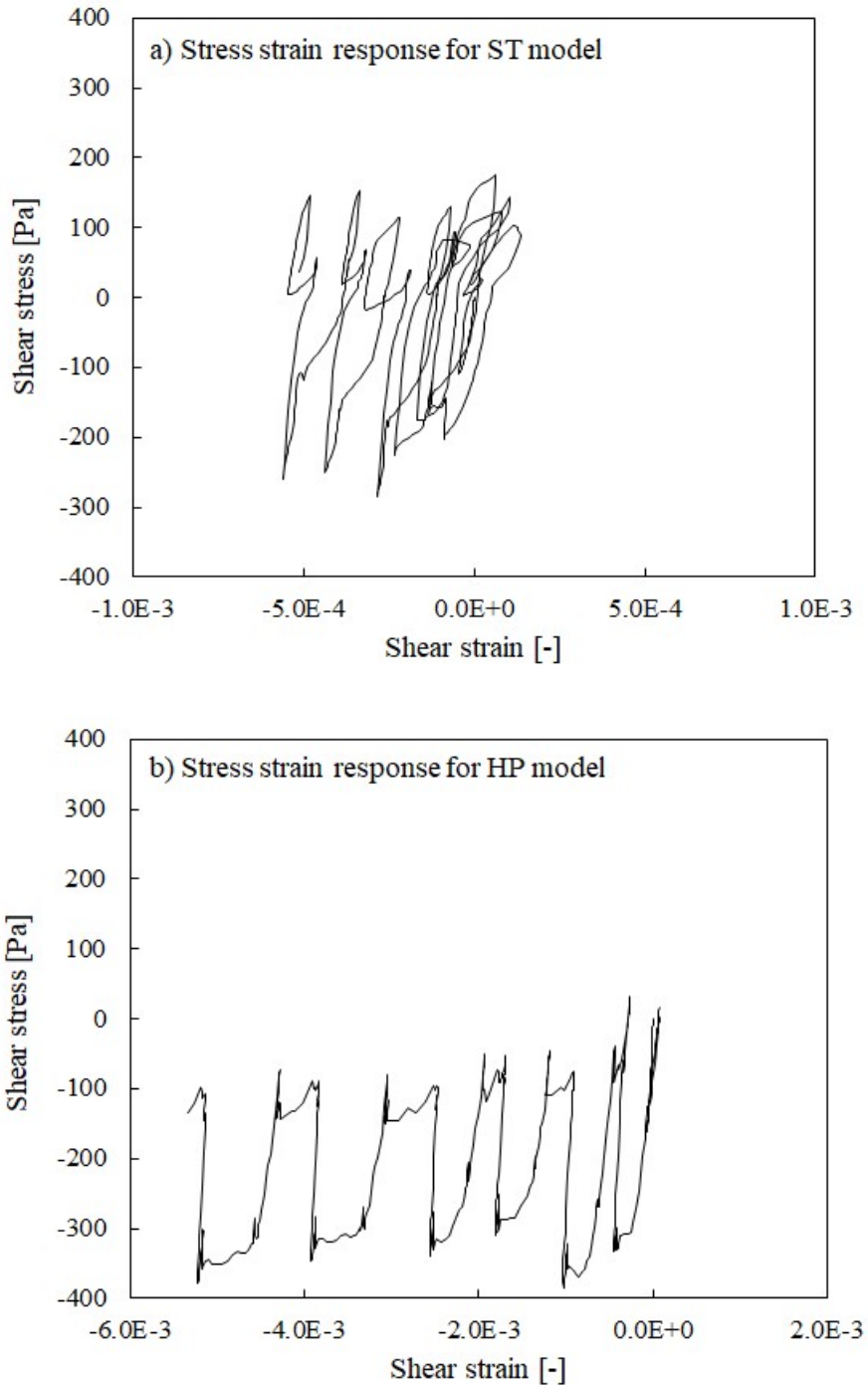


Fig. 49. Stress-strain curves for element no.5 in vicinity of kinematic pile with SDOF structure at around 90mm depth for: a) ST model, b) HP model (note different scale on shear strain axis).

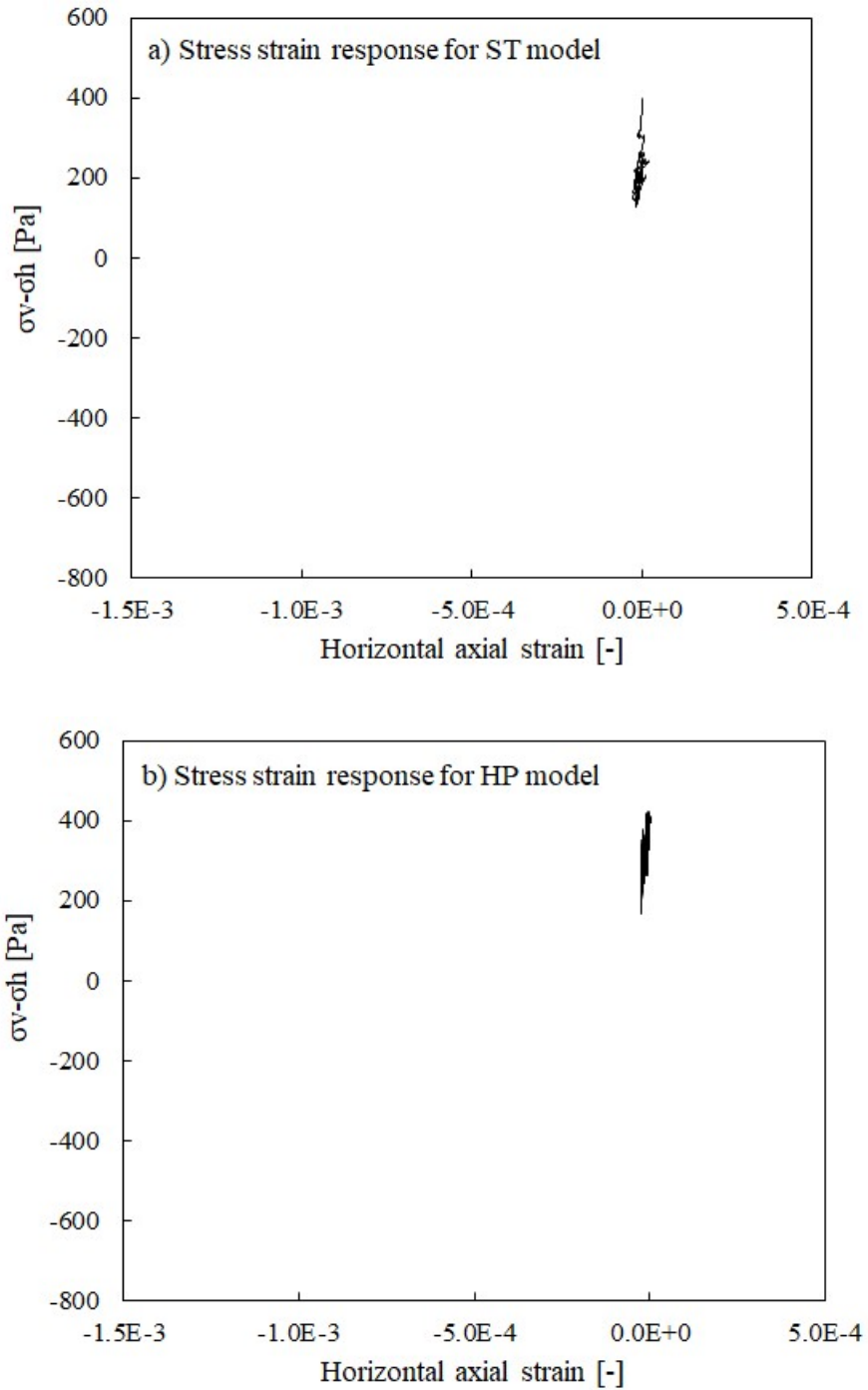


Fig. 50. Biaxial stress-strain curves for element no.1 at around 90mm depth for: a) ST model, b) HP model.

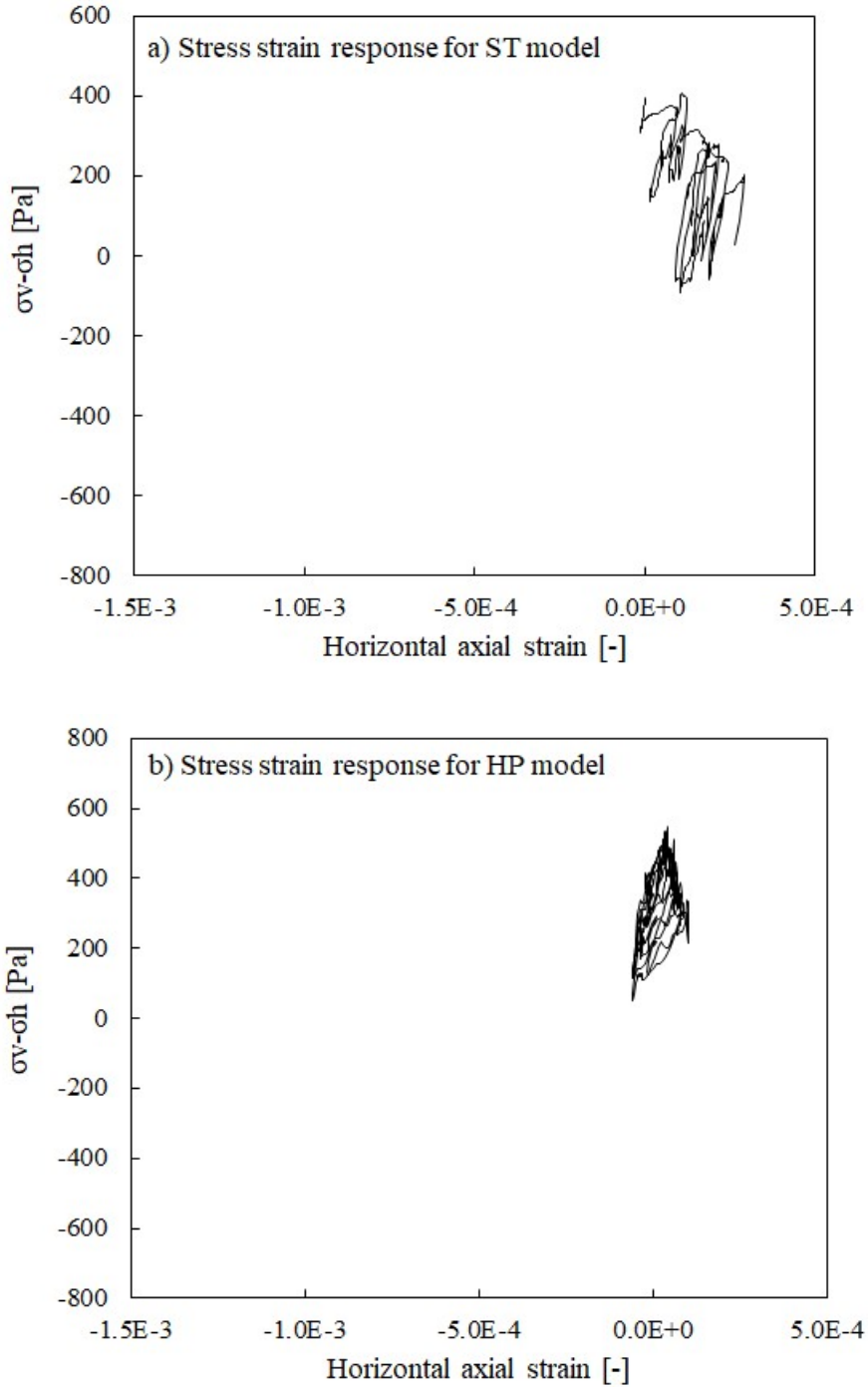


Fig. 51. Biaxial stress-strain curves for element no.3 in vicinity of kinematic pile at around 90mm depth for: a) ST model, b) HP model.

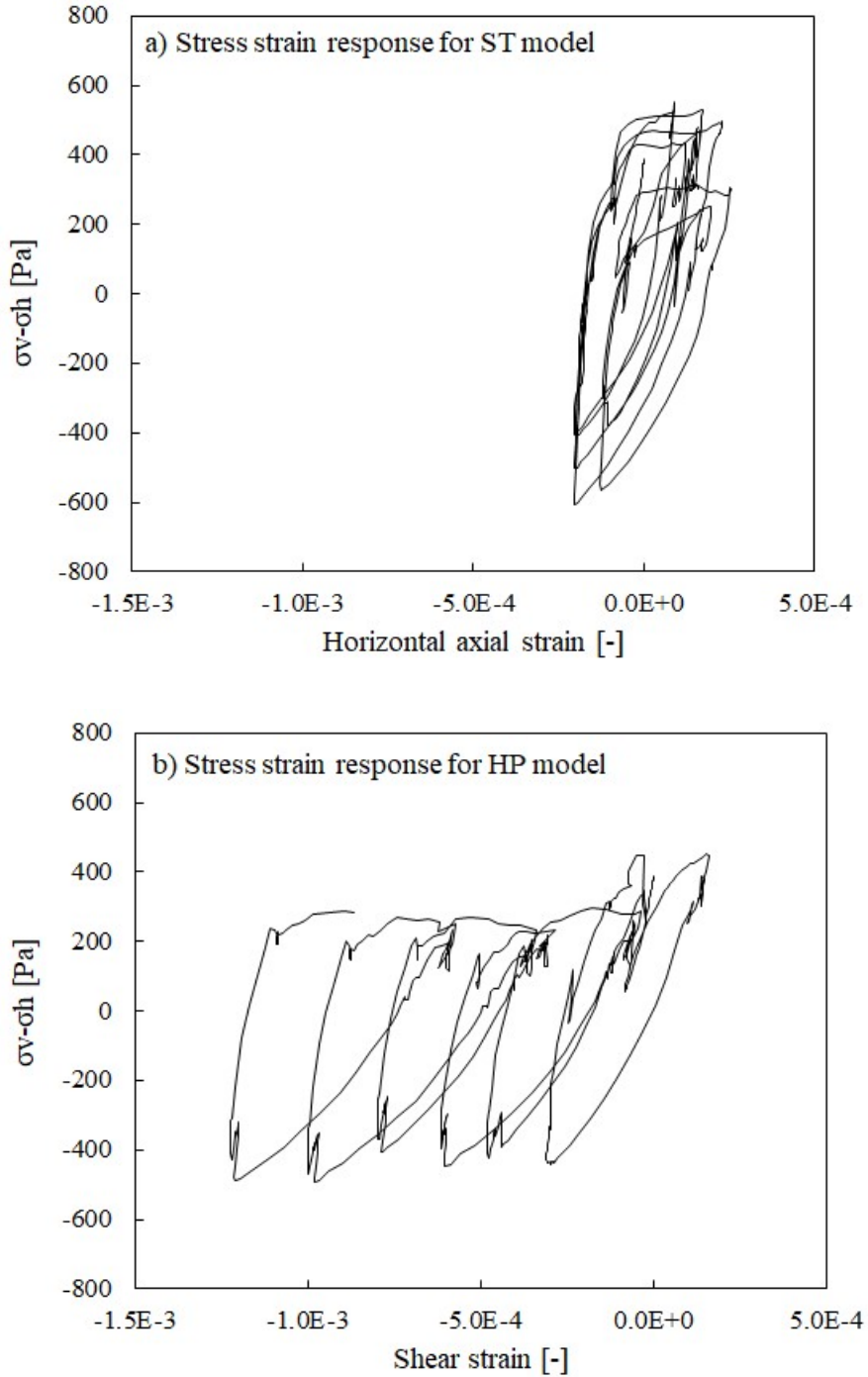


Fig. 52. Biaxial stress-strain curves for element no.5 in vicinity of kinematic pile with SDOF structure at around 90mm depth for: a) ST model, b) HP model.

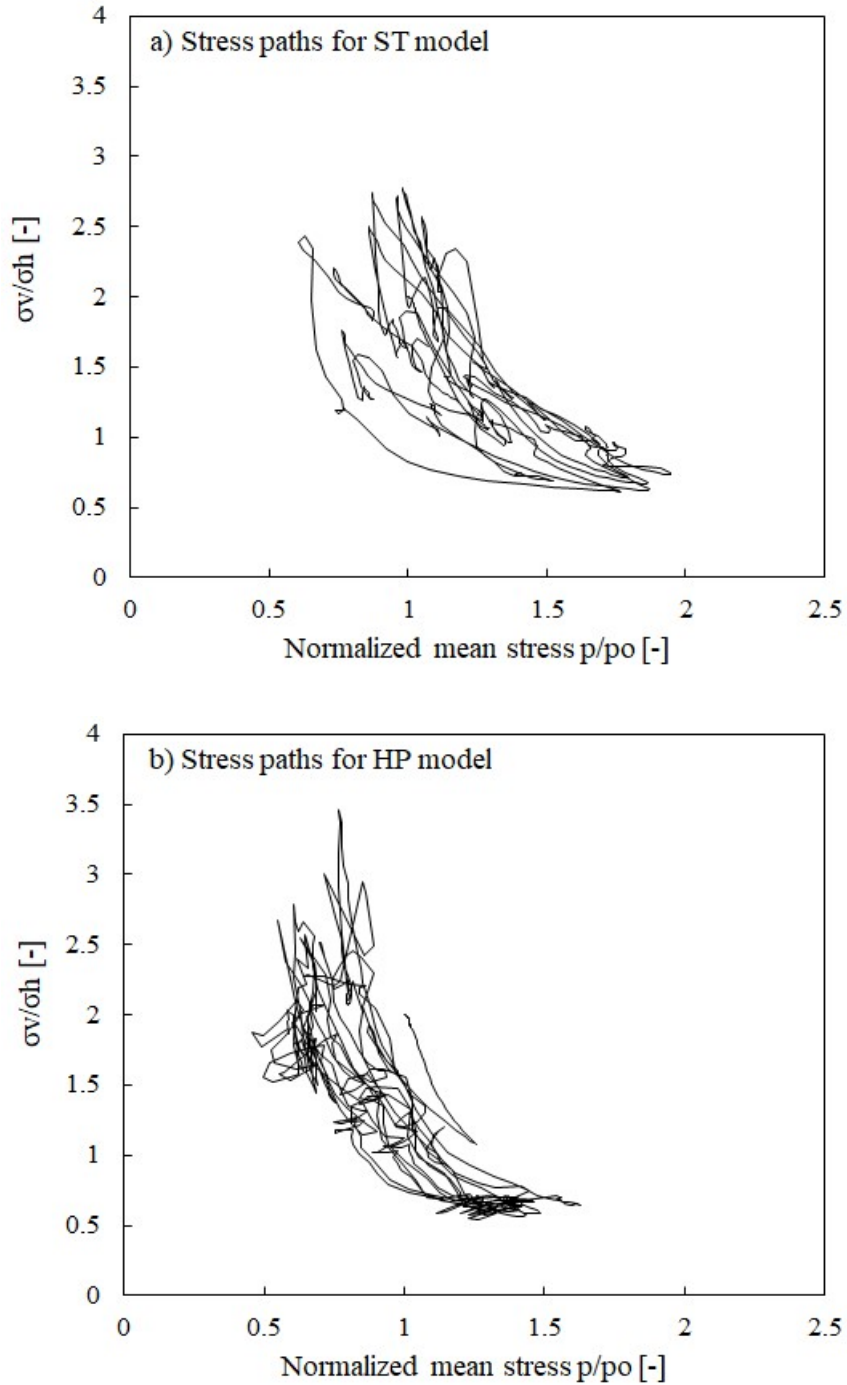


Fig. 53. Stress paths for element no.5 in vicinity of kinematic pile with SDOF structure at around 90mm depth for: a) ST model, b) HP model.

4.2. Importance of elasticity and soil fabric in simulation of shear stack tests

The modern soil constitutive modelling discusses uses of various complex constitutive ingredients to account for soil complexities observed at laboratory test level. Therefore, some questions arise when thinking of soil behaviour under seismic conditions, i.e. one may want to know how important are: elasticity, soil fabric, stiffness anisotropy and their changes during seismic loading in the analysis of soil and soil-structure interaction. Is soil during shearing disturbed enough to cause changes in fabric that affect in consequence soil stiffness characteristics and anisotropy? A subsequent question, if the fabric effect was important, could be the following: where to place a constitutive feature such as a fabric tensor in the model formulation, i.e. should it modify the elastic stiffness, the plastic stiffness or maybe dilatancy. This section attempts to look at the experimental data from the past studies and the numerical results from this thesis to give some consideration to these aspects. Firstly, looking in the response of free field, secondly looking in the vicinity of piles. Note that the potential importance of the elasticity in soil seismic behaviour has been already recognized in Chapter 2 dealing with the presence of higher frequency motion. This aspect will not be treated more in this section.

First of all, the response in shear stack, although the relative lateral displacement is typically less than 0.2mm (Durante, 2015), is driven by plastic strains. Settlement and volumetric changes (alternate compression and dilation) during the tests were observed by Durante (2015) and some extracts of these showed also in Sections 2 and 3 of this chapter. On the other hand, these changes were very small. Durante (2015) evaluated changes in void ratio based on the observed settlement (cumulative 10mm during 5 days of testing). These changes, if attributed solely to the upper soil layer, would result in the change in a void ratio as small as 0.06 (i.e. from 0.91 to 0.85). Such a change in the void ratio would not be expected to affect significantly the stiffness characteristics or soil fabric. This is confirmed on Figure 54 which presents a comparison of the lateral displacements from the experimental tests with 25Hz input motions of similar amplitudes carried out between 1st testing day and 4th testing day. The measured displacements do not differ between the initial and the final runs. In addition, no changes within single tests, i.e. from one sine cycle to the other sine cycle within the same shaking time history, can be noticed. Therefore, it can be concluded that the soil stiffness (elastic and plastic) in shear stack tests remains fairly constant both, during the span of a single test as well as during the span of few testing days.

The numerical studies also confirm the observation of irreversible behaviour being dominant. Chapter 2 showed higher harmonic generation for input motion as low as 0.037g (i.e. based on the carried-out studies the higher harmonic generation is not expected for linear or nearly linear elastic behaviour as shown in Appendix B).

Figure 55a shows changes in mean effective stresses as predicted by the constitutive models due to: P-wave generation (measured also in the experiments) as a result of volumetric changes in soil in a single loading cycle and an increase in lateral stresses due to cumulative densification (note that the densification is mostly overestimated in this study by the constitutive models). It is recognized that these changes are still minor, thus, the elastic shear stiffness and anisotropy should not change significantly during the shaking.

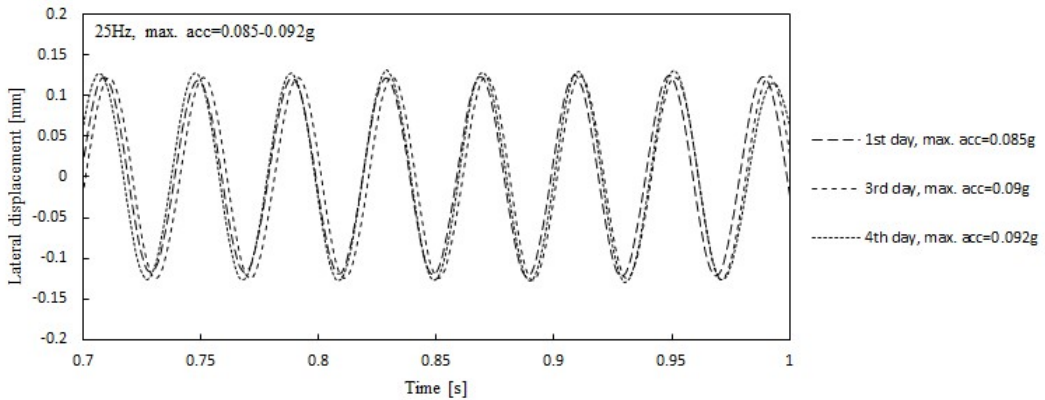


Fig. 54. Displacements measured experimentally on top of shear stack for 25Hz input motions applied at 1st, 3rd and 4th day of testing campaign.

What is more, Kuwano & Jardine (2002) indicated that for a stress ratio (vertical stress over horizontal stress) less than 2.2 (i.e. such as in case of the stress state in the shear stack) the elastic stiffness is governed mainly by mean effective pressure (which does not change significantly in shear stack as shown on Fig. 55a) and to a lower extent by a void ratio (the latter changing again only slightly due to some densification in the shear stack experiments). The past history does not play a role for the stress ratios lower than 2.2. Therefore, it can be concluded that the stiffness characteristics are functions of mean stress and a void ratio, and the stiffness characteristics and the soil fabric of the shear stack soil remain practically the same throughout the whole experimental campaign.

Another aspect to consider is inherent anisotropy. Initial anisotropy in dense sand in isotropic stress state was shown to be negligible (Gajo et al., 2000). On the other hand, in shear stack some initial anisotropy is expected due to deposition by pluviation method resulting in approximately $K_0=0.5$ conditions. The evolution of anisotropy with increasing stress ratio η and for large strains was also shown by Gajo et al. (2000). However, this is not expected to happen in shear stack tests since the strain range is very small and stresses are far from reaching peak strength. Besides, since the free field in shear stack tests is subjected to simple shear stress path and the

models are calibrated for this behaviour, as a consequence the inherent anisotropy is of less importance in free field.

To sum up, the soil behaviour in shear stack tests in free field is driven by plastic strains but of relatively small magnitudes. The soil fabric is practically not affected, thus, the stiffness characteristics such as anisotropy and its development are of less importance in dry soil. On the other hand, anisotropy and its development would be expected to be more important in saturated tests approaching liquefaction or cyclic mobility as it was shown in the past (Li & Dafalias, 2012).

All that described above focuses on soil response in simple shear as it is dominant in shear stack tests. However, the above conclusions could differ when looking at stress paths close to the piles, especially when the structure is also modelled. Therefore, it is more interesting to look what happens in the vicinity of the pile with a SDOF structure. Here the mean effective pressure varies considerably (Figure 55b). Two simultaneous stress paths are experienced, i.e. simple shear and a sort of “biaxial” loading with pile pushing into the adjacent soil and moving away from it (as shown in Section 4.1 on Figure 52). The changes in the ratio of vertical stress versus horizontal in-plane stress in the vicinity of the pile no.3 are shown on Figure 53. Dramatic changes from 0.5 to 3.5 are experienced in soil for this stress ratio. Thus, according to Kuwano & Jardine (2002), fabric effects such as sudden stiffness degradation are expected to happen for such large changes in the stress ratio. Therefore, the effects of fabric can be important for improvements in simulating soil-structure interaction. Future studies incorporating constitutive models with constitutive features accounting for fabric and its evolution should be employed to investigate further this observation.

For completeness, some ideas on the future studies including fabric effects are given below. One of the ways to model more realistically the effects of changes in soil fabric close to a structure could be by means of including more sophisticated feature such as a fabric tensor in the model formulation. The fabric tensors can act on other different constitutive ingredients in the formulation of the model, e.g. the fabric tensor in the DM model acts on the volumetric response. A different approach is to use an advanced hyperelastic soil law with an incorporated fabric tensor as was shown by Gajo (2010). The elasticity law in the ST model version used in this thesis has been simplified and discarded any anisotropy, either inherent (fabric tensor $\mathbf{B}=\mathbf{I}$) or plastic strain induced anisotropy (no evolution of tensor \mathbf{B} in the model version used in this thesis). However, future numerical studies, when compared with more reliable experimental data on soil-structure interaction, could also look in detail on how important more sophisticated approach to elastic soil stiffness modelling is. In such a case, one may want to refine the mesh size around pile tops in order to further enhance the reliability of such a study. This has not been done in this thesis, as it has not been intended to look at such details of constitutive modelling (i.e. none of the models possesses relevant constitutive features).

To conclude the changes in small strain soil stiffness (elastic stiffness) and soil fabric are found to be negligible in the shear stack in free field. These changes can be

more important in the vicinity of the piles; however, this aspect has not been investigated in detail in this thesis.

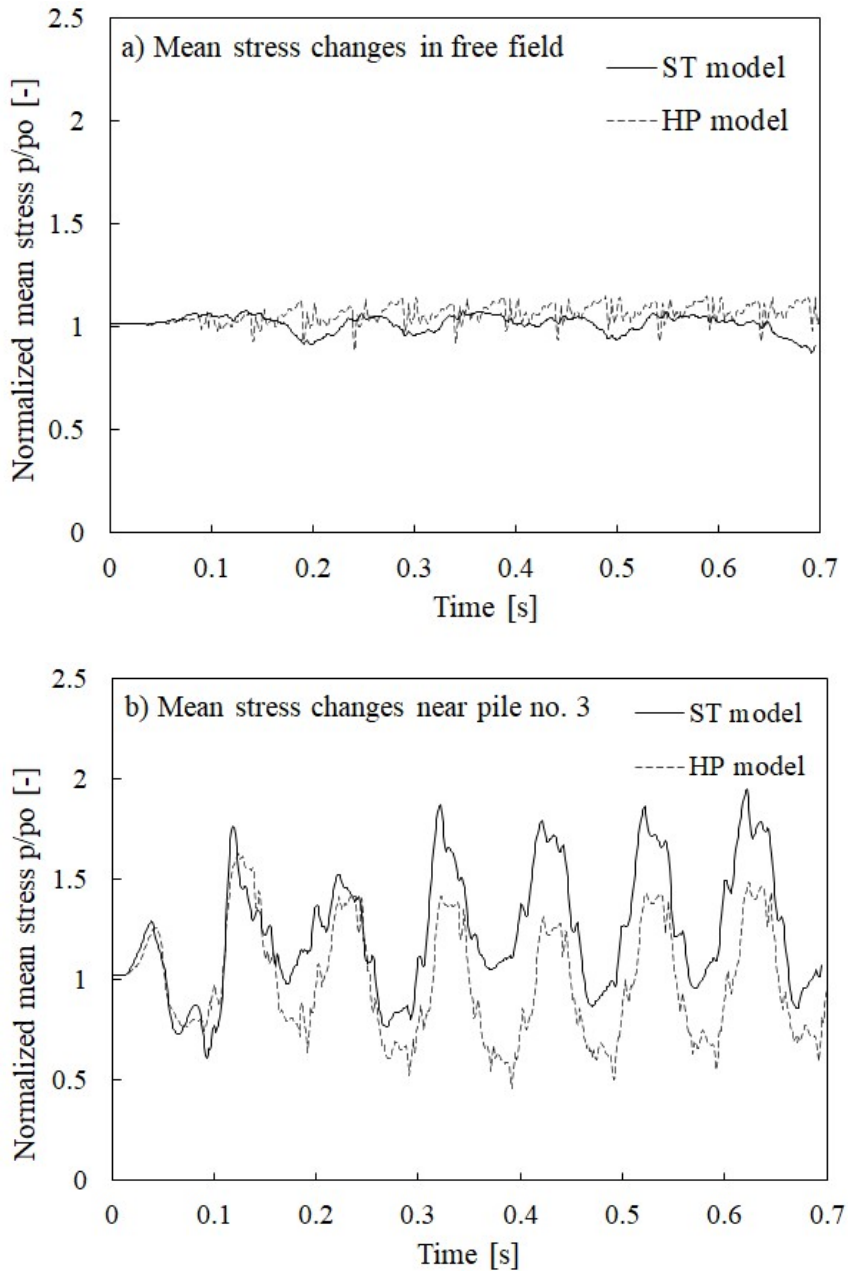


Fig. 55. Changes in mean effective pressure computed by numerical models for 25Hz input motion (0.077g) in: a) free field and b) close to pile with SDOF structure (as per elements no. 1 and no. 5 in Figure 44, respectively).

4.3. Effect of smooth stress-strain response

A constitutive feature, which has been found important in this research, is a feature allowing predictions of smooth stress-strain response during the loading in all strain ranges. Typically, the problem can occur when changing from elastic to plastic stiffness characteristics.

The ST model achieves a smooth stress strain curve through the α parameter introduced by Gajo (2010). A smooth stress- strain relationship is achieved by the HP model in the tensorial equation (eq. 27, Chapter 1) including the intergranular strain concept. On the other hand, the DM model does not possess a likewise constitutive ingredient. The plastic stiffness definition includes the unitless elastic stiffness constant G_0 in its definition (see eq. 48 in Chapter 1). However, other input parameters modify the value in such a way that a corner between the elastic and plastic stiffness definition may be obtained. In this thesis, particular care has been paid to the calibration at small strain levels, and comparable G/G_0 curves between all the three constitutive models, thus the calibration of the DM model has been “sort of” optimized to hide the lack of the “smoothing” feature. Therefore, for the comparison purpose in this subsection of the thesis, the DM model will also be shown as per the original calibration for Toyoura sand. This calibration is understood not to be calibrated for small strain range but rather larger strain levels but often used by others in seismic analysis (e.g. McAllister et al., 2015; Taiebat et al., 2010). Note that Chapter 1 (Section 5.4, Figure 12) presented the resulting G/G_0 curves obtained using this calibration, and a clear sharp change of stiffness is observed after exceeding the yield stress. Similar findings are also shown below.

Figure 56 shows the computed accelerations at the depth of 12.5mm (middle of the top element in a column made of 32 elements of the 25mm element size) and Figure 57 presents the corresponding τ - γ stress-strain curves for a 2D soil column. Figures 58 and 59 present the same set of results but at depth of 187.5mm (middle of the element no. 8 counting from the top). The chosen input motion is 25Hz of the maximum amplitude of 0.077g. Only first 0.15sec of time history is shown, i.e. before the effects of fast elastic unloading waves (shear strain discontinuity occurrence) dominate the response and all the models respond generating spurious oscillations due to the inefficiency of the adopted finite element formulation (as explained in Chapter 2).

The acceleration records on Figures 56 and 58 clearly show that the first model to experience “wobbling” in the computed accelerations is the DM model. This is visible in particular for the original calibration, and only when investigating the curves in the “zoom in window” (Figure 56b and 58b), for the calibration used in this thesis. Looking at the stress strain curves an obvious difference can be observed, the ST and the HP models have smooth stress strain behaviour, whereas the DM model “suffers” from having an edge between elastic and plastic stiffnesses, again this is particularly

visible for the original calibration of the DM model (Figure 57d and 59d; note the shear strain axis of a different scale as the original calibration of the DM model is also “softer” than it is required for the shear stack analysis).

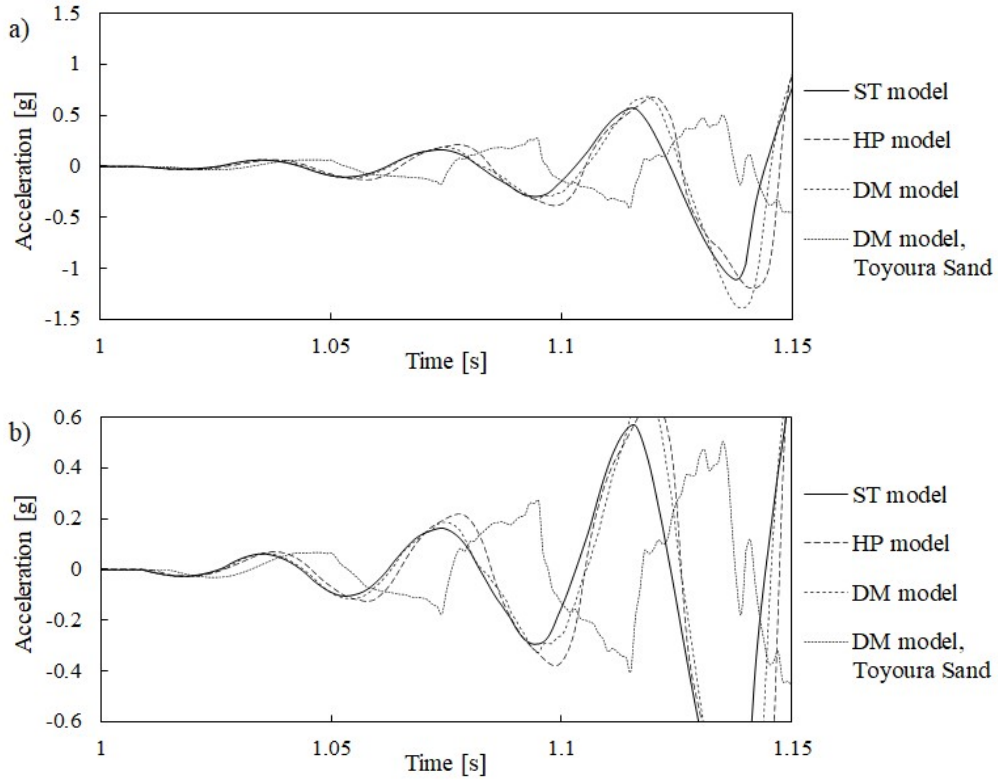


Fig. 56. Computed accelerations at depth of 12.5mm: a) zoom out, b) zoom in.

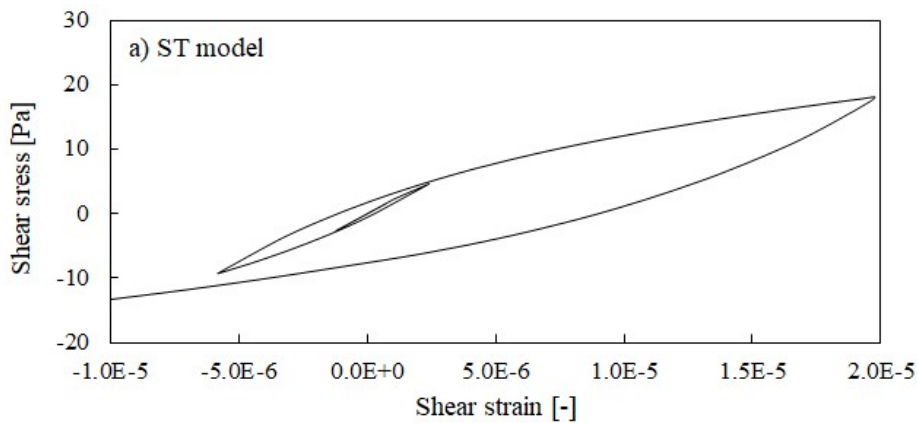


Fig. 57. (continuation on the next page)

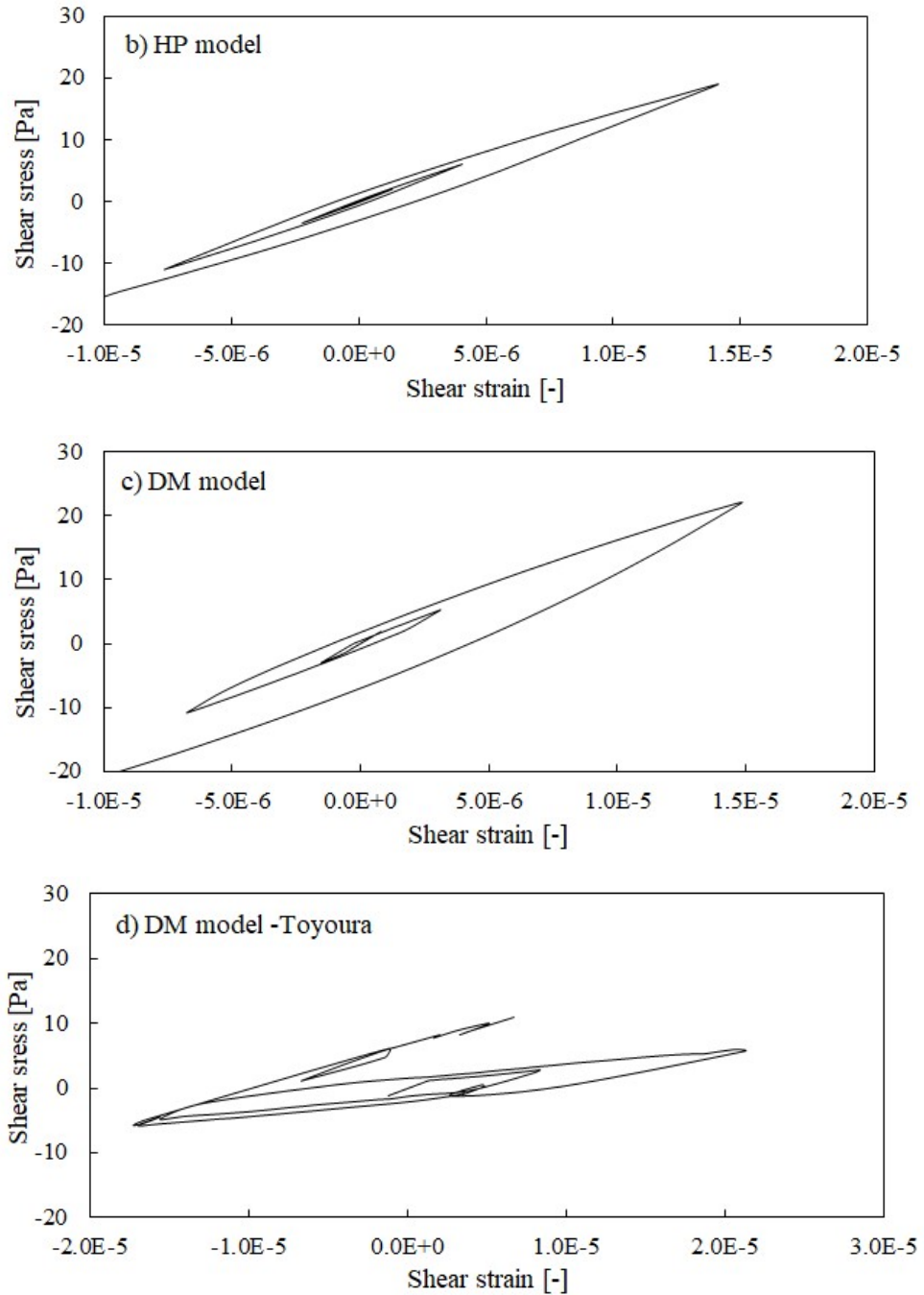


Fig. 57. Computed stress-strain curves at depth of 12.5mm: a) ST model, b) HP model, c) DM model, calibration for the shear stack, d) DM model, calibration for Toyoura sand (note here shear strain axis of different scale as explained in text).

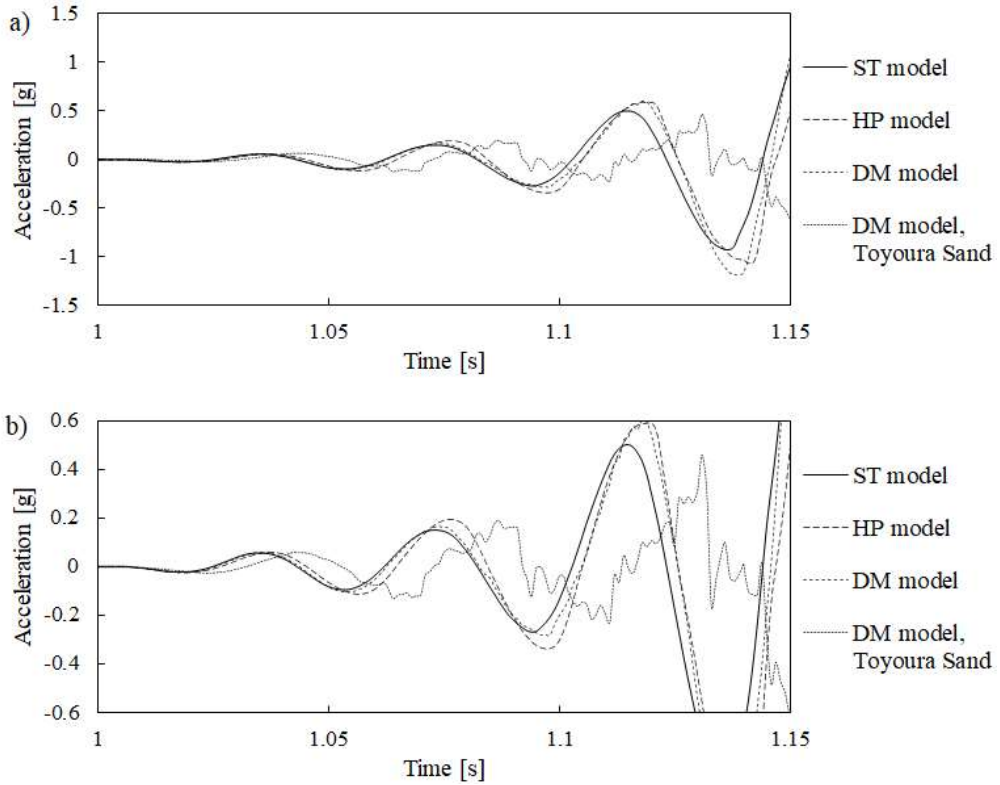


Fig. 58. Computed accelerations at depth of 187.5mm: a) zoom out, b) zoom in.

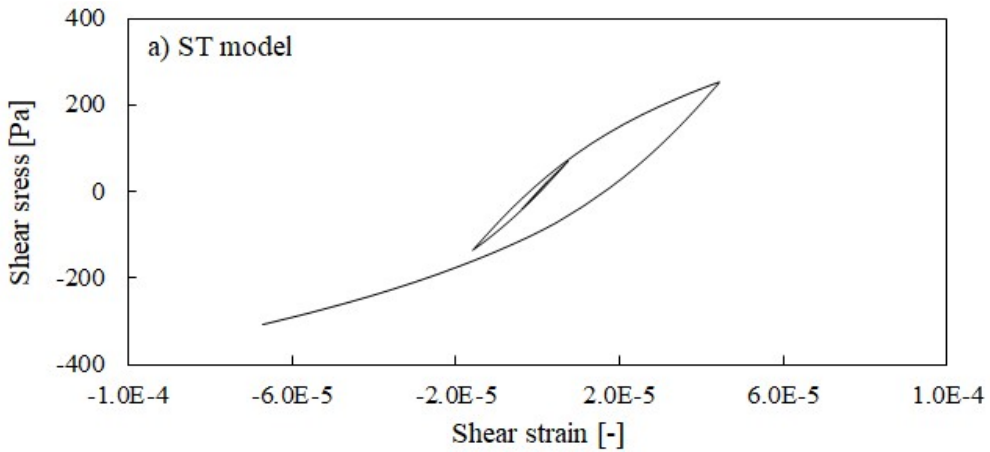


Fig. 59. (continuation on the next page)

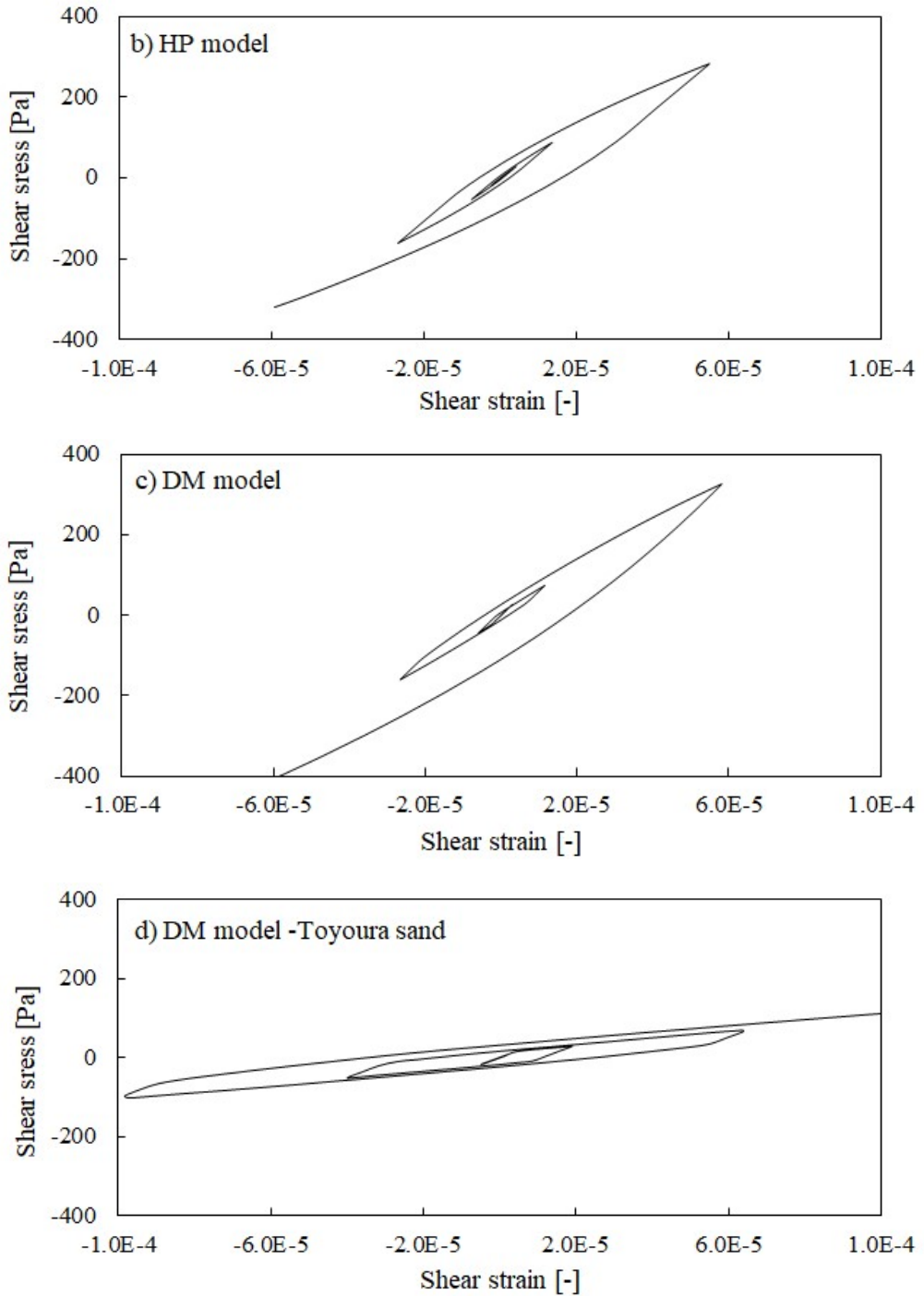


Fig. 59. Computed stress-strain curves at depth of 187.5mm: a) ST model, b) HP model, c) DM model, calibration for the shear stack, d) DM model, calibration for Toyoura sand (note here shear strain axis of different scale as explained in text).

On top of the above findings, as mentioned before, it was also found that fitting G/G_0 curve for the strain range of the interest in this thesis (i.e. less than 0.1%) was easier when a “smoothing” constitutive feature was present. Otherwise, it seems to be particularly difficult to calibrate and to cover with a single set of parameters the small and large strain behaviour. In addition, the lack of a “smoothing” feature resulted in an obligatory single yield surface size throughout the soil profile for the DM model for both sand layers. Namely, different yield surface sizes (such as adopted for the ST model in this thesis, i.e. 0.02 for the top and 0.01 for the bottom) could lead to the unacceptable situation when the top layer has higher stiffness than the lower layer within certain ranges of strain (i.e. the smaller yield surface at the soil bottom is reached but the larger yield surface at the soil top is not).

To conclude the above short study, smooth stress strain response allows to obtain predictions of smooth acceleration records and facilitates the calibration procedure. Typically, such smooth stress-strain behaviour is also observed in the experimental results, thus it can be considered to be physical. Therefore, a smoothing constitutive feature improves the predictions of dynamic soil behaviour and should be desired in the advanced soil constitutive models.

4.4. Settlement predictions

This section is focused on the volumetric response in the shear stack analyses as computed by the two models (ST and HP models) since they both, in general, tend to overpredict the settlement in the 3D analysis shown in Section 3 of this chapter.

Numerous numerical studies have been focused on replicating soil and soil-structure interaction in seismic conditions and settlement predictions have been typically problematic. For instance, Bilotta et al. (2014) showed significant underestimation of the settlement calculated by constitutive models when comparing with the experimental data. Similar findings were shown by Ramirez et al. (2018) or Ochmanski et al. (2019). Usually, this type of studies is focused on G/G_0 calibration in small strain region where no data on volumetric changes is available.

First of all, some doubt is highlighted on the measured settlements. Figure 60 shows the settlement recordings during only a couple of cycles of input motion. Two input motions are considered, 10Hz (maximum amplitude 0.137g, 11th test during the 1st testing day of the experimental campaign) and 25Hz (maximum amplitude 0.077g, 15th test during the 1st testing day of the experimental campaign). Both input motions generate very similar lateral displacements at the soil surface level (see Figures 19 and 25 in Section 3). However, the settlement records are distinctively different. The reversal in the lateral displacement causes initial compression as noticed for both input motions followed subsequently by dilation which agrees with typical behaviour of dense sand. However, the rates of the initial compression and especially subsequent dilation are distinctively different for both input motions. This could be due to the fact that the 10Hz time history applied some days before could still produce more settlement due to the initial reposition of the grains, i.e. the pluviation method could result in initially non-uniform density in the shear stack. This is author's speculation only. Anyway, another important observation from the experimental results is that the compression and dilation phases within a single loading cycle can be distinguished clearly. This observation is important when evaluating the performance of both of the constitutive models.

The numerical results on settlement are presented in Chapter 3 on Figures 20 and 26 for the input motions presented in Figure 60. The observation is that the problem of the overestimated settlement shown in Section 3 of this chapter is not related to ratcheting but rather to the rate of compression within a single cycle of the applied shear strain history, i.e. amount of the volumetric compression observed even for dense sands before dilation occurs. Such rate of compression seems to be generally overestimated by both models.

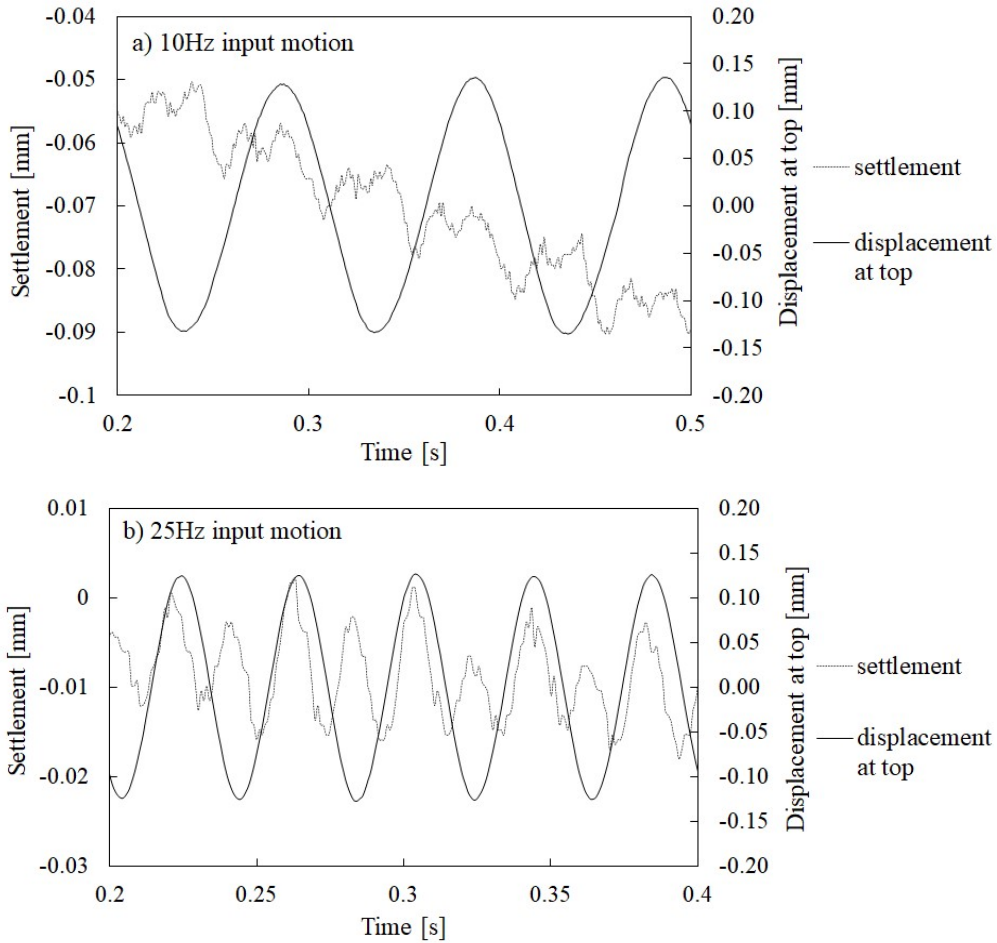


Fig. 60. Comparison of experimentally measured volumetric response from two input motions applied during the same testing day: a) 10Hz, 0.137g, test no. 11, b) 25Hz, 0.077g, test no. 15 (note vertical axis scale differs for both).

Regarding the predictions of the ST model, some improvements of the predicted volumetric response could be obtained by readjusting the dilatancy parameters (i.e. A or k_d). Decreasing A or increasing k_d values results in lower global volumetric compression in the shear stack studies. The proposed values of $A=0.1$ and $k_d=5.0$ and their impact on the settlement computations are shown on Figure 61. Note that these values of A and k_d lie significantly outside the typical ranges of values (shown in Table 1, Chapter 1). Nevertheless, an improvement in the global settlement prediction, i.e. a reduction in the computed settlement can be observed. On the other hand, the compressive and dilative phases within a single sine cycle seem still not to be well predicted by the ST model and the compressive behaviour dominates over dilative.

It could also be interesting to see if changes in the flow rule formulation of the ST model could improve the model volumetric response at small strain levels. Generally, sand in shear stack (although in relatively loose state, $e=0.91$ for the top layer) behaves as a dense sand due to low mean effective pressure. As a result of that, it can be concluded that the ST model seems to overestimate the initial compressive response observed typically also for dense sands before dilation occurs.

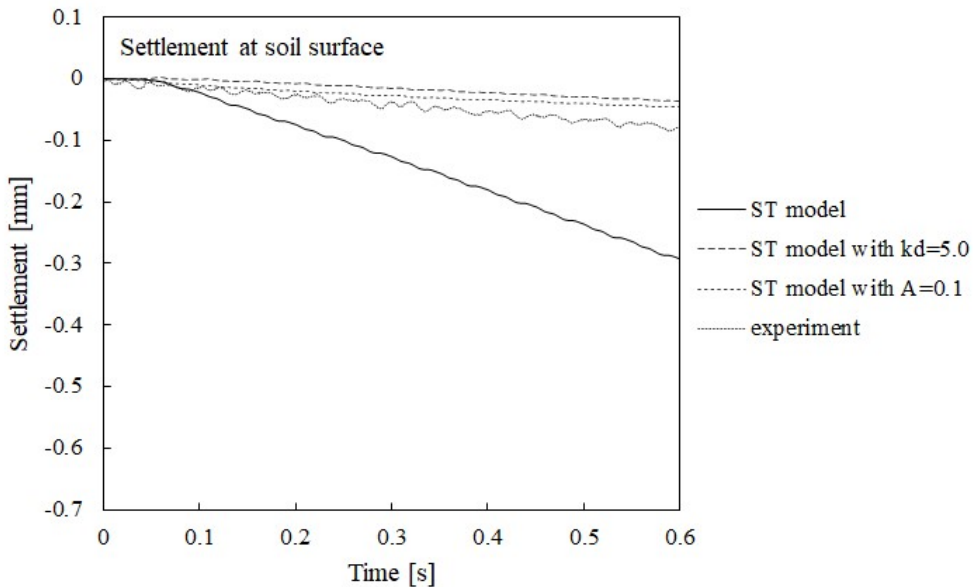


Fig. 61. Settlement predictions with ST model with dilatancy parameters changed to $A=0.1$ (a) and $k_d=5.0$ (b) for 10Hz input motion (0.137g).

Regarding the HP model, it is important to mention that the updated version of the intergranular strain concept from Wegener & Herle (2014) helps significantly in controlling the cumulative volumetric response in a straightforward way, i.e. through modification of only a single model parameter which does not affect significantly other aspects of soil behaviour. Therefore, an option to improve the settlement predictions could be increasing the value of the ϑ parameter from 5 to 10. Figure 62 illustrates the improvement achieved by this change. Note that also in this case the adopted value of $\vartheta=10$ results in ratio $\vartheta/\chi=20$ which is twice than the typical maximum ratio for these two parameters (e.g. Wegener & Herle, 2014).

To sum up, the two models with their original calibration used in this thesis showed inconsistent settlement computations when compared with the experiments. These could be improved by changes in the calibrations, although with the new values of the model parameters being outside their typical ranges. Potential changes in the model formulations could be a next step to improve the future predictions of settlements in small strain regions. In any case, it is reminded here that the volumetric

changes in shear stack tests are very small (even in the overpredicted computations by the two models) and do not influence the soil behaviour significantly (as shown in Section 4.2 of this chapter).

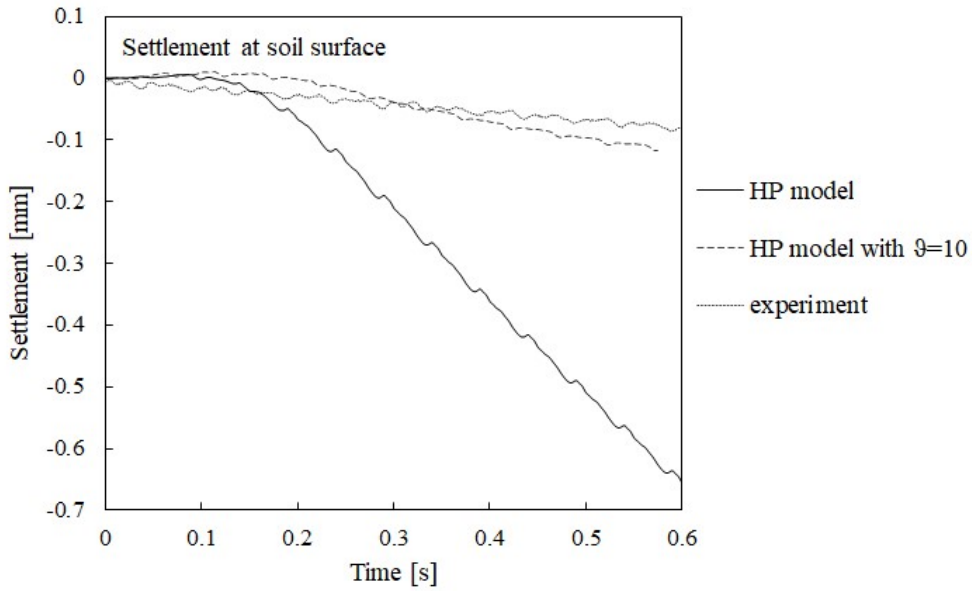


Fig. 62. Settlement predictions with HP model with $\vartheta=10$ for 10Hz input motion (0.137g).

4.5. Ratcheting in low strain cycles

In addition to the discussion on the predictions of settlements in Section 4.4, the problem of ratcheting is discussed in this section. For this purpose, firstly, the model of a 2D column has been run with a sequence of sine dwell input motions as shown in Table 2 and the response of the two models is shown on Figure 63. Secondly, an input motion of 10Hz (0.137g) was extended to last for 20 seconds to see the response of the models to constant shearing ratio at very small strains and this is illustrated on Figure 64. Note that the calibration in the ratcheting study has been used as presented in Chapter 1, i.e. without recalibration to improve settlement predictions (as discussed in Section 4.4).

The cumulative settlement from the sequence of the six analysed tests shown in Table 2 was measured in the experiments to be around 0.5mm (only some tests were available to the author, thus this magnitude is indicative) with the input motions no. 11 and 13 generating the highest settlements, and input motion no. 16 not showing any settlement.

The volumetric response of the constitutive models subjected to the same time history of the input motions presented in Table 2 is depicted on Figure 63. This shows that the ST model is not able to reduce the rate of compression with the already accumulated compressive strain. On the other hand, although still overpredicting the global settlement, the HP model seems to perform better, predicts the highest compression rate for the 20Hz input motion and a sudden shakedown and a change from strongly compressive into lightly dilative response when the test no. 15 starts (25Hz, 0.077g).

For completeness, the volumetric response of the two models is shown on Figure 64 for the extended 20s long 10Hz input motion. It can be observed that both models predict stiffening in stress-strain response (Figure 65). However, either no change (ST model) or a very slight change (HP model) in the rate of compression during shaking can be observed in the computed settlements.

On the other hand, it is recalled that both models, especially the ST model, show the ability to reduce the rate of volumetric changes due to consecutive loading cycles for larger strain levels (e.g. such as shown in Section 6 of Chapter 1 in this thesis). Therefore, the problem of ratcheting in the two models may be limited to the initial compression observed in dense sands at very small strains prior dilation occurs at larger strains. In any case, for seismic loadings, such as the those analysed in this thesis, the ability of the models to deal with ratcheting is considered to be of minor importance, since the loading histories are relatively short (i.e. soil is subjected to low number of cycles) and the volumetric changes are also relatively small, thus soil stiffness characteristics are affected in a very limited way as shown in Section 4.2.

Table 2 Sequence of input motions on 1st testing day (phase I) and measured experimentally settlements

Test no.	Frequency [Hz]	Amplitude [g]	Duration [s]	Settlement [mm]
11	10	0.137	1.2	0.14
12	15	0.104	0.8	-
13	20	0.086	0.6	0.24
14	25	0.085	0.5	0.024
15	25	0.077	0.5	0.015
16	30	0.055	0.5	0

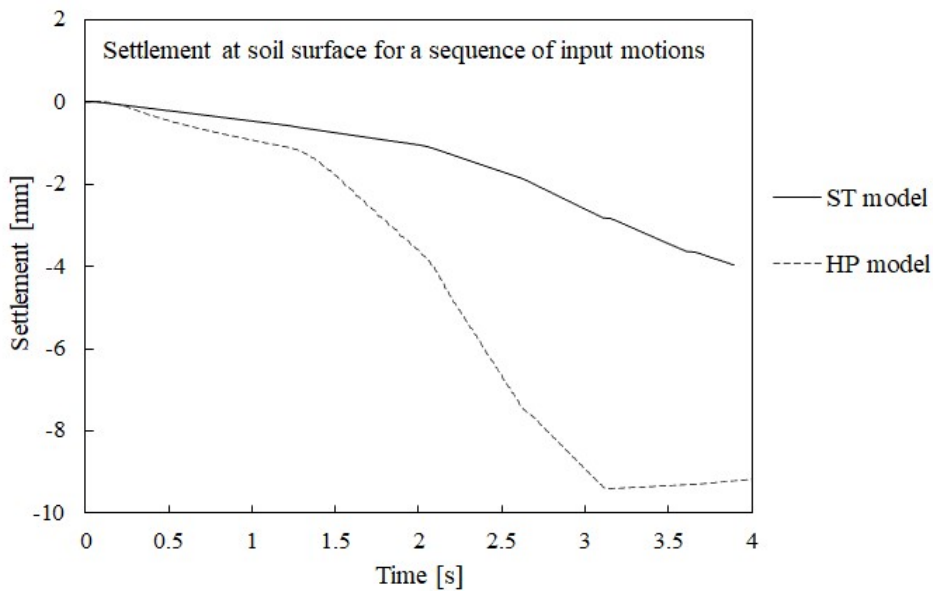


Fig. 63. Settlement prediction to sequence of input motions as per Table 2.

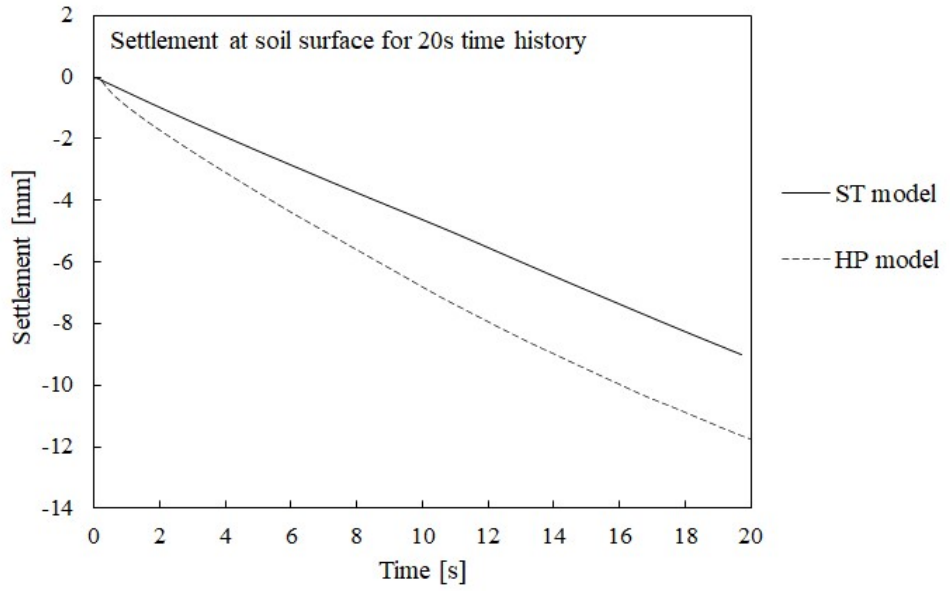


Fig. 64. Settlement prediction to extended 10Hz input motion (0.137g).

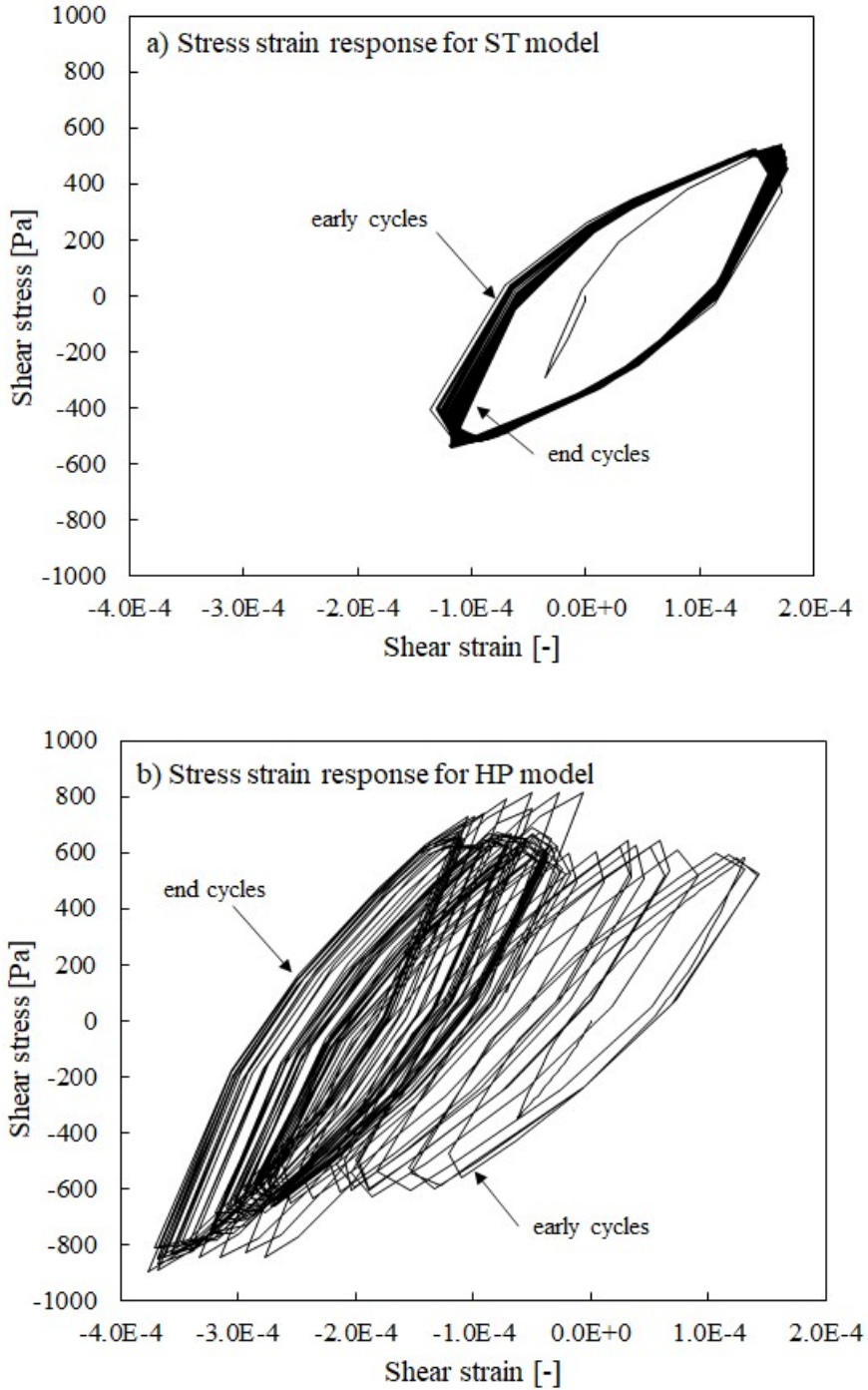


Fig. 65. Stress strain curves at depth of 225mm for ST and HP models.

4.6. Pressure dependence of models in large range of mean stresses

This section investigates the ability of the chosen calibration of the two constitutive models to simulate stiffness degradation in much higher mean effective pressures (i.e. 400kPa) and is compared with G/G_0 curves obtained by Lanzano et al. (2016) for Leighton Buzzard sand, fraction E.

The predictions of the shear stiffness degradation with the increasing strain levels computed by both models are shown in Figure 66. Note that the comparison is for $p'=400\text{kPa}$ and $K_\theta=0.5$ so assuming deposition similar to this in the shear stack but at much higher depths.

The results reveal that the stiffness degradation curve obtained from the HP model remains fixed around the recommended G/G_0 curve for shear stack analysis (Dietz & Wood, 2007) even though the mean stresses are much higher. The ST model performance is much better in this respect. This is a confirmation of a similar study shown by Gajo (2010) where the ST model with a single set of model parameters showed ability to capture, at least qualitatively, stiffness degradation in the range of mean effective stresses between 30 and 1700 kPa.

The fact that the calibration of the HP model adopted in this thesis seems to be too “soft” for 400kPa mean effective pressure is not surprising. Chapter 1 of this thesis showed an opposite situation, i.e. the calibrations of the HP model for Leighton Buzzard sand, fraction E, in much higher mean effective pressures (e.g. Hleibieh et al., 2014; Ochmanski et al., 2019) have been shown to result in too “stiff” predictions for shear stack analysis.

For completeness, the G/G_0 curves are also computed for the top ($p'=1\text{kPa}$) and the bottom of the shear stack ($p'=10\text{kPa}$) and compared with each other on Figure 67. This comparison shows that the ST model predicts faster stiffness degradation with increasing strain than the HP model at the top of the shear stack ($p'=1\text{kPa}$) and slower stiffness degradation at the bottom of the shear stack. Basically, the stiffness degradation curve in the HP model seems to be pressure independent and fixed in one position. This is not the case of the initial stiffness G_0 , which is shown in Table 3 for both models, and which is always stress dependent. Note that the initial stiffness G_0 is slightly lower for the HP model as explained in the calibration section of this thesis (Section 5 in Chapter 1) in order to result in better overall predictions of the soil behaviour in shear stack modelling.

In addition, one may note that the G/G_0 curve at $p'=1\text{kPa}$ for the ST model lies below the limits specified by Seed & Idris (1970). To the best of author’s knowledge, there is no studies on derived G/G_0 curves at mean stresses as low as $p'=1\text{kPa}$. Therefore, it is difficult to say whether the ST model possibly overpredicts the stiffness degradation at very low mean effective stresses.

Most importantly, the above findings could explain the differences in the predictions of both of the models shown in Section 3 of this chapter, such as, for

instance: higher lateral displacements at the mid-height of the shear stack shown by the HP model or the maximum pile axial strains of different magnitudes and at different depths predicted sometimes by both models.

The conclusion of this section is that the HP model in the current form is not able to predict stiffness degradation curves due to soil pressure dependency for large range of mean stresses with a single calibration. Possibly modifying the model formulation in such a way that the parameter χ , which controls the rate of the stiffness degradation, changes with changing mean effective pressure could be a simple way to improve the model predictions. A promising attempt to such modification is shown on Figure 68 where the hypoplastic umat has been updated in a way to allow linear variation of the parameter χ on mean effective stresses. Here the parameter χ differs from 0.4 (at $p' = 0$ kPa at the top of a shear stack) to 0.6 (at $p' = 10$ kPa at the bottom of a shear stack). One may observe an obvious improvement in the model predictions (although the implemented linear variation may not be the most suitable), i.e. the G/G_0 curves do not overlap with each other, but lower mean effective stresses result in faster stiffness degradation than higher mean effective stresses.

Table 3 Pressure dependence of initial stiffness G_0 for two constitutive models

	G_0 for ST model [MPa]	G_0 for HP model [MPa]
$p' = 1$ kPa	7.8	5.6
$p' = 5$ kPa	18.2	14.3
$p' = 10$ kPa	26.1	21.3
$p' = 400$ kPa	169.3	179.0

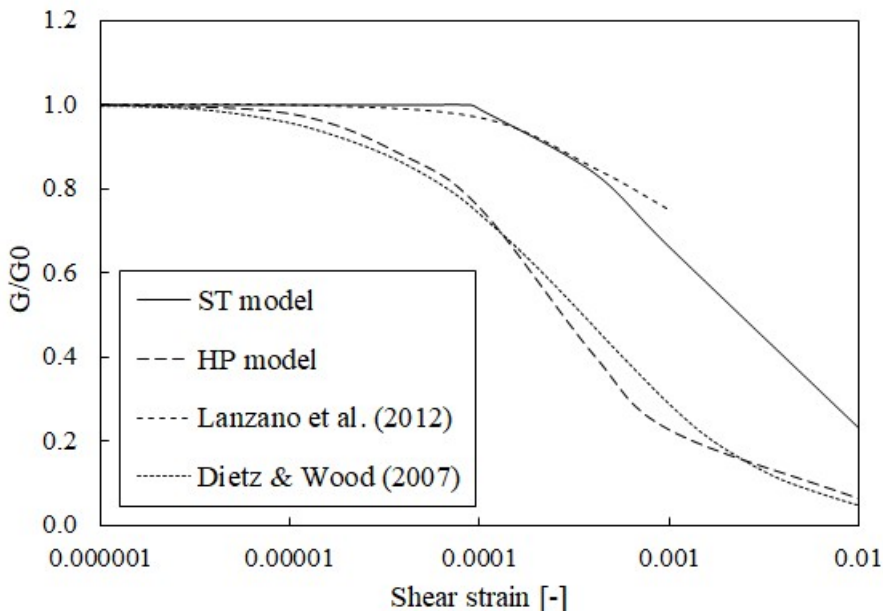


Fig. 66. Stiffness degradation curves at $p'=400\text{kPa}$ ($K_0=0.5$) computed by ST and HP model and compared with experiments (Lanzano et al., 2016).

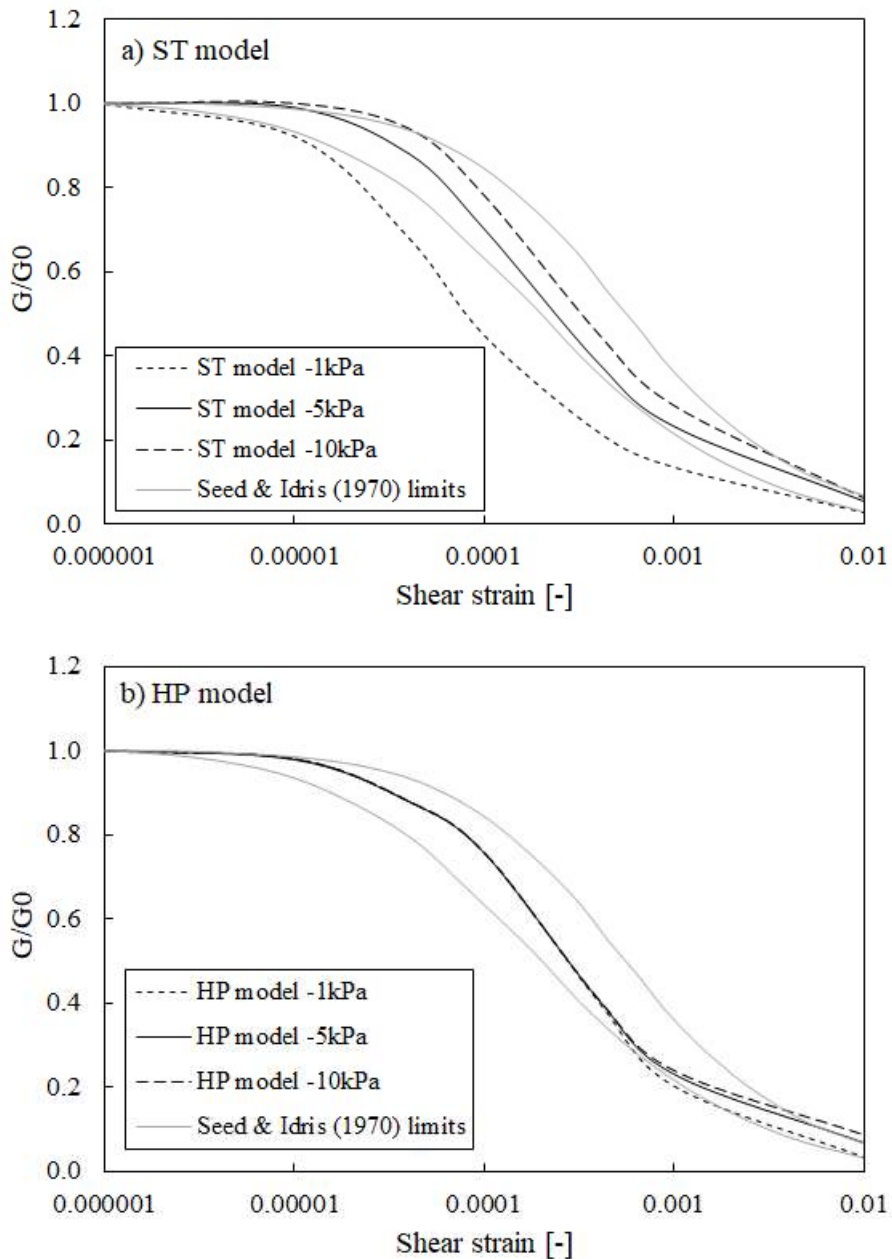


Fig. 67. Stiffness degradation computed by ST model (a) and HP model (b) at three different levels of mean effective stresses in shear stack 1kPa, 5kPa and 10kPa.

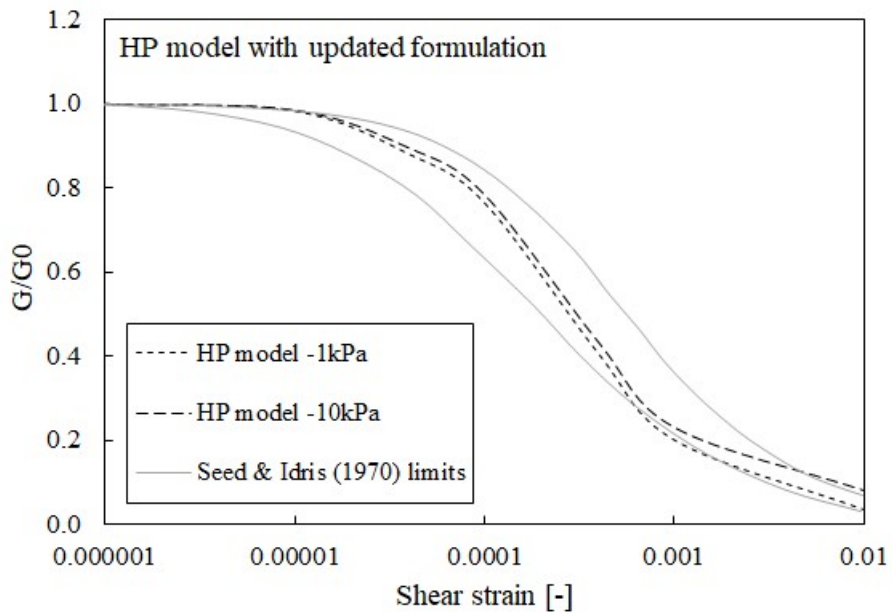


Fig. 68. Stiffness degradation at two different levels of mean effective stresses in shear stack 1kPa and 10kPa computed by HP model with updated formulation.

4.7. Occasional problems with ST model

This subsection illustrates some problems observed in the calculations performed by means of the ST model. Although they are minor, their occurrence is rare, these are presented here for completeness. In addition, the problems presented here could potentially occur more often in future numerical studies, for instance due to different calibration or different application of the model.

Figure 69 shows stress strain behaviour in around the top of soil surface for 10Hz 0.137g input motion. This input motion results in the “wobble” presence at the top of the soil column as shown in Chapter 2 due to elastic part of a wave separating from the plastic part. As a result of the “wobble”, very small strain unloading-reloading loops show in stress-strain behaviour. The problem observed in Figure 69 is related to overshooting (noted also in other constitutive models, e.g. Cudny & Truty, 2020). Too stiff response in the reloading part of the stress-strain curve is observed. Such reloading would rather be expected to follow the curvature of the preceding loading curve after only initially stiffer response. This model prediction is a result of the dependence of the small strain stiffness on the model parameter α rather than the parameter B . Thus, a solution to that could be a modification in the equation (11) in Chapter 1 in order to reduce the range of strains where the parameter α dictates the stiffness definition.

Note that the section *Occasional problems with ST model* is shorter than the equivalent section for the HP model. This is due to the fact that some problems with the ST model have been fixed during the course of this work or “covered” in the numerical “tricks” of increasing the yield surface of the top layer to a size of 0.02 and introducing a very small amount of cohesion of 1Pa. The problems encountered during the course of the project included, for instance, just to mention few: the elastic predictor “jumping” significantly outside the yield surface, a need to increase the number of substepping, problems with the load increments tangential to the yield surface or updating the initial stress state on load reversals. The origin of these problems was primarily associated with very low mean effective stresses in shear stack environment. The improvements in the model formulation are not detailed here as have not been made by the author of the thesis but the author of the umat (Gajo, 2017).

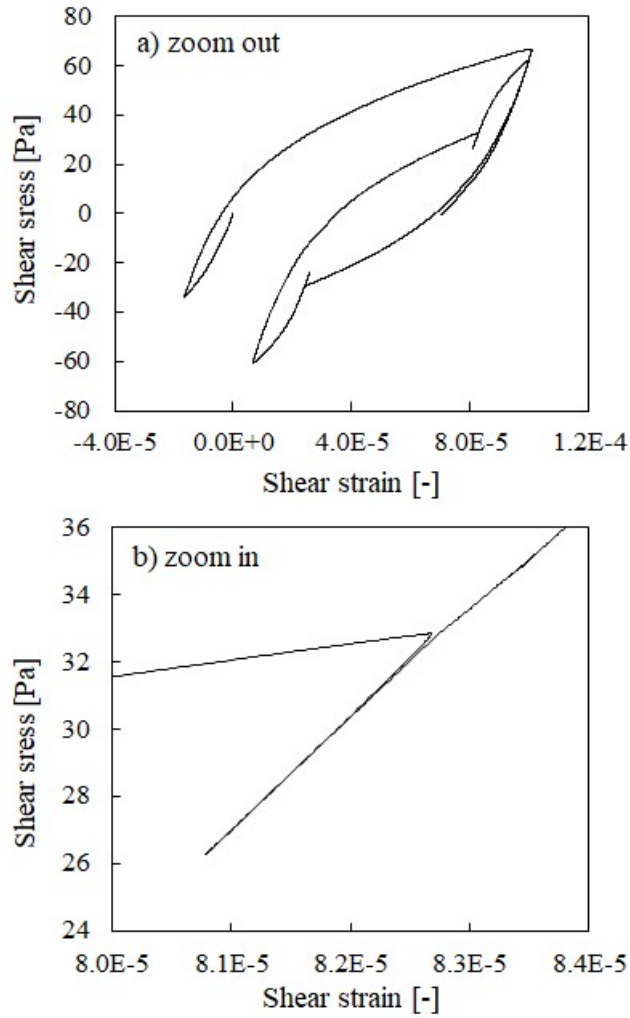


Fig. 69. Stress strain behaviour of ST model in upper layers of soil column in: a) zoom out, b) zoom in.

4.8. Occasional problems with HP model

This subsection presents some minor problems encountered when using the HP model. Similarly to the subsection 4.7, the indicated problems are either of rare occurrence or are deemed to affect the calculations presented in this thesis in a minor manner.

The first problem encountered with the HP model occurred during the calibration process. Initially, a calibration as per Toyoura sand (Herle & Gudehus, 1999) was considered due to similarities between this sand and Leighton Buzzard sand. The cyclic simple shear tests (Figure 70) performed with this calibration gave very accurate predictions of the experimental results (Shahnazari & Towhata, 2002), both, in terms of stress strain and volumetric response (see experimental results in Chapter 1, Section 6, Figure 15). Generally, the shear stiffness increases with cycles and is accompanied by a reduction in volume. Subsequently, another cyclic simple shear test was performed, this time within a much smaller strain range but applicable to seismic conditions, i.e. 0.1%. This time, although exactly the same calibration was used, strange behaviour was observed. In detail, shear stiffness reduction observed with loading cycles was accompanied by contraction of the sample which is not realistic. Note that Figures 70 and 71 show results when using *umat* without the updated intergranular strain concept by Wegener (2013) and Wegener & Herle (2014). However, the problem persists if this improvement is implemented.

A similar problem occurs in the calibration used in this thesis. Although the response in the cyclic simple shear tests subjected to large strain cycles seems reasonable, i.e. dilation is accompanied by a slight decrease of stiffness (Figure 17, Chapter 1) and compression by a slight increase of stiffness (Figure 20, Chapter 1), a reduction in the strain level to 0.1% would result in the opposite nonphysical response. Nevertheless, the volumetric changes in seismic motions analysed in this thesis have been shown to be minute (e.g. Sections 4.2 and 4.4 of this chapter) and practically not affecting the soil stiffness in consecutive loading cycles. Most importantly, this effect (of almost constant stiffnesses during the subsequent loading cycles) has been captured correctly by the HP model even if the volumetric predictions experienced some minor inconsistencies.

As mentioned in the previous section of this thesis, the formulation of the ST model has been updated in the course of the project. The same has not been the case for the HP model, which results in slightly longer section than the equivalent section 4.7 for the ST model.

Finally, some additional final studies by the author revealed that the problem presented in this section may not be limited to the HP model only. In detail, the author found that the ST model and the DM model with their original calibrations also experience similar contradictory behaviour. It could be also noticed that the horizontal stresses change significantly in such test and affect the mean effective pressure which

later seem to rule in this problem. Possibly including some constitutive features accounting for anisotropy evolution would improve predictions.

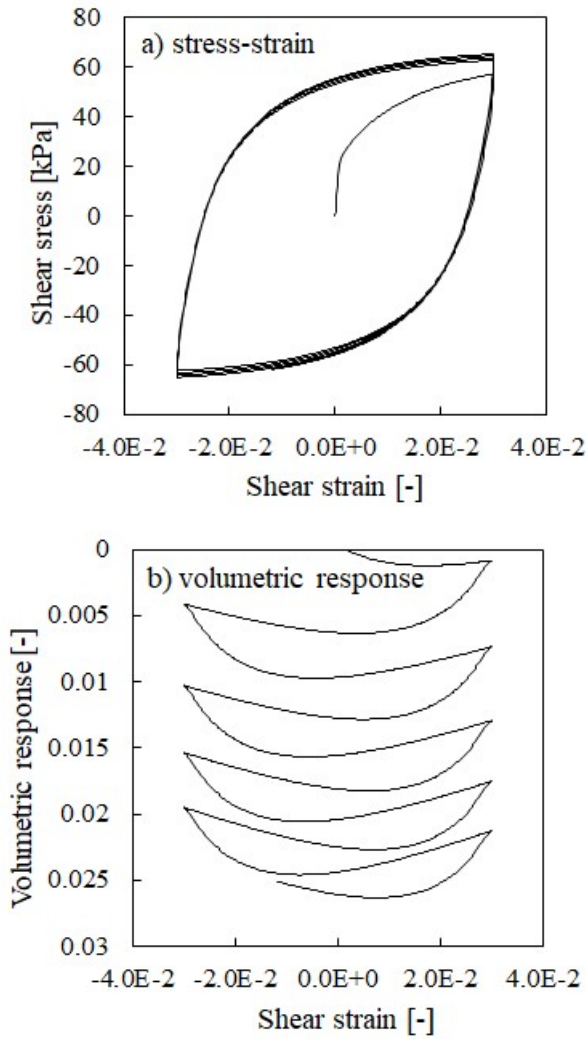


Fig. 70. Cyclic simple shear test simulated with HP model calibrated as per Toyoura sand (to be compared with experimental results on Figure 15 in Chapter 1).

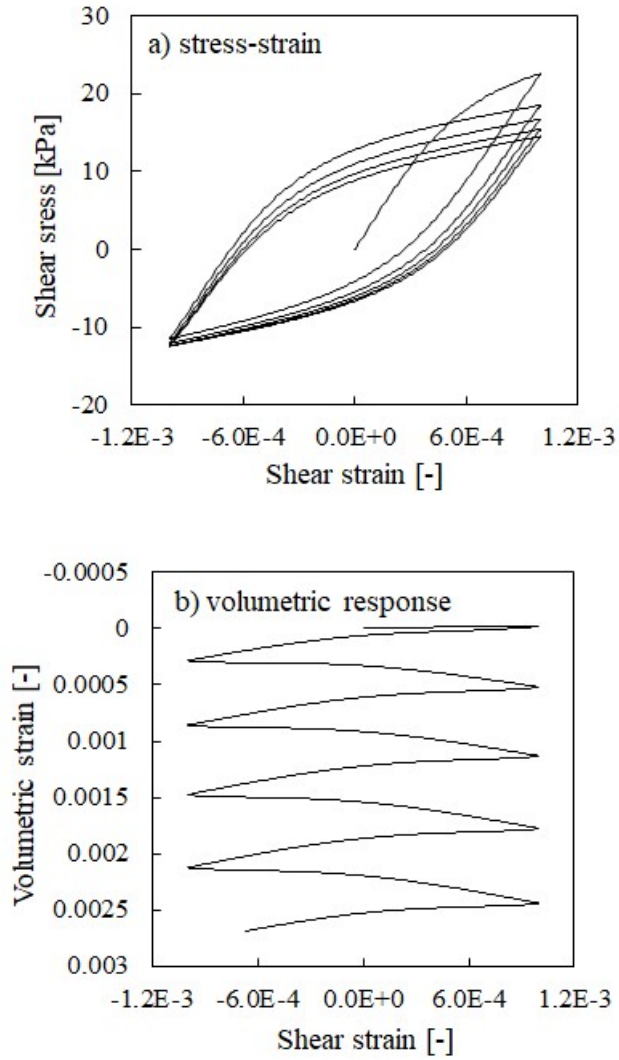


Fig. 71. Cyclic simple shear test simulated with HP model calibrated as per Toyoura sand within small strain range.

4.9. Effect of addition of viscous damping on higher frequency motion

The numerical studies often “suffer” from high frequency oscillations being particularly visible in the computed accelerations. Typical remedies to reduce the amount of oscillations is to filter the results, as has been done in Chapter 2, or to use viscous (Rayleigh) damping. The use of the latter for the predictions of the ST model is discussed in this section of Chapter 3 of this thesis.

Numerous numerical studies have reported using viscous damping in different amounts for various advanced soil constitutive models. For instance, Gajo & Wood (1997) used 20% Rayleigh damping for Mohr Coulomb and Pastor-Zienkiewicz (Pastor et al., 1990) models, Abate et al. (2010) up to 25%, Bilotta et al. (2014) pointed out two teams within the numerical round robin competition that used Rayleigh damping between 4-6%. Ramirez et al. (2018) reported that three predicting teams used Rayleigh damping of 2.24-3%. Ghofrani & Arduino (2018) limited the use of Rayleigh damping to 0.5% only when using the DM model for a saturated soil slope. On the other hand, Pisano & Jeremic (2014) proposed a visco-elastic-plastic constitutive law to account for small strain damping with two dissipative sources, i.e. hysteretic or viscous, both included in the model formulation. The justification of the use of Rayleigh damping is explained by some studies as a need to account for damping at very small strain levels (e.g. Reyes et al., 2009, Bilotta et al., 2014). This subsequently allows to damp out very high frequencies.

In this subsection of the thesis, Rayleigh damping is shown to be able to remove a part of the higher frequencies due to fast elastic unloading waves. Only the ST model has been used in this section. The chosen input motion is 10Hz 0.137g. The results in this section are not filtered as in the previous section (as such can be compared with those in Chapter 2, Section 3.3). Only the effect of the viscous damping is studied. Note that very initial studies focused also on the effect of numerical damping and it was concluded that it was unsuccessful in removing the observed oscillations. In addition, the initial studies showed that damping on a mass matrix is inefficient. Therefore, the viscous damping in this thesis has been implemented only on stiffness matrix by Gajo (2017). The introduced damping was aimed at the driving frequency of 10Hz and applied in the amounts of 2%, 5% and 10%.

Figure 72 shows the acceleration time history at the top of the soil column as computed with different amounts of Rayleigh damping. Note that the analysed 2D soil column assumes only a single soil layer (i.e. Leighton Buzzard, fraction E) in order to avoid any generation of spurious frequencies due to interface on two soil layers. It can be observed (Figure 72a and 72b) that the accelerations become smoother and smoother with the increased amount of stiffness proportional damping. In addition, one can observe that the generally distorted shape of the perfect sine input wave is maintained for all the results. Importantly, it can be noticed that the increasing amount of Rayleigh damping starts to remove higher frequencies due to fast elastic waves,

which as shown in Chapter 2 might be physical. On the other hand, Rayleigh damping removes also very high frequency due to strain discontinuity appearing for longer propagation lengths (more obvious for the 25Hz input motion and not for the 10Hz input motion analysed in this section as explained in Section 3.3 of Chapter 2). Thus, the amount of Rayleigh damping applied to the soil mass should be a subject of a careful assessment. For completeness, Figures 72c and 72d show spectral analysis for different amounts of Rayleigh damping.

It is also interesting to see the effect of Rayleigh damping applied on soil and its effect on an elastic pile. It can clearly be noticed (Figure 73) that the amount of higher frequency of motion on piles reduces when Rayleigh damping is applied on soil.

To sum up, Rayleigh damping helps removing very high frequency records due to strain discontinuity due to fast elastic unloading waves. However, its amount needs to be chosen carefully, in order to represent other physical soil behaviours (i.e. the effect of elastic part separation). It would be interesting in the future to decide on the optimum amount of Rayleigh damping, in order to represent soil behaviour in a more realistic way and remove spurious numerical oscillations but maintain all the physical oscillations.

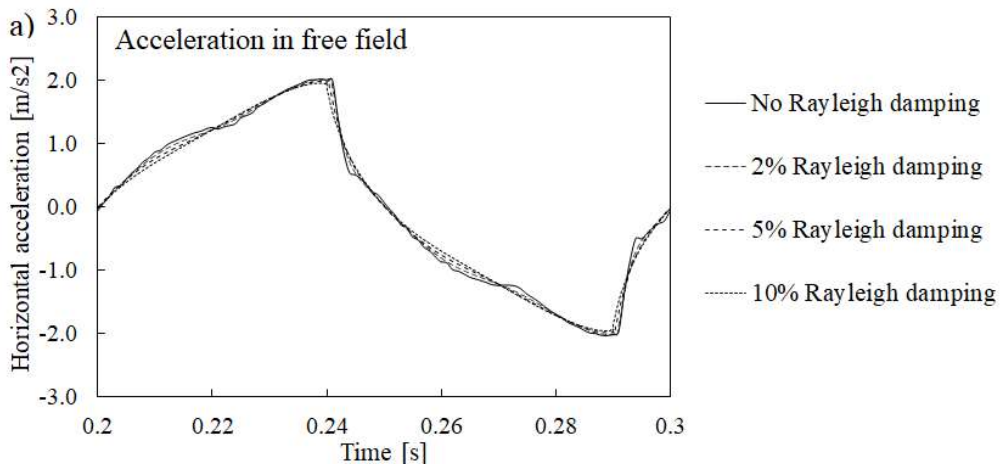


Fig. 72. (continuation on the next page)

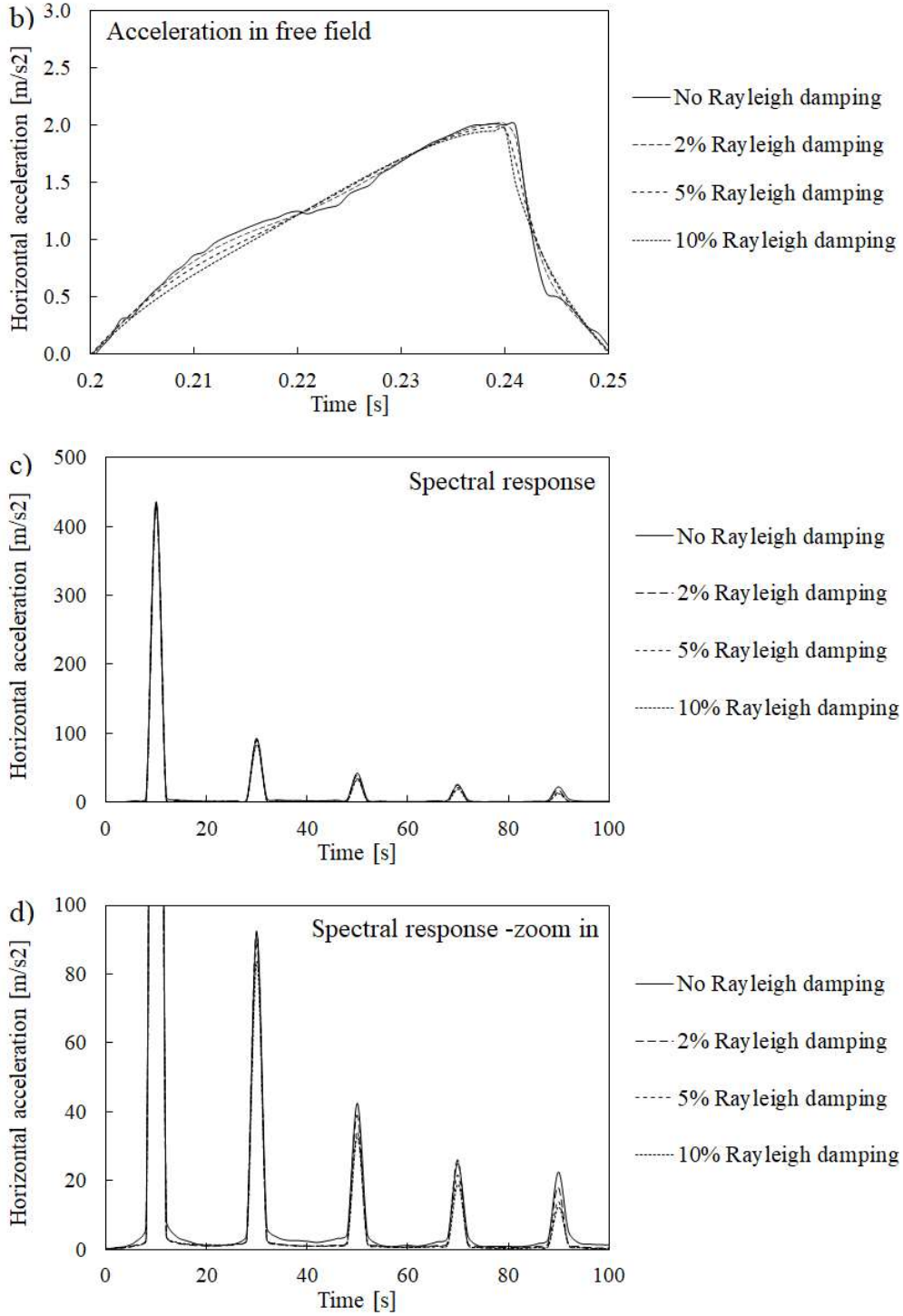


Fig. 72. Free field acceleration records with different amount of viscous damping at top of soil column (a), zoom in (b), spectral response (c), spectral response in zoom (d).

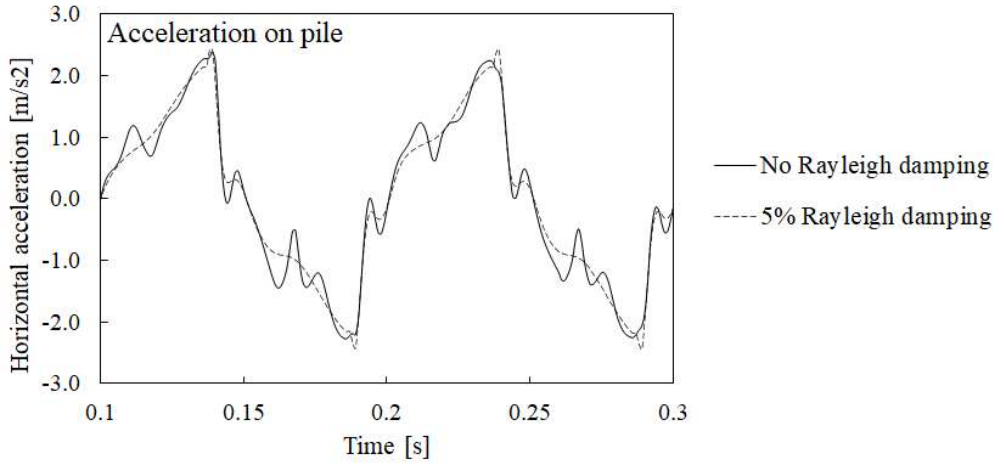


Fig. 73. Pile head acceleration records with and without viscous damping applied on soil mass.

4.10. Minimum corrections to constitutive features and their optimal complexity to simulate dynamic soil behaviour and seismic soil-structure interaction

The previous sections, in particular Section 4.2, showed that soil behaviour in shear stack tests under seismic loading is dominated by plastic deformation. As a result of that, the common attempts of using the linear elastic stiffness representation for soil behaviour in some numerical studies in the past can be considered as a crude assumption. The constitutive laws allowing irreversible deformation would be more suitable. The plastic deformation, although dominant, results in relatively small permanent volumetric changes, thus the soil stiffness characteristics and fabric do not change significantly during shaking, at least for the input motions of the maximum amplitude not exceeding 0.15g, such as studied in this thesis.

Based on the elastoplasticity formulation, the following consideration on the minimum potential corrections to the constitutive ingredients could be suggested for such models as the ST model in order to improve simulations in seismic analyses:

- Since plastic behaviour dominates, the elastic stiffness is of less importance, hypoelastic law would be believed to be sufficient, especially if free field response is in question. Importantly, this conclusion is based on studies on dry soil. It is expected that the elastic law would be much more important in case of saturated soil.
- Hyperbolic relationship for plastic stiffness degradation with strain should include a smoothening feature, such as the parameter α in the current formulation of the ST model. On the other hand, the current formulation of the α parameter is aimed at large strain behaviour, thus it is parameter α that dominates the stiffness reduction in small strain region which causes some problems as shown in Section 4.7 of this chapter. Therefore, it would be interesting to formulate the stiffness degradation in a way to depend more on the parameter B and less on the parameter α , also in the small strain region. This would help avoiding situations such as shown on Figure 68.
- A more refined flow rule to account better for volumetric changes in small strain region, i.e. optimising the rate of the initial compression for dense sands in case of the ST model, could improve the settlement predictions.

- The permanent volumetric changes shown experimentally and typical low number of loading cycles in seismic conditions lead to the conclusion that additional features (such as memory surface) to limit ratcheting are not expected to yield significant improvement, if no high number of loading cycles occur. This assumption would be valid for seismic applications. However, the constitutive models still could aim at capturing the ratcheting phenomena better if used in other applications (e.g. offshore geotechnics).
- Addition of a relatively small amount of Rayleigh damping can be considered as a remedy to remove numerical very high frequency oscillations before finite elements codes implement formulations dealing with shock formation. Note that an excessive amount of Rayleigh damping may remove higher frequencies generated in soil, thus, its amount should be a subject of a careful assessment.

The proposed set of corrections to constitutive ingredients needed to simulate accurately (and with limited complexity) seismic soil and soil-structure interaction is based on the experimental work carried out in dry sand. It is recognized that similar studies in saturated sand could introduce some modifications to the proposed considerations, especially regarding importance of elastic stiffness.

Similarly, if looking at soil in the vicinity of a pile with a structure, potentially more sophisticated elastic law accounting for fabric changes and anisotropy evolution may be needed, e.g. hyperelastic law in Gajo (2010).

Note that, the validation shown in this chapter deals with cases of shear wave propagation only. Chapter 2 of this thesis has shown that the ST and HP models are not capable of reproducing correctly vertical acceleration records for P-wave propagation. Therefore, the proposed above improvements of constitutive features, would need to be furtherly enhanced in order to improve capabilities of simulating more realistic cases where S-waves are simultaneously accompanied by P-waves. This could possibly be achieved by introducing a cap in the yield surface formulation within the elastoplasticity framework (e.g. such as Taiebat & Dafalias, 2008). Further studies would be needed to confirm that such cap in the yield surface formulation would be sufficient for improving simulations of P-waves.

4.11. Computational time

Computational times are provided in Table 4. The complexity of the numerical models includes: 1884 quadratic soil elements, 800 shell elements to represent piles which are in surface to surface contact with soil. The values in Table 1 are for using 64 CPUs. To recall, the chosen time increments are $2 \cdot 10^{-5}$ for the ST model, and $1 \cdot 10^{-4}$ for the HP model.

The computational times for the HP model are much shorter. This is related to many aspects, including chosen time increments, adopted integration schemes (implicit in the ST model, explicit in the HP model), probably not optimized substepping in the ST model or finally, and most importantly, general complexity of the elastoplastic models (i.e. consistency condition and stress corrections).

Table 4. Computational times in hours for different input motions for two models

Item	Type of input motion	Pile head conditions	Maximum acceleration	Duration of input motion	Time for ST [h]	Time for HP [h]
1	Sine 10Hz	FHP	0.137g	0.7s	82	12
2	Sine 25Hz	FHP	0.077g	0.42s	35	6
3	Sine 30Hz	FHP	0.041g	0.4s	46	6
4	Tolmezzo scaled earthquake	FHP	0.101g	0.8s	87	10
5	Sine 25Hz	SCAP	0.037	0.42s	47	8
6	Sine 10Hz	FHP+SDOF	0.155g	0.7s	102	25
7	Sine 25Hz	SCAP+SDOF	0.092g	0.42s	55	11

4.12. Additional comments

The validation of the constitutive models in this chapter has been carried out in low pressure environment experienced in a small-scale 1g experiment. Therefore, it is valid for the extrapolation of the constitutive models from the usual field pressure to low pressure environment. On the other hand, both the ST model and the HP models are typically considered to be capable of dealing with pressure dependency (but see Section 4.6) in this chapter. Especially for elastoplastic models, but probably also for hypoplastic models (see Wegener, 2013; addition of numerical cohesion of 5kPa at low pressures), validation in low mean stresses can be considered to be more demanding. Therefore, similar findings as shown in this chapter would be expected under higher mean stresses applicable to field conditions.

It is recalled here that the constitutive models have been calibrated for small strain behaviour where they performed reasonably well as shown in Chapters 2 and 3. The chosen calibrations show also qualitatively good performance in large strains (Chapter 1). On the other hand, it still seems challenging to calibrate the models in a way to cover quantitatively simulations in small and large strain ranges together. Similar conclusions were drawn by Ramirez et al. (2018) who pointed out that the calibrations for the DM model from small element tests (large strains) and from centrifuge (small strains) were different. Therefore, currently it would probably be troublesome to analyse realistically a time history including small and large soil deformation within a single numerical model with a single calibration of model parameters.

Finally, it is of the author's opinion that the development and improvements of advanced soil constitutive models should come in line with parallel improvements in repeatability of experimental setups. It was shown in the past (e.g. Kutter et al., 2019) how the measured response of theoretically the same experimental setup can vary from one experimental laboratory to the other one and how difficult it is to numerically simulate theoretically the same experimental setup from various experimental research centres with only a single set of model parameters (Ghofrani & Arduino, 2018). The experimental results obtained in the two phases of the shear stack tests and discussed in this thesis, although reasonably consistent in terms of free field response, did also produce some discrepancy for pile measurements. Therefore, care is needed when drawing conclusions based on comparisons with such experiments, in particular, when trying to refine the validation to details as these details may have not been well captured in the experimental studies. Note that the work presented in Chapter 3 is believed to be an attempt of such careful validation bearing in mind the limitations of experimental work.

5. Conclusions

This chapter has shown that the two constitutive models, namely the ST model and the HP model, are capable of simulating seismic soil behaviour and seismic soil-structure interaction at least qualitatively, and in most cases with satisfactory accuracy. The comparison with the experimental data included free field response, kinematic and inertial soil-structure interaction under various input motions and pile head conditions. A link between Chapter 2 and Chapter 3 has been shown by highlighting the impact of the generated harmonics (due to fast elastic unloading waves) on the response of the top of the pile and the structure.

Free field response has been generally well captured, whereas some discrepancies have been encountered, mainly when predicting settlements and sporadically, when analysing structural response. The former could be improved by recalibrating parameters of the models (although outside the typical range of values) for global settlement predictions but not for compressive and dilative phases within a single loading cycle. The latter was suggested to be potentially the result of: the lack of a constitutive feature dealing with fabric effects in the employed constitutive models, the inconsistent experimental measurements regarding structural aspects or to the lower extent, the lack of laboratory data for Leighton Buzzard sand (fraction B+E) for a more refined calibration of the constitutive models.

Nonetheless the doubts on the model calibrations, model formulations and experimental repeatability, some inconsistencies have been found in the model predictions (believed not to be related to the above uncertainties) and highlighted in detail. The most important aspects of numerical and constitutive modelling have been discussed and followed by recommendations on how to possibly improve the predictions of the constitutive models under seismic loading conditions in the future.

Future work, if more repetitive experimental data on soil-structure interaction is available, should focus on soil fabric changes in the proximity of a structure. Further improvements of the formulation of the models could, therefore, include accounting for changes in fabric and related aspects of anisotropy and its development due to past loading history.

References

- Abate, G., Massimino, M. R., Maugeri, M., Muir Wood, D. (2010). Numerical modelling of a shaking table test for soil-foundation-superstructure interaction by means of a soil constitutive model implemented in a FEM code. *Geotechnical and Geological Engineering* 28(1): 37-59
- Benz, T. (2007). Small-strain stiffness of soils and its numerical consequences. *PhD Thesis*. Universitat Stuttgart (Germany).
- Bilotta, E., Lanzano, G., Madabushi, S.P.G., Silvestri, F. (2014). A numerical Round Robin on tunnels under seismic actions. *Acta Geotechnica* 9:563-579.
- Boulanger, R., Ziotopoulou, K. (2015). PM4Sand Version 3: A sand plasticity model for earthquake engineering applications. *Technical Report*.
- Cairo, R., Chidichimo, A., Dente, G., Simonelli, A. L., Di Sarno, L., Sica, S., Durante, M.G. (2011). TA4 SERIES Piles -Results -Phase II. *Report*.
- Chidichimo, A., Cairo, R., Dente, G., Taylor, C. A., Mylonakis, G. (2014). 1-g experimental investigation of bi-layer soil response and kinematic pile bending. *Soil Dynamics and Earthquake Engineering* 67, 219-232.
- Conti, R., Madabhushi, G. S. P., Viggiani, G. M. B. (2012). On the behaviour of flexible retaining walls under seismic actions. *Géotechnique* 62(12), 1081-1094.
- Crewe, A., J., Lings, M., L., Taylor, C., A., Yeung, A., K., Andrighetto, R. (1995). Development of a large flexible shear stack for testing dry sand and simple direct foundations on a shaking table. *European seismic design practice, Elnashai (ed), Balkema, Rotterdam*.
- Cudny, M., Truty, A. (2020). Refinement of the hardening soil model within the small strain range. *Acta Geotechnica* 15, 2031-2051.
- Dafalias, Y., F., Manzari, M. T. (2004). A simple plasticity sand model accounting for fabric change effects. *Journal of Engineering Mechanics* 130(6), 622-634.
- Dafalias, Y., F., Papadimitriou, A. G., Li, X. S. (2004). Sand plasticity model accounting for inherent fabric anisotropy. *Journal of Engineering Mechanics* 130(11): 1319-1333.
- Dafalias, Y., F., Taiebat, M. (2016). SANISAND-Z: zero elastic range sand plasticity. *Geotechnique*, 66(12), 999-1013.
- Dar, A. R. (1993). Development of a flexible shear-stack for shaking table testing of geotechnical problems. *PhD Thesis*. University of Bristol.

Dietz, M., Muir Wood, D. (2007). Shaking table evaluation of dynamic soil properties. *In proceedings of: 4th International Conference of Earthquake Geotechnical Engineering*, June 25-28, Thessaloniki, Greece.

Durante, M. G. (2015). Experimental and numerical assessment of dynamic soil-pile-structure interaction. *PhD Thesis*. Università degli Studi di Napoli Federico II (Italy).

Durante, M. G., Di Sarno, L., Mylonakis, G., Taylor, C. A., Simonelli, A. L. (2016). Soil-pile-structure interaction: experimental outcomes from shaking table tests. *Earthquake Engineering and Structural Dynamics*, 45(7), 1041-1061.

Durante, M. G. (2019). *Personal communication*.

Gajo, A., Muir Wood, D. (1997). Numerical analyses of behaviour of shear stacks under dynamic loading. *Report on work performed under the EC project European Consortium of Earthquake Shaking Tables (ECOEST): Seismic bearing capacity of shallow foundations*.

Gajo, A., Muir Wood, D. (1999a). Severn-Trent sand: a kinematic hardening constitutive model for sands: the q-p formulation. *Géotechnique* 49(5), 595-614.

Gajo, A., Muir Wood, D. (1999b). A kinematic hardening constitutive model for sands: the multiaxial formulation. *International Journal for Numerical and Analytical Methods in Geomechanics* 23(9), 925-965.

Gajo, A., Bigoni, D., Muir Wood, D. (2000). Stress induced elastic anisotropy and strain localisation in sand. In H Muhlhaus *Localisation and bifurcation theory for soils and rocks*.

Gajo, A. (2010). Hyperelastic modelling of small-strain anisotropy of cyclically loaded sand. *International Journal for Numerical and Analytical Methods in Geomechanics* 34(2), 111-134.

Gajo, A. (2017). Fortran subroutine in a format of user defined material (UMAT) of implementation of the Severn-Trent sand model.

Ghofrani, A., Arduino, P. (2018). Prediction of LEAP centrifuge test results using a pressure-dependent bounding surface constitutive model. *Soil Dynamics and Earthquake Engineering* 113, 758-770.

Gudehus, G. (1996). A comprehensive constitutive equation for granular materials. *Soils and Foundations* 36(1), 1-12.

Hall, J. F., Beck, J. L (1986). Structural damage in Mexico City. *Geophysical Research Letters*, 13(6), 589-592.

- Herle, I., Gudehus, G. (1999). Determination of parameters of a hypoplastic constitutive model from properties of grain assemblies. *Mechanics of Cohesive and Frictional Materials* 4, 461-486.
- Hleibieh, J., Wegener, D., Herle, I. (2014). Numerical simulations of a tunnel surrounded by sand under earthquake using a hypoplastic model. *Acta Geotechnica* 9, 631-640.
- Hleibieh, J., Herle, I. (2019). The performance of a hypoplastic constitutive model in predictions of centrifuge experiments under earthquake conditions. *Soil Dynamics and Earthquake Engineering*, 122, 310-317.
- Kolymbas, D. (1991). Computer-aided design of constitutive laws. *International Journal of Numerical and Analytical Methods in Geomechanics* 15, 593-604.
- Kutter, B. L., Carey, T. J., Hashimoto, T., Zeghal, M., Abdoun, T., Kokkali, P., Madabhushi, G., Haigh, S. K., Burali d'Arezzo, F., Madabhushi, S., Hung, W.-Y., Lee, C.-J., Cheng, H.-C., Iai, S., Tobita, T., Ashino, T., Ren, J., Zhou, Y.-G., Chen, Y.-M., Sun, Z.-B., Manzari, M. T. (2018). LEAP-GWU-2015 experiment specifications, results and comparisons. *Soil Dynamics and Earthquake Engineering* 113, 616-628.
- Kutter, B. L., Carey, T. J., Stone, N., Li Zheng, B., Gavras, A., Manzari, M. T., Zeghal, M., Abdoun, T., Korre, E., Escoffier, S., Haigh, S. K., Madabushi, G. S. P., Madabushi, S. S. C., Hung, W.-Y., Liao, T.-W., Kim, D.-S., Kim, S.-N., Ha, J.-G., Kim, N. R., Okamura, M., Sjafruddin, A., N., Tobita, T., Ueda, K., Vargas, R., Zhou, Y.-G., Liu, K. (2019). LEAP-UCD-2017 Comparison of Centrifuge Test Results. In: B. Kutter et al. (Eds.), *Model tests and numerical simulations of liquefaction and lateral spreading: LEAP-UCD-2017*. New York: Springer.
- Kuwano, R., Jardine, R.J. (2002). On the applicability of cross-anisotropic elasticity to granular materials at very small strains. *Géotechnique* 52:727-749.
- Lanzano, G., Bilotta, E., Russo, G., Silvestri, F., Madabushi, S. P. G. (2012). Centrifuge modelling of seismic loading on tunnels in sand. *Geotechnical Testing Journal* 35(6), 854-869.
- Li, X. S., Dafalias, Y. F. (2002) Anisotropic Critical State Theory: Role of Fabric. *Journal of Engineering Mechanics* 138(3), 263-275.
- Loli, M., Apostolou, M., Gazetas, G., Gerolymos, N., Anastasopoulos, I. (2010). Soil failure can be used for seismic protection of structures. *Bulletin of Earthquake Engineering* 8: 309-326.
- Manzari, M. T., Dafalias, Y. F. (1997). A critical state two-surface plasticity model for sands. *Géotechnique* 47(2), 255-272.

Manzari, M. T., El Ghoraiby, M., Zeghal, M., Kutter, B. L., Arduino, P., Barrero, A. R., Bilotta, E., Chen, L., Chen, R., Chiaradonna, A., Elgamal, A., Fasano, G., Fukutake, K., Fuentes, W., Ghofrani, A., Haigh, S. K., Hung, W.-Y., Ichii, K., Kim, D. S., Kiriya, T., Lascarro, C., Madabushi, G. S. P., Mercado, V., Montgomery, J., Okamura, M., Ozutsumi, O., Qiu, Z., Taiebat, M., Tobita, T., Travasarou, T., Tsiaousi, D., Ueda, K., Ugalde, J., Wada, T., Wang, R., Yang, M., Zhang, J.-M., Zhou, Y.-G., Ziotopoulou, K. (2019). LEAP-2017: Comparison of the Type-B Numerical Simulations with Centrifuge Test Results. *In: B. Kutter et al. (Eds.), Model tests and numerical simulations of liquefaction and lateral spreading: LEAP-UCD-2017. New York: Springer.*

Mašín, D. (2018). Modelling of soil behaviour with hypoplasticity. Another approach to soil constitutive modelling. *Springer.*

Moccia, F. (2009). Seismic soil pile interaction: experimental evidence. *PhD Thesis. Universita degli Studi di Napoli Federico II (Italy).*

Mohammadi-Haji, B., Ardakani, A. (2018). Numerical prediction of circular tunnel seismic behaviour using hypoplastic soil constitutive model. *International Journal of Geotechnical Engineering* DOI:10.1080/19386362.2018.1438152

Muir Wood, D., Crewe, A., Taylor, C. (2002). Shaking table testing of geotechnical models. *IJPMG-International Journal of Physical Modelling in Geotechnics* 1:01-13.

Mylonakis, G., Gazetas, G. (2000). Seismic soil-structure interaction: beneficial or detrimental? *Journal of Earthquake Engineering*, 4(3), 277-301.

Niemunis, A. (2003). Extended hypoplastic models for soils. *Dissertation.*

Niemunis, A., Herle, I. (1997). Hypoplastic model for cohesionless soils with elastic strain range. *Mechanics of Cohesive-Frictional Materials* 2, 279-299.

Ochmanski, M., Delli Carpini, M., Salvatore, E., Modoni, G., Bilotta, E. (2019). Numerical simulation of centrifuge seismic tests on tunnel in sandy soil. *In proceedings of the 7th International Conference of Earthquake Geotechnical Engineering*, 17-20 June, Rome, Italy.

Pastor, M., Zienkiewicz, O.C., Chan, A.H.C. (1990). Generalized plasticity and the modelling of soil behaviour. *International Journal of Numerical Methods in Geomechanics* 14, 151-190.

Pisano, F., Jeremic, B. (2014). Simulating stiffness degradation and damping in soils via a simple visco-elastic-plastic model. *Soil Dynamics and Earthquake Engineering* 63, 98-109.

- Pitilakis, D., Dietz, M., Muir Wood, D., Clouteau, D., Modaressi, A. (2008). Numerical simulation of dynamic soil-structure interaction in shaking table testing. *Soil Dynamics and Earthquake Engineering* 28, 453-467.
- Ramirez, J., Barrero, A. R., Chen, L., Dashti, S., Ghofrani, A., Taiebat, M., Arduino, P. (2018). Site response in a layered liquefiable deposit: evaluation of different numerical tools and methodologies with centrifuge experimental results. *Journal of Geotechnical and Geoenvironmental Engineering* 144(10) 04018073.
- Régnier, J., Bonilla, L.-F., Bard, P.-Y., Bertrand, E., Hollender, F., Kawase, H., Sicilia, D., Arduino, P., Amorosi, A., Asimaki, D., Boldini, D., Chen, L., Chiaradonna, A., DeMartin, F., Elgamal, A., Falcone, G., Foerster, E., Foti, S., Garini, E., Gazetas, G., Gélis, C., Ghofrani, A., Giannakou, A., Gingery, J., Glinsky, N., Harmon, J., Hashash, Y., Iai, S., Kramer, S., Kontoe, S., Kristek, J., Lanzo, G., di Lernia, A., Lopez-Caballero, F., Marot, M., McAllister, G., Mercerat, E.D., Moczo, P., Montoya-Noguera, S., Musgrove, M., Nieto-Ferro, A., Pagliaroli, A., Passeri, F., Richterova, A., Sajana, S., Santisi d'Avila, M. P., Shi, J., Silvestri, F., Taiebat, M., Tropeano, G., Vandeputte, D., Verrucci, L. (2018) PRENOLIN: International benchmark on 1D nonlinear site-response analysis -validation phase exercise. *Bulletin of the Seismological Society of America* 108(2), 876-900.
- Reyes, D. K., Rodriguez-Marek, A., Lizcano, A. (2009). A hypoplastic model for site response analysis. *Soil Dynamics and Earthquake Engineering* 29, 173-184.
- Simonelli, A. L., Di Sarno, L., Durante, M. G., Sica, S., Bhattacharya, S., Dietz, M., Dihoru, L., Taylor, C. A., Cairo, R., Chichidimo, A., Dente, G., Modaressi, A., Todo Bom, L. A., Kaynia, A. M., Anoyatis, G., Mylonakis, G. (2014). Experimental assessment of seismic pile-soil interaction. Chapter 26. *Seismic evaluation and rehabilitation of structures*.
- Taiebat, M., Dafalias, Y. F. (2008). SANISAND: Simple anisotropic sand plasticity model. *International Journal of Numerical and Analytical Methods in Geomechanics*. 32, 915-948.
- Shahnazari, H., Towhata, I. (2002). Torsion shear tests on cyclic stress-dilatancy relationship of sand. *Soils and Foundations* 42(1), 105-119.
- Shirato, M., Nonomura, Y., Fukui, J., Nakatani, S. (2008). Large-scale shake table experiment and numerical simulation on the nonlinear behaviour of pile-groups subjected to large-scale earthquakes. *Soils and Foundations* 48(3), 375-396.
- Taiebat, M., Dafalias, Y. F. (2008). SANISAND: Simple anisotropic sand plasticity model. *International Journal of Numerical and Analytical Methods in Geomechanics* 32, 915-948.

Tokimatsu, K., Suzuki, H., Sato, M. (2005). Effects of inertial and kinematic interaction on seismic behaviour of pile with embedded foundation. *Soil Dynamics and Earthquake Engineering* 25(7-10), 753-762.

Uesugi, M., Kishida, H. (1986). Influential factors of friction between steel and dry sands. *Soils and Foundations* 26(2), 33-46.

Von Wolffersdorff, P. A. (1996). A hypoplastic relation for granular materials with a predefined limit state surface. *Mechanics of Cohesive and Frictional Materials* 1(3), 251-271.

Wegener, D. (2013). Numerical investigation of permanent displacements due to dynamic loading. *PhD thesis*. TU Dresden (Germany).

Wegener, D., Herle, I. (2014). Prediction of permanent soil deformations due to cyclic shearing with a hypoplastic constitutive model. *Geotechnik* 37(2), 113-122.

CHAPTER 4

Seismic frequency wandering of structures due to changes in soil pore pressure

1. Background

Many researchers have observed changes in modal characteristics of engineering structures due to seismic events. These changes can be permanent, and come mainly from structural damage, or temporary when the system recovers its initial stiffness. The temporary shifts of modal characteristics occurring during seismic events are usually referred to as frequency wandering. The reasons of the seismic-induced frequency wandering are not yet fully recognized.

Clinton et al. (2006) reported changes in natural frequencies observed for the Millikan Library (California). They indicated elongation of the natural periods of the building due to weather conditions (wind, rain, temperature) but also due to seismic events of low or high intensity. For example, an increase in natural frequency was observed directly after the rainfall had started with the potential explanation being associated with a change in soil saturation. Indeed, Todorovska & Al Rjoub (2006a, 2006b, 2009) derived a closed-form solution based on poroelasticity and showed that the increase in saturation can lead to the increase in the natural frequency of the Millikan Library. On the other hand, the permanent drop of the natural frequency presented by Clinton et al. (2006) reached 22% and was mainly associated with structural damage due to strong seismic events. The authors also indicated a temporary drop in the natural frequencies due to high-intensity earthquakes, usually around 20%. There was no clear indication on the recovery time, namely when or how fast, the recovery took place. Temporary changes in frequencies were also observed during low-intensity earthquake. The recovery here was almost instantaneous, i.e. within minutes. The source of a temporary drop was not recognized explicitly but the authors associated it potentially with soil-structure interaction, nonlinearities in the structure, or a combination of both of these effects. They noticed that pore pressure measurements from the site could be useful in better understanding of the observed effects.

Todorovska (2009a) claimed that some reasons of the frequency wanderings could be associated with structural nonlinearities and soil-structure interaction. For the latter, Todorovska (2009b) proposed a model where soil behaviour is enclosed in the

recoverable rocking component of the system. Todorovska (2009a, 2009b) also analysed the Millikan Library and focused on soil-structure interaction as a main source of the frequency wandering. The building is founded on medium dense to dense sands (shear velocity 300m/sec) of 30m depth, embedment is around 6-7m and the ground water level is 11m below ground level. The author splits the observed natural frequencies of the system into two components, a fixed-base component and a rocking component, the first associated with the horizontal shear deformation of the structure, the latter associated with the soil-structure interaction and accounting for the rocking behaviour of the building as a rigid block. The rocking component was amplitude dependent and recoverable. Both frequency components can be obtained from only two horizontal sensors, one at the roof and second at the base. Todorovska (2009a) showed that the recovery of a temporary drop in frequencies due to a rigid body rotation was not instantaneous but completed in a longer time scale. However, no clear indication about the recovery time was given.

Ceravolo et al. (2017) analysed a case of three representative buildings in Italy under consecutive low-intensity seismic events, i.e. aftershocks after the main earthquake. The results showed dependence of the modal parameters, namely natural frequency and a damping ratio, on the shaking level. The reasons of this dependence were not explicitly given by the authors (Ceravolo et al., 2017). However, the time of the seismic swarm of around two months was identified to be too short to allow environmental effects to play a role. Since no structural damage was reported in the three buildings, it was suspected that the frequency wandering came from amplitude-dependant reversible nonlinearities such as soil-structure interaction, nonlinear reversible behaviour of a structure (microcracking, slip in masonry), or the interaction of structural and non-structural elements or the combination of the three. According to the authors, the effects of soil-structure interaction, especially for one of the buildings (HC building) which was placed mostly on rock (actually on 5m of superficial soil overlying deeper sandstone), could be attributed to rocking and sliding. In addition, the authors accounted for soil-structure interaction in a simplified way. A finite element elastic analysis with an updating technique for the soil elastic modulus was carried out, showing the effects of the amplitude dependence of the equivalent elastic moduli of the soil, i.e. the higher the shaking level, the lower the equivalent soil elastic stiffness.

Trifunac et al. (2001a, 2001b) showed a decrease of natural frequency with the amplitude of seismic motion for a seven-story hotel VN7SH in Van Nuys (California). The decrease reached up to 64%, of which a large part was temporary and not associated with structural damage. Therefore, the authors associate this drop in natural frequency with a loss of foundation stiffness due to a gap creation around the foundation, followed by a “healing” process during compaction caused by aftershocks, leading to a return of the natural frequencies with time to the initial values.

Trifunac et al. (2001c) showed temporary frequency wandering of a Hollywood storage building (California) by means of transfer functions during low

and strong seismic events. The changes were explained by the same conceptual model developed by Trifunac et al. (2001a, 2001b), namely through the geometrical nonlinear effects (a gap between the structure and soil) caused by soil-structure interaction.

Muciarelli et al. (2011) used the time-frequency domain analysis to show the change of the natural frequency of a reinforced concrete building (in central Italy) during the aftershocks in the Abruzzo earthquake 2009. Their measurements showed a drop in the natural frequency during the high-amplitude part of the aftershock, with a gradual return to the initial value after the end of the aftershock.

Trifunac et al. (1999) analysed the response of five sites to San Fernando earthquake sequence, i.e. the main event and the aftershocks. They showed clear period elongation for the main event when comparing with the majority of the aftershocks, thus, the response of the sites was amplitude dependent.

Puglia et al. (2011) showed that relatively small changes of soil natural frequency were observed during the L'Aquila earthquake, and they could not be related to soil nonlinearity. They suggested that these changes might be due to pore pressure generation, but no piezometer measurements were available.

The frequency wandering and the impact of soil-structure interaction was shown in a different context by Barrios et al. (2019). The authors showed that the natural frequency of a standalone structure changes if another adjacent building is present. This effect can be attributed to the increased soil stresses below the structures, thus the increased soil stiffness. This is an example of a 'structure-soil-structure interaction' and its contribution towards frequency wandering due to changes in soil stress state.

A strong impact of soil-structure interaction on natural frequency was highlighted by de Silva et al. (2019) and Ceravolo et al. (2019) for a damaged school in Visso (Marche earthquake 2016, in central Italy), where also the changes in natural frequencies were captured during and between the sequence of aftershocks.

To sum up, the majority of the studies presented above suggest that the seismic frequency wandering can be related to soil-structure interaction as the frequency wandering is amplitude dependent and returns to the pre-event quantity if no structural damage has taken place. However, when considering soil-structure interaction, soil nonlinear behaviour is not the only factor contributing to frequency wandering, because the pore pressure build-up is a further important element that should be considered. An attempt to investigate the effect of pore pressure generation, reduction in effective stresses and soil stiffness, and gradual changes of frequency with time seem to be missing in the literature devoted to temporary natural frequency wandering.

On the other hand, recent earthquakes in Italy have shown that large pore pressures were generated, often leading to liquefaction (Lombardi & Bhattacharya, 2014; Fioravante et al., 2013). There was no specific data, showing natural frequency wandering in the liquefaction-prone areas, although the long-lasting effect of frequency wandering is also expected to happen on these sites. For example, during the Emilia Romagna earthquake 2012, the sites subjected to liquefaction were

characterized by soil profiles of sandy soil being covered by topsoil and silty layers which delayed the excess pressure dissipation from the underlying sand layer (Chiaradonna et al., 2018). A similar ground profile, with liquefiable soil placed deeper, can even lead to liquefaction in deeper layers (at depths of 8-10m), with no clear signs of liquefaction at ground level being observed (Cubrinovski et al., 2019).

The effects of pore pressure generation on structural response were analysed in some aspects by Oka et al. (2004), Corciulo et al. (2017) and Kementzetzidis et al. (2018, 2019). Oka et al. (2004) focused on the reduced structural demand due to strain localisation in a deep soft clay layer where significant excess pore pressure was induced, although natural frequencies were not considered. Corciulo et al. (2017) and Kementzetzidis et al. (2018, 2019) referred to the case of an offshore wind turbine. They showed turbine natural frequency being dependent on dynamic actions due to wind and waves which caused changes in pore pressure. These numerical studies were consistent with the evidence from field observations (Kallehave et al., 2015).

No specific experimental study dealing with changes in natural frequencies of structures due to pore pressure generation induced by seismic events has been performed, to the best of Author's knowledge. The only exception is a study by Lee (2005) who presented a simplified evaluation of the effects induced by pore pressure based on the measured reduction in shear wave velocity in centrifuge tests of quay walls in saturated sand during simulated earthquake input motions.

Similarly, site specific data dealing with pore pressure generation and reduction in soil stiffness is very rare. Arai (2006) measured shear wave velocities of a subsurface layer at two sites. The measurements indicated that these velocities were reduced during the strong motion event to the factor of 0.8. Later the velocities returned to their initial values, faster for sandy silt and slower for silty clay. However, the reason of the measured changes was not explicitly provided. Some interpretation was given towards nonlinear soil behaviour. Boulanger & Ziotopoulou (2015) associated this change with loss in cementation, later regained over time by new inter particle bonding being created. The effect of pore pressure was not considered among the potential explanations.

This chapter investigates through numerical analyses the impact of pore pressure and soil nonlinear behaviour on structural natural frequency wandering induced by earthquakes since previous studies did not show qualitatively such effects. The effects of pore pressure generation were preliminary examined on an idealized structure representative of the VN7SH hotel by Kowalczyk & Gajo (2020). These results were promising, although numerous assumptions were made. Herein, a more sound and careful examination is proposed, which is not site specific as the previous work, although it is inspired by some sites where the frequency wandering is very likely to have taken place, such as Mirandola in Emilia Romagna (Italy) during the earthquake of 2012, and by some buildings around the world (e.g. the Millikan Library, the hotel VN7SH, or the school in Visso). Therefore, an idealized case of a simple structure embedded in a granular saturated medium dense soil deposit is presented in

this chapter. The structure has been characterized numerically through dynamic analyses performed before and after the earthquake motion and the changes in natural frequency with time have been identified. The effects of soil permeability, soil density, seismic input motion, characteristics of a structure, and the sequence of a main event followed by an aftershock have been examined in detail.

2. Methodology

The numerical analyses presented here are focused on a simple structure representing a broad class of buildings resting on saturated sandy soils with an embedded substructure. This case will be referred below as the “basic case”. In addition, some parametric analyses will be presented for evaluating the impact of soil permeability, soil density, input motion and the type of a structure on frequency wandering. In addition, aftershock time history will be analysed to show different structural response during the main shock and the aftershock.

2.1 Numerical model for “basic case”

A plain strain finite element model has been analysed with Abaqus commercial FEM code (Dassault System, 2019). For the sake of simplicity, the structure is modelled as a simple cantilever beam embedded 4m in soil. Initial studies showed that the foundation of a finite size would also result in similar trends as those shown in this chapter. The structure is assumed to be elastic, weightless (but not massless) with the first natural frequency of 2.2Hz (for the geometry of Figure 1). The soil behaviour is simulated with the ST model in the form presented by Gajo (2010) as explained in Chapter 1.

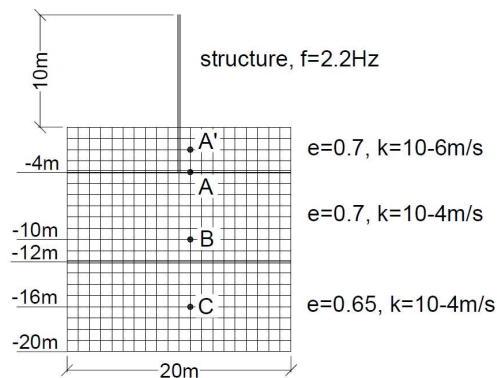


Fig. 1. Model mesh with characteristics of soil profile (where e is a void ratio, k is soil permeability, f is first natural frequency of a simplified structure)

A typical granular soil profile of 20m depth with the increasing density with depth has been considered (Figure 1). Deeper soil layers have been assumed to be overlaid by a less permeable layer (soil permeability $k=10^{-6}$ m/s). The ground water table is at the ground surface to simulate the ground conditions experienced in the Emilia Romagna region (Fioravante et al., 2013; Lombardi & Bhattacharya, 2014). Three points A, B and C along the depth of the soil profile are chosen as the reference points for the result presentation (Figure 1). In addition, an additional point (A') is specified when looking into the response of very dense sand.

The boundary conditions applied to the FEM models include impervious lateral and bottom boundaries and a tie-type connection between the lateral nodes to ensure periodic boundary conditions. No transmitting boundary was applied at the bottom of the mesh. This implies that rockhead is assumed to be placed at depth of 20m and the stiffness difference between rock and soil is so large that wave reflection from the rockhead occurs. In addition, only in-plane shearing motion is analysed, no impact of compression wave propagation on soil and structure response is considered due to the preliminary character of this study.

The element size has been selected from the shortest significant wavelength present in the input motion and the lowest elastic shear stiffness, i.e. around the top of the ground profile. The former has been taken as 10Hz as can be deduced from Figure 2, the elastic shear stiffness has been estimated to around 30MPa for the 4m depth. The standard rule of thumb of 10 nodes per shortest wavelength has given the minimum size of the element of 1.2m. Therefore, the final element size used throughout this study is 1m. It is noted that the reappraisal of the discretization rules for wave propagation problems presented by Watanabe et al. (2017) can be more strict in nonlinear analysis. Nevertheless, some preliminary initial studies have been carried out with the element size of 2m and the simulations showed the same trends evaluated with the more refined mesh size of 1m. This confirms that the accuracy and the reliability of the analyses performed with the 1m element size.

The time increment of 0.0005 second has been chosen in order to reduce the number of iterations required for each time step to reach convergence. This time increment is smaller than the time required for the fastest wave to be represented by a minimum twenty time increments (Haigh et al., 2005) and small enough to prevent a wave front from reaching two consecutive nodes at the same time (Watanabe et al., 2017).

Abaqus Standard (Dassault System, 2019) has been used with a user-defined element (Gajo, 2018) for simulating the transient soil dynamic behaviour in saturated soils. The hydromechanical coupling under dynamic equations is taken into account with the u-p formulation of the Biot's theory (Zienkiewicz et al., 1999). The user-defined finite element has been validated for P-wave propagation by Argani & Kowalczyk (2019) and subsequently Gajo & Argani (2020). In addition, a visualisation tool Abaquser (S. Roth et al., 2012) has been used for the result presentation in Abaqus CAE.

No numerical damping has been introduced in the system during the dynamic time steps. Rayleigh damping equivalent to damping of 5% and for the frequency range between 1-3Hz has been introduced in the definition of the elastic material for the structure as proportional to mass and stiffness matrices. A small amount of Rayleigh damping of 2%, proportional to the stiffness evaluated in the soil constitutive law has been introduced for soil in the same frequency range (1-3Hz) in order to account for the soil damping at very low strain levels.

The earthquake time history of the Mirandola site in the Emilia Romagna region which was affected by liquefaction during 2012 earthquake has been used as an input motion in the numerical studies (Figure 2). This motion has been downscaled by a factor of 0.5 in order to reduce the maximum acceleration amplitude to around 0.1g and apply shaking which is representative of an earthquake in which a typical structure will likely remain elastic.

An in-plane lateral component of the acceleration time history has only been considered. An out-of-plane lateral component and a vertical ground motion component have not been included due to a preliminary character of this study.

With a direct approach, the natural frequencies of soil and structure have been determined from the FFT of the input motion of a very low amplitude applied in a form of a pulse at the bottom of the soil, in this case the Ormsby wavelet (Figure 3) was used. Similarly, to the sinc function, the Ormsby wavelet also gives a flat power spectrum but the signal duration is shorter this is why it has been chosen here as an input motion for the structural identification purpose. The specified limits of the excited frequencies of interest are 1Hz up to 9Hz with a gradual increase from 0.1Hz and a gradual decrease to 10Hz, the maximum amplitude of the pulse is 0.0001g. The amplitude is chosen to ensure elastic response only in soil, thus, is representative of microtremors which would typically be used to measure the natural frequency of a structure in field. Transfer functions between the top of the structure and the motion recorded at the top of the soil in the free field identify the natural frequency of the structure including soil-structure interaction effects. The plots showing the transfer functions include only the range of dominant frequencies (i.e. from around 0.6 to 3.0Hz) in order to avoid misleading spurious peaks at very low frequencies.

The dynamic identification has been carried out immediately before the beginning of the earthquake and 5 minutes, 30 minutes and 20 hours after the end of the earthquake for all the analysed cases unless otherwise stated. Note that no dynamic identification has been carried out during the actual earthquake as the evaluation of Fast Fourier spectra for earthquake motions is typically not fully representative and more advanced identification methods are recommended especially in nonlinear systems (e.g. Ceravolo et al., 2013). Future studies may resource to such identification methods to further develop the findings of this chapter.

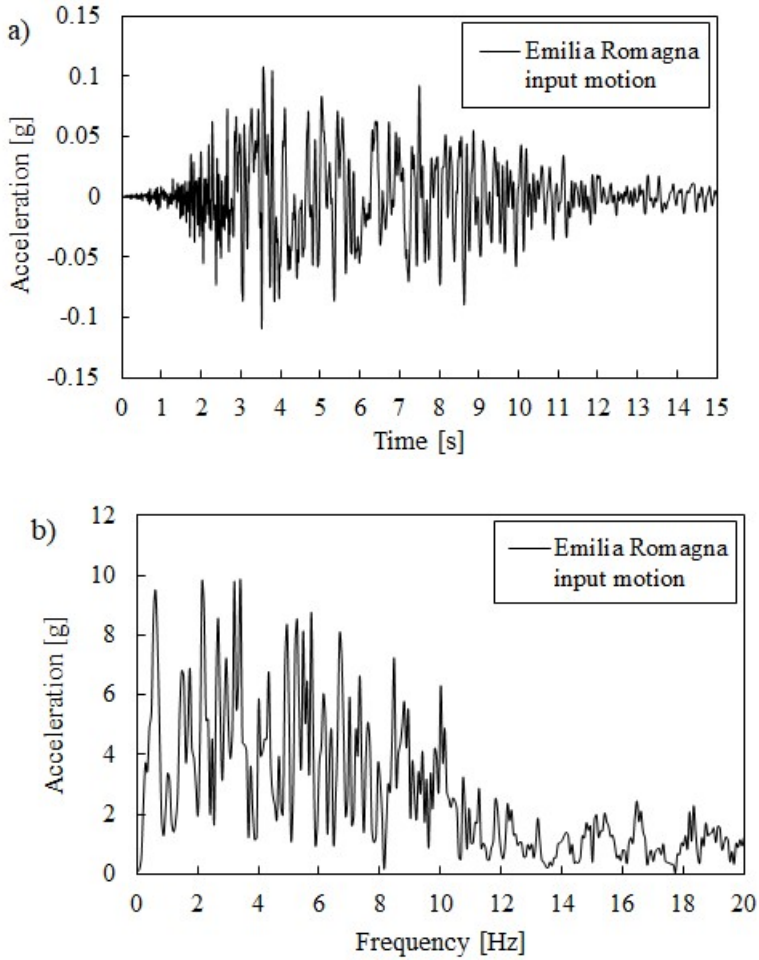


Fig. 2. a) Acceleration time history as recorded at Mirandola site downscaled to maximum amplitude of approximately 0.1g, b) spectral acceleration response.

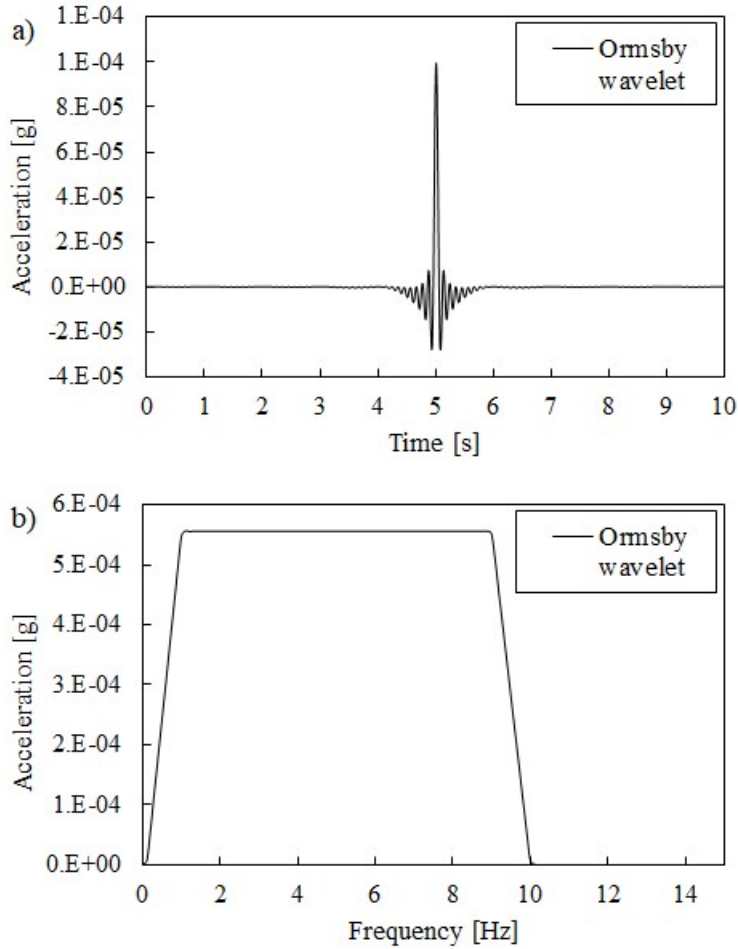


Fig. 3. Impulse in a form of Ormsby wavelet for structural identification purpose, amplitude versus time (a) and FFT of impulse (b).

2.2 Calibration of constitutive model

The ST model has been used to represent soil nonlinear behaviour. The version of the model used in this study is as per Gajo (2010). The model description is provided in Chapter 1. The model calibration has been obtained for the comparison with the shear stack experimental data on dry sand (Chapter 2 and 3), therefore, the behaviour in the small strain region could be represented realistically. Some minor changes to this calibration were needed to improve the simulation of cyclic undrained simple shear tests on data on other available sands (Zhao et al., 2019; Silva et al., 2015). Table 1 lists the input parameters of the model. The validation of the ST model in cyclic

undrained behaviour in simple shear is shown in the section concerning the validation of the constitutive model.

Table 1 Input parameters for ST model.

Parameter	Description	Value
v_A	Intercept for critical-state line in v - $\ln(p)$ plane at $p=1\text{Pa}$	2.194
A	Slope of critical state line in v - $\ln(p)$ plane	0.0267
φ_{cv}	Critical state angle of friction	33°
m	Parameter controlling deviatoric section of yield surface	0.8
k	Link between changes in state parameter and current size of yield surface	3.5
A	Multiplier in flow rule	0.7
k_d	State parameter contribution in flow rule	1.3
B	Parameter controlling hyperbolic stiffness relationship	0.015
α	Exponent controlling hyperbolic stiffness relationship	1.8
RR	Size of yield surface with respect to strength surface	0.01
ER	Fraction of G_0 used in computations	0.16

2.3 Parametric studies

A number of parametric studies have been carried out in order to examine the importance of various factors on seismic frequency wandering. The geometry of the problem is the one of the “basic case” (Figure 1), unless otherwise stated. The parametric studies are described in detail below. The following factors have been taken into account: soil permeability, soil density, input motion, type of a structure and a time history with an aftershock.

Soil permeability

At first the limit case of infinite permeability has been considered for the sake of validating the numerical procedures and to distinguish the effects due to soil non-

linearity with respect to those due to pore pressure generation. The limit case of infinite permeability has been achieved by constraining pore pressure DOF to remain constant. In this way, pore pressures and the vertical effective stress do not change during the dynamic analyses. The dynamic identification has been carried out only 5 minutes after the earthquake. Due to the lack of any excess pore pressure, any computed natural frequency wandering is expected to be associated only with plastic deformations.

In addition, the effect of soil permeability has been investigated in order to evaluate the time span in which the structure can be affected by the pore pressures generated by the seismic motion. In contrast to the profile of the soil permeability of Figure 1, in the parametric analyses the permeability of the top 4m layer has been considered to vary between 10^{-7} m/s and 10^{-4} m/s.

Soil density

A case of very dense sublayers of saturated soil (i.e. void ratio $e=0.6$ throughout the soil profile) has been analysed in order to show how soil density can affect the dynamic response of the structure. For this purpose, the initial void ratio for the three layers has been set to be 0.6 for the all layers to simulate very dense conditions.

Input motion

A different input motion, i.e. the San Fernando earthquake time history, as shown on Figure 4 has also been applied to inspect the effects of different duration and frequency content on the generated pore pressures and the reduction in natural frequencies. This input motion was registered on rock at the old seismological station in Pasadena, California.

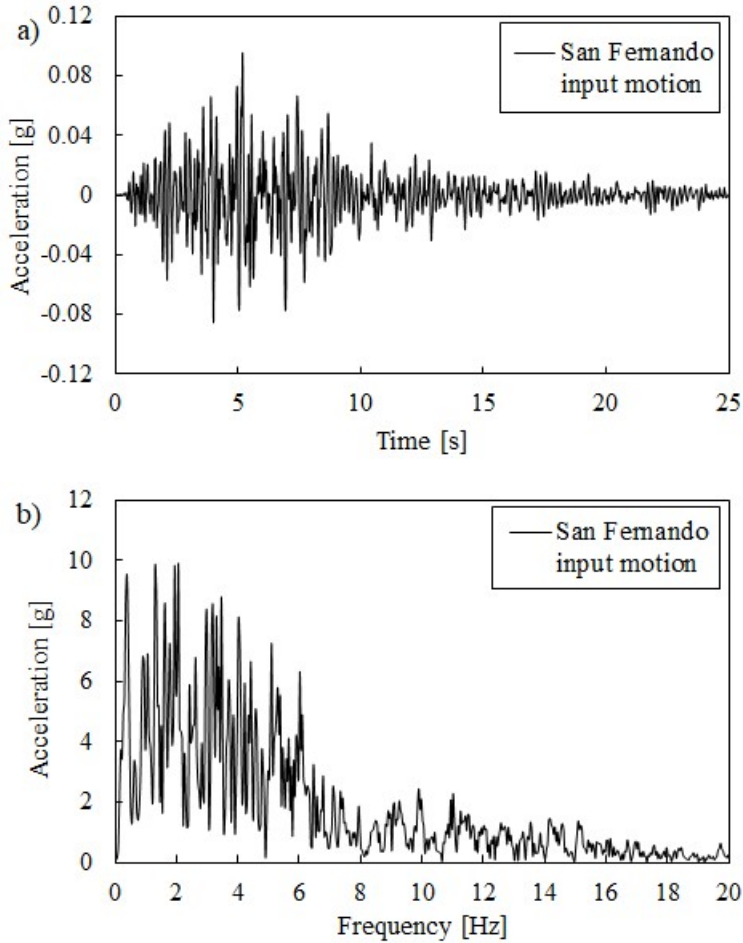


Fig. 4. a) Acceleration time history as recorded during San Fernando earthquake (1971), b) spectral acceleration response.

Type of structure

A slender structure with a compliant base, having a natural frequency of approximately 1.3Hz has also been analysed in order to consider slender buildings. The geometry of the slender structure is the same as in Figure 1 for the “basic case”, but the elastic stiffness has been reduced. Similarly, to the main case, the simplified structure is weightless and embedded 4m in soil.

Time history with aftershock

A time history inclusive of an aftershock has been analysed. The Emilia Romagna earthquake sequence including numerous strong aftershocks has been considered. Aftershocks are expected to be particularly important in the areas where pore pressure dissipation can be delayed due to a layered soil profile such as at the Mirandola site. Herein, the input motion for the aftershock of magnitude 5.5M (Figure 5) has been chosen among one of the aftershocks registered at the Mirandola site and applied 1h after the main event. The amplitude of the aftershock was downscaled by the factor of 0.5 in order to be consistent with the main input motion (Figure 2).

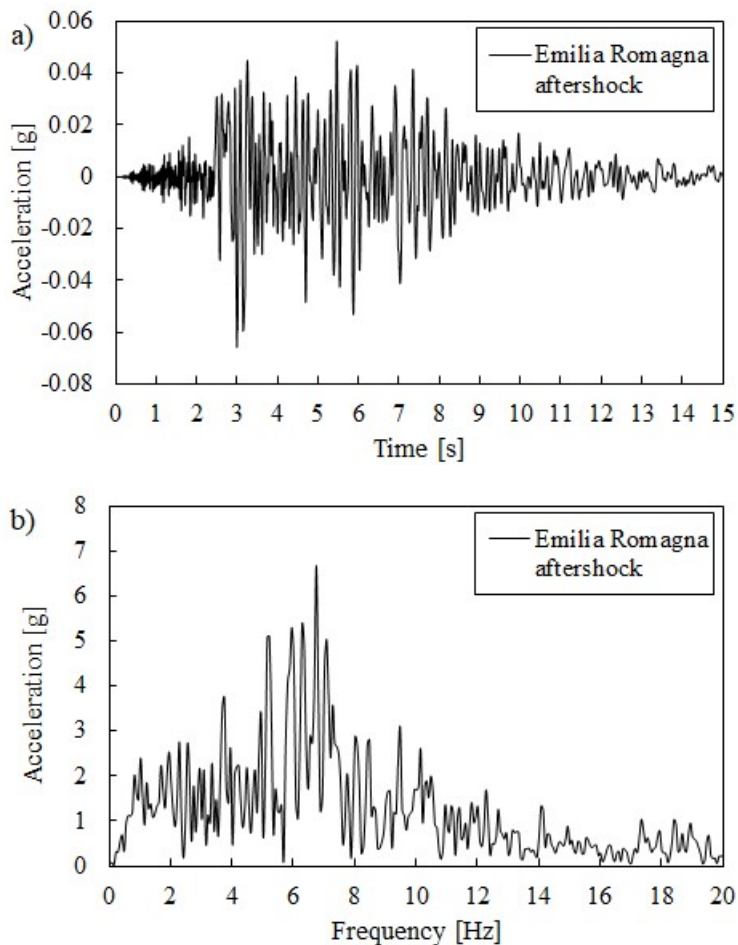


Figure 5. a) Acceleration time history for one of aftershocks as recorded at Mirandola site, b) corresponding spectral acceleration response.

3. Validation of constitutive model on laboratory tests

A set of cyclic, undrained, simple shear tests performed on sand samples with various initial densities have been selected for the model calibration. The comparison of the ST model predictions with some experimental results (Zhao et al., 2019; Silva et al. 2015) are shown on Figures 6-10. In each simulated test, the void ratio has been set as to be approximately equivalent to the relative density evaluated in the experimental work.

Generally, a good match has been obtained for dense sand (Figure 6) and loose sand (Figure 8) in terms of the stress-strain curves. In terms of the reduction of mean effective stresses with shear straining the loose soil (Figure 8) is very well represented, whereas the dense soil achieves the shakedown stage sooner in the numerical study than in the experiments (Figure 6). The comparison between the model simulations and the experimental results is a bit less consistent for medium dense sand. Figure 7 shows the inability of the constitutive model to achieve full cyclic mobility state and very large shear strains in the consecutive loading cycles. On the other hand, for Toyoura Sand (Figure 9), the simulations and the experimental results for medium dense sand at slightly higher CSR (cyclic stress ratios) are similar to each other. Figure 10 shows a satisfactory match too, although in this case the constitutive model reaches the shakedown at slightly higher mean effective stress than the experimental measurements and very large strains do not develop for the consecutive loading cycles.

The author and Gajo (2018) are aware of these limitations of the ST model. On the other hand, the drawbacks of the model do not affect the basic conclusions that will be drawn from this preliminary study.

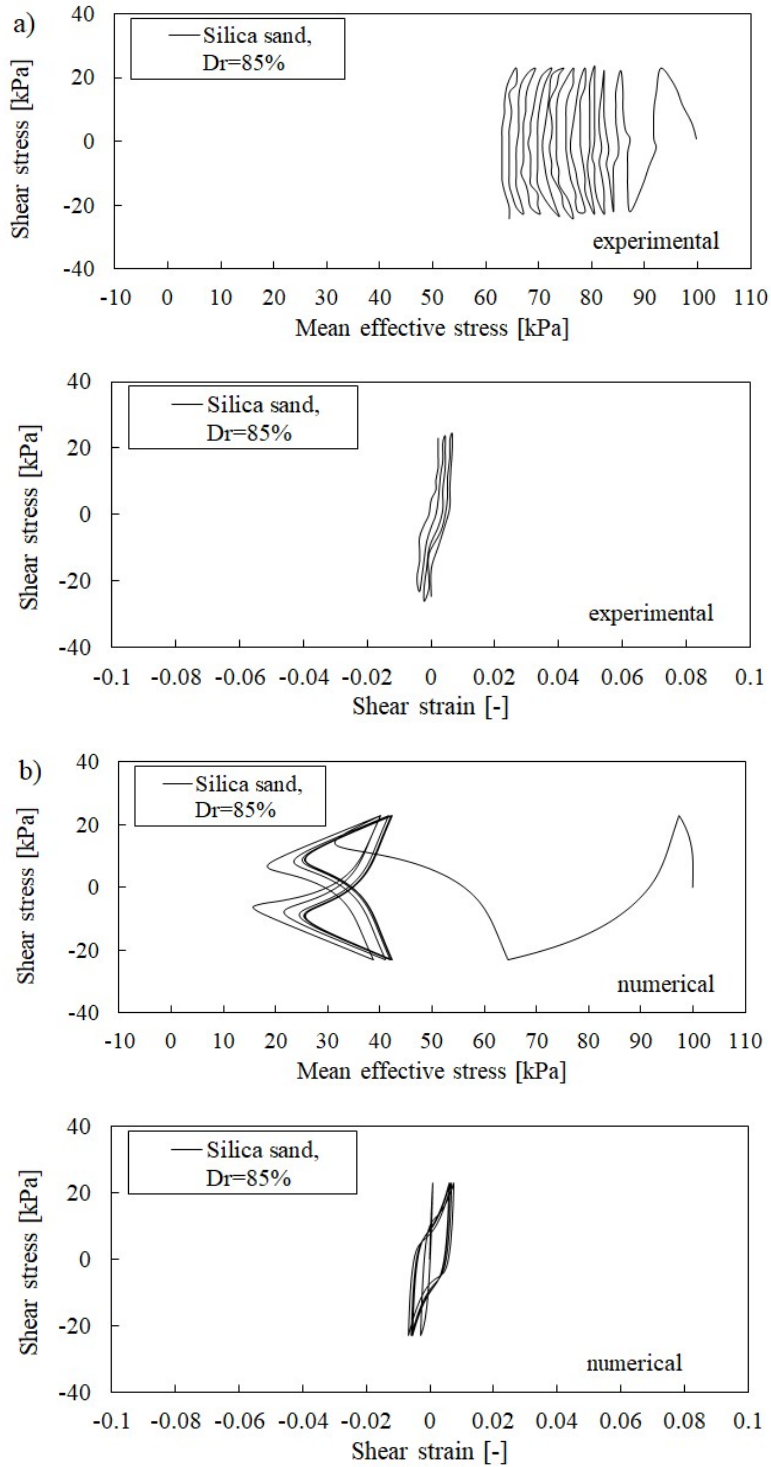


Fig. 6. Dense sand ($D_r=85\%$) in cyclic undrained simple shear tests with $CSR=0.23$: a) experimental data (Zhao et al., 2019), b) model simulations.

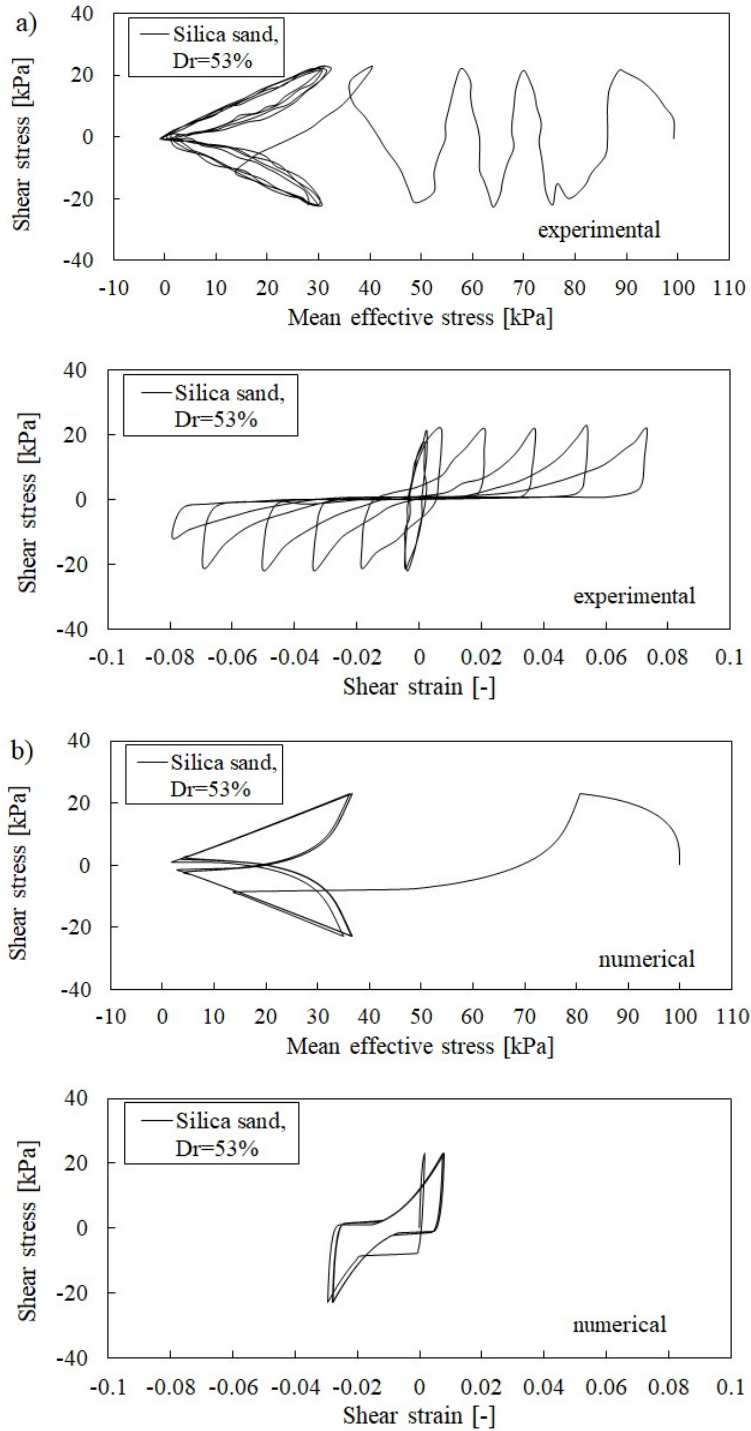


Fig. 7. Medium dense sand ($D_r=53\%$) in cyclic undrained simple shear tests with $CSR=0.23$: a) experimental data (Zhao et al., 2019), b) model simulations.

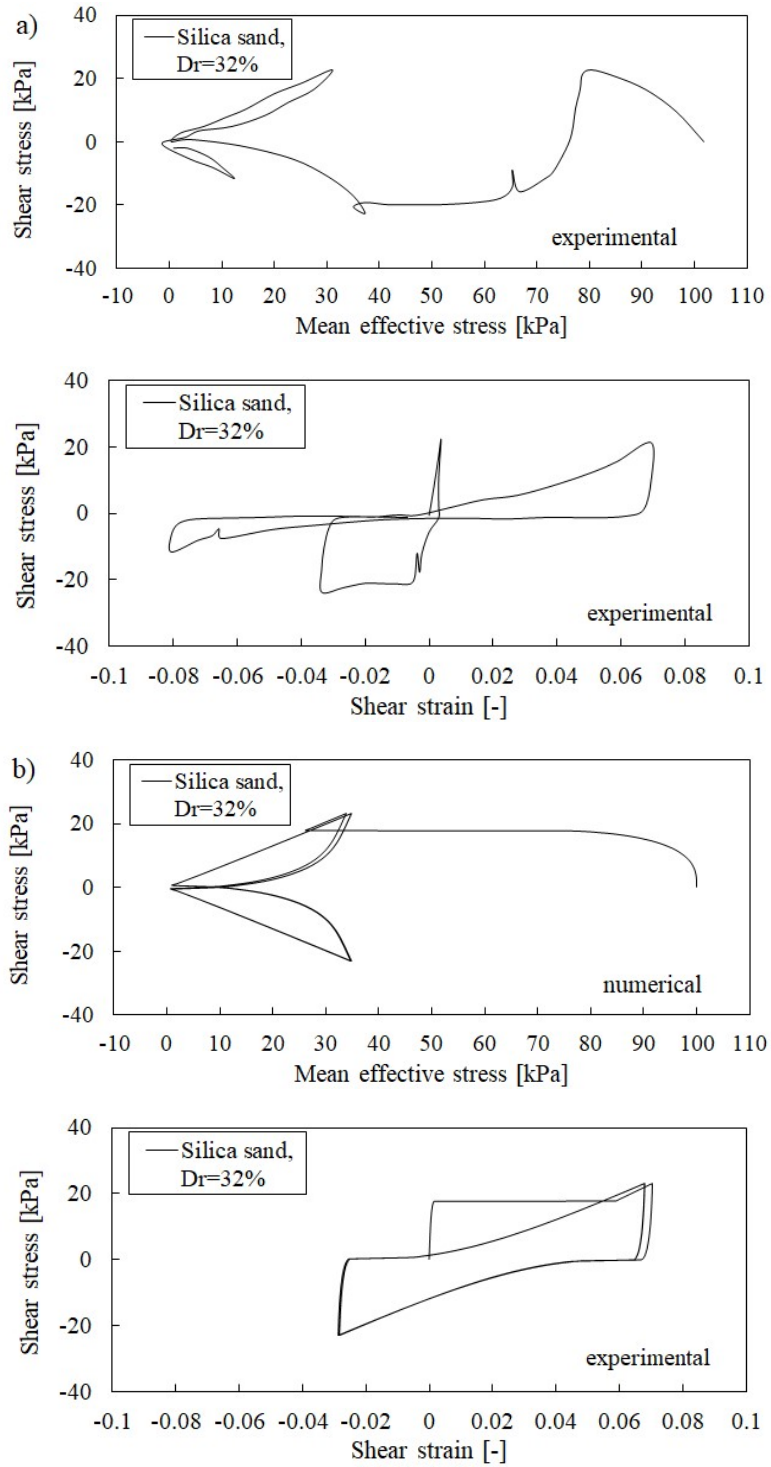


Fig. 8. Loose sand ($D_r=32\%$) in cyclic undrained simple shear tests with $CSR=0.23$: a) experimental data (Zhao et al., 2019), b) model simulations.

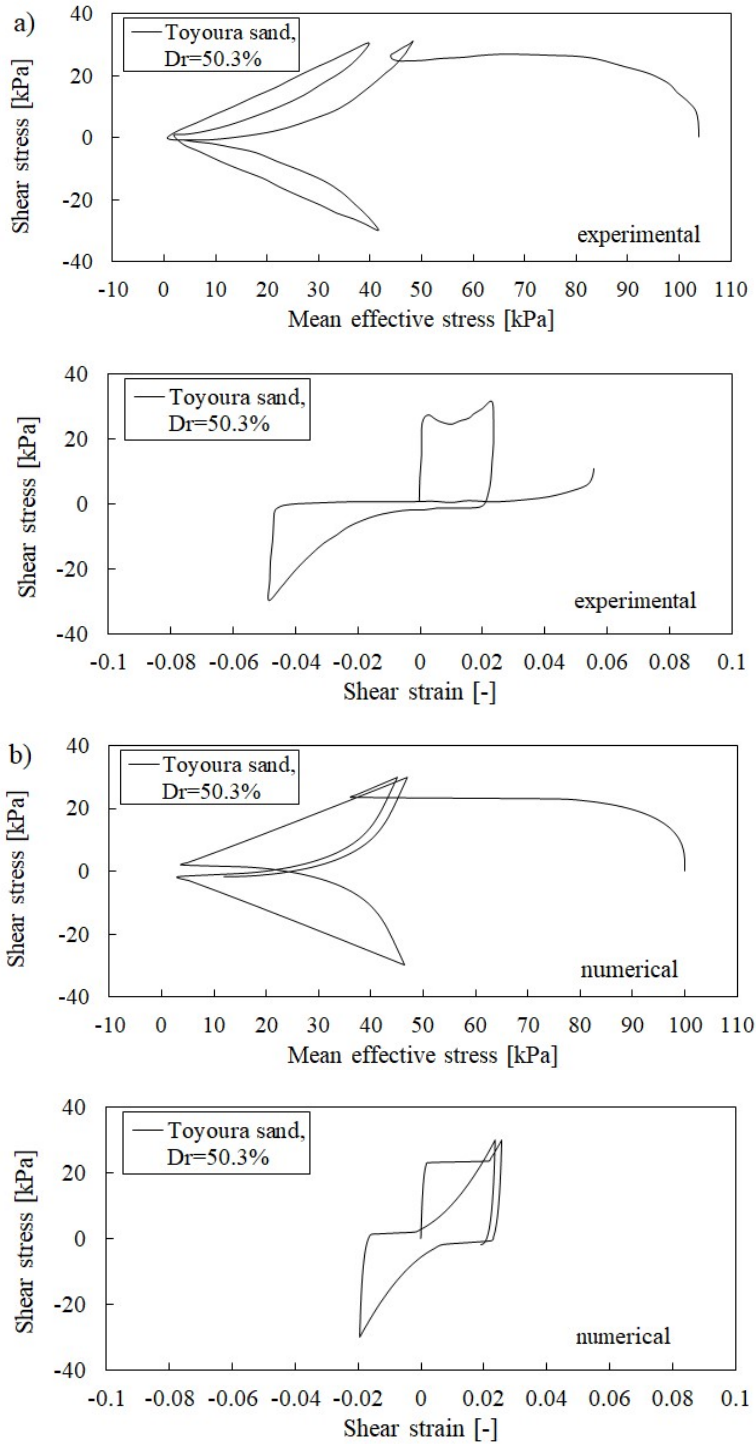


Fig. 9. Toyoura Sand, medium dense ($D_r=50.3\%$) in cyclic undrained simple shear tests with $CSR=0.30$: a) experimental data (Silva et al., 2015), b) model simulations.

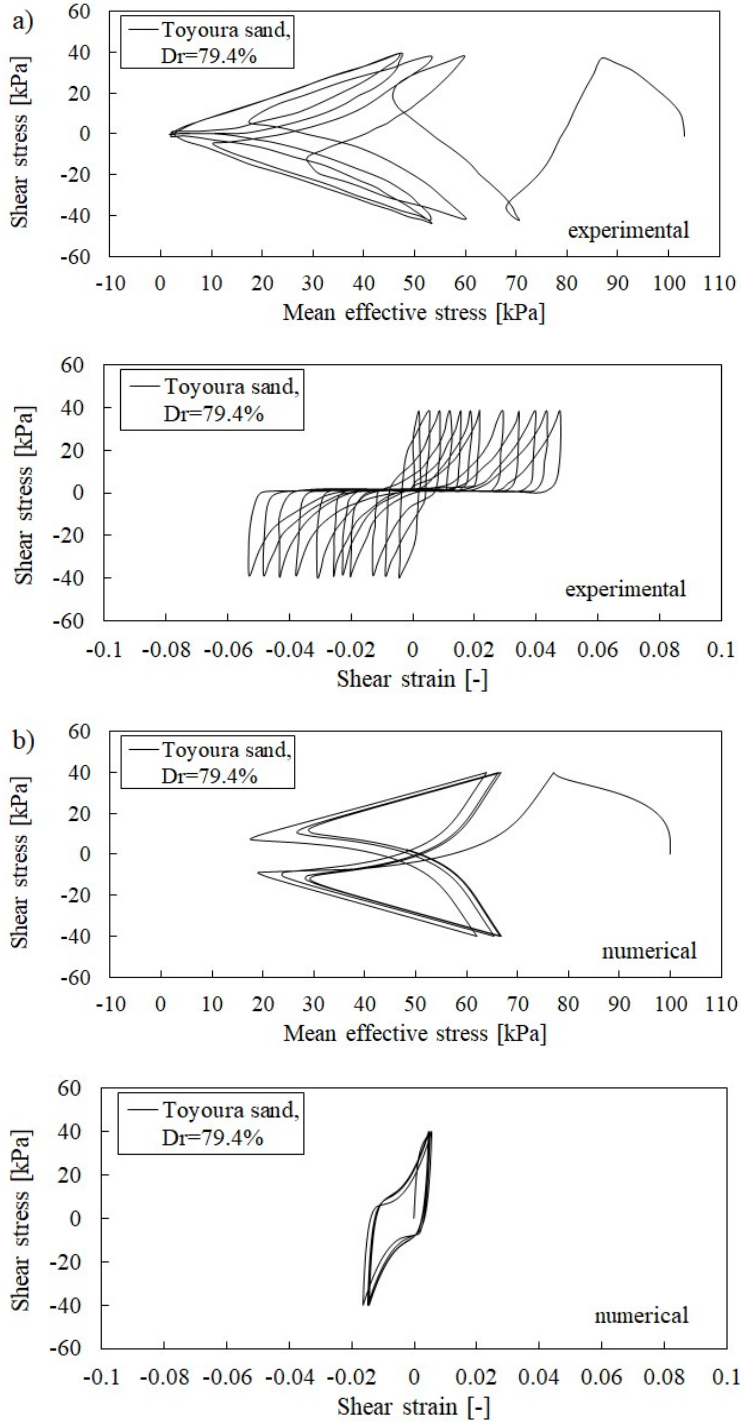


Fig. 10. Toyoura Sand, dense but at high ratio of shear stress/pressure ratio thus behaving as loose/m.dense, ($D_r=79.4\%$) in cyclic undrained simple shear tests with $CSR=0.4$: a) experimental data (Silva et al., 2015), b) model simulations.

4. Results

This section presents firstly the results for the “basic case” of saturated soil with an embedded structure and secondly the results of the parametric studies on: soil permeability, soil density, a type of structure, a type of ground motion and a time history with aftershock.

4.1 “Basic case”

The results of the “basic case” are shown on Figures 11-15. Figure 11 shows that the natural frequency of the soil and the structure reduces after the earthquake to the values of 1.0Hz for the soil (initially 1.5Hz) and 1.4Hz for the structure (initially 2.2Hz). The lowest frequencies are computed 5 minutes after the end of the earthquake. A gradual return to the initial values is observed with time, firstly at 30 minutes and later at 20 hours after the end of the earthquake when the computed frequencies return to their initial values. Noticeably, the peaks in the spectral response at 5 minutes after the earthquake have a smaller amplitude which can be associated with a softer soil response due to pore pressure generation. The reduction in frequencies and amplitudes is induced by the pore pressure generation and the corresponding reduction in effective stresses. Figure 12 shows the reduction of mean effective stresses at the three reference points, whereas Figure 13 shows the corresponding shear stress-strain curves. The reduction of effective stresses leads to a reduction of soil stiffness, which is particularly visible at the top of the soil profile.

The pore pressure generation is shown on Figure 14a. The values of the natural frequency return with time almost to their initial values due to pore pressure dissipation with time which is shown on Figure 14b. It can be observed that although soil regains completely its stiffness after 20h (Figure 11a), the natural frequency of the structure (Figure 11c) returns to a slightly lower value (2.1Hz) than the initial one (2.2Hz). This is probably related to a reduction in the mean effective stresses in the vicinity of the structure (Figure 15). For the sake of completeness, Figure 15 also shows pore pressure profiles along two vertical cross sections (in the vicinity of the structure and in free field).

Table 3 Changes in the computed natural frequency of the soil and structure with time.

	Before	5 mins after	30 mins after	20h after
Soil	1.5 Hz	1.0 Hz	1.2 Hz	1.5 Hz
Structure	2.2 Hz	1.4 Hz	1.6 Hz	2.1 Hz

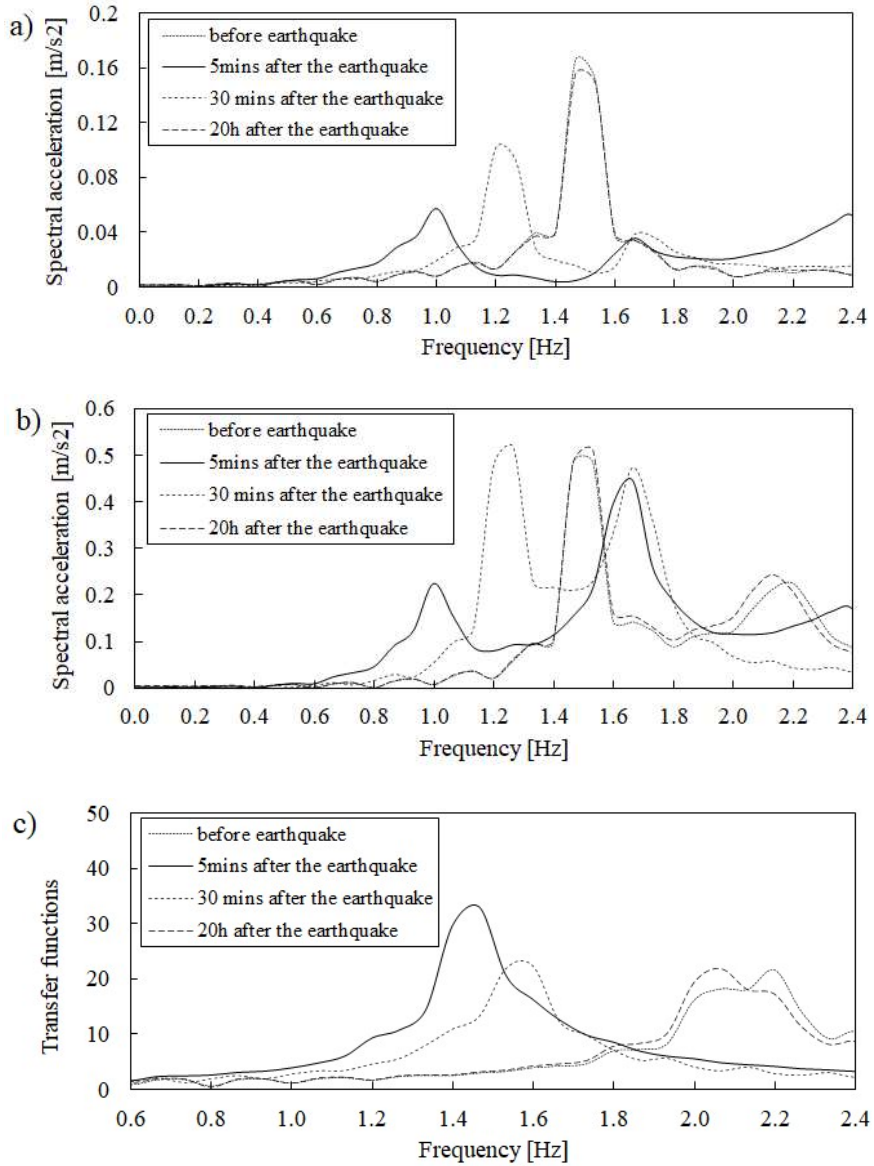


Fig. 11. Changes in natural frequency of soil (a), structure (b) and transfer functions for structure (c).

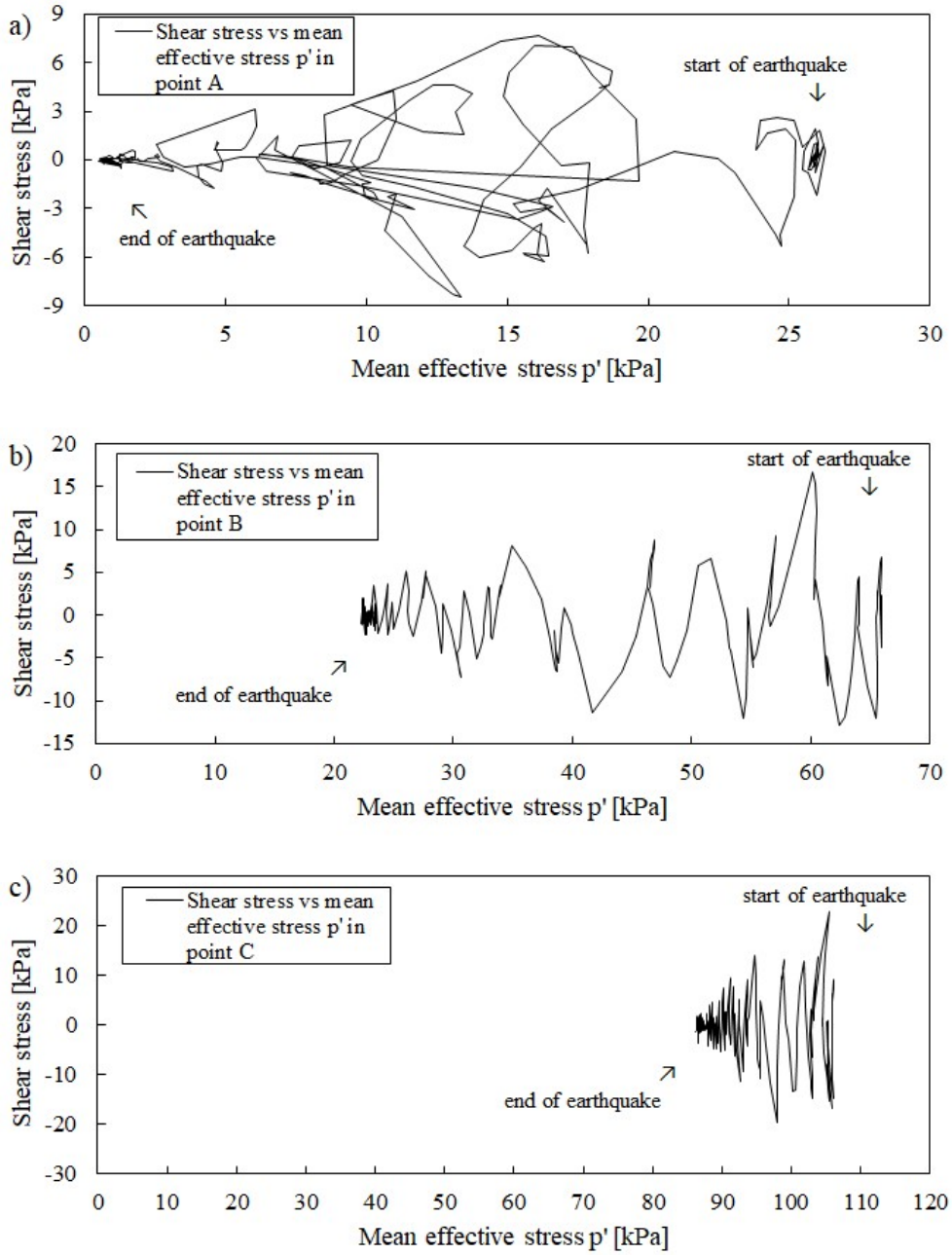


Fig. 12. Effective stress paths during shearing in reference points A, B and C.

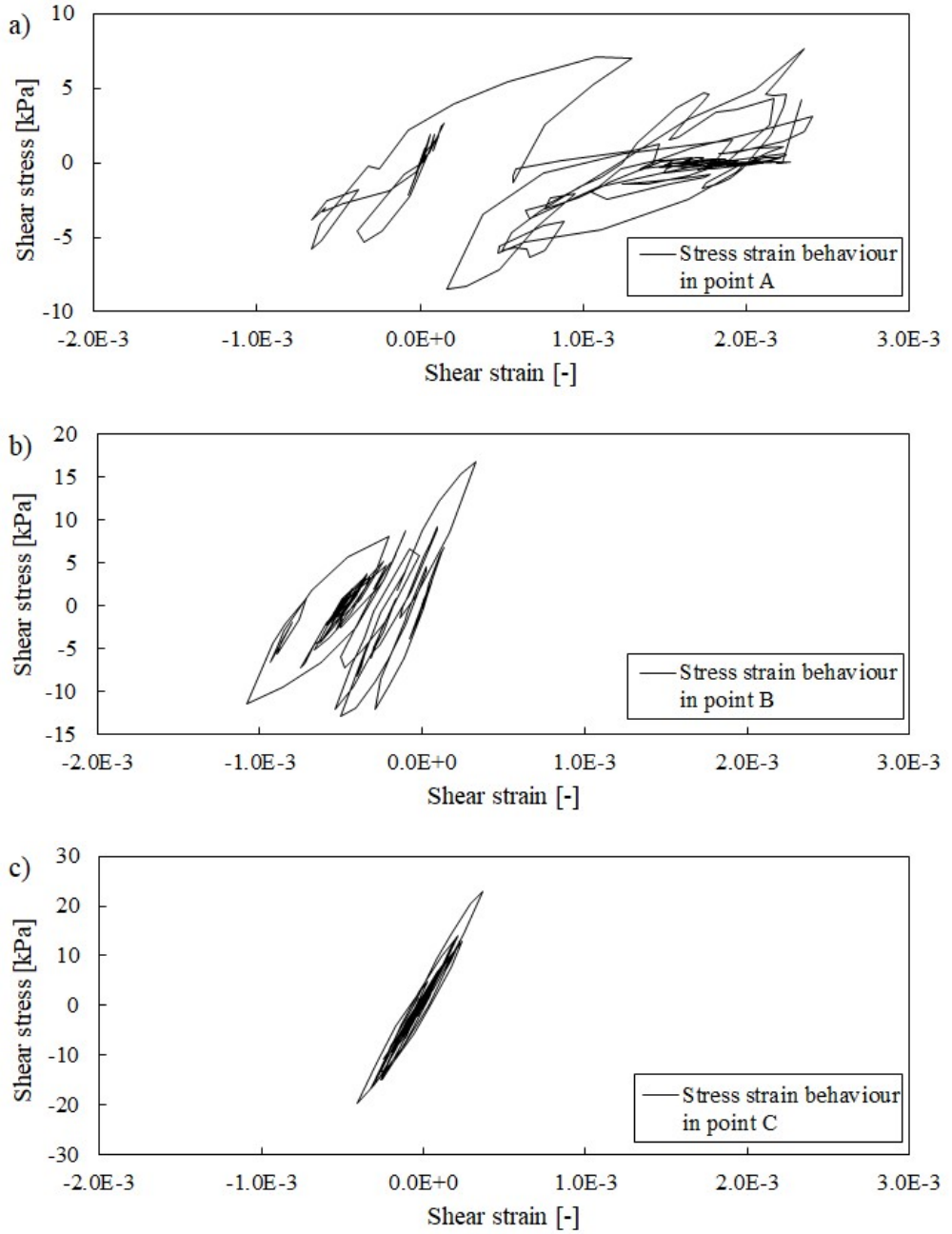


Fig. 13. Stress strain curves in reference points A, B and C.

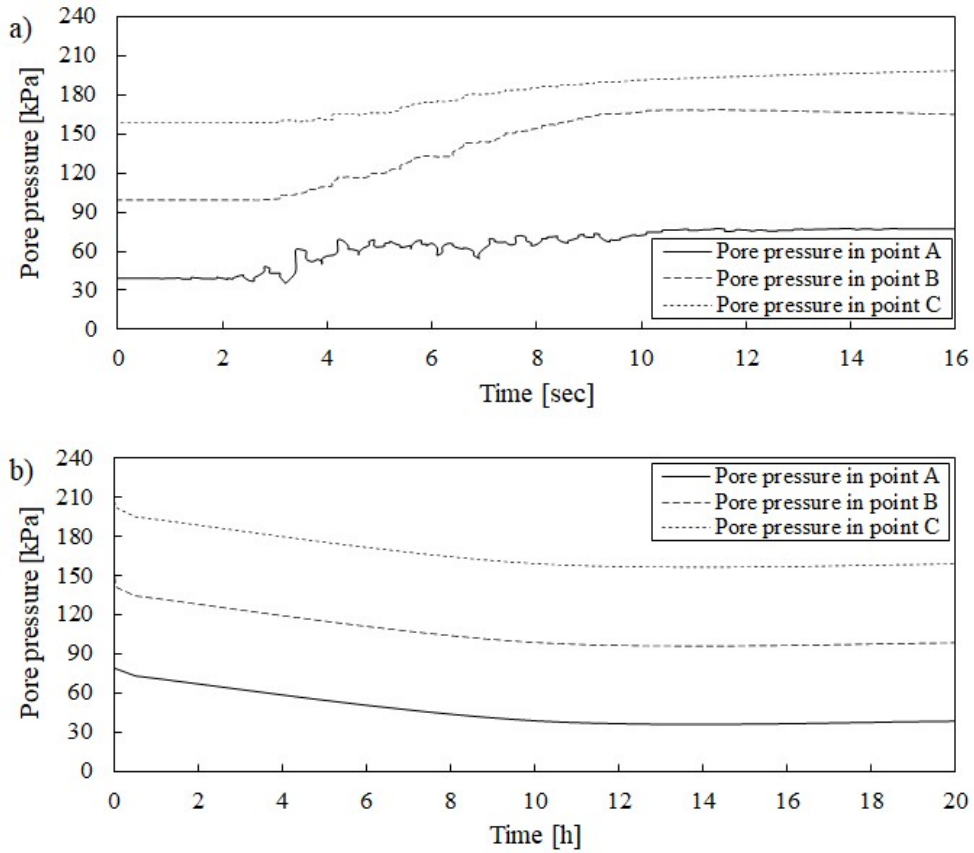


Fig. 14. Pore pressure generation (a) in reference points during earthquake and pore pressure dissipation (b) during following 20 hours.

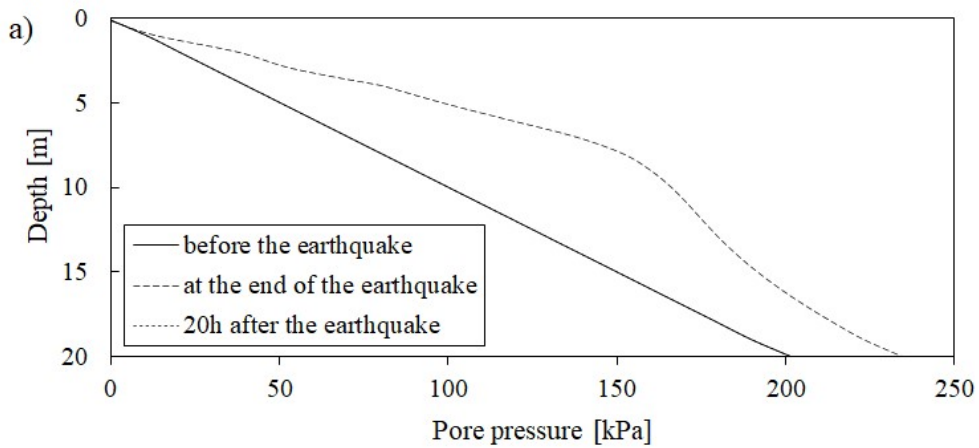


Fig. 15. (continuation on the next page)

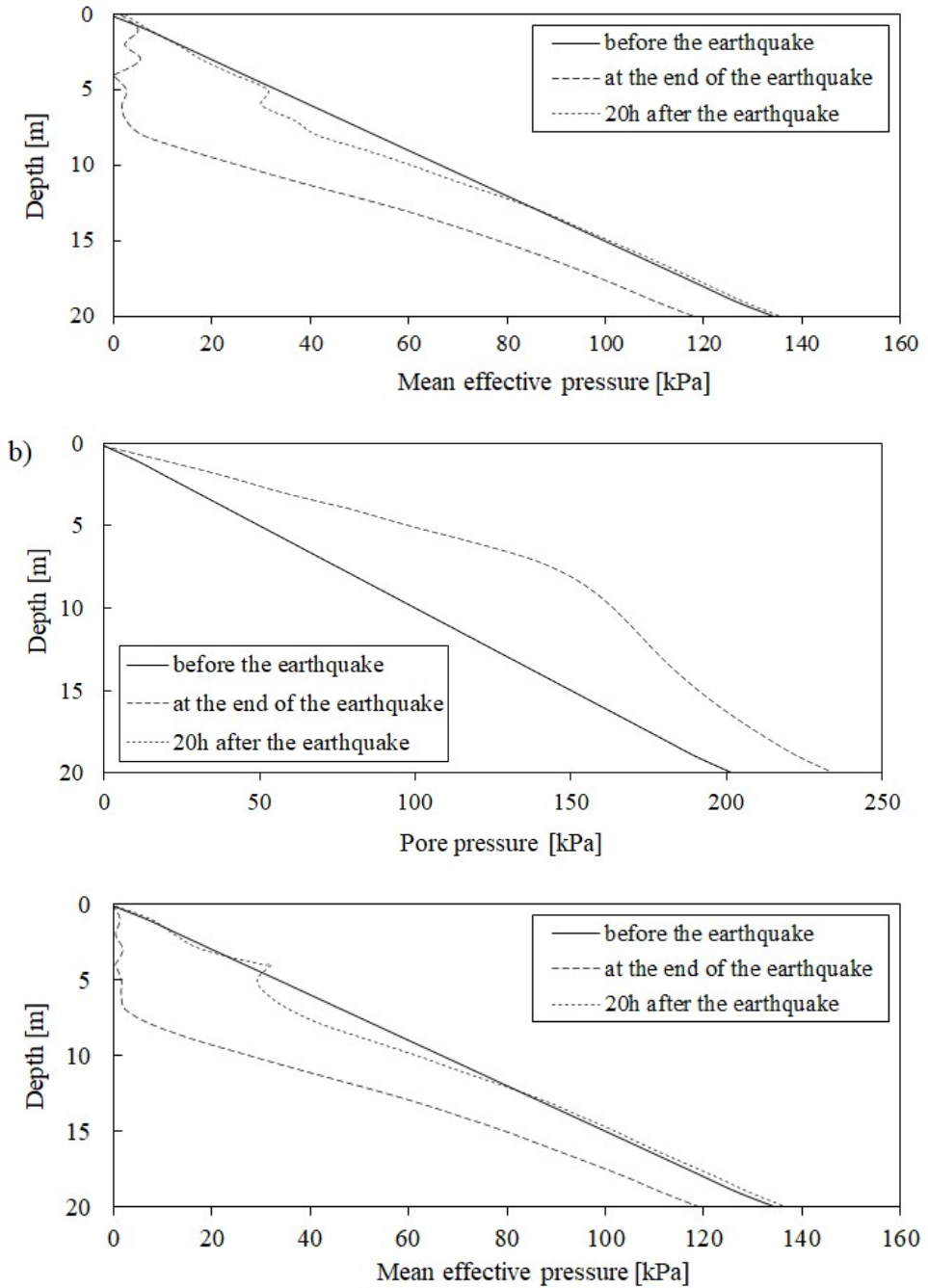


Fig. 15. Pore pressure and mean effective stresses within depth before, just after, and 20h after earthquake: a) in line of structure and b) in free field.

4.2 Parametric studies

Soil permeability

The limit case of infinite permeability shows natural frequency reduction due to inherent nonlinear soil behaviour. Figure 16 shows a slight increase in the natural frequency of the soil and structure. This can be associated with changes in density (Figure 17) due to settlement and densification or with changes in the stress state.

The effect of soil permeability has also been investigated with reference to the time span in which the structure is affected by the generated pore pressures. The permeability k in the top 4m layer is assumed to vary between 10^{-7} m/s and 10^{-4} m/s. The density and the permeability of the lower soil layers remain as per the “basic case” of Figure 1.

Figures 18-20 show the impact of the different permeabilities of the top 4m layer on the frequency wandering of the soil and structure. Figure 18 shows the results 5 minutes after the end of the earthquake. It can be observed that for the permeability of 10^{-4} m/s the natural frequencies return to their initial values almost immediately, i.e. practically within the 5-minute period. Figure 19 shows that a 30-minute period is enough to regain stiffness when considering the permeability of 10^{-5} m/s. On the other hand, for the case of the smallest permeability of 10^{-7} m/s the regain of the natural frequencies is not reached even after 20h as shown on Figure 20.

Figure 21 shows the pore pressure generation and dissipation as a function of the permeability in the reference point A. It can be observed that the pore pressure generated during the seismic motion is barely affected by soil permeability (thus, the response in very short term can be considered undrained), whereas the dissipation time varies from 5 minutes ($k=10^{-4}$ m/s) to 10 days ($k=10^{-7}$ m/s).

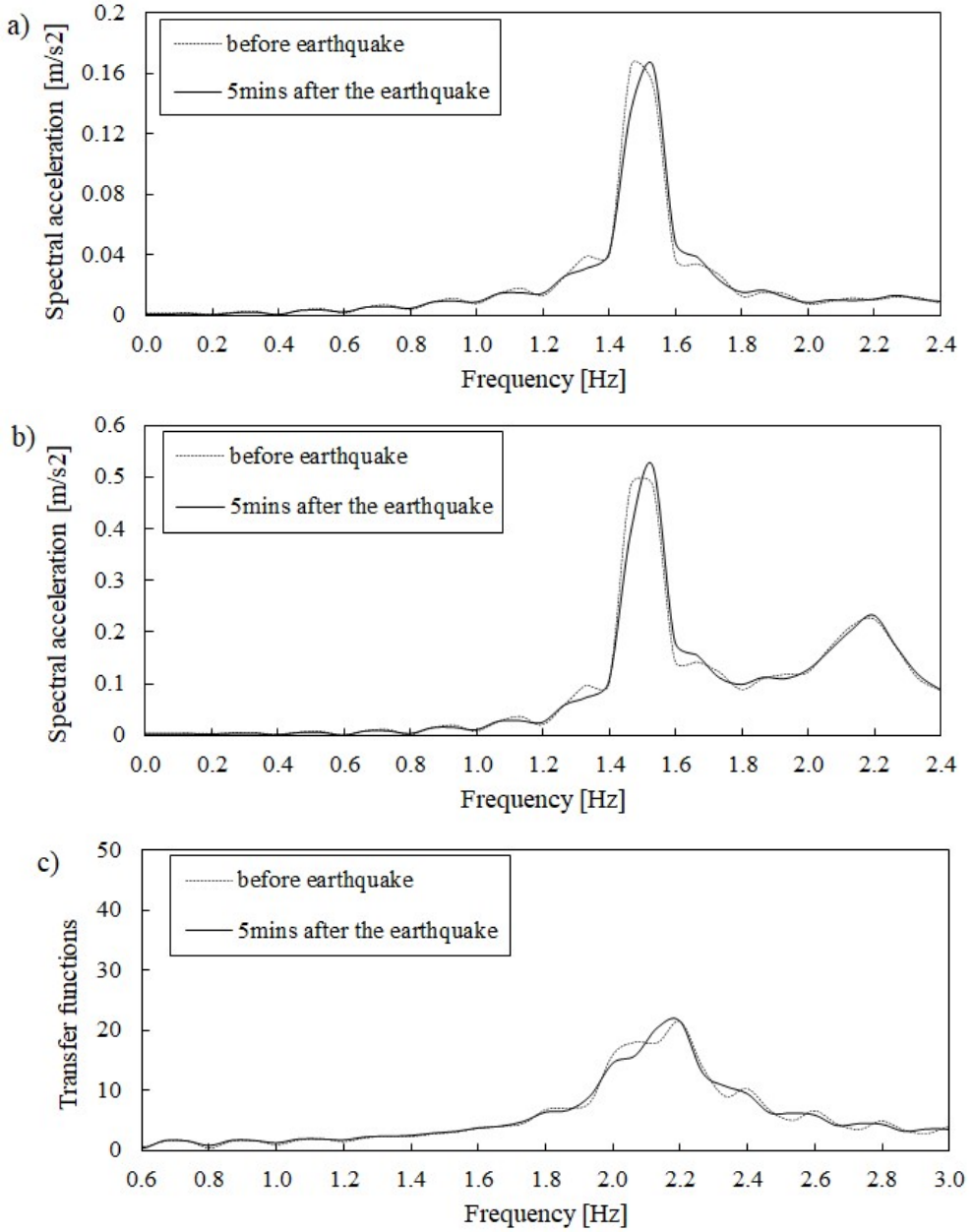


Fig. 16. Changes in natural frequency of soil and structure in case of infinite permeability.

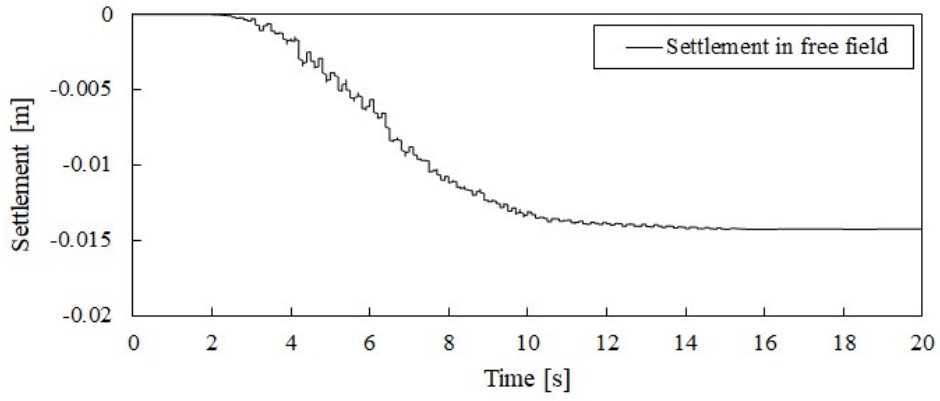


Fig. 17. Settlement calculation during earthquake in case of infinite permeability.

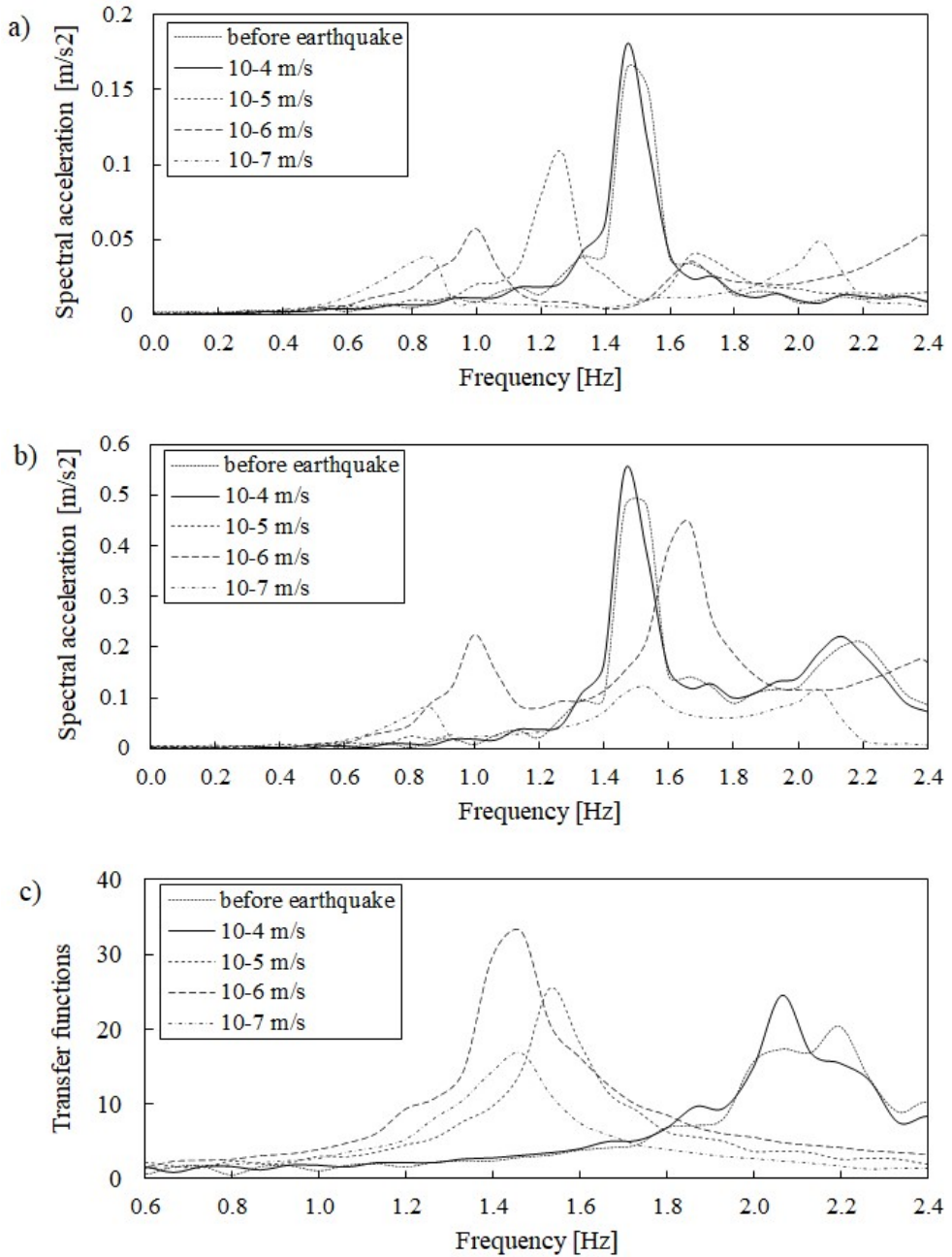


Fig. 18. Changes of natural frequency of soil and structure computed 5 minutes after earthquake as function of permeability of top soil layer: a) FFT for soil, b) FFT for structure, c) transfer functions for structure.

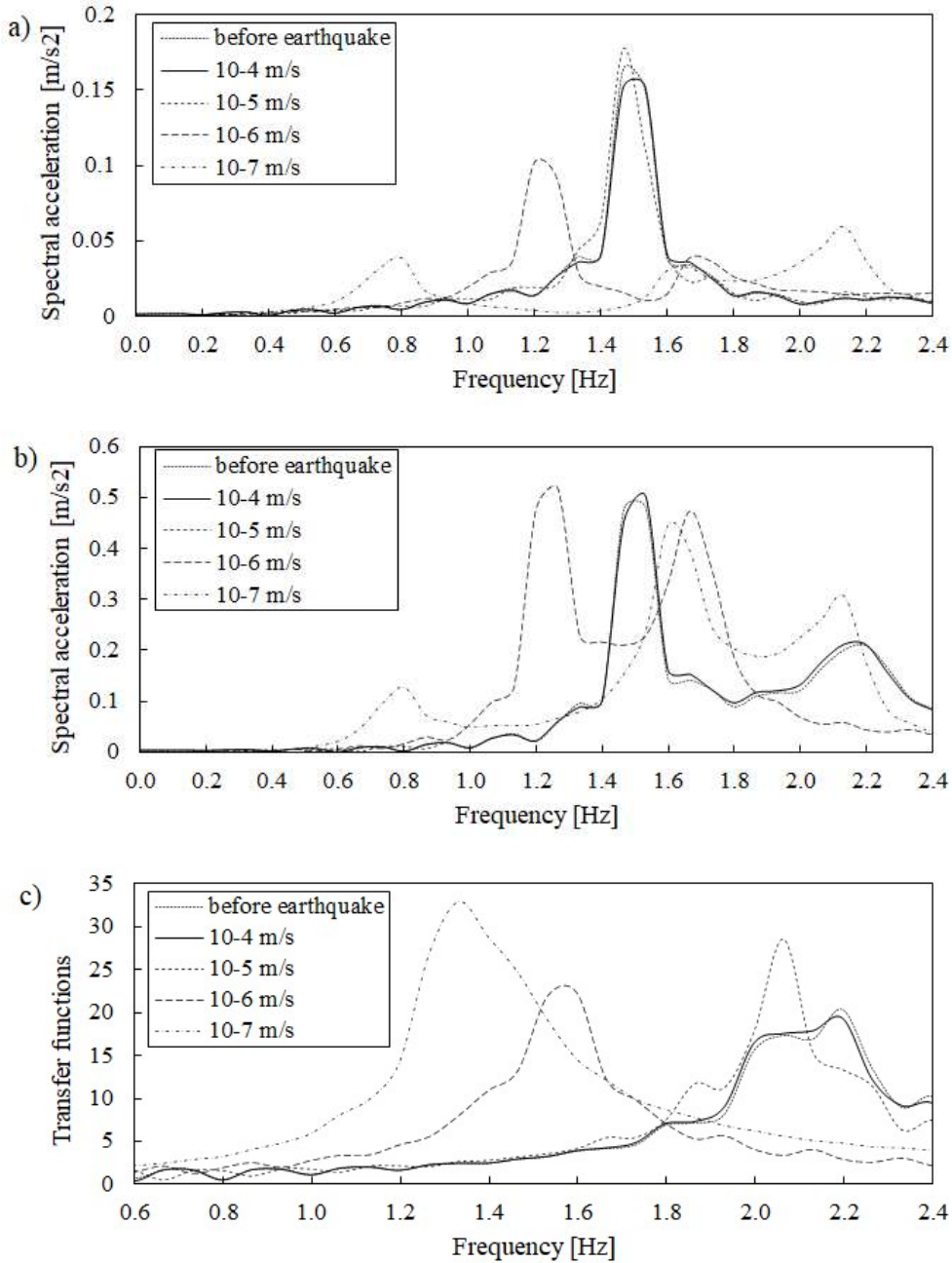


Fig. 19. Changes of natural frequency of soil and structure computed 30 minutes after earthquake as function of permeability of top soil layer: a) FFT for soil, b) FFT for structure, c) transfer functions for structure.

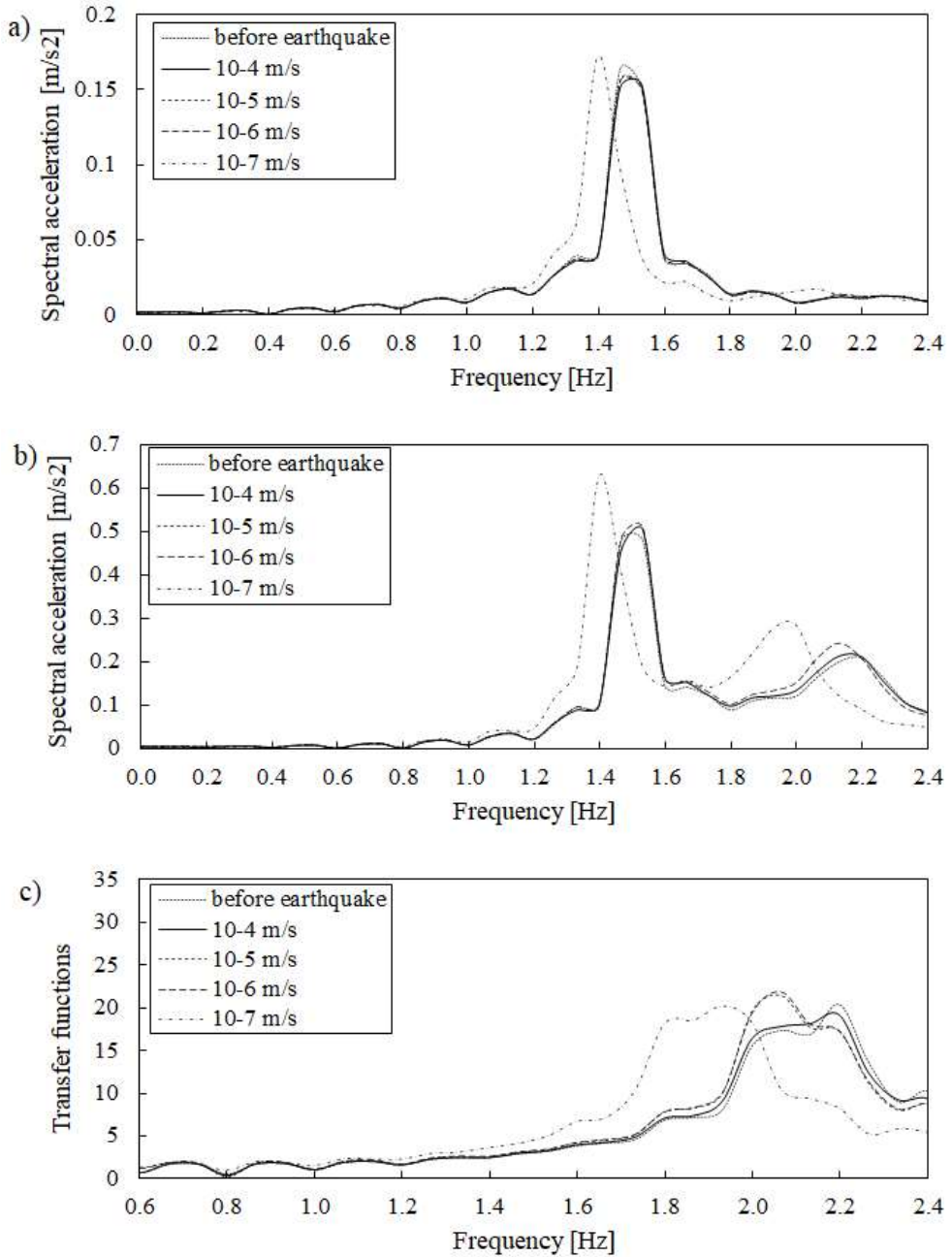


Fig. 20. Changes of natural frequency of soil and structure computed 20 hours after earthquake as function of permeability of top soil layer: a) FFT for soil, b) FFT for structure, c) transfer functions for structure.

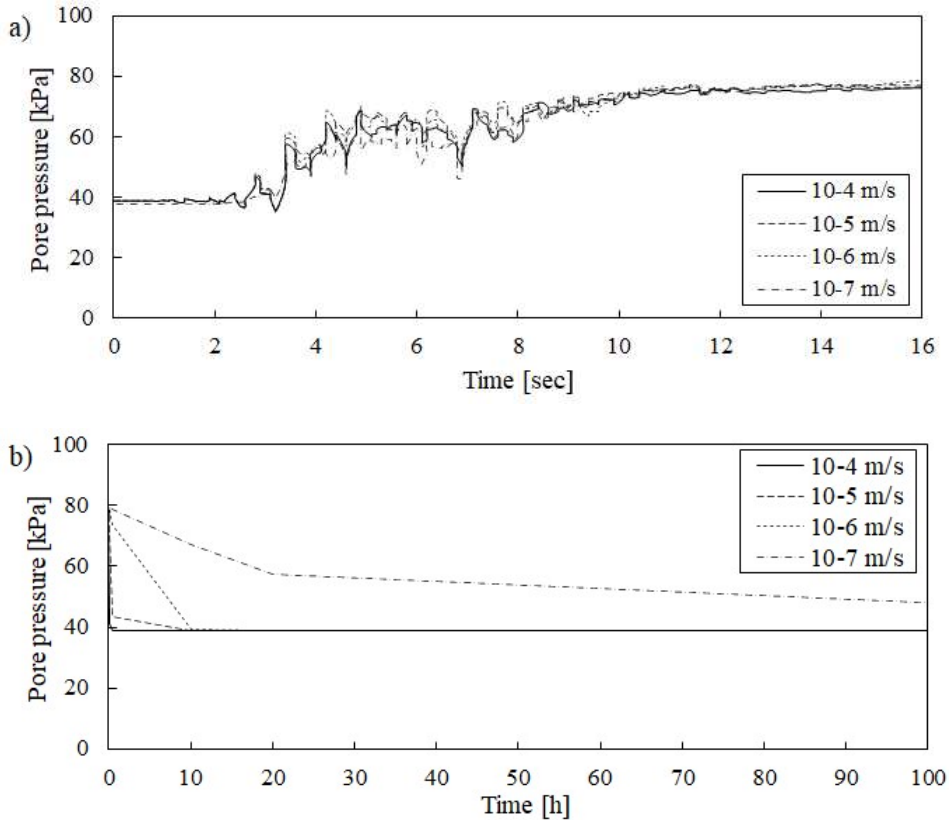


Fig. 21. Pore pressure generation (a) and dissipation (b) in reference point A as function of permeability.

Soil density

A case of very dense sublayers of saturated soil has been analysed in order to explore the effects of the relative density on the dynamic response of the structure. To this purpose, the initial void ratio of the three layers has been set to 0.6 to simulate very dense conditions. The permeabilities are equal to those of the “basic case” (Figure 1).

In contrast with the “basic case” including dense and medium dense sand, very dense sand leads to a slight increase of the natural frequency of the structure as shown in Figure 22. This effect is explained in Figure 23 which shows an increase in effective stress (due to a concurrent decrease of pore pressure) which is visible at the reference point A’ (at 2m depth) from 12kPa to 27kPa. This effect leads to the stiffening of the upper soil layer and to an increase of the natural frequency of the structure from 2.2Hz to 2.4Hz. On the other hand, the mean effective stress at the reference point B and C

decreases slightly and this is reflected in the calculated natural frequency of the soil column which also decreases slightly (the stiffening effect of the top soil layer is not sufficient to overcome this effect). Noticeably, the natural frequency of the structure does not return to its initial values even after 20h. This effect is achieved due to an increase in the lateral in-plane component of the effective stresses near the structure as shown on Figure 25.

Generally, the cumulative negative pore pressure excess in undrained seismic loading on dense sand may appear unexpected. Typically, laboratory simple shear tests performed at constant shear stress ratios show an increase of pore pressure (and thus a reduction in effective stresses), even for dense sand. However, in dense or very dense sand, the combination of partial drainage occurring at soil top, the erratic amplitude of shear strains, and the increase of horizontal stresses may lead to cumulative negative excess pore pressures. Further comments on the very dense case will be given in the discussion section.

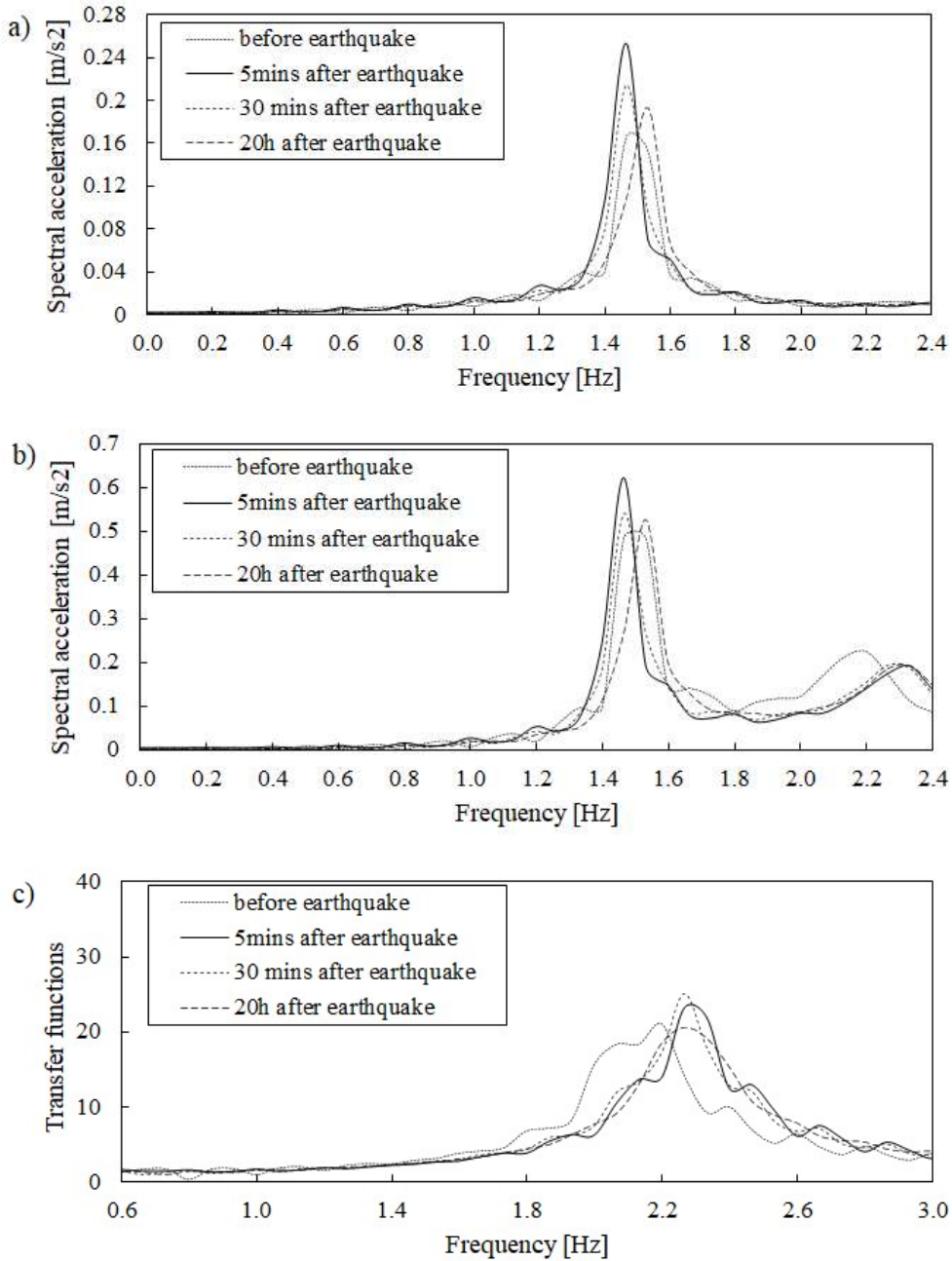


Fig. 22. Changes of natural frequency of soil evaluated: a) from FFT of free field motion, b) from FFT of motion of top of structure, c) from transfer functions of motion of top of structure and soil free field motion.

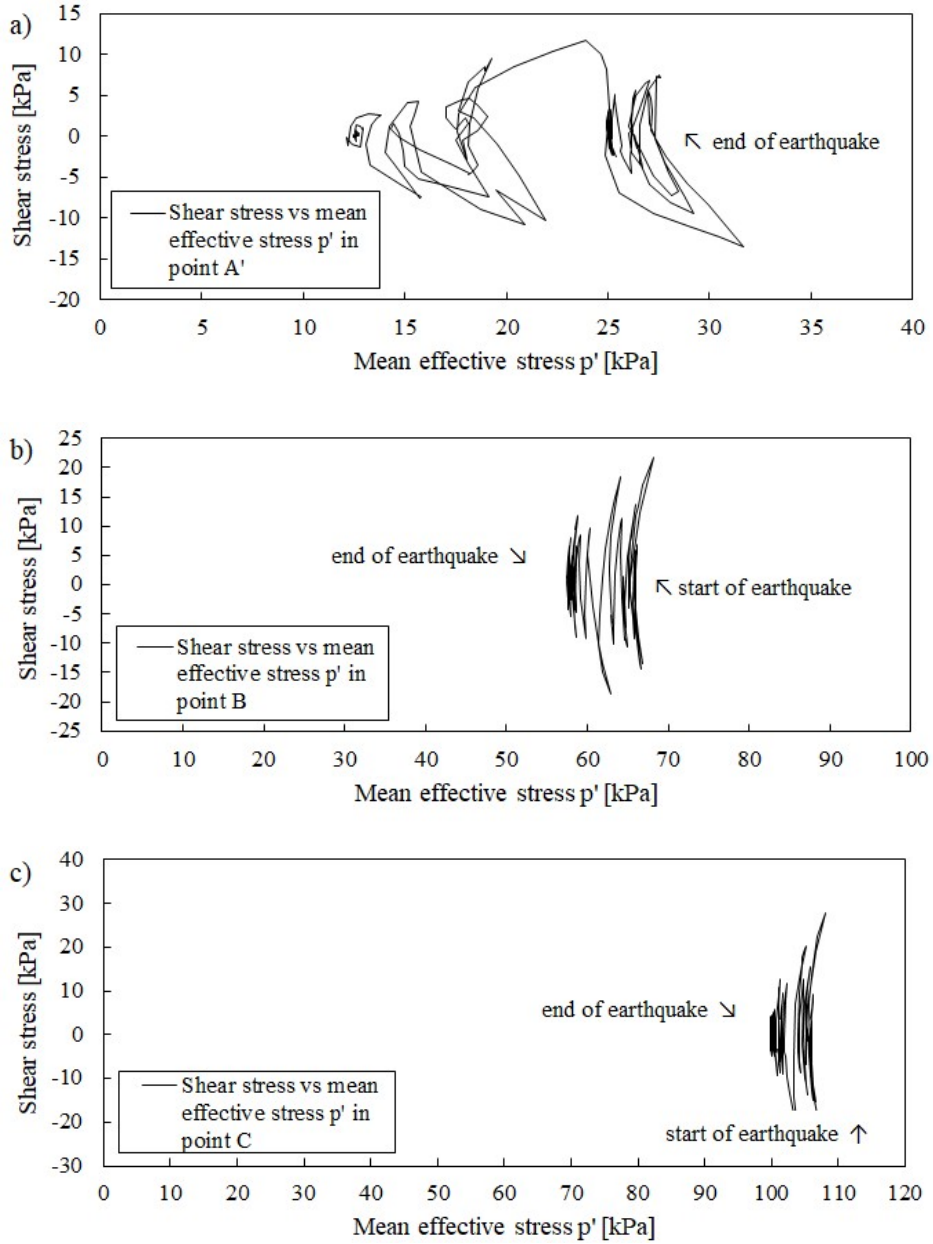


Fig. 23. Effective stress paths during shearing in reference points A', B and C.

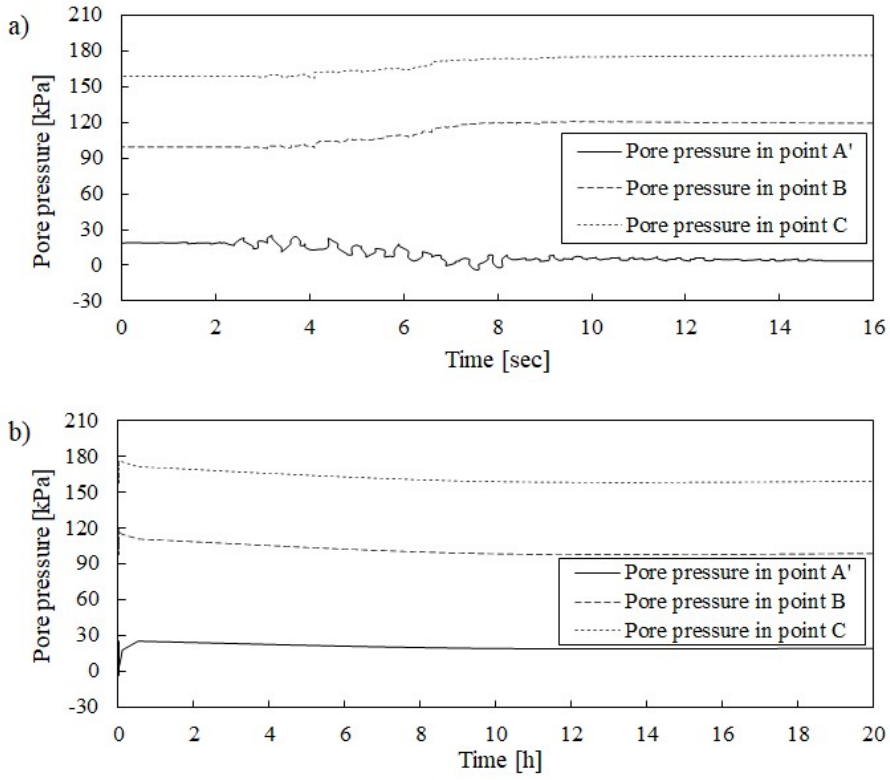


Fig. 24. Pore pressure generation (a) and dissipation (b) in reference points A', B and C during and after earthquake respectively.

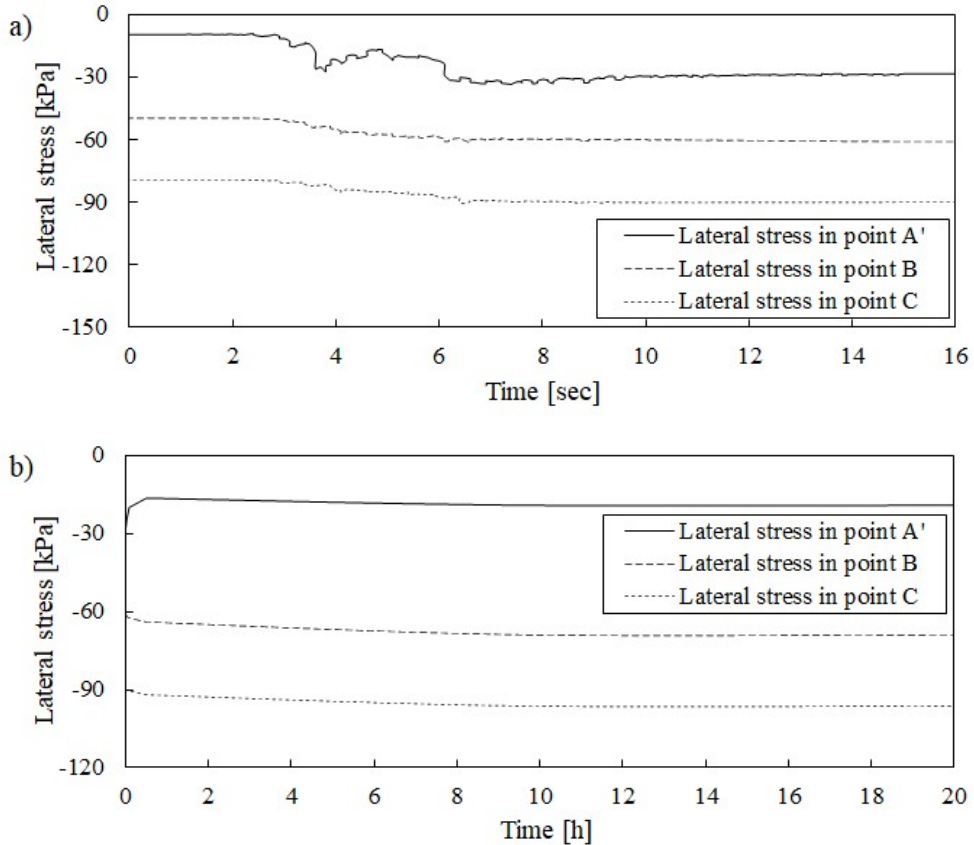


Fig. 25. Change of effective lateral in-plane stress component with time: a) during earthquake, b) during dissipation.

Input motion

This section investigates the impact of the input motion of the San Fernando earthquake on frequency wandering of the system shown on Figure 1. The San Fernando earthquake input motion (Figure 4) has longer duration and different frequency content than the one of the “basic case” (Figure 2).

Similarly, to the main study, the natural frequencies of the soil and the structure drop to 1.2 and 1.5 Hz, respectively. These values are larger than those obtained with the Emilia Romagna earthquake in the “basic case” where the maximum drop reaches 1.0Hz and 1.4Hz, respectively for the soil and for the structure. The smaller drop in the natural frequencies for the San Fernando input motion can be explained by the smaller amount of pore pressure generated by the San Fernando seismic motion with respect to the Emilia Romagna earthquake (Figure 27).

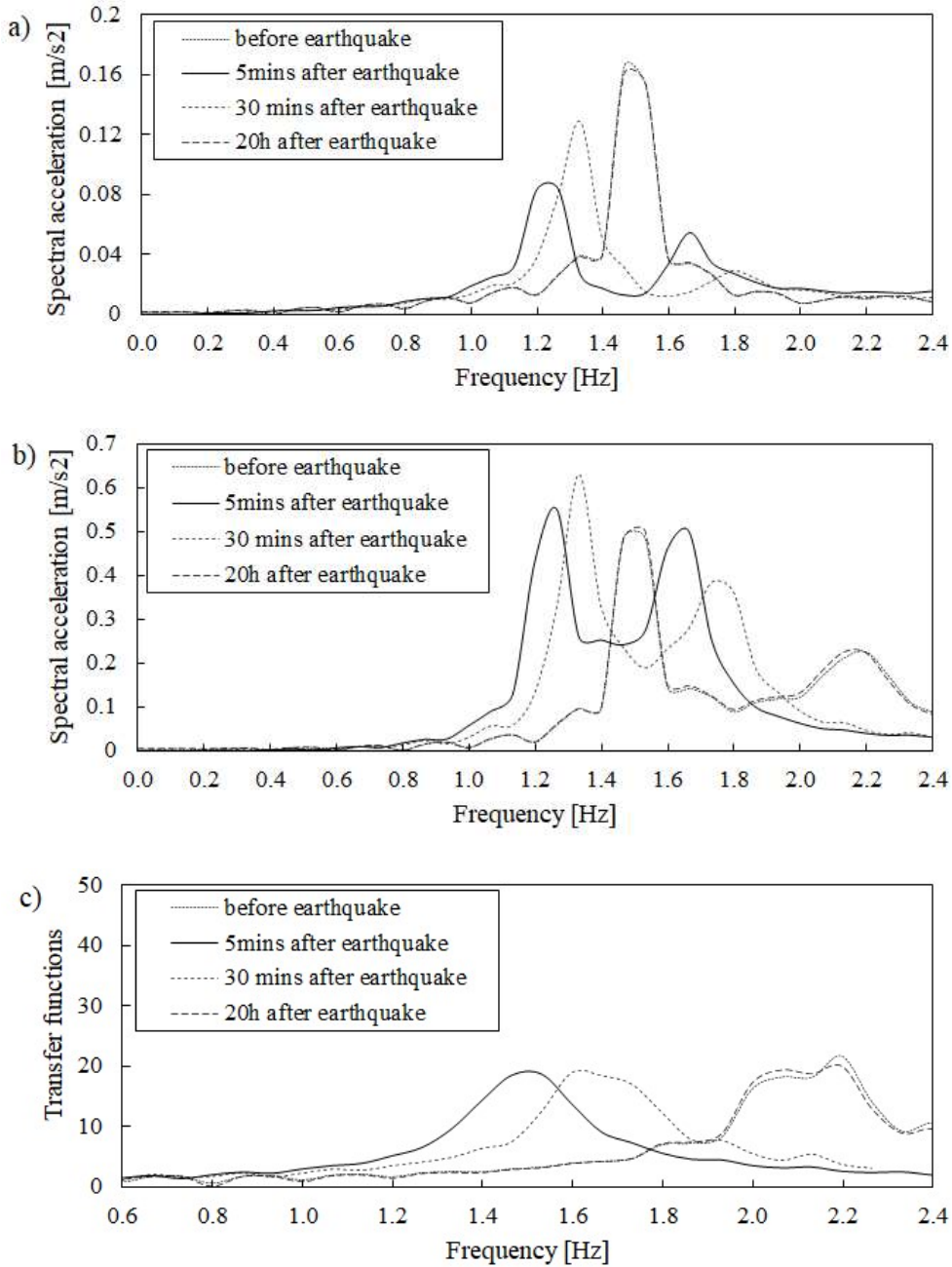


Fig. 26. Changes of natural frequency of soil evaluated: a) from FFT of free field motion, b) from FFT of motion of top of structure, c) from transfer functions of motion of top of structure and soil free field motion.

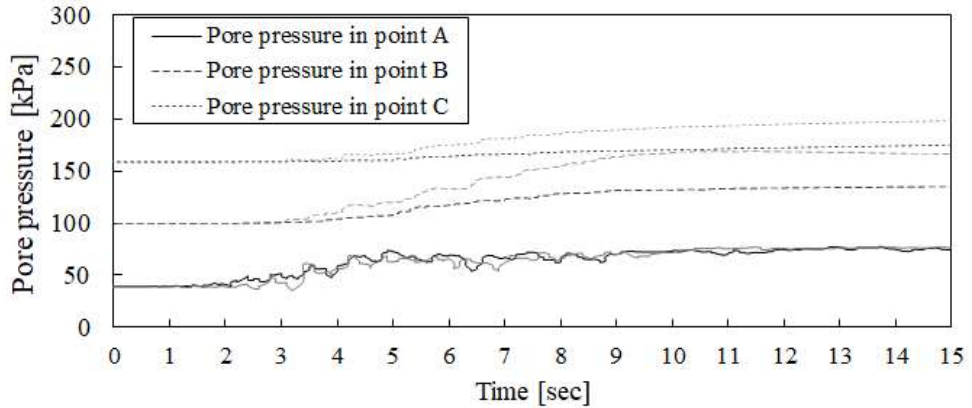


Fig. 27. Pore pressure generation in reference points A, B and C during earthquake (black -San Fernando earthquake, grey -Emilia Romagna earthquake).

Slender structure

This section investigates the impact of pore pressure generation on a slender type of structure of the compliant natural frequency of 1.3 Hz. Similarly, to the case of the “stocky” structure of the “basic case”, an initial drop in the value of the natural frequency and a gradual return to the initial value with time is observed (Figure 28). This is expected since the structure is elastic, and it is the soil that induces changes in the natural frequency of the structure. To sum up, the effect of frequency wandering happens in both, stocky and slender, types of structures.

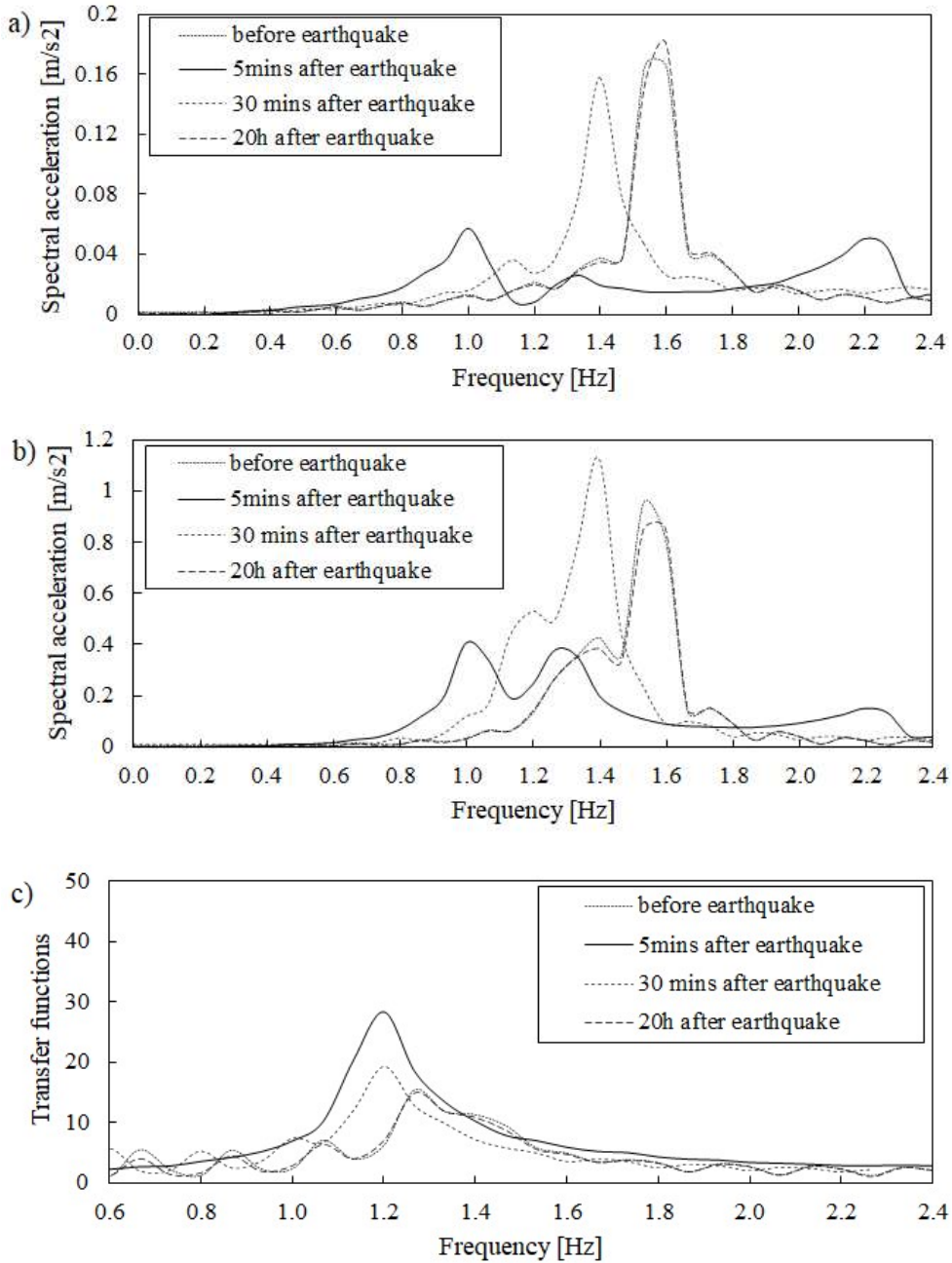


Fig. 28. Changes of natural frequency of soil evaluated from: a) FFT of free field motion, b) FFT of motion of top of structure, c) transfer functions of motion of top of structure and soil free field motion.

Time history with aftershock

The following section considers a case in which a strong aftershock is included in the time history. The time between the main shock (Figure 2) and the aftershock (Figure 5) is one hour, which is representative of the Emilia Romagna earthquake in 2012. The results on Figure 29 to 31 show clearly that the aftershock arrives before the full dissipation has taken place, thus the structural dynamic characteristics during the aftershock are different from what would be anticipated prior to the earthquake. Namely, the natural frequency of the structure drops to 1.4Hz, 5 minutes after the earthquake, returns to 1.65Hz 1h later just before the aftershock, and subsequently is reduced to 1.55Hz due to the aftershock (Figure 29 and 30). Figure 31 shows that some additional pore pressure is generated during the aftershock. However, this is less than the maximum pore pressure generated during the main event, thus, the drop in the natural frequency due to the aftershock does not reach the minimum value computed due to the earthquake. For completeness, Figure 32 presents a case when the aftershock is applied only 5 minutes after the earthquake. In this case, one may observe that the natural frequencies of soil and structure are reduced below those indicated after the main earthquake.

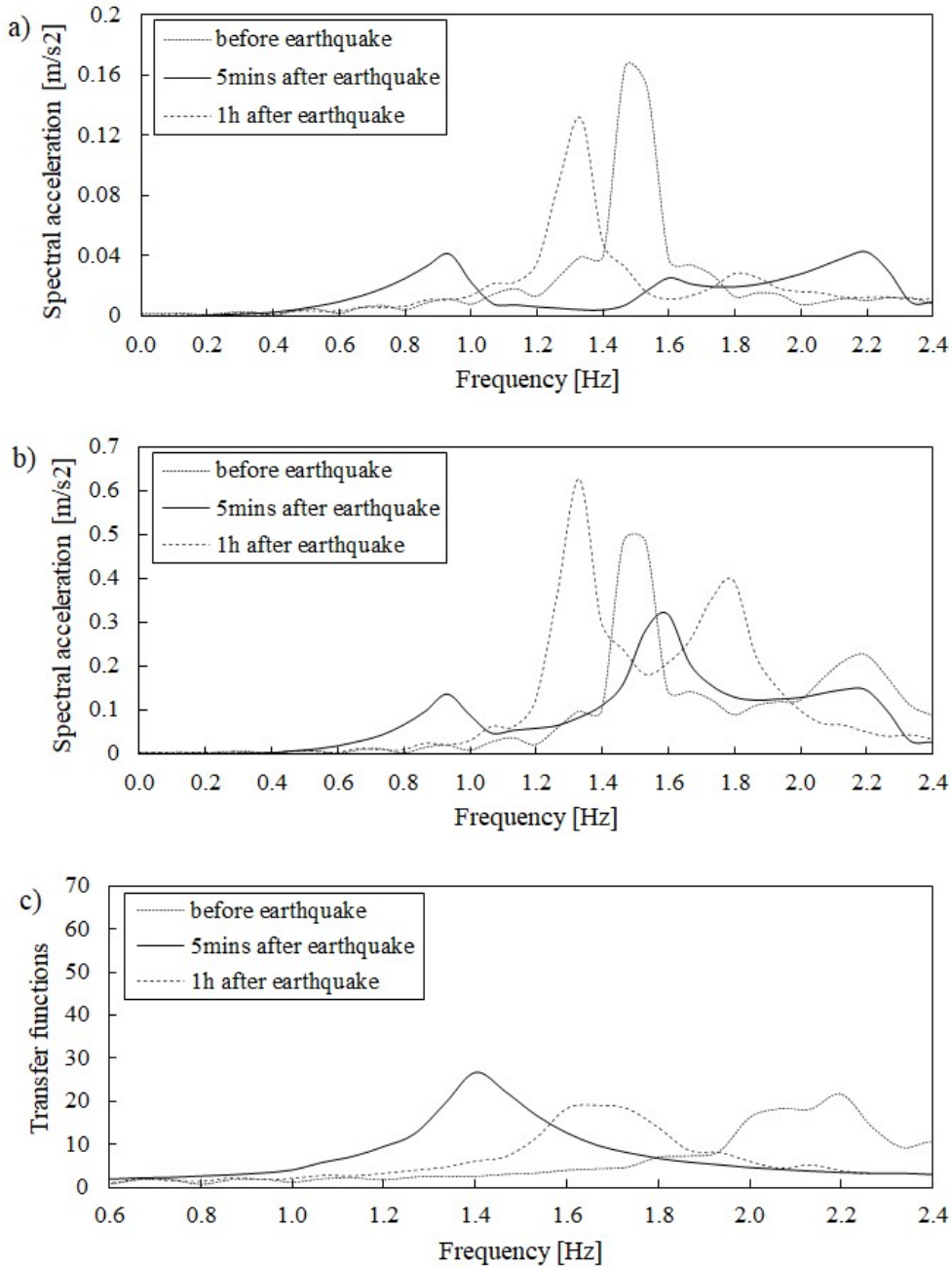


Fig. 29. Changes of natural frequency of soil and structure evaluated due to main shock: a) from FFT of free field motion, b) from FFT of motion of top of structure, c) from transfer functions of motion of top of structure and soil free field motion.

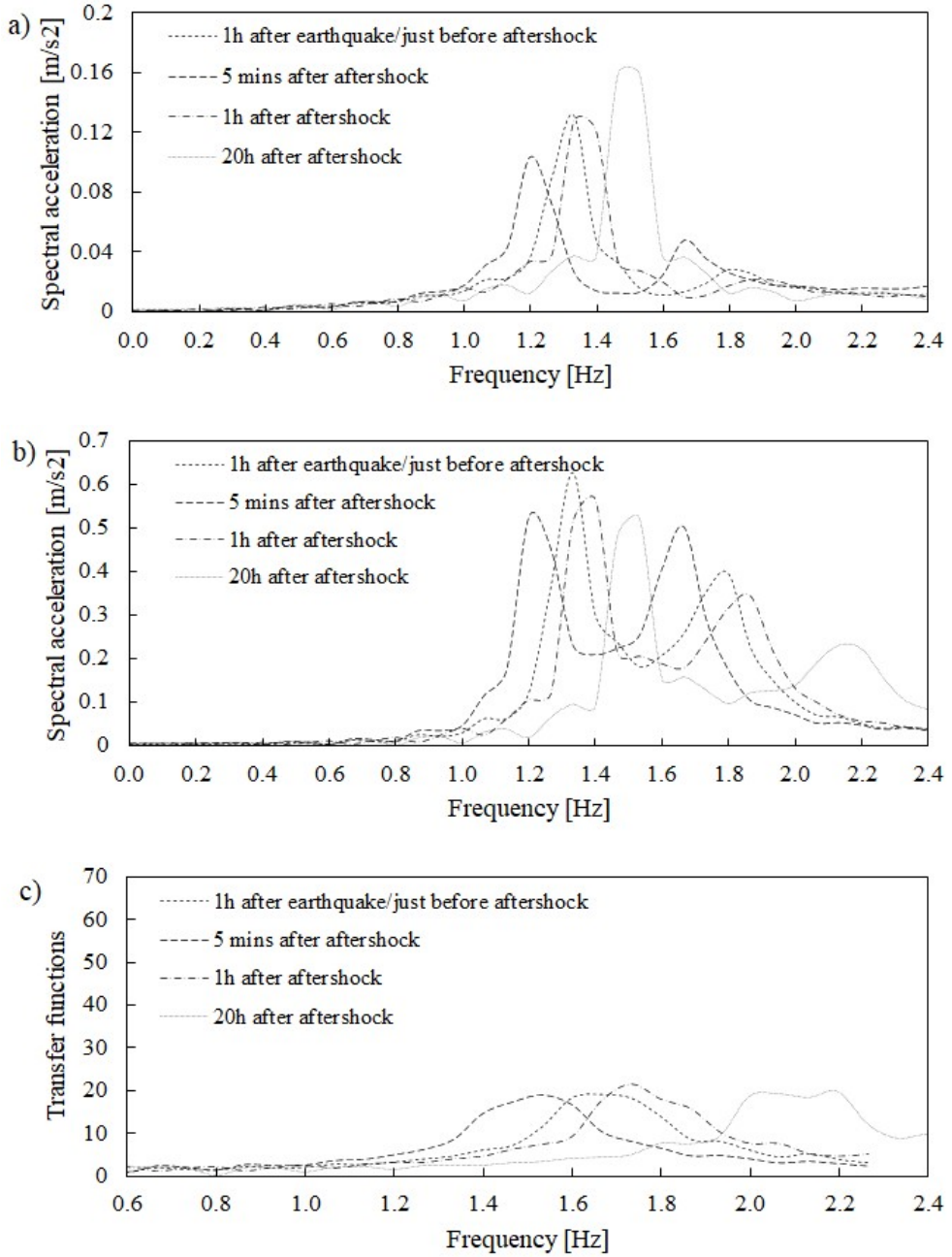


Fig. 30. Changes of natural frequency of soil and structure evaluated due to aftershock: a) from FFT of free field motion, b) from FFT of motion of top of structure, c) from transfer functions of motion of top of structure and soil free field motion.

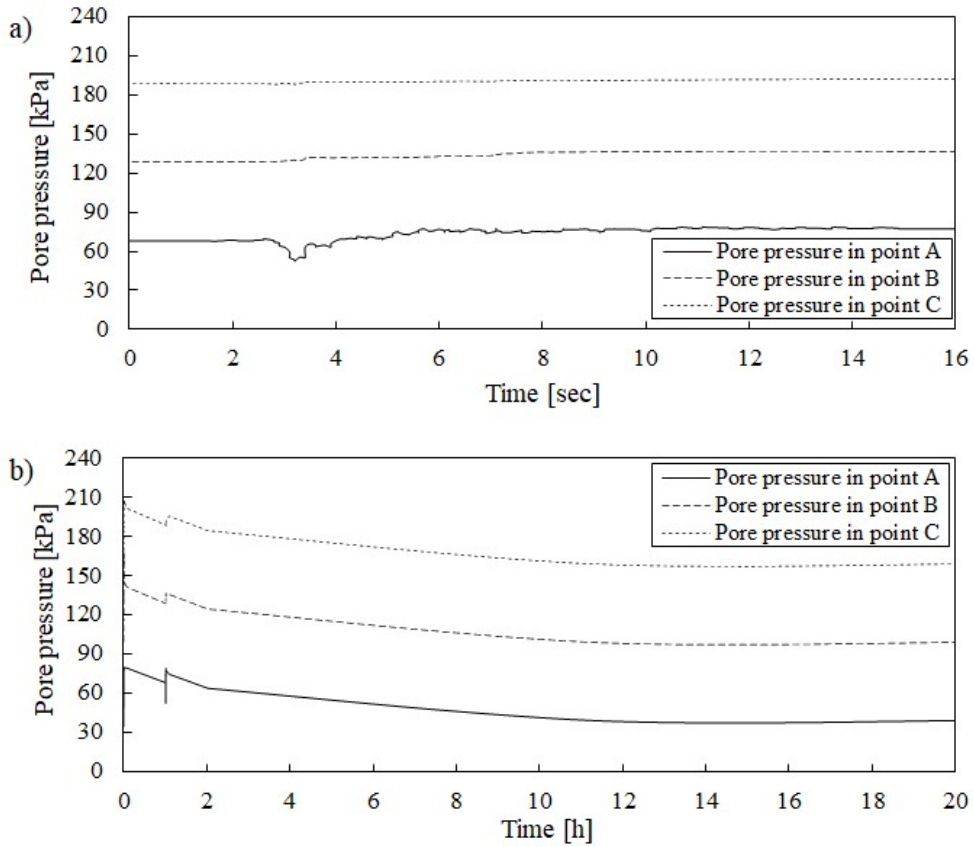


Fig. 31 Pore pressure generation (a) and pore pressure dissipation (b) in reference points A, B and C during and after aftershock respectively.

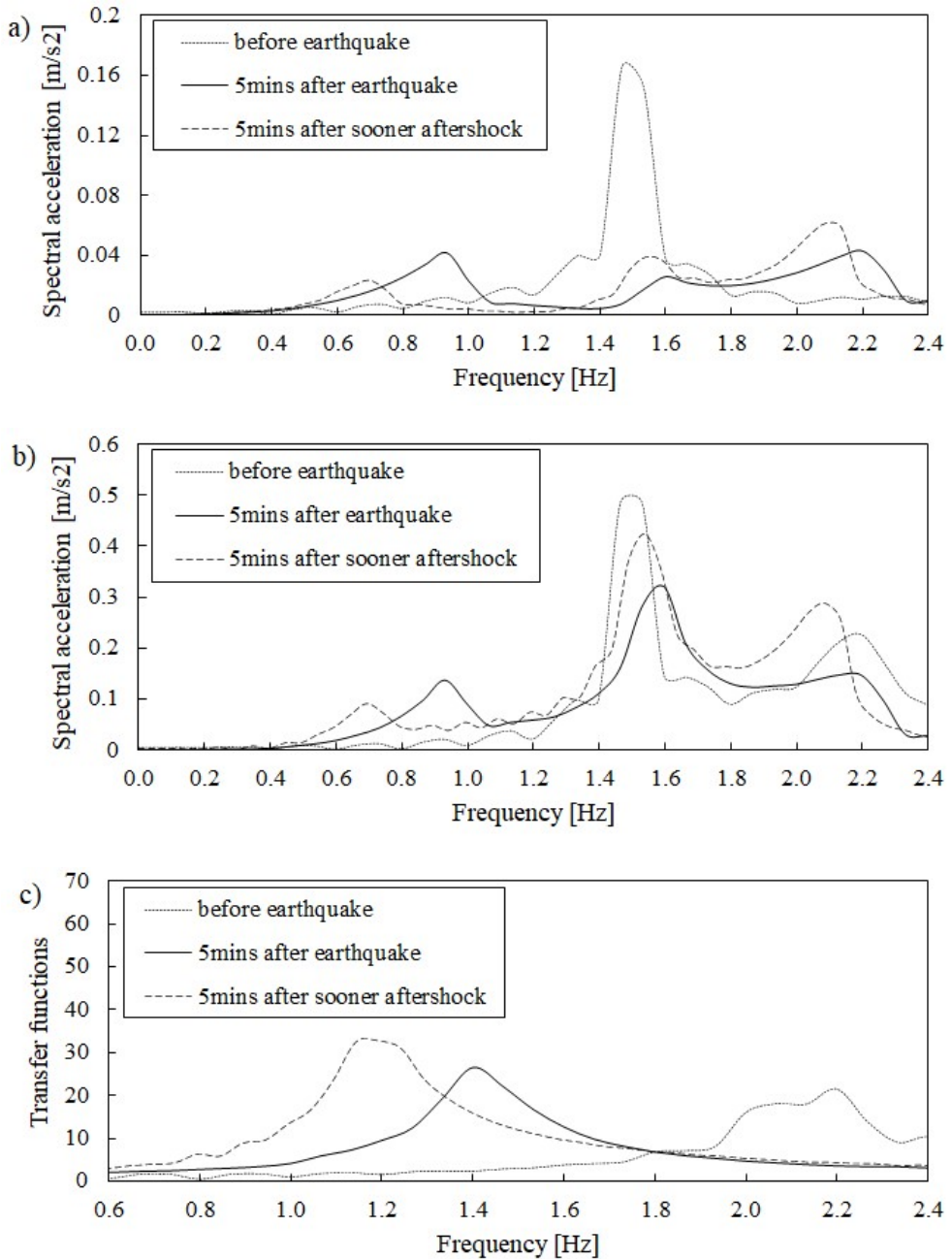


Fig. 32. Changes of natural frequency of soil and structure evaluated for aftershock applied 5 minutes after main event: a) from FFT of free field motion, b) from FFT of motion of top of structure, c) from transfer functions of motion of top of structure and soil free field motion.

5. Discussion

The simulations presented above show the clear impact of pore pressure generation on natural frequency wandering of structures. The general trend is independent of structure types or input motions. It has been shown that the natural frequency of the system returns to its initial value with time (if negligible soil plastic strains and changes in soil stress state have been developed). This study is focused on granular soil and the time required for the return to the initial conditions varied between 5 min (coarse material with large permeability) and 10 days (for less permeable soils and long drainage paths).

In this work, the reduction of the natural frequency turned out to be as large as 30% (from 2.2Hz to 1.5Hz). The literature gives examples of temporary drops in field measurements as large as 15% (Ceravolo et al., 2017), 20% (Clinton et al., 2006) up to 50% (Trifunac et al., 2001a; 2001b). In the latter study, the natural frequency was evaluated during the earthquake, therefore including also amplitude dependent effects (i.e. reversible nonlinearities in soil and structure). The study presented here has not considered dynamic identification during earthquakes, although further drop in natural frequencies would be expected (due to soil nonlinearity in addition to pore pressure excess).

Interestingly, the pore pressure build-up can also cause temporary stiffening effect in soil, therefore, increasing the system stiffness and the structural demand of a structure (the latter can likely be detrimental). This is in contradiction with the common expectations that the soil impact on structures leads only to softening of the system response. For example, as shown in the parametric studies of this chapter, for the very dense sand case, strong dilative behaviour is expected, thus leading to negative pore pressure excess accompanied by an increase in lateral effective stresses. Similar stiffening effect of dense sand on structural dynamic response due to cumulative negative pore pressure excess was suggested by Dakoulas & Gazetas (2008) and was associated to an increased rotation of a structure, as observed also in centrifuge tests by Lee (2005). Corciulo et al. (2017) also predicted cumulative negative excess pore pressure generation and an increase in the natural frequency of an offshore wind turbine in their numerical studies explaining this effect by crossing the phase transformation line (i.e. dilation effect). An unexpected increase in the natural frequency of a structure due to soil-structure interaction effects was presented by Trifunac et al. (2001a, 2001b) but no explicit explanation was given. Partial drainage in field conditions and erratic shear amplitude may lead to this sort of effect. On the other hand, to the author's knowledge, laboratory tests do not usually present an accumulation of negative pore pressure excess in cyclic loading (even in dense sand). Therefore, some experimental studies on very dense sand subjected to cyclic loading within the range of small strains could help to validate the results obtained on very dense sand shown in Section 4.2 of this chapter.

The importance of the aftershocks on soil behaviour and delayed liquefaction phenomenon was already recognized by Sinatra & Foti (2015) for the Emilia earthquake sequence (Italy, 2012). They analysed soil of low liquefaction potential subjected to a sequence of aftershocks. The aftershocks gradually increased the pore pressure in soil, eventually leading to liquefaction during one of the aftershocks. Herein, the time history with an aftershock applied one hour after the main shock has shown an increase in pore pressure but the maximum value of excess pore pressure computed for the main earthquake is not reached. Thus, the most detrimental effects are observed just after the main event. On the other hand, the parametric studies on soil permeability show significantly lower pore pressure dissipation rates for low permeabilities ($k=10^{-7}$ m/s). This would have consequences for the aftershock, possibly leading to a further increase of pore pressure with respect to the main shock as per the study by Sinatra & Foti (2015), and consequently, to a further decrease of natural frequencies. Actually, applying the aftershock earlier in the time history (i.e. 5 minutes after the main event as shown in this chapter) results in the same effect, the natural frequencies are reduced even more, below the values indicated after the earthquake. Some previous studies of site response to a sequence of the main event and the following aftershocks seem to confirm such thinking. For example, the work of Trifunac et al. (1999) showed a significant period elongation for a strong aftershock (5.6M) twelve hours after the main shock (6.7M). The period elongation is even stronger than for the main event, thus, cannot be associated only with the amplitude effects.

The actual extent of buildings that could be affected by frequency wandering due to pore pressure generation is not known. However, bearing in mind that earthquakes often cause pore pressure changes on sites with saturated granular soils, the structural modal response on or nearby these sites is expected to be somehow affected, even if no clear sign of liquefaction might be observed at ground surface. Therefore, it can reasonably be expected that many buildings resting on granular soils can be potentially affected by the wandering of their natural frequency during and just after earthquakes.

The analyses conducted in this chapter focus on granular soils thus the dissipation is relatively fast. It would be interesting to conduct a similar study on clay soils and identify in the expected much longer dissipation time. The elementary school in Visso (Italy) could potentially be a good example to study as it was founded on cohesive soils.

The shown patterns in structural dynamic behaviour such as in this chapter could have important consequences in terms of post-earthquake structural damage assessment, which should consider the possibility of a temporal change in modal characteristic due to pore pressure generation. The change in the modal characteristics may not necessarily be associated with structural damage only and can be regained with time, thus the structural damage assessments should consider possible temporal changes due to soil effects.

The presented study has not been carried out for any specific site or building. The author presented in the past an idealized case for the hotel VN7SH (Kowalczyk & Gajo, 2020) although it was based on some crude assumptions due to lack of enough input data. To the best of the author's knowledge, there is no known example of a fully monitored structure where pore pressures have also been recorded during earthquakes. Therefore, no accurate site-specific study of an existing building was possible. Nevertheless, there are some buildings that could be the subject of a detailed investigation in the future in order to assess potential effects of pore pressure generation on the observed natural frequency wandering if more data was available. The buildings potentially experiencing this type of behaviour include those mentioned before, namely: the Millikan Library (Clinton et al., 2006), the school in Visso (Ceravolo et al., 2019), the hotel VN7SH (Trifunac et al., 2001a, 2001b) or the Hollywood storage building (Trifunac et al., 2001c). The explanation of the observed seismic frequency wandering for the last two buildings was attributed to the gap opening between the buildings and the surrounding soil, thus reducing the effective embedment of the buildings and their rotational stiffness. Later, the gap was assumed to close during aftershocks which could result in the regain of the initial stiffness. However, no field evidence or numerical study was provided to support this mechanism. Therefore, pore pressure generation presented in this study can be considered as an interesting alternative explanation for the observed changes in natural frequencies.

Finally, it is recognized that the idealized cases presented herein can only contribute to the discussion on the phenomena of seismic frequency wandering. It would be beneficial for the future to analyse a case study of a structure where full structural monitoring data is available, including pore pressure measurements and comprehensive dynamic characterization before, during and after the seismic events. A more advanced numerical model (potentially 3D) would also likely be needed. All these would allow for a proper quantitative investigation into the real contribution of soil and soil-structure interaction to the phenomena of temporary seismic frequency wandering.

6. Conclusions

This chapter has presented a potential explanation for the observed temporary natural frequency wandering of structures shortly after seismic events. It has been shown that pore pressure generation and simultaneous mean effective stress reduction in soil can contribute to the change of structural behaviour under seismic actions. These changes are of a temporary character and generally decrease the natural frequency of a structure. Seismic frequency wandering of structures has also been shown to be independent from the type of input motion or the type of structure.

The natural frequency of a simplified structure has been shown to return to its initial values due to pore pressure dissipation with time. The time of the regain of the initial natural frequency is determined by soil permeability and boundary conditions. A time history with an aftershock has shown that the structural behaviour before the seismic event, just after the main event, and just after the aftershock is different.

Further studies, including fully monitored structures, would be needed for quantitative validation of the findings of this chapter.

References

- Arai, H. (2006). Detection of subsurface vs recovery process using microtremor and weak ground motion records in Ojiya, Japan. *In Proceedings of the 3rd International Conference on Urban Earthquake Engineering*, 6-7 March, Tokyo, Japan.
- Argani, L., Kowalczyk, P. (2019). Some considerations about vertical ground motions modelling in earthquake engineering. *In Proceedings of the 7th International Conference of on Earthquake Geotechnical Engineering*, June 17-20, Rome, Italy.
- Barrios, G., Nanayakkara, V., de Alwis, P., Chouw, N. (2019). Effects of slenderness and fundamental frequency on the dynamic response of adjacent structures. *International Journal of Structural Stability and Dynamics*, DOI: 10.1142/S0219455419501050.
- Boulanger, R., Ziotopoulou, K. (2015). PM4Sand Version 3: A sand plasticity model for earthquake engineering applications. *Technical Report*.
- Ceravolo, R., Erlicher, S., Zanotti Fragonara, L. (2013). Comparison of restoring force models for the identification of structures with hysteresis and degradation. *Journal of Sound and Vibration* 332(26) 6982-6999.
- Ceravolo, R., Matta, E., Quattrone, A., Zanotti Fragonara, L. (2017). Amplitude dependence of equivalent modal parameters in monitored buildings during earthquake swarms. *Earthquake Engineering & Structural Dynamics* 46(14) 2399-2417.
- Ceravolo, R., De Lucia, G., Matta, E., Miraglia, G., Parodi, L. (2019). Accounting for soil-structure interaction in the calibration of monitored buildings. *In Proceedings of 7th International Conference on Computational Methods in Structural Dynamics and Earthquake Engineering*, June 24-26, Crete, Greece.
- Chiaradonna, A., Tropeano, G., d'Onofrio, A., Silvestri, F. (2018). Interpreting the deformation phenomena of a levee damaged during the 2012 Emilia earthquake. *Soil Dynamics & Earthquake Engineering* 124, 389-398.
- Clinton, J. F., Bradford, S. C., Heaton, T. H., Favela, J. (2006). The observed wander of the natural frequencies in a structure. *Bulletin of the Seismological Society of America* 96(1), 237-257.
- Corciulo, S., Zanoli, O., Pisano, F. (2017). Transient response of offshore wind turbines on monopoles in sand: role of hydro-mechanical soil behaviour. *Computers and Geotechnics* 83, 221-238.
- Cubrinovski, M., Ntritsos, N., Dhakal, R., Rhodes, A. (2019). Key aspects in the engineering assessment of liquefaction. *In Proceedings of the 7th International Conference of on Earthquake Geotechnical Engineering*, June 17-20, Rome, Italy.

Dakoulas, P., Gazetas, G. (2008). Insight into seismic earth and water pressures against caisson quay walls. *Géotechnique* 58(2), 95-111.

Dassault Systèmes (2019). Abaqus Standard software package.

de Silva, F., Piro, A., Brunelli, A., Cattari, S., Parisi, F., Sica, S., Silvestri, F. (2019). On the soil-structure interaction in the seismic response of a monitored masonry school building struck by the 2016-2017 Central Italy Earthquake. In *Proceedings of 7th International Conference on Computational Methods in Structural Dynamics and Earthquake Engineering*, June 24-26, Crete, Greece.

De Silva, L. I. N., Koseki, J., Chiaro, G., Sato, T. (2015). A stress-strain description of saturated sand under undrained cyclic torsional shear loading. *Soils and Foundations*. 55(3), 559-574.

Fioravante, V., Boldini, D., Crespellani, T., Grasso, S., Maugeri, M., Santucci de Magistris, F., Giretti, D., Capilleri, P.P., Dezi, F., Lanzo, G., Pagliaroli, A., Sica, S., Abate, G., Cavallaro, A., Facciorusso, J., Madiari, C., Rainieri, C., Silvestri, F., Aversa, S., Chamlagain, D., Ghinelli, A., Massimino, M. R., Tropeano, G., Vannucchi, G. (2013). Earthquake geotechnical aspects: the 2012 Emilia –Romagna Earthquake (Italy). In *Proceedings of the 7th International Conference on Case Histories in Geotechnical Engineering and Symposium in Honor of Clyde Baker*, April 29- May 4, Wheeling (Chicago), USA.

Gajo, A., Muir Wood, D. (1999a). Severn-Trent sand: a kinematic hardening constitutive model for sands: the q-p formulation. *Géotechnique* 49(5), 595-614.

Gajo, A., Muir Wood, D. (1999b). A kinematic hardening constitutive model for sands: the multiaxial formulation. *International Journal for Numerical and Analytical Methods in Geomechanics* 23(9), 925-965.

Gajo, A. (2010). Hyperelastic modelling of small-strain stiffness anisotropy of cyclically loaded sand. *International Journal for Numerical and Analytical Methods in Geomechanics* 34(2), 111-134.

Gajo, A. (2018). Subroutine for a user-defined finite element with implemented constitutive law of the Severn-Trent sand model.

Gajo, A., Argani, L. (2020). New insights in seismic vertical ground motion modelling with u-p and u-U formulations. (*In preparation, title to be confirmed*).

Haigh, S.K., Ghosh, B., Madabushi, S.P.G. (2005). The effect of time step discretisation on dynamic finite element analysis. *Canadian Geotechnical Journal*, 42(3), 957-963.

Kallehave, D., Thilsted, C.L., Diaz, A.T (2015). Observed variations of monopile foundation stiffness. In: *Proceedings of the 3rd International Symposium on Frontiers in Offshore Geotechnics*. CRCPressLLC; 717–722.

Kementzetzidis, E., Versteijlen, W. G., Nernheim, A., Pisano, F. (2018). 3D FE dynamic modelling of offshore wind turbines in sand: natural frequency evolution in the pre- to after-storm transition. *In Proceedings of the 9th European Conference on Numerical Methods in Geotechnical Engineering (NUMGE 2018)*, June 25-27, Porto, Portugal.

Kementzetzidis, E., Corciulo, S., Versteijlen, W. G., Pisano, F. (2019). Geotechnical aspects of offshore wind turbine dynamics from 3D non-linear soil-structure simulations. *Soil Dynamics & Earthquake Engineering* 120, 181-199.

Kowalczyk, P., Gajo, A. (2020). Effects of pore pressure on wandering in structural natural frequency. *In Proceedings of the 16th International Conference of the International Association for Computer Methods and Advances in Geomechanics*, July 1-4, Torino, Italy.

Lee, C. J. (2005). Centrifuge modelling of the behaviour of caisson type quay walls during earthquakes. *Soil Dynamics and Earthquake Engineering* 25, 117-131.

Lombardi, D., Bhattacharya, S. (2014). Liquefaction of soil in the Emilia –Romagna region after the 2012 Northern Italy earthquake sequence. *Natural Hazards* 73, 1749-1770.

Muciarelli, M., Bianca, M., Ditomasso, R., Gallipoli, M.R., Masi, M., Milkereit, C., Parolai, S., Picozzi, M., Vona, M. (2011). Far field damage on RC buildings: the case study of Navelli during the L’Aquila (Italy) seismic sequence, 2009. *Bulletin of Earthquake Engineering* 9(1), 263-283.

Oka, F., Kodaka, T., Kim, Y.S. et al. (2004). A cyclic viscoelastic-viscoplastic constitutive model for clay and liquefaction analysis of multi-layered ground. *International Journal for Numerical and Analytical Methods in Geomechanics* 28(2), 131-179.

Puglia, R., Ditomasso, R., Pacor, F., Mucciarelli, M., Luzi, L., Bianca, M. (2011). Frequency variation in site response as observed from strong motion data of the L’Aquila (2009) seismic sequence. *Bulletin of Earthquake Engineering* 9(3), 869-892.

Roth, S., Hutter, G., Muhlich, U., Nassauer, B., Zybell, L., Kuna, M. (2012). Visualization of User Defined Finite Elements with ABAQUS/Viewer. *Gacm Report*. 7,7-14.

Sinatra, L., Foti, S. (2015). The role of aftershocks in the liquefaction phenomena caused by the Emilia 2012 seismic sequence. *Soil Dynamics and Earthquake Engineering* 75, 234-245.

Todorovska, M., Al Rjoub, Y. (2006a). Plain strain soil-structure interaction model for a building supported by a circular foundation embedded in a poroelastic half-space. *Soil Dynamics and Earthquake Engineering* 26, 694-707.

- Todorovska MI, Al Rjoub Y (2006b). Effects of rainfall on soil-structure system frequency: examples based on poroelasticity and a comparison with full-scale measurements. *Soil Dynamics and Earthquake Engineering* 26, 708-717.
- Todorovska, M. (2009a). Soil-Structure System Identification of Millikan Library North–South Response during Four Earthquakes (1970–2002): What Caused the Observed Wandering of the System Frequencies? *Bulletin of Seismological Society of America* 99(2A), 626-635.
- Todorovska, M. (2009b). Seismic Interferometry of a Soil-Structure Interaction Model with Coupled Horizontal and Rocking Response. *Bulletin of Seismological Society of America* 99(2A), 611-625.
- Todorovska, M., Al Rjoub, Y. (2009). Environmental effects on measured structural frequencies – model prediction of short-term shift during heavy rainfall and comparison with full-scale observations. *Structural Control and Health Monitoring* 16, 406-424.
- Trifunac, M., Hao, T.Y., Todorovska, M. (1999). On reoccurrence of site-specific response, *Soil Dynamics and Earthquake Engineering* 18, 569-592.
- Trifunac, M., Ivanovic, S., Todorovska, M. (2001a). Apparent Periods of a Building I: Fourier Analysis. *Journal of Structural Engineering* 127(5), 517-526.
- Trifunac, M., Ivanovic, S., Todorovska, M. (2001b). Apparent Periods of a Building II: Time Frequency Analysis. *Journal of Structural Engineering* 127(5), 527-537.
- Trifunac, M., Todorovska, M., Hao, T.-Y. (2001c). Full-scale experimental studies of soil-structure interaction – a review. In *Proceedings of the 2nd U.S. -Japan Workshop on Soil-Structure Interaction*, March 6-8, Tsukuba, Japan.
- Watanabe, K., Pisano, F., Jeremic, B. (2017). Discretization effects in the finite element simulation of seismic waves in elastic and elastic-plastic media. *Engineering with Computers* 33, 519-545.
- Zhao, C., Koseki, J., Weichen, L. (2019). Local deformation behaviour of saturated silica sand during undrained cyclic torsional shear tests using image analysis. *Géotechnique* (<https://doi.org/10.1680/jgeot.18.T.017>).
- Zienkiewicz, O., Chan, A. H. C., Pastor, M., Schrefler, B. A., Shiomi, T. (1999). *Computational Geomechanics with special Reference to Earthquake Engineering*. John Wiley & Sons.

Summary

This thesis presented validation and application of the most advanced available sand constitutive models under various seismic loading conditions. The results were presented in Chapters 2, 3 and 4.

Chapter 2, based on advanced numerical studies, revealed the potential origin of higher harmonics typically observed in experimental acceleration records to be the result of soil nonlinearity. The mutual interpretation of numerical and experimental results led to the possible observation of fast elastic unloading waves and their effects, namely wave distortion and separation of the elastic part of a wave, in soil seismic behaviour. In addition, these findings were shown to be important in understanding: wave propagation in real earthquakes, soil-structure interaction and limitations of currently available numerical techniques. Although the origins of higher harmonics in spectral response were presented in an explicit way, the conducted numerical studies and experimental setups were shown to have their limitations, thus, some ideas on future studies were given in order to develop and quantify the findings of this thesis.

Chapter 3 presented the validation of two advanced soil constitutive models regarding their performance in simulating soil and soil-structure interaction under seismic loading conditions. The results were shown for various input motions and pile head and oscillator configurations. Structural response was indicated to be affected by higher harmonic generation in soil. This and other aspects of soil-structure interaction were typically reproduced with satisfactory accuracy by both constitutive models. When some inconsistencies were found, improvements in the formulation of the models were suggested in order to improve the numerical predictions in the future. Some doubts and uncertainties over the extend of the carried-out validation and ideas on the validation studies in the future were also briefly drafted.

Chapter 4 illustrated the application of one of the advanced soil constitutive models in the phenomena of seismic frequency wandering of buildings. It was shown that pore pressure generated during earthquakes causes such temporary frequency wanderings. Subsequent parametric studies presented explicitly the effects of soil permeability, soil density, type of input motion, type of structure and time history with aftershocks on the computed frequency wanderings and the time span of these wanderings. Future studies on monitored buildings were encouraged to develop further the findings presented in Chapter 4.

To sum up, this thesis showed in an explicit way validation and application of advanced soil constitutive models in various aspects, ranging from free field analysis to soil-structure interaction, from dry to saturated soil, from detailed comparisons with experimental data to high fidelity predictions on novel engineering problems. Therefore, the results presented in this thesis can be considered of substantial importance for the earthquake geotechnical engineering.

Epilogue

The epilogue in this thesis is an attempt to sum up the PhD experience and to encapsulate the effort level, the state of mind of the author during the course of the research, his pre-PhD expectations versus the PhD reality and the author's key observation. All coming somewhere from the chaos of his thoughts.

Some parts of this epilogue were written in mountains.

Some other parts were written on the Mesiano "terrazza" considered by the author as one of his offices.

There is no technical input to the thesis in this epilogue.

The "puzzles" presented in this epilogue are not very well connected with each other.

Effort level and state of mind

(Celva, Falesia la Spina overlooking sunset over the Brenta Group)

XP-Resilience workshop in Rome. It is now less than two months before the end of the 3rd year of the PhD program and the admission to the final stage of the PhD.

I have just left my hotel to look for a place for a dinner. Normally, when travelling, I would search for places full of people, best full of locals, this is always a clear indication of the food quality.

Tonight, I am going to a Thai restaurant, the one ... from yesterday. It perfectly suits my current priorities. The tables outside are occupied, instead, it is empty inside. And, most importantly, quiet.

A glimpse on the menu, and I remove my notes from the rucksack to let my mind to jump into the ocean of seismic waves.

(Malga Casnago, Puez Odle, Dolomiti)

It is the last XP-Resilience meeting for my group, again only some weeks before the end of the 3rd year of the PhD program.

Immediately after landing in Vienna I am heading to the recommended train link with the Vienna City Centre. When entering the platform, the train is already waiting there. What catches my attention is the repeated everywhere writing: "16 minutes to the City Centre". May seem little but when entering the train, I already know how I will use these 16 minutes (Figure 1).

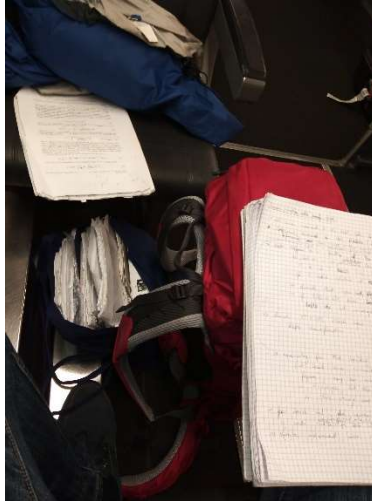


Fig. 1. Notes on my lap with a bag of papers in the background accompanying my 3-day stay in Vienna.

(Celva, the viewing spot towards Marzola, Povo and Trento on a very windy summer evening)

Running again! I got to a ticket machine, fast glance on the clock ... 8 minutes to the train departure! Perfect. Having experience from Italy, buying a ticket 2-3 minutes before the departure I am almost sure to get my train.

The machine spat the ticket. Running again... Platform 2? Where? Right, here it is.

The train is also already here. A glimpse of an eye on the train door before entering, the names Lille and Rennes scrolling rapidly on a small screen like trying to represent a TGV train linking east of France with its far west. Great! In the last moment but I got it again.

I am not even trying to find my coach. The Italian experience of fast trains is simple, the most quiet places in trains, thus perfect for work, are “bistro” compartments. This is also my choice today for the journey Paris-Rennes.

With a short delay, the train starts slowly crawling out of the underground station Paris Montparnasse.

While ordering a coffee and a snack, I spot a train officer and briefly ask about the exact time of the arrival to Rennes. He peeks at me suspiciously, asks for the ticket and taking some time to probably formulate a sentence in English says:

“Sir! This train is to Lille! You have to get off on the next station...”

.....

Now me taking time to receive and proceed this information.

“Ehi... And which is the next station?”

“Lille...”

(Caldonazzo from Calceranica)

I am driving again with my van on the way Italy-Poland, probably now for the last time. It will be a minimum 12-hour straggle to stay focused on the monotonous 1200km of a straight road with six-seven turns. The turns are the only moments requiring real focus. All the rest of the journey can be filled with some sort of entertainment. Typically, it was listening radio in the past.

Unfortunately, my van suffers from a particular issue (possibly typical for old cars). Every time it goes to a car service, three problems are removed but one new is born. The last time, following the change of the fuse box, the new problem became lack of radio....

Before I head on for the journey, I imagine nervously driving my 27-year old van with no radio for more than a thousand of kilometers.

Finally, here I am, driving the red van for all this long way. Surprising the help comes from ... the PhD. I spent all the journey thinking of the most recent results on unloading waves. When some interesting thought arrives, it ends up in my notepad (Figure 2) placed on the passenger’s seat.

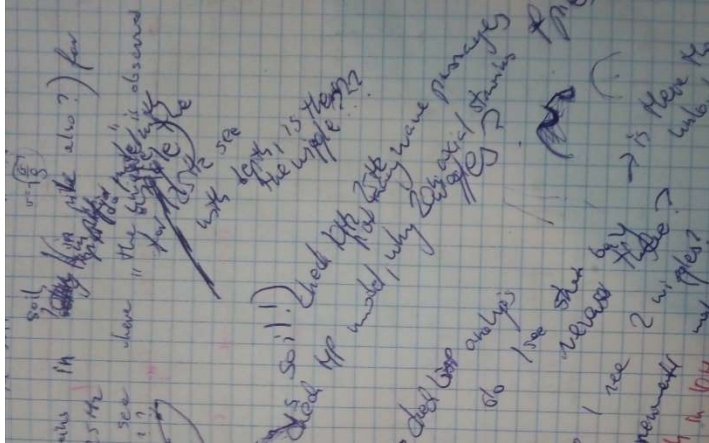


Fig. 2. Notes taken during driving to Poland (The notes are barely legible due to “blind” writing with eyes on road “supported” additionally by the fact that the van currently has also no internal lights...).

(Cima Marzola Sud between Trento and Valsugana)

Airport in Bergamo two years ago on the evening 25th May 2018. I was heading for the wedding of my cousin the day after.

I am already waiting in the queue for boarding. I noticed the boarding started later than scheduled so we are probably going to be late. In the meantime, I am exchanging emails on my mobile with my supervisor.

Prof. Gajo:

“(…) I realized that some stresses are positive (…)”

Me:

“NON RAGGIUNTA LA CONVERGENZA DEL EL. 441 (…)

stressi - 4842.27675710850 -2838.32158796387 -6726.01048833869 (…)”

Prof. Gajo:

“(…) I suspect that it might be due to substepping (…)”

Me:

“(...) maybe positive values come from umat (...)”

In the meantime, I find myself in front of the boarding desk. After intuitively passing the boarding pass to a flight attendant, she has raised her head up and says:

“*ddjhcbej sajeujxz*”

Me still thinking whether these values could be positive directly from umat.

The flight attendant:

“Signore, *jsakhhsda aklidan*”

Me:

“?”

The flight attendant:

“Excuse me, Sir. It is”

Me:

“Sorry?”

The flight attendant:

“It is not your flight. Your flight is from gate X. I think they called you. They are closing NOW! Hurry up! Gate no. X!”

So I run my fastest ever 100m on an airport ever just before the gates were closed, boarding as the last passenger...

But were those stresses positive because of the convention used in the umat?

(Polsa, 1550m, just below Bivacco Madonnina and overlooking Caldonazzo)

Leaving Mesiano now. It is almost 2am, certainly I am the last person in Mesiano, and I know it is Nicola who is today at the “portineria”. Nicola is a good soul of Mesiano in the night, taking care of each person left, each open door and each turned on light. He will never leave his desk knowing someone is still in the building. So, I cannot stay today until 4am as it happened a couple of times before.

I am approaching the book to sign out from the building. I am glimpsing towards Nicola. Since it is pretty late today it seems he is trying to have a nap in front of a computer as it happens sometimes if I am leaving very late. So, I am opening and closing the heavy bulky main door of Mesiano in the most quiet possible way. It takes literally something like one minute to slowly open and close it without any noise. Everything in order not to disturb Nicola.

Having left the building I am approaching slowly the main gate, thinking, whether at least this time, I managed to close the door so Nicola did not wake up, so I feel less guilty of my night shift working. In any case, I will leave the fortress of Mesiano. In my early times here, it happened to jump over the fence to enter or to leave the office outside the usual working hours. For the last couple of years, I resource myself to the Cuban way of opening and closing the gate (Camillo, 2018).

So here I am, right in front of the main gate of Mesiano. In this moment, the little light on the intercom starts flickering and I can hear the buzzer opening the gate.

So, Nicola again did not sleep? Or should I take even longer to close the bulky door next time?

The PhD experience in my case was not limited to the official working hours. I was swimming and diving in the ocean of seismic waves when waiting for a bus, during a train journey or even when sleeping. Sometimes, after waking up in the morning, I was not able to say if some thoughts were conscious or not.

Such dedication may be considered as a poor life balance. On the other hand, it is fascinating and rewarding to know that your mind explores ideas that probably have never been considered before.

Pre-PhD expectations vs PhD reality

Prior to joining the PhD program, my motivations for such a step were a desire to challenge myself and to finally excel something.

I believe I succeeded in terms of challenging myself although not having results for long during my research. However, the success needed enormous effort levels which I decided to increase during the course of my research and which were attempted to be described in the previous section.

Now I like the idea of combing this intellectual challenge and the arrival at the intellectual summit with climbing an 8a project (Marco!) and peaking up Monte Bianco (Gabri!) in some nearest future.

Excellence? I believe I only gained appreciation for the vast complexity of the world. I am not even close to any sort of feeling of having excelled something.

Professor Wood and his co-workers (see Wood et al., 2002, reference after Chapter 3) when introducing seismic geotechnical engineering cite an aphorism: “*Engineering is the art of modelling materials we do not wholly understand, into shapes we cannot properly analyse, so as to withstand forces we cannot properly assess, in such a way that the public has no reason to suspect the extend of our ignorance*”.

Following my PhD experience, I feel like this aphorism could not be more true. The author hopes that those who will read this thesis will not realize how much the author still does not understand. Note that even these words of non-technical character are added to this thesis after the thesis submission to the examination committee (just in case...).

Details in big picture

My observation is that the key point is to be able to see details and a big picture at the same time. It may sound banal, but I have seen many who struggle with such approach.

A line that makes a history. A dream. Fifteen meters of a slab with an initial roof and a traverse. In total almost thirty meters of grey limestone.

Details? Ankles, diet, twisting fingers in the first pocket on the slab, taking the “book crimp” with three fingers, jumping to a hidden pocket with one finger instead of two, repeating the moves in head, overcoming fear of falling, choosing partners, conditions.

It is like putting puzzles together. We find a piece here, a piece there and there, and we try to see how the pieces fit, or can they fit? Can we see a big picture yet? Or do we still need one or two more pieces to get a clear big picture? My thesis is an attempt of putting such “puzzles” together. I am sure some “puzzles” are still missing.

“Details in big picture” is not only about science or climbing. It is also about people around us. Single puzzles need to fit into a bigger picture. The message is placed here.

Sometimes it is difficult. Some people can put additional “fake” puzzles into the game but still “construct a façade of normalcy”. It is here, where the ability to see the big picture is so important. Only being able to see the big picture you realize that some puzzles might be “fake”. Once you know that, you can try to complete the picture using those “fake” puzzles. Just rearrange them into a new place in the big picture.

Science also helps here (see Hare, 1999, page 113).

Epilogue of epilogue

Science is not much different from climbing projects.

I never know when ideas will come. And if they come, it is less than 16 minutes.

I was lost during the PhD time many times. It did happen to think I had entered a “train” to “Rennes”, only later to realize that I was going opposite direction to “Lille”.

Wait a second... Am I actually sure this “train” now is to “Rennes”?

The end?

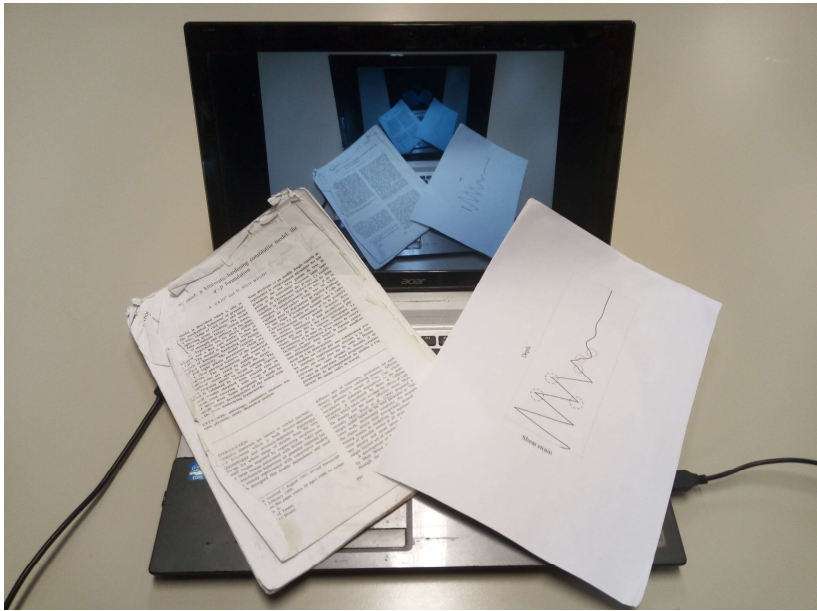


Fig. 3. The end?

Appendices

Appendix A

Additional numerical studies on higher harmonic generation

The additional studies for Chapter 2 in Appendix A are mainly for the 25Hz input motion of the maximum amplitude of 0.077g and investigate the impact of imperfect sine input motion, the physical presence of the shear stack and a bi-layered soil profile on higher harmonic generation presented in Chapter 2. Only the ST model has been used here as the response of all the models to S-wave propagation and their ability to higher harmonic generation has been found to be very comparable.

Note that citations in the Appendices are listed in the references at the end of the corresponding chapters.

1. Effect of imperfect sine input motion

This part of Appendix A shows numerical results when the input motion at the base of the soil column contains some higher harmonics being present (Figure A-1), i.e. in case of the chosen input motion some additional content of 50Hz harmonic could be observed at the base level. However, Figure A-2 shows that the impact of this higher harmonic can be considered negligible, as the odd harmonic 75Hz is generated at soil top in any case. For the case of the recorded input motion, some amount of the second harmonic can also be seen at the soil top, however, it is not amplified within the soil mass. Therefore, the higher harmonic generation within the soil mass can be fully attributed to soil nonlinearity and fast elastic unloading waves.

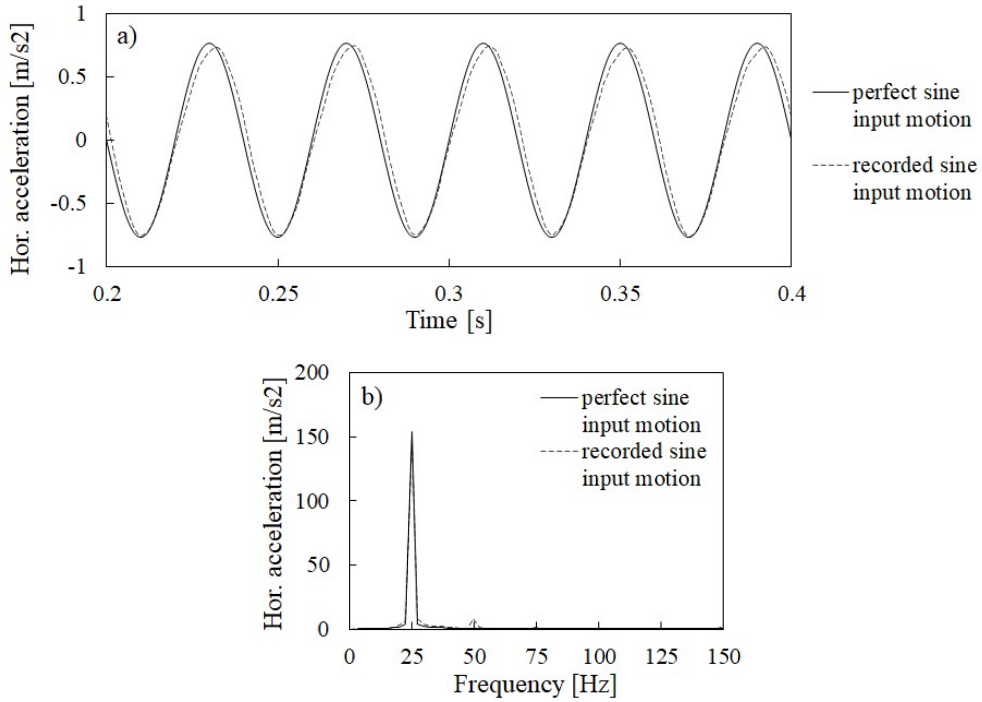


Fig. A-1. Applied acceleration time history (a) and spectral response (b) for perfect sine and recorded sine input motions.

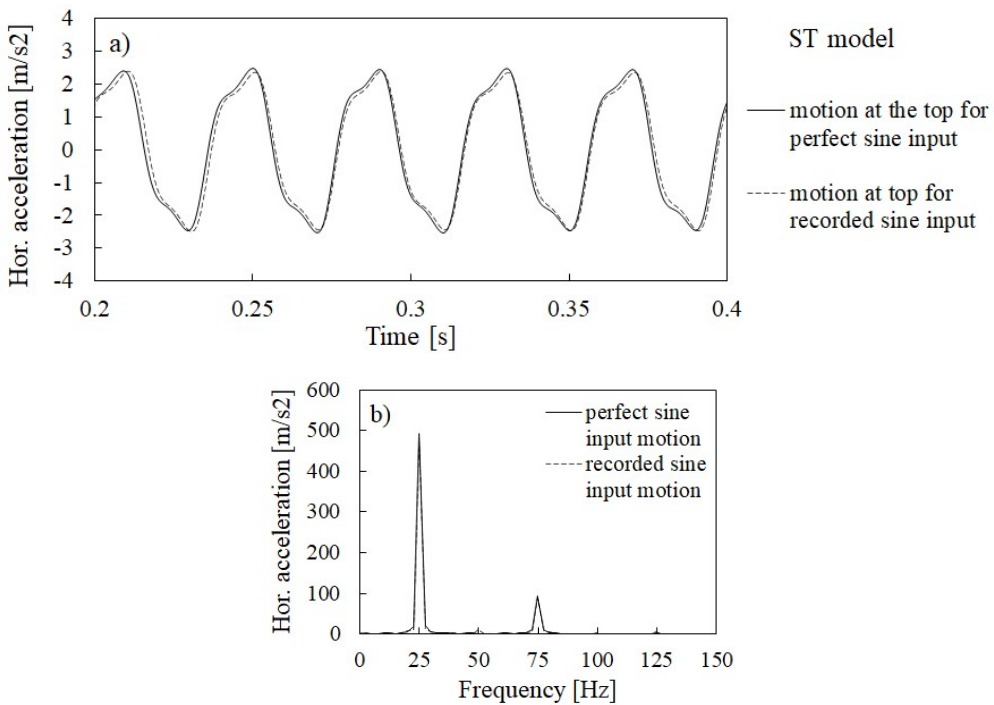


Fig. A-2. Computed acceleration time history (a) and spectral accelerations (b) at soil surface for perfect sine and recorded sine input motions.

2. Effect of shear stack

This part of Appendix A investigates the impact of the shear stack on soil behaviour, in particular on the generation of higher harmonics. Typically, numerical studies omit including shear stacks or laminar boxes (e.g. Bilotta et al., 2014). Some other studies say directly the impact of the shear stack is negligible (Gajo & Wood, 1997; Dietz & Wood, 2007). Herein, a trial is attempted to see the impact of the shear stack on soil behaviour, in particular on higher harmonic generation. The simulations have been carried out by a 1D model consisting of two columns representing soil and shear stack, respectively.

Shear stack has been modelled as “smeared” weight and stiffness over the shear stack dimensions similarly to the previous comparison (Gajo & Wood, 1997). The mass of the currently used shear stack in Bristol is around 132kg which includes the mass of aluminium stacks, rubber parts on the short side and aluminium filling sections on the long side. The density of the shear stack in the 1D model has been calculated as follows:

$$\rho = \frac{132}{(0.8 \cdot 1.2 \cdot 0.55)} = 250 \frac{kg}{m^3} \quad (1)$$

The stiffness has been chosen in a way to ensure that the first natural frequency mode is 6Hz as measured for the empty shear stack.

$$f = \left(\frac{1}{4H}\right) \sqrt{\frac{G}{\rho}} \quad (2)$$

$$G = (4 \cdot 0.8 \cdot 6)^2 \cdot 0.250 = 92kPa \quad (3)$$

The damping ratio is 3%. The damping parameters are: $\alpha=4.7124$, $\beta=0.000191$.

The accelerations are filtered as per other numerical and experimental data shown in this thesis. The results are shown in terms of accelerations, relative displacements and spectral response on Figures A-3 and A-4. Top surface of the soil and mid-height have been considered.

The results are presented for two input motions of 25Hz, the first one of the maximum accelerations of 0.037g and the second one of the maximum acceleration of 0.077g. The results on Figure A-3 show the accelerations and relative displacements calculated at soil surface and at mid-height for the lower acceleration input motion. It can be observed that the motion is amplified more when shear stack is present. The

explanation to that is the increased inertia, coming from the shear stack mass, which acts laterally on the soil. On the other hand, the impact of the shear stack stiffness is negligible here, it is still the soil that controls the response. However, the results shown on Figure A-4 present that the increased input motion causes the shear stack stiffness to affect the response of the soil. This could happen, as for stronger input motions, the soil reaches higher strain levels, thus its stiffness reduces below the stiffness of the shear stack, which, in this case, starts to constrain the soil movement. However, most importantly, in terms of generated harmonics, the results for both cases, without and with the shear stack, do not seem to be affected (note that the signal length taken to evaluate the spectral response is less in this Appendix than that in Chapter 2, thus the amount of harmonics is also less than in Chapter 2).

The short study above, based on a very simplified numerical modelling approach, shows that there can be some impact from the shear stack on soil. However, most importantly, the higher harmonic generation is not affected by the presence of the shear stack. The general impact of the shear stack is not significant either, therefore, further work in this thesis does not include shear stack modelling. This in line with common assumption in numerical studies where the presence of the shear stack is neglected. As a side note to the above conclusions, it would be interesting to carry out a full 3D analysis of the soil and detailed shear stack geometry being included to identify more realistically the impact of the shear stack on soil. This would allow further clarification and possibly going back to experimental work in a longer shear stack (i.e. 5m in case of the Bristol facility), where the effect of the boundaries are expected to be reduced.

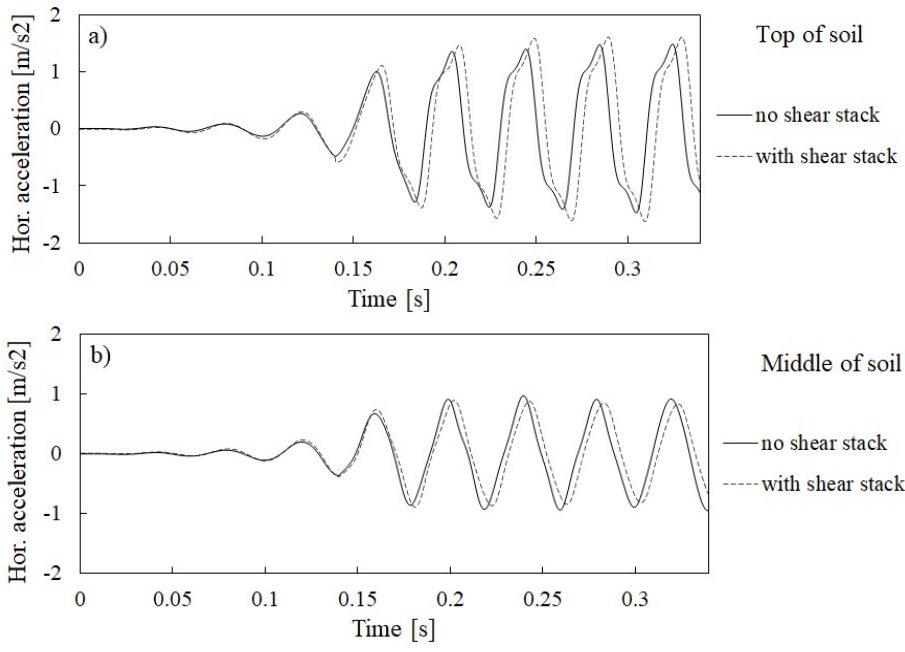


Fig. A-3. (continuation on the next page)

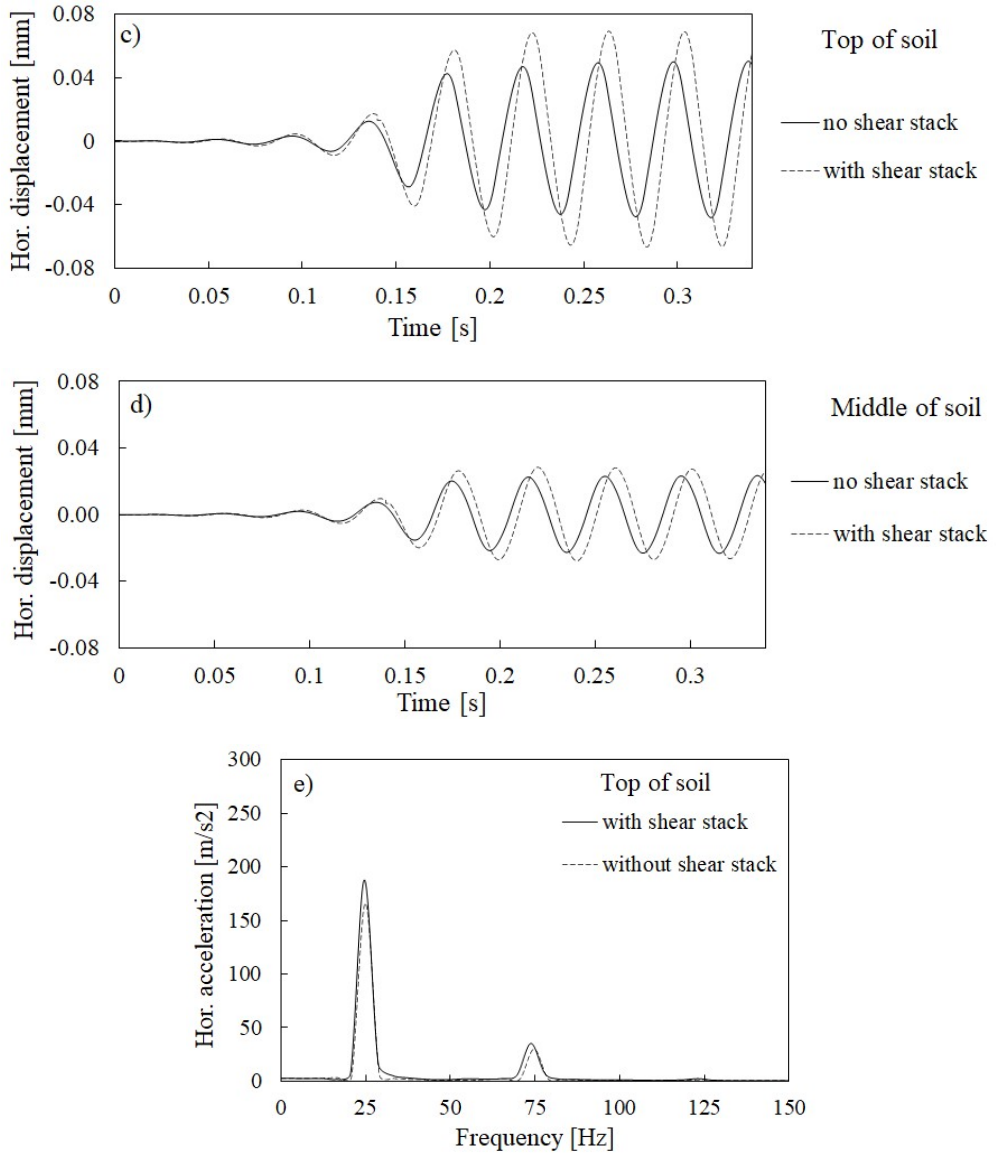


Fig. A-3. Computed accelerations, displacements and spectral accelerations with and without shear stack for 25Hz input motion of maximum amplitude of 0.037g.

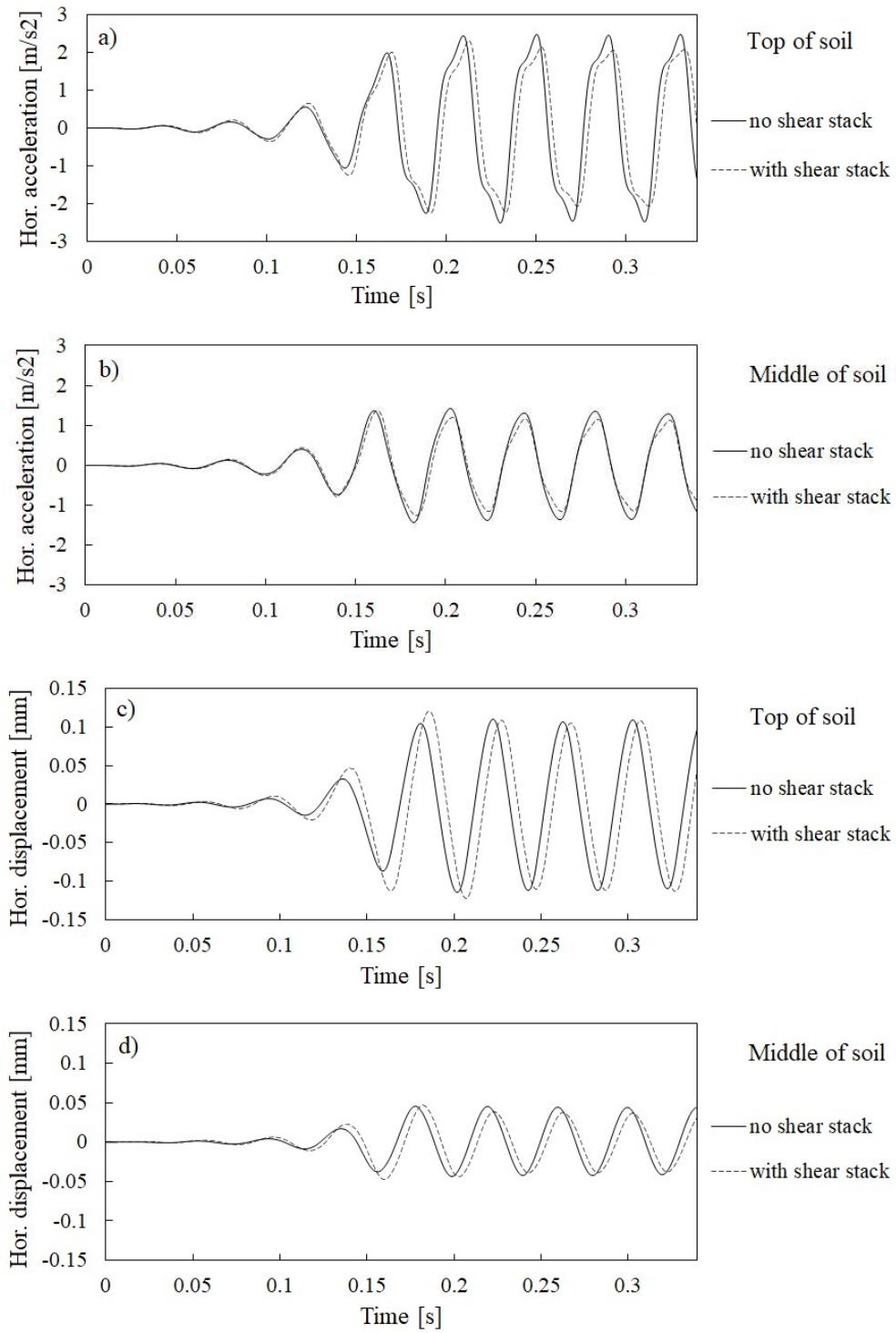


Fig. A-4. (continuation on the next page)

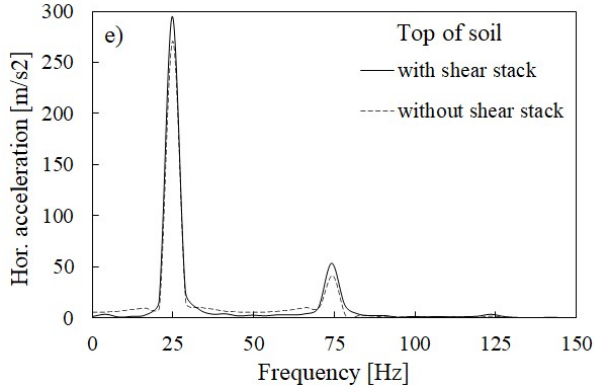


Fig. A-4. Computed accelerations, displacements and spectral accelerations with and without shear stack for 25Hz input motion of maximum amplitude of 0.077g.

3. Effect of bi-layered soil profile

This section of Appendix A compares accelerations computed assuming a single soil layer in shear stack experiments (i.e. Leighton Buzzard sand, fraction E, with $e=0.91$, density 1332kg/m^3) with those obtained assuming a bi-layered soil profile (i.e. Leighton Buzzard sand, fraction E in the top with $e=0.91$ and density 1332kg/m^3 ; Leighton Buzzard sand, fraction B+E in the bottom with $e=0.85$ and density 1800kg/m^3).

The filtered results shown on Fig. A-5 and A-6 are very similar. The “wobble” is still present, and its position is almost the same, thus, no spectral response is presented. Some difference can be spotted regarding the motion amplification ratio and slight shift in phase between the two computations. However, these are expected as the single soil layer is slightly “softer”.

To conclude, although some difference in the computed accelerations for the single and two-layered soil profiles can be noticed, the main conclusions in Chapter 2 on higher harmonic generation are not affected.

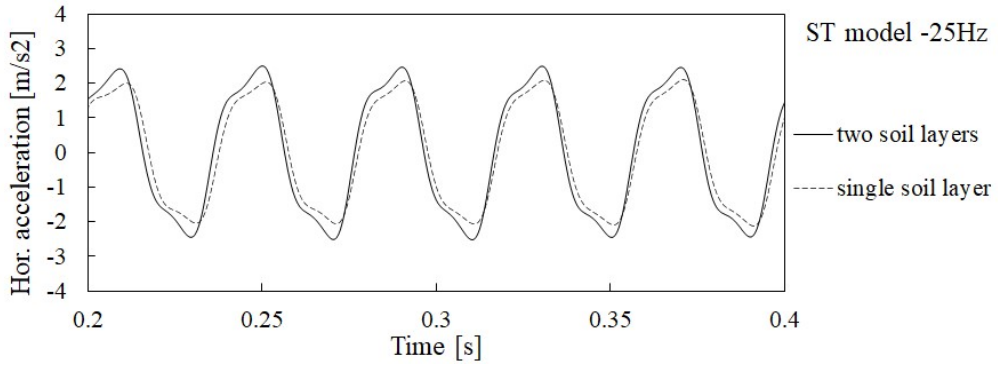


Fig. A-5. Computed accelerations for 25Hz input motions with single soil layer and two soil layers.

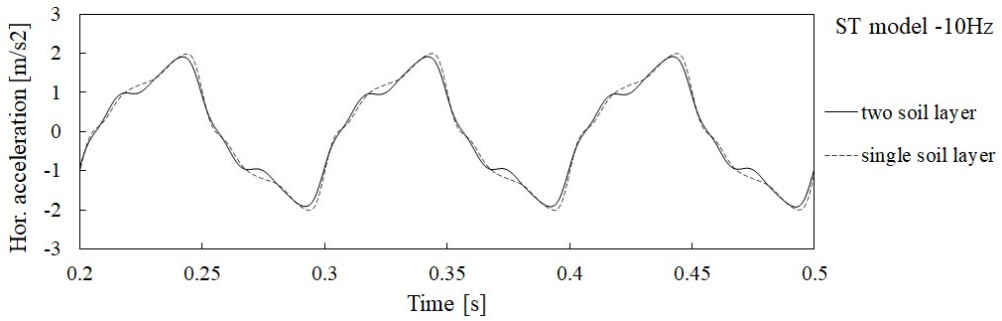


Fig. A-6. Computed accelerations for 10Hz input motions with single soil layer and two soil layers.

Appendix B

Numerical investigation on elastic region determination

This Appendix shows a short numerical study on small amplitude input motions and it is a supplement to Chapter 2. Such input motions would expect to result in only elastic soil response, thus, the higher harmonics due to soil nonlinearity and elastic unloading wave would not be generated.

Indeed, Figure B-1 shows that the generated harmonic 75Hz reduces in the 25Hz input motion of 0.02g acceleration and disappears (ST model) or almost disappears (HP model and DM model) for 0.01g input motion. Of course, the disappearance of higher harmonics in this study would a consequence of the chosen elastic region size. It would be interesting in the future to try to identify the elastic region also in shear stack experiments when subjecting the shear stack to low amplitude shaking. Some indication of such identification could be achieved also by swept-sine input motion, i.e. motion which starts with high driving frequency and high amplitude, and gradually reduces both, frequency and amplitude with time. Indeed, Figure B-2 (Madabhushi, 2014) shows such an example, where higher harmonics (3ω , 5ω) seem to disappear before the driving frequency ω . The limits drawn on the original figure (vertical black lines) at $\omega= 0.8\text{Hz}$, $3\omega= 2.4\text{Hz}$ ($3*0.8\text{Hz}$) and $5\omega= 4.0\text{Hz}$ ($5*0.8\text{Hz}$), seem to confirm such speculation, i.e. higher harmonics disappear from the left of the chosen limits (so could be representative of an elastic region) whereas the driving frequency ω is still present to the left of the chosen limit and only furtherly reduces in frequency and amplitude.

Note that the results in this section have been obtained at earlier stage of this research and due to time constraints not updated in the final version of the thesis, thus some minor inconsistencies may be encountered.

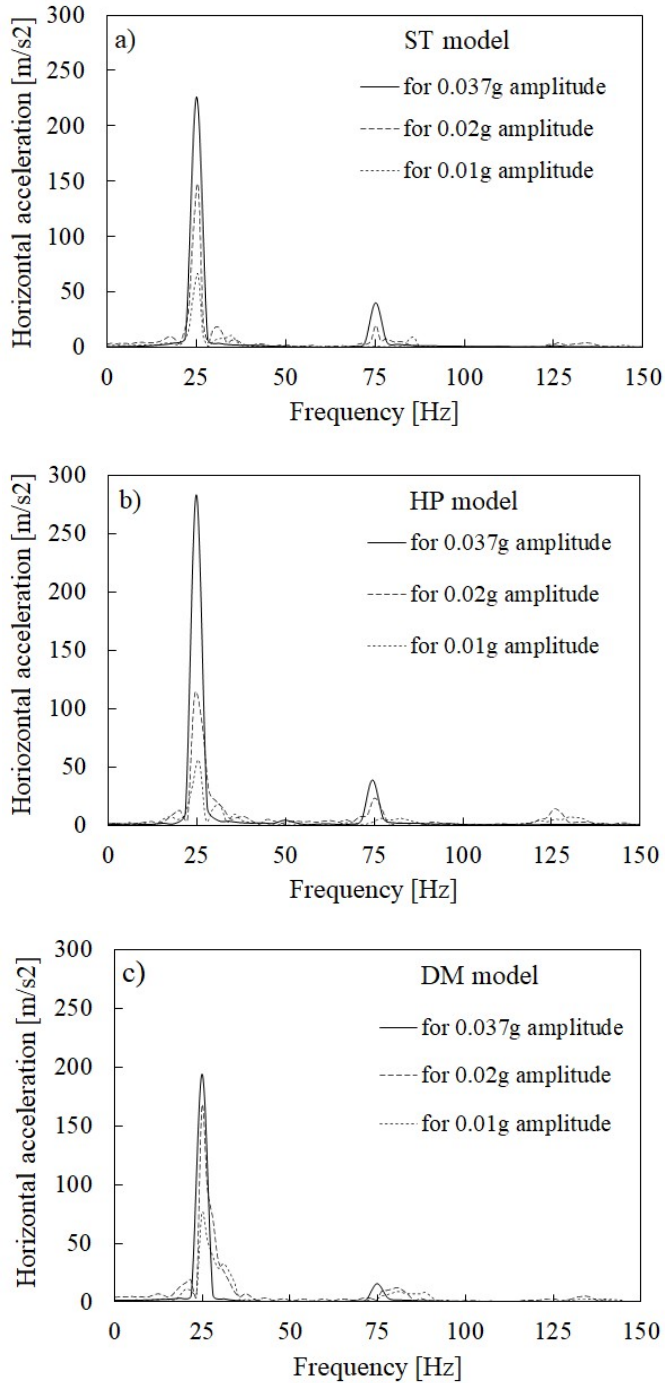


Fig. B-1. Spectral response for low amplitude input motions for: a) ST model, b) HP model and c) DM model.

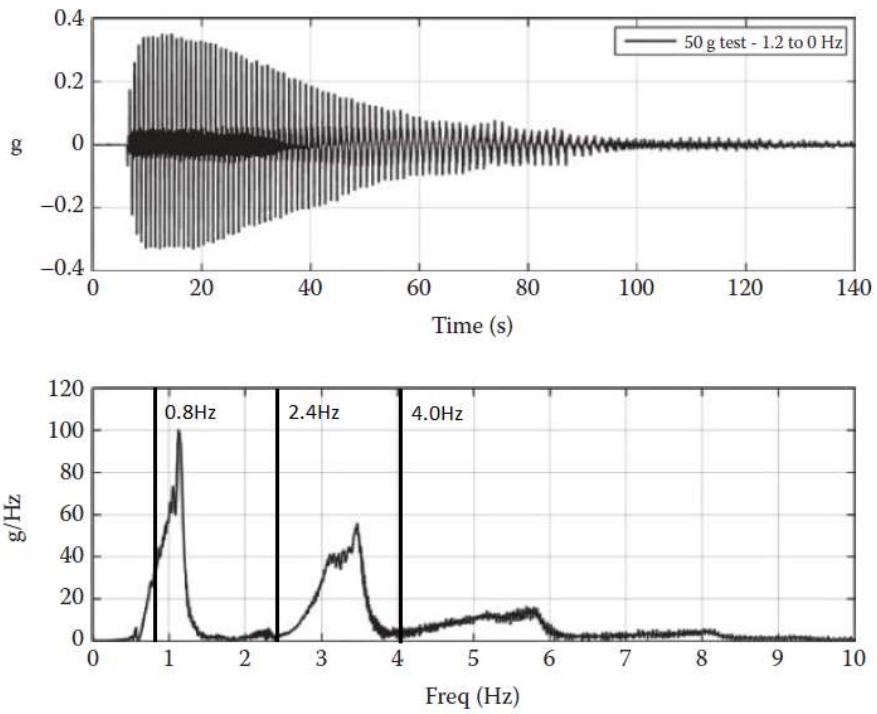


Fig. B-2. An example of swept-sine input motion possible to be applied in centrifuge (original figure from Madabhushi, 2014).

Appendix C

This appendix supplements Chapter 2, Section 3.5. The Section 3.5 showed a case of how kinematic piles are affected by higher frequency motion generated in soil due to the effects of fast elastic unloading waves. Numerical and experimental results have been presented. In detail, it was shown that the pile top (with a small mass on top) behaves as an oscillator and resonates with higher harmonics of motion generated in soil. Nevertheless, the numerical and experimental models comprised a pile group of five piles embedded in a bi-layered soil profile. As such, one may think that the higher harmonics of motion come from those factors due to wave reflection between the piles or wave reflection and refraction on the interface of the bi-layered soil profile. This appendix presents a numerical study on a perfect experimental setup. This means that the author used only a single pile placed in the shear stack (Figure C-1) and a single soil layer. The pile characteristics are as per the pile modelled in Chapter 3. The soil layer characteristics are as per Leighton Buzzard sand, fraction E (see Chapter 1, Section 5.1). The chosen input motion is 10Hz of 0.137g amplitude.

Figure C-2 presents the computed accelerations in soil and on pile at different depths and heights. The accelerations were filtered in order to remove very high frequency motion (80 Hz Butterworth filter, 5th order). Figure C-2a clearly shows that the top of the pile, although still driven by soil, is heavily affected by the additional harmonics generated in soil even if no other piles are present and the soil profile comprises of a single soil layer. This effect decreases with depth, for example, at the depth of 300mm the accelerations in soil and on the pile match each other (Figure C-2b), thus, the pile at this depth behaves fully as a kinematic pile (note that higher harmonics are also present at this depth, the wave is clearly distorted towards a “square wave”).

Further investigation with such a model could comprise various parametric studies, for example studies in which stiffness characteristics of a pile differ to see how such a change influences higher frequency motions on the pile.

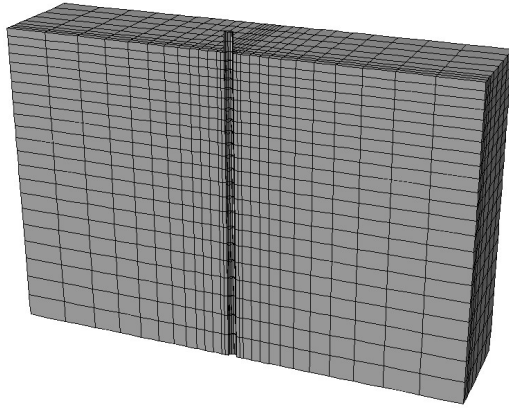


Fig. C-1. Numerical model with single pile and single soil layer.

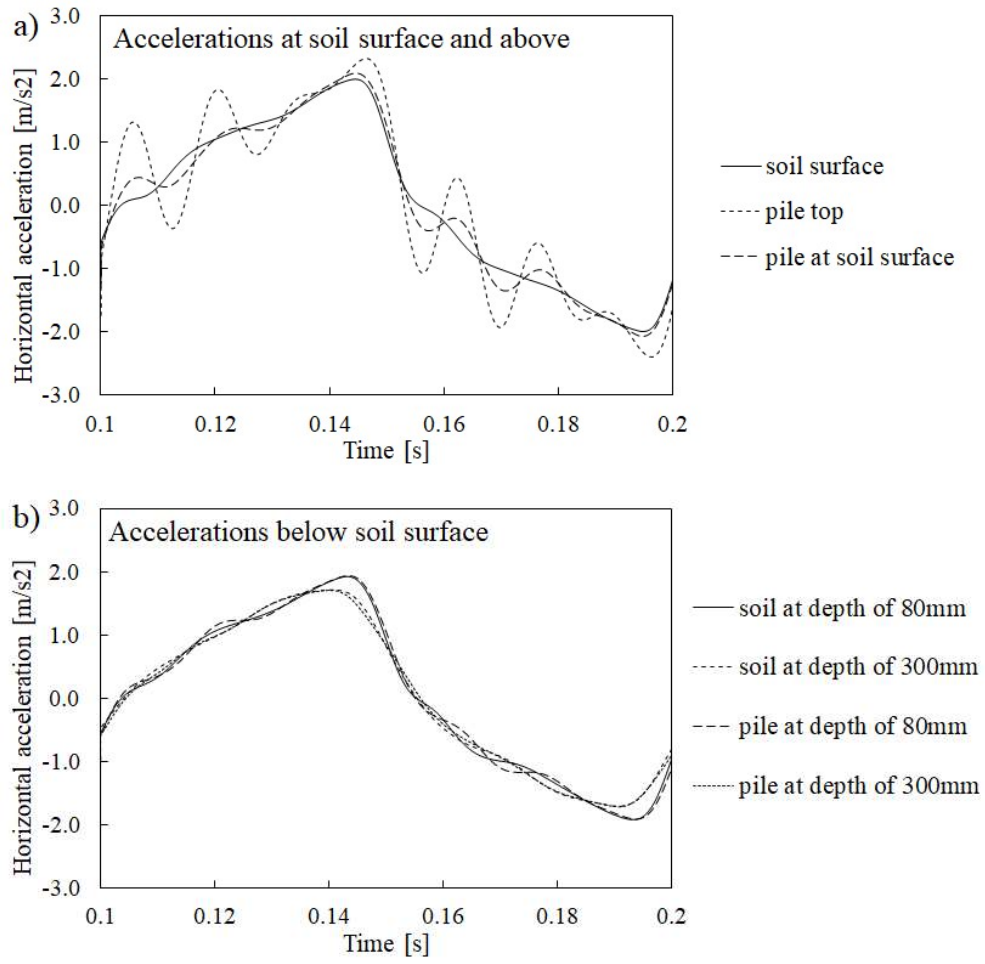


Fig. C-2. Computed filtered accelerations in soil and on pile: a) at soil surface and above, b) below soil surface.

Appendix D

Numerical simulation of Dar's shear stack tests (1993)

This appendix constitutes a part of Chapter 2 and discusses experimental and results obtained on dry sand subjected to shear stack tests at 1g by Dar (1993) and representative numerical analyses. Single 10Hz sine input motion of a maximum amplitude of 0.41g is considered.

One may note that Durante (2015) did not apply higher amplitudes of sinusoidal input motion than 0.15g. On the other hand, the first experimental studies with a shear stack (Dar, 1993) also included cases with higher amplitudes of sinusoidal input motions, e.g. 0.41g (for 10Hz input motion). Such high amplitude input motions resulted in a “double peak” being observed at the soil surface level (Figure D-1). The original explanation for such a “double peak” was attributed to shear localisation at shallow depths (Dar, 1993). However, the typical response in terms of lateral displacements for the 0.41g input motion shown by Gajo & Wood (1997) based on the measurements by Dar (1993) was approximately 2-3mm, thus, still rather low for shear localisation. Therefore here, an alternative explanation is attempted by means of a short numerical study. The results of three advanced soil constitutive models are presented when the amplitude input motion is increased to 0.41g (10Hz sine dwell). Although the soil characteristics are as per work of Durante (2015), the numerical results are filtered with 80Hz cut-off frequency (no data available on whether acceleration results were filtered by Dar, 1993), the three constitutive models predict a “double peak” in the acceleration records at soil surface (Figure D-2). This “double peak” is more pronounced for the ST and DM models and less visible for the HP model (although filtering with higher cut-off frequency filter would reveal also in this case the “double peak” feature). These horizontal accelerations are accompanied by lateral displacements between approximately 0.8mm (DM model) and 1.5mm (HP model). Therefore, one may be tempted to draw a conclusion that such a “double peak” as observed in the experimental work by Dar (1993) could also potentially be explained by soil nonlinearity and fast elastic unloading waves in soil as described in Chapter 2 of this thesis. In particular, the Section 3.2 of Chapter 2 shows that for the input motions of higher amplitudes, the separated elastic parts arrive just after the unloading, thus, possibly close to the acceleration peaks. Such explanation of double peaks as provided here is a speculation only (since the author lacks experimental experience) and would need further investigation in the future to determine whether the reason for the “double peak” is strain localisation, soil nonlinear behaviour and fast elastic unloading waves, increased interaction between the shear stack and the soil or maybe some other mechanism.

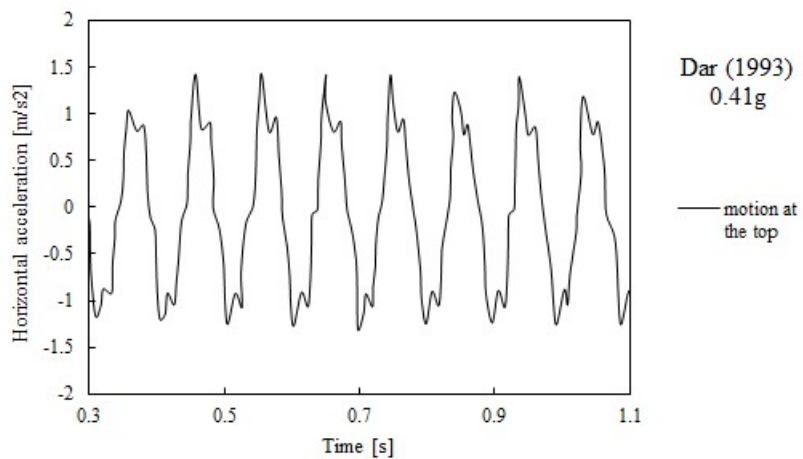


Fig. D-1. Horizontal acceleration records around top of soil for 10Hz sine input motion with maximum acceleration of 0.41g (digitalized from Gajo & Wood, 1997; original source: Dar, 1993).

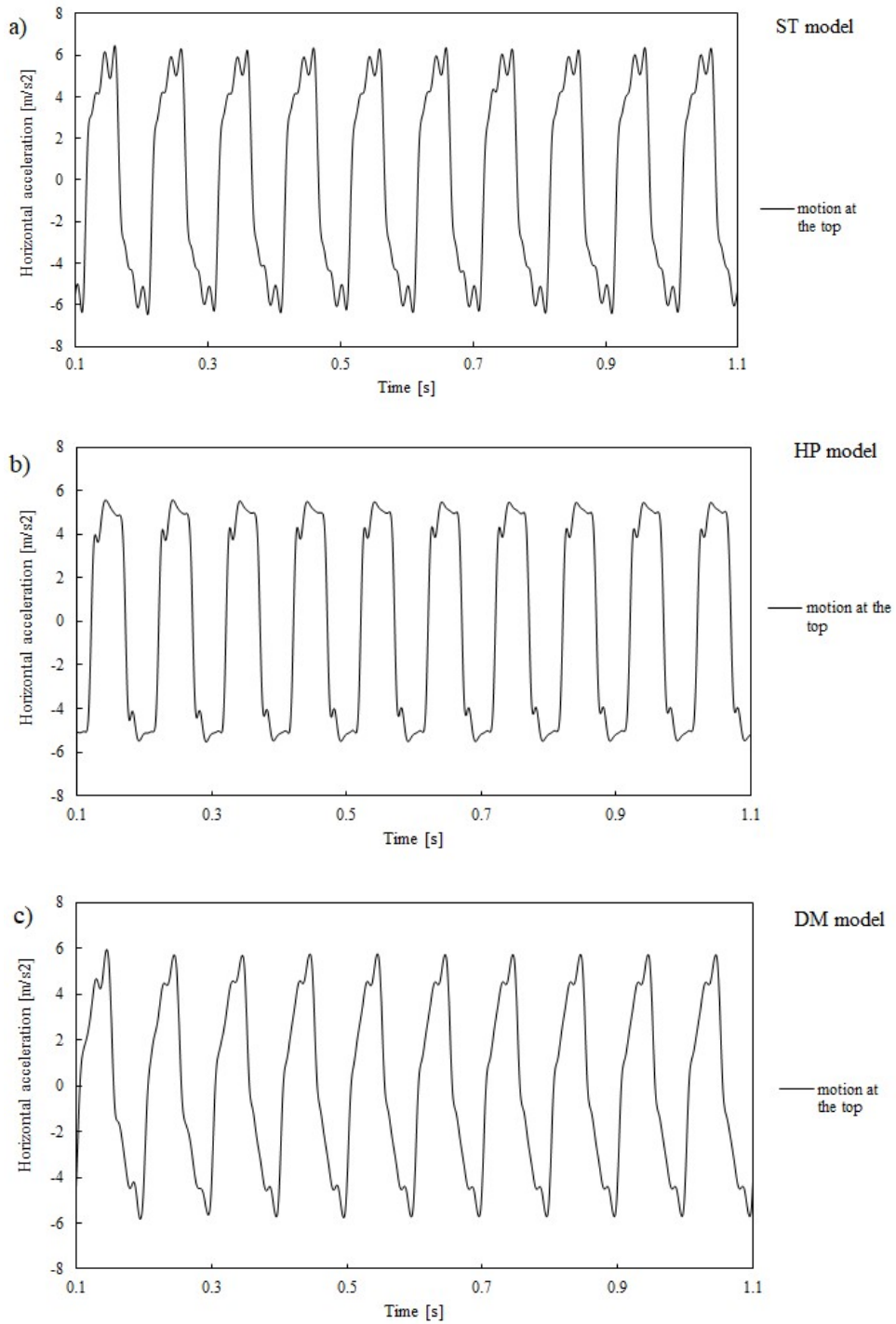


Fig. D-2. Horizontal acceleration records at top of soil for 10Hz sine input motion with maximum acceleration of 0.41g: a) ST model, b) HP model, c) DM model.

Appendix E

Additional numerical and experimental comparison on piles

This appendix presents additional computational runs for Section 3 in Chapter 3. Three additional input motions are analysed, two for free pile head conditions, and one with a small pile cap spanning piles no. 1, 2 and 3.

1. Free head piles

30Hz sine dwell, 0.041g (Fig. E-1 to E-6)

Figures E-1 to E-3 show free field response. This is generally very well captured by both models, with the exceptions of the lateral displacements at mid-height where the HP model overestimates the response (the explanation to such behaviour is shown in Section 4.6 of Chapter 3) and of the overpredicted settlement by the ST model.

The pile accelerations are matched quite well although the number of harmonics on piles has been underestimated by the two models. This can be related to the fact that the mass of a plastic cap (i.e. a cap to place instrumentation) has not been evaluated very precisely (in fact, only a photograph was used to evaluate such mass). On the other hand, the lateral displacements for pile no. 3 are well predicted by the ST model and slightly underpredicted by the HP model.

The pile axial strains are shown on Figure E-6. The computed values by the HP model are inconsistent with those computed by the ST model or from the experiments. On the other hand, it has been explicitly checked that all five piles experience the same maximum axial strains, thus at least error in data reading is avoided here. Note that similar maximum pile axial strains have been found also around the top of the piles in the computations of the HP model. Indeed, as explained in Section 2.1 of Chapter 3, the embedded piles behave as kinematic piles only to a certain depth, over which their behaviour resembles an oscillator, thus some bending moments are also expected at shallower depths. On top of that, some difference in pressure dependence of both of the models have been shown in Section 4.6. All these can lead to rather complex interactions which have not been studied in detail in this thesis.

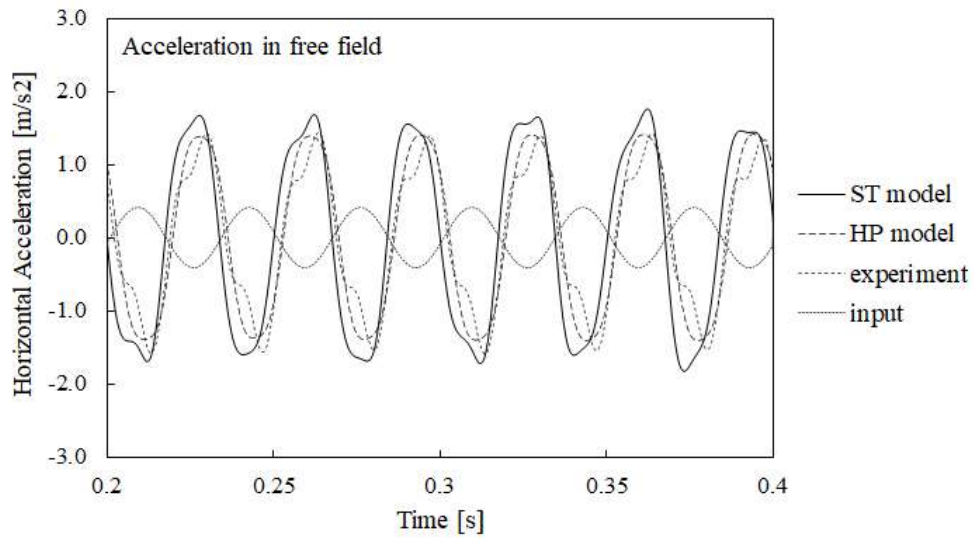


Fig. E-1. Comparison of measured and computed horizontal accelerations in free field at soil surface level.

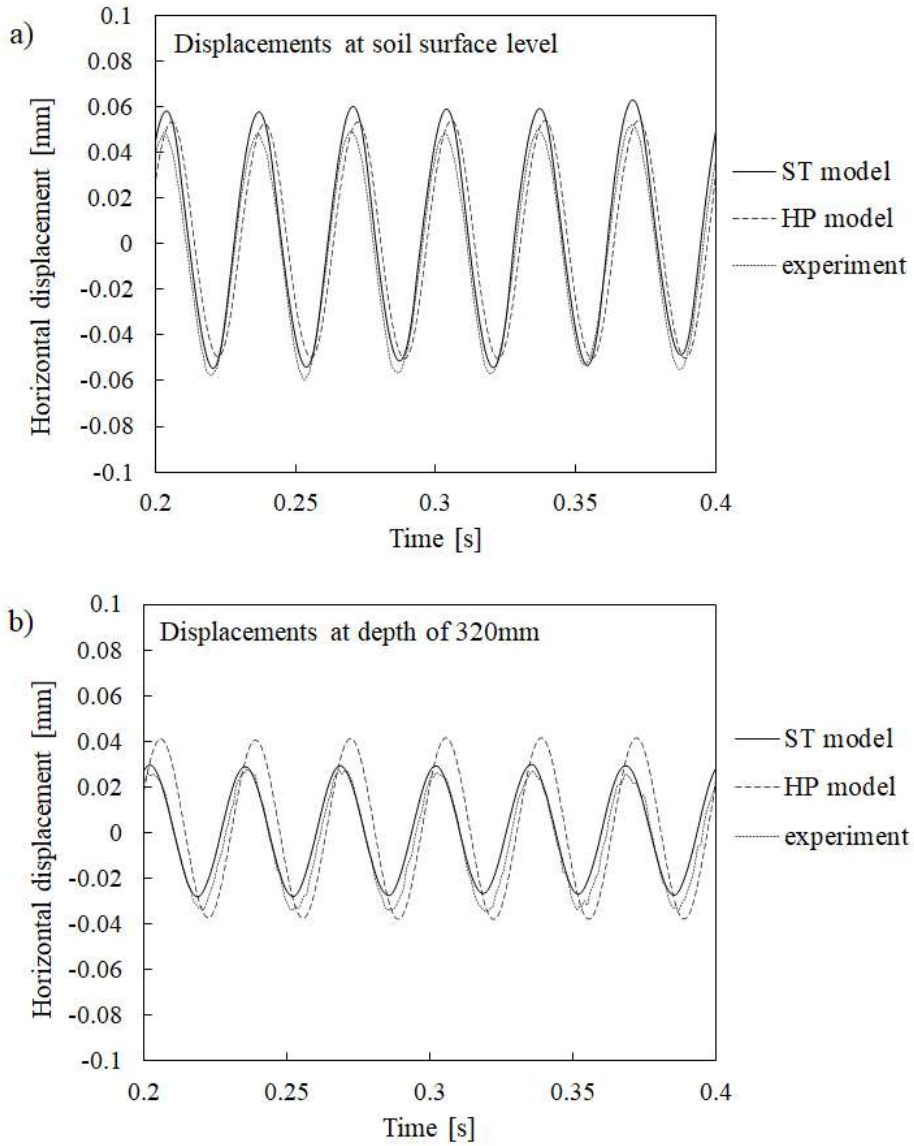


Fig. E-2. Comparison of measured and computed lateral displacements in free field at soil surface level (a) and at mid-height (b).

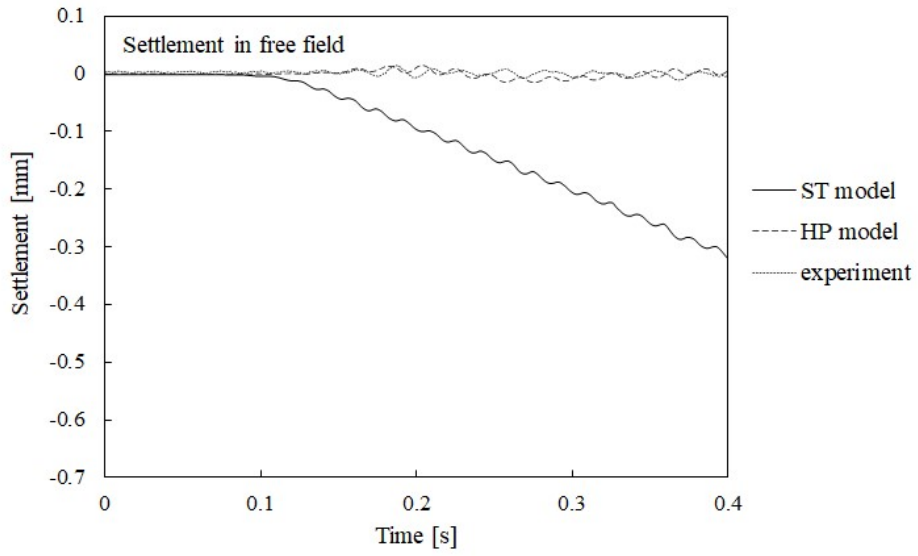


Fig. E-3. Comparison of measured and computed settlements in at soil surface level.

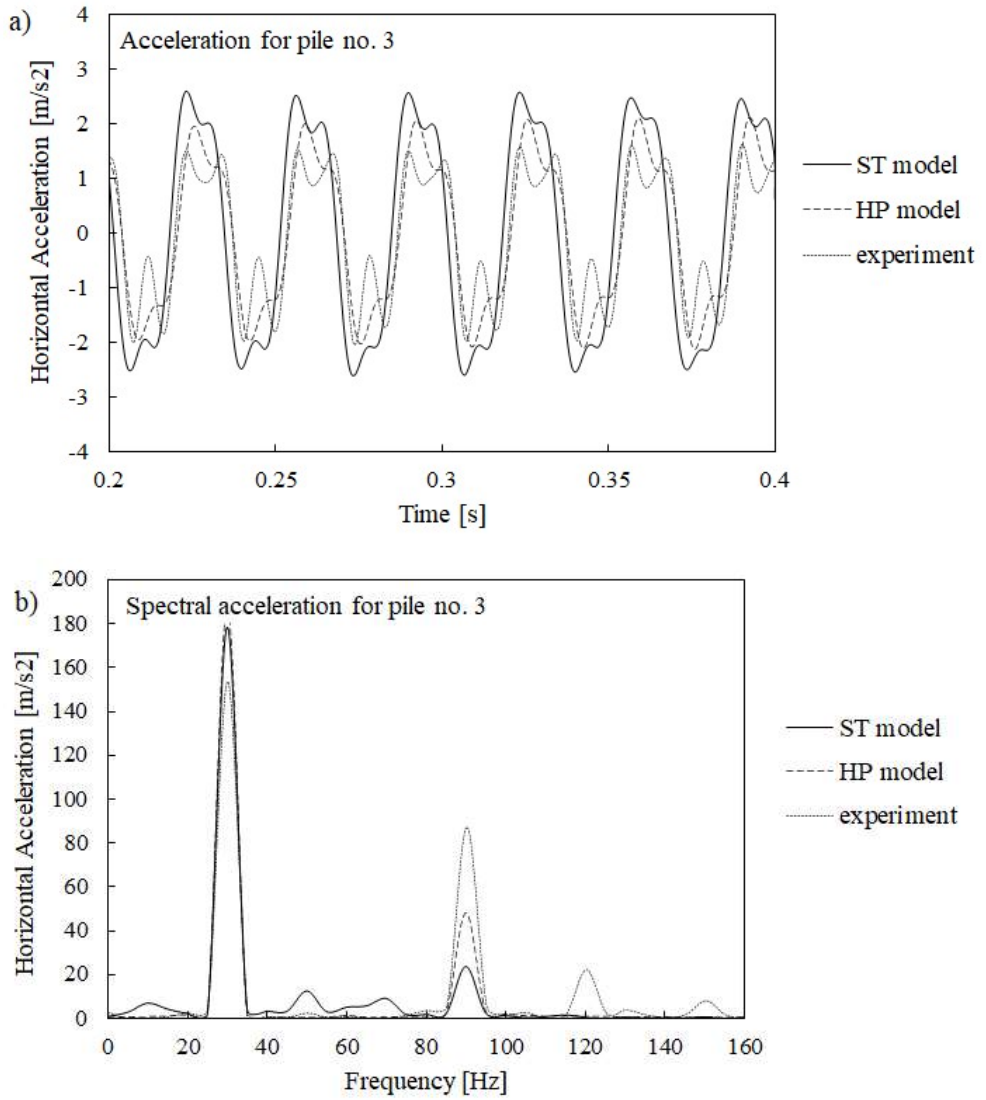


Fig. E-4. Comparison of measured and computed horizontal accelerations at top of pile no.3 and corresponding spectral accelerations.

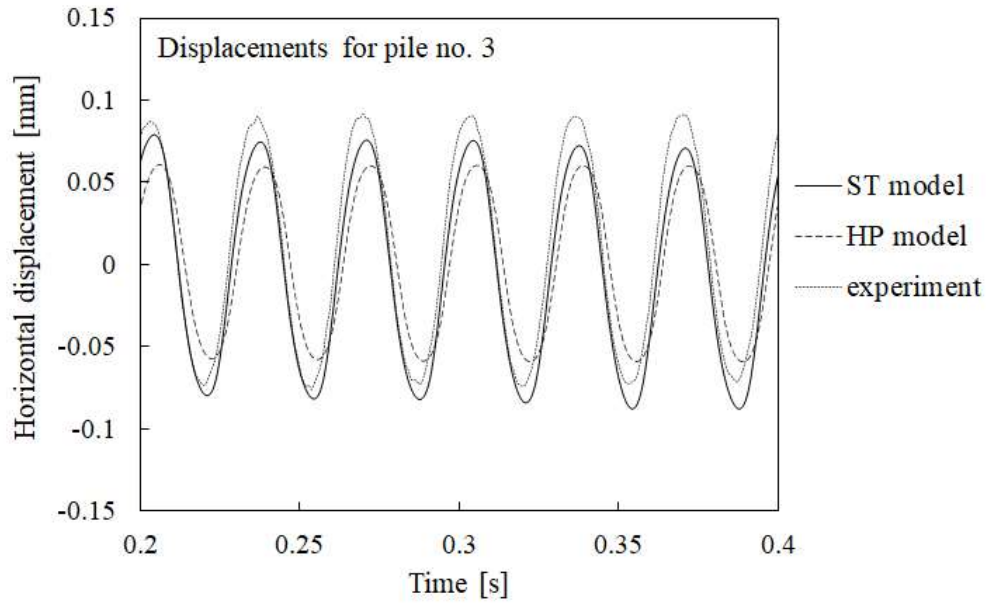


Fig. E-5. Comparison of measured and computed lateral displacements at top of pile no.3.

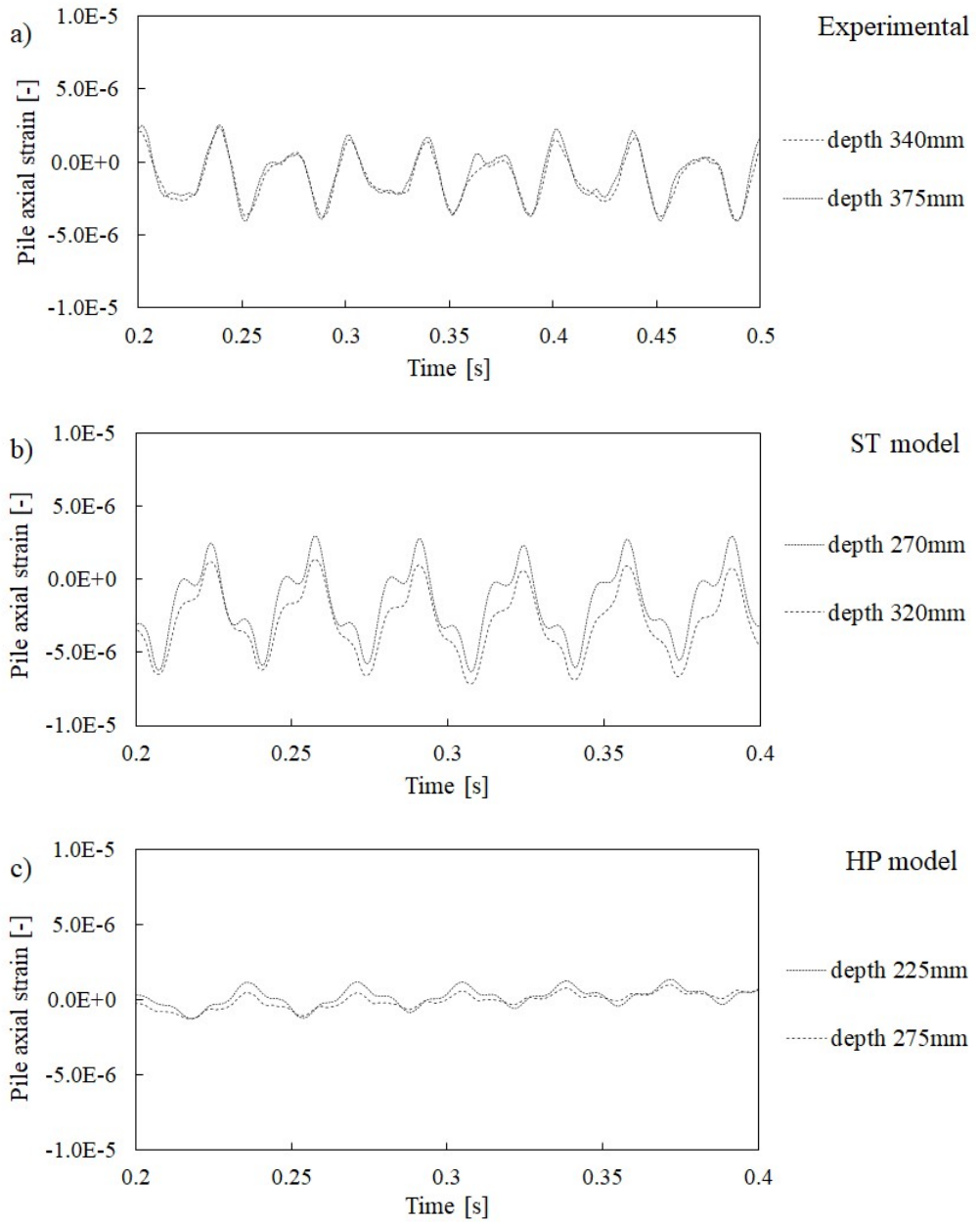


Fig. E-6. Comparison of maximum measured and computed pile axial strains of pile no. 3.

Tolmezzo scaled earthquake, maximum amplitude 0.101g (Fig. E-7 to E-12)

Earthquake time history can be more demanding for numerical models as the loading reloading cycles are erratic and not regular. However, both models, when subjected to 0.101 scaled earthquake present very promising predictions for free field response shown on Figures E-7 to E-9.

The same applies to the comparison between the pile accelerations and displacements where very satisfactory consistency can be observed (see Figures E-10 to E-11). Note that the numerical accelerations for the pile no. 3 are compared with experimental accelerations for the pile no. 2 due to a broken accelerometer on the pile no. 3. Finally, the pile axial strains are shown on Figure E-12. The inconsistency between predictions of the two models can be observed, and possibly attributed to some difference in how pressure dependence is predicted by the two models. Moreover, significant discrepancy can be observed between the numerical computations and experimental measurements (note different scale for strain on Figure E-12). This discrepancy is due to the experimental problems mentioned before in Section 2 of Chapter 3 and depicted on Figure 12.

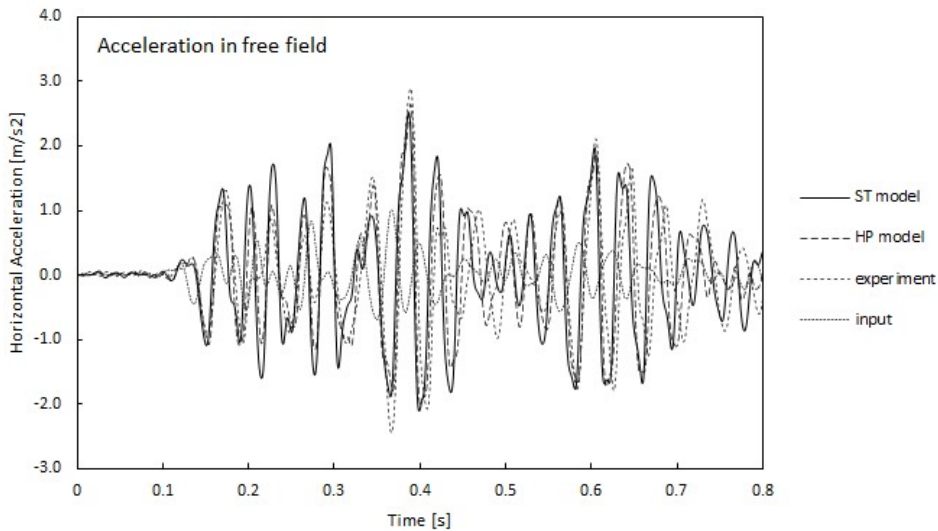


Fig. E-7. Comparison of measured and computed horizontal accelerations in free field at soil surface level.

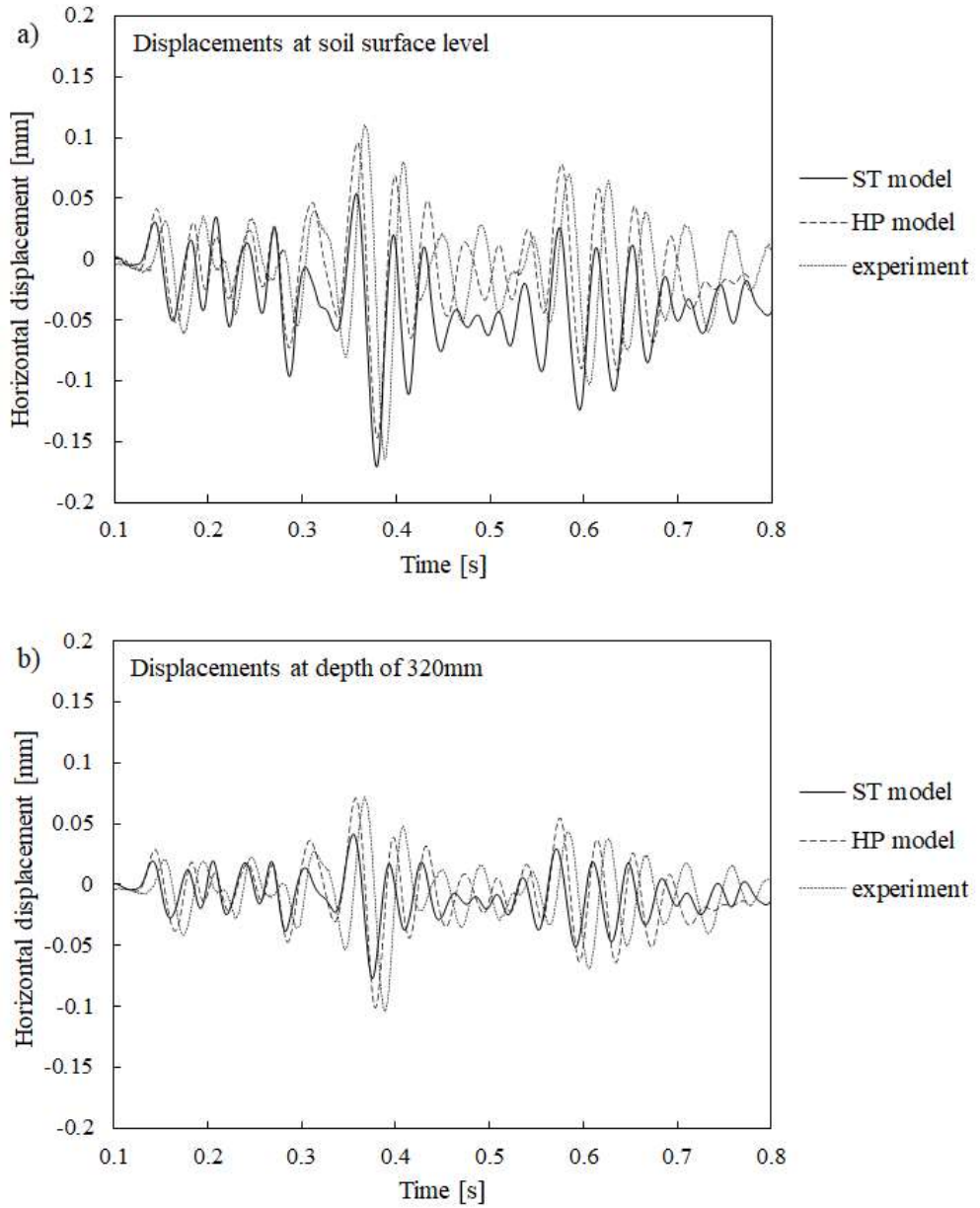


Fig. E-8. Comparison of measured and computed lateral displacements in free field at soil surface level (a) and at mid-height (b).

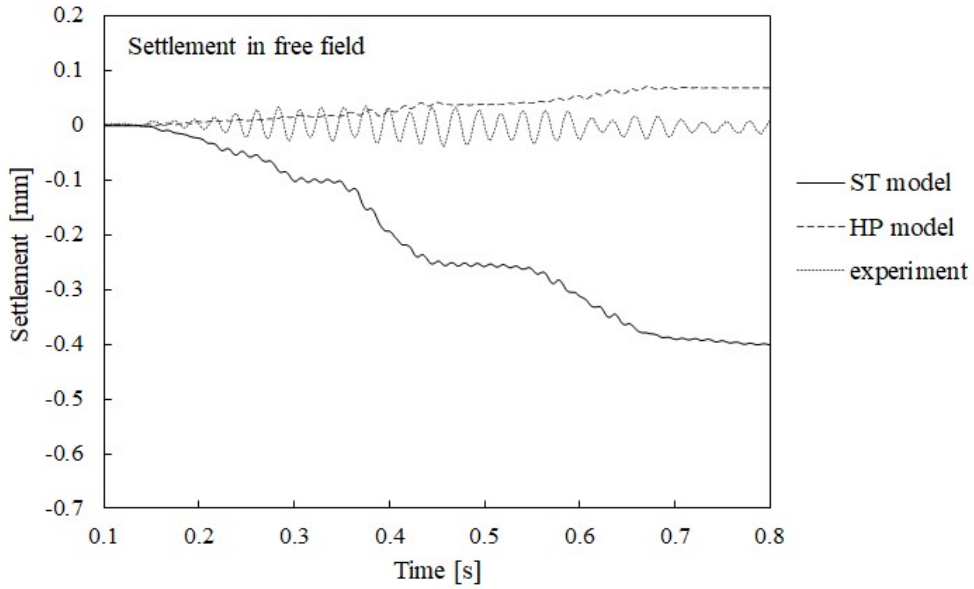


Fig. E-9. Comparison of measured and computed settlements in at soil surface level.

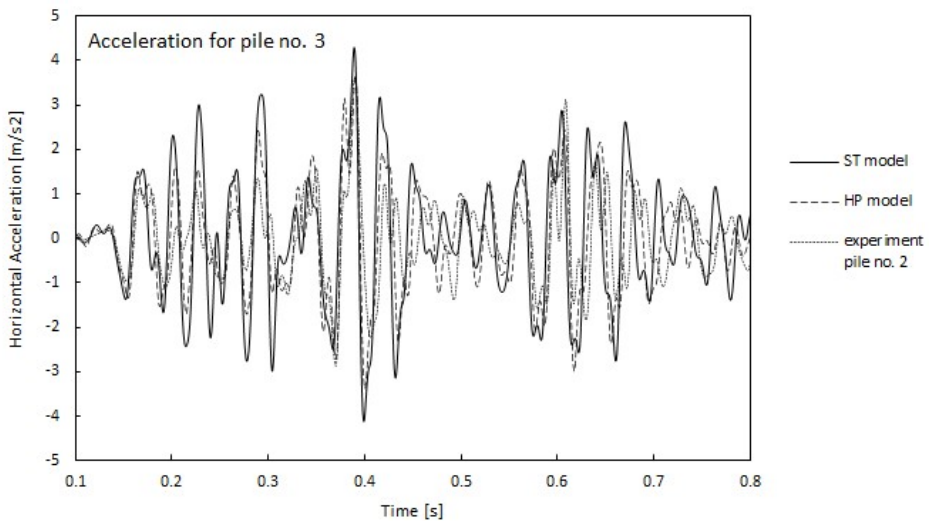


Fig. E-10. Comparison of measured and computed horizontal accelerations at top of pile no.3.

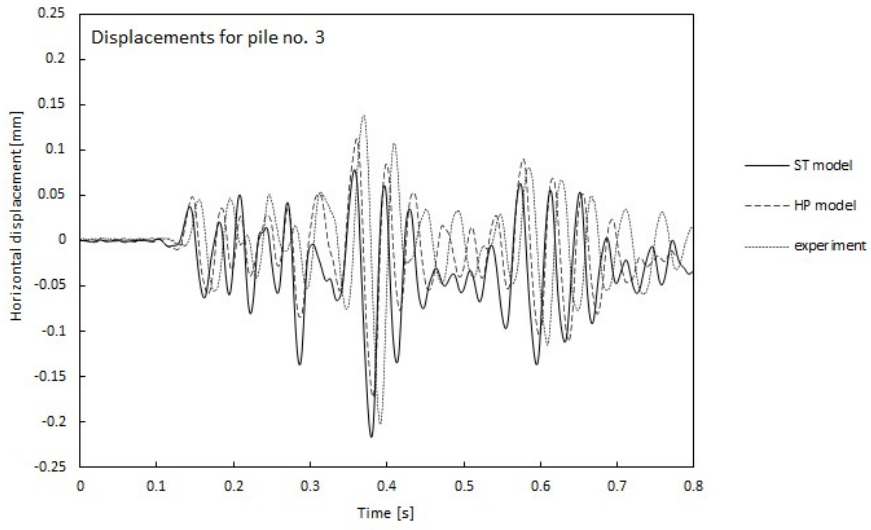


Fig. E-11. Comparison of measured and computed lateral displacements at top of pile no.3.

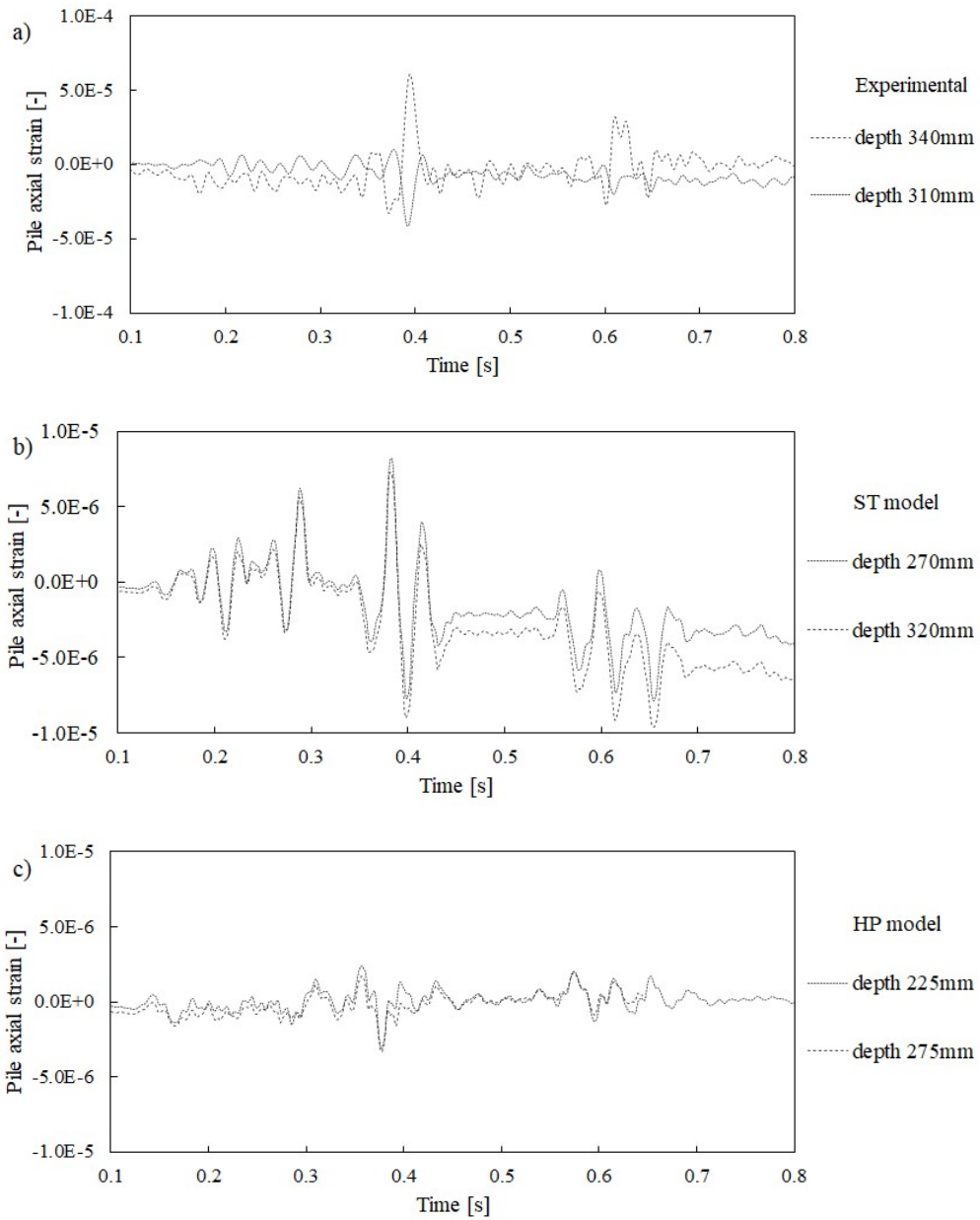


Fig. E-12. Comparison of maximum measured and computed pile axial strains of pile no. 3 (note different scale on vertical axis for the experimental results).

2. Pile group with small cap

This section analyses a case of input motion when a small cap spans three piles no. 1, 2 and 3. The free field response shows very good agreement of the computed accelerations with measurements (Figure E-13), including the generated “wobble”. Very good and fairly good agreement for lateral displacements (Figure E-14) can be observed for the HP and ST model, respectively. The experiment for rather low amplitude motion (0.037g) does not register any settlement, on the other hand some small permanent volumetric changes (Figure E-15) are predicted by the ST model (compression) and the HP model (dilation).

Figure E-16 shows the comparison of the experimental and numerical accelerations for the pile no. 3 which show very good match. In fact, the pile accelerations resemble very closely those registered in free field (Figure E-13). The reason for that, as mentioned before in the main body in Chapter 3, is the fixity of the three piles, which mitigates the effect of piles behaving as oscillators. This has been verified by inspection for the pile no. 5 where the typical response with strong presence of harmonics is observed (not shown here for brevity). The pile lateral displacements are shown on Figure E-17 and both models seem to underestimate the measurements. On the other hand, it is recalled that some doubts are over the experimentally measured values (i.e. much higher measurements for piles than for soil surface), thus, the numerical predictions can still be considered quite reliable in this case. Finally, the pile maximum axial strains are shown on Figure E-18 with very good match between the numerical and experimental data, both in terms of magnitude and in terms of location along the pile length.

25Hz sine dwell, 0.037g (Fig. E-13 to E-18)

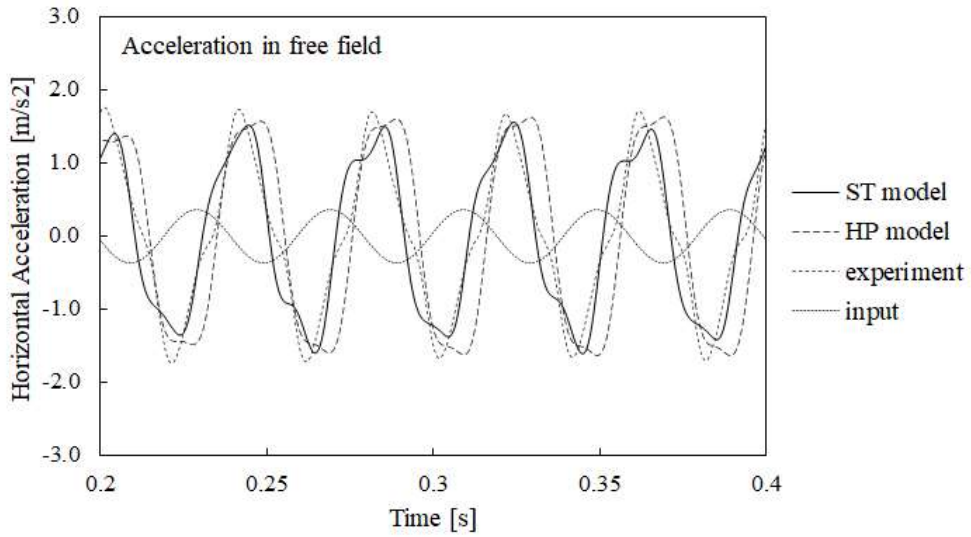


Fig. E-13. Comparison of measured and computed horizontal accelerations in free field at soil surface level.

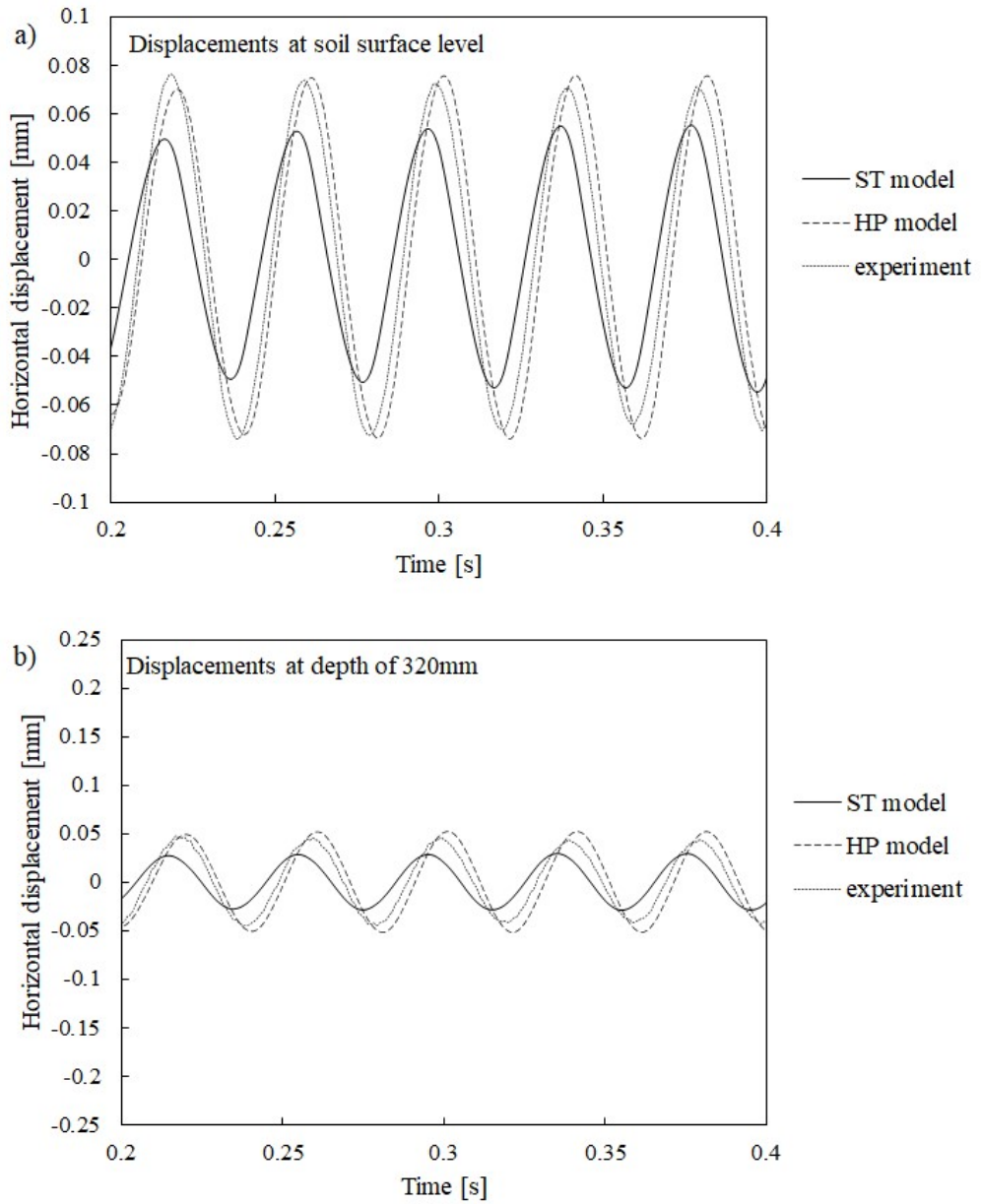


Fig. E-14. Comparison of measured and computed lateral displacements in free field at soil surface level (a) and at mid-height (b).

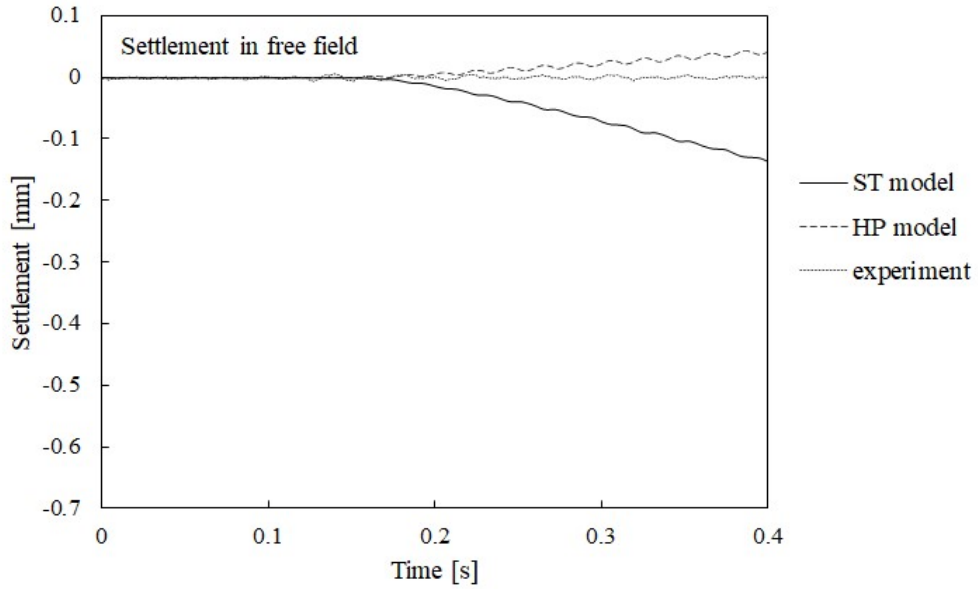


Fig. E-15. Comparison of measured and computed settlements in at soil surface level.

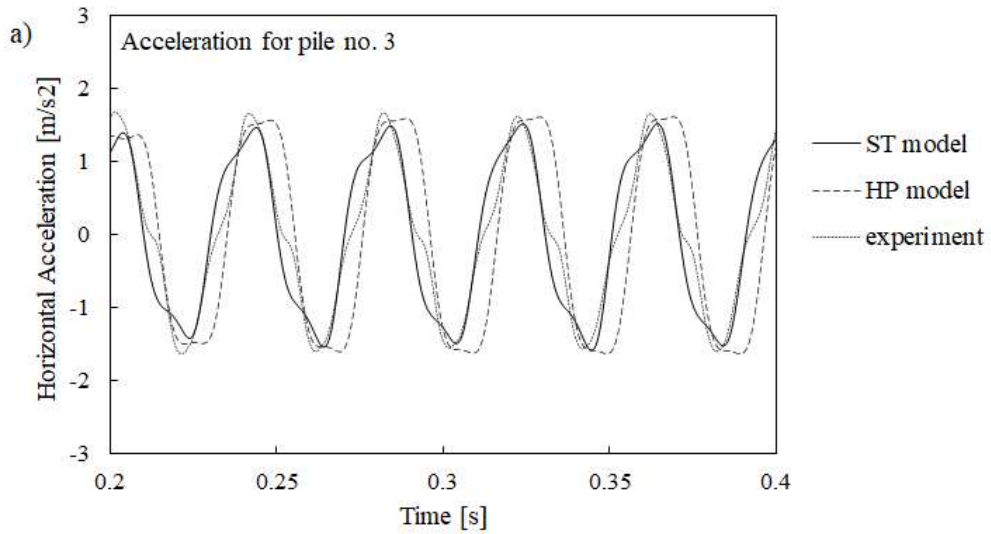


Fig. E-16. Comparison of measured and computed horizontal accelerations at top of pile no.3.

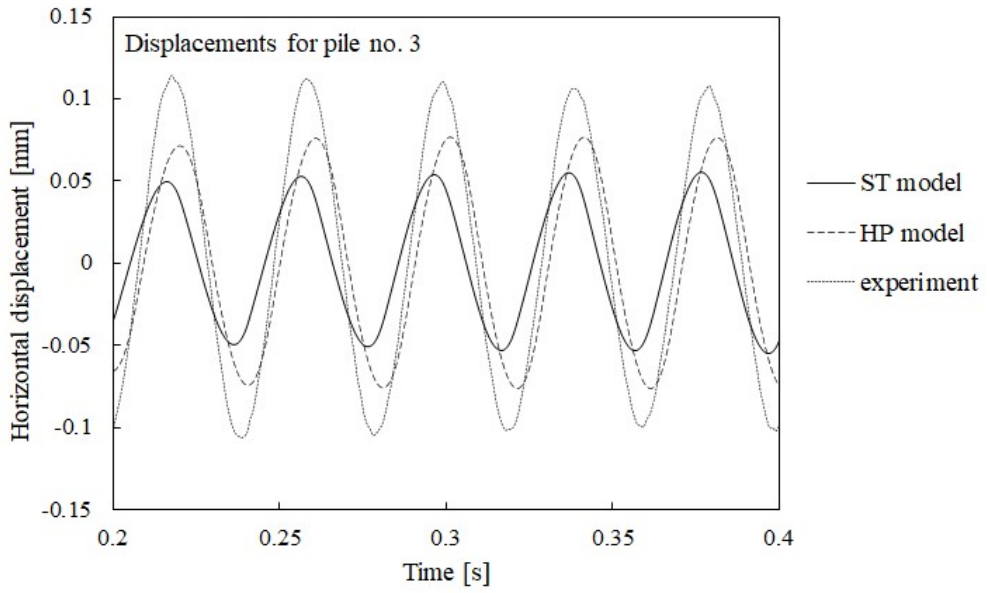


Fig. E-17. Comparison of measured and computed lateral displacements at top of pile no.3.

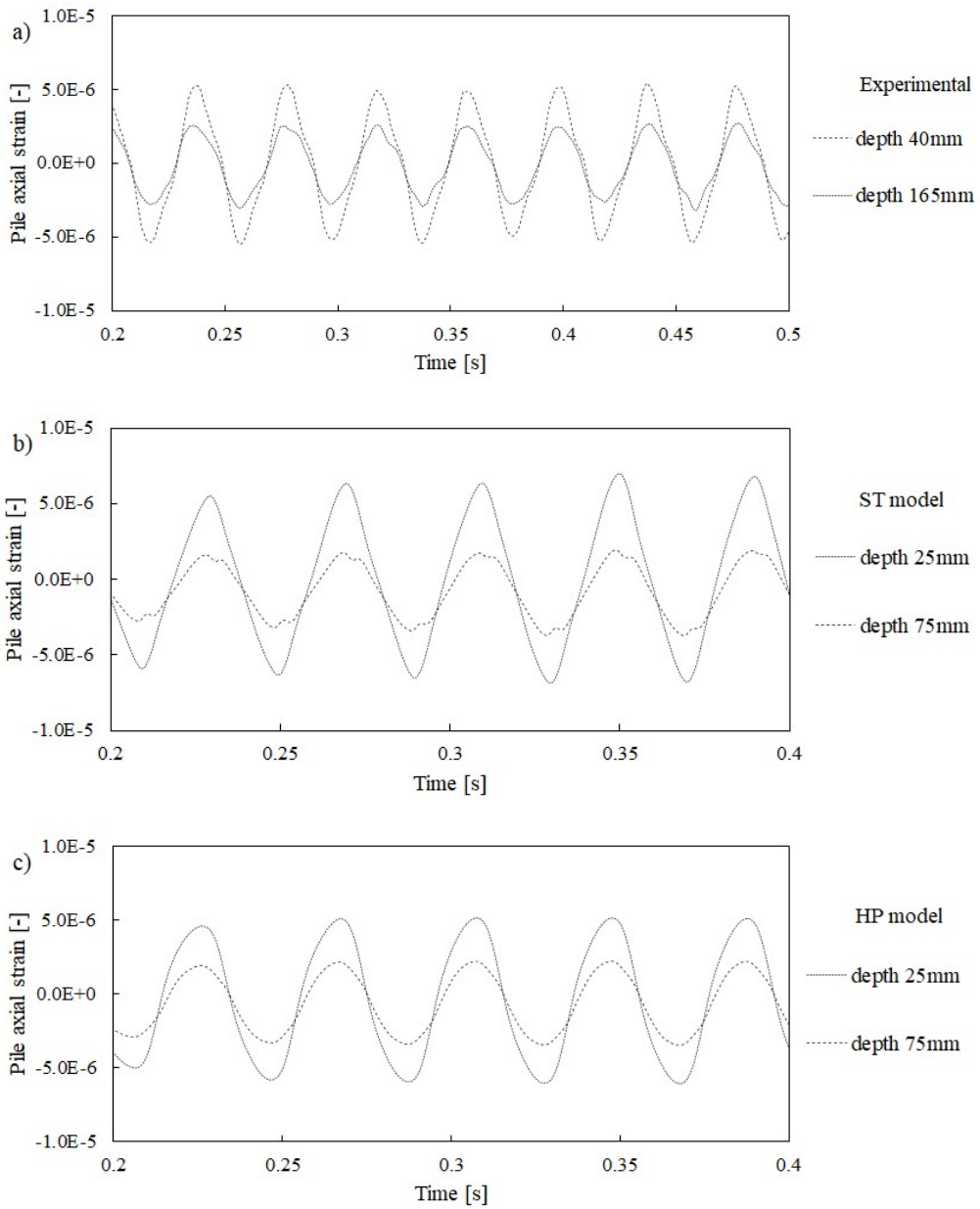


Fig. E-18. Comparison of maximum measured and computed pile axial strains of pile no. 3.

This thesis presents validation and application of advanced soil constitutive models in cases of seismic loading conditions.

Firstly, results of three advanced soil constitutive models are compared with examples of shear stack experimental data for free field response in dry sand for shear wave propagation. Higher harmonic generation in acceleration records, observed in experimental works, is shown to be the result of elastic unloading waves. The latter has never been observed before in soil seismic behaviour. This finding is shown to have high importance on structural response, real earthquake records and reliability of conventionally employed numerical methods.

Secondly, two advanced soil constitutive models are used, and their performance is assessed based on the examples of experimental data on piles in dry sand in order to validate the ability of the constitutive models to simulate seismic soil-structure interaction. The validation includes various experimental configurations and input motions. The discussion on the results focuses on constitutive and numerical modelling aspects. Some improvements in the formulations of the models are suggested based on the detailed investigation.

Finally, the application of one of the advanced soil constitutive models is shown in regard to temporary natural frequency wandering observed in structures subjected to earthquakes. Results show that pore pressure generated during seismic events causes changes in soil stiffness, thus affecting the natural frequency of an idealized structure shortly after the seismic event. Parametric studies present how soil permeability, soil density, input motion or a type of structure may affect structural natural frequency and the time for its return to the initial value. In addition, a time history with an aftershock is analysed to investigate the potential difference in structural response during the main shock and the aftershock.

Piotr Kowalczyk obtained his first Master Degree in Structural Engineering from University of Technology in Cracow (Poland) and his second Master Degree in Geotechnical Engineering from Strathclyde University in Glasgow (Scotland), both with distinction. He has in total five years of experience in bridge and geotechnical engineering consultancy in Poland and Scotland. He was rewarded prizes for academic performance and was a finalist of Cooling Prize for Young Geotechnical Engineers in the UK. Currently he is a PhD candidate at University of Trento (Italy) and his research interests lie within the broad field of soil-structure interaction under seismic conditions.